Lipidic cubic phase crystallization of the adenosine A_{2B} receptor in complex with antagonists

Dissertation

zur

Erlangung des Doktorgrades (Dr. rer. nat.)

der

Mathematisch-Naturwissenschaftlichen Fakultät

der

Rheinischen Friedrich-Wilhelms-Universität Bonn

vorgelegt von

Victoria Johanna Vaaßen

aus Düren

Bonn 2024

Angefertigt mit Genehmigung der Mathematisch-Naturwissenschaftlichen Fakultät

der Rheinischen Friedrich-Wilhelms-Universität Bonn

Gutachterin/Betreuerin: Prof. Dr. Christa E. Müller

Gutachter: Prof. Dr. Finn Hansen

Tag der Promotion: 11.07.2024

Erscheinungsjahr: 2024

Table of Contents

List of Figures

List of Tables

List of Abbreviations

7-AAD	7-Aminoactinomycin D
7-TM	Seven-transmembrane
A_1AR	Adenosine A_1 receptor
$A_{2A}AR$	Adenosine A_{2A} receptor
$A_{2B}AR$	Adenosine A_{2B} receptor
A_3AR	Adenosine A_3 receptor
ADA	2,2′-[(2-Amino-2-oxoethyl)azanediyl]diacetic acid
APS	Ammonium persulfate
AR	Adenosine receptor
ATP	Adenosine 5'-triphosphate
bRIL	Thermostabilized apocytochrome b_{562}
BSA	Bovine serum albumin
cAMP	Cyclic adenosine monophosphate
CD	Cluster of differentiation
CHS	Cholesteryl hemisuccinate
CMC	Critical micelle concentration
Conc.	Concentrated
CPM	7-Diethylamino-3-(4'-maleimidylphenyl)-4-methylcoumarin
Cryo-EM	Cryogenic electron microscopy
CV	Column volume
D_4R	Dopamine D_4 receptor
DAD	Diode array detector
DAG	Diacylglycerol
DC	Dendritic cells, Dendritic cells
DDM	Dodecyl-β-D-maltoside
DESY	Deutsches Elektronen-Synchroton
DME	Dimethyl ether
DMSO	Dimethyl sulfoxide
DTT	Dithiothreitol
ECL	Extracellular loop
EDTA	Ethylenediaminetetraacetic acid
FITC	Fluorescein isothiocyanate
FPLC	Fast protein liquid chromatography
GAP	GTPase activating protein/protein domain
GDP	Guanosine diphosphate
Gp64	Glycoprotein 64
GPCR	G protein-coupled receptor
GRK	G protein-coupled receptor kinase
HEPES	4-(2-Hydroxyethyl)-1-piperazineethanesulfonic acid
His-tag	Histidine tag
HPLC	High-performance liquid chromatography
HSP	Heat shock protein
IMAC	Immobilized metal affinity chromatography
IP_3	Inositol trisphosphate
IPTG	Isopropyl β-D-1-thiogalactopyranoside
Irrev.	Irreversible

LB	Lysogeny broth
LCP	Lipidic cubic phase
LMNG	Lauryl maltose neopentyl glycol
LXP-FP1	Undisclosed fusion protein 1 from leadXpro
LXP-FP2	Undisclosed fusion protein 2 from leadXpro
M_4R	Muscarinic M_4 receptor
MAG	Monoacylglycerol
MAPK	Mitogen-activated protein kinase
MD	Molecular dynamics
MDSC	Myeloid-derived suppressor cells
MME	Methyl ether
MO	Monoolein
MOPS	3-(Morpholin-4-yl)propane-1-sulfonic acid
MP	Monopalmitolein
MV	Monovaccenin
MWCO	Molecular weight cut-off
N.d.	Not determined
NECA	5'-*N*-Ethylcarboxamidoadenosine
NK cells	Natural killer cells
OB1	Optimized variant 1 of bRIL
PBS	Phosphate-buffered saline
PBS-T	Phosphate-buffered saline with 0.1 % Tween 20
PCR	Polymerase chain reaction
PE	Phycoerythrin
PGS	*Pyrococcus abyssi* glycogen synthase
PSI	Paul Scherrer Institute
PTM	Post-translational modification
Rev.	Reversible
RMSD	Root-mean-square deviation
RT	Room temperature
S.E.	Salt exchange
SDS-PAGE	Sodium dodecyl sulfate – polyacrylamide gel electrophoresis
SEC	Size-exclusion chromatography
Sf9	Clonal isolate from *Spodoptera frugiperda* IPLB-Sf21-AE cells
T4L	Chain A of the lysozyme from *Tequatrovirus T4*
TBS	Tris-buffered saline
TC	Test construct
TEMED	*N*,*N*,*N′*,*N′*-Tetramethylethane-1,2-diamine
TM	Transmembrane
T_M	Melting temperature
TME	Tumor microenvironment
Tni	*Trichoplusia ni*
Tris	2-Amino-2-(hydroxymethyl)propane-1,3-diol
Unconc.	Unconcentrated
WB	Wash buffer
wt	Wildtype
X-Gal	5-Bromo-4-chloro-3-indolyl-β-D-galactopyranoside
β_2AR	β_2 adrenergic receptor

1 Introduction

1.1 G protein-coupled receptors

One of the fundamental hallmarks of life is the ability to perceive and respond to information from the environment through complex cellular processes termed "signal transduction".[1–3] The sensing of a signal, may it be e.g. a peptide, a nucleotide or just a photon,[4] is the first step of such a signal transduction event, which is accomplished by diverse classes of proteins.[5] One of the most important and abundant families of these signal-sensing proteins are the G protein-coupled receptors (GPCRs).[6] The importance of these seven-transmembrane (7-TM) receptors is highlighted by the fact that they represent one of the largest protein families,[7] encompassing 67 % of all membrane-bound receptors, that are coded by more than 900 different genes.[8] Structurally, GPCRs feature seven α-helices that weave through the cell membrane, connected by three intracellular and three extracellular loops.[5] The amino-terminal end of the protein (*N*-terminus) is located extracellularly and the carboxy-terminal tail (*C*-terminus), including a short eighth α-helix, is located intracellularly. Their embedment in the cell membrane enables them to transduce extracellular signals, mediated mostly by chemical entities, the so-called ligands, to the inside of the cell where various different responses can be stimulated, or inhibited.[9, 10]

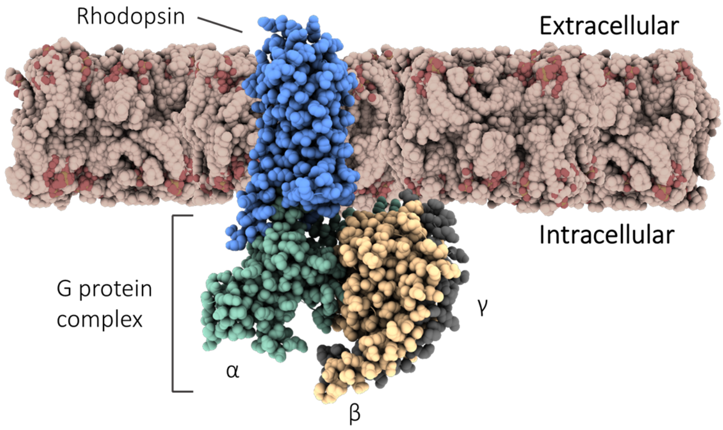

Figure 1. Illustration of the GPCR rhodopsin in complex with a heterotrimeric G protein (α-, β-, γ-subunit) embedded in a lipid bilayer, presented in spheres (PDB-IDs 6OY9, 2MLR).[11, 12]

As their name suggests, the main intracellular signaling partner for GPCRs are G proteins, which are heterotrimeric guanine nucleotide-binding regulatory proteins, consisting of an α-, β- and γ-subunit.[13] The latter two form a tightly associated dimer, which can be regarded as one functional signaling unit, whereas the Gα subunit propagates signals by itself.[14] G proteins are classified according to the function and sequence of the Gα subtype and belong to one of four classes, namely $G\alpha_s$, $G\alpha_{i/o}$, $G\alpha_{q/11}$ or $G\alpha_{12/13}$.[15] Upon ligand binding and activation, GPCRs display a distinct signaling profile; they can interact with several members of one Gα class,[16] or multiple of the four different classes which, in part, even exhibit opposite functions.[17, 18] In contrast to the broad diversity of GPCRs, the G protein family comprises only few isotypes, with the Gα subunit being coded by only 16 genes, Gβ by 5 genes and Gγ by 12 different genes.[19, 20] This suggests that the activation of G proteins is a conserved process among the various representatives of the family, which is supported by the comparably low diversity of the intracellular regions of the receptors, to which the G proteins bind.[10, 21, 22]

One of the more exclusive signaling partners is the G protein $G\alpha_t$, which belongs to the $G\alpha_{i/o}$ class of G proteins.[13] $G\alpha_t$, also named transducin, is the main signal transducer of the photoreceptor rhodopsin, which is present on rod cells of the retina and responsible for low-light vision in vertebrates.[23] The light-detecting system in vertebrates exhibits an astonishing sensitivity. Over 80 years ago, studies revealed that a rod cell can be excited by one single photon.[24, 25] This reliable, absolute sensitivity of the light-detecting system, with the signal transduction from the GPCR rhodopsin to the G protein transducin at its core, has since been replicated and confirmed in several studies.[26] Regarding the signaling processes, the visual phototransduction pathway is thought to be a prototypical system, in which the signal from a single photon is amplified through several mediators to result in a relevant physiological effect, in this case a neuronal response.[11, 27]

1.2 Canonical GPCR-mediated signal transduction

GPCR signaling pathways exhibit an enormous complexity that includes cross-talk and feedback mechanisms, and it is spurred by the fact that GPCRs can interact with a variety of different signal transducer proteins, each feeding into different signaling cascades.[28] The comprehensive presentation of these pathways would go beyond the scope of this introduction, however, a brief overview of the canonical GPCR-mediated signal transduction pathways is provided in order to understand the high therapeutic relevance of GPCRs.[29]

In short, the canonical signaling of GPCRs through G proteins proceeds as follows: Binding of an activating ligand (agonist) to the orthosteric binding site presumably induces structural changes within the GPCR, which in turn increases the affinity for G proteins. In their inactive form, the guanosine diphosphate- (GDP-)bound Gα protein associates with the Gβγ dimer to form a heterotrimeric unit. Upon activation, the GPCR acts as a guanine nucleotide exchange factor by stimulating the release of GDP from the Gα protein, which is immediately replaced by readily available GTP, present inside the cells at high concentration. The binding of GTP results in conformational changes of the Gα protein. Consequently, the heterotrimer dissociates from the receptor and splits into two functional units, Gα and Gβγ, each of which modulates the activity of various downstream effector proteins, depending on the type of G protein.[10, 14, 20, 30] The G protein-unbound active receptor can subsequently bind and activate other G proteins; this constitutes the first level of signal amplification.[27, 31] As briefly mentioned briefly, the effects of different G protein classes can be of opposite nature. For example, $G\alpha_s$ proteins directly activate adenylate cyclases which results in an increase in the production of the second messenger cyclic adenosine monophosphate (cAMP), whereas $G\alpha_{i/o}$ proteins inhibit adenylate clyclases. Further typical interaction partners of Gα proteins include, for example, phospholipase β ($G\alpha_{q/11}$) or Rho guanine nucleotide exchange factors ($G\alpha_{12/13}$).[30] Effector proteins of the Gβγ subunit include, but are not limited to, protein kinases like mitogen-activated protein kinases (MAPKs) and G protein-coupled receptor kinases (GRKs).[32]

The latter play a pivotal role in the attenuation of the signaling cascade, since GRKs phosphorylate serine and threonine residues of the intracellular region of GPCRs, which can lead to the recruitment of β-arrestins.[33] β-Arrestins are 48 kDa large proteins that bind to phosphorylated receptors and, among other effects, sterically hinder the activation of further G proteins by the active GPCR, and promote its internalization.[20, 34] Nowadays, it is widely accepted that β-arrestins have their own role in signal transduction, e.g. through activation of MAPKs. However, it is not conclusive whether these signaling events are dependent or independent of G protein activation.[35–37]

The attenuation of the G protein itself is regulated through the intrinsic GTPase activity of the Gα subunit, which results in the hydrolysis of GTP to GDP and inorganic phosphate (P_i). The kinetics of this hydrolysis can be accelerated by GTPase activating proteins or protein domains, called GAPs.[38] The GDP-bound Gα protein then re-associates with the Gβγ dimer and is available to enter a new cycle of activation.[30]

The effector proteins downstream of the G proteins catalyze the production of second messenger molecules like cAMP, inositol trisphosphate (IP_3) or diacylglycerol (DAG), which can modulate various physiological functions, depending on the targeted cell, tissue or organ.[14] As an example, stimulation of the β_2-adrenergic receptor (β_2AR) in airway smooth muscle cells by the endogenous ligand adrenaline, e.g. in a fight-or-flight situation, leads to an activation of $G\alpha_s$ proteins. This, in turn, stimulates adenylate cyclase to produce cAMP, whereupon this second messenger activates protein kinase A, resulting in the phosphorylation and deactivation of other proteins, which otherwise mediate the contraction of airway smooth muscles. Consequently, relaxation of the of airway smooth muscle occurs leading to bronchodilatation and reduced airway resistance, which can be vital in such a situation.[39–41]

Figure 2 illustrates the most important pathways in the canonical signaling of GPCRs.

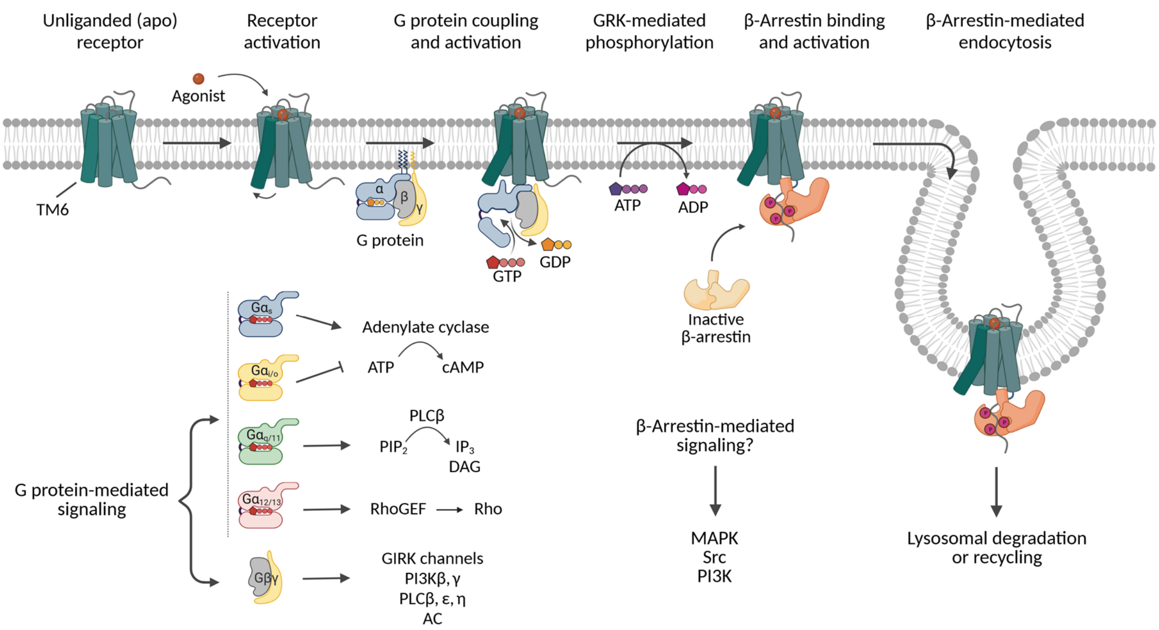

Figure 2. Schematic representation of the canonical GPCR signaling pathways. Figure inspired by Hilger.[42]

Rhodopsin is not only regarded as a prototypical GPCR in terms of its signaling, but it is also the prototype of the largest group of GPCRs, as classified by the A-F system, which is termed "rhodopsin-like family" or class A GPCRs. The over 900 different GPCRs were classified in a total of six different classes, labeled A-F, based in their amino acid sequence and functional similarities.[43] The class A receptors account for 85 % of all GPCRs and it is the most widely studied class in terms structural and functional characteristics.[44] Also in this regard, rhodopsin has played a key role, as it was the very first GPCR to be structurally elucidated in the year 2000.[45] Ever since, rhodopsin has served as a model system for the entire class A receptor family and has been elucidated in various states, including inactive,[45] active[11, 46] and intermediate states,[47, 48] as well as in complex with arrestin,[49] and a GRK.[50] Of interest, rhodopsin is still the only GPCR that has been crystallized in full sequence, including the third intracellular loop (ICL3), as well as the *C*-terminus.[51, 52]

The following section will focus on the structural aspects of class A GPCRs.

1.3 Structural aspects of class A GPCRs

Until 2007, when the structure of the inactive state of the human β_2-adrenergic receptor was revealed, bovine rhodopsin was the only GPCR for which a high-resolution structure had been available.[53] However, since the elucidation of the first GPCR structures, structural insights into more than 250 different GPCRs are now available, achieved mostly by X-ray crystallography or by cryogenic electron microscopy (cryo-EM). Of these structures, approximately 200 account for members of class A GPCRs.[52] Thanks to the tremendous progress in the field of structural biology of GPCRs, several features of active and inactive states of class A GPCRs were identified. In fact, recently, a class-wide common activation mechanism was proposed, that connects the changes in the ligand binding pocket, made up of residues near the extracellular portion of TM3, TM5, TM6 and TM7,[54] to the G protein-binding domain in the intracellular region of the receptors.[55]

1.3.1 Common features of class A GPCR activation

In order to facilitate signal transduction, GPCRs undergo a global reorganization of their intracellular TM regions, especially TM6 and TM7, which is triggered by smaller movements in the side chains of conserved motifs. The most prominent reorganization is the outward swing of the cytoplasmatic end of TM6 whose magnitude can differ distinctly between different GPCRs and activation states.[56, 57] In the G protein-coupled, active state of the β_2AR, for example, the tip of TM6 swings out by as much as 14 Å, whereas for the partially activated adenosine A_{2A} receptor (A_{2A}AR) this movement spans only 3.5 Å.[56] The involved motifs include the CWxP, PIF, Na^+ pocket, NPxxY and DRY motifs, which are located between the ligand binding pocket and G protein-coupling region.[55] Zhou et al. proposed the following common rearrangements during the activation of class A GPCRs, which in parts aligns with previous findings of other research groups:[22, 55, 56, 58–60]

i. Repacking and formation of new contacts within the more extracellular motifs CWxP and PIF (e.g. between 6.48 and 3.40 (Ballesteros-Weinstein numbering)[61]) triggers the rotation of the intracellular tip of TM6.
ii. Collapse of the Na^+ pocket through strengthening of the contacts within the pocket (2.50, 3.39, 7.45 and 7.49) initiates a movement of TM7 towards TM3.
iii. The "hydrophobic lock" between 3.43, 6.40 and 6.41 breaks, which thereby loosens this association of TM3 and TM6. Instead, a new interaction between 3.43 and 7.49 is formed, fueling the movement of TM7 towards TM3.

iv. Interactions involving residue $Y^{7.53}$ of the NPxxY motif rearrange and further strengthen the packing of TM7 and TM3 (e.g. strengthened interaction of $Y^{7.53}$ with 3.43).

v. The salt bridge between $R^{3.50}$ and $D/E^{3.49}$, and the less conserved ionic lock between $R^{3.50}$ and $D/E^{6.30}$ break, as well as the interaction between $R^{3.50}$ and 6.37. This terminates the last remaining interaction of TM3 and TM6 at their cytoplasmatic ends and thereby enables the full-scope outward swing of TM6.

vi. $R^{3.50}$ forms new contacts, e.g. with $Y^{7.53}$ of the NPxxY motif, and further rearrangements on the intracellular ends of TM3, TM5 and TM6 facilitate the binding of the G protein.

Figure 3 provides a schematic representation of the main structural reorganizations that happen upon activation, and the postulated interplay of the different conserved motifs.

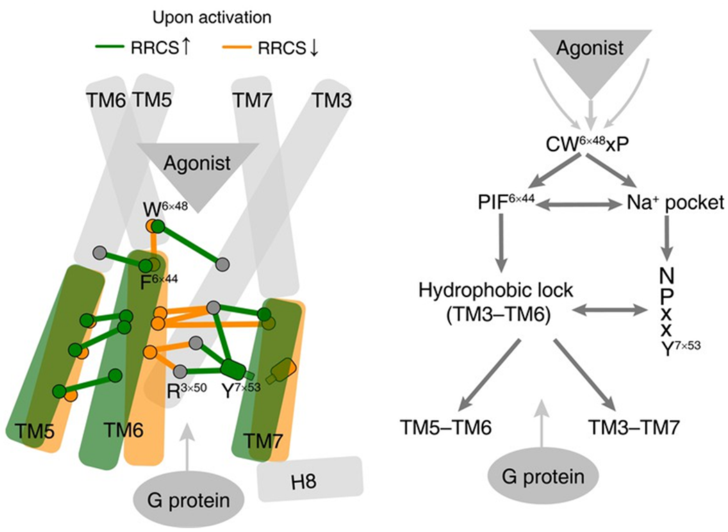

Figure 3. Schematic representation of the proposed common activation model for class A GPCRs. Structural features and contacts of the inactive state are depicted in orange, whereas those of the active state are shown in green. RRCS refers to residue-residue contact score. Figure taken from Zhou et al.[55]

Despite extensive efforts in discovering a universal mechanism of activation, it is unsurprising that some aspects of the ligand-associated GPCR activation differ among GPCRs, considering the diversity of ligands, sequences and functions across class A GPCRs.[55, 59] Also, there are limiting factors for a detailed deciphering of the activation mechanisms and other structural details, such as the resolution of the structures used for the interpretation. For example, many inactive, and especially active state structures elucidated by cryo-EM mostly do not reveal crucial water molecules, that frequently bridge interactions.[62, 63] Additionally, with regard to the inactive structures, one limiting factor is the oftentimes extensive protein engineering, specifically of the TM5-ICL3-TM6 interface, that is often modified for their structural elucidation by X-ray crystallography.[64] And generally, each crystal structure and cryo-EM structure represents only a static snapshot. Consequently, their comparison can hardly do justice to the highly dynamic processes and variety of conformational states of each receptor, and further analyses like nuclear magnetic resonance, fluorescent spectroscopy and molecular dynamics (MD) simulations are needed in this context.[42, 55–57, 64]

Nevertheless, knowledge of the features and differences in active and inactive state GPCRs, is important for understanding the roles of GPCRs in (patho-)physiology and for utilizing them for rational drug design.[64] But also in the context of protein engineering of GPCRs, specifically for X-ray crystallography, this knowledge can be useful to stabilize a receptor in the desired state.

1.3.2 The Na^+ binding pocket

In this regard the Na^+ ion binding site was of particular interest for this study, which was first revealed through elucidation of the high-resolution structure (1.8 Å) of the inactive A_{2A}AR in the year 2012.[65] Owing to further high-resolution crystal structures e.g. of the δ opioid receptor,[66] the $β_1$AR[67] and the dopamine D_4 receptor (D_4R)[68], it is now established that the Na^+ ion is bound in the middle of the TM region by aspartate $D^{2.50}$ and serine $S^{3.39}$ in the inactive state of the receptors. The pocket, which is lined by 16 conserved residues in class A GPCRs, partially collapses upon activation due to the inward movement of the TM7. TM7 directly clashes with the Na^+ binding site, whereupon the Na^+ is released towards the cytoplasm.[58, 69] The negative allosteric effect that Na^+ exhibits on agonist binding in many GPCRs can be abolished by replacement of the negatively charged main anchor of the ion, $D^{2.50}$, with a neutral amino acid.[42, 70, 71] Conversely, mimicking of Na^+ binding, e.g. through a Na^+-mimicking ligand, or protein engineering on the Na^+ binding site, can lock a GPCR in its inactive state.[72–74]

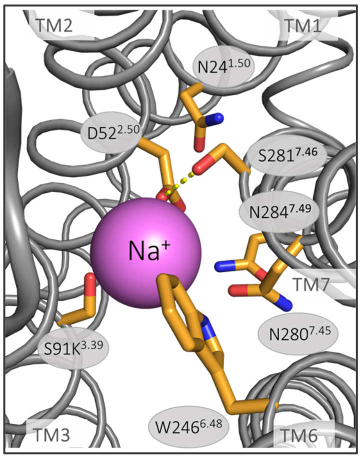

Figure 4. Example of the Na^+ pocket of the $A_{2A}AR$. PDB-ID: 4EIY.

Interestingly, the D_4R was crystallized in a Na^+-bound and a Na^+-free form and neither the overall receptor, nor the residues lining the Na^+ pocket showed notable conformational differences in both structures.[68] This observation suggests that the Na^+ does not induce any specific conformation, but instead might shift the equilibrium of the receptor towards the same inactive state, that was observed in the absence of Na^+.[69]

All these insights explain and confirm observations that were made decades before the first structural evidence for the Na^+ pocket was obtained. First reports of an allosteric Na^+ effect on opioid receptors in mouse brain extracts were published already 50 years ago.[75, 76] Subsequently, observations of similar effects were described for numerous other GPCRs, including dopamine receptors, adrenergic receptors as well as adenosine receptors (ARs).[76] For ARs, the allosteric effect of Na^+ was first mentioned for the adenosine A_1 receptor (A_1AR) in 1996,[77] and for the $A_{2A}AR$ in the year 2000.[78] A more recent study, performed after elucidation of the high-resolution structure of the $A_{2A}AR$, provided a further in-depth analysis of the cation's effect on the receptor explored by MD stimulation studies, radioligand binding experiments, and thermo-stability assessments. The study demonstrated that for the $A_{2A}AR$

i. Na^+ increased binding of the antagonist [^{3}H]ZM241385 and reduced binding of the agonist [^{3}H]NECA in a concentration dependent manner,
ii. binding of Na^+ and agonists is mutually exclusive, and
iii. the presence of Na^+ increases the thermostability of the purified $A_{2A}AR$.[79]

Specifically, the radioligand binding data is in agreement with observations on the other members of the AR family.[77, 80–82] Consequently, all of the AR subtypes, including the receptor of interest in the present study, the $A_{2B}AR$, are expected to form a Na^+ binding pocket. The conservation of the amino acids of the respective residues, lining the Na^+ pocket, [69] supports this proposition, as illustrated in Figure 5.

Position	1.50	1.53	2.46	2.47	2.49	2.50	3.35	3.39	3.43	6.44	6.48	7.45	7.46	7.49	7.50	7.53
α-branch GPCRs	N	V	L	A	A	D	F / L	S	L	F	W	N	S	N	P	Y
	100	83	88	79	58	97	26 / 18	84	81	89	92	82	77	82	93	93

Position / Receptor	1.50	1.53	2.46	2.47	2.49	2.50	3.35	3.39	3.43	6.44	6.48	7.45	7.46	7.49	7.50	7.53
A_1AR	N	V	L	A	A	D	L	S	L	F	W	N	S	N	P	Y
$A_{2A}AR$	N	V	L	A	A	D	L	S	L	F	W	N	S	N	P	Y
$A_{2B}AR$	N	V	L	A	A	D	L	S	L	F	W	N	S	N	P	Y
A_3AR	N	V	L	A	A	D	F	S	L	F	W	N	S	N	P	Y

Figure 5. Conservation of amino acids in the Na^+ binding pocket of ARs. Top: Residue conservation in the Na^+ binding site of α-branch GPCRs. Numbers correspond to conservation [%].[69] Bottom: Residue conservation among the ARs.[83] Numbering of residues according to Ballesteros-Weinstein nomenclature.[61] Adapted from Zarzycka et al.[69]

1.3.3 Further structural aspects of class A GPCRs

Besides the conserved transmembrane motifs involved in the activation process of class A GPCRs, they exhibit further structural features that are noteworthy in the context of this thesis.

1.3.3.1 The conserved disulfide bridge

One example of such a feature is the disulfide bridge between the cysteine at position 3.25, near the extracellular end of TM3, and the cysteine residue 45.50 in the extracellular loop 2 (ECL2) of the receptors. This disulfide bridge is thought to be present in the vast majority of human GPCRs and likely stabilizes the conformation of the extracellular region and shapes the entrance to the orthosteric ligand binding pocket.[84–86] Its disruption was shown to be detrimental to the function of several class A GPCRs, such as rhodopsin and the β_2AR,[85, 87, 88] and it was shown to affect ligand binding at different receptors.[89] For some receptors, such as the melanocortin receptors and the $A_{2A}AR$, additional disulfide bonds were observed in the extracellular region, which further constrain the ECLs and form the entry to the ligand binding site.[85] In case of the $A_{2A}AR$, for example, two additional disulfide bonds are present (C71^{ECL1} to C159^{ECL2} and C74$^{3.22}$ to C146^{ECL2}), which proved to be essential for potency and efficacy of the endogenous ligand adenosine.[90]

1.3.3.2 The diversity of the ECL2

In general, the ECL2 is of very high functional importance for class A GPCRs. Among all ECLs, the ECL2 is the largest and structurally most diverse one. Due to its proximity to the orthosteric binding site, the ECL2 can facilitate or block ligand entry, trap ligands within the TM domain, change the shape of the orthosteric binding site, influence selectivity, and directly or indirectly participate in ligand binding.[85, 91, 92] It can exhibit either α-helices or β-sheets or lack a secondary structure altogether.[91] Interestingly, the longest ECL2 across all classes of human GPCRs is present in the class A anaphylatoxin chemotactic C3a receptor, with an astonishing 172 amino acids inserted between its TM4 and TM5.[52, 93] To date, two cryo-EM structures of this receptor have been published, but unsurprisingly, the ECL2 was not fully resolved in either of them.[93] For comparison, the ECL2s of rhodopsin, the $A_{2A}AR$ and the β_2AR are composed of 23, 28 and 22 amino acids, respectively, and the whole sequence of the prototypical class A GPCR rhodopsin is 348 amino acids long.[52]

1.3.3.3 The extracellular N-glycosylation

Another typical feature on the extracellular face of class A GPCRs is its post-translational modification (PTM) with glycans. Today it is assumed that, with few exceptions, most mammalian GPCRs are glycosylated at either their extracellular *N*-terminus or the ECLs, which may substantially regulate the GPCR biology with regard to trafficking, ligand binding, dimerization and signaling.[94, 95] However, the exact effects are variable between different receptors. Functionally, the most consistent role of glycosylation seems to be the link between the presence of N-glycans and correct receptor folding and trafficking from the endoplasmic reticulum to the cell membrane.[96] N-Glycosylation occurs at the side chain amide of an asparagine residue of the consensus sequence N-X-S/T, with X being any amino acid except for proline, and it is the most common form of glycosylation found in GPCRs, typically at their *N*-terminus or ECL2.[85, 95] For many GPCRs the requirement of at least one N-glycan for efficient trafficking was reported, including the β_2AR,[97] the δ opioid receptor,[98] and the angiotensin II receptor type 1.[96, 99]

Unfortunately, structural information on N-glycans and other PTMs on GPCRs from crystal structures and cryo-EM structures is rare, partly due to their presence in flexible regions such as the *N*-/*C*-terminus or the ECL2.[95, 100] Another contributing factor is that for structural studies of GPCRs overexpression of the receptor of interest is typically necessary, which is most commonly performed in insect cells.[101, 102] Insect cells perform different PTMs compared to mammalian cells. For example, N-glycosylations produced in insect cells are less complex compared to those of higher eukaryotes, and exhibit a higher mannose content.[103] Also, upon overexpression of GPCRs in insect cells, a large portion of the recombinant protein is often not glycosylated at all, likely due to the saturation of the glycosylation machinery.[104] Since this heterogeneity in glycosylation may affect crystallization, N-glycosylation sites are sometimes removed enzymatically or by mutation/truncation, preventing their structural elucidation altogether.[102, 105–108]

1.3.3.4 The orthosteric binding site in GPCR subfamilies

Besides these features involving the extracellular domain of class A GPCRs, another common observation among members of the same family of GPCRs is their highly conserved orthosteric binding site. This was observed, for example, for muscarinic acetylcholine receptors, serotonin receptors, β adrenergic receptors, as well as ARs.[109–112] Unfortunately, due to their in parts different coupling partners, tissue distribution and consequently differing physiological effects, the unwanted simultaneous targeting of several family members of a specific sub-family can result in side effects of drugs.[44, 110, 113] An example of that are the β_1AR and the β_2AR, whose orthosteric binding site only differs by the presence of one hydroxyl group (phenylalanine vs. tyrosine residue). Blockade of the β_1AR in the heart is favorable e.g. for treating hypertension, but antagonism of the β_2AR is detrimental e.g. for patients with asthma.[112]

Figure 6 exemplarily compares the orthosteric binding pocket of the four AR family members.

	3.32	3.33	3.36	3.37	ECL2	ECL2	5.38	5.42	5.47	6.48	6.51	6.52	6.55	7.35	7.39	7.42	7.43
A_1AR	V	L	T	Q	F	E	M	N	V	W	L	H	N	T	I	T	H
A_{2A}AR	V	L	T	Q	F	E	M	N	V	W	L	H	N	M	I	S	H
A_{2B}AR	V	L	T	Q	F	E	M	N	V	W	V	H	N	M	I	S	H
A_3AR	L	L	T	H	F	V	M	S	I	W	L	S	N	L	I	S	H

Figure 6. Sequence alignment of residues lining the orthosteric ligand binding pocket of the ARs. Differences compared to A_{2A}AR are highlighted in red. Adapted from Chen et al.[111]

One way to overcome this challenge of selectively targeting one specific receptor subtype is the detailed structural elucidation of the binding site of each member of the sub-family. This information can facilitate the exploitation of minor differences in the binding site, as well as potentially less conserved secondary binding sites,[114] for increased selectivity of new drug candidates.[115, 116] This highlights the importance of obtaining co-crystal structures and cryo-EM structures for improving therapeutic intervention. The next section will focus on the role of GPCRs as drug targets, specifically regarding the receptors of interest in the present study, the ARs.

1.4 GPCRs as drug targets

As briefly mentioned before, GPCRs display a multitude of functions, as they are expressed in most of the body's tissues and contribute to virtually all aspects of human physiology.[4] Consequently, their dysregulation has been linked to a large number of diseases including type 2 diabetes, cardiovascular diseases, central nervous system disorders, neurodegenerative disorders, cancer, and many more.[110, 117] The exact (patho-)physiological functions of the different GPCRs depends largely on the context, and receptor-related dysfunctions can be caused in several different ways. Consequently, different approaches must be undertaken to target these malfunctions.[118]

The silver lining of the GPCR's frequent involvement in diseases is the fact that they present themselves as interesting drug targets for several reasons:[119]

i. Their orthosteric binding site is accessible from the extracellular space, meaning drugs do not need to pass the plasma membrane to induce intracellular effects.
ii. The binding site is typically well-suited in size and shape for small synthetic molecules to bind.
iii. The GPCRs can be either activated or inactivated, depending on the desired effect.

Additionally, some researchers propose a potential to further fine-tune receptor signaling through biased ligands, thereby reducing the side effects of drugs.[120–122]

Indeed, as of 2018, approximately 700 drugs targeted GPCRs, accounting for 35 % of all drugs approved in the United States and the European Union.[29] As such, GPCRs constitute the largest family of proteins that are targeted by approved drugs, despite the fact that less than 40 % of the approximately 360 potentially druggable human GPCRs (excluding the sensory GPCRs) are addressed so far.[29] However, it should be noted that according to that study, only approximately two thirds of the targeted GPCRs are thought to be the primary targets that mediate the desired therapeutic effect. Moreover, numerous approved drugs represent the physiological agonists of the respective GPCRs.[29] This leaves a major, still unfulfilled potential for selective therapeutic intervention on numerous GPCR-linked diseases. Accordingly, a multitude of agents targeting GPCRs are currently in clinical trials, of which dozens address potentially novel GPCR targets without an approved drug.[123]

One interesting class of drug targets, currently investigated in over 40 ongoing clinical trials, are the ARs.[124]

1.5 The adenosine receptors

It was over 40 years ago, that the existence of ARs was first reported, based on observations of cAMP decrease or increase upon treatment of cultured brain cells with different concentrations of adenosine. Back then, the ARs were subdivided into A_1 receptors and A_2 receptors accounting for the contradictory effects on cAMP accumulation.[125] Nowadays, it is clear that there are more than two members of the AR family, namely the A_1AR, the A_{2A}AR, the main receptor of interest in the present study, the $A_{2B}AR$, as well as the A_3AR.[126] Nevertheless, the distinction between inhibitory and stimulatory ARs held true, as the A_1- and the A_3AR couple preferentially to $G\alpha_i$ proteins, inhibiting cAMP production, whereas the A_{2A}- and the $A_{2B}AR$ couple preferentially to $G\alpha_S$, stimulating cAMP synthesis.[127] ARs belong to the class A family of GPCRs and contribute to the broader phenomenon of purinergic signaling, which refers to the signal transduction mediated by extracellular nucleosides and nucleotides, such as adenosine and adenosine 5'-triphosphate (ATP).[128, 129] In this context, the ARs form one of the three main subfamilies involved in purinergic signaling that are termed P1, P2Y and P2X receptors. The P1 receptors, or ARs, are activated by adenosine, whereas the family of P2Y GPCRs is activated by various nucleotides, depending on the subtype.[128] P2X receptors are transmembrane receptors activated mainly by ATP, however they constitute ionotropic receptors, i.e. ATP-gated cation channels for Na^+, K^+ and Ca^{2+}.[130] Figure 7 depicts an overview of the receptors involved in purinergic signaling.

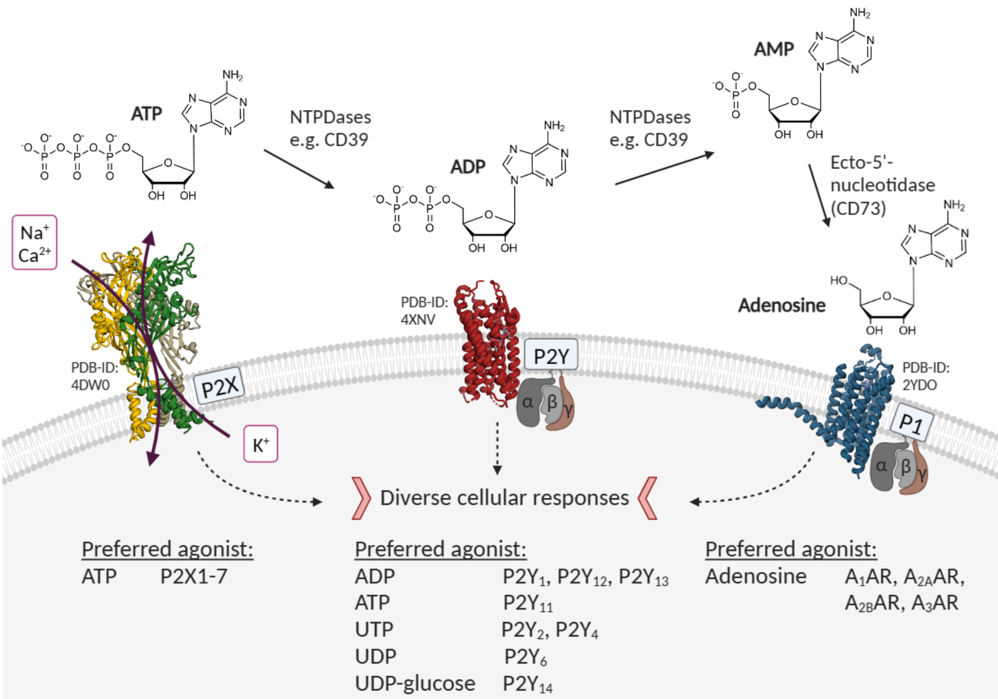

Figure 7. Canonical extracellular purinergic signaling. Figure adapted from Menzies et al.[131]

1.5.1 Physiological roles of adenosine mediated through ARs

Despite their common endogenous agonist, ARs exhibit distinct tissue distributions, expression levels, signaling profiles and affinities for adenosine, and are therefore involved in diverse cellular processes.[127] The common theme, however, is that through ARs, adenosine acts as a cytoprotective modulator in response to stress in an organ or tissue, which in the case of adenosine overproduction, can also have pathophysiological implications.[132]

The abundance of extracellular adenosine largely depends on the metabolic state of a cell. Under normal conditions extracellular concentrations are in the nanomolar range, but in states of high metabolic or oxygen demand, such as ischemia, inflammation and cancer, the extracellular concentration of the short-lived nucleoside adenosine rises up to the micromolar range, by up to 100-fold.[127, 132, 133] At low concentration, adenosine would activate only the A_1-, the A_{2A}- and the A_3ARs, the latter only if highly expressed, whereas at high concentrations the general activation of all four present AR subtypes can be expected, even that of the A_{2B}AR for which adenosine exhibits the lowest affinity.[127, 132] Extracellular adenosine levels rise either by its active release from the cells e.g. via adenosine transporters,[134] or by its extracellular production through the action of ectonucleotidases such as cluster of differentiation (CD) 39 and CD73 from adenine nucleotides (AMP, ADP and ATP, see to Figure 7).[127, 135] The adenine nucleotides, especially ATP, which is intracellularly present in millimolar concentration,[136] are released either through regulated pathways or resulting from plasma membrane damage or cell death.[137] The AR-mediated protective measures include e.g. an increased oxygen and energy supply/demand ratio, the stimulation of angiogenesis, ischemic preconditioning and anti-inflammatory effects.[138, 139]

1.5.2 ARs as drug targets

Even long before the understanding of these functions and the discovery of the biological target of adenosine, the nucleoside and its derivatives were used clinically for the treatment of arrhythmia and/or vasodilation.[140, 141] Today, adenosine is still used as a treatment for arrhythmia, specifically for treating paroxysmal supraventricular tachycardia, and for the diagnosis of coronary artery disease through myocardial perfusion imaging.[142–144] Besides adenosine, the synthetic $A_{2A}AR$ agonist regadenoson is in clinical use. Its application is solely for diagnosis of coronary artery disease in subjects that cannot fulfill an exercise stress test for studying blood vessel dilation.[144, 145] Recently, further clinical trials for agonists of the various AR subtypes were conducted for conditions ranging e.g. from pain and heart failure to hepatitis.[146]

Antagonism of AR signaling is also of clinical value. The natural alkaloids caffeine and theophylline, present e.g. in tea and coffee preparations, have also been applied long before their mechanism of action, namely blockade of ARs, was known.[147] Both xanthine derivatives, caffeine and theophylline, are approved drugs since many decades.[124] Currently several antagonists targeting ARs are approved drugs (see Table 1).

Table 1. List of approved drugs primarily targeting ARs. [124]

Drug	Target	Indication
Caffeine	All ARs	Apnea of prematurity
Theophylline, Aminophylline	All ARs	Reversible airway obstruction
Istradefylline	$A_{2A}AR$	"Wearing-off" episodes of Parkinson's disease, adjunctive treatment

Additionally, caffeine is employed as an adjuvant in analgesic formulations, e.g. in combination with non-steroidal anti-inflammatory drugs,[148] and exhibits stimulating properties on the central nervous system.[149]

The chemical structures of approved AR agonists and antagonists are depicted in Figure 8.

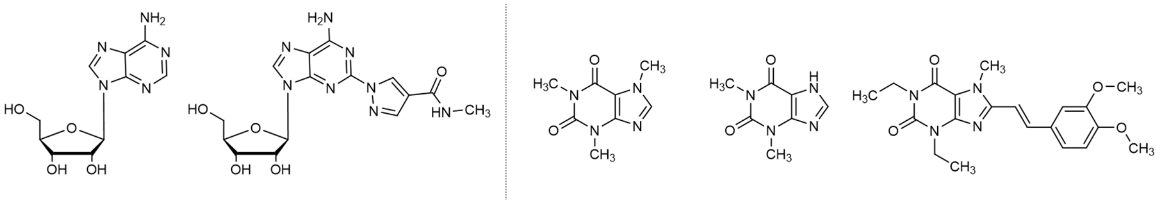

Adenosine Regadenoson Caffeine Theophylline Istradefylline

Figure 8. Chemical structures of approved AR-targeting drugs. Left: Agonists. Right: Antagonists. Aminophylline is the ethylenediamine salt of theophylline and therefore not explicitly shown.

Considering the AR's vast involvement in many (patho-)physiological processes, it is clear that for this receptor subfamily, the therapeutical potential is underexplored and underexploited, especially in terms of selective antagonists. Encouragingly, several selective inhibitory candidates are currently investigated in clinical trials, as recently compiled by Kutryb-Zając et al. and presented in the following Table 2.

Table 2. List of selected current clinical trials of drug (candidates) primarily targeting ARs.[124]

Drug	Target	Indication	Phase
Caffeine	All ARs	Alzheimer's disease	3
		Bronchopulmonary dysplasia	3
		Carcinoma breast after mastectomy	2
Theophylline	All ARs	Chronic obstructive pulmonary disease	3
Aminophylline	All ARs	Complete heart block	4
		Acute kidney injury	4
Istradefylline	A_{2A}AR	Amyotrophic lateral sclerosis	1/2
		Parkinson's disease with cognitive impairment	2
		Spinal cord injuries, myelopathy	1/2
Ciforadenant	A_{2A}AR	Advanced cancers	1
		Renal cell carcinoma	1/2
Taminadenant	A_{2A}AR	Solid tumors, non-Hodgkin lymphoma	2
PBF-1129	A_{2B}AR	Non-small cell lung cancer	1
TT-702	A_{2B}AR	Advanced solid tumors	1/2
Etrumadenant	A_{2A}AR/A_{2B}AR	Prostate cancer	1/2
		Rectal cancer	2
		Non-small cell lung cancer	2
		Prostate cancer	2
M1069	A_{2A}AR/A_{2B}AR	Unresectable solid tumors	1

Their chemical structures are illustrated in Figure 9.

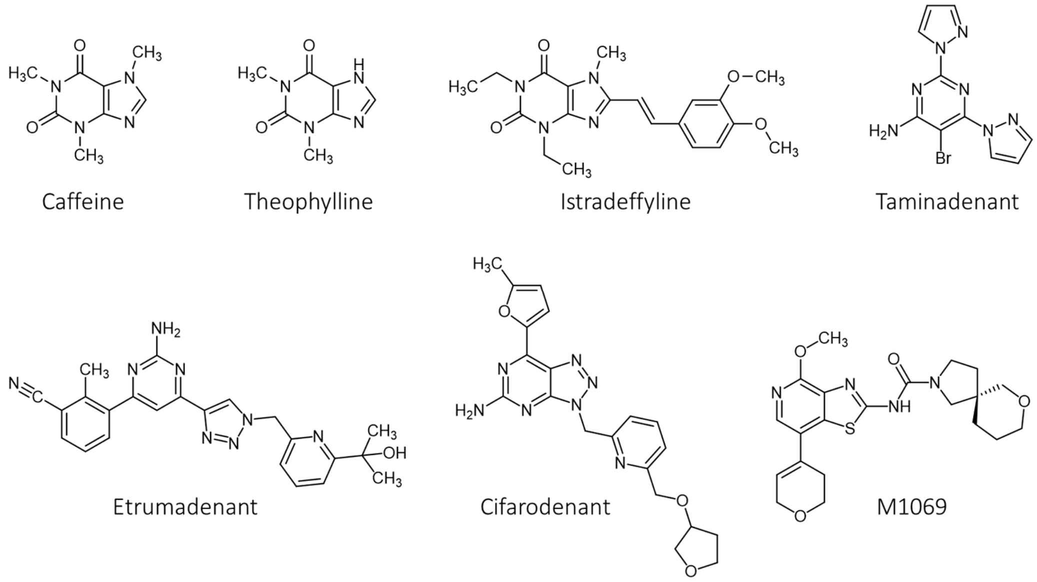

Figure 9. Chemical structures of selected AR-targeting drug (candidates) currently investigated in clinical trials. Aminophylline is the ethylenediamine salt of theophylline and therefore not explicitly shown. Structures of PBF-1129 and TT-702 are undisclosed.

As evident from this list of selected ongoing clinical trials, the intended therapeutic use, specifically for the selective A_{2A}AR and/or A_{2B}AR antagonists, is focused on the treatment of neurodegenerative disorders, and, most importantly, cancer. This reflects the expanding appreciation of the importance of the A_{2A}AR and A_{2B}AR for the immunotherapy of cancer.

1.5.3 ARs as targets for the immunotherapy of cancer

Cancer is as complex as the cellular systems it hijacks.[150] Today it is believed that the majority of cancers descend from a single abnormal cell, whose abnormality is caused by mutation and other alterations of their genetic material.[151, 152] It is estimated that 10^{16} cell divisions take place in a normal human body in the course of a lifetime, and each time the limit of accuracy of the DNA replication and repair is tested.[153, 154] Taking into account this accuracy, every gene undergoes mutation in billions of separate occasions throughout the lifetime of any individual human being.[154] Luckily, a single mutation in an otherwise healthy cell is typically not sufficient to initiate cancer,[154, 155] and in the early stages, abnormal cells are detected and eliminated by the surveillance system of the immune system.[156] In theory, the immune system has an outstanding potential for specific and sustained destruction of cancer without toxicity to healthy tissue, and a long-term memory that can prevent cancer recurrence.[156] However, oftentimes cancers change their microenvironment to evade this destructive immunity.[157] One key pathway by which tumors achieve this immune system evasion is the upregulation of the adenosine concentration in their microenvironment.[158]

Under normal conditions, one way by which adenosine fulfills its physiological role as a cytoprotective modulator, is by protection against an excessive immune response that otherwise may lead to tissue damage or loss of organ function.[158, 159] This immunosuppressive function of adenosine can be exploited by cancer cells.[158] In the chronically hypoxic tumor microenvironments (TME), the adenosine concentration is drastically elevated as a result of the overexpression of the ectonucleotidases CD39 and CD73, among other mechanisms.[160, 161] The expression of these enzymes is upregulated through hypoxia-mediated mechanisms and a positive feedback loop in response to the adenosine signaling through ARs.[161–163] Consequently, the concentration of the immunosuppressive extracellular adenosine in the TME can rise approximately 200-fold over the basal level, protecting cancer cells from the attack by the immune system.[158, 164]

Among the ARs, the A_{2A}AR- and A_{2B}AR are believed to be primarily responsible for adenosine-mediated immunosuppressive signaling. This is the result of their stimulatory effect on intracellular cAMP accumulation, leading to transcriptomic modulation towards suppression of immune functions.[165, 166] Stimulation of the A_{2A}AR generally inhibits the activities of many cells of the immune system, including T cells, natural killer cells, macrophages and dendritic cells (DCs), as well as neutrophils.[160] The immunosuppressive mechanisms of A_{2B}AR activation are different from those of the A_{2A}AR, as the A_{2B}AR-mediated regulation affects mainly myeloid immune cells, e.g. DCs and macrophages.[160, 166] Both of the receptors are expressed not only on immune cells, but often also on cancer cells, where they are frequently upregulated.[167–169] The blockage of the receptors is consequently a promising approach to restore the immune system's firepower against cancer, either alone or in combination with already established immune checkpoint inhibitors, or other anti-cancer drugs.[158, 165]

Among the two A_2ARs, the $A_{2A}AR$ represents the more established target for the immunotherapy of cancer,[165] however, there are some factors that render the $A_{2B}AR$ specifically interesting for this purpose. For one, in contrast to the other ARs which are activated by adenosine even under basal conditions (EC_{50} = 0.3 – 0.7 µM) , the $A_{2B}AR$ is only significantly activated by much higher adenosine concentrations (EC_{50} = 24 µM), present only under pathological conditions.[170,171] Consequently, despite its ubiquitous expression,[172] blockade of the $A_{2B}AR$ might predominantly affect the signaling in a pathological context and therefore exhibit fewer side-effects. Moreover, $A_{2B}ARs$ expression, although ubiquitous, is mostly low to moderate in healthy conditions,[159] but highly upregulated under hypoxic, ischemic and inflammatory conditions by several transcription factors, including the hypoxia-inducible factor-1α (HIF-1α).[173,174] Also, it is now appreciated that $A_{2A}AR$ and $A_{2B}AR$ play a nonredundant role in immunosuppression and the utilization of dual-antagonists might provide an additional benefit.[165] For example, the high expression, especially of the $A_{2B}AR$ subtype by many cancers, promoting cell proliferation, tumor angiogenesis, and metastasis,[169] is an additional reason for developing $A_{2B}AR$ antagonists for the treatment of cancer. Furthermore, $A_{2B}AR$ antagonists were demonstrated to mediate antinociceptive effects,[175,176] which is valuable for cancer treatment as well.

Figure 10 illustrates key aspects of adenosine-mediated signaling in the context of immunotherapy.

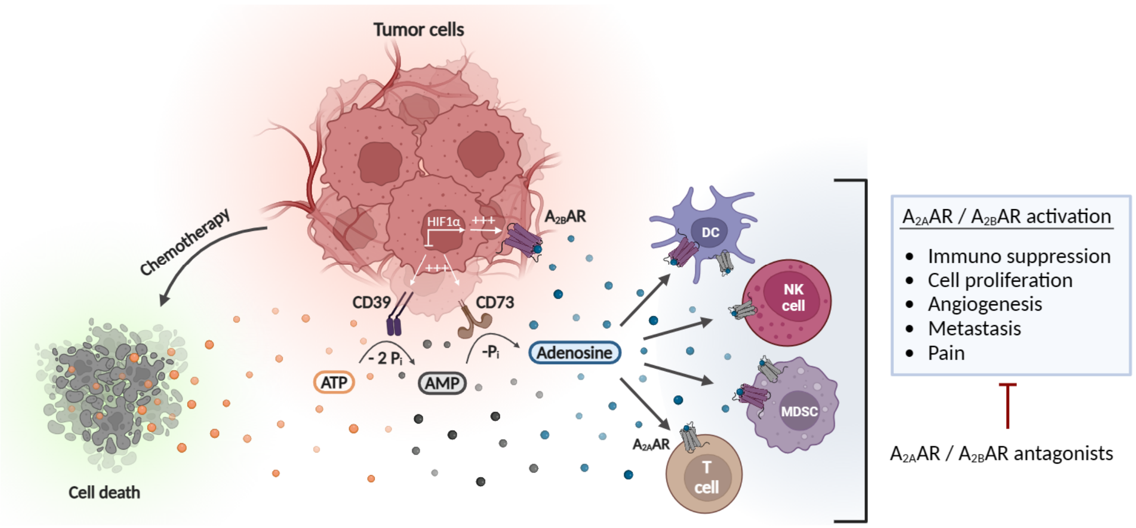

Figure 10. A_{2A}- and A_{2B}-AR as targets in the immunotherapy of cancer. Figure inspired by Khadela et al., Augustin et al. and Gao et al.[177–179] Abbreviations: NK cells = natural killer cells, DC = dendritic cells, MDSC = myeloid-derived suppressor cells.

Due to the importance of the $A_{2B}AR$ as a potential drug target, structural insights into the exact binding mode of its ligands, specifically its antagonists, would be of high value. The next section will focus on the structural insights into the $A_{2B}AR$ that are already available, and which information is still missing.

1.6 Structural insights into the adenosine A_{2B} receptor

At beginning of this study, no experimental structural information on the $A_{2B}AR$ was available. However, after the elucidation of the first crystal structure of the closely related $A_{2A}AR$ in 2008, which was only the fourth unique GPCR structure solved up to this date,[180] first homology models of the $A_{2B}AR$ were built based on these initial structural insights of the $A_{2A}AR$.[181–183] Indeed, due to the comparably high sequence identity of 58 % and sequence similarity of 73 % between these two AR subtypes,[90] the $A_{2A}AR$ structures were in principle an ideal template for the generation of such homology models.[181] As demonstrated in section 1.3.3.4 on page 12, especially the orthosteric binding site is almost identical in both receptors, with a difference of just one amino acid at position 6.51. At this position, the $A_{2A}AR$ and $A_{2B}AR$ sequence harbor a leucine and valine residue, respectively, two amino acids that differ only slightly in the length of their aliphatic side chain. Nevertheless, or exactly for that reason, these models were not able to explain the striking differences in the affinity observed for the endogenous ligand adenosine and its derivatives, which typically show significantly higher affinity for the $A_{2A}AR$ compared to the $A_{2B}AR$, by up to 1000-fold.[90, 92]

1.6.1 The ECL2 of the $A_{2B}AR$

Today, it is established that the ECL2 of the $A_{2B}AR$, which is one of the least conserved regions between the $A_{2A}AR$ and $A_{2B}AR$ exhibiting an identity of 34 %, is largely involved in ligand selectivity and receptor activation. One hypothesis is that the ECL2 of the $A_{2B}AR$ might directly form part of the orthosteric binding site and even provide a "meta-binding site" for some ligands to bind to, before their entry into the orthosteric pocket.[92] However, the exact structural mechanism by which the ECL2 affects ligand binding remains elusive.[111, 184, 185] What is known about $A_{2B}AR$'s ECL2 is that it harbors an extraordinarily high number of four cysteines within its 34 amino acid long sequence, which is the longest among the ECL2s of all AR subtypes.[52, 186] Of these, only the class A-wide conserved disulfide bridge between residues 3.25 and 45.50 was found to be essential for $A_{2B}AR$ ligand binding and function, based on site-directed mutagenesis studies.[187] Consequently, the nonessential cysteine residues may have different functions.[184] An additional aspect of the $A_{2B}AR$'s ECL2, which will be of interest later, is the presence of two potential N-glycosylation sites, which is in contrast to the other AR subtypes which only carry one potential N-glycosylation site.[52]

1.6.2 General considerations on cryo-EM

In recent years, the field of structurally biology of GPCRs experienced another acceleration, driven by the technical advances in the field of cryo-EM. Until 2017, X-ray crystallography was the method of choice to obtain high-resolution structures of GPCRs, and structures were determined mostly in the inactive or intermediate state. Since then, cryo-EM structures have vastly outnumbered the X-ray structures solved in the same timeframe.[188] From December of 2022 to end of November 2023, 128 new structures of GPCRs have been deposited at the Protein Data Bank (www.rcsb.org), as compiled by the GPCRdb (gpcrdb.org).[52] Of those 128 structures, 113 were solved by cryo-EM and only 14 were solved by X-ray crystallography, 88 % and 11 %, respectively.[52] The main reason for this explosion in cryo-EM structures is the ease of structure determination by this method, which typically does not necessitate the time-consuming construct and process optimizations that are necessary to obtain a GPCR's crystal structure.[188] Importantly however, most of the cryo-EM structures are solved of the active state of GPCRs. Within the last year, for example, 112 of the published cryo-EM GPCR structures were solved of the receptors in their active state, and only one showed a receptor in the inactive conformation.[52, 189] At the very end of the year 2022, among these active state structures were four of the $A_{2B}AR$, independently solved by two different research groups. The following section will focus on the structural insights obtained from these cryo-EM structures.[111, 185]

1.6.3 Cryo-EM structures of the active state A2BAR

The four active state A2BAR structures were solved in complex with three distinct agonists, namely adenosine, its derivative 5'-*N*-ethylcarboxamidoadenosine (NECA), and the partial agonist BAY 60-6583 which is present in two of the structures. Table 3 contrasts the general aspects of these structures.

Table 3. Comparison of general aspects of the active state A2BAR cryo-EM structures.[111, 185]

A)	B)	C)	D)
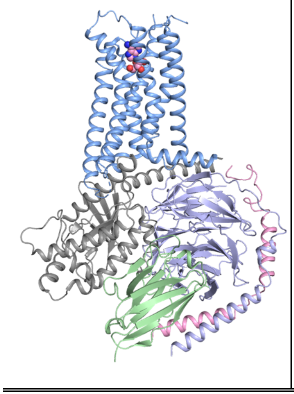	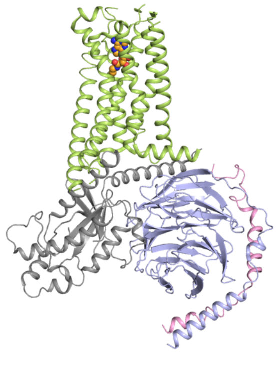	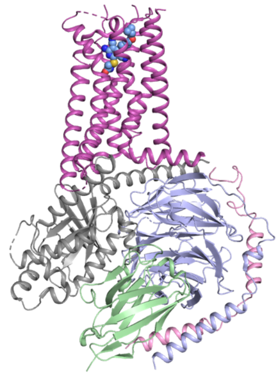	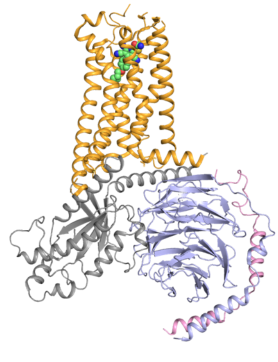
Ligand			
Adenosine	NECA	BAY 60-6583	
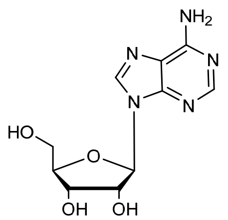	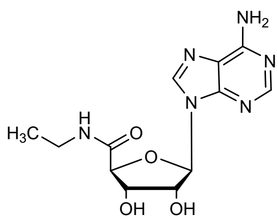	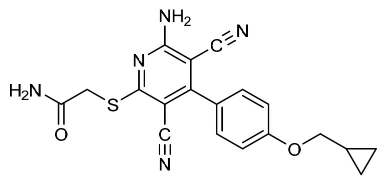	
PDB-ID, authors			
8HDP, Cai et al.[185]	7XY7, Chen et al.[111]	8HDO, Cai et al.[185]	7XY6, Chen et al.[111]
Overall resolution			
3.2 Å	3.3 Å	2.9 Å	3.0 Å
A2BAR sequence modifications			
wt human A2BAR (full length)	wt human A2BAR, (residues 2 – 332), *N*-terminal bRIL, *C*-terminal LgBiT	wt human A2BAR (full length)	wt human A2BAR, (residues 2 – 332), *N*-terminal bRIL, *C*-terminal LgBiT
Further complex proteins			
mini-Gαs, Gβ1, Gγ2, nanobody 35	Gγ2-mini-GαsIN, Gβ1-SmBiT	mini-Gαs, Gβ1, Gγ2, nanobody 35	Gγ2-mini-GαsIN, Gβ1-SmBiT

All four structures were obtained of the human A_{2B}AR without any mutations, and in complex with a G protein complex formed by a modified Gα_s, a Gβ_1 and a Gγ_2 subunit. The G protein complex of the structures in columns A) and C) of Table 3 were additionally stabilized by the nanobody 35 that binds across the interface of the Gαs and Gβ subunits.[190] For the structures presented in column B) and D), the formation of a stable complex was facilitated using the NanoBiT tethering strategy, for which the *C*-terminus of the receptor and the Gβ_1 were fused with a LgBiT and a SmBiT, respectively. The interaction of the LgBiT and SmBiT is thought to improve the complex formation and decelerate its dissociation.[191]

As expected, in the presence of (partial) agonists each structure displays the typical major features of GPCR activation, specifically the outwards-swung TM5 and TM6, as well the inwards moved TM7. Importantly, due to the unavailability of inactive state structures of the A_{2B}AR, the structures could only be compared to an inactive state structure of the A_{2A}AR (PDB-ID 4EIY)[65]. However, since the comparison of the NECA-bound cryo-EM structure of the A_{2B}AR with the NECA-bound cryo-EM structure of the A_{2A}AR (PDB-ID 6GDG)[192] revealed a high similarity with a Cα root-mean-square deviation (RMSD) of 1.1 Å, the comparison of these major movements seems valid.[111] Within the two sets of structures, 1) PDB-IDs 7XY6/7XY7 and 2) PDB-IDs 8HDO/8HDP, the Cα RMSD of the receptors are 0.4 Å and 0.5 Å, respectively, indicating a generally high similarity of the structures.[111, 185] Interestingly, BAY 60-6583, although it is only a partial agonist, does not limit the magnitude of the TM5, TM6 and TM7 movements, compared to the full agonist-bound structures.

1.6.3.1 The ECL2s in the A_{2B}AR cryo-EM structures

For medicinal chemists, one of the most interesting parts of the structures is the ligand binding pocket, including the ECL2 of the receptor. Unfortunately, the ECL2 is not fully resolved, in neither of the A_{2B}AR structures, missing between 15 and 23 of the 34 residues. The following Figure 11 highlights the (partly missing) ECL2s, along with TM4 and TM5 that are connected by them.

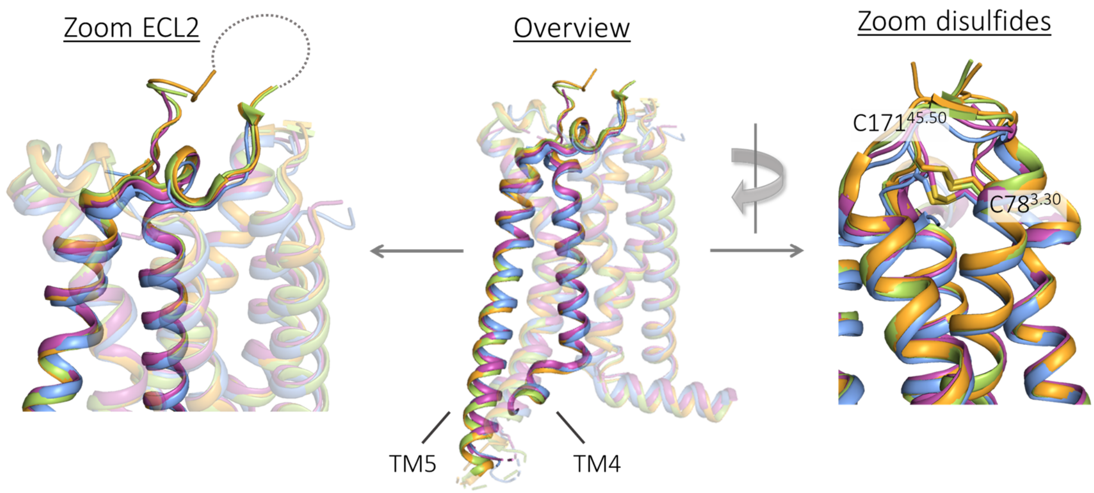

Figure 11. Comparison of the ECL2 region of all available A_{2B}AR cryo-EM structures. For improved visibility of TM4 in the back of this representation, TM1 – TM3 and TM6 – H8 are presented transparent in the images on the left and in the middle. The image on the right displays the conserved disulfide bridge present in all four structures.

Of the previously mentioned four ECL2 cysteine residues, only the conserved residue at position C171$^{45.50}$ is resolved which forms a disulfide bond to C78$^{3.30}$ (present in all four structures), as expected based on previous site-directed mutagenesis studies.[187] With regard to clear additional densities around C72^{ECL1} in the structures 7XY6 and 7XY7, it is predicted that one of the three elusive cysteines of the ECL2 forms a disulfide bond with C72^{ECL1}, which is similarly also present in the A_{2A}AR (C71^{ECL1} – C159^{ECL2}). Considering the pair-wise conservation of the cysteine-pairs C72^{ECL1} – C166^{ECL2} and C154^{ECL2} – C167^{ECL2} across six species, it is furthermore speculated that these specific pairs might form disulfides, implying that each of the cysteines in the A_{2B}AR's extracellular regions can be involved in disulfide bridges. Regarding the missing impact of these disulfide bonds, it was argued that all of them, except for the conserved one, might be flexible and alter receptor function only indirectly.[111]

1.6.3.2 The A_{2B}AR structures in complex with adenosine and NECA

Among the interactions of the ECL2, direct interactions of the residue F173^{ECL2} with both, adenosine and NECA, were observed, as illustrated in the presentation of the two binding sites in the following Figure 12.

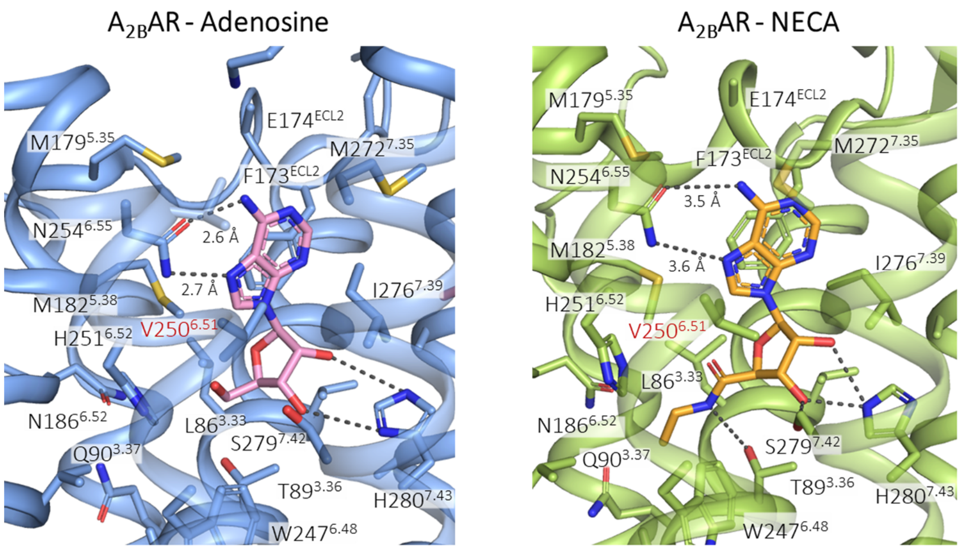

Figure 12. Detailed illustration of the binding modes of adenosine and NECA in the A_{2B}AR.

The general binding modes of adenosine and NECA in the A_{2B}AR are similar to ones observed in the A_1AR-adenosine (PDB-ID 7LD3)[193] and the A_{2A}AR-NECA (PDB-IDs 5G53, 6GDG)[192, 194] structures. The conserved interactions include:

i. π- π -stacking with F173^{ECL2} (present behind the adenine core in Figure 12),
ii. hydrogen bonding with (T89$^{3.36}$), N254$^{6.55}$, (S279$^{7.42}$), and H280$^{7.43}$, and
iii. hydrophobic interactions with V85$^{3.32}$, L86$^{3.33}$, M182$^{5.38}$, V191$^{5.47}$, W247$^{6.48}$, V250$^{6.51}$, and I276$^{7.39}$.[111]

Hydrogen bond interactions with T89$^{3.36}$ and S279$^{7.42}$ are observed only with NECA.

V250$^{6.51}$ is the only residue that differs between the orthosteric binding pockets of the A_{2A}AR and A_{2B}AR, and all AR subtypes except for the A_{2B}AR harbor the slightly larger amino acid leucine at this position. Despite the similar binding mode, some small variations are observed in the interactions with the two agonists. One notable difference is the hydrogen bond between S279$^{7.42}$ and the 3'-OH of the ribose moiety, which is present in the NECA-bound structure, but absent in the adenosine-bound one, due to a differently modeled rotation of the serine's side chain at this position, in which the OH-group from serine is flipped away from the ribose structure. However, looking at the cryo-EM map of the adenosine-bound structure, only a poorly resolved map is observed for that sidechain. Consequently, the rotamer is not modeled with high confidence, and the structural relevance of the different rotamer is unclear. Pharmacological characterization of the S279$^{7.42}$A mutant by Thimm et al.

demonstrated an even more drastic reduction of potency for adenosine (> 6200-fold), compared to NECA (> 1000-fold), determined in cAMP assays.[195] This further implies a direct interaction between the 3'-OH of the ribose with S279$^{7.42}$, not only for NECA, but also for adenosine.

Additionally, the interactions between the 2'-OH and 3'-OH of the ribose moiety with H280$^{7.43}$ are presented differently in the two publications. While these hydroxyl groups in the publication on the adenosine-bound structure are both presented to form a hydrogen bond with a different nitrogen atom of H280$^{7.43}$, the authors of the NECA-bound structure expect hydrogen bonds with both OH-groups to be formed with just one of the nitrogen atoms of H280$^{7.43}$. The reason for the discrepancy between both publications lies in the differently modeled side chain of the histidine, which is rotated by 180° in one structure, as compared to the other. The rotamer presented in the adenosine structure is likely not correct, since the bond length and angles do not align well with hydrogen bond characteristics. Thus, it can be assumed that the interaction presented in the NECA-bound structure is the relevant one and likely applies to the binding mode of adenosine as well.

Notably, also the distance of the presumed hydrogen bonds, differs among the structure. The distance between the hydrogen groups and the nitrogen atoms in H280$^{7.43}$ is ~ 3.5 Å in the adenosine-bound structure, and 2.7 Å, and 3.1 Å, respectively, in the NECA-bound structure. In contrast, the distance between the hydrogen bond partners N254$^{6.55}$ and *N*7 and N^6H_2 of the adenine core of the agonists is shorter for adenosine, as annotated in the structures in Figure 12. This reflects the slightly different relative position of adenosine and NECA in these structures. One potential cause for that could be the interaction between T89$^{3.36}$ and the nitrogen of NECA's additional 5'-*N*-ethylcarboxamide moiety.

As mentioned previously, adenosine displays strikingly different potencies at the $A_{2A}AR$ as compared to the $A_{2B}AR$, with EC_{50} values of 0.7 µM and 24 µM, respectively, and the same holds true for NECA, with K_i values of 20 nM and 1900 nM, respectively.[170, 196] Chen et al. speculate that the residue E174^{ECL2} might be a key determining factor for these differences.[111] In case of the $A_{2A}AR$, the amino acid corresponding to E174^{ECL2} in the $A_{2B}AR$, namely E169^{ECL2}, was observed to form a salt bridge to a histidine residue in the $A_{2A}AR$'s ECL3 in some crystal structures, which was shown to play a role in the dissociation of orthosteric ligands.[111, 194, 197] Mutation of either of the salt bridge-forming residues $E169^{ECL2}$ and $H264^{ECL3}$ in the $A_{2A}AR$ increased the dissociation rate for ligands with long residence times.[198]

The fact that the side chain of $E174^{ECL2}$ is not resolved in the NECA-bound cryo-EM structure of the $A_{2B}AR$ is an indication to the authors that this residue is not involved in any significant interaction. One interaction would be a hydrogen bond formed with the adjacent N^6H_2 of the adenine core of NECA.[111]

Importantly, however, it was not mentioned in the publication of the $A_{2B}AR$ structure that in the NECA-bound cryo-EM structure of the $A_{2A}AR$ (PDB-ID 6GDG, 4.1 Å)[192], the respective $E169^{ECL2}$ is not resolved either. Two years before the elucidation of the NECA-bound cryo-EM structure of the $A_{2A}AR$, the active state co-crystal structure of the NECA-bound $A_{2A}AR$ in complex with an engineered $G\alpha_s$ protein had already been solved (PDB-ID 5G53, 3.4 Å).[194] In contrast to the cryo-EM structure, an interaction of $E169^{ECL2}$ and the N^6H_2 of the adenine core was well resolved in that crystal structure. In the publication on the cryo-EM structure of the $A_{2A}AR$, it was argued that the missing interaction of $E169^{ECL2}$ with NECA is likely due to the high flexibility of the ECL2 at a physiological pH.[192] In many crystal structures of the $A_{2A}AR$ that were determined at a pH < 6, a salt bridge between $E169^{ECL2}$ and $H264^{ECL3}$ is observed.[73, 192] The NECA-bound cryo-EM structure of the $A_{2A}AR$, however, was solved at a physiological pH of 7.5, at which the ionic bond between $E169^{ECL2}$ and $H264^{ECL3}$ is not favored, due to the deprotonated state of histidine ($pK_a \sim 6$).[192, 199] This missing interaction of $E169^{ECL2}$ likely resulted in a more disordered ECL2, which might have been the reason for the the low-resolution of the cryo-EM map for this residue in the NECA-bound cryo-EM structure of the $A_{2A}AR$.[192] Of interest, the $A_{2B}AR$ does nor harbor a respective histidine in its ECL3, but two lysines.[52]

In any way, the limited map quality for $E174^{ECL2}$ that was observed in the adenosine- and NECA-bound structures is not a unique feature of the $A_{2B}AR$ cryo-EM structures, and does not provide a structural reason for the vastly different affinities of adenosine and NECA towards the $A_{2B}AR$, compared e.g. to the $A_{2A}AR$.

Another hypothesis is that a slight rotation of NECA and the nearby residues H251$^{6.52}$ and N254$^{6.55}$ in the A_{2B}AR, compared to the A_{2A}AR (NECA), might contribute to the different affinities. Figure 13 details the different rotamers of H$^{6.52}$ among the A_1-, A_{2A}- and A_{2B}AR.

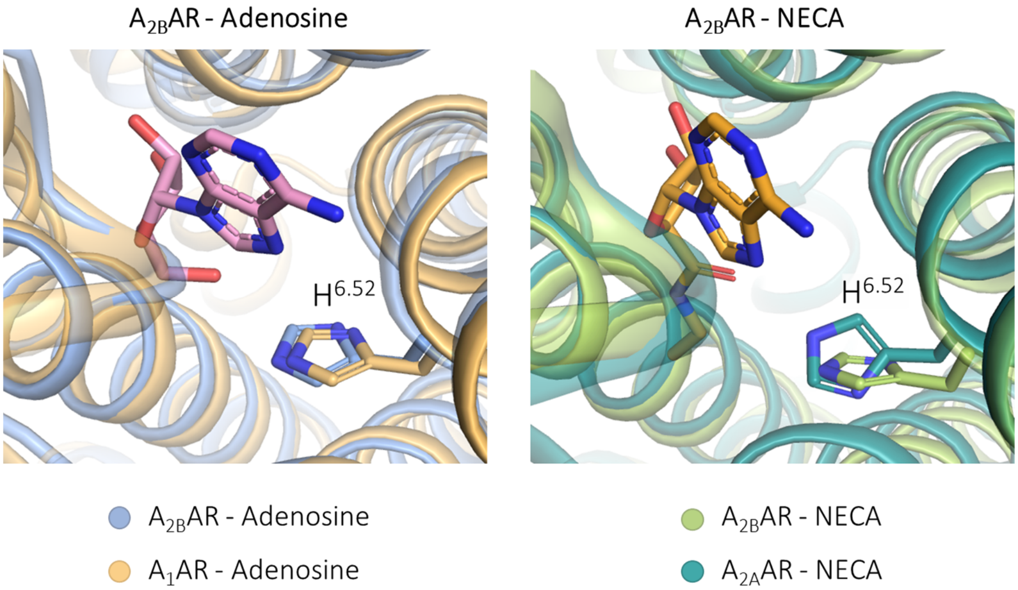

Figure 13. Comparison of the rotamers of residue H$^{6.52}$ in the cryo-EM structures of A_1-, A_{2A}- and A_{2B}AR. PDB-IDs: A_{2B}AR-Adenosine: 8HDO,[185] A_{2B}AR-NECA: 7XY7,[111] A_1AR-Adenosine: 5UEN,[193] A_{2A}AR-NECA: 6GDG.[192]

The difference in the rotation of residue H$^{6.52}$, specifically observed in the NECA-bound structure presented on the right, is thought to be caused by the presence of V250 at position 6.51 of the A_{2B}AR, and might result in a slightly compromised interaction between NECA and H251$^{6.52}$ of the A_{2B}AR. Interestingly, in the adenosine-bound structure of the A_{2B}AR this rotation is not observed, as the H$^{6.52}$ rotamer is modeled identically to the respective H$^{6.52}$ of the adenosine-bound A_1AR (see left panel of Figure 13). However, as evident from the differences in the adenosine-bound A_1AR and the adenosine- and NECA-bound A_{2A}AR structures, the interactions of the 5'-OH of adenosine and the 5'-*N*-ethylcarboxamide moiety of NECA are likely different. In the adenosine-bound structures of the A_1AR (PDB-ID 5UEN)[193] and the A_{2A}AR (PDB-ID 2YDO)[200], the 5'OH forms hydrogen bonds via a water molecule to N$^{5.42}$ (and H$^{6.52}$ in A_{2A}AR), whereas in the NECA-bound A_{2A}AR cryo-EM structure a direct interaction between its carbonyl group and H$^{6.52}$ is observed. Assuming the same interactions in the A_{2B}AR, the different rotamers of H250$^{6.52}$ among the NECA- and adenosine-bound A_{2B}AR structures might be explained by the involvement of unresolved water molecules in the interaction of adenosine with the receptor. Also, the map quality for the H250$^{6.52}$ residue in the adenosine-bound structure is not ideal, and the presence of a different rotamer cannot be excluded.

Consequently, the underlying structural determinants for the low affinity of adenosine towards the $A_{2B}AR$ remain elusive. However, for NECA, the well-resolved unusual rotamer of H$^{6.52}$ might indeed be a contributing factor for its receptor selectivity. Unclear is, if this structural difference is the only plausible reason for the selectivity, or if it is accompanied by other unique structural features of the receptor, e.g. in the poorly-resolved ECL2 region.

1.6.3.3 The $A_{2B}AR$ structures in complex with BAY 60-6583

Apart from the two $A_{2B}AR$ structures with the endogenous agonist and its derivative, both research groups also solved structures with the non-nucleoside partial agonist BAY 60-6583. Surprisingly, the proposed binding mode of the agonist is different among the two structures, as illustrated in Figure 14 stated below.

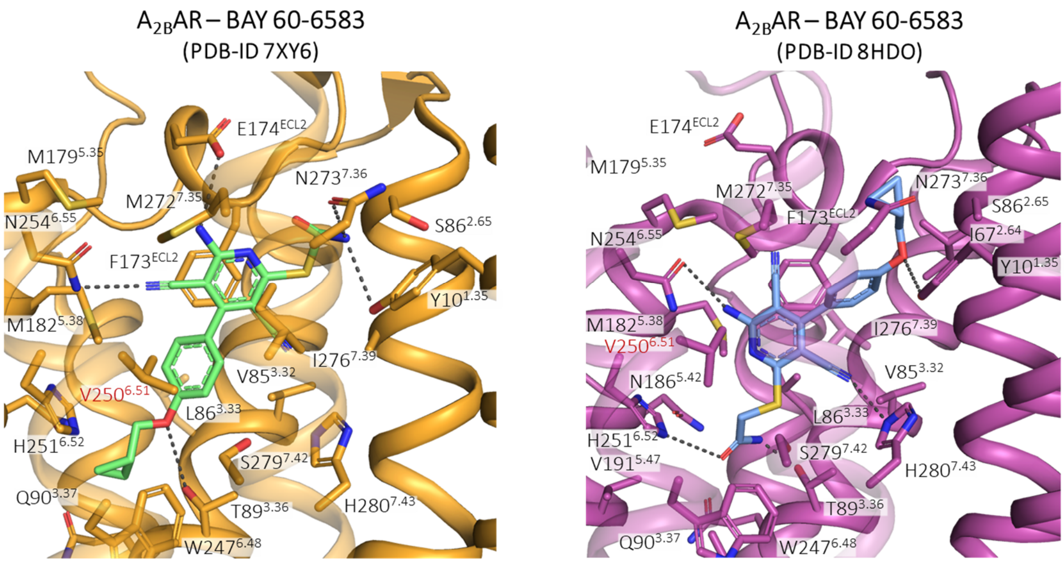

Figure 14. Detailed illustration of the differently modeled binding modes of BAY 60-6583 in the two $A_{2B}AR$ cryo-EM structures.

The structure with the PDB-ID 7XY6, listed in column D in Table 3 and presented in orange and green, was solved by Chen et al.,[111] while the structure with the PDB-ID 8HDO, listed in column C in Table 3 and presented in purple and blue was solved by Cai et al.[185] Comparing the structures, many of the sidechains of the orthosteric binding pocket are oriented similarly, yet the cyclopropyl moiety of the ligand points towards the core of the receptor in one, and towards the extracellular domain in the other structure. Despite the differently assumed binding modes, both groups identified or proposed several interactions, also with residues that were found to be involved in the binding of adenosine/NECA, e.g. N254$^{6.55}$, T89$^{3.36}$, H280$^{7.43}$ for polar interactions.

However, looking at the cryo-EM maps of both complexes, it seems that in the purple/blue structure presented on the right-hand side of Figure 14, the ligand might be modeled incorrectly. Figure 15 displays the map of the ligand and some adjacent sidechains of that structure. Additionally, the modeled binding modes of BAY 60-6583 of both structures are superimposed in the same density for comparison.

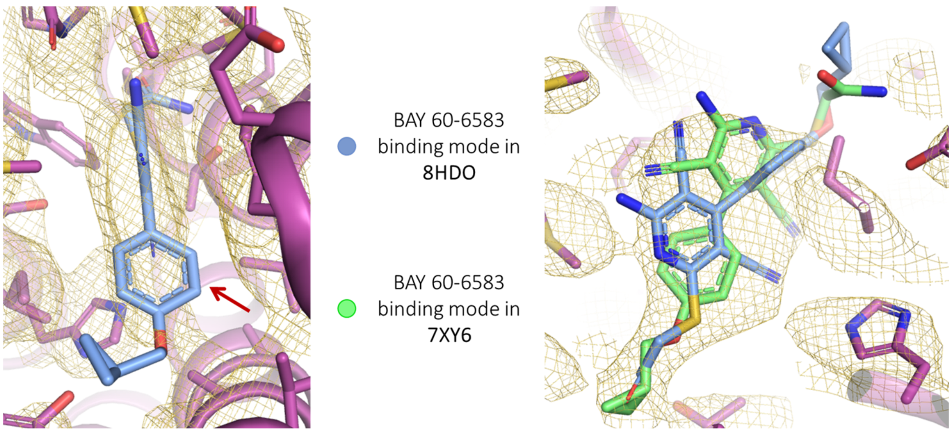

Figure 15. Presentation of the map of the ligand and some adjacent side chains of the structure 8HDO.

One irregularity in the model of structure 8HDO is the position of the phenyl moiety, which is modeled perpendicular to the observed map and with incorrect bond lengths. Also, in the 8HDO structure the lipophilic cyclopropyl residue is pointing towards the surface of the receptor, instead of the aliphatic residues at the bottom of the orthosteric binding pocket. The authors state that the N^6H_2 of BAY 60-6583 forms hydrogen bond interactions with N254$^{6.55}$ (see Figure 14), however, the distance and angles are unfavorable for hydrogen bond interactions (N-O distance 3.6 Å, φ = 114°). Instead, the binding mode of BAY 60-6583 as modeled in the structure 7XY6 aligns well with the observed ligand map of structure 8HDO, and is similar to the binding mode of the resembling partial agonist LUF5833 at the $A_{2A}AR$, as observed in an X-ray crystal structure.[201]

For these reasons, the binding mode observed in the 7XY6 structure solved by Chen et al., presented on the left in Figure 14, seems more likely. Additionally, in their publication more functional data, in form of cAMP assays, was provided to validate the structure. Therefore, only that structure will be regarded in the following discussion. In that structure, BAY 60-6583's position overlaps with the previously observed binding site of NECA, and its cyclopropyl moiety makes close hydrophobic contacts with residues, which were also involved in interactions with NECA or adenosine, such as L86$^{3.33}$, V191$^{5.47}$, W247$^{6.48}$, and H251$^{6.52}$. However, some contacts previously observed with the ribose groups of NECA and adenosine, namely S279$^{7.42}$ and H280$^{7.43}$, are not observed for the partial agonist. Residue E174^{ECL2}, which was not resolved in the NECA-bound structure, is resolved in the BAY 60-6583-bound complex where it forms a weak interaction with the amino group on the pyridine ring of the ligand.[111] Additionally, BAY 60-6583 occupies a "secondary binding pocket", formed by the extracellular ends of TM1, TM2 and TM7, where the acetamide of the partial agonist is thought to interact with Y10$^{1.35}$ and N273$^{7.36}$ by hydrogen bonds.[111]

Figure 16 compares the positions of NECA and BAY 60-6583 in the A_{2B}AR binding pocket and illustrates the position of the acetamide moiety of the latter.

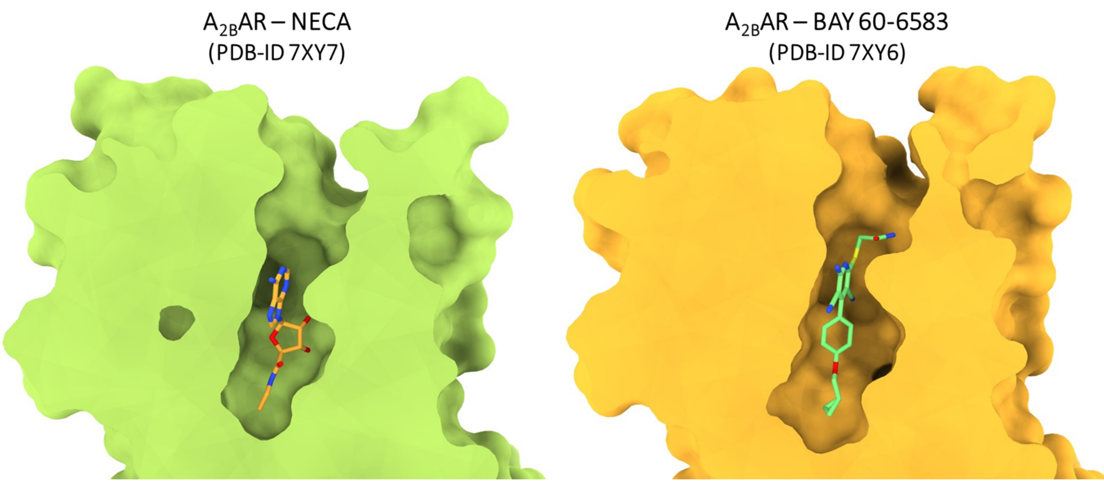

Figure 16. Comparison of the binding modes of NECA and BAY 60-6583 in the A_{2B}AR illustrated in cross section.

Of these two residues, the interaction with N273$^{7.36}$ is presumed to be partly responsible for the selectivity of the compound, especially towards the A_{2A}AR (K_i > 10,000 nM).[111, 196] In the A_{2A}AR, position 7.36 is occupied by a tyrosine whose bulky side chain potentially interferes with the accommodation of the acetamide group. This hypothesis is supported by results of cAMP assays that were performed with interchanged mutants of both receptors. The same was noticed with regard to $V250^{6.51}$, which is thought to be the key determinant for the high selectivity of BAY 60-6583 towards the $A_{2B}AR$. Mutation of residue $L249^{6.51}$ to $V249^{6.51}$ in the $A_{2A}AR$ resulted in a > 700-fold increase in potency in cAMP assays, from an EC_{50} value of 4.17 mM for the wt $A_{2A}AR$, to an EC_{50} value of 5.82 nM for the $L249^{6.51}V$ mutant. For comparison, the EC_{50} value of BAY 60-6583 for the wt $A_{2B}AR$ was determined to be 3.67 nM in the same experimental set-up.[111]

1.6.4 Conclusion and open questions

The four agonist-bound cryo-EM structures published at the end of 2022 present valuable first structural insights into the $A_{2B}AR$. While the NECA- and BAY 60-6583-bound structures published by Chen et al. elucidated some structural differences between the $A_{2B}AR$ and the A_1- and $A_{2A}AR$ subtypes that could contribute to the striking pharmacological profile of these agonists, these aspects are most likely not exhaustive. With regard to the adenosine structure, no structural determinants for the vastly different potency of the endogenous ligand towards the $A_{2B}AR$ were provided. One clear drawback of the structures is the low resolution of the ECL2 region, which was proven to have a significant influence on the potency and selectivity of ligands towards the $A_{2B}AR$.[92]

As evident from the ongoing clinical trials, the biggest pharmacological potential regarding the $A_{2B}AR$ is currently seen in the utilization of antagonists in the immunotherapy of cancer.[124] Therefore, knowledge on the exact binding pose of antagonists would be of even greater use to support the development of selective or dual-acting antagonists with suitable pharmacodynamic and pharmacokinetic profiles. Currently, despite the emergence of numerous cryo-EM structures and ongoing progress in the field,[202] antagonist-bound structures of GPCRs are still typically solved by X-ray crystallography. According to GPCRdb, of the over 600 published cryo-EM structures solved of GPCRs, only 12 were solved in complex with antagonists and only six of those were structures of class A GPCRs. This stands in contrast to the 214 published antagonist-bound GPCR structures solved by X-ray crystallography, of which 204 structures were of class A GPCRs.[52] Consequently, X-ray crystallography is still the method of choice for the experimental structure determination of antagonist-bound class A GPCRs, including the $A_{2B}AR$.

Also, the recent advance in protein structure predictions using e.g. AlphaFold cannot close this gap in experimental antagonist-bound structures, since the presence of ligands and other factors such as covalent modifications, environmental factors, different conformational states and protein-protein interactions are not (sufficiently) accounted for in these models, yet.[203, 204] Therefore, in order to truly and reliably capture the complexity of a GPCR's interaction, experimental structures are still indispensable. Nevertheless, also in the course of this thesis, AlphaFold structure predictions were used to support the process of experimental structure determination, specifically with regard to protein engineering which is necessary to facilitate the crystallization of GPCRs. The engineering of GPCRs and other important aspects of the crystallography project will be the focus of the upcoming sections.

1.7 Methods for X-ray crystallography

In order to crystallize any protein, a multitude of different techniques must be employed, from the cloning of the protein, to its expression, purification and crystallization. The flowchart depicted in Figure 17 provides an outline of the standard workflow which is followed throughout the process. The theoretical background on the key aspects of this workflow will be addressed in the following sections.

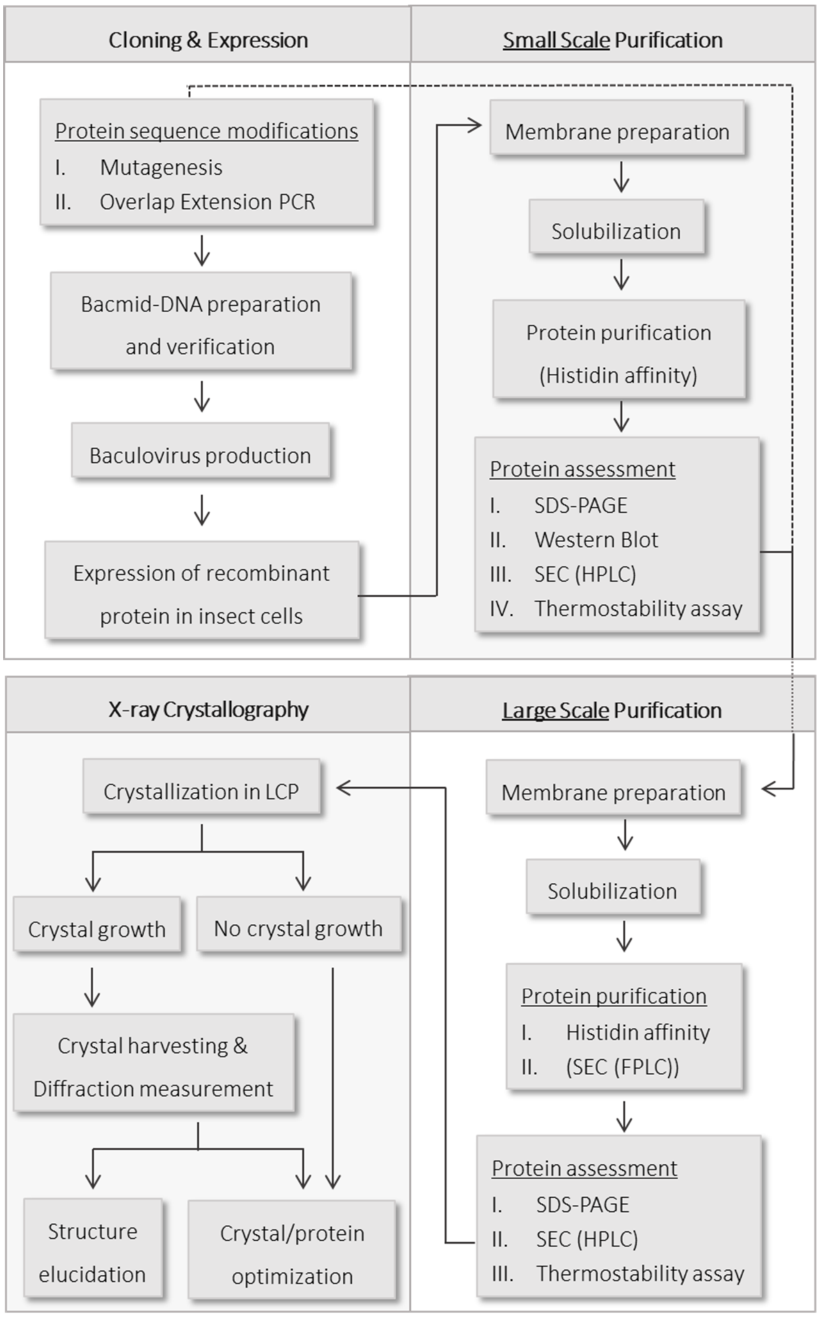

Abbreviations:

PCR = polymerase chain reaction

DNA = deoxyribonucleic acid

SDS-PAGE = sodium dodecyl sulfate polyamide gel electrophoresis

SEC = size-exclusion chromatography

HPLC = high-performance liquid chromatography

FPLC = fast protein liquid chromatography

LCP = lipidic cubic phase

Figure 17. General workflow from protein sequence modifications to the crystallization of the $A_{2B}AR$.

1.7.1 GPCR engineering

The crystallization of GPCRs often poses significant challenges, and hurdles are encountered at every stage of the process.[106] Firstly, the overexpression of native GPCRs often proves insufficient to generate the high quantities of protein required for their crystallization. Secondly, purifying the receptors involves extracting them from the cell membranes, which can result in their destabilization. Thirdly, GPCRs exhibit an inherent flexibility that, although crucial for their signaling function in the physiological context, may inhibit the formation of well-ordered crystals. And lastly, they have only a limited polar surface area available to form the crystal contacts that are necessary for obtaining well-ordered, diffraction quality crystals.[106, 205]

With the exception of rhodopsin, the structure elucidation of all GPCRs by X-ray crystallography has required extensive protein sequence modification to overcome the above-mentioned hurdles. These modifications encompass e.g. the introduction of fusion partners, point mutations, the truncation of flexible *N*-/*C*-termini and/or the utilization of conformation-specific antibodies.[52, 205] Especially the application of a fusion partner enabled a major breakthrough in the field of GPCR X-ray crystallography.[206]

The term fusion partner refers to a small, soluble, ordered and crystallization-prone protein,[106] and the approach of replacing the inherently flexible ICL3 with such a fusion protein was first used on a GPCR in 2007, for the crystallization of the β_2AR.[206, 207] By placing the fusion protein between TM5 and TM6 of the receptors, two hurdles are tackled at once: The inherent flexibility, mainly attributed to the major outward swing of TM6 upon activation, and the scarcity of hydrophilic regions for crystal contacts. Today, GPCRs have been crystallized with various fusion proteins displaying a variety of secondary structures. These include e.g. the chain A of lysozyme from *tequatrovirus T4* (e.g. β_2AR),[207] thermostabilized apocytochrome b_{562} from *escherichia coli* (e.g. A_{2A}AR),[65] flavodoxin from *desulfovibrio vulgaris* (e.g. cannabinoid receptor 1),[208] and the glycogen synthase from *pyrococcus abysii* (e.g. orexin receptor 1).[209]

Another strategy that must oftentimes be employed to facilitate the crystallization of GPCRs is site-directed mutagenesis, which can fulfill several purposes:[205, 210]

i. An increase in protein expression,
ii. Enhancement of thermo-/detergent-stability of the protein,
iii. locking of the receptor in the desired conformation, and
iv. removal of PTM sites that could introduce microheterogeneity.

One approach to identify beneficial point mutations is the alanine scanning, i. e. the individual mutation of each amino acid of the receptor to alanine followed by purification and evaluation.[211] Alternatively, point mutations previously utilized in related GPCRs could be useful for identifying favorable point mutations. Also, the evaluation of different amino acids in known and conserved structural motifs may be considered. Either way, the identification and especially the combination of point mutations is a labor-intensive undertaking, as the effect of several otherwise advantageous single mutations can be detrimental on the receptor, when combined.[205] Additionally, each mutation could potentially interfere e.g. with ligand binding capacity of the receptor, even if mutations directly in the ligand binding site are avoided.[212]

1.7.2 Solubilization

In order to purify GPCRs, they have to be isolated from the expression host's cell membrane in a process termed solubilization. In order to obtain a stable GPCR sample upon solubilization, two inherently contradictory events must overlap: The extraction of the mainly hydrophobic membrane proteins from the lipid membrane, and their stabilization in an aqueous environment instead.[213] The conventional method of solubilization, which is also the prevalent method in GPCR crystallography, is the utilization of detergents. The standardly used detergents are n-dodecyl-β-D-maltoside (DDM) and lauryl maltose neopentyl glycol (LMNG) which are strong enough to extract the 7-TM proteins from the membrane, yet mild enough to maintain their stability.[210, 214] Both are amphipathic molecules consisting of a nonionic polar head group and a hydrophobic chain that spontaneously form micelles which protect the hydrophobic protein surfaces from water, when used above their critical micelle concentration (CMC).[213, 215] For an efficient solubilization of the proteins from the membrane a typically very high concentration of detergent is employed (e.g. 1 % (w/v)). For the subsequent purification steps the detergent concentration is usually gradually lowered (e.g. to 0.025 % (w/v)), but must always remain above the CMC to prevent micelle disruption and aggregation of the protein.[210] Oftentimes the detergent-soluble cholesterol analog cholesteryl hemisuccinate (CHS) is added to the main detergent solution, since it was shown to be critical for maintaining the protein stability of many GPCRs.[216] The chemical structures of the two most commonly used detergents and CHS are provided in Figure 18.

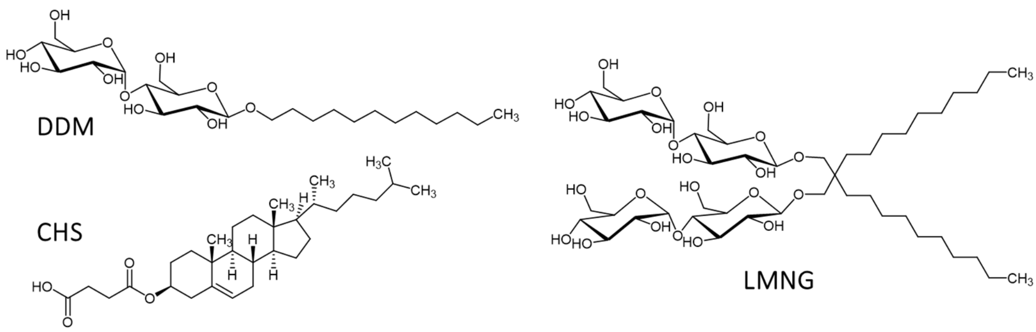

Figure 18. Chemical structures of the detergents DDM, CHS and LMNG.

1.7.3 Histidine affinity purification

The successful crystallization of a protein requires a high purity of the sample.[217] Today, many different methods are available for the purification of proteins, broadly classified into physiochemical purification methods and affinity purification methods. Examples for affinity-based purification methods are the use of antibodies, substrates, ligands and metal ions that are immobilized on a solid matrix to be used in a chromatography setting.[218] For structural studies, recombinant GPCRs are oftentimes equipped with one or more specific tag sequences which enables their effective purification.[219] Among all tags, histidine tags (His-tags) are the most commonly used since they are small, less disruptive than other tags, and facilitate an effective purification at quite high recovery rates.[102, 218] Polyhistidine-tagged proteins can be purified based on their interaction with cations such as Ni^{2+} and Co^{2+} that are immobilized on a polymer matrix, a principle which was termed “immobilized metal affinity chromatography”, first introduced in 1975.[220] Upon binding, the recombinant proteins can be gradually freed from protein contaminants and eluted from the polymer matrix under mild, non-destructive conditions, using e.g. competitive displacement with increasing imidazole concentrations.[221, 222]

1.7.4 Size-exclusion chromatography

Sometimes, structural studies require an additional polishing purification step for the protein of interest, which can be achieved e.g. by size-exclusion chromatography (SEC).[102] SEC is a form of liquid chromatography that allows for the separation of proteins relative to their hydrodynamic radius, based on the proteins' interaction with the spherical, porous particles of the stationary phase.[223] The proteins are passed over the porous particles as part of the mobile phase of the chromatography system, whereby large proteins, that are unable to penetrate the defined pores, pass over the stationary phase more quickly and elute first. With decreasing hydrodynamic radius, or simplified molecular size, the molecules penetrate better into the pores and consequently their elution is retarded.[224] Thus, this method can be used to differentiate between large protein aggregates, the monodisperse protein of interest, and protein impurities, in case they exhibit a different hydrodynamic volume.[223] With the appropriate column and chromatography system, this separation can be performed in a preparative manner to yield a highly homogenous and pure protein sample. For the crystallization of GPCRs "in meso", which was performed in this thesis and will be addressed in the upcoming section 1.7.6, this polishing step is oftentimes not necessary, since this method tolerates larger amounts of impurities and aggregates, compared to other crystallization methods.[102] In contrast, the analytical application of SEC is indispensable for the characterization of protein variants with regard to their monodispersity, protein yield and potentially their thermostability.[225, 226] Figure 19 illustrates the principle of SEC.

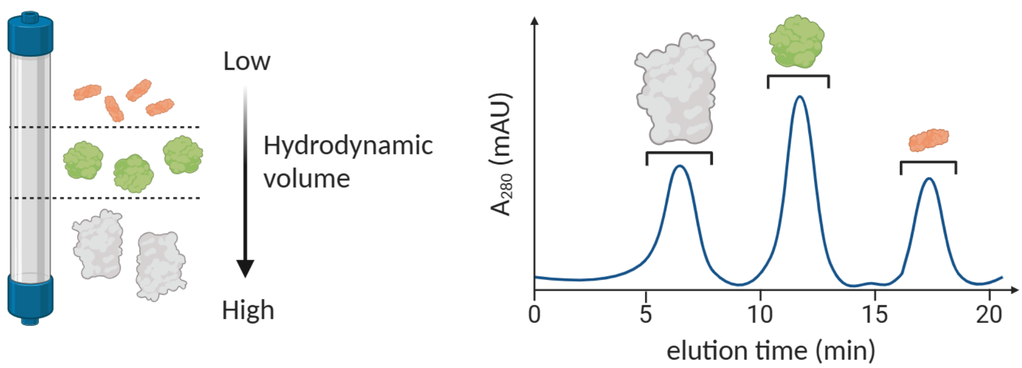

Figure 19. Illustration of the principle of size exclusion chromatography.

1.7.5 Thermostability assessment

Although the assessment of a protein's thermostability can be conducted using an analytical SEC, a different method was generally used in the course of this thesis, namely the CPM-based thermostability assay. CPM is the abbreviation for 7-diethylamino-3-(4'-maleimidylphenyl)-4-methylcoumarin which is a thiol-specific fluorochrome that is practically nonfluorescent in its unbound form.[227, 228] However, upon reaction with thiols, such as the thiol-groups in the native cysteines of a protein, and excitation with a wavelength of 384 nm, the thiol-CPM adduct emits a fluorescence that can be measured at a wavelength of 470 nm. In folded proteins, cysteine residues are typically situated within the protein's interior where they engage in helix-helix interactions. The gradual, temperature-induced unfolding of the protein exposes them to the solvent and the CPM dye, which results in a temperature-dependent rise in fluorescence. Due to the inaccessibility of cysteines in well-folded proteins, this rise in fluorescence correlates with the overall integrity of a protein.[228] Typically, the obtained fluorescence signal results in a sigmoidal curve that can be fitted using nonlinear regression equations. The melting temperature of a protein is defined as the point of inflection of these sigmoidal curves.[229]

The advantage of this thermostability assay is the limited protein amount that is necessary for its conduction, as well as the simultaneous analysis of multiple samples.[228] Generally, the assessment of a protein's thermostability is a useful method for the characterization of protein variants, as the thermostability is one of the best indicators for the crystallization potential of a membrane protein.[225] The following Figure 20 illustrates the basic principle of the CPM assay.

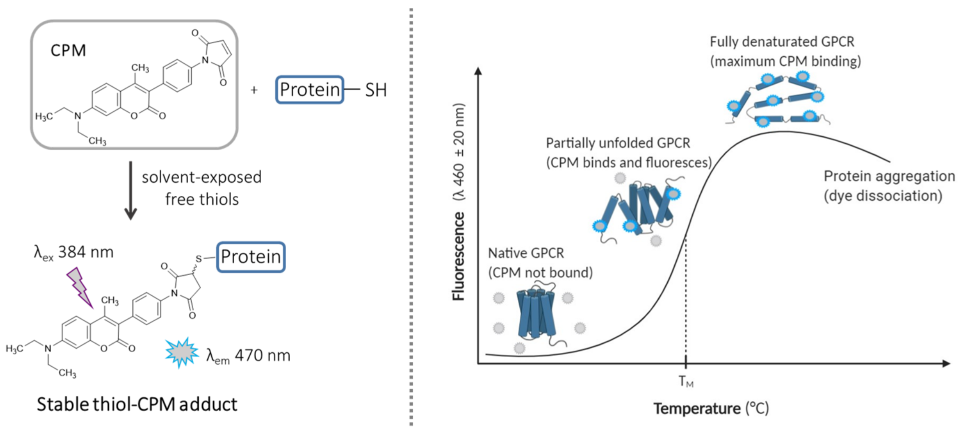

Figure 20. Schematic representation of the CPM reaction and a typical sigmoidal curve.

1.7.6 Crystallization in LCP

Several methods are available for the crystallization of membrane proteins, which can be divided into two major types: The *in surfo* and the *in meso* methods. *In surfo* refers to the crystallization of membrane proteins directly in the presence of the detergents, whereas *in meso* requires the reconstitution of the membrane proteins into a lipid bilayer of a "cubic mesophase" which is assumed to be more native and functionally relevant.[230, 231] Due to the protein's reconstitution into the cubic phase, this method is also commonly termed lipidic cubic phase (LCP) method.[230]

This method makes use of the fact that lipids, when mixed with an aqueous (protein) solution, can self-assemble in a variety of different mesophases, depending on factors such as their chemical structure, but also temperature, hydration, and composition of the aqueous solution.[232] Several of these mesophases can support the crystallization of membrane proteins, including the LCP, but also other mesophases like the lipidic sponge phase,[231, 232] which will also be of interest in this thesis. The success of the crystallization in LCP, especially for GPCRs,[233] can be attributed to several factors. One aspect is its compatibility with many different precipitant conditions which are necessary to reduce the protein's solubility and therefore induce the nucleation and growth of the protein crystals.[232, 234] Additionally, the LCP was shown to tolerate higher rates of protein impurities, since its spacial constraints prohibit the diffusion of larger impurities and aggregates.[232, 235] Importantly, the LCP favors a certain type of crystal packing (type I) that contributes to a better order of the molecules within the crystal and a better diffraction.[236]

The process by which the crystallization of membrane proteins occurs is thought to happen in several stages:[231, 237]

i. The protein is reconstituted into the "bicontinuous" cubic mesophase, which can be imagined as a three-dimensional molecular sponge. The lipid bilayer makes up the "fabric" of the sponge and aqueous channels within the LCP correspond to the pores that run throughout the sponge.
ii. An excess of precipitant solution is added to the LCP, which destabilizes this system by diffusion of the components into the mesophase. The mesophase does not normally dissolve during this stage, but stays intact.

iii. The components of the precipitant solution initiate a series of phase transitions and separations. One of the sheet-like separated phases gets enriched with protein, which ultimately leads to nucleation and growth of the protein crystal.

Figure 21 illustrates the principle of crystal nucleation starting from the bicontinuous cubic mesophase.

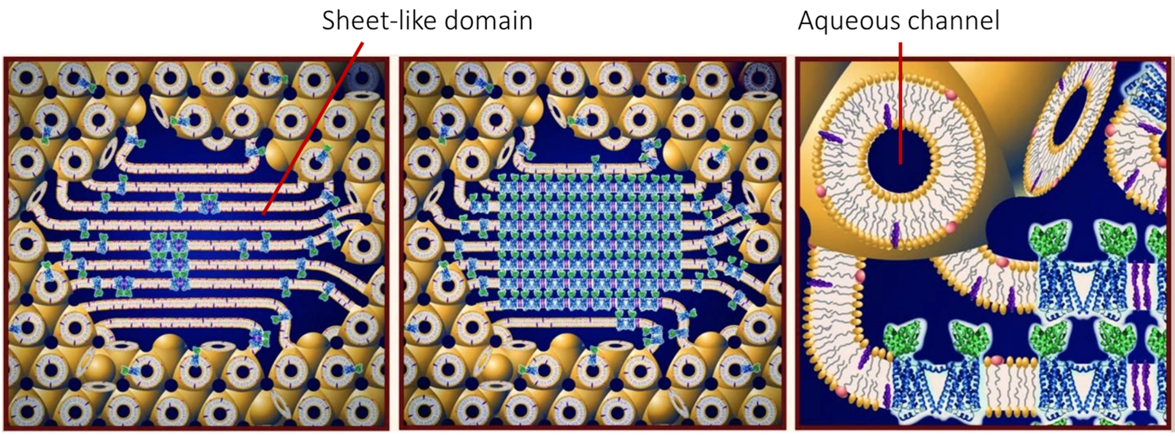

Figure 21. Schematic representation of the proposed events during the crystallization of membrane proteins. Modified from Caffrey.[237]

The most common class of "host lipids" used for LCP crystallization are monoacylglycerols (MAGs), for GPCRs specifically the MAG monoolein, which is the one that was standardly used throughout this thesis. But also other MAGs have been utilized successfully, e.g. monopalmitolein and monovaccenin, which differ from monoolein in the length of their acyl chain or the position of the olefinic bond.[210, 238] The acyl chain characteristic of the host lipid can have a significant effect on the *in meso* crystallogenesis of a protein. For example, with decreased acyl chain lengths the thickness of the lipid bilayer decreases as well and the diameters of the aqueous channels within the LCP expands, which might be of special interest for membrane proteins with larger extra- or intracellular domains.[239–241] Therefore, the screening of different host lipids might be beneficial, specifically for proteins that behave well but exhibit a limited crystal formation with the standard MAG monoolein.[242] Another important factor regarding the host lipid is the observation that the addition of cholesterol to the MAG proved to be essential for the production of structure-grade crystals of several GPCRs and cholesterol is therefore commonly added to the main host lipid (e.g. 10 % (w/w)).[210, 237] The chemical structures of the MAGs mentioned herein is depicted in panel A) of Figure 22.

While different mesophases are observed at a broad range of lipid:water ratios and temperatures, the desired LCP is formed only at very specific conditions. Generally, the temperature-composition phase behavior of most MAGs is very similar to that of monoolein, provided in panel B) of Figure 22.[240] Yet some MAGs, such as monopalmitolein and monovaccenin, require a higher water content compared to the approximately 40 % required for the LCP formation with monoolein.[243, 244] Another difference to consider is that e.g. monovaccenin tolerates only little variation in the relative water content and the surrounding temperature.[243] The monoolein-based LCP is stable at temperatures between 18 °C and 22 °C; below or above these temperatures the LCP shifts into the lamellar phase or sponge phase, respectively.[245] Therefore, experimental steps involving the LCP are standardly performed at 20 °C.

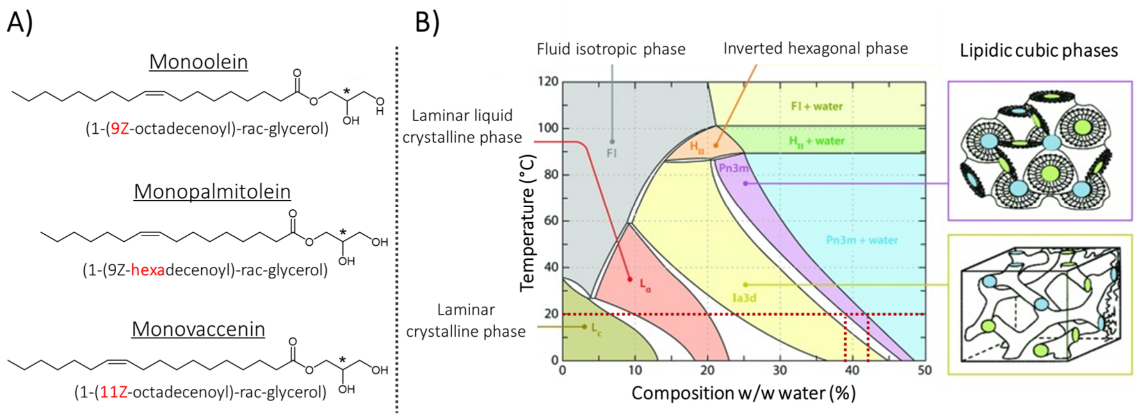

Figure 22. Chemical structures of the three relevant MAGs (A) and phase diagram of the monoolein-water system (B) Figure adapted from Caffrey and Rupp.[237, 246]

2 Aim of the Thesis

Since its discovery in 1992, the physiological relevance of the A_{2B}AR has oftentimes been underestimated in comparison to the other AR subtypes, perhaps due to the strikingly low affinity of the endogenous agonist adenosine for the receptor. Nowadays, the unique functions of the A_{2B}AR are well established, specifically its involvement in pathological conditions such as hypoxia, inflammation and cancer.[169, 179, 247] In this regard, adenosine's distinctive affinity even renders the receptor particularly intriguing as a drug target, as it is thought to remain silent under healthy, physiological conditions and is activated mainly in pathological states.[248] This perspective is reflected in several ongoing clinical studies investigating the potential use of A_{2B}AR antagonists, specifically for the treatment of tumors/cancers.[124]

In the beginning of this project, structural insights into the A_{2B}AR were non-existent, and even in the light of the recent cryo-EM structures, there are still many open questions regarding the structural basis of the A_{2B}AR's unique pharmacology. Also, while the cryo-EM structures provided insights into the active state of the receptor, the antagonist-bound state remains elusive. Yet, this information would be particularly valuable for the development of A_{2B}AR antagonists with improved properties, e.g. for the immunotherapy of cancer and the treatment of pain. In addition, a crystal structure could potentially illuminate the structural features of the receptor's ECL2, which was shown to be a key determining factor for the selectivity of several ligands,[92, 249] but was only partially resolved in the cryo-EM structures of the A_{2B}AR.[111, 185]

Therefore, the goal of this study was to:

i. Generate a highly stable, well-expressing A_{2B}AR construct,
   that is suitable to

ii. Crystallize the receptor using the LCP method,
   in order to eventually

iii. Solve the first antagonist-bound crystal structure of the A_{2B}AR.

3 Results and Discussion

As discussed in section 1.7 of the introduction, the crystallization of GPCRs mostly requires extensive receptor modifications. On this account, a total of 233 distinct receptor constructs of the $A_{2B}AR$ were designed and analyzed in the effort of solving the first crystal structure of the receptor. The initial 58 of those constructs were analyzed during my master's thesis. The remaining 175 receptor constructs were conceptualized and processed as part of this doctoral thesis.

Figure 23 visually depicts the general architecture of the $A_{2B}AR$ constructs:

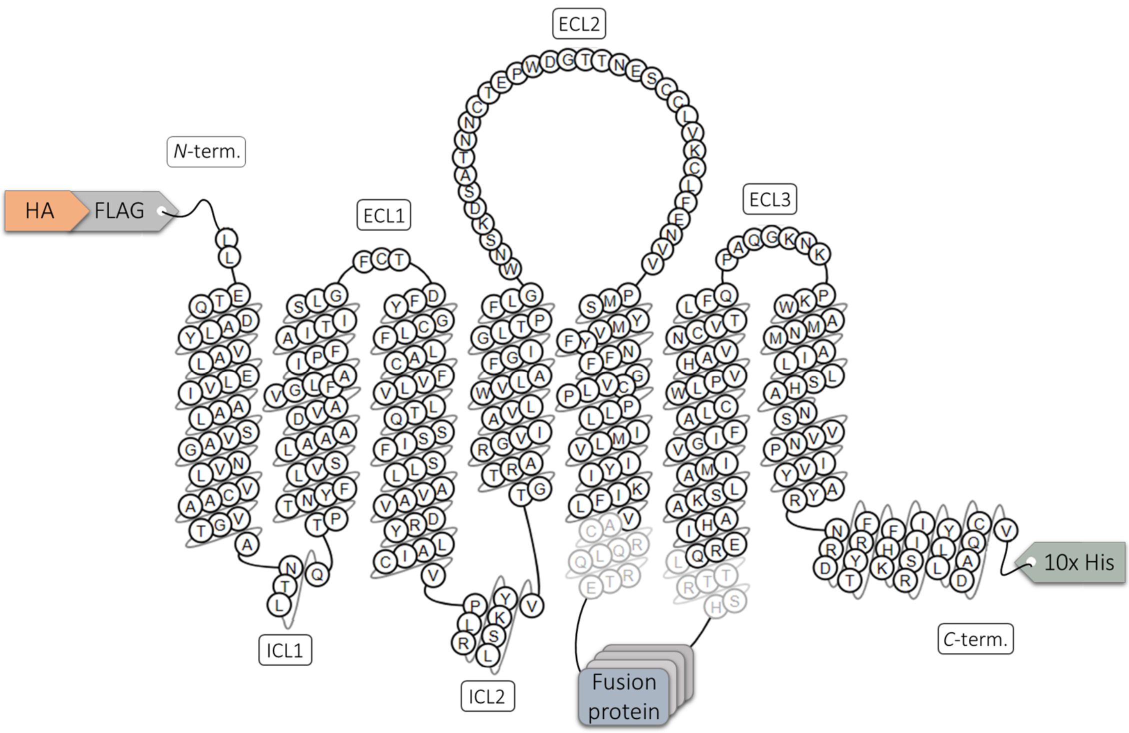

Figure 23. General architecture of the $A_{2B}AR$ constructs. Snake plot modified from GPCRdb.[52]

The general architecture of the recombinant $A_{2B}AR$ constructs was as follows: The *N*-terminal methionine was truncated and replaced by a signal sequence from influenza hemagglutinin,[250] in short HA-tag, and a FLAG-tag (sequence DYKDDDK)[251]. The fusion proteins were typically inserted between TM5 and TM6. In the process of optimizing this insertion site, e.g. for different fusion proteins, the exact insertion sites varied. In Figure 23 this is indicated by the faded outlines of the respective variable residues of TM5 and TM6. For the vast majority of the construct, and unless stated otherwise, the thermostabilized apocytochrome b_{562} from *Escherichia coli*, bRIL, was used as the fusion partner and was inserted between L213$^{5.69}$ and H221$^{6.22}$. On the *C*-terminus, the amino acids K316 to L332 were truncated and a deca-histidine tag was added to facilitate the purification of the receptor.

In order to stabilize the A_{2B}AR for crystallization, several strategies were applied:

I. A plasmid exchange from the original pFastBac1™ plasmid to a modified one,
II. the screening of numerous point mutations and their combination,
III. application of all in-house available fusion partners to either the *N*-terminus or the ICL3,
IV. the exchange from A_{2B}AR's native TM1 to A_{2A}AR's native TM1,
V. deletion of all *N*-terminal tags, and finally
VI. application of *N*-terminal truncations and linkers.

Please note that the that items III., application of all in-house available fusion partners to either the *N*-terminus or the ICL3, and IV., the exchange of A_{2B}AR's native TM1 for A_{2A}ARs native TM1, were already conducted as part of my master's thesis mentioned above.

Owing to the extensive range of receptor constructs, we assigned numerical labels to the various constructs based on the order in which they were conceived, ranging from test construct (TC) 1 to TC233. To enhance clarity, the data in the result graphs will be referenced using these numerical labels. Nevertheless, each section will provide an outline of the distinctions among the presented constructs. Furthermore, a comprehensive list of all modifications made to the A_{2B}AR constructs presented in this thesis is given in section 7.2 of the appendix, from page 305 onwards.

3.1 Starting point for this doctoral thesis

The project of crystallizing the A_{2B}AR was initiated shortly before the beginning of my master's thesis, which was submitted in September of 2019, entitled "Stabilization of the adenosine A_{2B} receptor for crystallization".[252] During the course of this thesis, I processed 58 A_{2B}AR constructs, which resulted in first improvements in the stability of the receptor. To provide an insight into the starting point for this doctoral thesis, the most important finding of this master's thesis will shortly be summarized.

The most significant improvement was achieved by exchanging the entire native TM1 of $A_{2B}AR$, with the entire native TM1 of $A_{2A}AR$. The rationale behind this extensive modification was based on the comparison of SEC results of the very first $A_{2B}AR$ constructs with the $A_{2A}AR$ construct, shown in Figure 24:

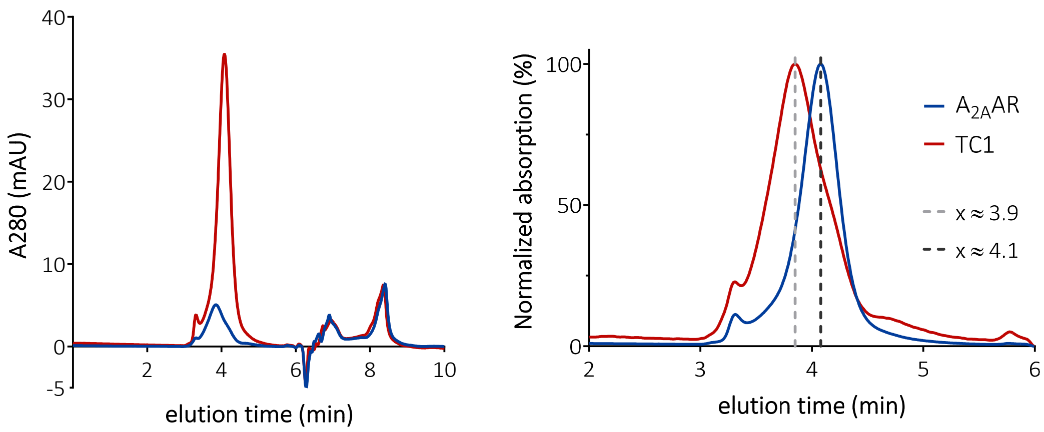

$A_{2A}AR$	$A_{2A}AR$ – No mutations
TC1	$A_{2B}AR$ – No mutations

Figure 24. Comparison of SEC results of the unmutated $A_{2A}AR$ and $A_{2B}AR$ constructs. This graph presents data collected in the course of my master's thesis.

Due to the extensive *C*-terminal truncation of both the $A_{2B}AR$ and $A_{2A}AR$ constructs used for this project (ΔK316-L332 for $A_{2B}AR$ and ΔA317-S412 for $A_{2A}AR$), the receptors share a molecular weight of approximately 50 kDa (including *N*-terminal tags and fusion partner bRIL). Consequently, it was previously assumed that these receptors would exhibit similar elution times in size-exclusion chromatography (SEC) analysis.

However, the notable shift of all initial $A_{2B}AR$ constructs to an earlier elution time in SEC was observed. Given that an earlier elution in the SEC column typically suggests a protein form with a larger volume, it led to the hypothesis that within our purified protein solution, the $A_{2B}AR$ might be present in an oligomeric state. This conjecture was further supported by a proposed homodimer model by Vittorio Limongelli (Universita della Svizzera italiana, Lugano), which suggests that the $A_{2B}AR$ can indeed form homodimers, and that TM1 and TM5 of the $A_{2B}AR$ may constitute an interface for the potential homodimeric arrangement of the receptor (see Figure 25).

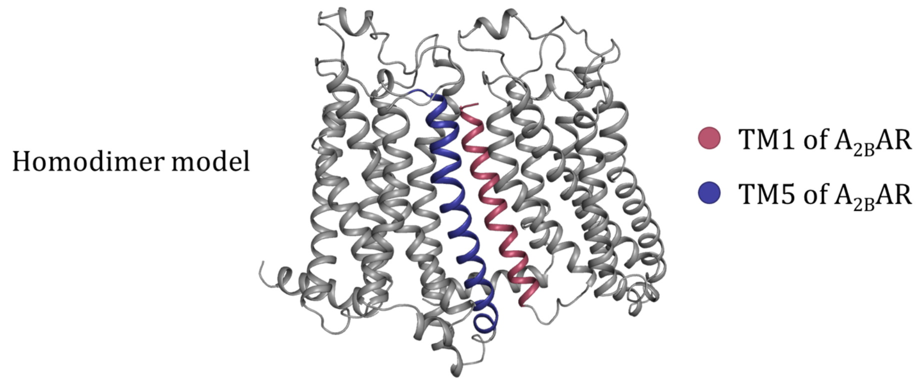

Figure 25. Homodimer model of the $A_{2B}AR$ as proposed by Vittorio Limongelli.

Since the $A_{2A}AR$ appears to predominantly exist in a monomeric state, one straightforward approach to disrupt this interface was to substitute one of the involved TM domains of the $A_{2B}AR$ with the corresponding TM domain of the $A_{2A}AR$. Therefore, the entire TM1 region of the $A_{2B}AR$ was replaced with the corresponding TM1 region of the $A_{2A}AR$, as TM1, unlike TM5, is believed not to play a significant role in the ligand binding pocket, which is of primary interest in the context of a potential co-crystal structure.

The result of this exchange is shown in the following Figure 26.

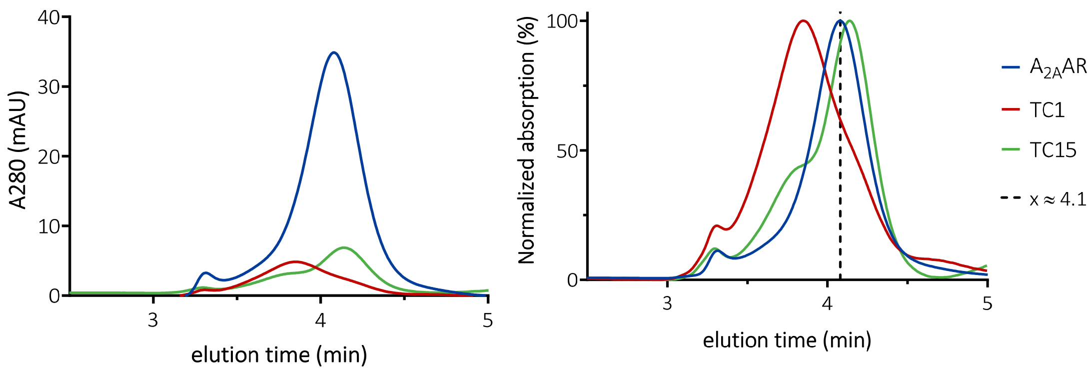

$A_{2A}AR$	$A_{2A}AR$ – No mutations
TC1	$A_{2B}AR$ – No mutations
TC15	$A_{2B}AR$ – TM1 exchange

Figure 26. Comparison of the unmutated $A_{2A}AR$ and $A_{2B}AR$ constructs with the $A_{2B}AR$ TM1 exchange construct. This graph presents data collected in the course of my master's thesis.

After exchanging TM1, the main peak of the $A_{2B}AR$ displayed a distinct shift to the right and eluted at similar time points as its stable counterpart $A_{2A}AR$. Through the utilization of a thermostability assay and "thermal SEC", this rightward shift was later confirmed to indicate enhanced stability of the modified protein. The results of these assessments are presented in the following Figure 27 and Figure 28.

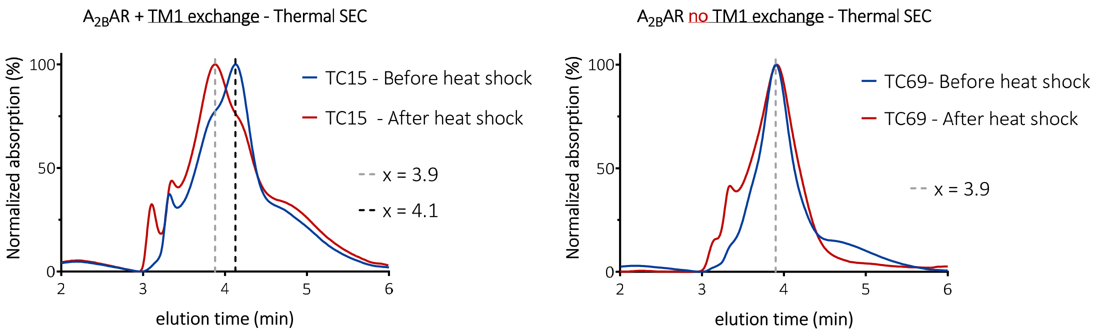

TC15	$A_{2B}AR$ – TM1 exchange
TC69	$A_{2B}AR$ – No TM1 exchange, no mutations

Figure 27. Results of the thermal SEC assessment of one $A_{2B}AR$ construct with TM1 exchange, and one construct without TM1 exchange. This graph presents data collected in the course of this doctoral thesis.

"Thermal SEC" refers to a method, during which a purified protein solution is exposed to a controlled heat shock, at a specific temperature and for a specific time, before subjecting it to SEC analysis.

The results of the thermal SEC showed a notable difference between the TM1 exchange construct, and an $A_{2B}AR$ construct without such a modification. Interestingly, the right-shift of TC15's main peak was reversed following the heat treatment at 42 °C for 5 min. The main peak eluted at 3.9 min, matching the elution time of the unaltered $A_{2B}AR$ construct. In contrast, the main peak of the $A_{2B}AR$ construct without the TM1 exchange eluted at 3.9 min, regardless of the heat treatment. As previously noted, an earlier elution in the SEC column indicates a larger protein volume, possibly due to (partial) unfolding or aggregation. Consequently, these findings suggest that the protein eluting earlier corresponds to unstable or incorrectly folded protein rather than receptor oligomers.

The unstable nature of the unmodified $A_{2B}AR$ constructs was also apparent from the thermal shift assay, presented in Figure 28:

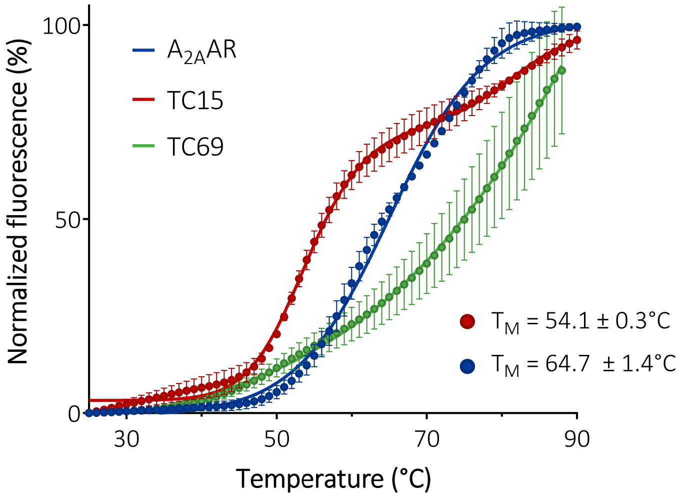

$A_{2A}AR$	$A_{2A}AR$ – No mutations
TC15	$A_{2B}AR$ – TM1 exchange
TC69	$A_{2B}AR$ – No TM1 exchange

Figure 28. Thermal shift assay results of $A_{2A}AR$, TC15 and TC69. Nonlinear fit (Boltzmann sigmoidal fit for $A_{2A}AR$ and TC69, biphasic sigmoidal fit for TC15) of normalized fluorescence data. The normalized fluorescence data is shown as dots ± their SD (n=2). The mean melting temperature is given. This graph partially presents data collected as part of my master's thesis ($A_{2A}AR$ & TC15).

For all early $A_{2B}AR$ constructs without the TM1 exchange, the thermostability results looked like those exemplarily shown for TC69. Only upon TM1 exchange, the desirable sigmoidal curve was observed, and a melting temperature (T_M) could be calculated. For TC15, the T_M was calculated to be 54 °C, approximately 10 °C less compared to its counterpart $A_{2A}AR$.

Upon closer inspection of the results of TC15, it becomes apparent that while the curve showed the intended sigmoidal behavior, it also displayed a biphasic nature. This characteristic is commonly observed in the early $A_{2B}AR$ constructs and can mostly be attributed to their relatively low expression levels. As expression levels increase, the Co^{2+} beads used in the purification process approach their binding capacity, leading to a reduction in non-specific binding of impurities. A visualization of this is given in the following Figure 29.

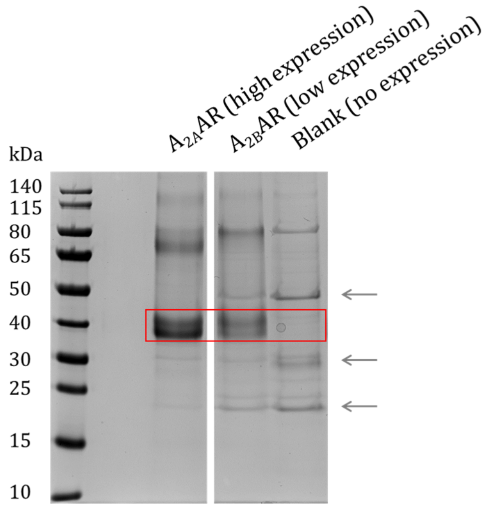

Figure 29. SDS-PAGE analysis of the indicated protein samples on a 10 % bis-Tris gel and subsequent staining with Coomassie R-250. For comparison of impurities, equal volumes of each protein were loaded. The gray arrows mark the most prominent impurities.

In order to account for the biphasic nature observed in the thermostability assay results of TC15 and other early constructs, a biphasic sigmoidal fit was occasionally applied to characterize the normalized data.

Based on these results, the hypothesis of existing homodimers of the $A_{2B}AR$ was put aside, but the positive effect of the TM1 exchange remained. Due to the improved stability of the TM1 exchange constructs, it was later used as a template to evaluate further strategies, such as plasmid exchange and other strategies that were employed in the course of this doctoral thesis. These results will be shown in the following sections.

3.2 Plasmid exchange to “GP64-pFastBac1”

Following the TM1 exchange, the “plasmid exchange” showed the next major improvement with regard to monodispersity of the receptor.

The initial rationale behind the plasmid exchange is based on the fact that the pFastBac1™ plasmid housing the gene of the highly expressed and stable $A_{2A}AR$ construct is not the original plasmid initially designed by Invitrogen, but a modified one.[73] The expression of the $A_{2A}AR$ previously employed the promoter of glycoprotein 64 (GP64),[73, 180, 253] an integral membrane protein that is essential for the virus's cell-to-cell transmission.[254, 255] In contrast, the original pFastBac1™

plasmid utilizes the polyhedrin promoter, which drives protein expression for a soluble virion structural protein.[256] Considering that the $A_{2B}AR$'s expression in the original plasmid was notably less efficient compared to that of the $A_{2A}AR$, plasmid exchange to the modified GP64-pFastBac1 plasmid was an obvious approach to enhance $A_{2B}AR$ expression levels.

The results of this approach are shown in the following Figure 30:

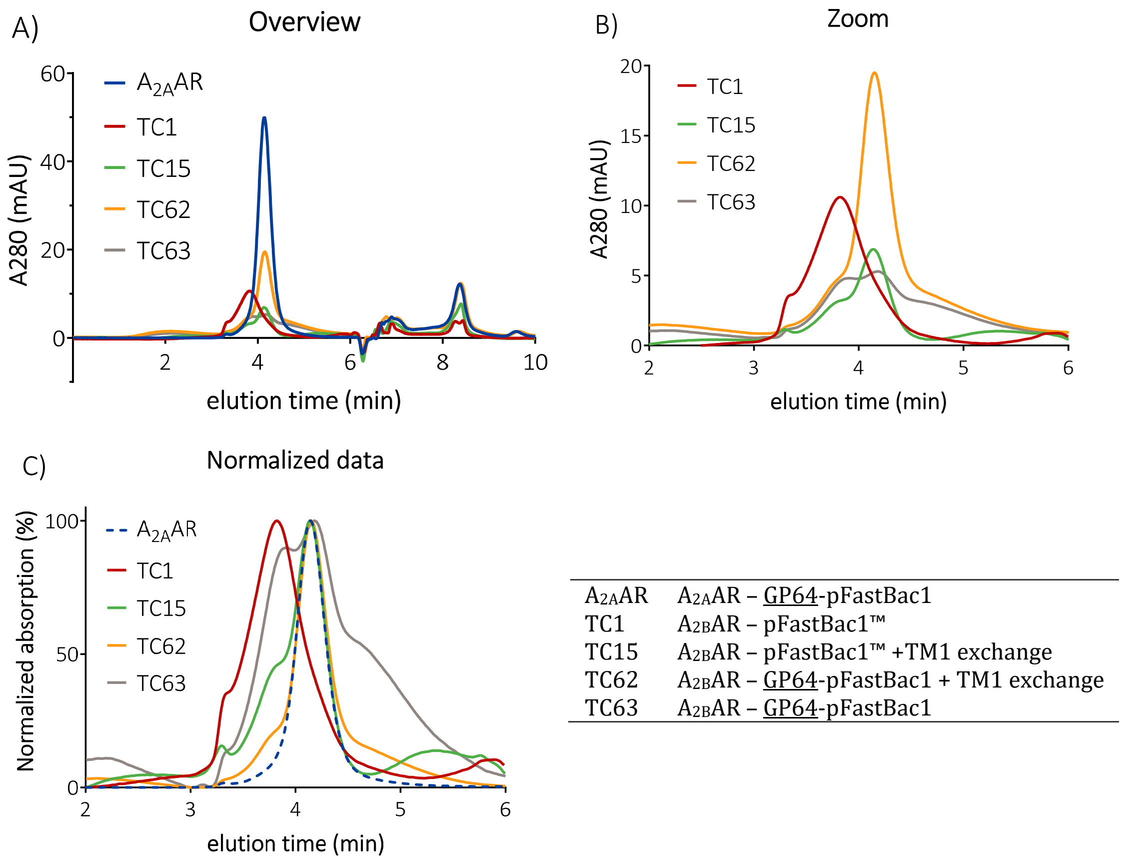

$A_{2A}AR$	$A_{2A}AR$ – GP64-pFastBac1
TC1	$A_{2B}AR$ – pFastBac1™
TC15	$A_{2B}AR$ – pFastBac1™ +TM1 exchange
TC62	$A_{2B}AR$ – GP64-pFastBac1 + TM1 exchange
TC63	$A_{2B}AR$ – GP64-pFastBac1

Figure 30. Analysis of the plasmid exchange for two $A_{2B}AR$ constructs and their comparison with $A_{2A}AR$. A) Complete elution profile of the SEC analysis. B) Elution profile of the region of interest of the SEC analysis. C) Normalized SEC data of the region of interest.

As seen in panel B) of the graph above, our goal to improve $A_{2B}AR$'s protein yield by exchanging the promotor was only partially reached. While for the TM1 exchange construct (shown in green and orange) the A280 nm signal was elevated from approximately 7 to 19 mAU, the yield of the $A_{2B}AR$ construct without further modifications (shown in red and gray) was even declined. However, the remarkable characteristic was not the protein yield of the plasmid exchange constructs, but their elution time. Interestingly, the sole act of switching promotors resulted in a noticeable stabilization of the receptor, evident by its primary peak appearing at an elution time of approximately 4.2 minutes. As discussed before, this later elution is believed to correspond to a more stable receptor construct.

The fact that plasmid exchange alone resulted in such an effect is particularly fortunate since this enhancement was achieved without any direct modification to the protein itself. Up to now, the precise mechanism behind this improved monodispersity remains unclear, given that the expressed protein should not differ from the previously expressed proteins using the the original pFastBac1™ plasmid.

The thermostability of these constructs was also assessed, as shown in Figure 31:

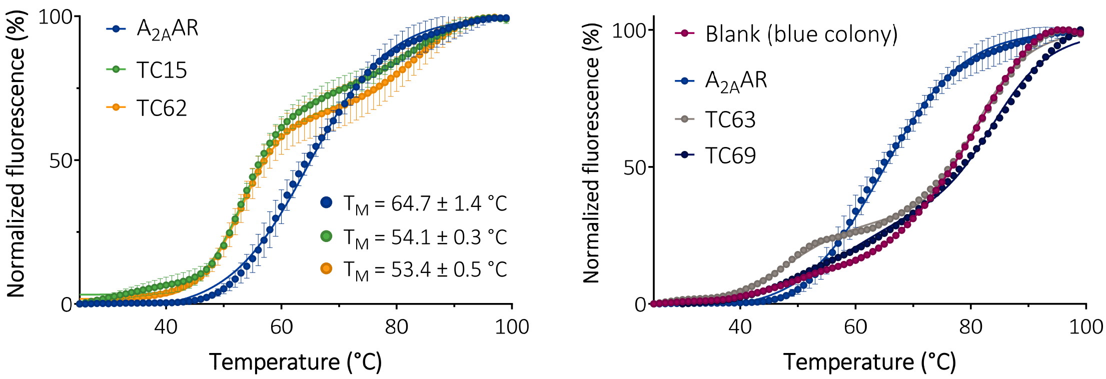

$A_{2A}AR$	$A_{2A}AR$ – GP64-pFastBac1
TC15	$A_{2B}AR$ – pFastBac1™ +TM1 exchange
TC62	$A_{2B}AR$ – GP64-pFastBac1 + TM1 exchange
TC63	$A_{2B}AR$ – GP64-pFastBac1
TC69	$A_{2B}AR$ – pFastBac1™
Blank	“Purified” sample of non-expressing, infected cells

Figure 31. Thermal shift assay of $A_{2A}AR$, selected $A_{2B}AR$ constructs with plasmid and/or TM1 exchange. Nonlinear fit ($A_{2A}AR$: Boltzmann sigmoidal, others: biphasic sigmoidal) of normalized fluorescence data. The mean, normalized fluorescence data is shown as dots ± SD (n=3 for $A_{2A}AR$ and TC62, n=2 for TC15, n=1 for remaining samples). The T_M was calculated as the mean ± SD of the first inflection point for $A_{2B}AR$ constructs and the only inflection point for $A_{2A}AR$ (TC15 n=2, TC62 and $A_{2A}AR$ n=3).

Judging from the thermostability data of the TM1 exchange constructs, it becomes apparent that despite the enhanced monodispersity, the plasmid exchange did not yield any advantage in terms of thermostability when compared to the original plasmid. In the case of the constructs lacking TM1 exchange, namely TC63 and TC69, the GP64-pFastBac1 plasmid induced a subtle sigmoidal signal, likely originating from the $A_{2B}AR$. This can particularly be seen when the results are compared to the blank sample.

The “blank” sample refers a sample that was processed in the same manner as all other samples, including the infection of insect cells, membrane preparation, and purification. The distinguishing factor is that this sample originated from cells infected with a baculovirus that lacked the genetic information of the A_{2B}AR, or any other recombinant protein. Consequently, it functions as a control to estimate the (in this case fluorescence) signal that can be attributed to common impurities, which are to be expected when working with proteins expressed at low levels. As illustrated in Figure 31, this signal resembles the characteristic curve shape observed in early A_{2B}AR constructs, such as TC69.

Summing up the data provided above, the plasmid exchange contributed to enhanced expression and monodispersity of the A_{2B}AR, particularly evident in the TM1 exchange construct. In terms of thermostability, there was no observed increase in the T_M. Nonetheless, the plasmid exchange has been validated, and as a result, the GP64-pFastBac1 plasmid was adopted as the standard vector for future A_{2B}AR constructs.

Since typically numerous constructs are processed simultaneously, not all newer constructs immediately incorporated this latest advancement. Therefore, some of the constructs presented in the following section were assessed using the original, inferior plasmid. Any constructs expressed in the original pFastBac1™ plasmid will be specifically indicated, as from here on the GP64-pFastBac1 plasmid will be regarded as the standard.

3.3 Point mutations

In the course of my master’s thesis, I conducted the assessment of many point mutations, including nine mutations utilized in the A_{2A}AR-StaR2(-bRIL) construct, which facilitated the co-crystal structures with 24 different ligands to date.[107] Seemingly, none of these mutations led to a significant improvement of A_{2B}AR’s stability.[252] However, prior to the TM1 exchange and the profound investigation addressing the unexpected SEC and thermostability results of the early A_{2B}AR constructs, it was not clear how such improvements would manifest.

As demonstrated in the previous chapter, the TM1 exchange construct expressed in the GP64-pFastBac1 plasmid showed a distinct improvement in monodispersity, stability and protein yield. Nevertheless, these characteristics were not yet sufficient for an initial crystallization attempt. Additionally, replacing an entire helix would represent a substantial modification, and achieving a crystal structure with such a chimeric protein could raise concerns about the authenticity and significance of the results. Therefore, the next objectives were as follows:

i. To further improve the monodispersity, thermostability and protein yield, and
ii. to reduce the modifications in the receptor's TM1.

3.3.1 Single point mutations in $A_{2B}AR$'s TM1

Therefore, the next point on the agenda was to narrow down which amino acids of $A_{2A}AR$'s TM1 might be primarily responsible for the stabilizing effect on the $A_{2B}AR$. For this cause, each amino acid of $A_{2B}AR$'s TM1 was individually replaced by the respective amino acid of the $A_{2A}AR$.

Figure 32 gives an overview of the respective amino acid sequences of both TM1s.

```
TM1 A2BAR         1.35          1.45          1.55
                   MLLETQDALYXALELVIAALSVAGNVLVCAAVGTAN
TM1 A2AAR                   |   || || |   |||||| ||
                    MPIMGSSVYITVELAIAVLAILGNVLVCWAVWLNS
```

Figure 32. Comparison of the TM1 domain amino acids between the $A_{2B}AR$ and the $A_{2A}AR$.

Since some of the residues in the TM1s are identical, a total of 20 constructs were designed to pinpoint the responsible, stabilizing amino acids.

The SEC results of these single point mutations are presented in the following Figure 33. With exception of three constructs, all of these TM1 mutation constructs were processed in parallel with the plasmid exchange constructs described earlier, and were therefore expressed using the original pFastBac1™ plasmid.

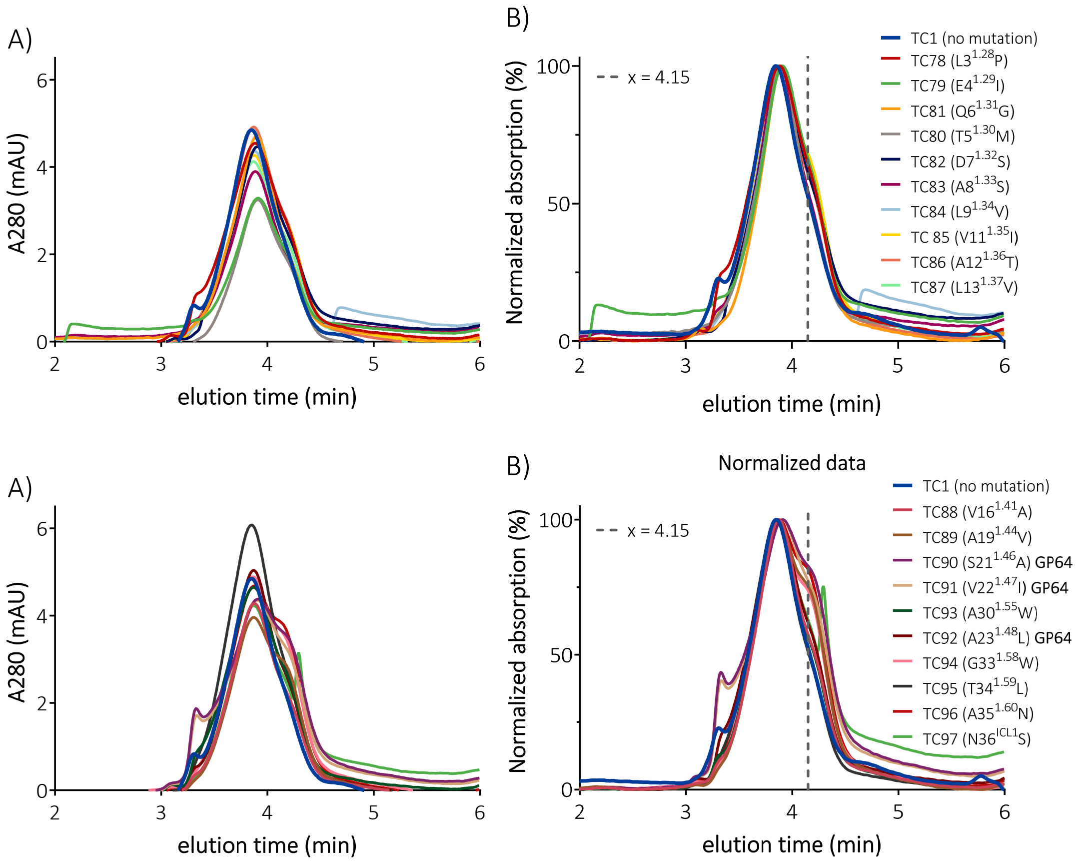

Figure 33. Evaluation of 20 single-point mutations in A_{2B}AR's TM1. For clarity, the results are divided into two sets. A) Elution profile for the region of interest in the SEC analysis. B) Normalized data from SEC analysis for the same region of interest.

Most of the point-mutated receptor constructs did not show a substantial difference, compared to the unmodified A_{2B}AR. However, some of the constructs in the lower part of the graph displayed a distinct small shoulder with an elution time of approximately 4.1 – 4.2 min. These six constructs will be focused on in the following Figure 34.

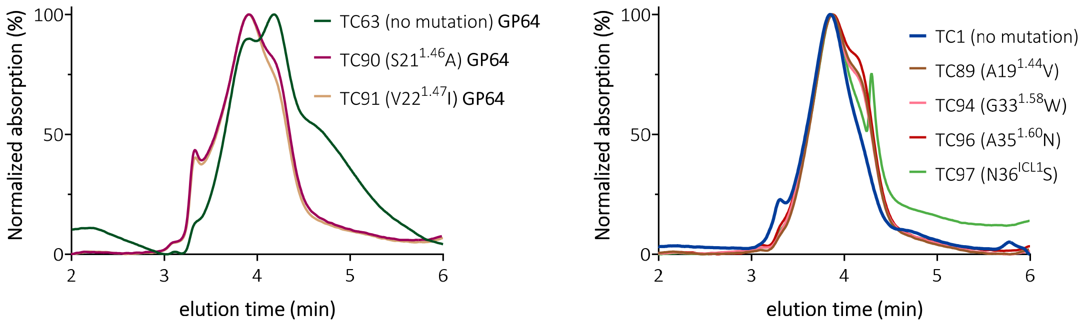

Figure 34. Evaluation of six selected single-point mutations in A_{2B}AR's TM1.

Unfortunate for the comparison, two of the six A_{2B}AR constructs displaying the favorable elution profile were expressed using the GP64-pFastBac1 plasmid, due to problems in obtaining recombinant baculovirus with the original pFastBac1™ plasmid. As shown before, the sole exchange of plasmids results in a (partial) right-shift of the elution profile. However, when compared to the results of the unmutated A_{2B}AR that was expressed using the GP64-pFastBac1 plasmid, the mutated constructs (TC90 and TC91) fall short, as their elution profile is less distinct at 4.1 to 4.2 min. Consequently, only the constructs presented in the right graph of Figure 34 were considered further.

Of those, the mutant N36^{ICL1}S elutes mainly at 3.9 min, as the other constructs do as well, but additionally shows an unusually sharp peak at 4.3 min, which is even later than the elution profile seen from the favorable TM1 exchange constructs. Therefore, also this construct was not considered further. The remaining three constructs, namely TC89, TC94 and TC94, corresponding to mutations A19$^{1.44}$V, G33$^{1.58}$W and A35$^{1.60}$N, all showed an advanced elution profile. Among these mutations, the A35$^{1.60}$N mutation showed the most substantial change. The A19$^{1.44}$V and G33$^{1.58}$W mutations showed a comparable peak form (see right panel of Figure 34), however, construct A19$^{1.44}$V showed a small decline in protein yield in comparison to the other point mutants as well as the unmutated receptor form (Figure 33).

Regarding the thermostability of these mutants, the assessment unfortunately did not yield the sigmoidal curves that are required for the analysis of this parameter. For this reason, it is not possible to make a statement about the thermostabilizing effect of these mutations.

Later, these three single point mutations in TM1 were combined, however, not until some other, promising mutations were discovered, which will be presented in the following chapters.

3.3.2 Mutations in the Na^+ binding site

The following section will focus on all point mutations involved in formation of the presumed Na^+ pocket of the receptor. Most of these mutations (up to TC35) were analyzed in the course of my master's thesis, and are shown for the sake of comparison. Figure 35 gives an overview of every SEC result of these mutants. Of note, all of the presented $A_{2B}AR$ constructs, shown in the following figures, were expressed using the original pFastBac1™ plasmid.

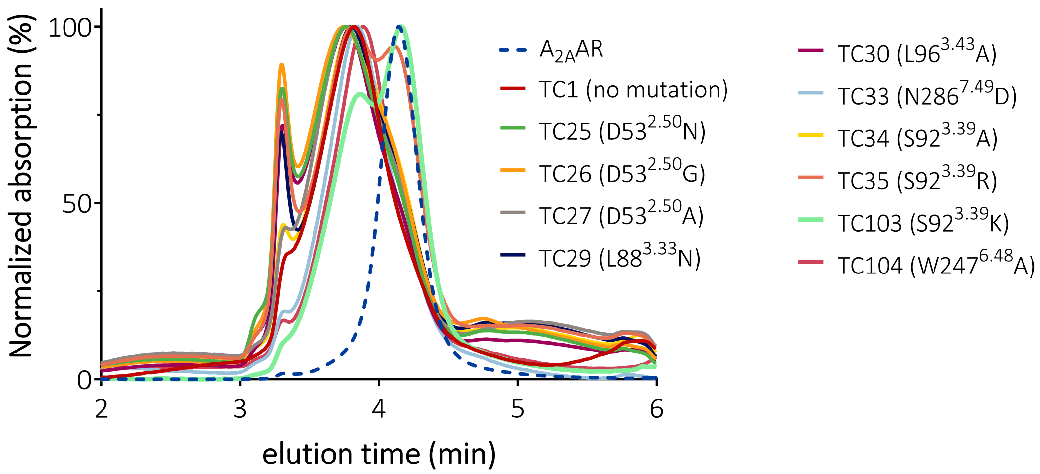

Figure 35. Analysis of all point mutations involving the presumed Na^+ binding pocket and comparison with $A_{2A}AR$ and unmutated $A_{2B}AR$. The normalized SEC data of the region of interest is shown. The constructs up to TC35 were processed in the course of my master's thesis.

As one can see from the overview of all Na^+ site mutations, the majority of alterations had a significant impact on the receptors' homogeneity. Next to the typical main peak at 3.8 min, most of the constructs show a distinct increase of the peak at 3.3 min, corresponding to aggregated protein.

The mutation of the residue $S92^{3.39}$ to basic amino acids, however, also led to the occurrence the protein peak at the favorable elution time of 4.2 min, as seen in the following Figure 36.

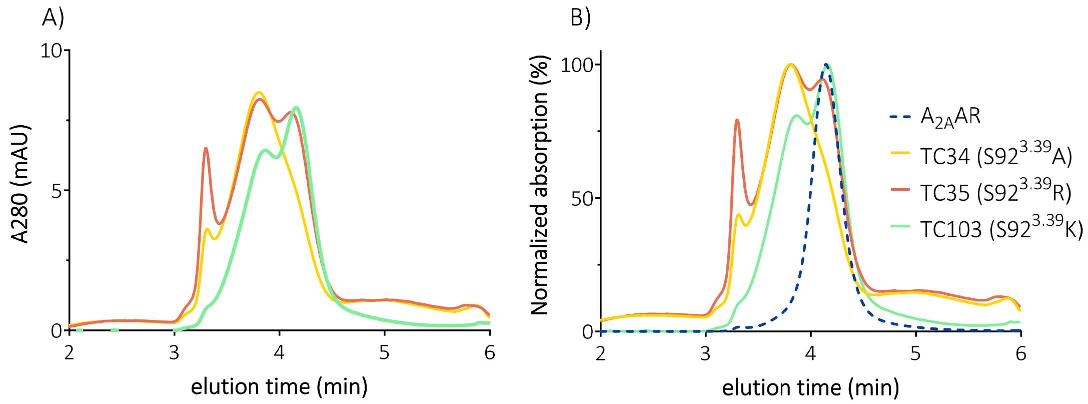

Figure 36. Analysis of three selected point mutations involving the presumed Na^+ binding pocket and comparison with $A_{2A}AR$ and unmodified $A_{2B}AR$. A) Elution profile of the region of interest of the SEC analysis. B) Normalized SEC data of the region of interest. TC34 and TC35 were analyzed in the course of my master's thesis.

The $S92^{3.39}R$ mutation, which was introduced based on a suggestion of the GPCRdb "Construct Design Tool",[52] displays both, a very prominent aggregation peak at 3.3 min, as well as the favorable peak at 4.2 min. At the time of the assessment, this receptor construct was not further considered due to the substantial aggregation and the fact that back then, it was not clear whether the peak at 3.8 min or 4.2 min corresponds to the favorable protein form.

However, this mutation site came back to light when the structure and function prediction tool "I-TASSER" (Zhang lab, University of Michigan)[257] was employed. I-TASSER is a top-ranked automated protein 3D structure prediction tool, that gives numerous analysis and predictions for a protein of interest, just by submitting its amino acid sequence.[257] Of note, these predictions were performed before the publication of AlphaFold.[203] One of the analyses included the prediction, which proteins, whose X-ray structure has been successfully solved before, might be the structurally most closely related to the protein of interest, in our case the $A_{2B}AR$. The result of this analysis is shown in the following Figure 37.

Top 10 Identified stuctural analogs in PDB

Click to view	Rank	PDB Hit	TM-score	RMSD^a	IDEN^a	Cov	Alignment	
	1	2ydvA	0.874	2.24	0.575	0.949	Download	Human adenosine A_{2A} receptor
	2	5uenA	0.860	2.39	0.479	0.928	Download	Human adenosine A_1 receptor
	3	3emlA	0.837	1.99	0.615	0.892	Download	Haemophilus influenzae Hia trimeric autotransporter
	4	2y00B	0.804	2.18	0.334	0.868	Download	Turkey β_1 adrenergic receptor
	5	2rh1A	0.790	2.64	0.297	0.874	Download	Human β_2 adrenergic receptor
	6	6a93A	0.787	2.69	0.241	0.874	Download	Human serotonine 5-HT_{2A} receptor
	7	5zbhA	0.786	3.08	0.207	0.898	Download	Human neuropeptide Y_1 receptor
	8	4ib4A	0.785	2.71	0.254	0.876	Download	Human serotonine 5-HT_{2B} receptor
	9	5ztyA	0.783	2.62	0.233	0.865	Download	Human cannabinoid CB_2 receptor
	10	4rnbA	0.780	2.60	0.249	0.858	Download	Human orexin OX_2 receptor

(a) Query structure is shown in cartoon, while the structural analog is displayed using backbone trace.
(b) Ranking of proteins is based on TM-score of the structural alignment between the query structure and known structures in the PDB library.
(c) RMSD^a is the RMSD between residues that are structurally aligned by TM-align.
(d) IDEN^a is the percentage sequence identity in the structurally aligned region.
(e) Cov represents the coverage of the alignment by TM-align and is equal to the number of structurally aligned residues divided by length of the query protein.

Figure 37. One of the results of the analysis performed by I-TASSER in 2020.The top 10 identified structural analogs to the A_{AB}AR are listed and various scores of the structural alignment are given. Highlighted in red is the personal annotation of the respective proteins, based on the PDB entry provided by the program.

As usual in the field of GPCR crystallography, several point mutations were applied to each of the presumably structurally related receptors in order to obtain their X-ray structure. One strategy to find suitable point mutations for the A_{2B}AR was therefore to analyze the mutation sites of these GPCRs and compare their native amino acids to the respective amino acids of the A_{2B}AR. When the native amino acids of the mutation sites were identical or similar between the receptors and the A_{2B}AR, the point mutations were transferred to the A_{2B}AR.

This led to the discovery of the S92$^{3.39}$K mutation, whose analog, S162$^{3.39}$K, was one of two thermostabilizing mutations that were introduced for the crystallization of the human serotonin 5-HT_{2A} receptor,[74] one of the predicted structural analogs of the A_{2B}AR. But even before that, the position 3.39 had already been argued to be a hotspot residue for the stabilization of class A GPCRs in the inactive state.[58, 258]

For the A_{2B}AR, the mutation S92$^{3.39}$K showed a significantly reduced aggregation peak as well as an enhanced peak at 4.2 min, compared to the previous S92$^{3.39}$R mutation. These improvements were similar to the TM1 exchange, with the advantage that only a single point mutation was necessary to achieve them. Another advantage was the increased thermostability that this mutation displayed, as shown in Figure 38.

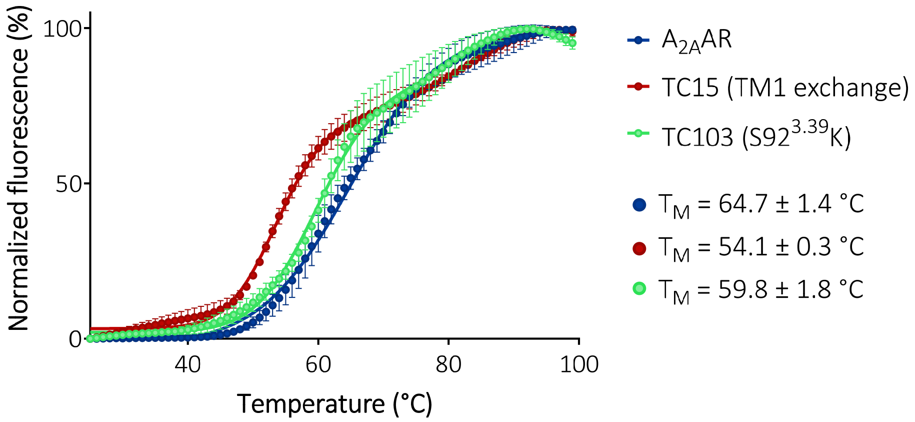

Figure 38. Thermal shift assay of $A_{2A}AR$, TC15 and TC103. Nonlinear fit ($A_{2A}AR$: Boltzmann sigmoidal, others: biphasic sigmoidal) of normalized fluorescence data. The mean, normalized fluorescence data is shown as dots ± SD. The T_M was calculated as the mean ± SD of the first inflection point for $A_{2B}AR$ constructs (n=2) and the only inflection point for $A_{2A}AR$ (n=3).

The $S92^{3.39}K$ mutation is the very first point mutation that enabled a convincing thermostability assessment, and additionally, it even showed a distinctly higher T_M as compared to the TM1 exchange construct (> 5°C).

Examination of this residue in a structure model of $A_{2B}AR$ gave a possible explanation for the substantial positive impact of this construct, as seen in Figure 39.

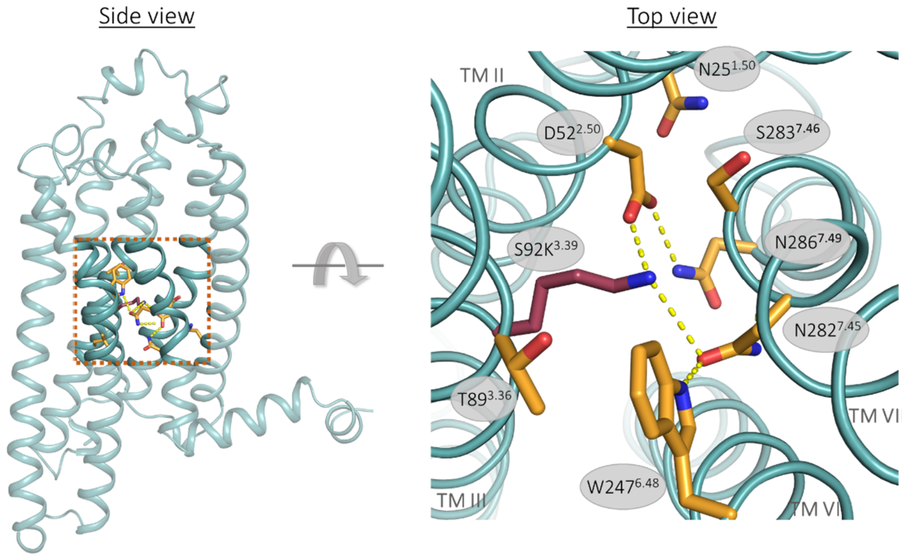

Figure 39. Possible interaction between the K92$^{3.39}$ residue of the described A_{2B}AR construct and the amino acids forming the presumed Na^+ pocket of the receptor. The scheme is based on the structure model of the A_{2B}AR from GPCRdb, April 2020.[52]

The reason for the stabilization was attributed to the occupation of the Na^+ binding site by the protonated amine of the lysine side chain. This interaction was presumed to induce similar effects as Na^+ on the inactive state of various receptors.[69]

Following the discovery of the beneficial impact of this mutation at the Na^+ binding site for the A_{2B}AR, it has since been successfully utilized in our laboratory to facilitate the crystallization of the related A_{2A}AR with seven distinct ligands.[259] These structures provide valuable insights into the mechanism of the S$^{3.39}$K mutation, as the A_{2A}AR has been structurally elucidated both with and without the mutation. As anticipated, these structures confirmed that the positively charged amine of the lysine side chain indeed occupies the allosteric Na^+ binding site, effectively mimicking sodium's stabilizing influence on inactive state GPCRs.[73, 107] Furthermore, it was demonstrated that despite its substantial stabilizing impact, the introduction of the mutation did not alter the receptor's overall transmembrane helix geometry.[73]

Later, this promising S92$^{3.39}$K construct was also expressed using the superior GP64-pFastBac1 plasmid, as shown in Figure 40.

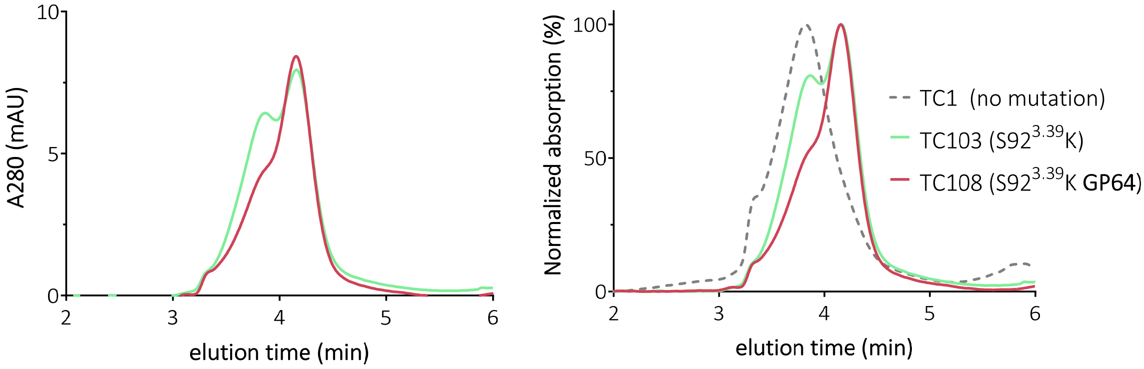

Figure 40. Analysis of the plasmid exchange for the S92$^{3.39}$K A_{2B}AR construct. A) Elution profile of the region of interest of the SEC analysis. B) Normalized SEC data of the region of interest.

Similar to the results observed in the other plasmid exchange constructs, the SEC analysis of the S92$^{3.39}$K-mutated A_{2B}AR construct revealed a pronounced monodispersity at an elution time of approximately 4.2 min upon application of the GP64-pFastBac1 plasmid. Compared to the unmutated A_{2B}AR in the original pFastBac1™ plasmid, the implementation of just this single point mutation and the promotor exchange resulted in a significantly improved elution profile. However, in contrast to the TM1 exchange constructs with the plasmid exchange (see TC15 and TC62 in Figure 30), the protein yield did not improve upon plasmid exchange.

In terms of thermostability, the results align with those of the other plasmid exchange constructs, since the T_M was nearly identical between the two constructs (see Figure 41).

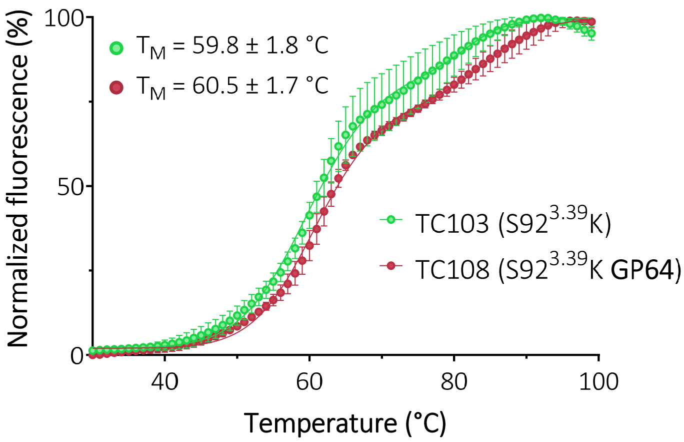

Figure 41. Thermal shift assay of TC103 and TC108. Nonlinear fit (biphasic sigmoidal) of normalized fluorescence data. The mean, normalized fluorescence data is shown as dots ± SD. The T_M was calculated as the mean ± SD of the first inflection point (TC103: n=2, TC108: n=3).

Naturally, the S92$^{3.39}$K mutation was also combined with the TM1 exchange, expressed in the GP64-pFastBac1 vector, in construct TC117 which is presented in the following Figure 42.

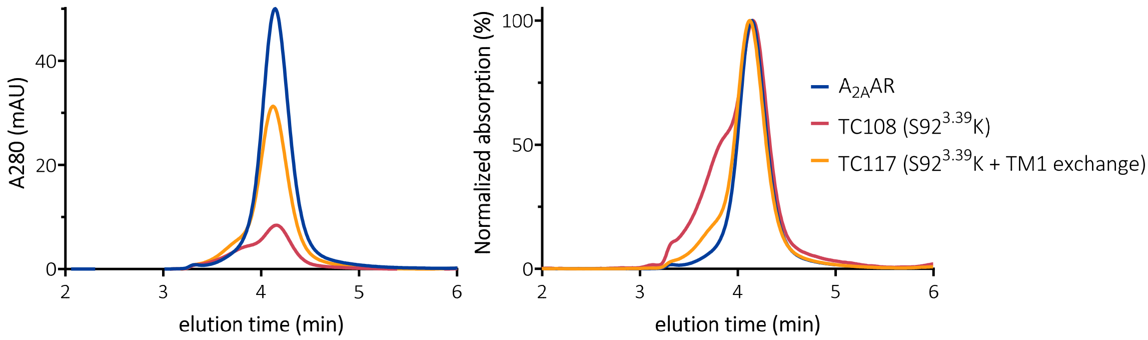

Figure 42. Comparison of construct TC108 and TC117 with A_{2A}AR. A) Elution profile of the region of interest of the SEC analysis. B) Normalized SEC data of the region of interest.

When all three stabilization approaches were employed in combination, the monodispersity of the A_{2B}AR closely resembled that of the benchmark A_{2A}AR, with only a minor early-eluting protein fraction noticeable in the SEC analysis. This also held true for the construct's thermostability, which, in comparison to TC108, showed an improvement by approximately 4°C and reached the same T_M as the A_{2A}AR, as depicted in Figure 43 below.

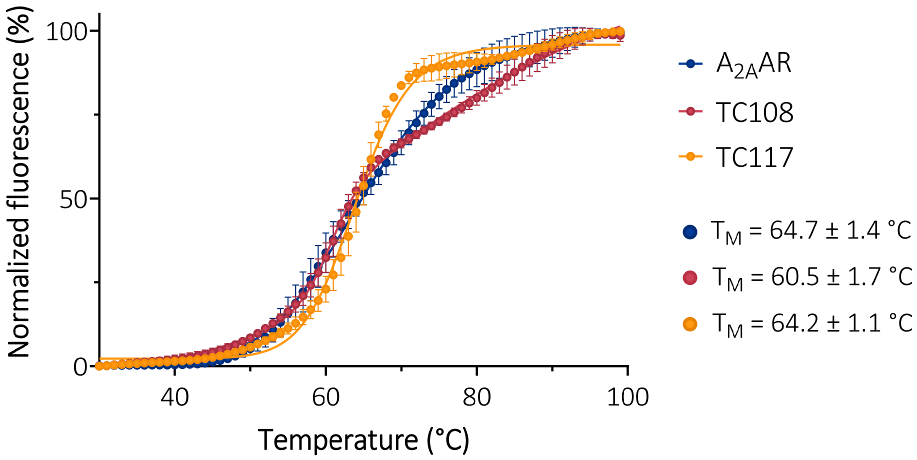

Figure 43. Thermal shift assay of TC108, TC117 and $A_{2A}AR$. Nonlinear fit (TC108: biphasic sigmoidal, others: Boltzmann sigmoidal) of normalized fluorescence data. The mean, normalized fluorescence data is shown as dots ± SD. The T_M was calculated as the mean ± SD of the first/only inflection point (TC108 and $A_{2A}AR$: n=3, TC117: n=2).

The only comparison that fell significantly short between TC117 and the $A_{2A}AR$ was the protein yield, which is a critical factor in crystallography projects, since the successful formation of crystals in LCP requires a high protein concentration.[260] For that reason, the protein yield continued to be a key item on the agenda towards an $A_{2B}AR$ crystallization construct.[260] Nevertheless, construct TC117 had been the most monodisperse, thermostable and well-expressing $A_{2B}AR$ construct up to that point.

3.3.3 Selected point mutations

In addition to the TM1 mutations and the $S92^{3.39}K$ mutation, among the numerous tested point mutations, other mutations also exhibited favorable characteristics.

One example of that is the $C29^{1.54}I$ mutation, which also dates back to the time when the left-shifted elution profile of the early $A_{2B}AR$ constructs was thought to be associated with oligomerization of the receptor. During the comparison of the sequences of TM1 and TM5 of the $A_{2B}AR$ with the sequences of the related A_1AR, $A_{2A}AR$ and A_3AR two cysteines stood out: $C29^{1.54}$ and $C210^{5.66}$. In position 1.54 the A_1AR as well as the A_3AR both harbor an isoleucine, instead of the cysteine in $A_{2B}AR$ and $A_{2A}AR$. In position 5.66, all of the related ARs harbor an arginine residue, instead of the cysteine in $A_{2B}AR$. Back then, one hypothesis was that these cysteines might be involved in the formation of disulfide bridges during the formation of homodimers of the receptor. Therefore, both of the sidechains were mutated to the analogs of the related receptors. The results are shown in the following Figure 44.

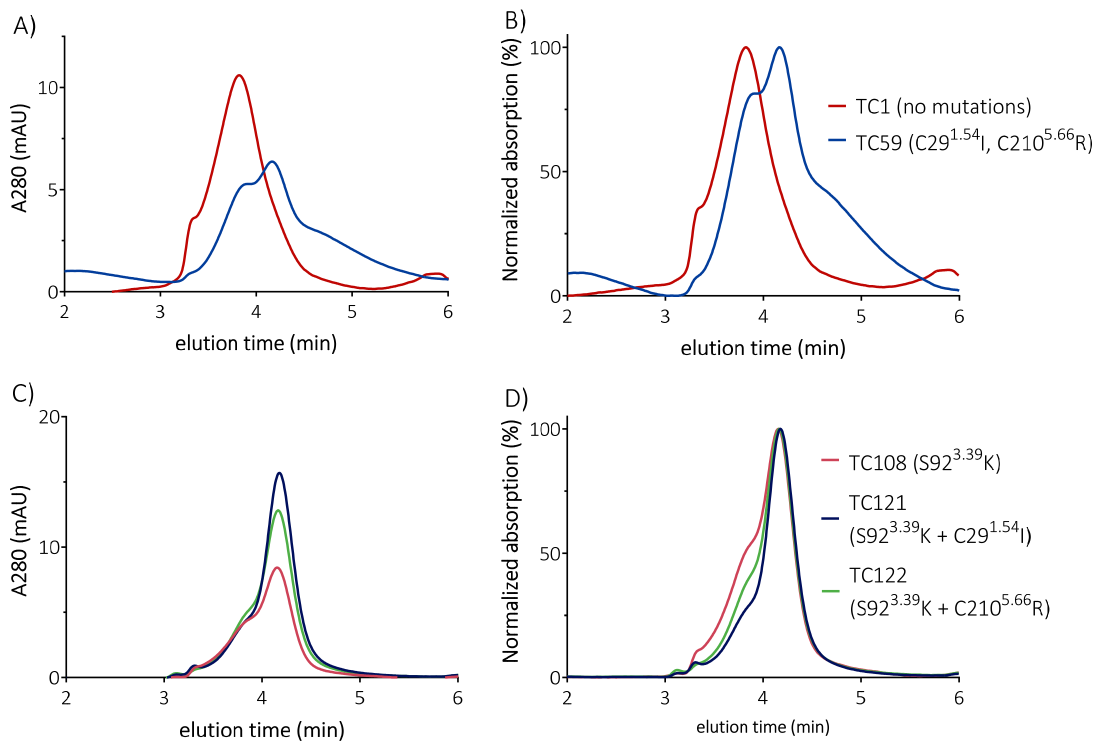

Figure 44. Analysis of the mutations C29$^{1.54}$I and C210$^{5.66}$R. A) Elution profile of the region of interest of the SEC analysis for TC1 and TC59 (expressed in original pFastBac1™). B) Normalized SEC data of the region of interest of TC1 and TC59. C) Elution profile of the region of interest of the SEC analysis for TC108, TC121 and TC122 (expressed in GP64-pFastBac1). B) Normalized SEC data of the region of interest of TC108, TC121 and TC122.

The results in panel A and B of Figure 44 show the initial result of the combined mutation of both cysteine residues performed using the original pFastBac1™ plasmid. Similar to the S92$^{3.39}$K construct, this construct showed a clearly improved elution profile in the SEC analysis. Unfortunately, the protein yield of this construct was comparably low. However, in the instance of very low protein yields, as seen for these earlier A_{2B}AR constructs, such differences in protein yield can also result from small variation in the expression or purification process. Due to the interesting SEC profile, these mutations were later revisited and individually combined with the S92$^{3.39}$K mutation, expressed in the GP64-pFastBac1 plasmid, as shown in panel C and D of the previous figure. Also individually, both of these mutations significantly improved the monodispersity, and fortunately also the protein yield, compared to the control

TC108. In both aspects, the construct TC121 with the C29$^{1.54}$I mutation showed a more favorable effect on the protein.

In terms of thermostability, construct TC121 was superior compared to TC122 as well, as illustrated in Figure 45.

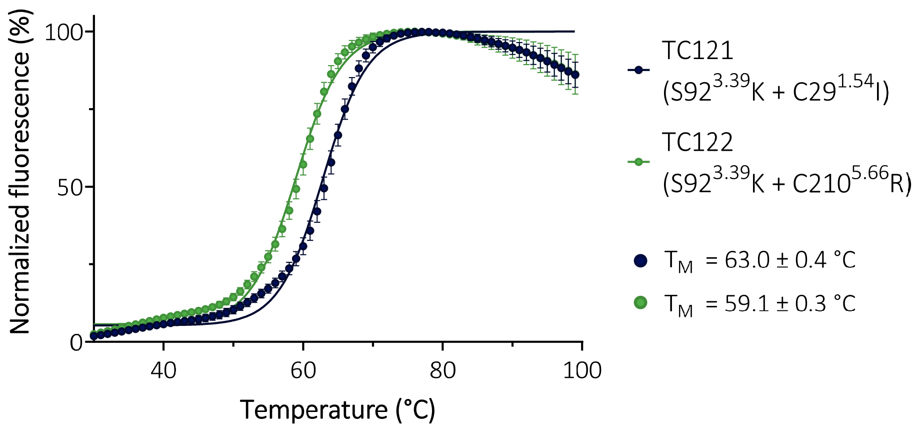

Figure 45. Thermal shift assay of TC121 and TC122. Nonlinear fit (Boltzmann sigmoidal) of normalized fluorescence data. The mean, normalized fluorescence data is shown as dots ± SD (n=2). The T_M was calculated as the mean ± SD of the first inflection point (n=3).

The additional cysteine mutations, C29$^{1.54}$I increased the T_M by approximately 3 °C (60.5 ± 1.7 °C for TC108 vs. 63.0 ± 0.4 °C for TC121), in comparison to TC108, whereas the C210$^{5.66}$R mutation did not show a positive impact on the thermostability of the receptor. With its T_M of approximately 63.0 °C, construct TC121 exhibited a similar thermostability as the gold standard A_{2A}AR, and the so-far best A_{2B}AR construct TC117, which featured the entire TM1 exchange.

Later, both cysteine mutations were combined with the S92$^{3.39}$K mutation in construct TC153. Between these analyses, another modification was introduced to the receptor, involving the elimination of N-glycosylation sites in the ECL2 of A_{2B}AR. As a result, TC153 incorporates a total of five point mutations: C29$^{1.54}$I, S92$^{3.39}$K, N153^{ECL2}Q, N163^{ECL2}Q, and C210$^{5.66}$R. A more comprehensive discussion of the removal of the N-glycosylation sites will be provided in chapter 3.4. It is worth noting that the removal of these glycosylation sites did not (negatively) impact protein yield, monodispersity, or thermostability. Therefore, a comparison of TC121, TC122, and TC153 is presented in Figure 46.

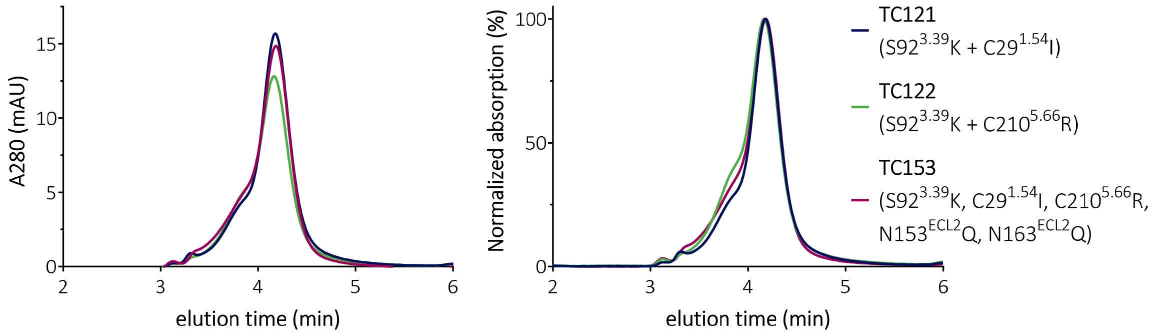

Figure 46. Analysis of the combination of mutations C29$^{1.54}$I and C210$^{5.66}$R. Elution profile of the region of interest of the SEC analysis and normalized SEC data of the region of interest.

Interestingly, while each individual mutation led to a notable enhancement in both protein yield and monodispersity compared to the construct with just the S92$^{3.39}$K mutation, their combination did not yield any further improvements. Instead, the protein yield and monodispersity were in between the results obtained from the single cysteine mutants. As a result of its superior attributes and the preference of preserving the native state of TM5 for potential crystal structure, the C29$^{1.54}$I mutation was selected for combination with other mutations, including the other TM1 mutations.

The thermostability data of the selected point mutations is compared in the column representation of the T_M values (Figure 47):

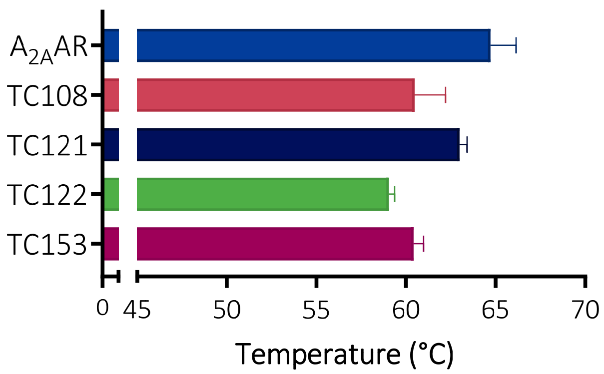

Construct	Mutations	T_M value:
$A_{2A}AR$	-	64.7 ± 1.4 °C
TC108	S92$^{3.39}$K	60.5 ± 1.7 °C
TC121	C29$^{1.54}$I, S92$^{3.39}$K	63.0 ± 0.4 °C
TC122	S92$^{3.39}$K, C210$^{5.66}$R	59.1 ± 0.3 °C
TC153	C29$^{1.54}$I, S92$^{3.39}$K, N153^{ECL2}Q, N163^{ECL2}Q, C210$^{5.66}$R	60.4 ± 0.6 °C

Figure 47. Comparison of the T_M ± SD values of the $A_{2B}AR$ constructs involving the cysteine mutations in TM1 and TM5.

Another modification with a positive effect was the mutation of amino acid A232$^{6.33}$. The idea behind these constructs was to reduce flexibility within the receptor by introducing an amino acid with an acidic sidechain (i.e. E or D), to form an ionic lock with R103$^{3.50}$ of the DRY motif. The result of this hypothesis is presented in the following Figure 48.

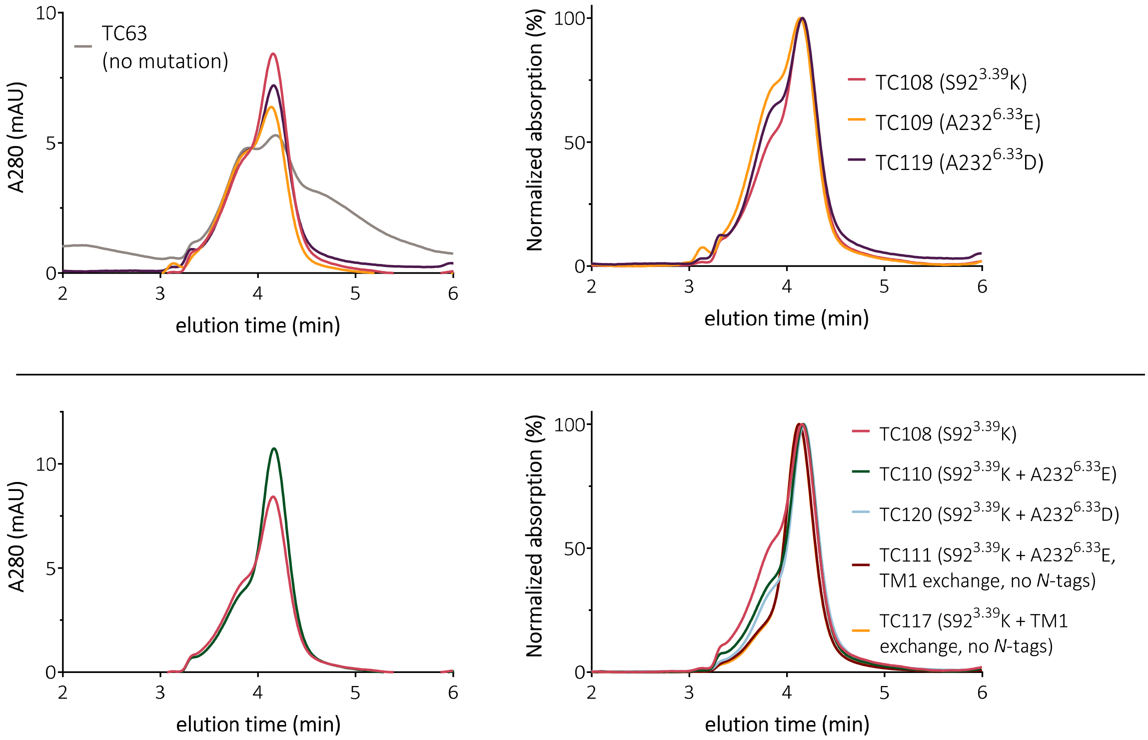

Figure 48. Analysis of the mutation site A232$^{6.33}$. Upper panel: Elution profile of the region of interest of the SEC analysis and normalized SEC data of the region of interest for TC108, TC109 and TC119. Lower panel: The same analyses for TC108, TC110, TC120, TC111 and TC117.

As illustrated in the upper panel of Figure 48, the introduction of the acidic amino acids aspartic and glutamic acid indeed had a positive impact on the receptor's elution profile in the SEC analysis. In comparison to TC63, there was a noticeable enhancement in the peak at the desirable elution time of approximately 4.2 minutes, although not as pronounced as with TC108. The substitution of the alanine with aspartic acid yielded more favorable results between than glutamic acid.

The lower panel of the figure presents the outcomes of combining the A232$^{6.33}$E and A232$^{6.33}$D mutation and the S92$^{3.39}$K mutation, with and without the TM1 exchange. In this case as well, the combination with only the Na^+ binding pocket mutation resulted in a significantly improved elution profile. However, when combined with

S92$^{3.39}$K and the TM1 exchange, the results were completely identical in terms of monodispersity and protein yield (data not shown). At this point, it should be noted, that both TC111 and TC117 include an additional modification, specifically the removal of *N*-terminal tags, which will be presented in section 3.6.1, page 80. Given that both constructs share this additional modification, a direct comparison between them is feasible.

The thermostability data of the A232$^{6.33}$ mutations is additionally given in form of a column representation of the T_M values in Figure 49:

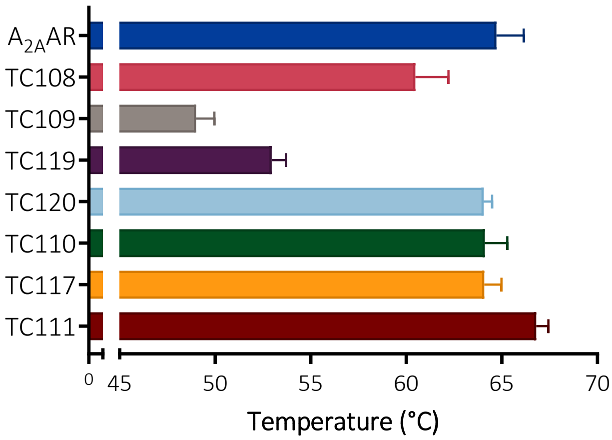

Construct	Mutations	T_M value:
$A_{2A}AR$	-	64.7 ± 1.4 °C
TC108	S92$^{3.39}$K	60.5 ± 1.7 °C
TC109	A232$^{6.33}$E	49.0 ± 1.0 °C
TC119	A232$^{6.33}$D	53.0 ± 0.8 °C
TC110	S92$^{3.39}$K, A232$^{6.33}$E	64.1 ± 1.2 °C
TC120	S92$^{3.39}$K, A232$^{6.33}$D	64.1 ± 0.4 °C
TC117	S92$^{3.39}$K, TM1 exchange	64.1 ± 0.9 °C
TC111	S92$^{3.39}$K, A232$^{6.33}$E, TM1 exchange	66.8 ± 0.6 °C

Figure 49. Comparison of the T_M ± SD values of the $A_{2B}AR$ constructs involving the A232$^{6.33}$ mutations (TC109: n=2, others: n=3).

This thermostability data demonstrates that the inclusion of each of the A232$^{6.33}$ mutations results in an increased T_M. Notably, despite TC111 and TC117 having identical elution profiles, TC111, featuring the A232$^{6.33}$E mutation, exhibited superior thermostability and emerged as the most thermostable construct up to that point. Therefore, TC111 was the first $A_{2B}AR$ construct employed in a crystallization experiment, which will be presented in a later chapter of this thesis (section 3.9, page 106). Eventually, however, other more promising leads, that did not require the possible construction of an artificial salt bridge within the receptor, led to the decision to not further consider the mutation site A232$^{6.33}$ for the crystallization constructs.

3.4 Removal of N-glycosylation sites

As briefly mentioned during the discussion of the results for TC153 in section 3.3.3, page 67, at some point in the course of this study, the two predicted N-glycosylation sites in the ECL2 of the receptor were removed. The reasoning behind this modification lies in the potential structural heterogeneity of N-glycans, which might negatively affect the outcome of crystallization experiments,[105, 261, 262] e.g. by preventing the formation of well-ordered crystals.[102] However, N-glycosylation sites can be crucial for expression, folding and functionality of GPCRs,[95, 96] and the consequences of their removal must always be investigated.

In case of the A_{2B}AR, the asparagine residues in the N-glycosylation consensus sequence N–X–S/T (X ≠ P)) were replaced by glutamines. The effect of this modification was analyzed by SEC, providing an assessment of the expression and protein folding, and the thermostability assay. The results of this assessment are shown in the following Figure 147.

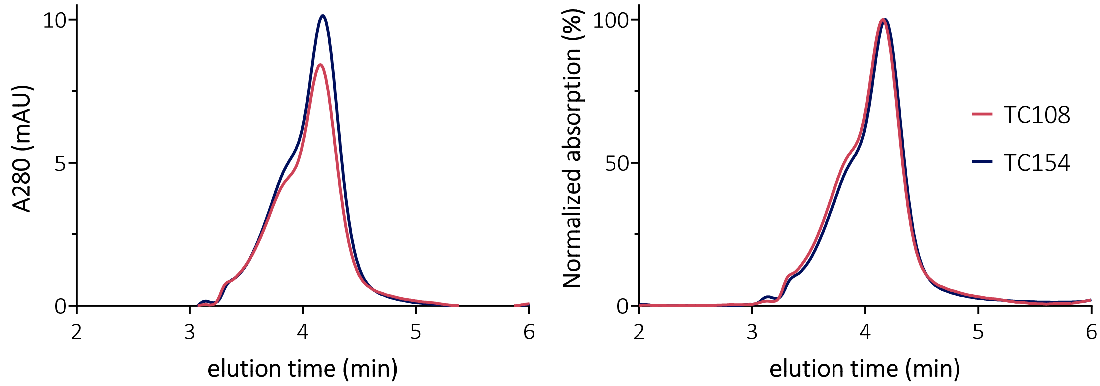

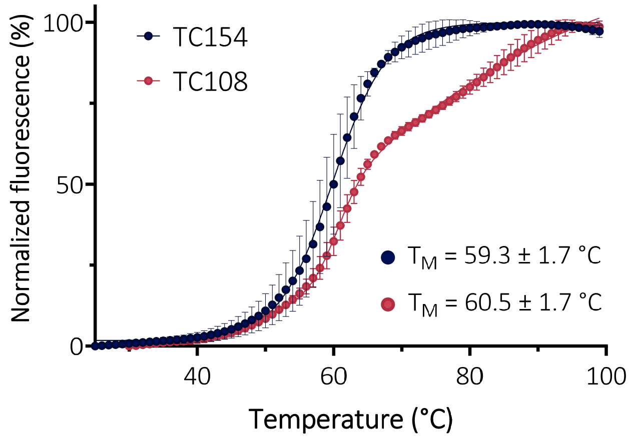

TC108	S92$^{3.39}$K
TC154	S92$^{3.39}$K, N153^{ECL2}Q, N163^{ECL2}Q

Figure 50. Results of the SEC and thermostability assessment for the removal of N-glycosylation sites. Upper half: Elution profile of the region of interest of the SEC analysis and normalized SEC data of the region of interest for TC108 and TC154. Bottom left: Thermal shift assay. Nonlinear fit (TC108: biphasic sigmoidal, TC154: Boltzmann sigmoidal) of normalized fluorescence data. The mean, normalized fluorescence data is shown as dots ± SD (n=3 for TC108, n=2 for TC154). The T_M was calculated as the mean ± SD of the first/only inflection point (n=3).

As evident from the SEC results presented earlier, the removal of N-glycosylation sites, fortunately, did not lead to a reduction in protein yield. In fact, the data suggests a potential increase in protein yield, particularly when considering the fact that a portion of the membrane preparation, used for the purification of the protein, was also extracted for assessment in a radioligand binding assay. As always, it is important to note that the expression and purification of the two constructs occurred at different times, so the interpretation of small differences in protein yield should be made with caution. In terms of monodispersity, the elimination of the N-glycosylation sites had no adverse effects on the stabilized A_{2B}AR construct.

Regarding the thermostability, TC154 exhibited a similar T_M value compared to the control TC108. Taken together, the removal of the glycosylation sites showed no negative impact on the $A_{2B}AR$ protein, and therefore, this opportunity to reduce potential structural heterogeneity was taken.

As mentioned earlier, numerous constructs are commonly processed at the same time, wherefore not all newer constructs immediately incorporated this latest modification.

3.5 Combination of TM1 mutations

Having identified many advantageous individual mutations, the next step was to combine them to create an even better construct that would exhibit strong expression, monodispersity, and thermostability, while retaining $A_{2B}AR$'s native TM1, or only slightly modifying it. Typically, the process of combining point mutations is not very straightforward, and the beneficial effects of individual mutations can sometimes counteract each other rather than being additive.[205] Consequently, it is often necessary to screen multiple combinations in order to identify a truly superior construct, which is what occurred also in case of the $A_{2B}AR$.

The first approach to supersede the entire TM1 exchange, was to combine the most promising TM1 mutations, namely A35$^{1.60}$N (see Figure 34), with the already successful combination of the C29$^{1.54}$I and S92$^{3.39}$K mutations. Furthermore, all the identified hits from the TM1 mutation screening were combined with the aforesaid mutations as well. The outcomes of these combinations are illustrated in the following Figure 51.

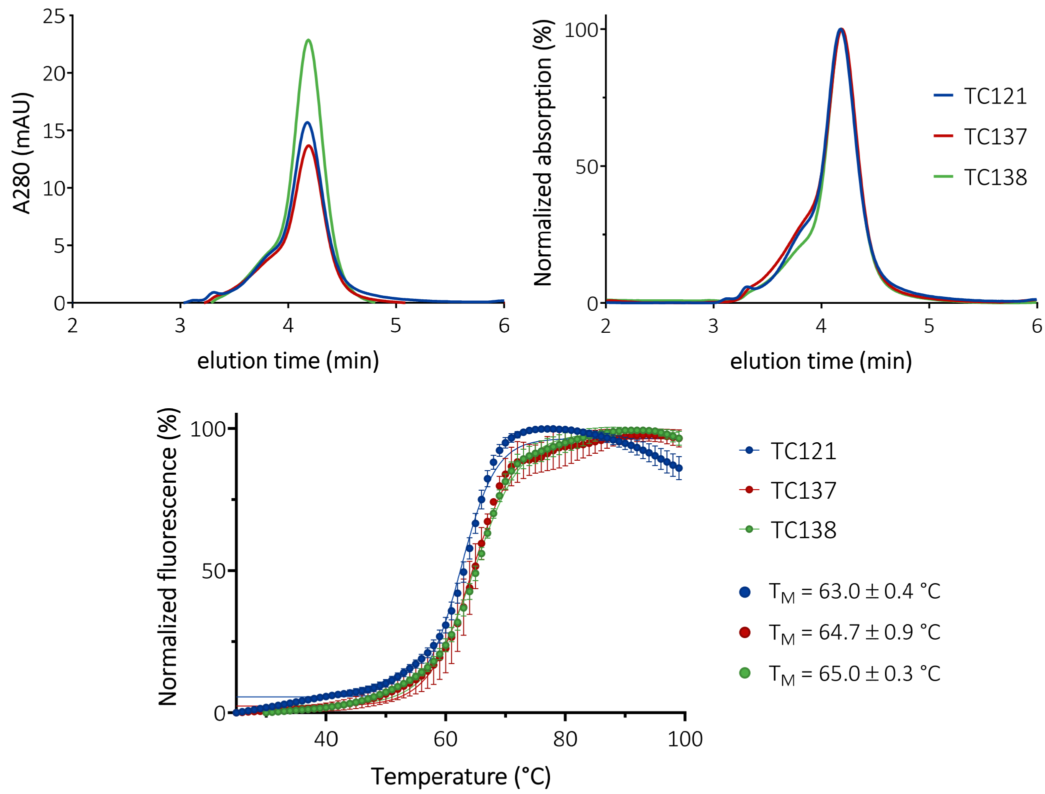

TC121	C29$^{1.54}$I, S92$^{3.39}$K
TC137	C29$^{1.54}$I, A35$^{1.60}$N, S92$^{3.39}$K, N153^{ECL2}Q, N163^{ECL2}Q
TC138	A19$^{1.44}$V, C29$^{1.54}$I, G33$^{1.58}$W, A35$^{1.60}$N, S92$^{3.39}$K, N153^{ECL2}Q, N163^{ECL2}Q

Figure 51. Comparison of the SEC and thermostability assessment for TC121, TC137 and TC138. Upper half: Elution profile of the region of interest of the SEC analysis and normalized SEC data of the region of interest. Lower half: Thermal shift assay. Nonlinear fit (Boltzmann sigmoidal) of normalized fluorescence data. The mean, normalized fluorescence data is shown as dots ± SD (n=3 for TC137 and TC138, n=2 for TC21). The T_M was calculated as the mean ± SD of the first/only inflection point (n=3).

In terms of the yield and monodispersity of the protein, TC137 with its additional A35$^{1.60}$N mutation, did not exhibit any advantage over construct TC121, which lacked this mutation. The only noticeable improvement of this construct was a slight improvement by approximately 1.5 °C of its T_M. Construct TC138, however, harboring all of the favorable TM1 mutations, demonstrated a considerable improvement compared to TC121, especially with respect to the protein yield that was achieved. Furthermore, the monodispersity and the T_M were slightly elevated by the three additional TM1 mutations. The absence of a distinct positive effect of the seemingly most favorable TM1 mutation A35$^{1.60}$N motivated a closer examination to identify which TM1 mutations actually showed an additive positive effect, when combined. Figure 52 presents the results of this investigation:

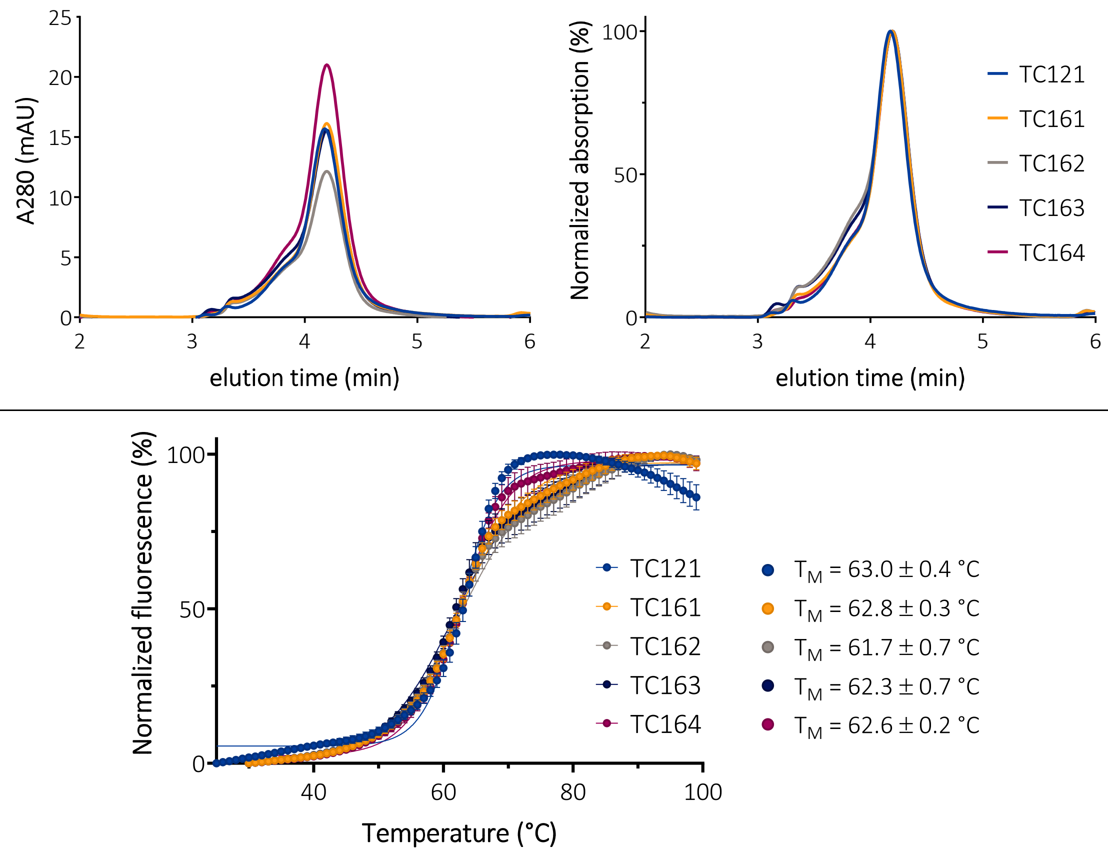

TC121	C29$^{1.54}$I, S92$^{3.39}$K
TC161	A19$^{1.44}$V, C29$^{1.54}$I, G33$^{1.58}$W, S92$^{3.39}$K, N153^{ECL2}Q, N163^{ECL2}Q / **- A35$^{1.60}$N**
TC162	A19$^{1.44}$V, C29$^{1.54}$I, S92$^{3.39}$K, N153^{ECL2}Q, N163^{ECL2}Q / **- G33$^{1.58}$W, - A35$^{1.60}$N**
TC163	C29$^{1.54}$I, G33$^{1.58W}$, S92$^{3.39}$K, N153^{ECL2}Q, N163^{ECL2}Q / **- A19$^{1.44}$V, A35$^{1.60}$N**
TC164	A19$^{1.44}$V, G33$^{1.58}$W, A35$^{1.60}$N S92$^{3.39}$K, N153^{ECL2}Q, N163^{ECL2}Q / **- C29$^{1.54}$I**

Figure 52. Evaluation of the SEC and thermostability assessment for TC121, and TC161-164. Upper half: Elution profile and normalized SEC data of the region of interest. Lower half: Thermal shift assay. Nonlinear fit (Boltzmann sigmoidal) of normalized fluorescence data. The mean, normalized fluorescence data is shown as dots ± SD (n=2 for TC21, n=3 for rest). The T$_M$ was calculated as the mean ± SD of the first/only inflection point (n=3).

Notably, while the inclusion of the A35$^{1.60}$N mutation alongside C29$^{1.54}$N and S92$^{3.39}$K did not yield any further benefits, the removal of this mutation had an unfavorable effect regarding all aspects, when compared to TC138, which contained all four of the TM1 mutations. Instead, the results of construct TC161, identical to TC138 but lacking the A35$^{1.60}$N mutation, resembled those of TC121, with just the C29$^{1.54}$I and S92$^{3.39}$K mutations. The same pattern was observed with constructs TC162 and TC163, where the A35$^{1.60}$N as well as one of the two additional mutations from the TM1 exchange screening were omitted, which overall performed even worse than TC121.

In order to investigate if the absence of the additive effect could be attributed to the combination of A35$^{1.60}$N and C29$^{1.54}$I, construct TC164 was evaluated, which contained all the TM1 mutations except for C29$^{1.54}$I. Although this construct outperformed TC161, featuring all TM1 mutations except A35$^{1.60}$N, it still showed an inferior performance in terms of monodispersity, protein yield and thermostability, when compared to TC138 with all its TM1 mutations (compare with Figure 51).

The outcome of this extended investigation confirmed that indeed, the combination of all identified TM1 mutations is essential for achieving the most positive effect on the receptor. With its T_M of 65.0 ± 0.3 °C, TC138 was the most thermostable construct up to this point that didn't require the exchange of the entire TM1. Also, both the monodispersity and protein yield, assessed by the height of the main peak in the SEC analysis, exceeded the results of any other construct without the TM1 exchange.

Figure 53 presents a comparison of the superior TC138 construct with its counterpart TC117, which includes the whole TM1 exchange instead of the four single TM1 mutations.

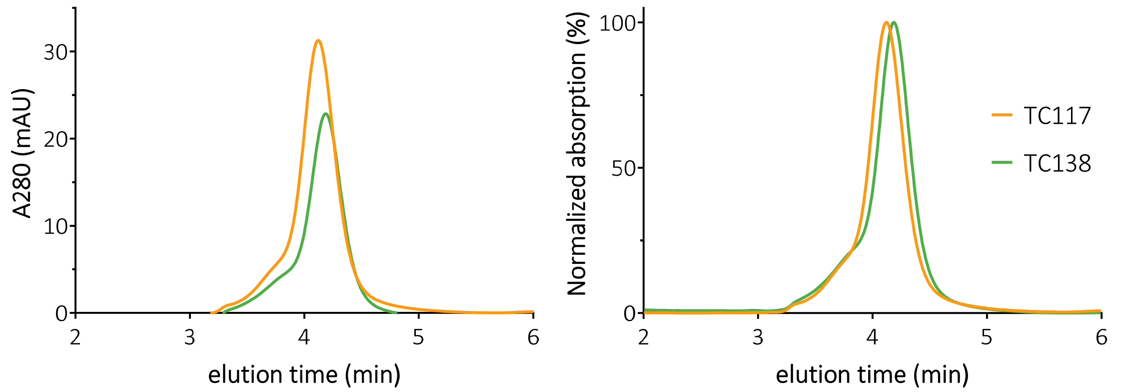

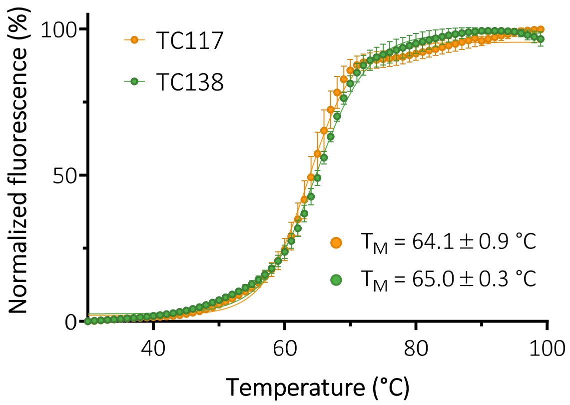

TC117	S92$^{3.39}$K, TM1 exchange, no *N*-tags
TC138	A19$^{1.44}$V, C29$^{1.54}$I, G33$^{1.58}$W, A35$^{1.60}$N, S92$^{3.39}$K, N153^{ECL2}Q, N163^{ECL2}Q

Figure 53. SEC and thermostability results for TC117 and TC138. Upper half: Elution profile and normalized SEC data of the region of interest. Lower half: Thermal shift assay. Nonlinear fit (Boltzmann sigmoidal) of normalized fluorescence data. The mean, normalized fluorescence data is shown as dots ± SD (n=3). The T_M was calculated as the mean ± SD of the first/only inflection point (n=3).

Based on these results, both receptor constructs exhibited the same monodispersity, despite the fact that construct TC138 harbors only four mutations in TM1, in contrast to the 19 amino acids that are altered by the entire TM1 exchange. Also, the thermostability of TC138 matches that of TC117. The only distinction between these constructs lies in the superior protein yield of TC117. However, it must be considered that TC117 also includes the removal of all *N*-terminal tags, which has the potential to significantly increase the protein yield, as will be explained in the upcoming section 3.6.1, page on 80 ff. A proper comparison of the respective A_{2B}AR construct, featuring the TM1 mutations without *N*-terminal tags, will follow in that section as well.

Taken together, the comparison of TC117 and TC138 already confirmed the effectiveness of the effort to replace the TM1 exchange with a limited number of individual TM1 mutations, as demonstrated by the identical monodispersity and thermostability of the respective constructs. As soon as the protein yield of the latest $A_{2B}AR$ construct were further enhanced, the whole TM1 exchange would be obsolete.

3.6 *N*-terminal modifications

Parallel to the plasmid exchange and point mutations, presented in the previous chapters, different *N*-terminal modifications on the receptor were assessed as well. Modifying the *N*-terminus is a common strategy in the field of GPCR crystallization since the *N*-terminus plays a significant role in determining protein stability and expression levels.[263, 264] An exemplary case of *N*-terminal modification is the A_1AR, where a crystal construct of the receptor was altered by incorporating 22 amino acids from the highly-glycosylated *N*-terminus of the muscarinic M_4 (M_4R) receptor in order to enhance expression levels.[265] This, and other approaches were also performed on the $A_{2B}AR$, as seen in the following sections.

3.6.1 Deletion of *N*-terminal tags

The first *N*-terminal modification is the deletion of the *N*-terminal tags. Standardly, the $A_{2B}AR$ constructs carried an HA-tag for improved trafficking,[250] as well as a FLAG-tag for expression control[266] at their *N*-terminus (see Figure 23). In an effort to analyze the impact of these tags on the receptor, they were (partially) removed and the protein was characterized using SEC and the thermostability assay. The results are presented in the following Figure 54 and Figure 55.

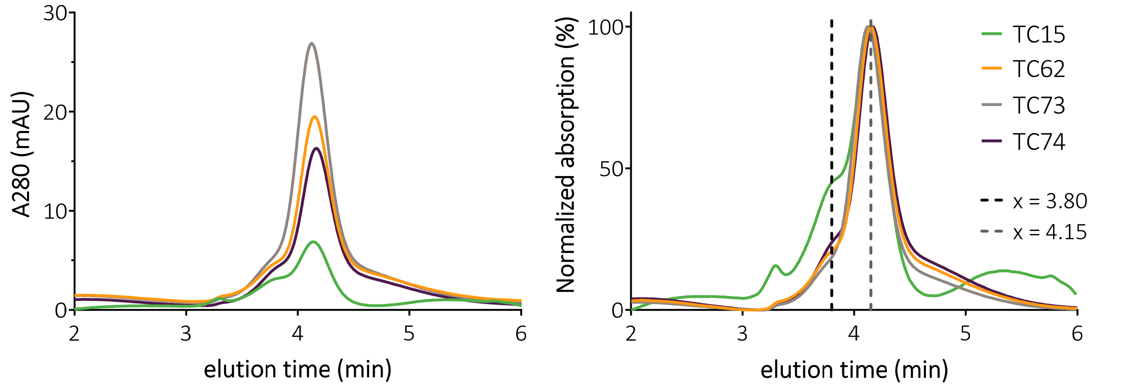

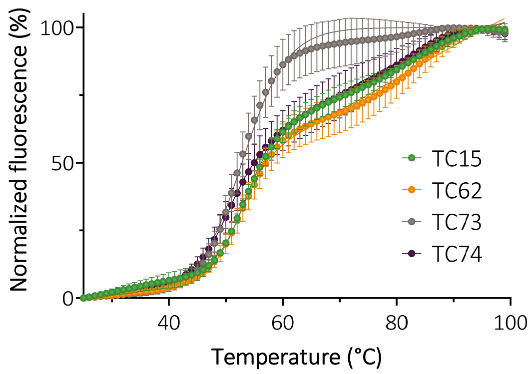

TC15	$A_{2B}AR$ – pFastBac1™ +TM1 exchange
TC62	$A_{2B}AR$ – GP64-pFastBac1 + TM1 exchange
TC73	$A_{2B}AR$ – GP64-pFastBac1 +TM1 exchange, no *N*-tags
TC74	$A_{2B}AR$ – pFastBac1™ +TM1 exchange, no *N*-tags
TC15	T_M = 54.1 ± 0.3 °C
TC62	T_M = 53.4 ± 0.5 °C
TC73	T_M = 52.3 ± 0.5 °C
TC74	T_M = 52.7 ± 0.5 °C

Figure 54. Results of the SEC and thermostability assessment for the removal of N-terminal tags. Upper half: Elution profile of the region of interest of the SEC analysis and normalized SEC data of the region of interest for TC15, TC62, TC73 and TC74. Bottom left: Thermal shift assay. Nonlinear fit (TC73: Boltzmann sigmoidal, others: biphasic sigmoidal) of normalized fluorescence data. The mean, normalized fluorescence data is shown as dots ± SD (TC15: n=2, others: n=3). The T_M was calculated as the mean ± SD of the first/only inflection point (TC15: n=2, others: n=3).

Presented in Figure 54 are the results from the deletion of all *N*-terminal tags, performed on the TM1 exchange constructs. Interestingly, in case of the TM1 exchange constructs expressed in the original pFastBac1™ plasmid, the deletion of the tags resulted in a reduction of the unfavorable peak at 3.8 min, and therefore an increase in monodispersity, in reference to the peak between 4.1 min and 4.2 min elution time. However, concerning the comparison of monodispersity it must be noted that this factor is also dependent on the protein yield. Low protein yields give rise to unwanted impurities in the sample (as demonstrated in Figure 29), which could also appear in the SEC analysis. Therefore, when comparing receptor constructs with substantial disparities in protein yield, differences in monodispersity should not be over-interpreted. Anyhow, as previously mentioned, high protein yield is a crucial factor for successful crystallization.[260, 267] Hence, the unexpected increase of protein yield, despite the HA-tag's conventional role in enhancing expression and plasma membrane localization,[250] was a promising result. For the TM1 exchange constructs expressed in the superior GP64-pFastBac1 plasmid, a similar increase in protein yield was observed, while the monodispersity was unchanged. Regarding the thermostability of these new constructs, a slight potential decrease of the T_M of approximately 1 – 1.5 °C could be observed. However, given the increase in protein yield, this slight potential decrease was an acceptable trade-off.

The impact of removing the *N*-terminal tags was also examined on the $S92^{3.39}K$ mutated A_{2B}AR without its N-glycosylation sites. In this case, the removal of the HA-tag alone was assessed, since the FLAG-tag serves as a useful tool to track the expression and receptor localization, a standard procedure performed after each protein expression and thus indispensable. The result of this removal is displayed in the following Figure 55.

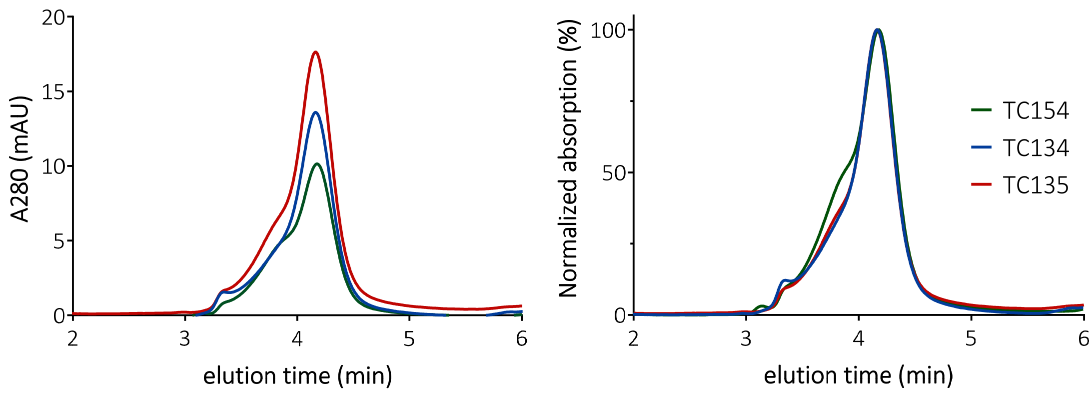

TC154	A_{2B}AR – $S92^{3.39}K$, N153Q, N163Q	T_M = 59.4 ± 1.6 °C
TC134	A_{2B}AR – A_{2B}AR – $S92^{3.39}K$, N153Q, N163Q, no *N*-tags	T_M = 60.0 ± 1.1 °C
TC135	A_{2B}AR – $S92^{3.39}K$, N153Q, N163Q, no *N*-terminal HA tag	T_M = 58.9 ± 1.3 °C

Figure 55. Results of the SEC assessment for the removal of N-terminal tags. Elution profile of the region of interest of the SEC analysis and normalized SEC data of the region of interest for TC134, TC135 and TC154. The T_M was calculated as the mean ± SD of the first/only inflection point (n=3).

Just as observed with the TM1 exchange constructs, the (partial) *N*-terminal tag removal similarly resulted in an increased monodispersity for A_{2B}AR constructs with a native TM1, as well as an increased protein yield. In the case of TC135, where only the HA-tag was removed, it even demonstrated a higher protein yield compared to its counterpart TC134 lacking both FLAG- and HA-tags. In terms of thermostability, the T_M values were similar across all three constructs, suggesting no significant drawback from this *N*-terminal modification.

As mentioned in the previous chapter 3.5, the *N*-terminal modification was also applied to the so-far best $A_{2B}AR$ construct, TC138, which does not involve the TM1 exchange. Following the rationale discussed above, the FLAG-tag remained unchanged, and only the HA-tag was removed from the construct. The results of this modification are presented in Figure 56 stated below.

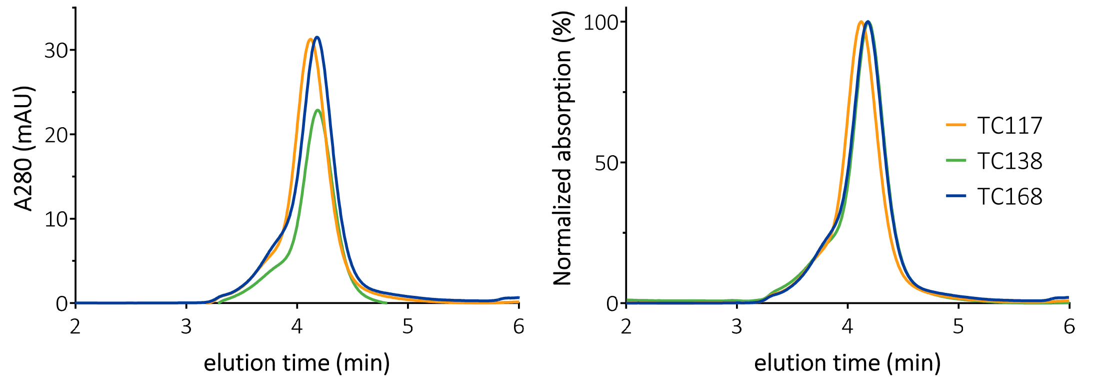

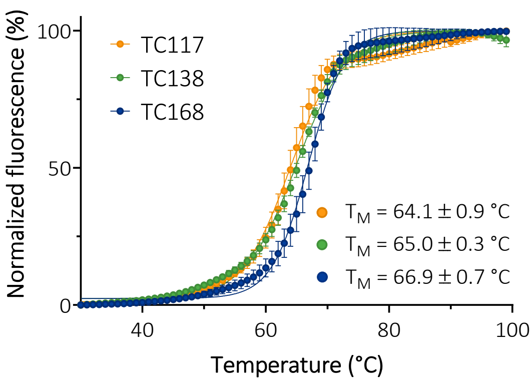

TC117	S92$^{3.39}$K, TM1 exchange, no *N*-tags
TC138	A19$^{1.44}$V, C29$^{1.54}$I, G33$^{1.58}$W, A35$^{1.60}$N, S92$^{3.39}$K, N153^{ECL2}Q, N163^{ECL2}Q
TC168	A19$^{1.44}$V, C29$^{1.54}$I, G33$^{1.58}$W, A35$^{1.60}$N, S92$^{3.39}$K, N153^{ECL2}Q, N163^{ECL2}Q, **no HA-tag**

Figure 56. Results of the SEC and thermostability assessment for TC117, TC138 and TC168. Upper half: Elution profile and normalized SEC data of the region of interest. Bottom left: Thermal shift assay. Nonlinear fit (Boltzmann sigmoidal) of normalized fluorescence data. The mean, normalized fluorescence data is shown as dots ± SD (n=3). The T_M was calculated as the mean ± SD of the first/only inflection point (n=3).

The removal of the *N*-terminal HA-tag did not enhance the monodispersity, which is not surprising considering the fact that the proteins are identical after HA-tag cleavage.[250] However, it significantly elevated the protein yield, matching that of TC117, the construct with the whole TM1 exchange, the S92$^{3.39}$K mutation, and without *N*-terminal tags. Additionally, the thermostability was assessed to be 66.9 ± 0.7 °C, surpassing both TC117 and TC138. As a result, TC168 emerged as the very first crystallization construct without the TM1 exchange, and it was employed in several crystallization trials, as detailed in section 3.11, page on 111 ff.

Due to the across the board positive effect of the (partial) *N*-tag removal, this modification was additionally considered and assessed in some of the newer A_{2B}AR constructs. However, another *N*-terminal modification that proved to be even more effective came to light shortly after, as will be detailed in the upcoming section 3.6.2.

3.6.2 *N*-terminal linker

In parallel to the course of this thesis, Dr. Jonathan G. Schlegel pursued his doctoral research, focusing on the development of a receptor model for structural studies of the A_3AR. One noteworthy finding of his thesis was that maintaining the native *N*-terminus of the A_3AR distinctly enhanced the protein yield for this receptor.[268] For the A_3AR, the observed effect aligned with the positive results seen for the addition of the M_4R's *N*-terminus, which is a practice that was already established in the crystallization construct of the related A_1AR.[265] At first, the improvement was attributed to the existence of two *N*-glycosylation sites in the A_3AR's *N*-terminus (P*NN*STAL), but later on Dr. Jonathan G. Schlegel uncovered that it was, in fact, the presence of a linker between the *N*-terminal tag HA- and FLAG-tag that was responsible for the difference.

Considering that the addition of the M_4R *N*-terminus did not result in an increased protein yield for an early A_{2B}AR construct, as previously examined during my master's thesis (not shown), the introduction of an *N*-terminal linker presented an alternative strategy to further improve A_{2B}AR's protein yield. Just as in case of the A_3AR, the linkers NNST, as well as the standard-linker sequence GSGS, were introduced at various positions into A_{2B}AR's *N*-terminus. The outcomes of these modifications are presented in the following figures.

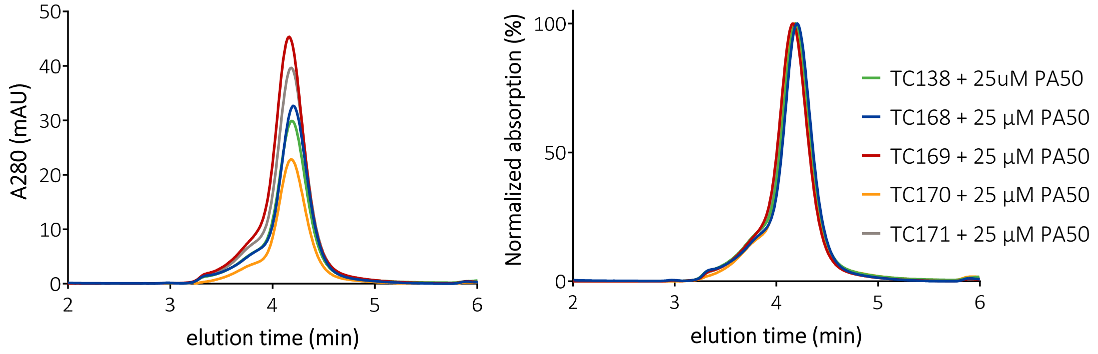

TC138	$A19^{1.44}V$, $C29^{1.54}I$, $G33^{1.58}W$, $A35^{1.60}N$, $S92^{3.39}K$, $N153^{ECL2}Q$, $N163^{ECL2}Q$
TC168	$A19^{1.44}V$, $C29^{1.54}I$, $G33^{1.58}W$, $A35^{1.60}N$, $S92^{3.39}K$, $N153^{ECL2}Q$, $N163^{ECL2}Q$, **no HA-tag**
TC169	$A19^{1.44}V$, $C29^{1.54}I$, $G33^{1.58}W$, $A35^{1.60}N$, $S92^{3.39}K$, $N153^{ECL2}Q$, $N163^{ECL2}Q$, HA-**NNST**-FLAG
TC170	$A19^{1.44}V$, $C29^{1.54}I$, $G33^{1.58}W$, $A35^{1.60}N$, $S92^{3.39}K$, $N153^{ECL2}Q$, $N163^{ECL2}Q$, HA-**NNST-HA**-FLAG
TC171	$A19^{1.44}V$, $C29^{1.54}I$, $G33^{1.58}W$, $A35^{1.60}N$, $S92^{3.39}K$, $N153^{ECL2}Q$, $N163^{ECL2}Q$, **NNST**-HA-FLAG

Figure 57. Comparison of the SEC analysis of the four N-terminally modified constructs TC168 – TC171 and their control TC138, all purified in presence of 25 µM PA50. Left: Elution profile of the region of interest of the SEC analysis. Right: Normalized SEC data of the region of interest.

Presented in Figure 57 are the results of four $A_{2B}AR$ constructs with diverse *N*-termini, namely TC168 – TC171. Among those, TC169 – TC171 are constructs harboring the NNST-linker, introduced before. In TC169, this NNST-linker is placed between the HA- and the FLAG-tag. For constructs TC170 and TC171, however, this sequence is placed ahead of the HA-tag, or in between two HA-tags. The reasoning for this was that, upon the post-translational cleavage of the HA-tag which has been postulated,[250] the potentially structurally heterogenous N-glycans would be removed as well.

Differing from the previously displayed protein purifications, the proteins presented above were purified in complex with 25 µM of the $A_{2B}AR$ antagonist PA50, a compound that proved to be highly stabilizing during the screening of various ligands, as detailed in the upcoming chapter 3.8. This approach aimed to estimate the highest possible monodispersity, protein yield and thermostability of these constructs in preparation for the upcoming crystallization trials.

As evident from the left panel of Figure 57, the introduced modifications were partially very successful. For the constructs with the *N*-terminal HA-NNST-FLAG (TC169) and NNST-HA-FLAG (TC171) tags, the modifications clearly elevated their protein yields, reaching levels of 45 mAU and 40 mAU, respectively. By comparison, the previously best-performing constructs displayed peak heights of approximately

30 mAU in the apo state. Construct TC170, however, featuring the *N*-terminal HA-NNST-HA-FLAG sequence, displayed a marked decrease in protein yield compared to the control TC138. Regarding TC138 and TC168, it must be noted that the difference in protein yield between the two was significantly more pronounced, when the proteins were purified in the apo state, as presented in Figure 56. In terms of monodispersity, all of the constructs presented above showed a similar performance, as demonstrated in the right panel of Figure 57.

The thermostability properties of these constructs were virtually, as seen in the following Figure 58.

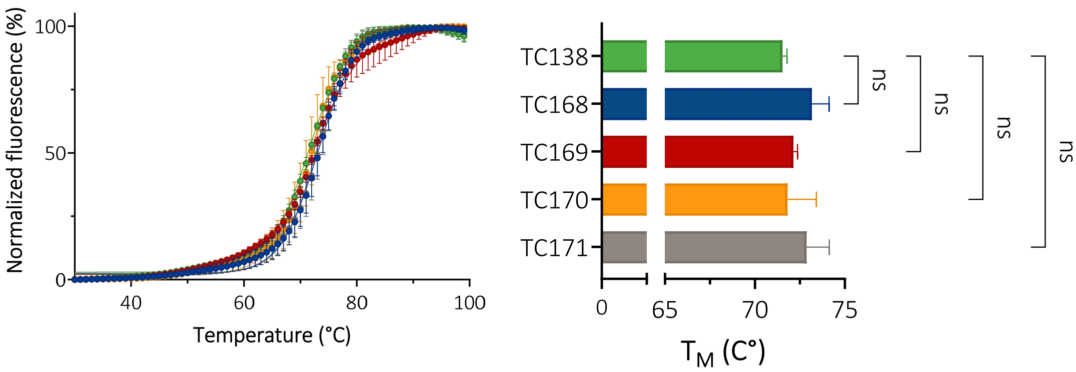

TC138	A19$^{1.44}$V, C29$^{1.54}$I, G33$^{1.58}$W, A35$^{1.60}$N, S92$^{3.39}$K, N153^{ECL2}Q, N163^{ECL2}Q
TC168	A19$^{1.44}$V, C29$^{1.54}$I, G33$^{1.58}$W, A35$^{1.60}$N, S92$^{3.39}$K, N153^{ECL2}Q, N163^{ECL2}Q, **no HA-tag**
TC169	A19$^{1.44}$V, C29$^{1.54}$I, G33$^{1.58}$W, A35$^{1.60}$N, S92$^{3.39}$K, N153^{ECL2}Q, N163^{ECL2}Q, HA-**NNST**-FLAG
TC170	A19$^{1.44}$V, C29$^{1.54}$I, G33$^{1.58}$W, A35$^{1.60}$N, S92$^{3.39}$K, N153^{ECL2}Q, N163^{ECL2}Q, HA-**NNST**-**HA**-FLAG
TC171	A19$^{1.44}$V, C29$^{1.54}$I, G33$^{1.58}$W, A35$^{1.60}$N, S92$^{3.39}$K, N153^{ECL2}Q, N163^{ECL2}Q, **NNST**-HA-FLAG

TC138 + 25 µM PA50	T_M = 71.3 ± 0.3 °C
TC168 + 25 µM PA50	T_M = 73.2 ± 1.0 °C
TC169 + 25 µM PA50	T_M = 72.2 ± 0.2 °C
TC170 + 25 µM PA50	T_M = 71.8 ± 1.6 °C
TC171 + 25 µM PA50	T_M = 72.9 ± 1.3 °C

Figure 58. Thermal shift assay of TC138 and TC168 – TC171 the control in complex with PA50 Left: Nonlinear fit (Boltzmann sigmoidal) of normalized fluorescence data. The mean, normalized fluorescence data is shown as dots ± SD (n=3). The T_M was calculated as the mean ± SD of the first/only inflection point (n=3). Right: Column representation of the mean melting temperatures and their SD of 3 repeated measurements. For evaluation of significance, the result of N-terminally modified construct was compared to the control using Dunnett's multiple comparison test (ns: P > 0.05).

In summary, the *N*-terminal modifications involving the NNST-linker proved to be successful also for the A_{2B}AR, with two of the constructs significantly enhancing the protein yield of the receptor, and thereby addressing the main limitation of the receptor. Due to the superior performance of construct TC169, this construct was later utilized in one of the crystallization trials, which will be presented in section 3.10, on page 108 ff.

As mentioned in the introduction to this chapter, Dr. Jonathan G. Schlegel later discovered that the generic GSGS-linker without any N-glycosylation sites, resulted in a similar protein yield compared to the same construct, carrying the NNST-linker.[268] Therefore, the most successful *N*-terminal sequence, namely HA-NNST-FLAG, was replaced by its analog HA-GSGS-FLAG in the construct TC190. The results of this alteration are displayed in the following Figure 59.

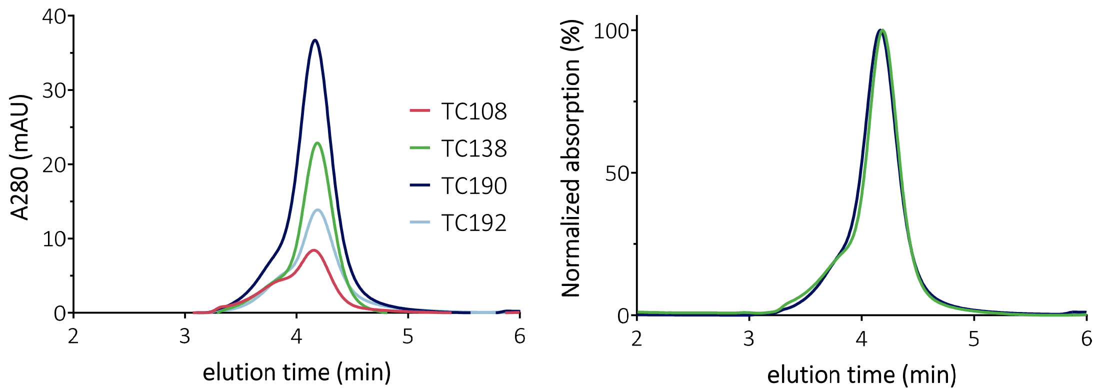

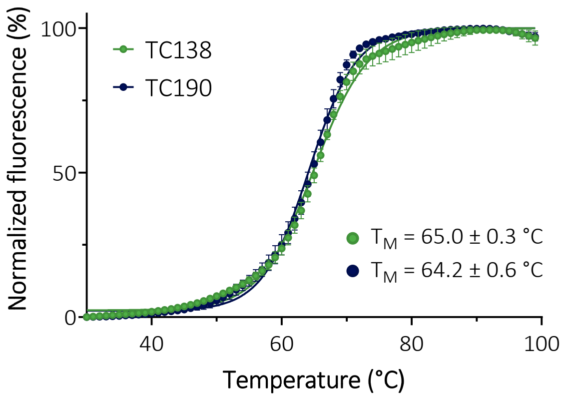

TC108	S92$^{3.39}$K
TC138	A19$^{1.44}$V, C29$^{1.54}$I, G33$^{1.58}$W, A35$^{1.60}$N, S92$^{3.39}$K, N153^{ECL2}Q, N163^{ECL2}Q
TC190	A19$^{1.44}$V, C29$^{1.54}$I, G33$^{1.58}$W, A35$^{1.60}$N, S92$^{3.39}$K, N153^{ECL2}Q, N163^{ECL2}Q, HA-**GSGS**-FLAG
TC192	S92$^{3.39}$K, HA-**GSGS**-FLAG

Figure 59. Results of the SEC and thermostability assessment for TC108, TC138, TC190 and TC192. Upper half: Elution profile and normalized SEC data of the region of interest. Bottom left: Thermal shift assay. Nonlinear fit (Boltzmann sigmoidal) of normalized fluorescence data. The mean, normalized fluorescence data is shown as dots ± SD (n=3). The T_M was calculated as the mean ± SD of the inflection point (n=3).

Similar to the NNST-linker, the introduction of the GSGS-linker between HA- and FLAG-tag significantly increased the protein yield for both tested $A_{2B}AR$ constructs (TC108 → TC192, TC138 → TC190). In this regard it is important to note that the total protein yields were lower compared to the previous analysis, due to the fact that these proteins were once again purified in their apo state. As for the constructs containing the NNST-linker, the monodispersity and thermostability remained unchanged by the GSGS-linker as well. Thus, the GSGS-linker emerged as a small, yet highly-effective *N*-terminal modification, and as a result, TC190 became one of the most frequently utilized constructs in crystallization trials in this study.

To recapitulate, TC190 encompasses the human sequence of the $A_{2B}AR$ with the following features (additionally illustrated in Figure 60):

i. *N*-terminal HA-GSGS-FLAG sequence,
ii. four TM1 point mutations (namely A19$^{1.44}$V, C29$^{1.54}$I, G33$^{1.58}$W, A35$^{1.60}$N),
iii. one point mutation in the Na^{+} binding pocket (S92$^{3.39}$K),
iv. no potential N-glycosylation sites (N153^{ECL2}Q, N163^{ECL2}Q),
v. fusion partner bRIL inserted between L213$^{5.69}$ and H221$^{6.22}$,
vi. *C*-terminal truncation of K316$^{8.69}$ to L332,
vii. 10x histidine tag,
viii. and it is expressed in the superior GP64-pFastBac1 vector.

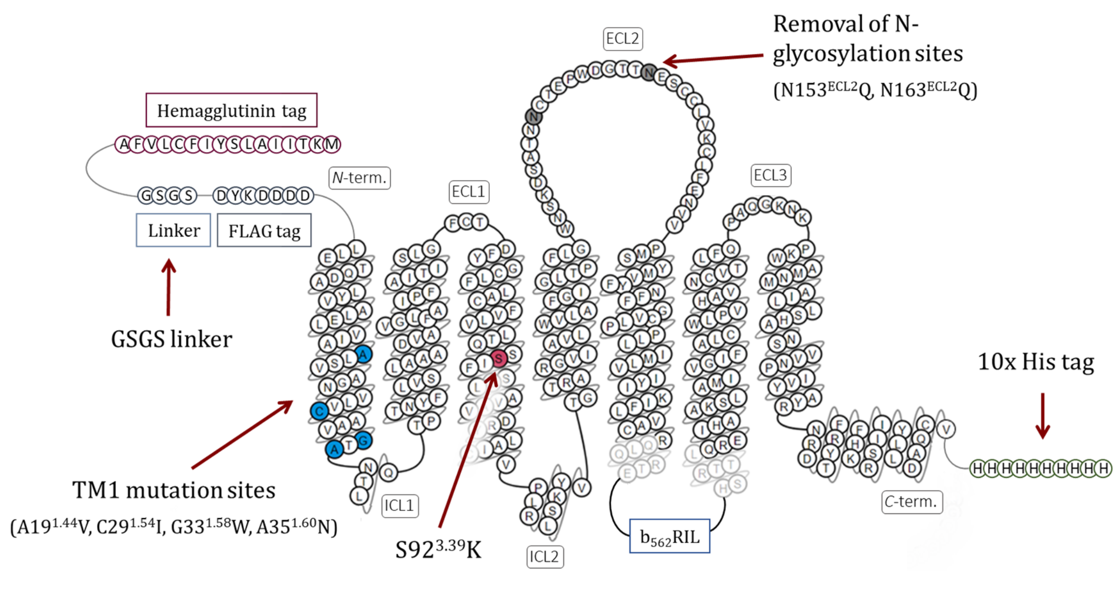

Figure 60. Construct design of TC190, presented in a SnakePlot (modified from GPCRdb)[52].

The previous sections have deeply focused on the origin of most of these features. The selection and precise placement of the fusion partner bRIL, however, was not part of the discussion yet. This is what the following section 3.7 will focus on.

3.7 Junction site optimization for bRIL in the ICL3

At the beginning of this project, during my master's thesis, all in-house available fusion partners were applied to both the *N*-terminus and the ICL3 of the $A_{2B}AR$.[252] Initially, the only distinguishable difference among the fusion partners appeared to be an increase in protein yield when the receptor was fused with the chain A of the lysozyme from tequatrovirus T4 (in short T4L).[252] During the course of this thesis, the two T4L fusion partner variations (*N*-terminal and in ICL3), were assessed once more, in order to potentially enhance $A_{2B}AR$'s protein yield and possibly other characteristics as well, this time by using the $A_{2B}AR$ construct featuring the S92$^{3.39}$K mutation, expressed in the GP64-pFastBac1 vector. The results of this assessment are provided in the following Figure 61.

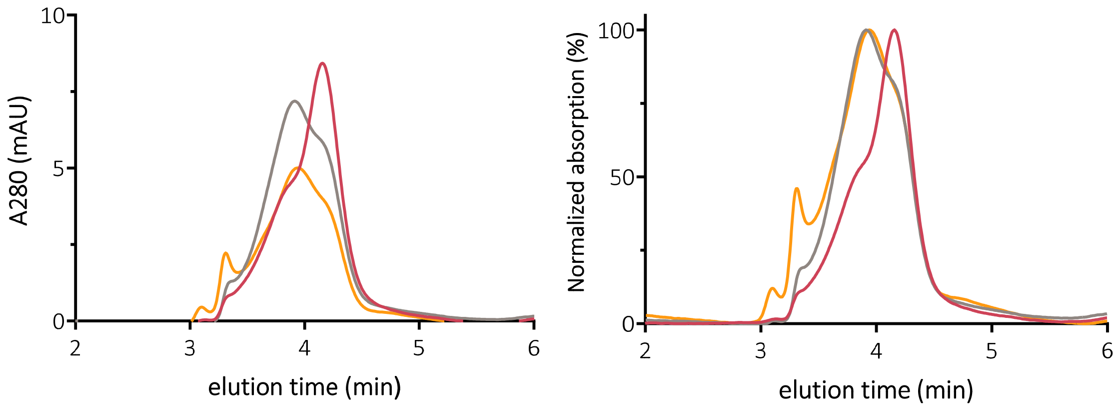

TC108	S92$^{3.39}$K, bRIL inserted between L213$^{5.69}$ and H221$^{6.22}$
TC132	S92$^{3.39}$K, T4 lysozyme fragment inserted between L213$^{5.69}$ and H221$^{6.22}$
TC133	S92$^{3.39}$K, T4 lysozyme fragment added to the *N*-terminus, native ICL3

Figure 61. Comparison of the SEC analysis of the two constructs with T4L as fusion partner (TC132, TC133) with the control TC108. Left: Elution profile of the region of interest of the SEC analysis. Right: Normalized SEC data of the region of interest.

This time, the application of the fusion partner T4L resulted in more diverse chromatograms. The reason that such a difference was not apparent in the earlier assessment can likely be attributed to the previous use of a the very stable "basis construct", which was the unmutated $A_{2B}AR$ expressed in the original pFastBac1™ plasmid. The initial hypothesis that the T4L fusion could lead to an increased protein yield was not confirmed. Among the three fusion partner options presented above, the insertion of bRIL into the ICL3 emerged as the superior choice, since the other two constructs showed a decreased signal at the elution time of 4.1 – 4.2 min, corresponding to a stable receptor, and resulted in increased protein aggregation.

In principle, a comprehensive analysis of all available fusion partners using the advanced "basis construct" (TC108) would have been advisable. However, considering that such an assessment would have required the junction site optimization of each fusion partner, the effort would have been immense and disproportionate, considering the already good results that were achieved with the fusion partner bRIL in ICL3. Thus, junction size optimization was exclusively carried out for bRIL. In this process, the standard junction site, which was adapted from the crystal constructs of the $A_{2A}AR$, was systematically shifted by one amino acid at a time (± 5 amino acids) to evaluate the optimal distance between the intracellular tips on helices five and six for the bRIL fusion in $A_{2B}AR$'s ICL3, as judged by the SEC and thermostability analysis.

The results of this junction site optimization are illustrated in the following Figure 62.

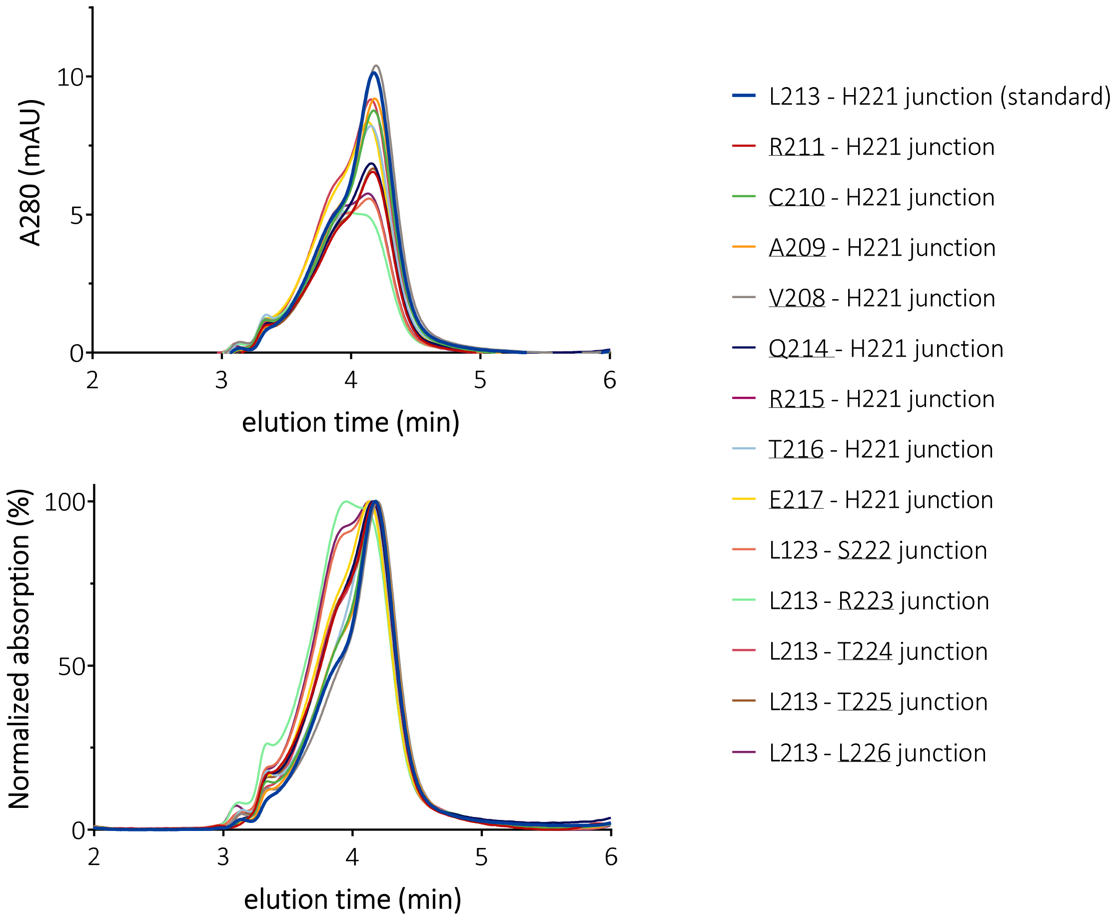

Figure 62. Results of the standard SEC analysis of the S92$^{3.39}$K, N153^{ECL2}Q and N163^{ECL2}Q mutated $A_{2B}AR$ analyzed with 14 different junction sites of bRIL in ICL3. Top: Elution profile of the region of interest of the SEC analysis. Bottom: Normalized SEC data of the region of interest.

As evident from the results presented above, the junction site that has typically been used (L213 – H221, highlighted as a thick line) showed the best monodispersity and protein yield among all of the examined junction sites. Only the V208 – H221 junction, shown in gray, appeared to cause a marginal improvement regarding these aspects. However, an examination of the melting temperatures for all constructs unveiled a considerable decrease in thermostability for this particular construct. The thermostability data for all constructs featuring junction site modifications are presented in Figure 63 below.

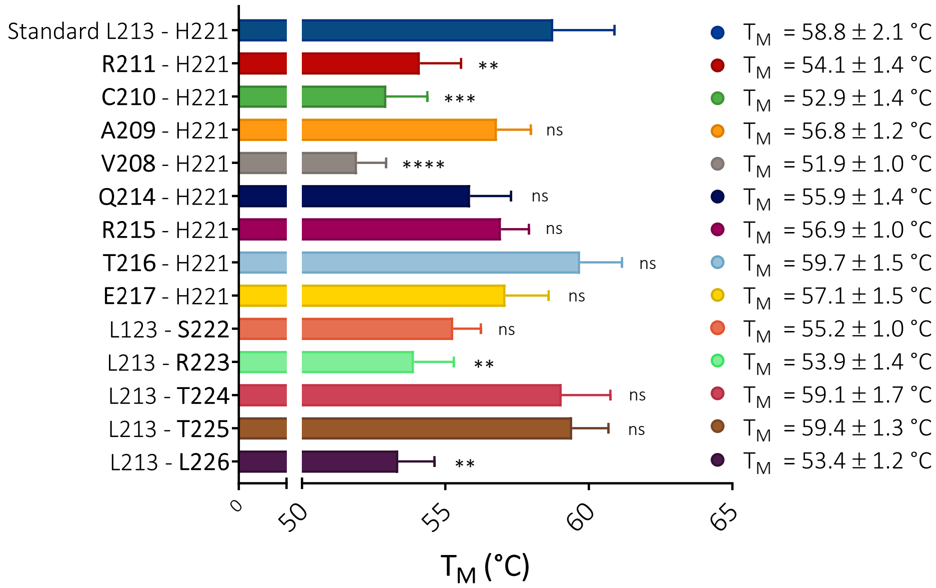

*Figure 63. Column representation of the mean melting temperatures and their SD for the 14 receptor constructs with different junction sites for bRIL in ICL3. The presented data is the average of 3 repeated measurements. For evaluation of the significance, the result of each receptor construct was compared to the receptor with the standard junction site using the Dunnett's multiple comparison test (ns: P > 0.05, * P ≤ 0.05, ** P ≤ 0.01, *** P ≤ 0.001, **** P ≤ 0.0001).*

Regarding thermostability, the standard junction site of bRIL also proved to be one of the best among the tested constructs. In contrast to that, the V208 – H221 junction resulted in a notably reduced T_M of only 51.8 °C, which is a decrease of almost 8 °C compared to the standard construct, which showed a T_M of 59.4 °C. With approximately 60 °C, three other candidates (junctions T216 – H221, L213 – T224 and L213 – T225) showed a slightly higher T_M compared to the standard insertion position. Unfortunately, the SEC results of these constructs, highlighted in the following Figure 64, do not indicate any advantages over the current junction site, neither in protein yield nor monodispersity. Therefore, the standard junction site (L213 – H221) was maintained for further constructs.

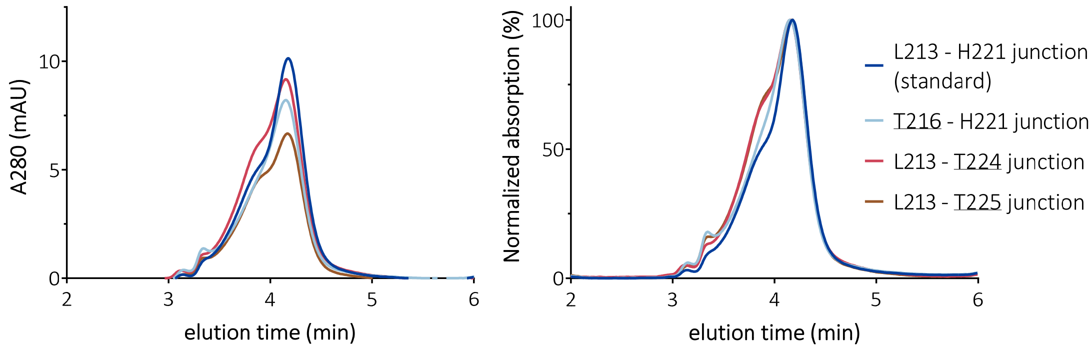

Figure 64. Comparison of the four most thermostable receptor constructs with different junction sites of bRIL in ICL3. Left: Elution profile of the region of interest of the SEC analysis. Right: Normalized SEC data of the region of interest.

3.8 Ligand Screening

One critical aspect in obtaining a co-crystal structure is the selection of a suitable ligand. Achieving protein stabilization does not only depend on modifying its amino acid sequence; the presence of ligands can also have a significant impact on the protein's yield, monodispersity and thermostability. All the proteins presented thus far were expressed and purified either in the apo form, or in the presence of 25 µM of the A_{2B}AR antagonist ISAM140, unless stated otherwise. As I will demonstrate in the following section, proteins purified with this ligand did not exhibit any noteworthily different behavior compared to apo proteins.

To determine the most suitable of the many available A_{2B}AR antagonists, two ligand screening campaigns were performed in this study. The first ligand screening took place in the early stage of this thesis and involved TC108 carrying the S92$^{3.39}$K mutation and expressed using the GP64-pFastBac1. The second screening was conducted using TC168, which is identical to TC108 but with all four TM1 mutations and without the HA-tag. To ensure consistent results, infection and membrane preparation were performed in large scale, whereupon the membrane preparation was split into equal parts for the subsequent solubilization and purification process.

3.8.1 First ligand screening with TC108

In the first ligand screening, the receptor was purified in the presence of 15 different ligands, each at a concentration of 25 µM. The ligands were selected based on their a) availability, b) solubility in aqueous solution, c) lacking fluorescence at the relevant wavelength (λ_{ex} 365 nm, λ_{em} 460 nm), which would prevent CPM-based thermostability analysis, and d) the diversity of scaffolds. The ligands utilized in this first ligand screening are depicted in Table 4.

Table 4. Overview of all ligands used for the first ligand screening for the $A_{2B}AR$.

Compound	Affinity for $A_{2B}AR$ (nM)	Structure
AT249	5.51	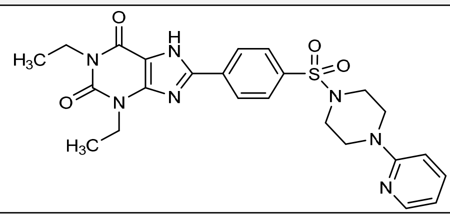
BAY 60-6583	110[196], 212[82]	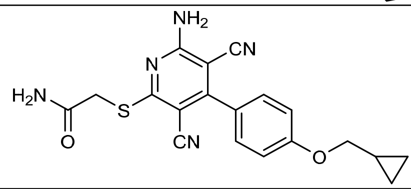
CGS15943	32.4[196], 44[269]	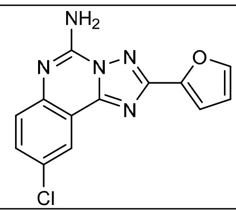
ISAM140	3.49[270]	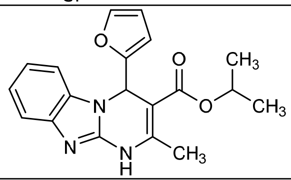
JH15079	0.971	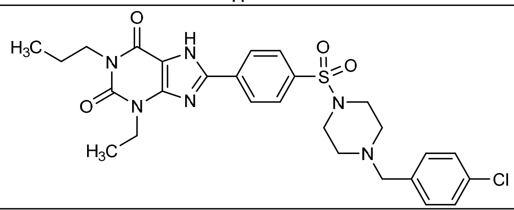
JH15100	0.180	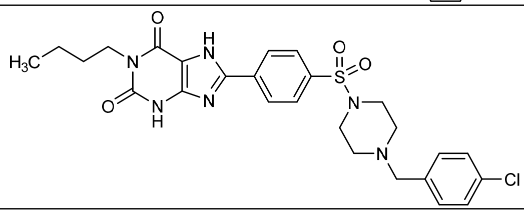

JJ1509	0.0846	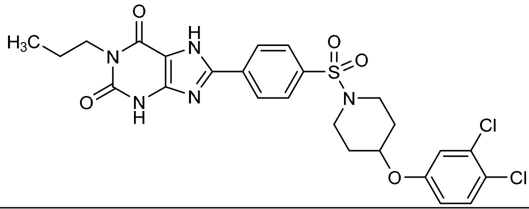
JJ1613	1.87	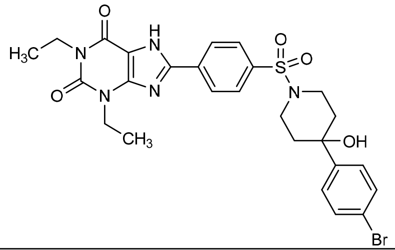
PA50	1.09	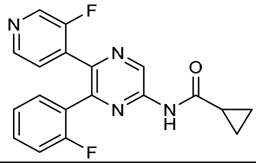
PSB-1115	53.4[271]	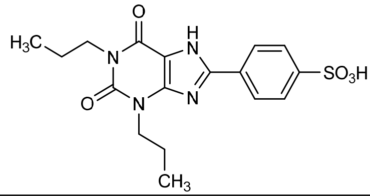
PSB-09120	0.16[272]	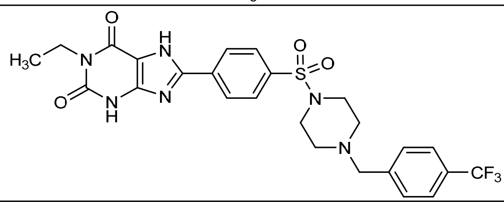
SL507	15.2	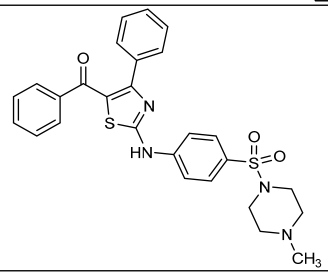
VCP746	55.0[273]	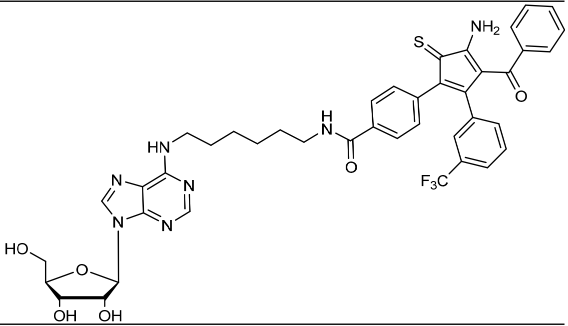
ZM-241385	31.6[274], 65.7[270], 75[275]	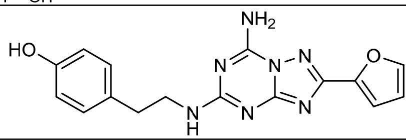

2FPYFU	2.51	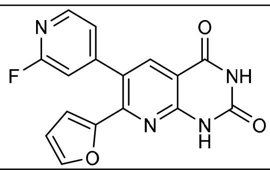

To evaluate the various ligands, a standard SEC analysis, a thermal SEC analysis and the thermostability assay were conducted. The results of the standard SEC analysis are presented in Figure 65 stated below.

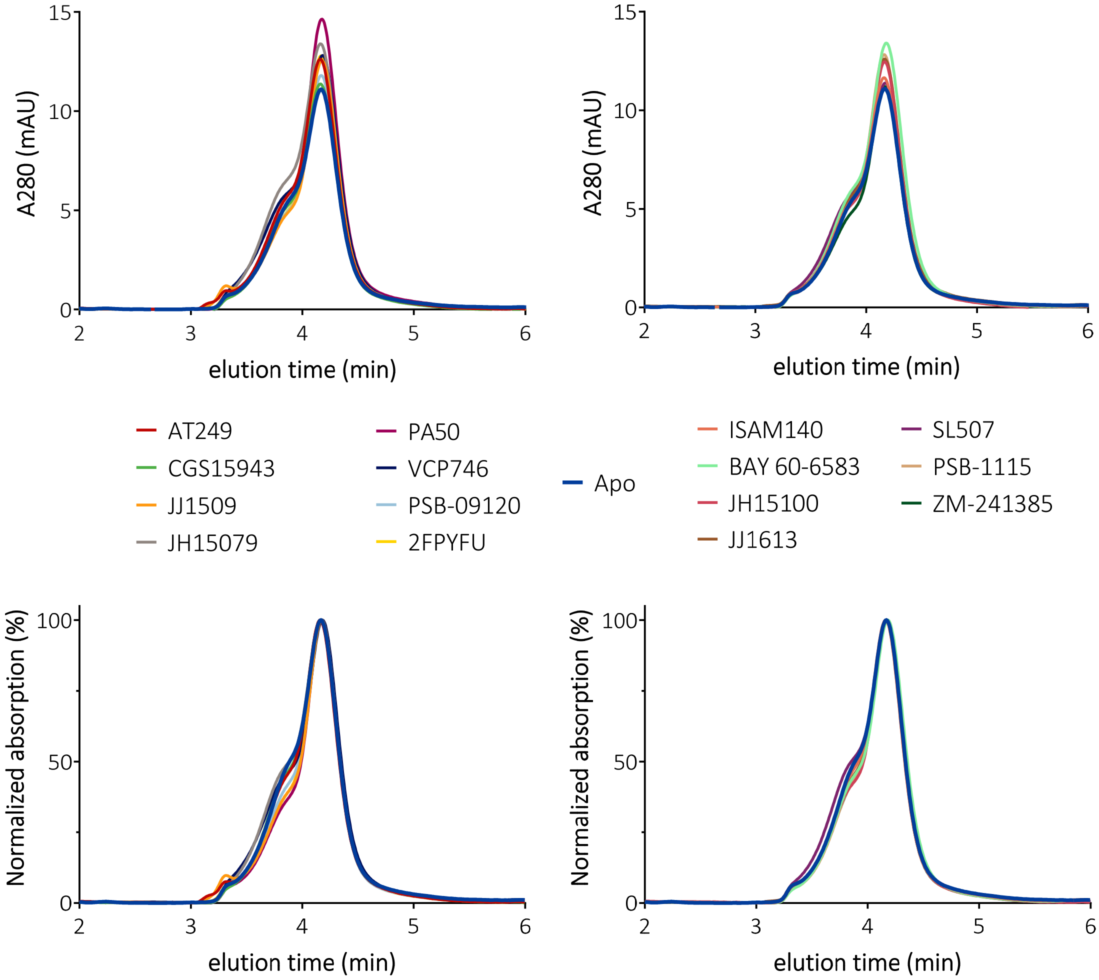

Figure 65. Standard SEC analysis of 16 A_{2B}AR samples, each purified with a distinct ligand or in apo state. Top: Elution profiles of the region of interest of the SEC analysis. Bottom: Normalized SEC data of the region of interest. For clarity, the results are split in 2x2 graphs and the results of the apo receptor are shown in each graph.

Overall, the SEC results without a heat shock prior to the analysis show a high degree of similarity. Comparing these results with the apo receptor, indicated by the red dotted line, it is notable that most of the tested ligand increased the protein yield, and the majority of them also improved the monodispersity. The ligands PSB-09120, 2FPYFU and PA50 showed the most substantial effect in this regard, and are therefore additionally focused on in the following Figure 66. In addition, the results of ISAM140, mentioned earlier in this chapter for showing no difference, are included for comparison.

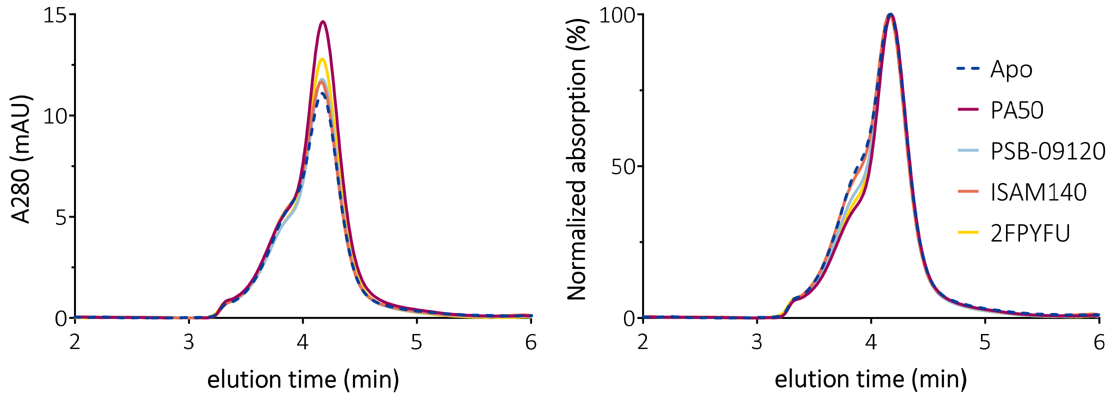

Figure 66. Comparison of selected results of the standard SEC analysis shown before. Left: Elution profile of the region of interest of the SEC analysis. Right: Normalized SEC data of the region of interest.

The purification with 25 µM PA50 resulted in the highest protein yield and monodispersity compared to all other ligands. Even though the ligands 2FYPFU and PSB-09120 showed only a slightly lower monodispersity than protein purified in the presence of PA50, neither of these ligands matched the increase in protein yield observed with PA50. In this assessment, ISAM140 (depicted in orange) showed essentially the same behavior compared to the apo receptor regarding the protein yield and monodispersity.

Typically, when analyzing the stabilizing effect of modifications applied to the receptor, the thermostability of each sample is examined. However, since some of the tested ligands are fluorescent and, therefore, cannot be properly analyzed in the standard thermostability assay, a thermal SEC analysis was conducted. For this, each sample was exposed to 55 °C for 5 min prior to their SEC analysis. This setting was pretested in a previous experiment to ensure that the receptor would not denature completely at this temperature, but would be affected enough to enable a proper evaluation of the stabilizing effect of the ligands. The results of this thermal SEC are depicted in the following Figure 67.

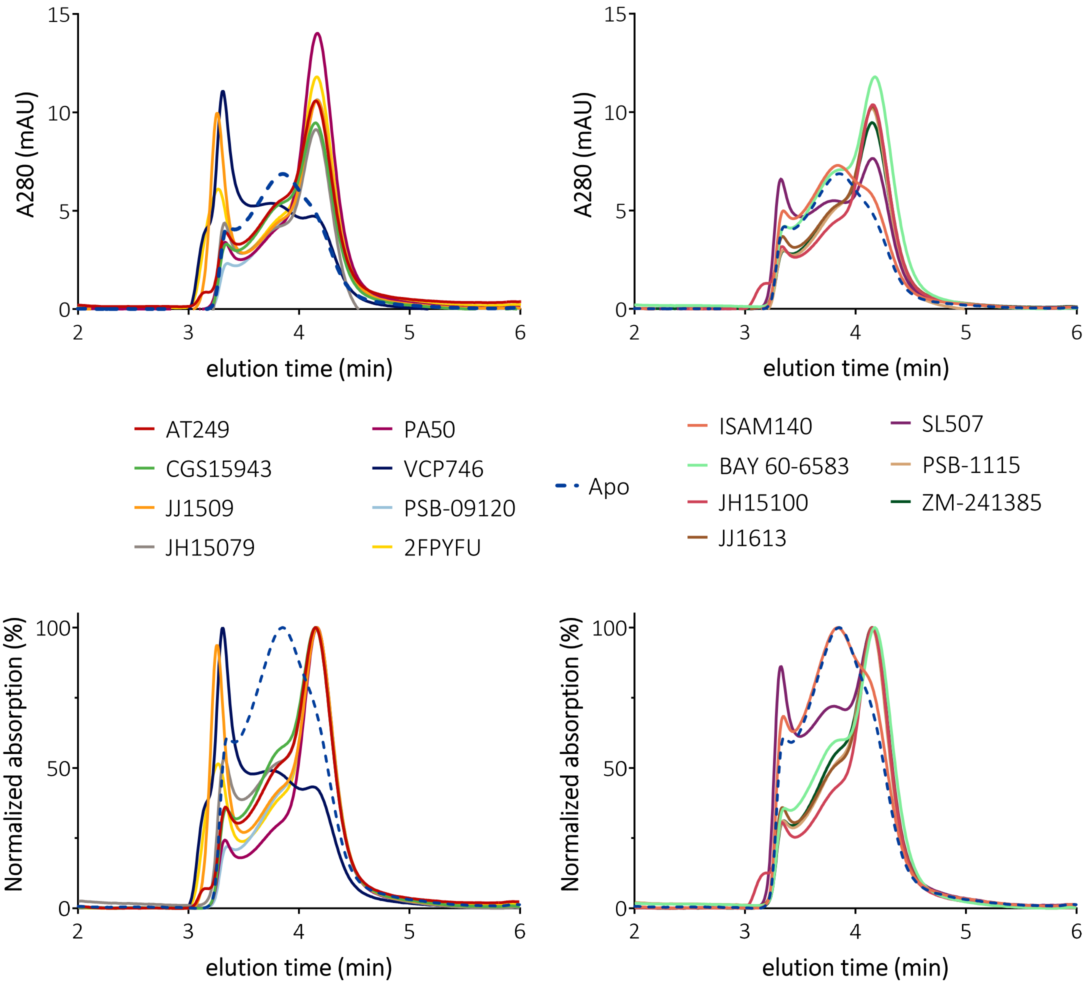

Figure 67. Thermal SEC analysis of 16 $A_{2B}AR$ samples, each purified with a distinct ligand or in apo state. Top: Elution profile of the region of interest of the SEC analysis. Bottom: Normalized SEC data of the region of interest. For clarity, the results are split in 2x2 graphs and the results of the apo receptor are shown in each graph.

The thermal SEC analysis yielded more heterogenous results than the standard SEC. Many samples displayed a distinct aggregation peak at around 3.3 min of elution time, and for some ligands (e.g. JJ1509, VCP746, SL507) this peak was even more pronounced than the aggregation peak observed for the apo receptor. In all cases, the heat shock resulted in a leftward shift in the signal, supporting the hypothesis that the premature elution of the early $A_{2B}AR$ constructs is likely caused by instable or incorrectly-folded protein, rather than homodimers of the receptor.

The proteins purified in the presence of PA50, PSB-09120, and JH15100 were the least affected by the heat shock, which is consistent with the findings from the standard

SEC analysis. The thermal SEC results of these superior ligands and ISAM140 are presented separately in Figure 68 given below.

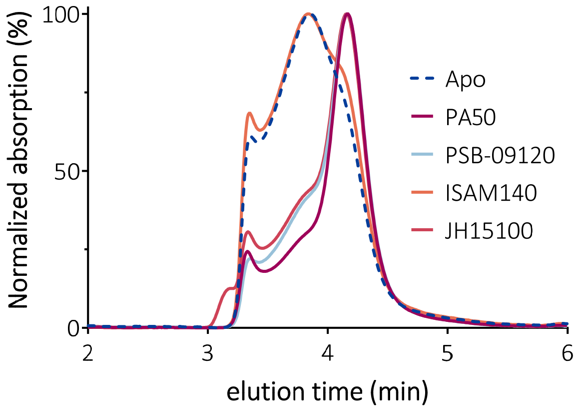

Figure 68. Normalized data of selected results of the thermal SEC analysis of the ligand screening.

Following heat shock, again only very minimal differences between the chromatograms of the apo receptor and the receptor purified with ISAM140 were observed. As previously observed, PA50 and PSB-09120 appeared to provide the best stabilization for the receptor, however, also the addition of JH15100 prevented destabilization and aggregation of the receptor. In contrast to that, the previously identified favorable ligand 2FPYFU resulted in more destabilization compared to the other ligands that demonstrated superior effects in the normal SEC analysis.

Even though some of the ligands exhibited fluorescence at 460 ± 20 nm, including the promising antagonists PSB-091290 and JH15100, the standard thermostability assay was conducted. Figure 69 compares the T_M of TC108 in apo form and in complex with 14 of the 15 tested ligands.

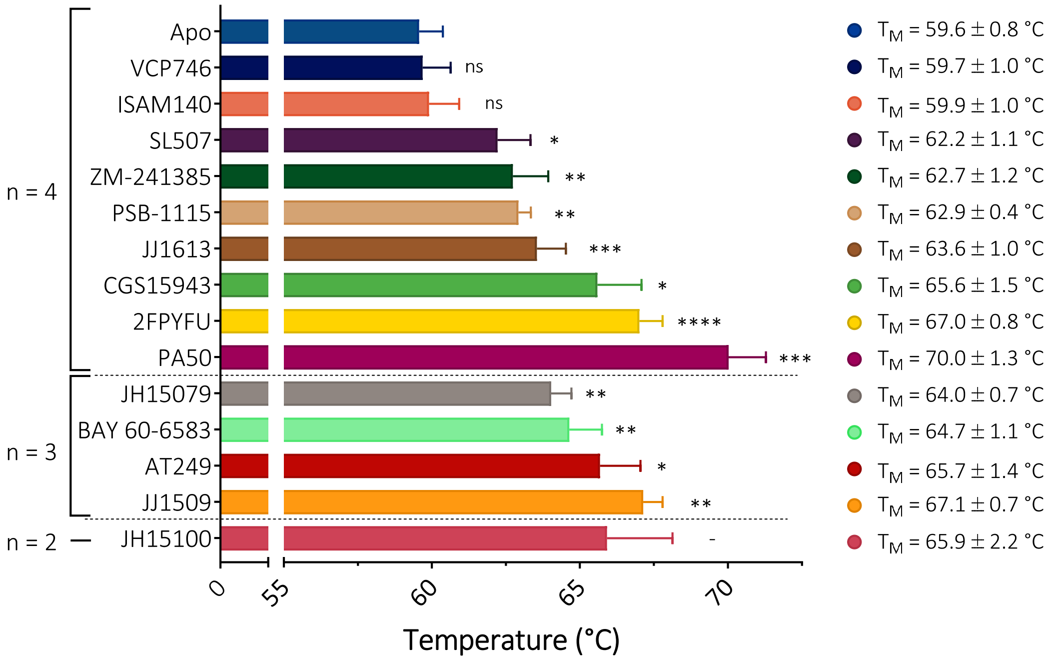

*Figure 69. Column representation of the mean melting temperatures and their SD for 14 ligand-bound receptors and the apo receptor TC108. The presented data is the average of 2-4 repeated measurements, as indicated on the left. For evaluation of the significance, the result of each ligand-bound receptor was compared to the apo receptor using the Dunnett's multiple comparison test (ns: P > 0.05, * P ≤ 0.05, ** P ≤ 0.01, *** P ≤ 0.001, **** P ≤ 0.0001).*

In most cases, the thermostability assessment was feasible. However, PSB-09120 posed an exception due to its high intrinsic fluorescence, which interfered with the required sigmoidal curve shape that is necessary for the meaningful interpretation of the results. Similar problems were observed with the ligands JH15079, BAY 60-6583, AT249, JJ1509 and JH15100, wherefore their results could be interpreted only two to three times out of the four repeated measurements.

In general, the thermostability assay substantiates the findings of both previous assays. With a melting temperature of 70.0 ± 1.3 °C PA50 exhibited the best stabilization of the receptor, followed by JJ1509 (T_M of 67.1 ± 0.7 °C), 2FPYFU (67.0 ± 0.8 °C) and JH15100 (65.9 ± 2.2 °C). Compared to the apo receptor, this represented an improvement of 6 – 10 °C. The fact that JJ1509 significantly increased the T_M despite exhibiting an even stronger aggregation upon heat shock compared to the apo receptor, was somewhat surprising. Apart from this observation, the results seem consistent between both of the thermostability assessments, suggesting that PSB-09120 likely enhances the thermostability similarly to the other promising ligands, even though data from the CPM-based thermostability assay is missing.

Nevertheless, it was PA50 that showed the most favorable effect in all aspects, from monodispersity to protein yield and thermostability.

ISAM140 consistently produced results similar to the apo receptor in all of the assays presented, with a T_M of 59.9 ± 1.0 °C versus 59.6 ± 0.8 °C for the apo receptor. This reaffirms the validity of comparing proteins purified with or without this ligand, in all aspects.

3.8.2 Second ligand screening with TC168

The results of the initial ligand screening led to the selection of PA50 as an antagonist for the very first crystallization trial with the $A_{2B}AR$ in our laboratory. However, before proceeding with the subsequent crystallization trials, involving the more advanced $A_{2B}AR$ constructs that harbor the four additional TM1 mutations (e.g. TC168), another ligand screening campaign was conducted.

Likewise, the first ligand screening, infection and membrane preparation were conducted in large scale to ensure comparability of the results. The membrane preparation was then split into 14 equal parts for purification in the presence of 13 different ligands, with concentrations ranging from 25 µM to 100 µM, as well as in apo form. The specific ligands that were assessed, and their affinity, used concentration and chemical structure are provided in the following Table 5.

Table 5. Overview of ligands used for the second $A_{2B}AR$ ligand screening campaign.

Compound	Affinity for $A_{2B}AR$ and used concentration	Structure
1-Propyl-xanthine	K_i 360 nM[276] Used at 50 µM	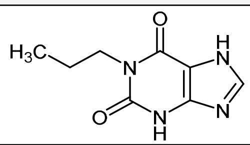
2FPYFU	K_i 2.51 nM Used at 50 µM	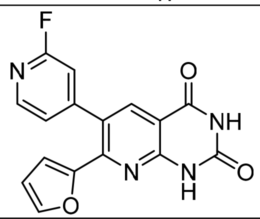
Caffeine	10.4 µM,[276] 33.8 µM[272] Used at 100 µM	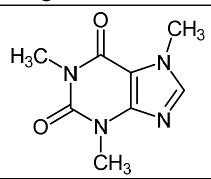

PA51	K_i 4.24 nM Used at 50 µM	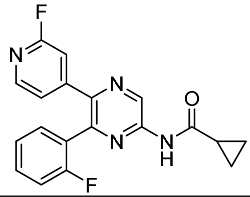
PSB-50	K_i 6.8 nM[271] Used at 50 µM	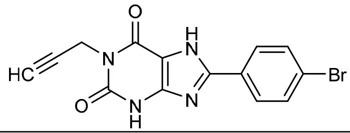
PSB-53	K_i 24 nM[271] Used at 50 µM	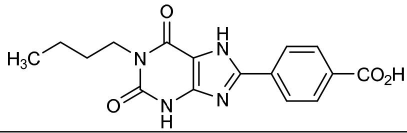
PSB-55	K_i 1.3 nM[271] Used at 25 µM	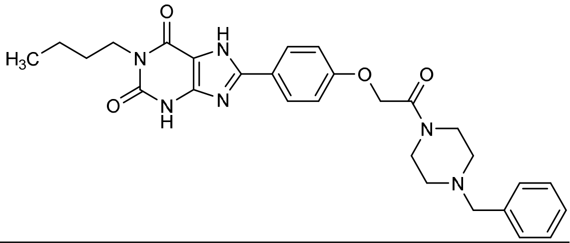
PSB-603	K_i 0.553 nM[272] Used at 50 µM	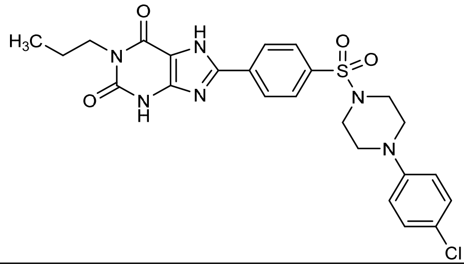
PSB-09120	K_i 0.157 nM[272] Used at 50 µM	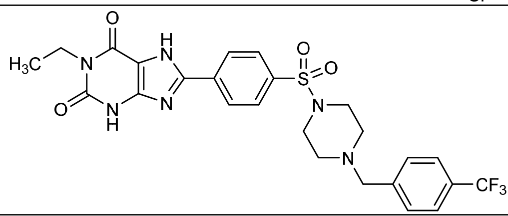
SL345	K_i 42.6 nM Used at 50 µM	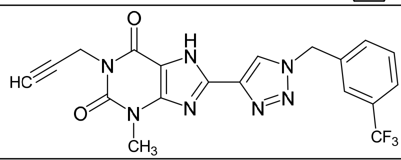
SL501	K_i 19.7 nM Used at 50 µM	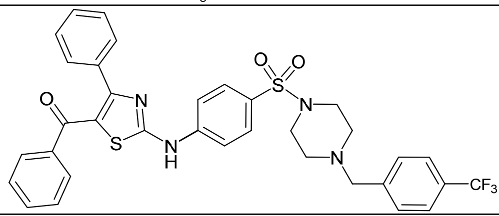
SL504	K_i 19.3 nM Used at 50 µM	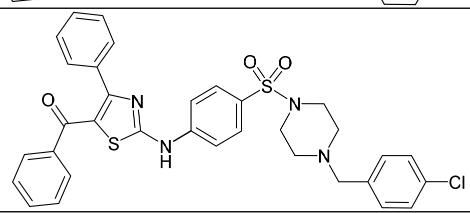

XAC	K_i 7.80 nM[277] Used at 25 µM	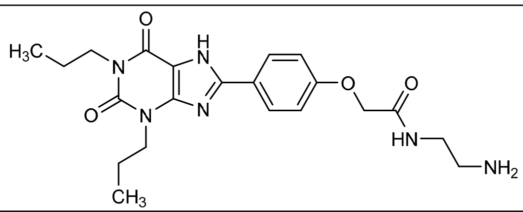

In order to evaluate the effects of the various ligands, a standard SEC analysis, a thermal SEC analysis and the CPM-based thermostability assay were conducted. The results of the standard SEC analysis are presented in Figure 70.

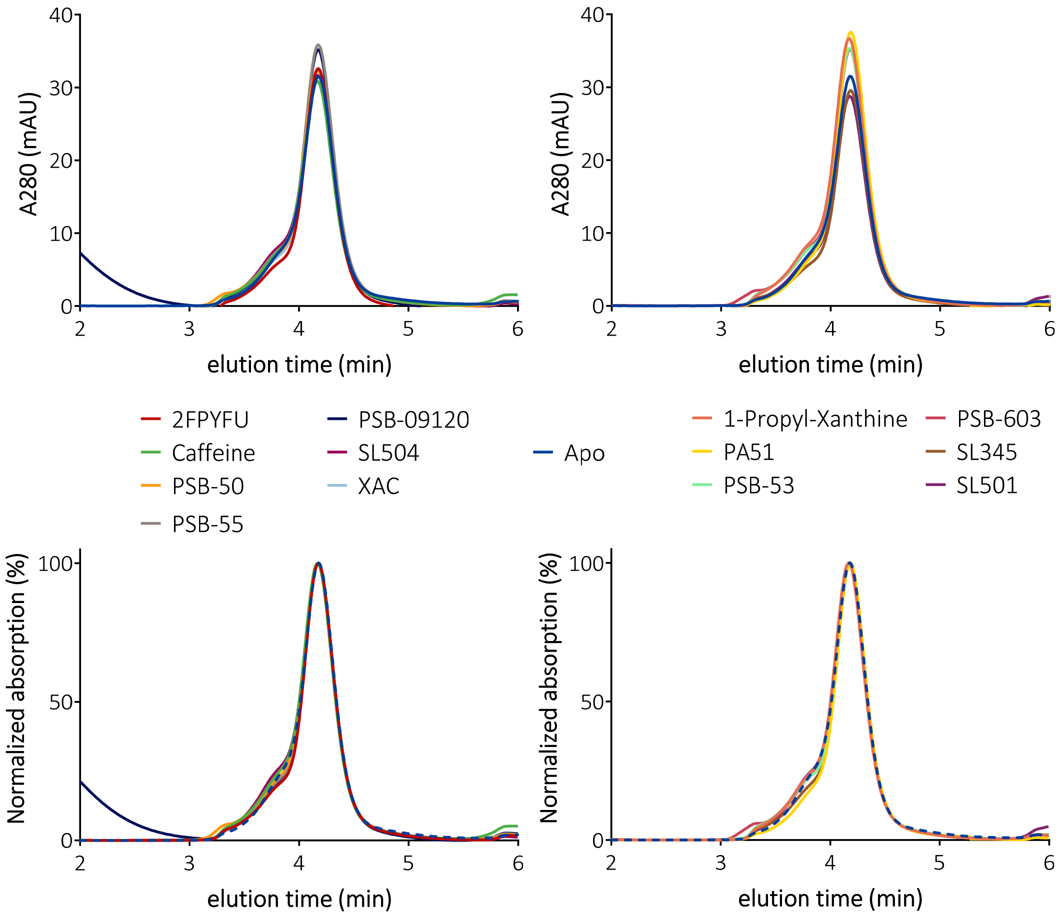

Figure 70. Standard SEC analysis of the 14 TC168 samples, each purified with a distinct ligand or in the apo state. Top: Elution profiles of the region of interest of the SEC analysis. Bottom: Normalized SEC data of the region of interest. For clarity, the results are split in 2x2 graphs. The result of the apo receptor is shown in each graph.

Much like the first ligand screening, the results of the standard SEC assessment without the heat shock showed high similarity. Nevertheless, several of the tested ligands did show improvements in the protein yield and some also increased monodispersity, as best seen in the lower panel of Figure 70. However, the effects were not as pronounced as those seen in the first ligand screening campaign with TC108. This time, the ligands 2FPYFU, PA51 (closely related to PA50, mentioned earlier) and SL345 exhibited the most significant effect regarding monodispersity. Therefore, these are additionally presented in the following Figure 71.

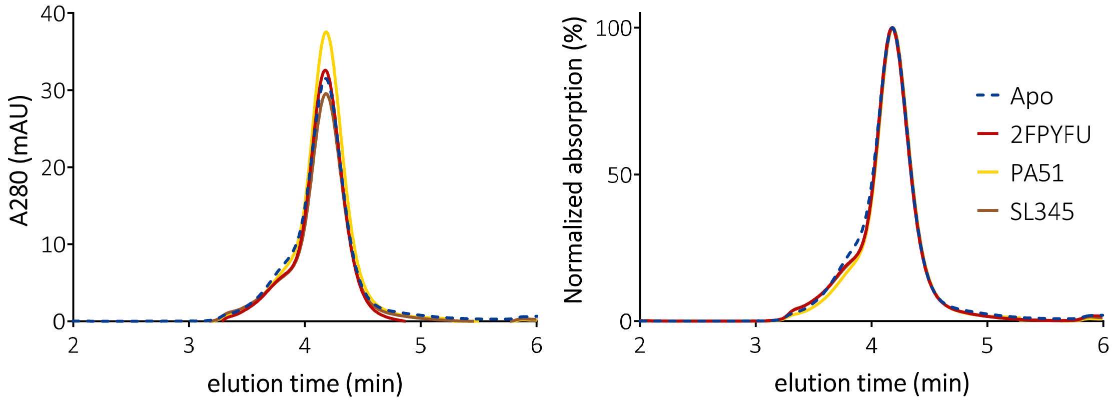

Figure 71. Comparison of selected results of the standard SEC analysis presented in Figure 70. Left: Elution profile of the region of interest of the SEC analysis. Right: Normalized SEC data of the region of interest.

Purification with PA51 resulted in the highest protein yield and monodispersity compared to all other ligands. In terms of monodispersity, 2FPYFU and SL345 showed similar effects, however, neither of them increased the protein yield. The ligand SL345 even slightly decreased the protein yield compared to the sample that was purified in the apo form.

Since some of the tested ligands or their impurities had previously shown fluorescence at the relevant wavelength, a thermal SEC was performed in addition to the fluorescence-based thermostability assay with CPM. This time, due to the higher inherent stability of TC168, the samples were incubated in a 60 °C water bath for 5 min prior to the SEC analysis. The results of this thermal SEC are illustrated in Figure 72 stated below.

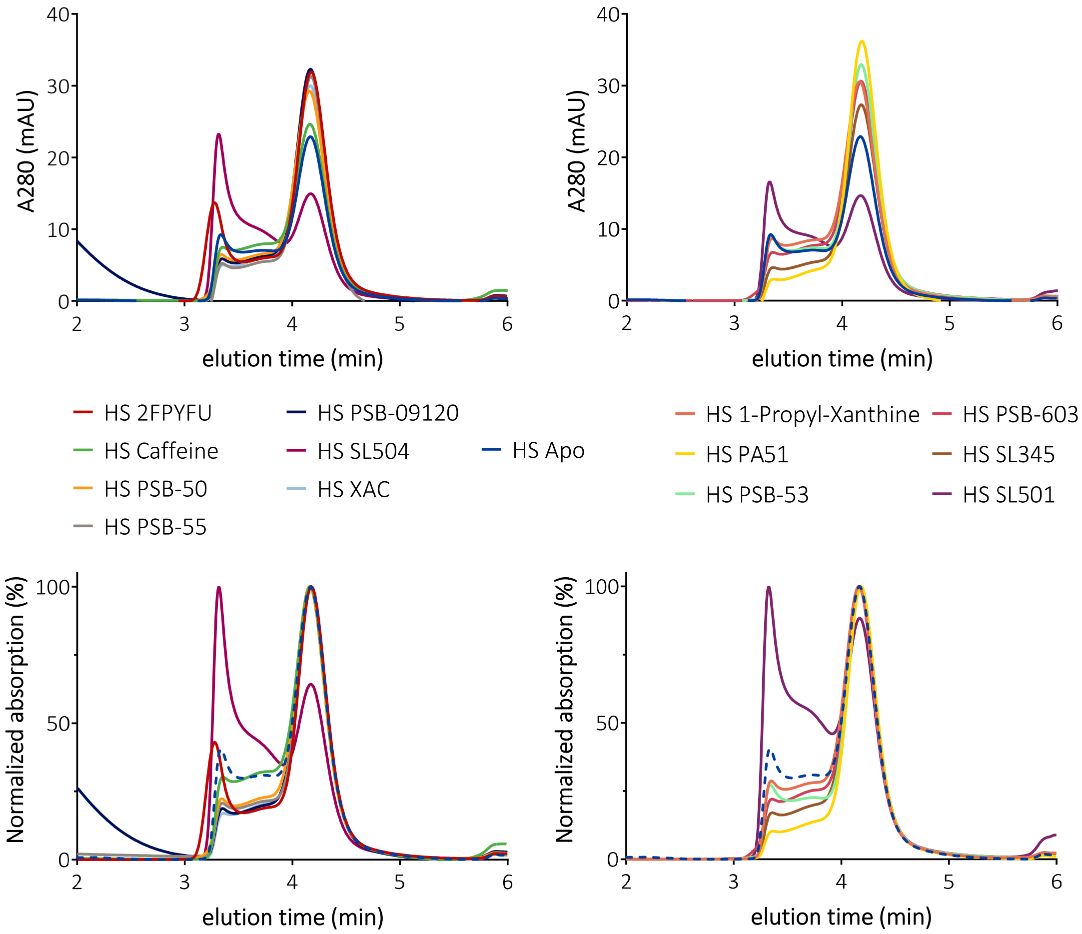

Figure 72. Thermal SEC analysis of the 14 TC168 samples, each purified with a distinct ligand or in the apo state. Top: Elution profiles of the region of interest of the SEC analysis. Bottom: Normalized SEC data of the region of interest. For clarity, the results are split in 2x2 graphs. The result of the apo receptor is shown in each graph.

Once again, the thermal SEC analysis resulted in more diverse results compared to the standard SEC. In some cases, distinct aggregation peaks appeared around 3.3 min elution time. Particularly for the antagonists SL501 and SL504 these peaks were significantly more prominent that the aggregation peak of the apo receptor. Still, most of the antagonists performed similarly. In hindsight, to highlight differences between the ligands, a more intense heat shock would have been advisable. Nevertheless, the sample that was purified in complex with PA51 was undoubtedly least affected by the heat shock, which aligns with the result from the standard SEC, as well as the results of the related PA50, presented above (section 3.8.1, page 93).

In addition to the thermal SEC, the standard thermostability assay was conducted. Figure 73 compares the T_M of TC168 in complex with the various ligands.

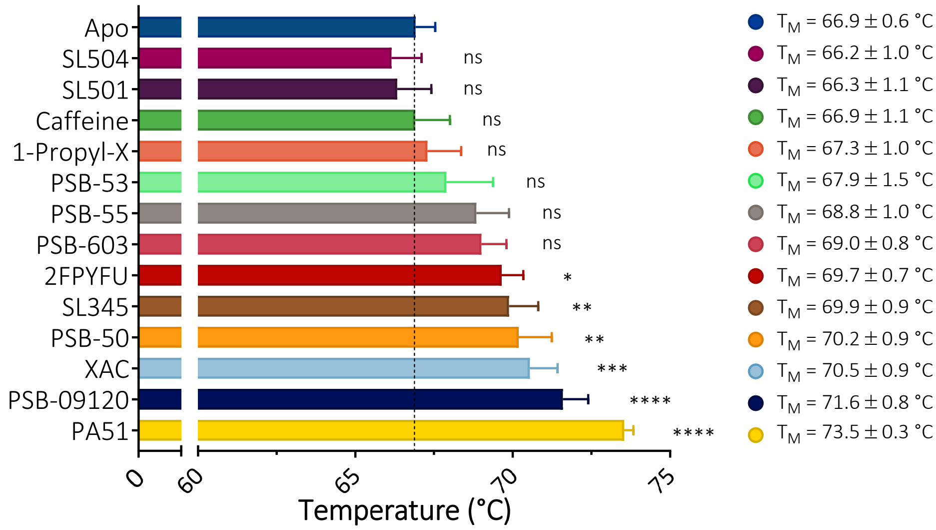

*Figure 73. Column representation of the mean melting temperatures and their SD for 13 ligand-bound receptors and the apo receptor TC168. The presented data is the average of 3 repeated measurements. For evaluation of significance, the result of each ligand-bound receptor was compared to the apo receptor using the Dunnett's multiple comparison test (ns: P > 0.05, * P ≤ 0.05, ** P ≤ 0.01, *** P ≤ 0.001, **** P ≤ 0.0001).*

In this thermostability assessment, each ligand was successfully evaluated, including the formerly problematic PSB-09120. Consistent with the findings from both of the SEC assays, the ligand PA51 demonstrated the highest thermostabilization in this CPM-based assay, followed by the in-house ligand PSB-09120. Interestingly, the ligands 2FPYU and SL345, which were among the best ligands with regard to the receptor monodispersity before heat-shock, caused a more modest increase in T_M, raising it by only 3 °C. Consistent with the results of the thermal SEC, the antagonists SL501 and SL504 showed a (slightly) negative impact on the receptor's thermostability, whereas the nonselective AR antagonist caffeine did not affect the T_M at all. In general, however, the differences in thermostability, observed in this ligand screening utilizing TC168, were less significant compared to the initial ligand screen using TC108, with a maximum T_M increase of 5 – 7 °C, compared to the > 10 °C increase seen for TC108 in the presence of PA50.

Nonetheless, PA51 proved to be the most advantageous ligand in this ligand screening campaign, regarding all aspects, namely monodispersity, thermostability and protein yield. But also the in-house ligand PSB-09120 with its xanthine scaffold demonstrated a significant degree of receptor stabilization, rendering both ligands promising options for crystallization experiments. The very first of these crystallization experiments is presented in the following section 3.9.

3.9 Crystallization of TC111 in complex with PA50

The first crystallization of the A_{2B}AR in our laboratory was performed with construct TC111 in complex with the antagonist PA50, added at a high concentration of 25 µM. To recapitulate, the three main features of this construct are a) the TM1 exchange, b) mutations S92$^{3.39}$K and A232$^{6.33}$E, and c) the absence of *N*-terminal tags.

Large-scale purification and crystallization were performed as described in sections 5.2.3 and 5.2.4; exact details of the purification process are provided in the appendix. In short, an equivalent of 450 mL of *Sf9* cell biomass was used, and all purification steps were performed in the presence of 25 µM PA50. The protein was eluted with 2 mL of elution buffer, and was subsequently concentrated in a 100 kDa molecular weight cut-off (MWCO) concentrator to the minimal volume of approximately 20 µL. It should be noted, that the concentrated protein sample used for the analysis, provided below, was prematurely removed from the concentrator when the volume amounted to approximately 30 µL. For crystallization, a total of six different 96-well plates with precipitant solutions (each containing 48 different salts at 100 mM and 300 mM), pH 5.0, 5.6, 6.0, 6.4, 7.0 and 7.4, were screened for their ability to facilitate protein crystal growth.

The results of all relevant assays, and the crystallization outcome are presented in the following Figure 74.

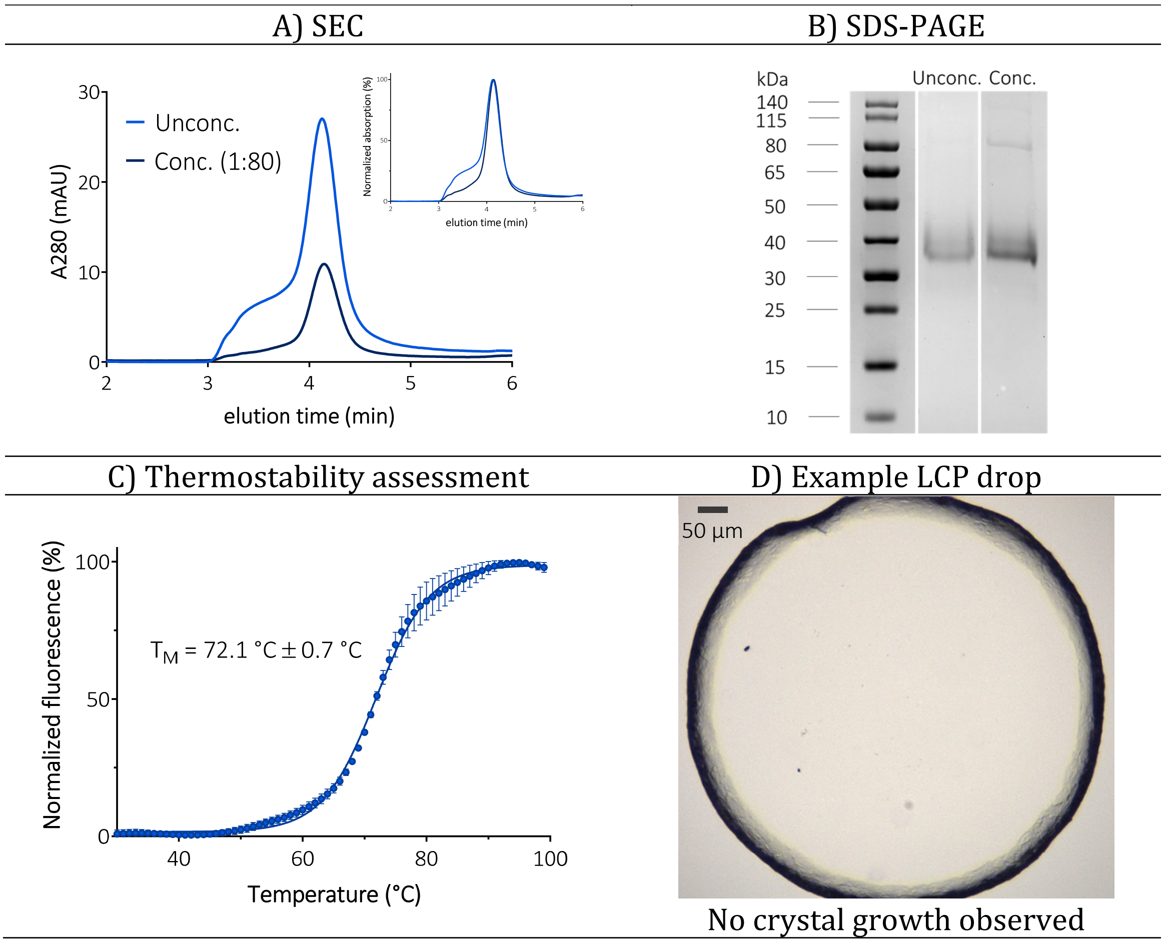

Figure 74. Protein analysis and crystallization of TC111 in complex with PA50. A) Region of interest of the SEC analysis of the (un-)concentrated protein samples (normalized results in the top right corner). B) SDS-PAGE of the purified samples, 30 µL each (concentrated sample (conc.) ~ 1:100 diluted). C) Thermostability assessment of the unconcentrated (unconc.) sample. Nonlinear fit (Boltzmann sigmoidal) of normalized fluorescence data. The mean, normalized fluorescence data is shown as dots ± SD (n=3). The T_M was calculated as the mean ± SD of the inflection point (n=3). D) Exemplary LCP drop from the crystallization experiment.

Large-scale purification of TC111 in complex with PA50 yielded a highly pure and sufficiently thermostable sample. Strikingly, the monodispersity of the sample before concentration was lower than that of the concentrated sample. One possible explanation for this observation could be that the unconcentrated sample contained a significant amount of smaller protein impurities, which were removed upon concentration with the 100 kDa MWCO concentrator. However, the SDS-PAGE of the unpurified sample did not indicate the presence of such impurities. Therefore, an alternative explanation could be related to a potential issue during the SEC analysis, possibly arising from fluctuations in pressure during the measurement.

Fortunately, the more crucial sample in this assessment, the concentrated sample (diluted 1:80-fold), displayed a more favorable monodispersity, however, unfortunately, a low protein amount as judged by the height of the main peak in panel A. As mentioned earlier, the protein was removed early from the concentrator, which means that the protein used for the crystallization experiment was indeed more concentrated than the analyzed protein sample. It is also possible that the partially concentrated protein solution was not entirely homogenous when the sample was taken, which could have contributed to the seemingly low protein peak. In any case, the purified and concentrated TC111 protein was reconstituted in LCP and was used to set up six 96-well plates with the precipitant conditions described above.

Unfortunately, the attempt to crystallize the protein was not successful. Most of the LCP drops were either empty (as presented in panel D of Figure 73), or the wells contained small crystals in both the LCP and the precipitant conditions, which were clearly identified as salt crystals. To improve the outcome of the next crystallization effort, it was advisable to increase the protein amount, potentially by purifying it from a larger amount of biomass. Additionally, as discussed in section 3.4 on page 73, the N-glycosylation sites which were still present in construct TC111 might have hindered the formation of protein crystals, due to potential heterogeneity of the glycans. Both of these issues were addressed in subsequent crystallization trials.

3.10 Crystallization of TC169 in complex with PA51

Thanks to the ongoing progress in construct optimization, the next crystallization experiment could be carried out using the less strongly modified construct TC169. In contrast to TC111 from the previous crystallization attempt, TC169 did not have any N-glycosylation sites in the ECL2 and showed an enhanced protein yield due to the incorporation of the NNST-linker between the HA- and FLAG-tag on the *N*-terminus. Additionally, this construct featured the four beneficial TM1 mutations, along with the crucial S92$^{3.39}$K mutation.

This time, the purification process was performed in the presence of 50 µM of the antagonist PA51, and it was carried out starting from an equivalent of 450 mL of biomass. Following the elution with 2 mL of elution buffer, the protein was concentrated to an approximate volume of 20 µL. In contrast to the previous crystallization, the protein concentration was completed it subjected to SEC analysis for the assessment of the protein amount and monodispersity of the sample.

The results of the SEC assessment, as well as other relevant results are presented in Figure 75 provided below.

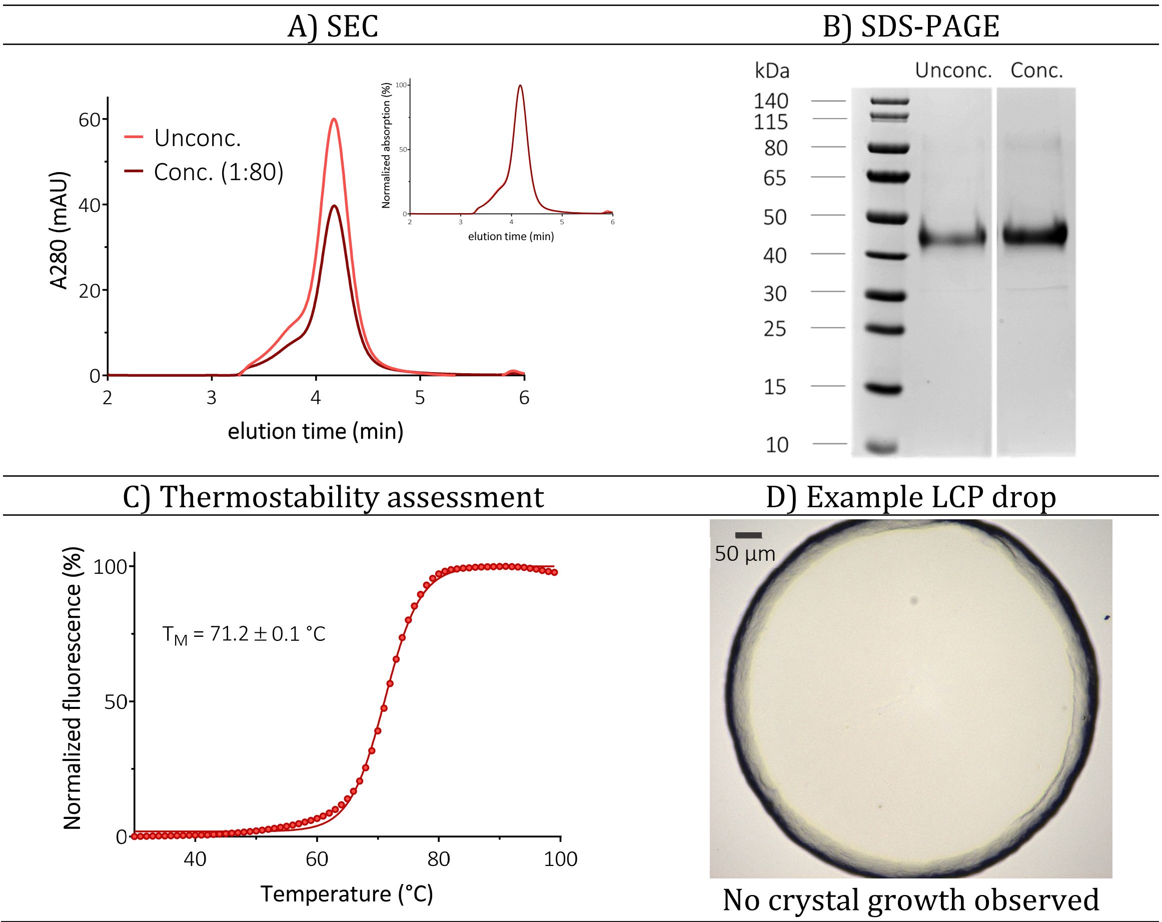

Figure 75. Protein analysis and crystallization of TC169 in complex with PA51. A) Region of interest of the SEC analysis of the (un-)concentrated protein samples (normalized results in the top right corner). B) SDS-PAGE of the purified samples, 30 µL each (conc. ~ 1:100 diluted). C) Thermostability assessment of the unconcentrated sample. Nonlinear fit (Boltzmann sigmoidal) of normalized fluorescence data. The mean, normalized fluorescence data is shown as dots ± SD (n=3). The T_M was calculated as the mean ± SD of the inflection point (n=3). D) Exemplary LCP drop from the crystallization experiment.

Similar to small-scale purification of TC169 in complex with PA50, presented in section 3.6.2 on page 84, large-scale purification with PA51 yielded a highly thermostable protein with good monodispersity, both before and after the concentration step. In comparison to the crystallization with TC111, the concentrated sample showed an approximately four-fold higher peak. Nevertheless, the 100-fold concentration (from 2 mL of unconcentrated sample to 20 µL of concentrated sample) did not result in a proportionally increased protein amount, which by experience is a common observation for (membrane) proteins. Regarding the purity, as assessed by SDS-PAGE presented in panel B), the protein sample displayed only minimal impurities at 30 kDa, demonstrating a satisfactory level of purity.

In this crystallization attempt, a total of nine different 96-well plates of precipitant solutions were tested. Six of the plates corresponded to the 48-salt plates at pH values ranging from pH 5.0 to pH 7.4, that were also utilized for the previously described crystallization attempt. In addition to those, the commercial screening plate PEG/Ion 400 from Hampton Research was employed twice, and one 96-well plate with crystallization conditions successfully used for the $A_{2A}AR$ was tested as well. Unfortunately, as in the previous attempt, the crystallization trial resulted in either empty wells or salt crystals, which were similarly present in the precipitant condition surrounding the LCP drop as well. Considering the significantly greater protein concentration in this case, the reasons for the unsuccessful outcome are less obvious. It was observed that during the incubation of the LCP drops with precipitant solution, the LCP drops disintegrated unusually fast and manifold, suggesting a potential problem with the monoolein/cholesterol stock, that was used in this crystallization trial for LCP formation (as described in section 5.2.4, page 249). Also, although construct TC169 does not harbor any N-glycosylation sites in the ECL2 anymore ($N153^{ECL2}Q$, $N163^{ECL2}Q$), it does possess two N-glycans at its *N*-terminus due the inclusion of the protein yield-increasing NNST linker. Possibly, these glycosylations hindered crystal formation.

To avoid these caveats for future crystallizations, a fresh stock of monoolein/cholesterol was prepared for the next crystallization. Moreover, TC168, which lacks any N-glycosylation sites, was chosen over TC169 for the next crystallization experiment, and our potent in-house ligand PSB-09120 was employed as an alternative ligand based on a different scaffold. The outcome of these changes is detailed in the following section.

3.11 Crystallization trials of TC168 with PSB-09120 (I - III)

3.11.1 Crystallization of TC168 in complex with PSB-09120 (I)

To compensate for the lower protein yield of TC168, compared to TC169 (see Figure 57 on page 85), and the change of ligands, the TC168 protein was purified from twice as much biomass as used previously for the crystallization of TC169. The other characteristics of the purification, e.g. elution volume and ligand concentration, were identical to those of the previous crystallization experiment. However, the ligand PSB-09120 was not completely dissolved at a concentration of 50 µM, due to its limited water-solubility. Therefore, insoluble ligand was removed by centrifugation before the analyses of the samples. The results of these analyses are provided in Figure 76.

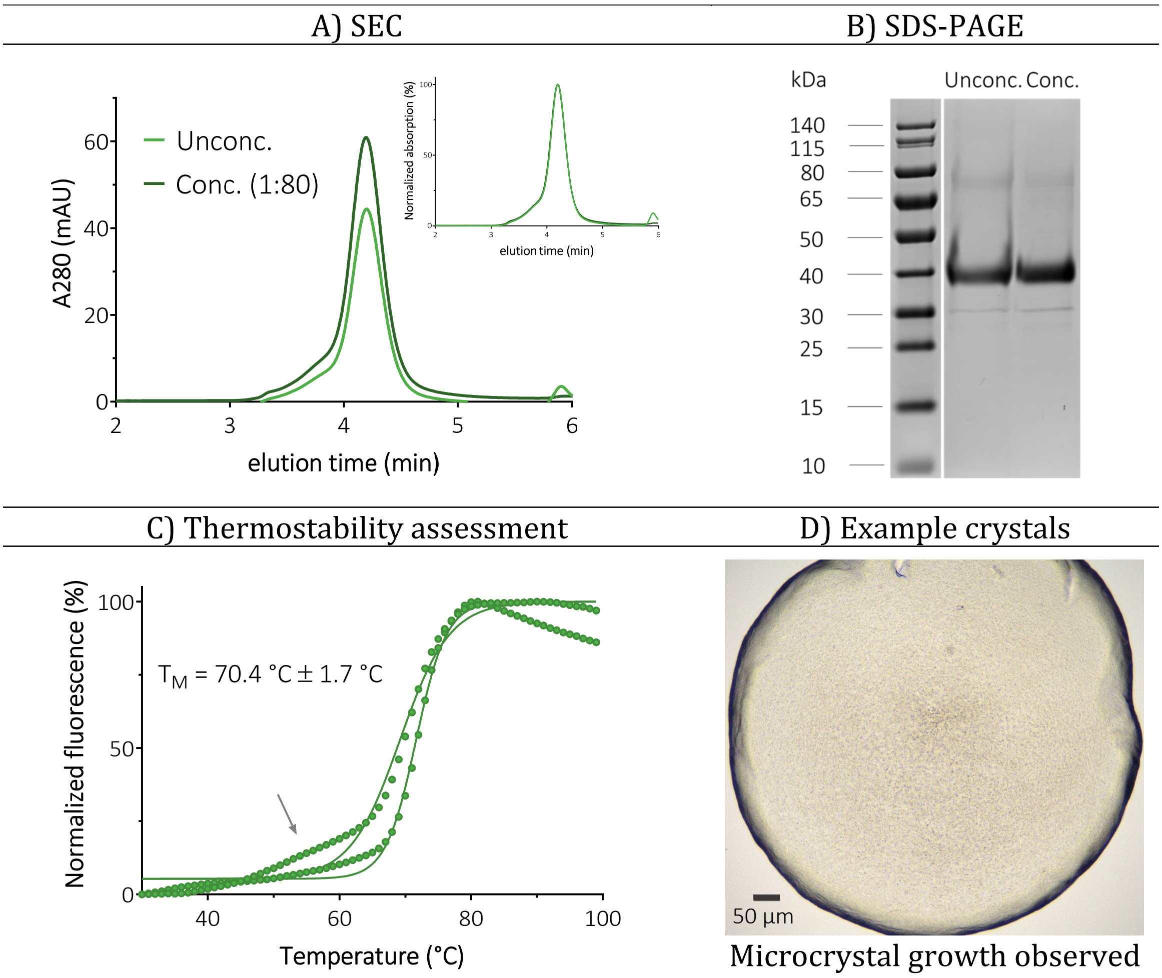

Figure 76. Protein analysis and crystallization of TC168 in complex with PSB-09120 (I). A) Region of interest of the SEC analysis of the (un-)concentrated protein samples (normalized results in the top right corner). B) SDS-PAGE of the purified samples, 30 µL each (conc. ~ 1:100 diluted). C) Thermostability assessment of the unconcentrated sample. Nonlinear fit (Boltzmann sigmoidal) of normalized fluorescence data. The T_M was calculated as the mean ± SD of the inflection point (n=2). D) Exemplary LCP drop from the crystallization experiment.

This crystallization resulted in the presumably very first crystals of the $A_{2B}AR$, as evident by the microcrystals presented in panel D) of the figure. In the typical analyses, the purified protein demonstrated a high monodispersity, both before and after concentration, and a high purity as evident from the SDS-PAGE. With a main protein peak height of around 60 mAU, the concentrated sample was in the same high range as the protein from the previous crystallization trial. As previously seen for the ligand PSB-09120, a meaningful thermostability assessment of the protein in complex with this ligand was only feasible in two of the three measurement. Also, the inflection points of the two curves, and conversely also the T_M, differed notably from each other. Either way, the measurements indicated high thermostability of the protein of around

70 °C, and a stability-shift compared to the apo protein (T_M ~ 67 °C) was observed, suggesting successful ligand binding.

In total, seven different 96-well plates of precipitant solutions were utilized to screen for conditions that might foster protein crystal growth. As before, six of these plates were 48-salt plates, but this time the pH ranged from pH 5.0 to pH 8.0 in increments of one. Additionally, the commercial PEG/Ion400 screen was utilized, which was the screen that had brought forth the microcrystals shown above. The exact condition for those crystal was as follows:

> 100 mM di-ammonium tartrate, 30 % (v/v) PEG 400, pH 6.5

Similar microcrystals grew also with the following condition: 300 mM ammonium formate, 30 % (v/v) PEG 400, 100 mM tri-sodium citrate dihydrate pH 7.0. However, the largest crystals of this trial were the following (presented in Figure 77), which grew with this condition:

> 100 mM tri-sodium citrate dihydrate, 30 % (v/v) PEG 400, 100 mM tri-sodium citrate dihydrate pH 5.0

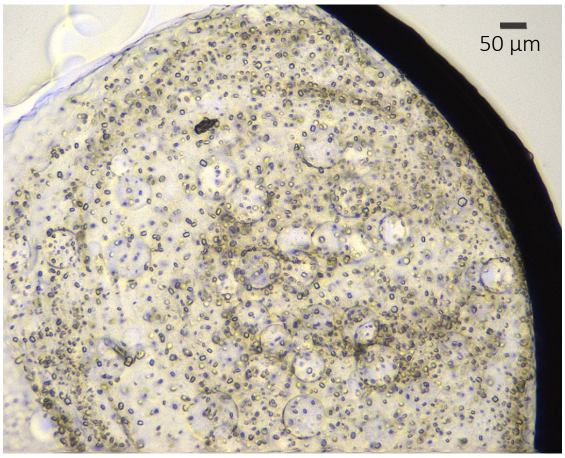

Figure 77. Disintegrated LCP drop with crystals.

Interestingly, those crystals only grew upon disintegration of the LCP, which for this drop happened between day 8 and 13. The size of these crystals was around 5 µm, with some reaching up to 10 µm.

In general, the LCP disintegrated less rapidly as seen before from the crystallization of TC168 in complex with PA51 (section 3.10, page 108), but still many of the drops disintegrated quickly. Potentially, the ratio of protein solution and lipid, or the sealing of the glass sandwich plates was not ideal. Unproper sealing of the drops with precipitant solutions could e.g. result in evaporation of water and therefore affect the concentration of the precipitant solution, considering that only 800 nL of the precipitant solutions are pipetted on the 50 nL LCP drops.

Due to the success of this crystallization trial, the next crystallization was performed with TC168 in complex with PSB-09120 as well.

3.11.2 Crystallization of TC168 in complex with PSB-09120 (II)

This next crystallization was performed similarly as the one described above, in order to assess the reproducibility of the observed crystal formation. Consistent with the previous procedure, the protein was purified from 900 mL of biomass. However, due to problems with a low flow rate during the wash and elution steps, that were encountered during the gravity flow purification of the previous protein, the amount of Co^{2+} beads was reduced by half. Additionally, the concentration of PSB-01920 was lowered to 25 µM for this crystallization attempt.

Figure 78 depicts the outcomes of this purification and crystallization attempt.

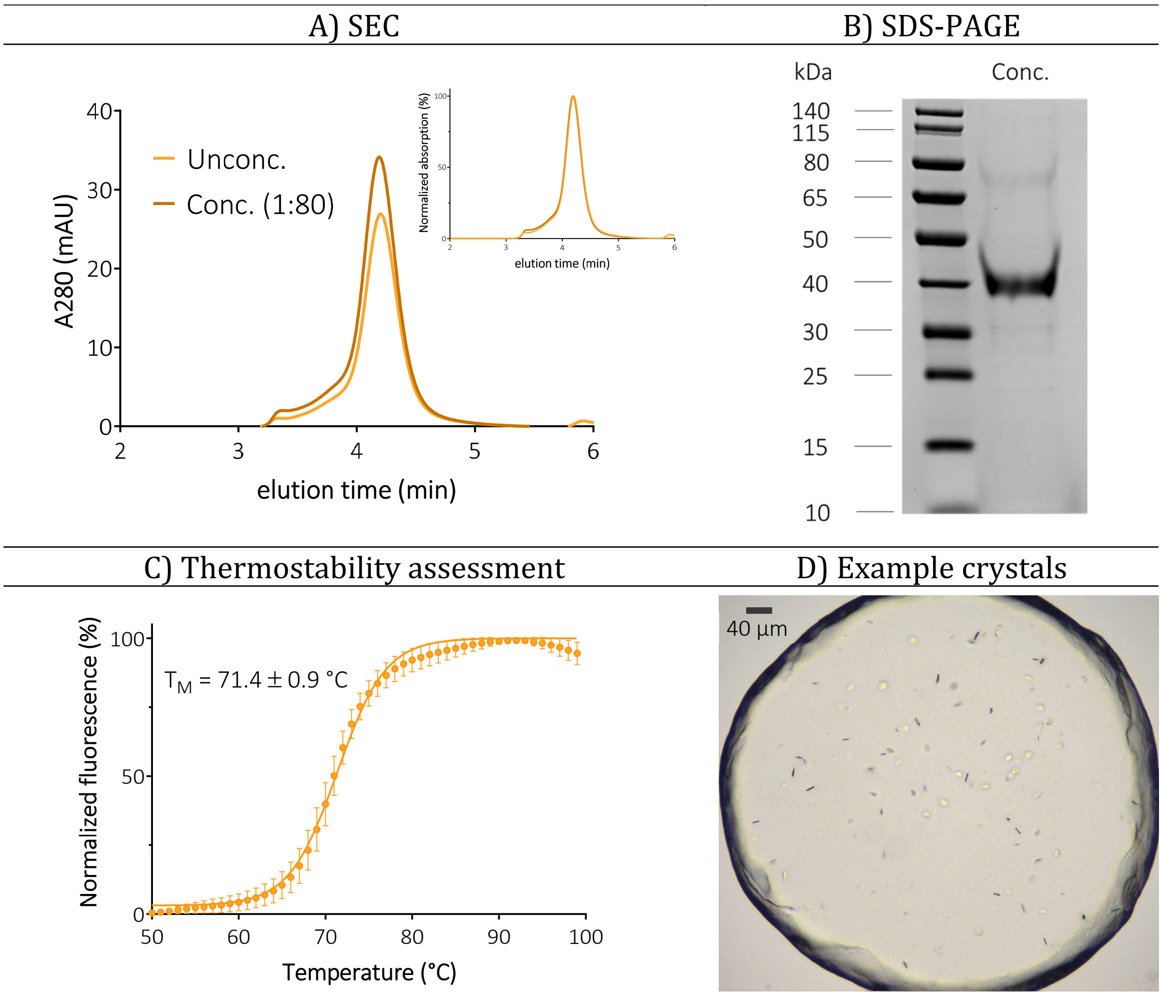

Figure 78. Protein analysis and crystallization of TC168 in complex with PSB-09120 (II). A) Region of interest of the SEC analysis of the (un-)concentrated protein samples (normalized results in the top right corner). B) SDS-PAGE of the concentrated sample, 10 µL (~ 1:100 diluted). C) Thermostability assessment of the unconcentrated sample. Nonlinear fit (Boltzmann sigmoidal) of normalized fluorescence data. The T_M was calculated as the mean ± SD of the inflection point (n=3). D) Exemplary LCP drop from the crystallization experiment.

Once again, the crystallization of TC168 in complex with PSB-09120 yielded crystals. Notably, the reduction of the ligand concentration did not have any adverse effects on neither the monodispersity, nor the thermostability of the protein. In fact, both characteristics were even improved in this experiment, compared to the previous one, and also the protein purity was adequate. The only downside encountered during this purification procedure was the decreased protein yield, since the main peak of the concentrated sample reaches only around 35 mAU, as opposed to the 60 mAU observed for the two previous crystallization attempts. Potentially, the amount of Co^{2+} beads, used for the purification of the His-tagged receptor, was reduced too much, despite their very high binding capacity of 5-15 mg of protein per mL of beads.[278] Unfortunately, the reduction of beads did not result in the anticipated improved flowrate during the wash end elution steps either. Therefore, further modifications of the purification process were considered for the next crystallization trials.

In spite of the relatively low protein yield, a crystallization experiment was conducted with this protein. The crystallization included the five 48-salt screens that were used previously, covering a pH from 4.0 to 8.0 in increments of one, along with the PEG/Ion 400 screen. This time, crystals grew in significantly more LCP drops and these crystals grew distinctly larger in comparison to the previous crystallization trial. Strikingly, for example, out of the 88 LCP drops that were successfully covered with the respective precipitant solution from the 48-salt screen at pH 4.0, 72 exhibited crystal growth, as evident from the overview provided in Figure 79.

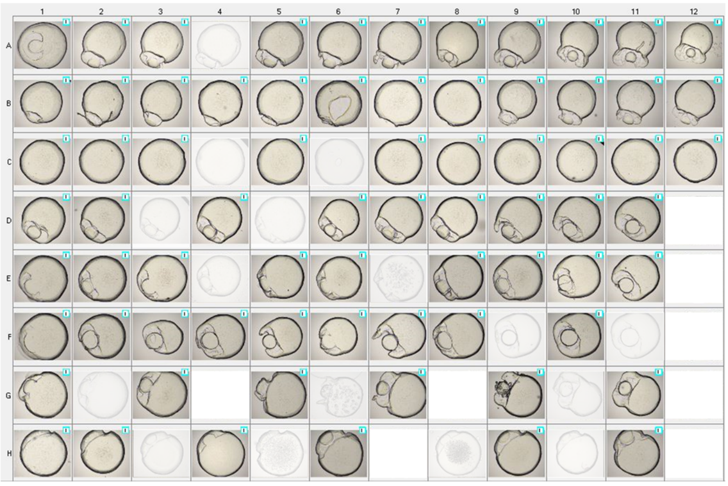

Figure 79. Overview of the 96-well plate with LCP drops covered with precipitant solutions at a pH of 4.0. The turquoise boxes in the top right corner of each well indicate the LCP drops in which crystal growth was observed.

Unfortunately, many of those crystals did not grow further after the first three days of the incubation period, and remained relatively small compared to crystals that developed after a longer incubation time and at higher pH values. However, also at pH 4.0, some crystals only started appearing after two to three weeks of incubation time and grew up to approximately 18 µm in size. These larger crystals were among the most remarkable crystals in this crystallization experiment. Representative examples of these observations are provided in the subsequent Figure 80.

A) B) C)

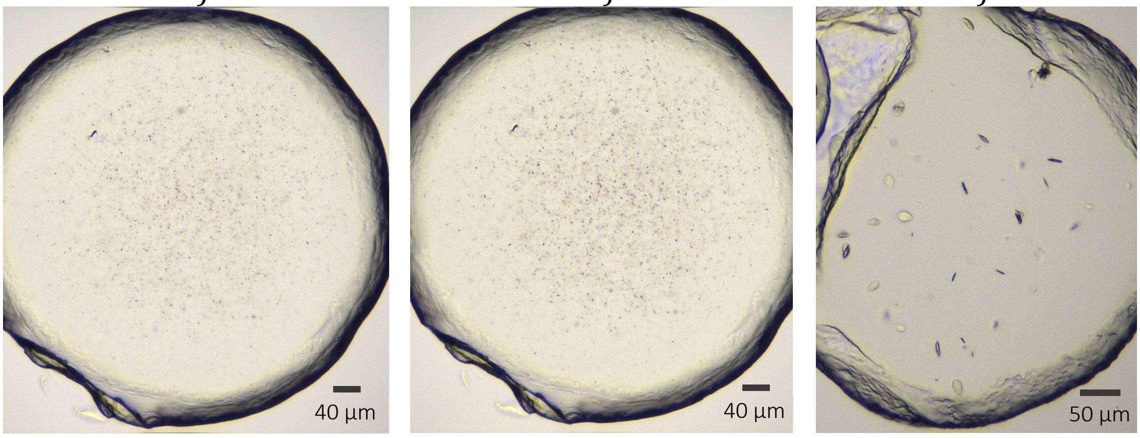

100 mM magnesium formate dihydrate – Day 3	100 mM magnesium formate dihydrate – Day 35	300 mM potassium thiocyanate – Day 35

+ 30 % (v/v) PEG 400
+ 100 mM Sodium acetate trihydrate pH 4.0

Figure 80. Representative LCP drops with crystals obtained with the indicated salts at pH 4.0. The day of the picture taking is indicated for each drop.

Apart from the crystals at pH 4.0, crystals also grew numerously at each of the other pH values. Especially precipitant solutions with a pH of 5.0 facilitated the manifold growth of comparably large crystals, with many reaching up to 15 µm in size. Figure 81 provides pictures of a selection of interesting crystals obtained at pH 5.0.

A) B) C)

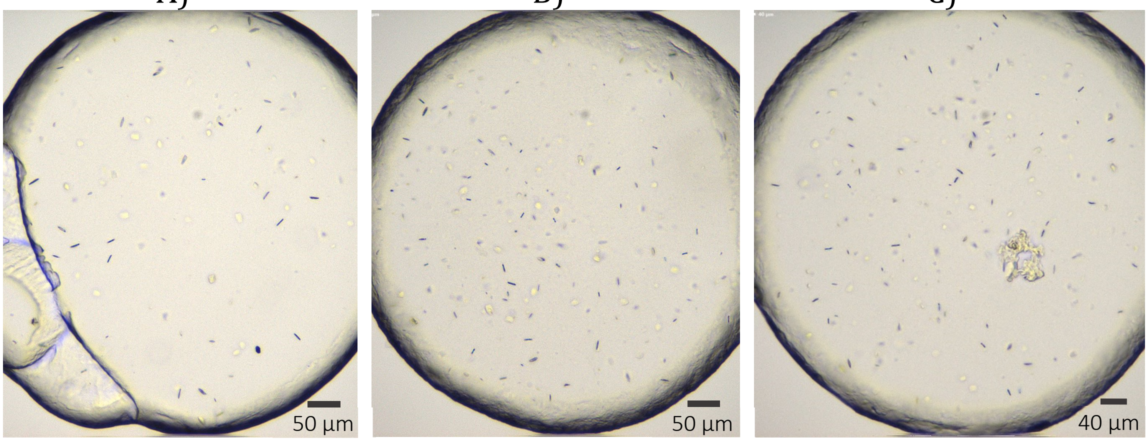

100 mM magnesium chloride hexahydrate	100 mM sodium dihydrogen phosphate	100 mM sodium thiocyanate

+ 30 % (v/v) PEG 400
+ 100 mM tri-sodium citrate dihydrate pH 5.0

Figure 81. Representative LCP drops with crystals obtained with the indicated salts at pH 5.0. Pictures taken on day 35.

Given the variety of conditions that facilitated crystal growth in this crystallization trial, it was a challenging task to decide which conditions were the most promising for a subsequent fine screening. In an effort to determine superior conditions, the precipitant solutions that yielded the best crystals at pH 5.0 were further investigated by assessing the crystal formation at different pH values and different concentrations of the respective salts. Among these conditions, it was noted that sodium dihydrogen phosphate consistently facilitated crystal growth across all tested pH levels, indicating a particularly beneficial influence on crystal formation. Additionally, precipitant solutions containing sodium thiocyanate showed promise for optimization, since crystals grown in those LCP drops, despite their smaller size, displayed a more three-dimensional structure compared to the plate-like crystals observed in most other LCP drops. Also, sodium thiocyanate facilitated crystal growth at various pH values, and had previously enabled the growth of diffraction-quality crystals of the A_{2A}AR.[279–281]

The abundance of crystals in so many of the LCP drops, also with varying pH values, gave rise to the suspicion that the crystals observed in this crystallization trial might have been composed of the ligand PSB-09120 instead of the protein. However, in the previous crystallization trial with an even higher ligand concentration, such crystal formation was not observed in any of the wells. In addition to the abundance of crystals, it was also striking that the crystals were all remarkably similar, despite growing in the presence of various different salts and pH values. Unfortunately, none of these crystals were harvested and analyzed to determine whether they were protein and ligand crystals, due to the unavailability of beamtime for diffraction measurements at the time. Also, it was hoped that through the optimization of the favorable precipitant solution, which had been a straightforward endeavor for the related A_{2A}AR, these crystals could be reproduced and improved in size, potentially even allowing for a successful structure determination of the A_{2B}AR, in case they were protein crystals. The result of this attempted optimization is presented in the following section.

3.11.3 Crystallization of TC168 in complex with PSB-09120 (III)

As mentioned above, the purpose of this crystallization was to enhance the quality the crystals that were observed in the second crystallization of TC168 in complex with PSB-09120. To that end, the purification was performed as previously described, starting from 900 mL of biomass and including 25 µM of the ligand in all buffers used for washing and elution of the protein from the Co^{2+} beads. This time, however, the amount of beads was reverted to the original quantity (500 µL in total), in response to the decreased protein yield that was observed in the previous attempt. Additionally, an extra bead washing step was introduced to enhance the flow rate during the gravity flow purification process, and to potentially further improve the protein purity.

Regarding the precipitant screens, four fine screens were designed and applied, incorporating the above-mentioned favorable salts:

i. Sodium thiocyanate, ranging from 10 – 200 mM along the columns, PEG 400 ranging from 20 – 34 % (v/v) along the rows, and 100 mM tri-sodium citrate dihydrate pH 5.0
ii. 100 mM sodium thiocyanate, 30 % (v/v) PEG 400, 100 mM tri-sodium citrate dihydrate pH 5.0 with 10 % additives
iii. Sodium dihydrogen phosphate, ranging from 10 – 200 mM along the columns, PEG 400 ranging from 20 – 34 % (v/v) along the rows, and 100 mM tri-sodium citrate dihydrate pH 5.0
iv. 100 mM sodium dihydrogen phosphate, 30 % (v/v) PEG 400, 100 mM tri-sodium citrate dihydrate pH 5.0 with 10 % additives

Additionally, the original 48-salt screen at pH 5.0 and the commercial PEG/Ion 400 screen were tested. The results of this purification and crystallization are provided in Figure 82 stated below.

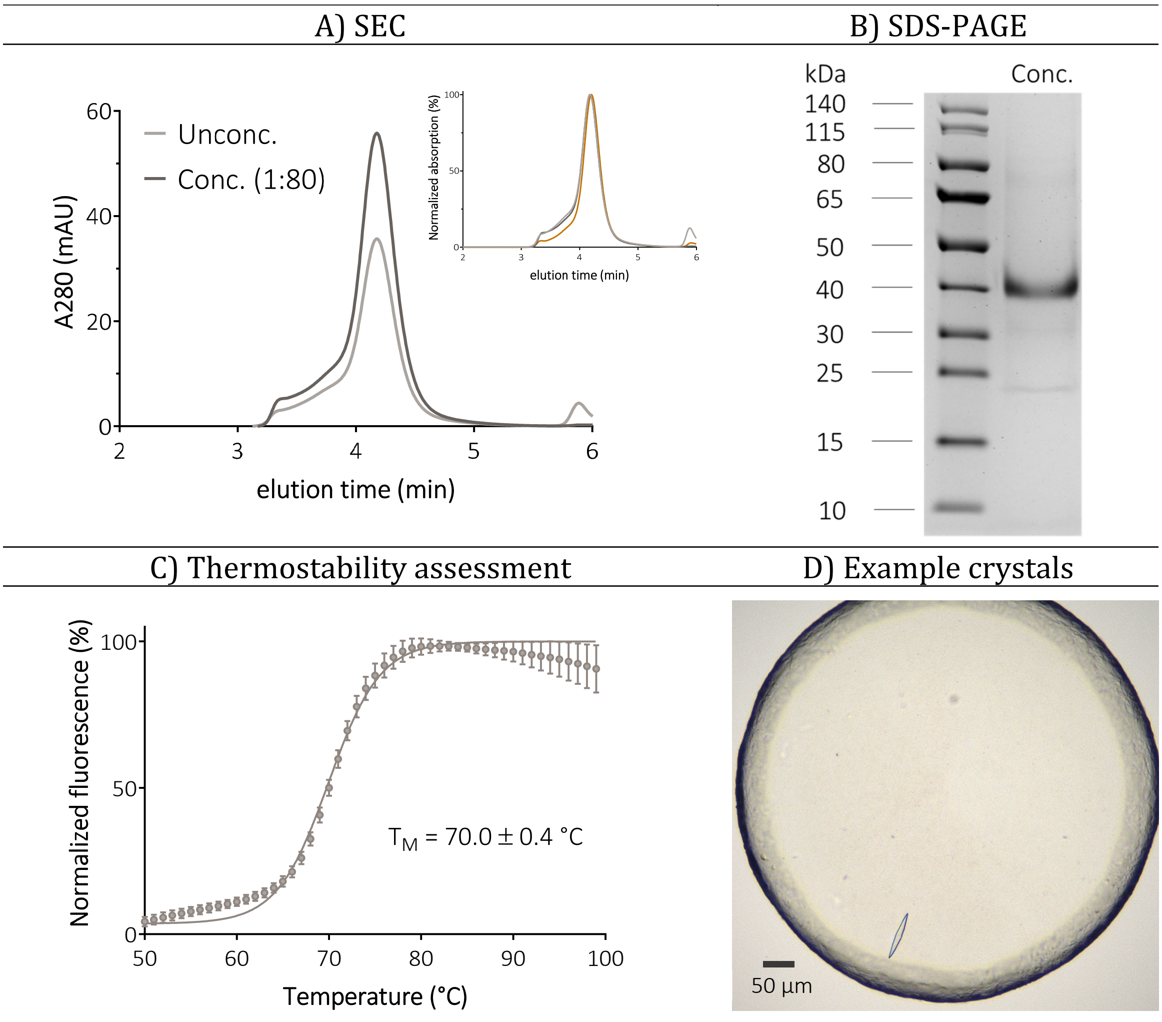

Figure 82. Protein analysis and crystallization of TC168 in complex with PSB-09120 (III). A) Region of interest of the SEC analysis of the (un-)concentrated protein samples (normalized results in the top right corner). B) SDS-PAGE of the concentrated sample, 10 µL (~ 1:100 diluted). C) Thermostability assessment of the unconcentrated sample. Nonlinear fit (Boltzmann sigmoidal) of normalized fluorescence data. The T_M was calculated as the mean ± SD of the inflection point (n=3). D) Exemplary LCP drop from the crystallization experiment.

Both modifications to the purification process proved to be successful. The flow rate during the wash and elution steps was notably faster, and the protein quantity, as indicated by the main peak's height, was significantly increased. Unfortunately, the protein displayed an inferior monodispersity compared to purification presented above, as depicted in the upper right corner of panel A in Figure 82, for both unconcentrated and concentrated protein sample. Also, the melting temperature of the protein was slightly reduced from formerly 71.4 °C to 70.0 °C. The precise reasons for this slight decrease in sample quality remained unclear, and it was unlikely that the additional wash step was responsible, since the buffer used for this additional wash step closely resembled wash buffer 1 (WB1). The only difference were the absence of the 20 mM imidazole and 8 mM ATP, the latter is typically added to the WB1 to remove chaperones from the protein.[282]

As indicated in panel D in the figure stated above, this crystallization trial also resulted in crystal growth, although compared to the second crystallization of TC168 with PSB-09120, the size and shape of these new crystals differed largely. In case of the 48-salt screen at pH 5.0, which previously resulted in numerous ~ 15 µm large crystals, the crystals grew considerably smaller and in fewer conditions than before. Also, crystal growth was observed in conditions that had not yielded any crystals before, and vice versa. An example of the decreased crystal growth is illustrated in the following Figure 83.

TC168 + PSB-09120 (III)	TC168 + PSB-09120 (II)
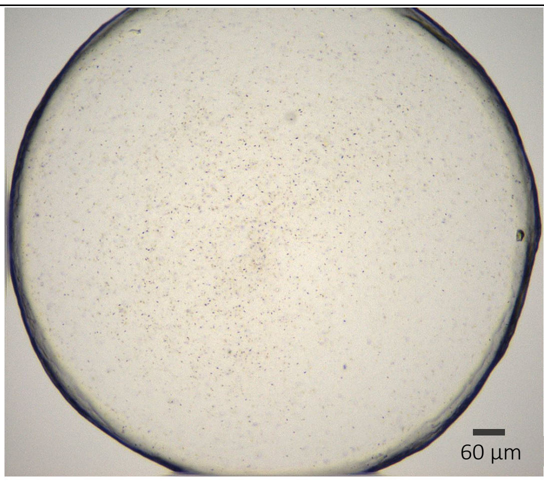	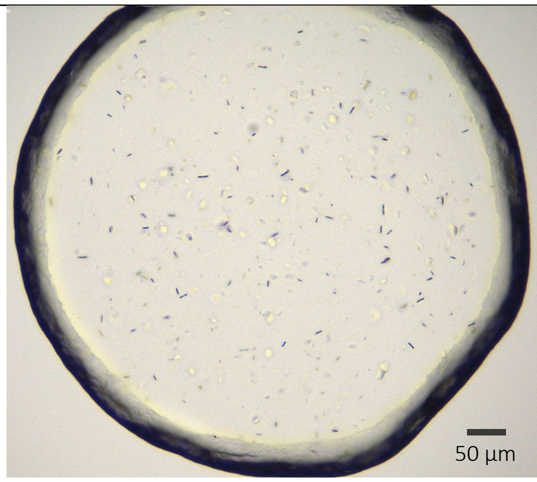
Day 27	Day 35
400 mM sodium chloride, 30 % PEG 400 (v/v), pH 5.8	

Figure 83. Comparison of two LCP drops from the second and third crystallization of TC168 in complex with PSB-09120. The drops were both covered with the same precipitant solution.

None of the LCP drops of this crystallization yielded crystals resembling those presented in the right panel of Figure 83, as most crystals remained microcrystals, similar to those depicted in the left panel of the figure. Approximately 35 wells of the optimized screening plates, however, exhibited the growth of one or two crystals of sizes ranging from 60 to 100 µm. These larger crystals mostly developed in the presence of the previously mentioned additives, and all of them shared the same shape. These additives have the potential to modify the interactions among the protein molecules and their interaction with the solvent and can therefore improve crystals or alter the sample solubility.[283] For the two screens in which additives were incorporated, the additive screen from Hampton Research was utilized, which encompasses various different classes of reagents, e.g. salts, carbohydrates and organic solvents.

Figure 84 details four examples of the crystals that predominantly grew in the presence of additives.

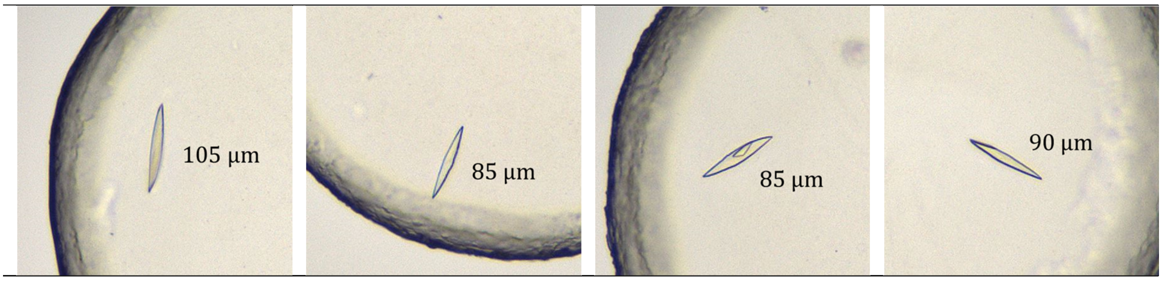

3 % dextran sulfate sodium salt	10 mM EDTA	100 mM guanidine hydrochloride	10 mM L-proline

+ 100 mM sodium thiocyanate
+ 30 % (v/v) PEG 400
+ 100 mM tri-sodium citrate dihydrate pH 5.0

Figure 84. Four examples of the approximately 35 large crystals, that occurred in the third crystallization trial of TC168 with PSB-09120. The pictures were taken after 27 days.

This time, the crystals were harvested and sent to the “Deutsches Elektronen-Synchroton” (DESY) in Hamburg for diffraction analysis. Unfortunately, none of the crystals showed diffraction patterns that could be attributed to protein. Instead, it was suspected that the submitted crystals were, in fact, formed by the ligand PSB-09120. Consequently, this raised the possibility that even the larger (~ 15 µm) crystals from the previous crystallization trial of TC168 with PSB-09120 might not have been protein crystals. Possibly, only the smaller microcrystals that were observed in all three of the crystallization trials with TC168 were indeed protein crystals, which emphasized the need for a new crystallization construct and/or a different ligand. Therefore, both of these aspects were addressed in preparation for the next crystallization experiments.

3.12 Crystallization trials of TC190 with PSB-21500 (I – V)

In parallel to the crystallization trials presented above, the $A_{2B}AR$ construct was further refined, with a special focus on the protein yield. As seen from the comparison of the crystallization of TC169 (section 3.10, page 108 ff.) and TC168 (section 3.11, page 111 ff.), the presence of the NNST-linker between the HA- and FLAG-tag of construct TC169 allowed for purification from only half of the amount of biomass, compared to TC168. This not only saved time and resources for every crystallization trial, but also provided flexibility in adjusting the protein concentration for crystallization, if necessary. The drawback of the potential microheterogeneity that is associated with the additional N-glycosylation sites introduced by the NNST-linker, was later overcome by the discovery that a GSGS-linker between the HA- and FLAG-tag results in the same increase in protein yield. The resulting construct TC190, which was introduced and discussed in detail in section 3.6.2, page 84, therefore emerged as the mostly utilized $A_{2B}AR$ construct in the following crystallization trials of the $A_{2B}AR$.

The other major alteration in the following crystallization trials was the utilization of a different ligand, namely PSB-21500. Its characteristics will be presented in section 3.12.1 below.

3.12.1 The covalent antagonist PSB-21500

The antagonist PSB-21500 was synthesized by Dr. Ahmed Temirak, in an effort to obtain the very first covalent antagonist for the $A_{2B}AR$. Throughout this project, a series of 8-*p*-sulfophenylxanthines with reactive sulfonyl fluoride groups were synthesized and characterized regarding their covalent behavior. For PSB-21500, we confirmed its irreversible binding to the $A_{2B}AR$ by radioligand binding and bioluminescence resonance energy transfer (BRET)-based assays involving wash-out experiments as well as kinetic studies. For detailed information on the synthesis and pharmacological characterization of this $A_{2B}AR$-selective compound, please refer to the respective recent publication.[284]

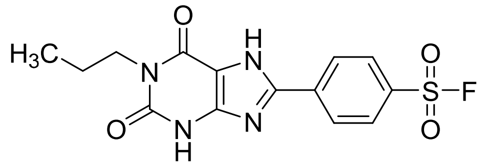

Figure 85. Chemical structure of PSB-21500.

Covalent antagonists can be very useful tools for structural studies. The crystal structures of the A_1AR in complex with the covalent antagonist DU172,[265] or the β_2AR in complex with the covalent agonist FAUC50[285] are just two of the examples of covalent ligands that facilitated the successful structure determination of a GPCR. The advantage of covalent ligands is that they can effectively lock the receptor in a specific conformation without dissociating. Thereby they permanently reduce the receptors flexibility and increase the stability of the purified protein,[286] which otherwise pose a major obstacle in the crystallization of the 7-TM proteins.[287] Another notable benefit of covalent antagonists is that, owing to their inability to dissociate, it is not necessary to supplement the elution buffer with the ligand. This essentially eliminates the likelihood of observing ligand crystals instead of protein crystals, as experienced previously.

Regarding the above-mentioned increase in stability, the A_1AR is a noteworthy example where the presence of the covalent antagonist DU172 increased the T_M of the crystallization construct by 16 °C.[265] To evaluate the stabilizing impact of the $A_{2B}AR$-selective irreversible antagonist PSB-21500 on the old and new crystallization constructs TC168 and TC190, the standard SEC and thermostability assessments were performed. The result of this is presented in the following Figure 86.

A) SEC

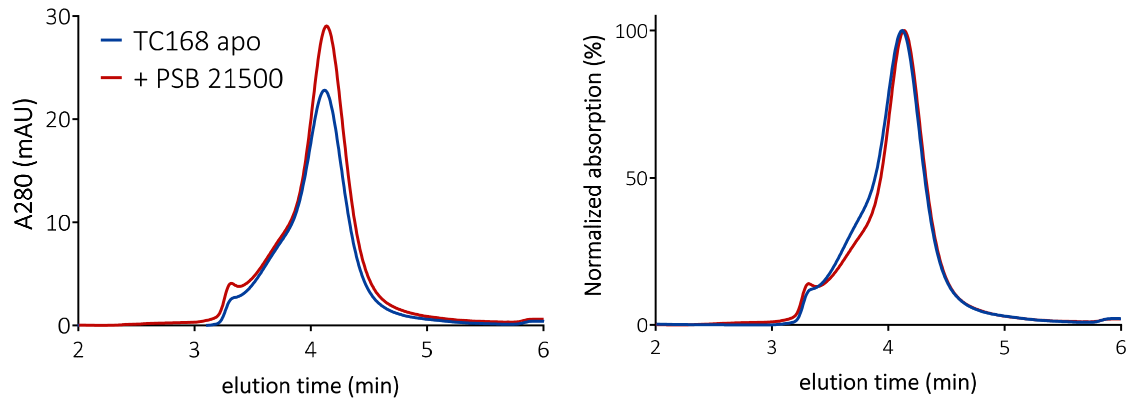

B) Thermostability assessment

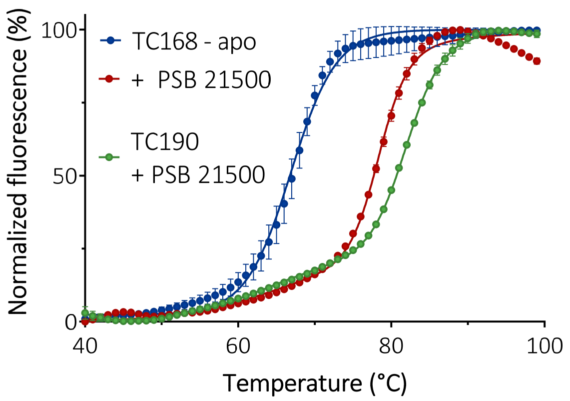

TC168 – Apo	T_M = 66.9 ± 0.7 °C
TC168 – PSB-21500	T_M = 77.9 ± 0.2 °C
TC190 – PSB-21500	T_M = 82.0 ± 0.1 °C

Figure 86. Protein analysis of TC168 and TC190 in complex with PSB-21500. A) Region of interest of the (normalized) SEC analysis of TC168 in apo form, and purified in complex with PSB-21500. B) Thermostability assessment of the TC168 samples and TC190 in complex with PSB-21500. Nonlinear fit (Boltzmann sigmoidal) of normalized fluorescence data. The T_M was calculated as the mean ± SD of the inflection point (n=3).

Similar to the A_1AR, the presence of a covalent antagonist, in this case PSB-21500, had a large impact on the stability of the A_{2B}AR. The presence of PSB-21500 during the purification resulted in an increased protein yield and monodispersity, in case of TC168, but most significantly, it greatly enhanced the thermostability of the receptor. For the former crystallization construct TC168, the ligand facilitated an increase in T_M of over 10 °C, compared to the purified apo receptor. With a T_M of almost 78 °C, a 4.5 °C increase over the previously best thermostabilizing antagonist PA51 was marked. In case of the new crystallization construct TC190, the T_M reached an even higher value with 82.0 °C. Both of these values are exceptionally high, and even surpassed the most thermostable A_{2A}AR complex, which raised hope for the success of future crystallization trials.

The upcoming sections will outline the results of all five crystallization trials of TC190 in complex with PSB-21500 that were performed. Following their presentation, the outcome of these crystallization trials will be jointly discussed.

3.12.2 Crystallization of TC190 in complex with PSB-21500 (I)

The results of the first purification and crystallization of TC190 in complex with PSB-21500 are presented in the following Figure 87.

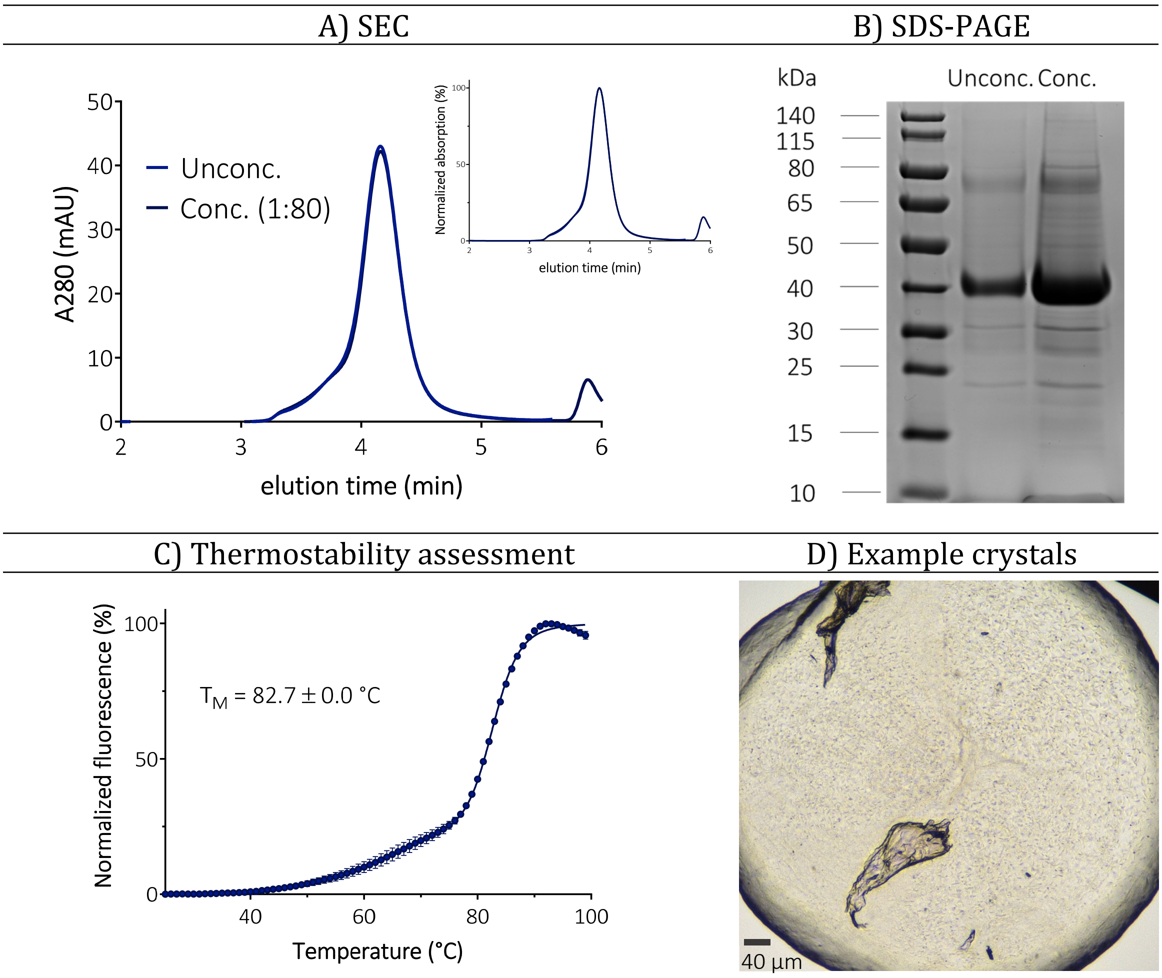

Figure 87. Protein analysis and crystallization of TC190 in complex with PSB-21500 (I). A) Region of interest of the SEC analysis of the (un-)concentrated protein samples (normalized results in the top right corner). B) SDS-PAGE of the concentrated sample, 10 µL (~ 1:100 diluted). C) Thermostability assessment of the unconcentrated sample. Nonlinear fit (biphasic) of normalized fluorescence data. The T_M was calculated as the mean ± SD of the later inflection point (n=3). D) Exemplary LCP drop from the crystallization experiment.

3.12.3 Crystallization of TC190 in complex with PSB-21500 (II)

Figure 88 illustrates the outcome of the second purification and crystallization of TC190 in the presence of PSB-21500.

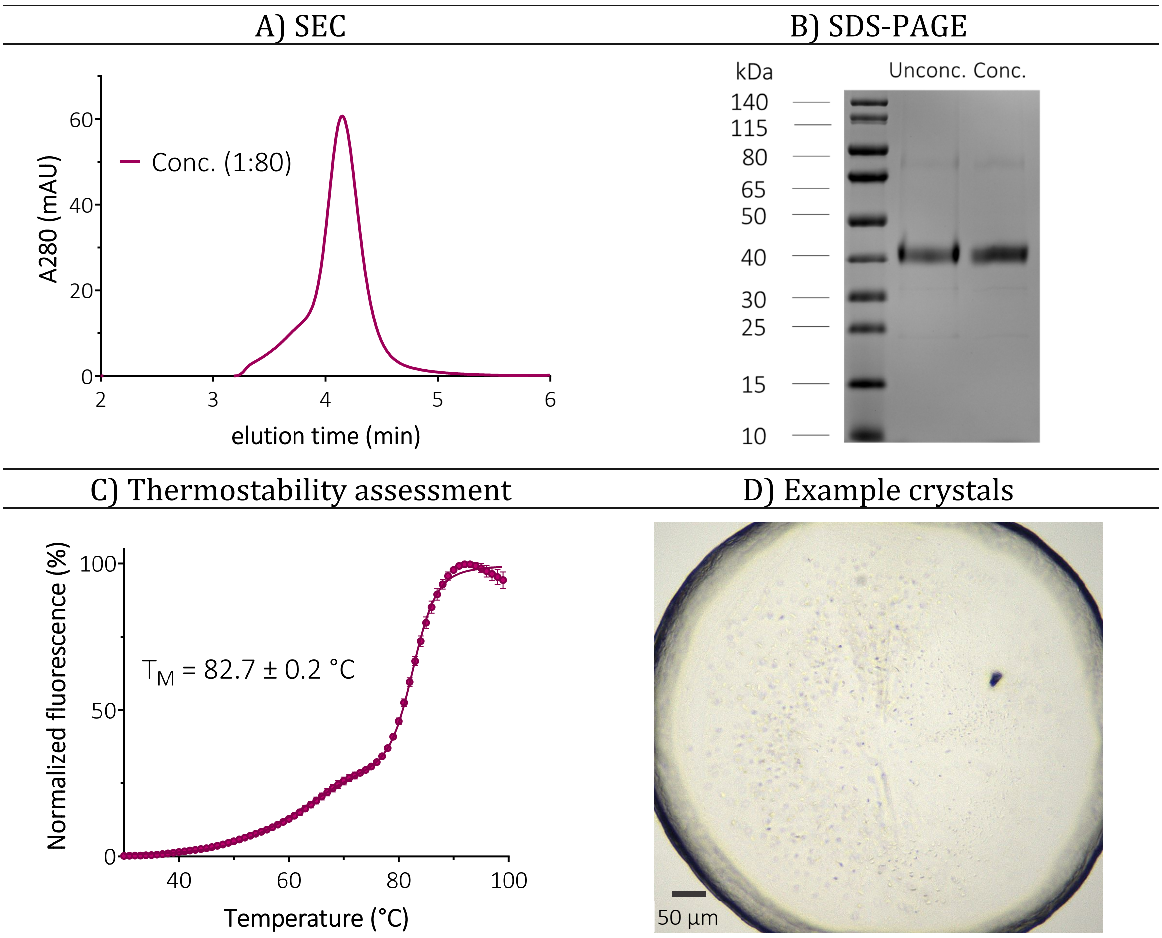

Figure 88. Protein analysis and crystallization of TC190 in complex with PSB-21500 (II). A) Region of interest of the SEC analysis of the concentrated protein samples. B) SDS-PAGE of the concentrated sample, 10 µL (~ 1:100 diluted). C) Thermostability assessment of the unconcentrated sample. Nonlinear fit (biphasic) of normalized fluorescence data. The T_M was calculated as the mean ± SD of the later inflection point (n=3). D) Exemplary LCP drop from the crystallization experiment.

3.12.4 Crystallization of TC190 in complex with PSB-21500 (III)

The third purification and crystallization of TC190 in complex with PSB-21500 is visualized in Figure 89 stated below.

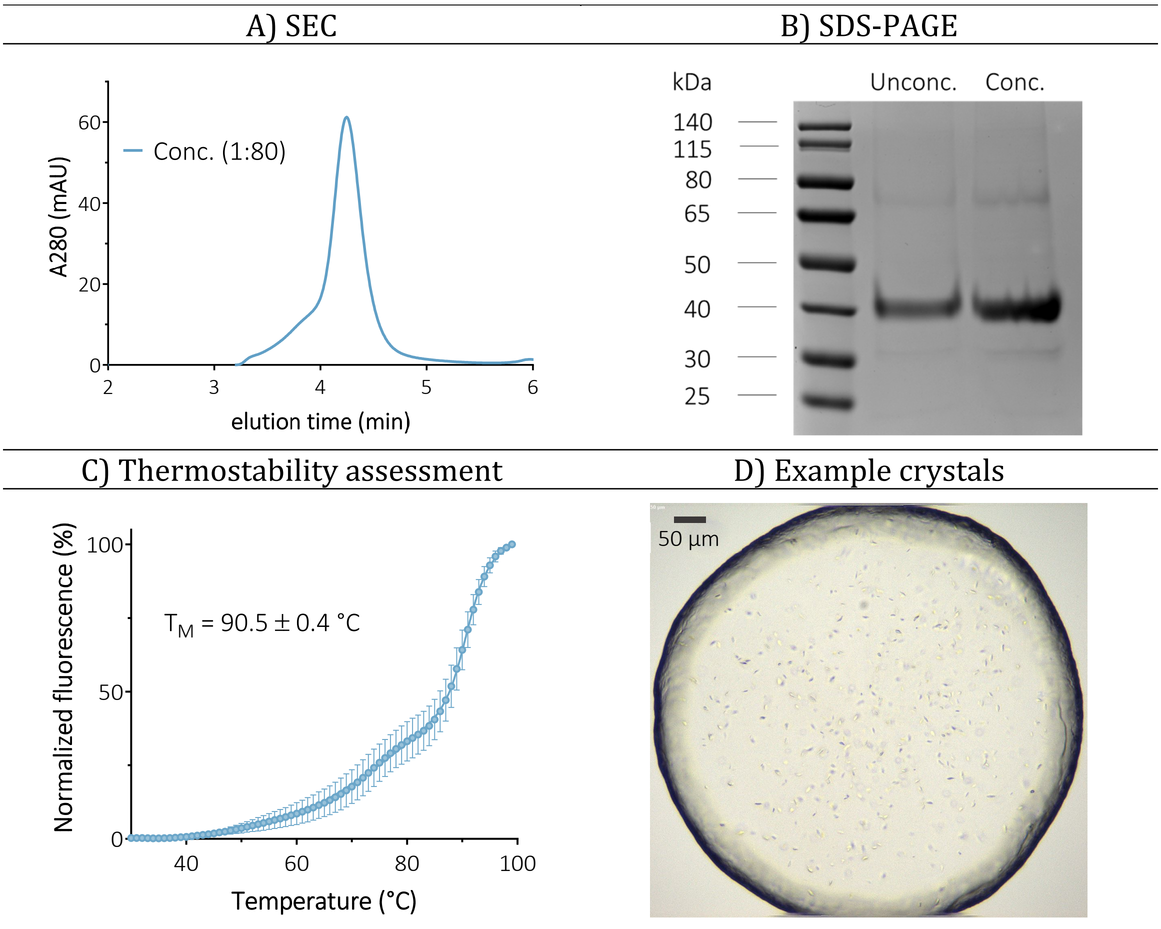

Figure 89. Protein analysis and crystallization of TC190 in complex with PSB-21500 (III). A) Region of interest of the SEC analysis of the concentrated protein samples. B) SDS-PAGE of the concentrated sample, 10 µL (~ 1:100 diluted). C) Thermostability assessment of the unconcentrated sample. Nonlinear fit (biphasic) of normalized fluorescence data. The T_M was calculated as the mean ± SD of the later inflection point (n=3). D) Exemplary LCP drop from the crystallization experiment.

3.12.5 Crystallization of TC190 in complex with PSB-21500 (IV)

The outcome of the purification and crystallization of the fourth time for TC190 and PSB-21500 are provided in Figure 90.

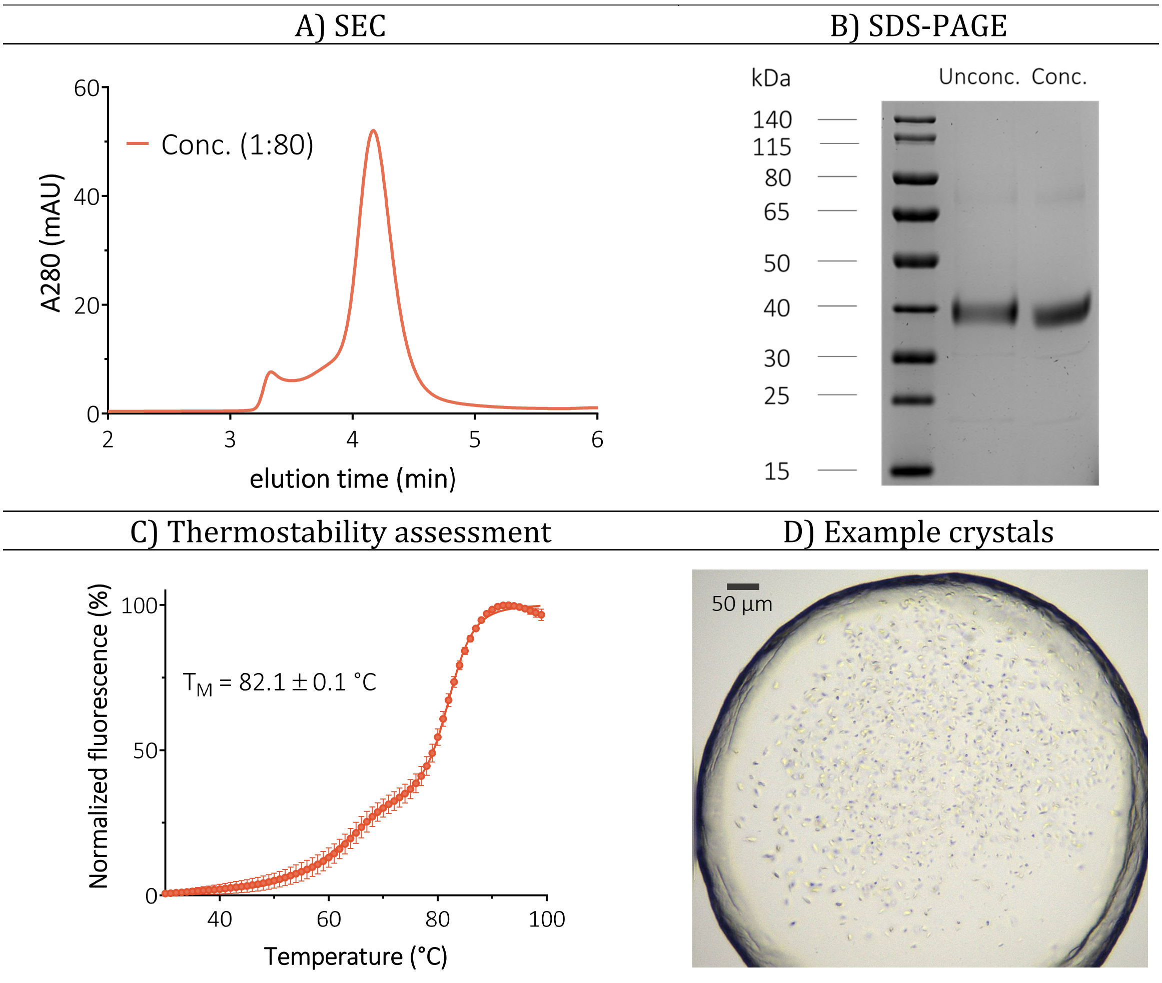

Figure 90. Protein analysis and crystallization of TC190 in complex with PSB-21500 (IV). A) Region of interest of the SEC analysis of the concentrated protein samples. B) SDS-PAGE of the concentrated sample, 10 µL (~ 1:100 diluted). C) Thermostability assessment of the unconcentrated sample. Nonlinear fit (biphasic) of normalized fluorescence data. The T_M was calculated as the mean ± SD of the later inflection point (n=3). D) Exemplary LCP drop from the crystallization experiment.

3.12.6 Crystallization of TC190 in complex with PSB-21500 (V)

Here, in Figure 91, the results of the fifth purification and crystallization of TC190 in complex with PSB-21500 are depicted.

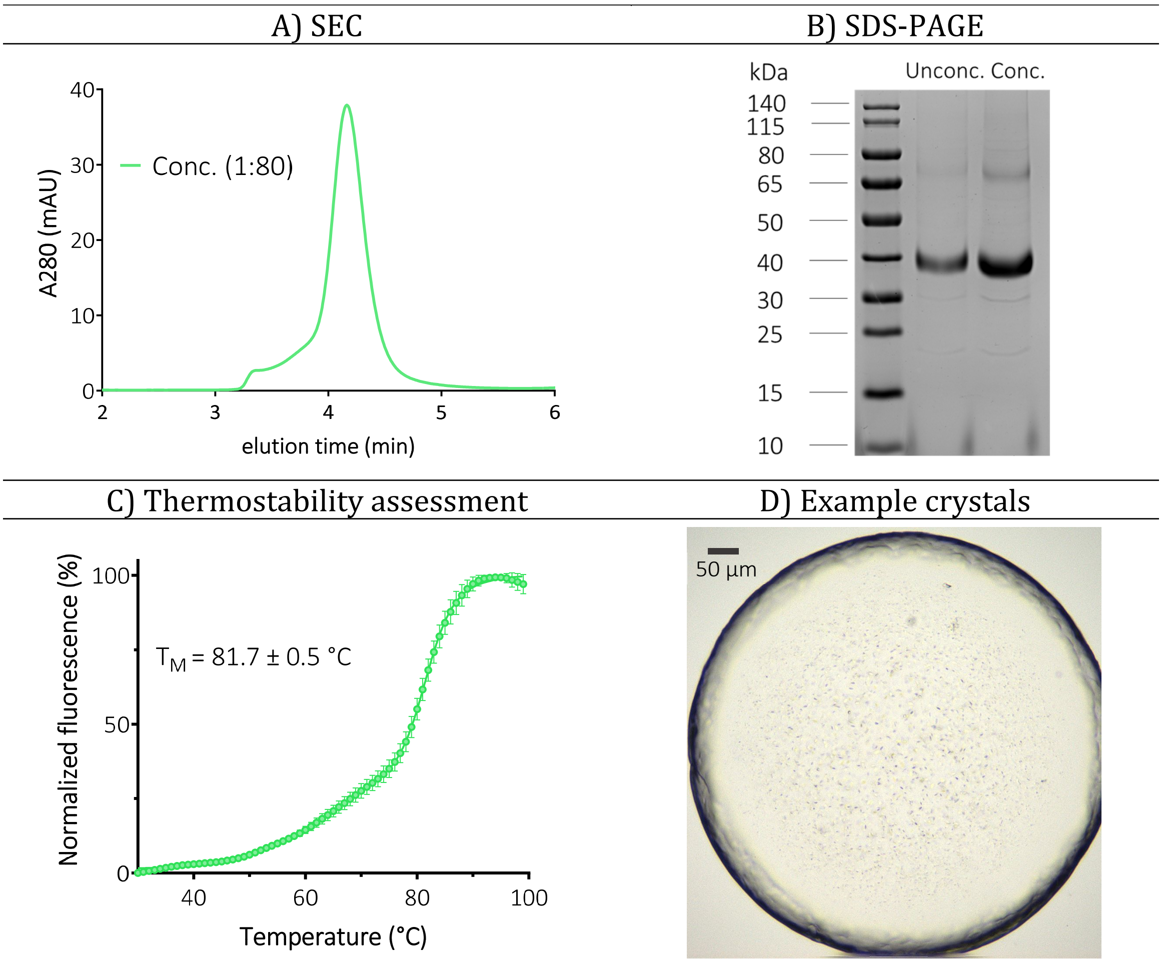

Figure 91. Protein analysis and crystallization of TC190 in complex with PSB-21500 (V). A) Region of interest of the SEC analysis of the concentrated protein samples. B) SDS-PAGE of the concentrated sample, 10 µL (~ 1:100 diluted). C) Thermostability assessment of the unconcentrated sample. Nonlinear fit (biphasic) of normalized fluorescence data. The T_M was calculated as the mean ± SD of the later inflection point (n=3). D) Exemplary LCP drop from the crystallization experiment.

3.12.7 Discussion of the crystallization trials (I – V)

All samples presented above were produced using similar purification processes, starting from 450 mL of biomass. The amount of ligand added during the purification was loosely based on the described purification procedure for the crystallization of the A_1AR in complex with DU172.[265] There, each purification step was performed in the presence of 0.2 µM DU172, which demonstrated an apparent affinity of approximately 40 nM towards the A_1AR.[265] For PSB-21500, which exhibited an apparent affinity of approximately 11 nM towards the wt $A_{2B}AR$,[284] the ligand concentration in each purification buffer, including the elution buffer, was set to 0.1 µM. During solubilization, however, a final concentration of 1 µM of PSB-21500 was chosen for each purification. In case of the fourth and fifth crystallization trial of TC190 with PSB-21500, the wash and elution buffers were devoid of the covalent ligand altogether in order to completely eliminate the possibility of ligand crystals.

Each crystallization trial with the refined construct TC190 in complex with the covalent antagonist PSB-21500 resulted in crystals, that could most likely be attributed to the $A_{2B}AR$. In terms of protein yield and monodispersity, the five crystallization trials differed to some degree. The peak height of the main peak during the SEC analysis ranged from approximately 40 mAU for the first and fifth crystallizations, (pages 126 and 130) to approximately 60 mAU for the samples from the other three crystallization trials. The monodispersity also showed some variability, with the most prominent protein aggregation observed in the sample of the fourth crystallization trial, as depicted on page 129.

Interestingly, this fourth crystallization, despite exhibiting an increased aggregation peak, yielded the best crystals. Even though neither the T_M nor the protein concentration of that sample were the highest, it outperformed the others, as detailed below. This underscores the unpredictability of which samples will produce the best crystals, and the fact that aggregation does not necessarily impede crystallization.

As evident also from the CPM assay of the small-scale purified TC190 sample in complex with PSB-21500, the thermostability of all five purified protein samples was remarkably high, with T_M values exceeding 80 °C. Surprisingly, the T_M for the third sample, presented on page 128, was even measured to be around 90 °C. The last analyzed characteristic was the purity of the samples, assessed by SDS-PAGE, which in each case, was acceptable for attempting crystallization of the proteins.

Throughout the course of these crystallization experiments, a diverse array of precipitant solutions was employed to determine the optimal conditions for this specific protein with this specific ligand. In the first crystallization of this series, only the 48-salt screens pH 5.0, 6.0 and 7.0 and the commercial PEG/Ion 400 screen from Hampton Research were tested. in the second crystallization trial, also two 48-salt screens (at pH 5.0 and pH 8.0) and the PEG/Ion 400 screen were used, and an additional commercial screen, namely JBScreen LCP from Jena Bioscience was tested as well. Furthermore, three of the refined screens that were originally designed for the crystallization of TC168 in complex with PSB-09120 were included, to review if those screens not only enhanced ligand crystal growth, but also promoted protein crystal growth, now that the presence of ligand crystals was essentially ruled out.

The best crystals from the first two crystallization trials of TC190 with PSB-21500 are showcased in the following Figure 92, presenting four different LCP drops.

TC190 + PSB-21500 (I)

400 mM di-ammonium tartrate, 30 % (v/v) PEG 400, pH 6.5

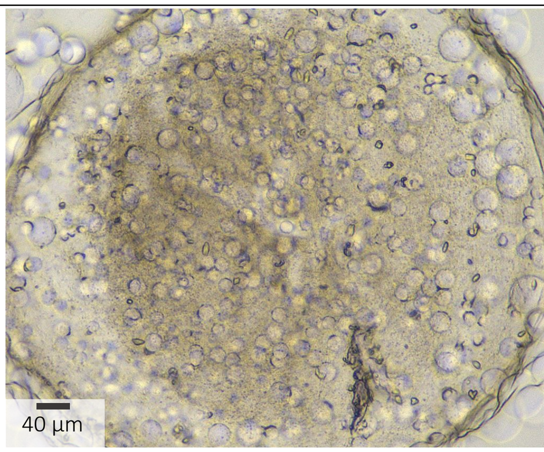

400 mM di-ammonium hydrogen phosphate, 30 % (v/v) PEG 400, pH 8.2

TC190 + PSB-21500 (II)

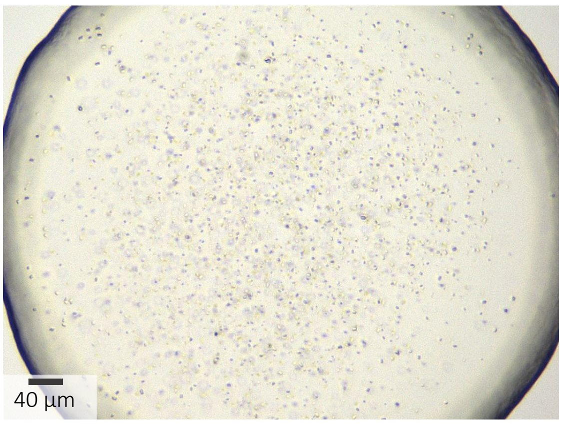

100 mM ammonium chloride, 30 % (v/v) PEG 400, pH 5.9

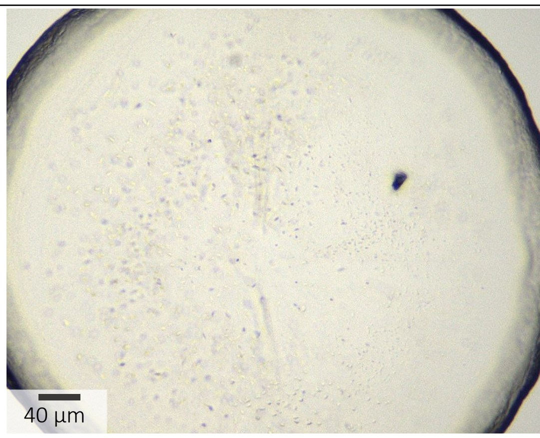

300 mM lithium sulfate monohydrate, 30 % (v/v) PEG 400, 100 mM tri-sodium citrate dihydrate pH 5.0

Figure 92. LCP drops from crystallizations of TC190 with PSB-21500 (I – II) with crystals obtained in the presence the indicated precipitant solutions. Pictures taken on day 21.

Both crystallizations resulted in small crystal growth in several wells, which reached a maximum size of approximately 10 µm. Regarding the second crystallization (TC190 + PSB-21500 (II)), the refined screens that previously generated many ligand crystals for the crystallization of TC168 with PSB-09120 (see page 119) did not result in any crystals this time. Instead, the precipitant solutions containing e.g. ammonium tartrate, di-ammonium hydrogen phosphate, lithium sulfate monohydrate and ammonium chloride demonstrated a positive effect on the (presumably protein) crystal growth. Therefore, these salts were selected for a new round of fine screens for upcoming crystallizations.

For the third crystallization, the following fine screens were employed:

i. Ammonium chloride ranging from 10 – 400 mM along the columns, PEG 400 ranging from 25 – 37 % (v/v) along the rows, and 100 mM tri-sodium citrate dihydrate pH 5.9
ii. Lithium sulfate monohydrate ranging from 40 to 440 mM along the columns, PEG 400 ranging from 25 – 37 % (v/v) along the rows, and 100 mM tri-sodium citrate dihydrate pH 5.0
iii. di-Ammonium hydrogen phosphate ranging from 50 to 700 mM along the columns, PEG 400 ranging from 22 – 36 % (v/v) along the rows, and 100 mM Tris-HCl pH 8.0

Some results of this fine screening campaign are presented in Figure 93.

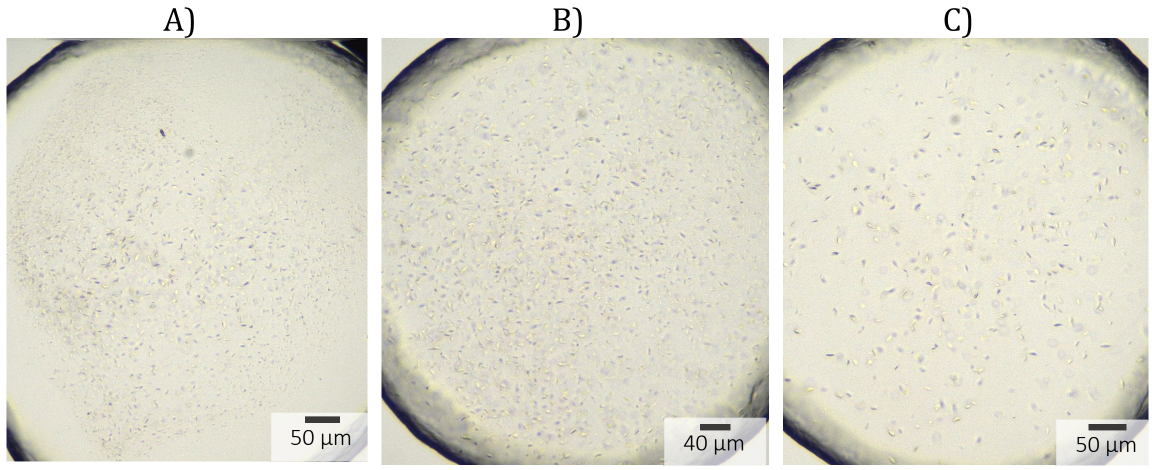

220 mM lithium sulfate monohydrate	300 mM di-ammonium hydrogen phosphate	
+ 33 % (v/v) PEG 400	+ 24 % (v/v) PEG 400	+ 26 % (v/v) PEG 400
+ 100 mM tri-sodium citrate dihydrate pH 5.0	+ 100 mM Tris-HCl pH 8.0	+ 100 mM Tris-HCl pH 8.0

Figure 93. Representative LCP drops from crystallization TC190 – PSB-21500 (III) with crystals obtained with the indicated conditions. The pictures were taken after 17 days of incubation at 20 °C.

In this third round of crystallizations, the initial crystal hits were validated, and the crystals successfully optimized with regard to size. Nevertheless, their size was still limited to approximately 10 – 15 µm, which is likely insufficient for successful structure determination. Despite this limitation, crystals from all three wells presented in Figure 93 were harvested and sent to the DESY to check for any low-resolution protein diffraction. Unfortunately, no clear protein diffraction was observed. However, in this case, the absence of any small-molecule diffraction suggests that these crystals were indeed protein crystals of the A_{2B}AR. Consequently, based on these crystal hits, further precipitant solutions were screened to find the optimal conditions. This time, the concentration range of the salts was narrowed around the conditions of the crystal hits presented above, and the pH value was varied slightly.

For lithium sulfate monohydrate, the concentration range was set from 200 –244 mM, with the PEG 400 concentration ranging from 30 – 36 % (v/v). Three of those plates were designed with pH values of 4.8, 5.0 and 5.2, respectively. In case of di-ammonium hydrogen phosphate the concentration ranged from 240 – 350 mM, and the PEG 400 concentration varied between 23 – 30 % (v/v). Again, three of those plates were designed with pH values of 7.8, 8.0 and 8.2. Noteworthy, at pH 7.8, HEPES was employed as the buffering agent instead of Tris-HCl.

All of these screens, in addition to the PEG/Ion 400 screen, were utilized for the fourth crystallization of TC190 with PSB-21500. Some exemplary results of this crystallization are depicted below in Figure 94.

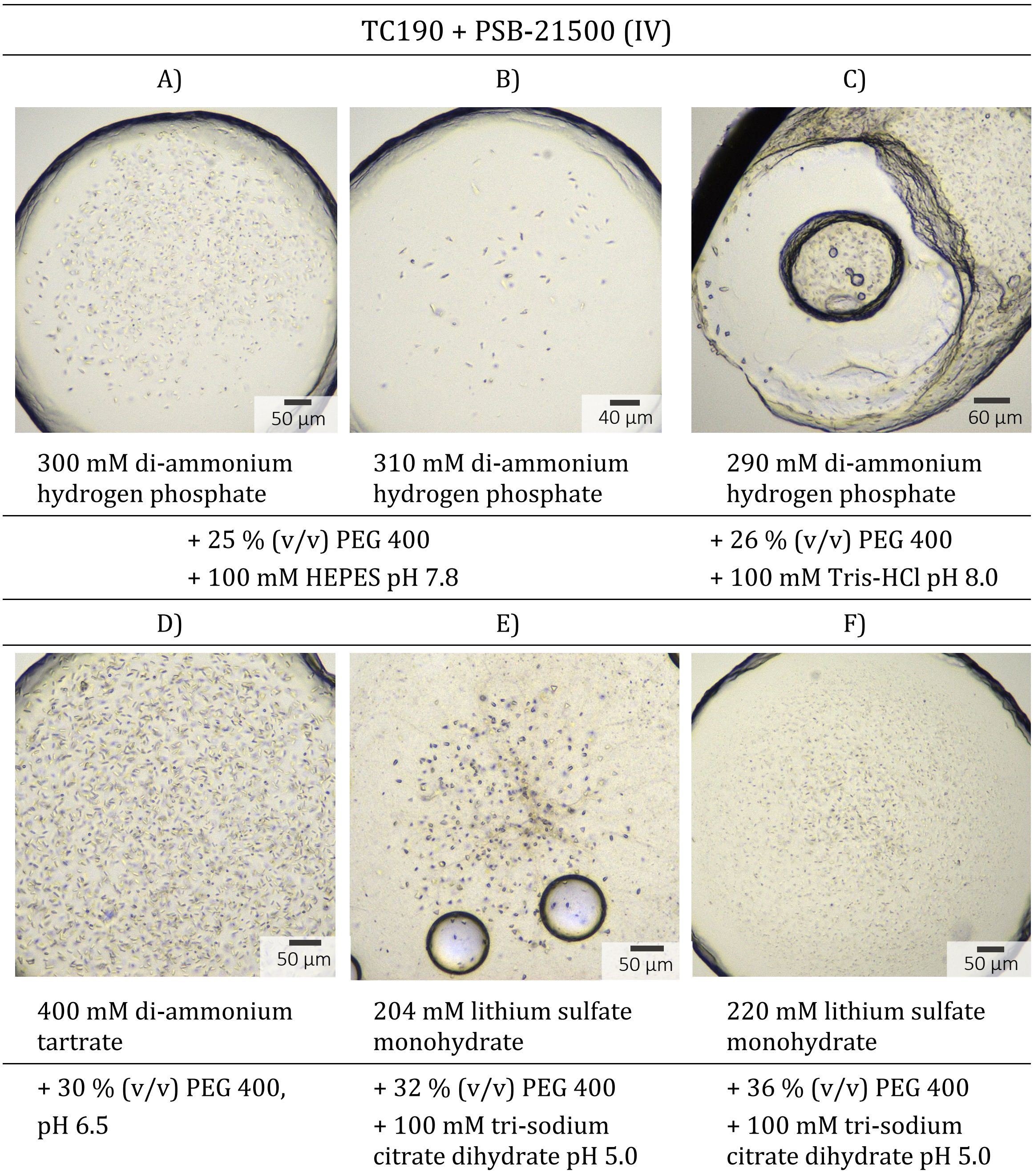

Figure 94. Exemplary LCP drops from crystallization TC190 – PSB-21500 (IV) with crystals obtained with the indicated conditions. Picture E) was taken after 40 days, the rest was taken after 21 days of incubation.

As stated in the beginning of this discussion, this fourth crystallization of TC190 with PSB-21500 proved to be the most successful one among all five trials presented here. The optimized fine screens facilitated the crystal growth in numerous LCP drops. Yet, the maximum size of the crystals was still limited to 15 – 20 µm, and thus showed only minor improvement compared to the previous crystallization. Once again, some crystals from the LCP drops presented above (except for panel E) were sent to the

DESY for measurement by our cooperation partners from the group of Prof. Dr. Norbert Sträter (University of Leipzig). Similar to the previous measurement, for most of the crystals, no diffraction could be observed. Only for the crystals from the LCP drop depicted in panel C) some low-resolution diffraction data was obtained, with the highest resolution reflection being around 15 Ångström (Å). This provided the first, direct evidence that these crystal hits produced in our lab were indeed protein crystals. Three of the diffraction images are provided in the following Figure 95.

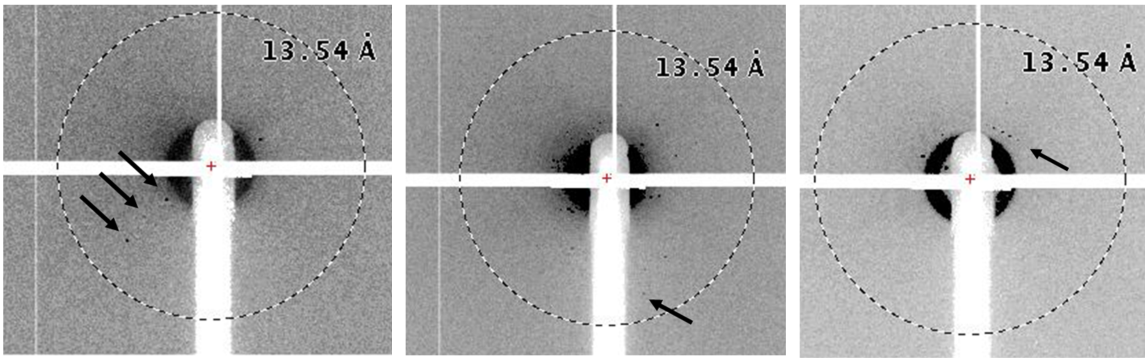

Figure 95. Diffraction images of protein diffraction observed from crystals presented in panel C) of Figure 94.

In another effort to further improve the crystal size and their diffraction quality, the precipitant solutions which yielded the best crystals in this fourth crystallization of TC190 with PSB-21500 were selected for combination with additives. The Hampton Research additive screen was used at two different concentrations: 10 %, as recommended by the manufacturer,[283] as well 3.33 %. The exact conditions were as follows:

i. 220 mM lithium sulfate monohydrate, 37 % (v/v) PEG 400, 100 mM tri-sodium citrate dihydrate pH 5.0 and 3.33 % or 10 % additives, respectively.
ii. 310 mM di-ammonium hydrogen phosphate, 25 % (v/v) PEG 400, 100 mM HEPES pH 7.8 and 3.33 % and 10 % additives, respectively.

Additionally, the original fine screens which had yielded the respective crystal hits were employed once again.

Unfortunately, despite the inclusion of additives, there was no further improvement in crystal formation. On the contrary, the crystals remained smaller and less abundant compared to the previous crystallization trial, even for the original fine screen. Potentially, the apparently lower protein concentration, judged by the peak of the SEC chromatogram, of this fifth crystallization (~ 40 mAU) compared to the previous crystallization (~ 60 mAU) may have contributed to this lack of success. Regardless of that, the crystal optimization proved to be challenging in the other crystallization trials as well, despite the similar peak height of those samples. Therefore, it was concluded that further optimization of the crystal construct was advisable.

Another possibility was that the irreversible antagonist did not support the crystal formation as anticipated, and potentially even hindered it, e.g. through unspecific reaction of the sulfonyl fluoride group with nucleophilic groups outside of the ligand binding pocket. However, compared to other cross-linking functions, sulfonyl fluorides demonstrate higher selectivity towards nucleophiles in a protein binding pocket, due to their moderate reactivity.[288] Cross-linking occurs only upon extended residence time on the protein, mediated by noncovalent binding interactions of the ligand's scaffold.[289] Anyhow, driven by the interest to obtain a potential crystal structure with other antagonists as well, TC190 was purified and crystallized with three interesting and promising reversible antagonists, including the previously employed antagonist PSB-09120. The results of these crystallizations are presented in the upcoming section 3.13.

3.13 Crystallization trials of TC190 with reversible ligands

Similar to previous sections, the results of the purifications and crystallization trials will be depicted in the upcoming sections 3.13.1 to 3.13.4, followed by a joint discussion in section 3.13.5 on page 143.

3.13.1 Crystallization of TC190 in complex with AB928

The dual $A_{2A}/A_{2B}AR$ antagonist AB928, also known as Etrumadenant, has been developed by Arcus Biosciences,[290] and is currently investigated in phase 2 clinical trials for the treatment of lung cancer, prostate cancer and colorectal cancer.[291–294]

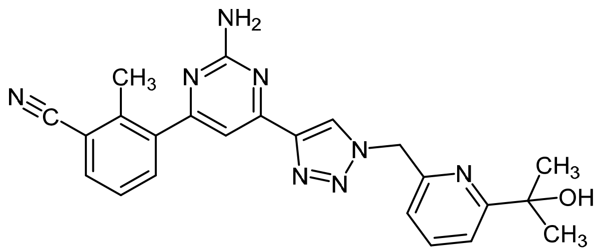

Figure 96. Chemical structure of AB928.

Recently, our group published the co-crystal structure of the $A_{2A}AR$ in complex with the antagonist AB928.[107] This structure provided insights into the binding mode of the small molecule and revealed an unprecedented interaction of the cyano group of AB928 to T88$^{3.36}$ of the $A_{2A}AR$, a residue commonly mutated to alanine in the majority of antagonist-bound co-crystal structures of the receptor.[107] Elucidation of the co-crystal structure of the clinical candidate in complex with the $A_{2B}AR$ receptor is of major interest, as it may have the potential to contribute the development of even more potent and selective dual $A_{2A}/A_{2B}AR$ antagonists.

The results of the purification and crystallization of TC190 in complex with AB928 are presented in the following Figure 97.

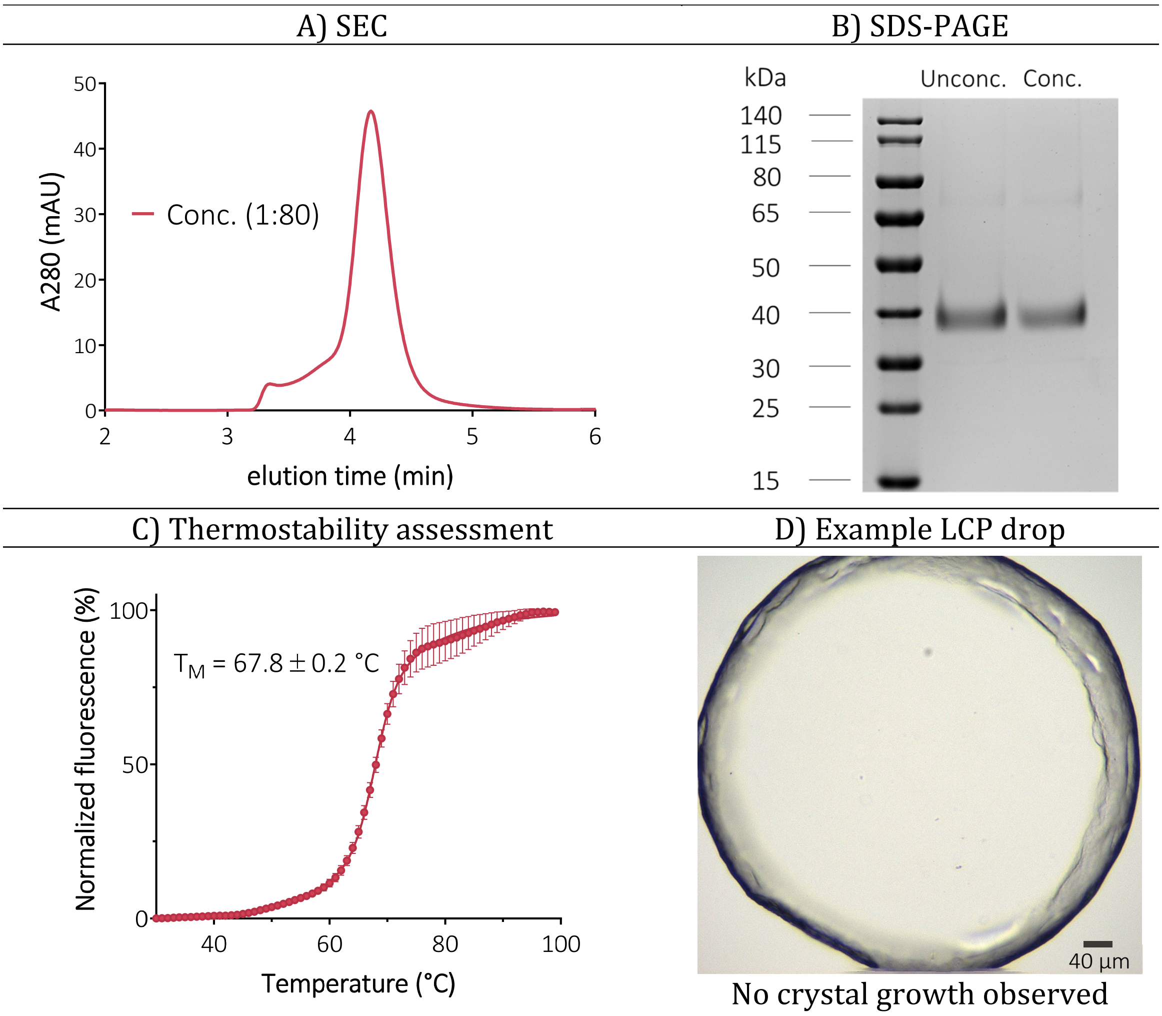

Figure 97. Protein analysis and crystallization of TC190 in complex with 25 µM AB928. A) Region of interest of the SEC analysis of the concentrated protein sample. B) SDS-PAGE of the concentrated sample, 10 µL (~ 1:100 diluted). C) Thermostability assessment of the unconcentrated sample. Nonlinear fit (Boltzmann sigmoidal) of normalized fluorescence data. The T_M was calculated as the mean ± SD of the inflection point (n=3). D) Exemplary LCP drop from the crystallization experiment.

3.13.2 Crystallization of TC190 in complex with PA51

In Figure 98, the results of the purification and crystallization of TC190 in complex with PA51 are depicted.

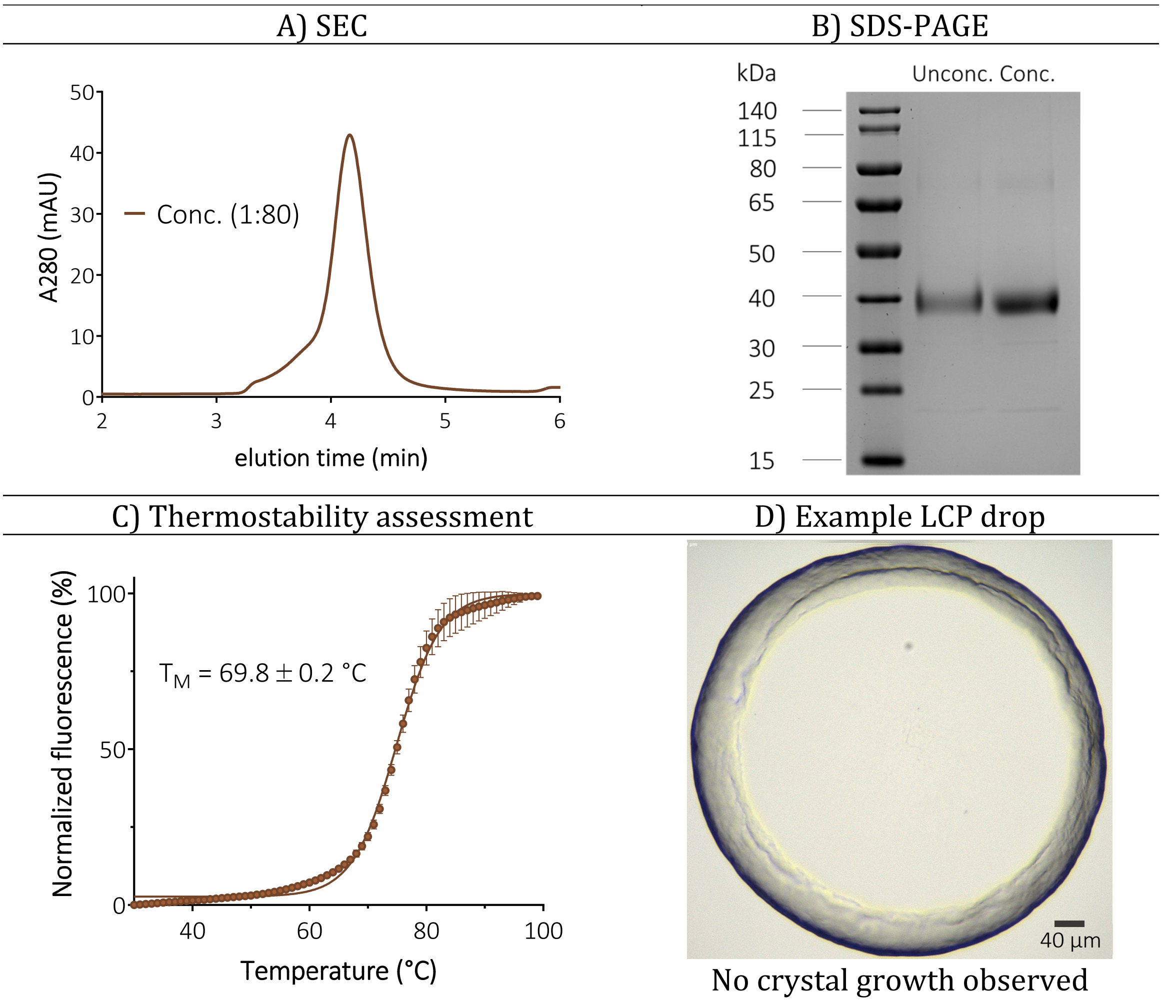

Figure 98. Protein analysis and crystallization of TC190 in complex with 25 µM PA51. A) Region of interest of the SEC analysis of the concentrated protein sample. B) SDS-PAGE of the (un-) concentrated sample, 10 µL (conc. ~ 1:100 diluted). C) Thermostability assessment of the unconcentrated sample. Nonlinear fit (Boltzmann sigmoidal) of normalized fluorescence data. The T_M was calculated as the mean ± SD of the inflection point (n=3). D) Exemplary LCP drop from the crystallization experiment.

3.13.3 Crystallization of TC190 in complex with PSB-09120 (I)

The outcome of the first purification and crystallization of TC190 in complex with PSB-09120 is provided in Figure 99.

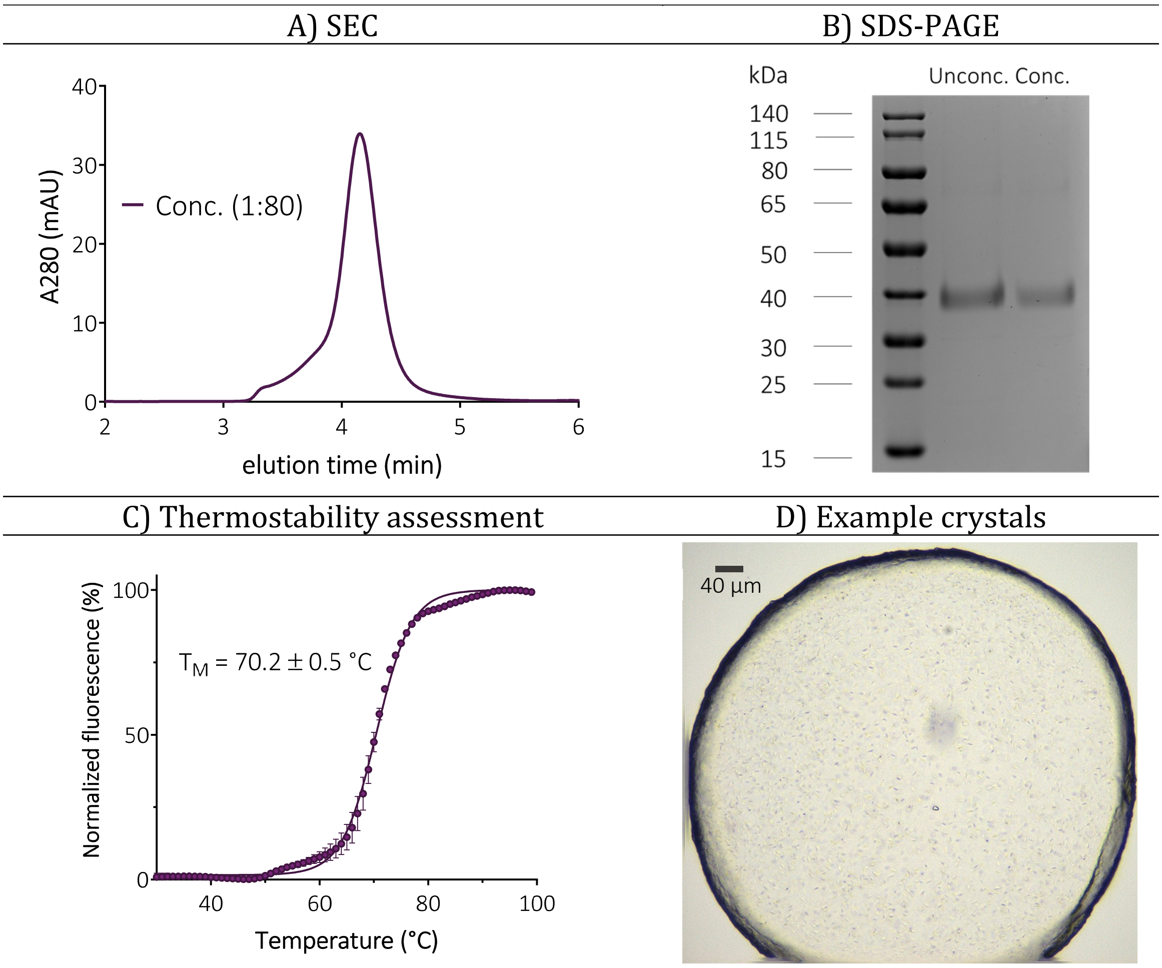

Figure 99. Protein analysis and crystallization of TC190 in complex with 25 µM PSB-09120. A) Region of interest of the SEC analysis of the concentrated protein sample. B) SDS-PAGE of the (un-) concentrated sample, 10 µL (conc. ~ 1:100 diluted). C) Thermostability assessment of the unconcentrated sample. Nonlinear fit (Boltzmann sigmoidal) of normalized fluorescence data. The T_M was calculated as the mean ± SD of the inflection point (n=3). D) Exemplary LCP drop from the crystallization experiment.

3.13.4 Crystallization of TC190 in complex with PSB-09120 (II)

The second purification and crystallization of TC190 in complex with PSB-09120 is visualized in Figure 100 shown below.

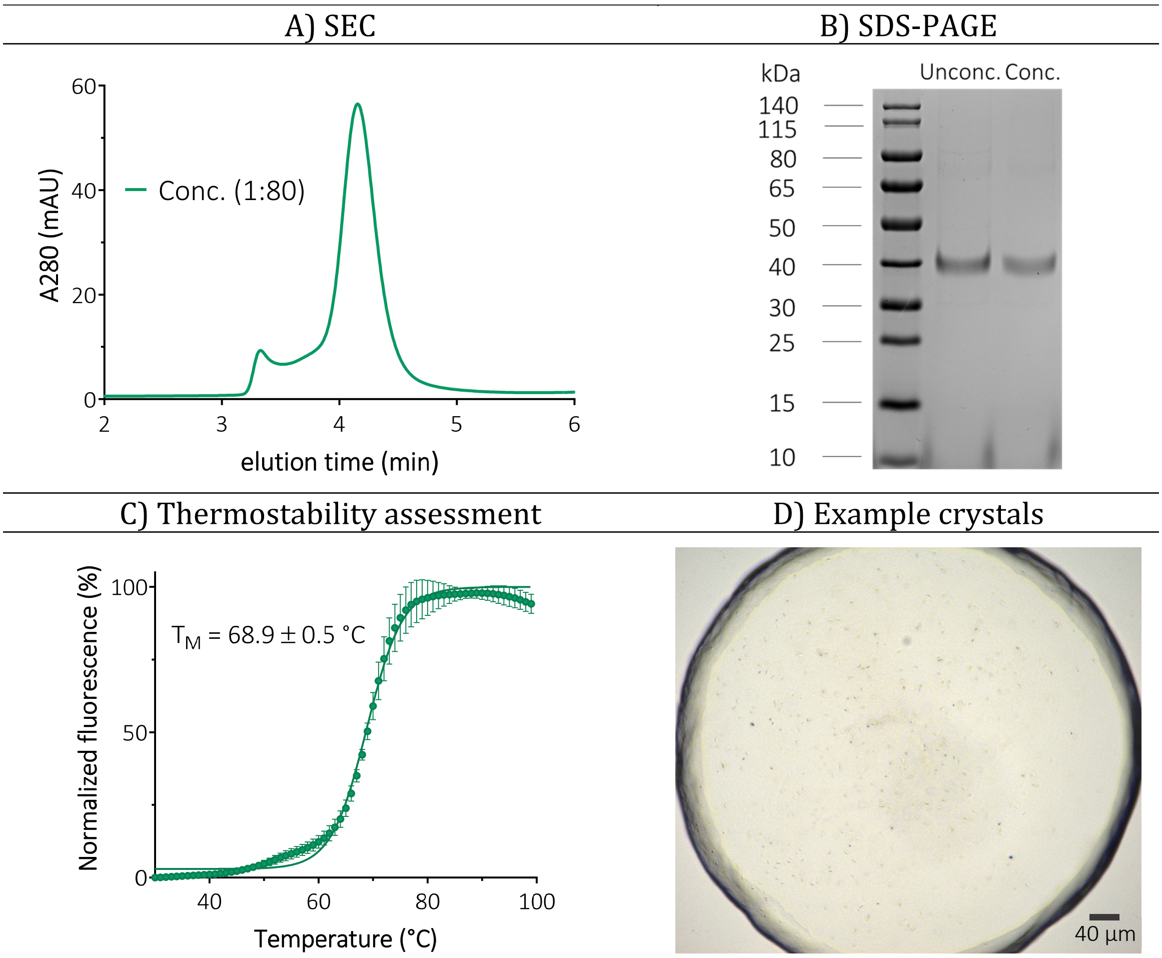

Figure 100. Protein analysis and crystallization of TC190 in complex with 25 µM PSB-09120. A) Region of interest of the SEC analysis of the concentrated protein sample. B) SDS-PAGE of the (un-) concentrated sample, 10 µL (conc. ~ 1:100 diluted). C) Thermostability assessment of the unconcentrated sample. Nonlinear fit (Boltzmann sigmoidal) of normalized fluorescence data. The T_M was calculated as the mean ± SD of the inflection point (n=3). D) Exemplary LCP drop from the crystallization experiment.

3.13.5 Discussion of the crystallization trials with reversible ligands

All of the four purification experiments resulted in relatively monodisperse protein samples, despite some elevated aggregation peaks observed for the purifications in complex with AB928 and PSB-09120 (II). The protein yields varied among the purifications, with SEC analysis peaks ranging form approximately 35 mAU for the first crystallization of TC190 with PSB-09120 (page 142), to approximately 60 mAU for the second crystallization of that complex, as presented above. The other two purifications in the presence of AB928 and PA51 showed peaks of around 45 mAU. Each ligand, when compared to the thermostability of the apo TC190 construct purified in small-scale (as demonstrated in section 3.6.2, page 87), elevated the T_M slightly by 3.5 to 6 °C. It is worth noting that, for the previously presented complex of TC190 with the irreversible antagonist PSB-21500, T_M values were > 10 °C higher than those observed for the reversible antagonists discussed here. Regarding the SDS-PAGE results, all samples were without major protein impurities.

Unfortunately, only two of the four crystallizations yielded crystals at all, specifically the first and second crystallization in presence of PSB-09120. No signs of crystal formation were observed in the presence of the non-xanthine antagonists AB928 and PA51, despite the samples' appropriate monodispersity and purity. The protein yield, as indicated by the SEC analysis, was in the same range or even higher as previously successful crystallizations of TC190 in complex with PSB-21500 (see crystallizations I, IV and V of section 3.12). Especially in the case of PA51, this demonstrates that an outstanding performance in thermostability or monodispersity does not necessarily indicate an outstanding crystallogenesis of the protein. It is possible that a different protein concentration or other factors in the purification process could be optimized for a better outcome with these ligands. For the elucidation of the very first crystal structure of the $A_{2B}AR$, however, it was decided to focus future experiments on ligands that had already successfully facilitated the protein crystal growth under the given purification conditions.

In the initial crystallization attempt of TC190 in complex with PSB-09120, the previously mentioned 48-salt screens, at pH values ranging from 4.0 to 8.0, along with the commercial screens PEG/Ion 400 and JBScreen LCP were utilized. Similar to other ligands, the crystal formation was relatively scarce, and the crystals' size was limited to 10 µm. The most promising crystals of this crystallization are depicted in Figure 101 stated below.

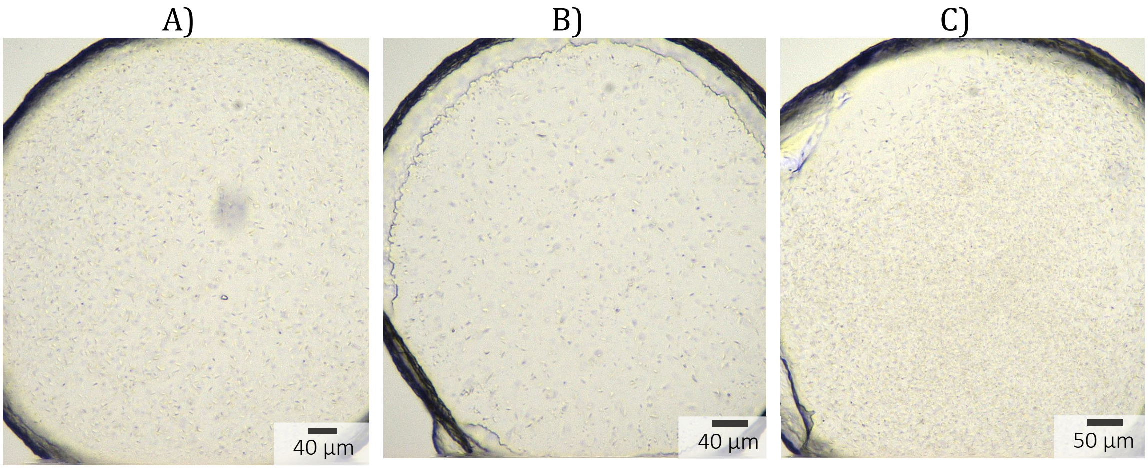

100 mM di-ammonium tartrate	400 mM sodium malonate	100 mM di-ammonium tartrate
+ 30 % (v/v) PEG 400 + 100 mM Tris-HCl pH 8.0	+ 30 % (v/v) PEG 400 pH 7.0	+ 30 % (v/v) PEG 400 pH 6.5

Figure 101. Representative LCP drops of the crystallization TC190 – PSB-09120 (I) with crystals obtained with the indicated precipitant solutions. The pictures were each taken after 21 days.

Based on the observed crystal hits, which resembled some of the hits from the crystallizations of TC190 in complex with PSB-21500, five previously formulated fine screens, including e.g. di-ammonium tartrate and di-ammonium hydrogen phosphate, were employed. As seen before, the optimization of the protein crystals proved to be a challenging task. The majority of LCP drops from the refined screens showed no signs of crystal formation, and the few crystals that did grow showed no improvement over the initial crystal hits.

To overcome this impasse of stagnating crystal sizes, which was observed with various irreversible and reversible antagonists, a further optimized $A_{2B}AR$ construct was chosen for subsequent crystallization trials.

3.14 Crystallization trials of TC196 with PSB-21500 (I + II)

The selected further refined crystallization construct was TC196. This construct comprises all features of TC190, but includes one additional point mutation: A233$^{6.34}$L. The rationale behind this mutation was based on the understanding that, for the β_2AR, L272$^{6.34}$ stabilizes the receptor in its inactive state, and mutation of that residue to alanine leads to increased basal activity and biochemical instability.[60] In the $A_{2B}AR$, this potentially destabilizing alanine in position 6.34 is naturally present, raising the hypothesis that this alanine might contribute to insufficient stabilization and thereby impeding the optimization of the observed protein crystal hits. The results of small-scale purification and its comparison to TC190 are provided in Figure 102.

A) SEC

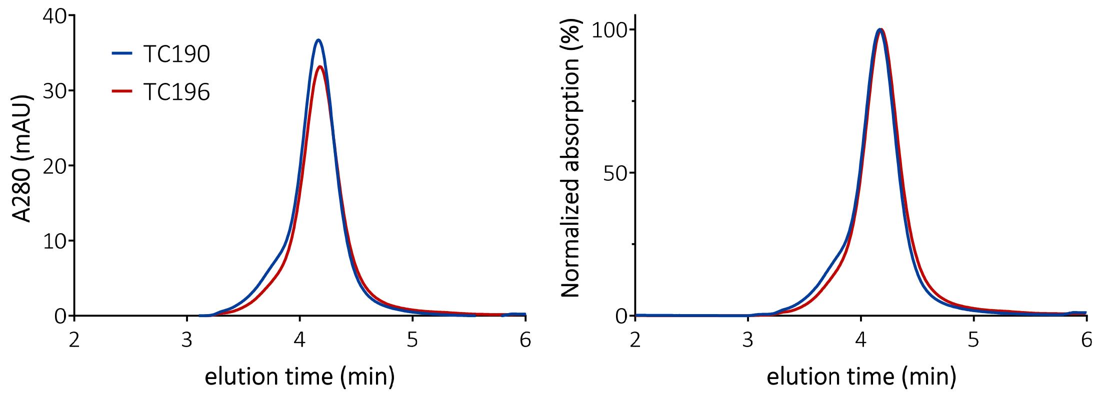

B) Thermostability assessment

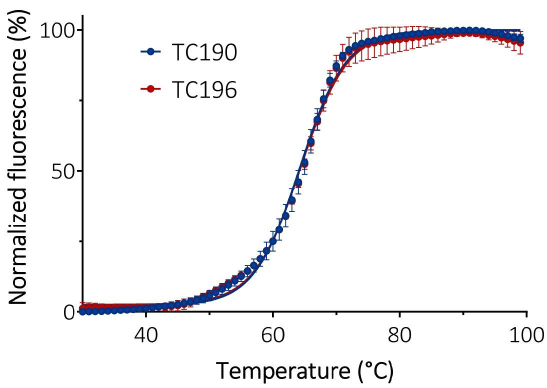

TC190 – Apo	$T_M = 64.2 \pm 0.6$ °C
TC196 – Apo	$T_M = 64.4 \pm 0.4$ °C

Figure 102. Comparison of the protein analyses of TC190 and TC196. A) Region of interest of the (normalized) SEC analysis of both proteins in apo form. B) Thermostability assessment of the TC190 and TC196 samples. Nonlinear fit (Boltzmann sigmoidal) of normalized fluorescence data. The T_M was calculated as the mean ± SD of the inflection point (n=3).

As evident from the data provided above, the introduction of the additional point mutation A233$^{6.34}$L in TM6 of the receptor had a slightly negative effect on the protein yield, and a slightly positive effect on the receptor's monodispersity. With regard to the thermostability, no differences in the T_M of both proteins were observed.

However, it is crucial to note that, at this stage of this crystallization project, slight changes in the monodispersity and thermostability of the protein were no longer meaningful indicators for successful crystal growth. Therefore, construct TC196 was put to the test by purifying and crystallizing it in presence of PSB-21500, which had shown superior performance among all tested $A_{2B}AR$ antagonists in the previous crystallization trials.

3.14.1 Crystallization of TC196 with PSB-21500 (I)

As for the earlier purifications of the protein TC190 with PSB-21500, TC196 was purified from 450 mL of *Sf9* biomass, in the presence of 1 µM of the ligand during solubilization, and 0.1 µM during the wash and elution steps. Regarding the utilized precipitant screens, two of the previously most successful fine screens (with lithium sulfate monohydrate at pH 5.0 and di-ammonium hydrogen phosphate at pH 7.8) were chosen. Each of these screens was employed twice, once with the addition of 2 µM of PSB-21500 and once without any extra ligand in the precipitant solutions. Additionally, the commercial screens PEG/Ion 400 and JBScreen LCP, as well as one ammonium chloride fine screen were tested. The results of this purification and crystallization attempt are presented in the following Figure 103.

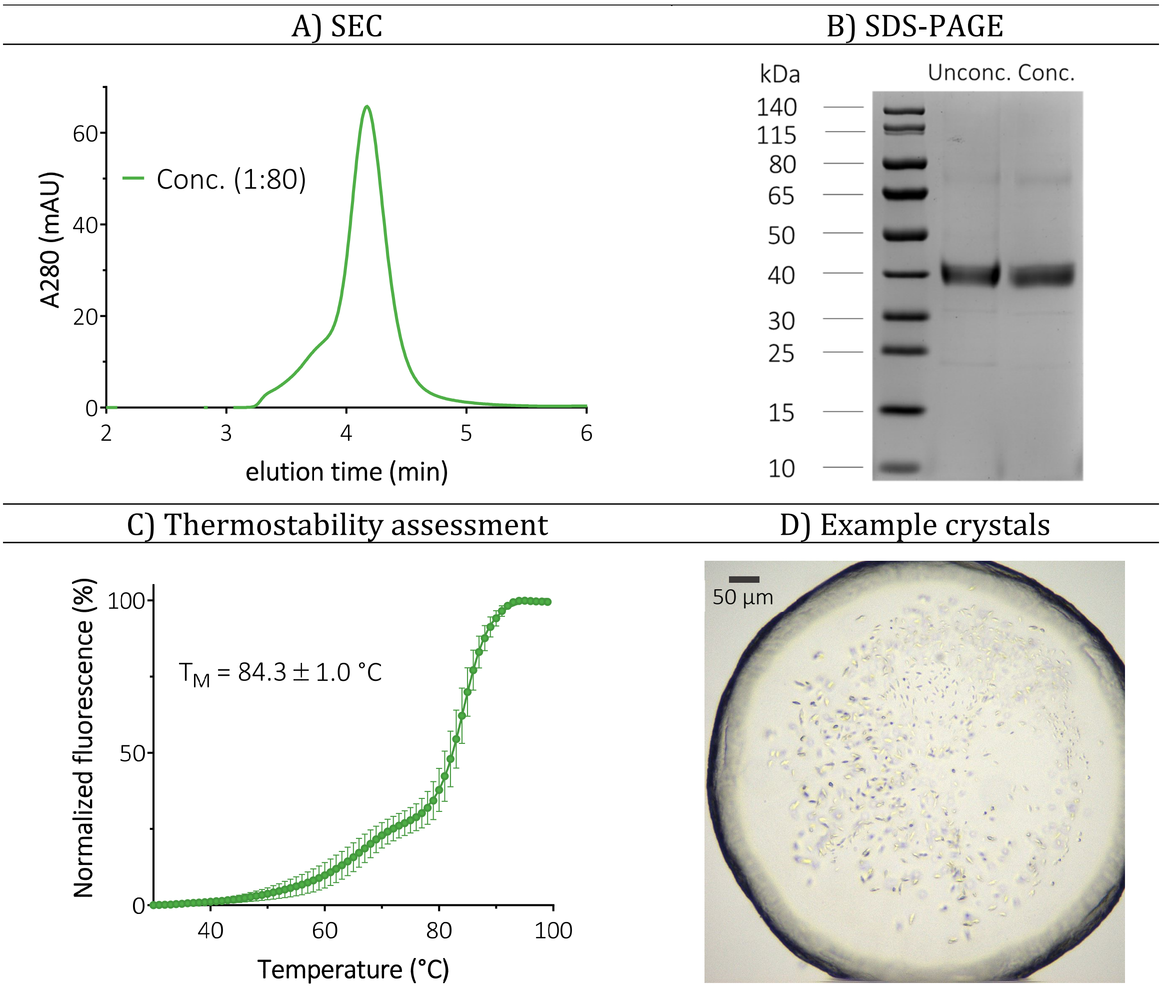

Figure 103. Protein analysis and crystallization of TC196 in complex with PSB-21500 (I). A) Region of interest of the SEC analysis of the concentrated protein sample. B) SDS-PAGE of the (un-) concentrated sample, 10 µL (conc. ~ 1:100 diluted). C) Thermostability assessment of the unconcentrated sample. Nonlinear fit (biphasic) of normalized fluorescence data. The T_M was calculated as the mean ± SD of the later inflection point (n=3). D) Exemplary LCP drop from the crystallization experiment.

The purification resulted in a quite monodisperse and pure sample of an apparently high protein yield, based on an approximately 70 mAU high peak of the SEC analysis. With a T_M of ~ 84 °C the thermostability was very high, consistent with all cases where the covalent ligand PSB-21500 was utilized. As anticipated, the crystallization with the new and potentially improved $A_{2B}AR$ construct was successful, given that many of the LPC drops exhibited extensive crystal formation. Particularly the fine screens with di-ammonium hydrogen phosphate resulted in large crystals, with sizes reaching up to 35 µm. However, also the fine screens with the other two salts resulted in crystal growth, albeit with smaller sizes. It should be noted, that the presence of the additional 2 µM of PSB-21500 in the precipitant solutions generally did not impact the crystallization events. Two representative results for each of the fine screen plates are provided in the following Figure 104.

TC196 + PSB-21500 (I)

A)

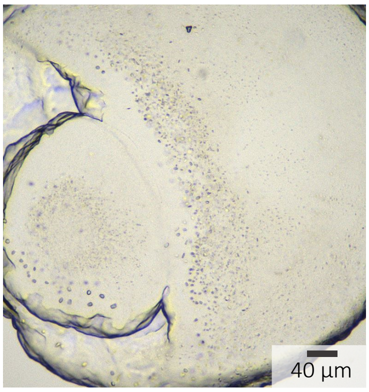

220 mM lithium sulfate monohydrate

+ 36 % (v/v) PEG 400
+ 100 mM tri-sodium citrate dihydrate pH 5.0

B)

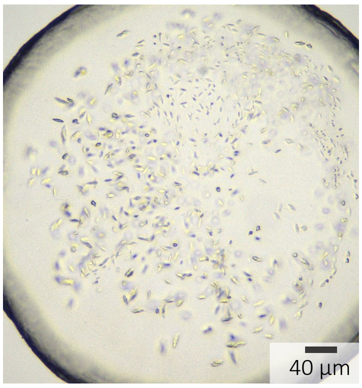

290 mM di-ammonium hydrogen phosphate

+ 26 % (v/v) PEG 400
+ 100 mM HEPES pH 7.8

C)

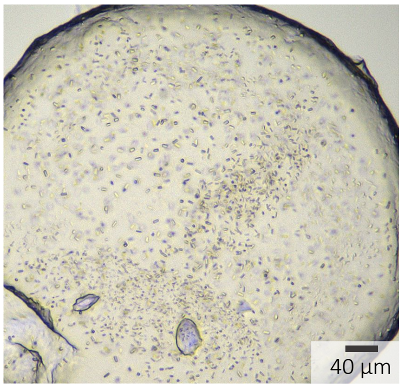

290 mM ammonium chloride

+ 33 % (v/v) PEG 400
+ 100 mM HEPES pH 7.0

D)

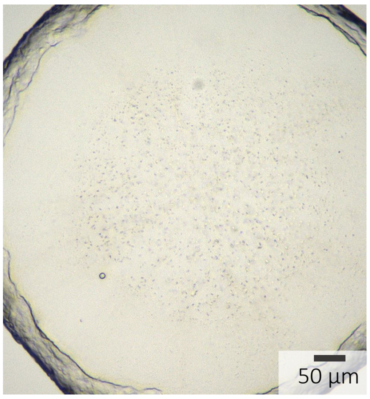

240 mM lithium sulfate monohydrate

+ 2 µM PSB-21500
+ 34 % (v/v) PEG 400
+ 100 mM tri-sodium citrate dihydrate pH 5.0

E)

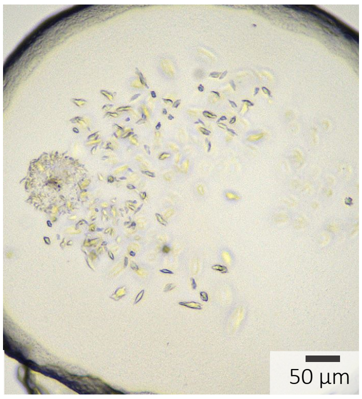

290 mM di-ammonium hydrogen phosphate

+ 2 µM PSB-21500
+ 26 % (v/v) PEG 400
+ 100 mM HEPES pH 7.8

F)

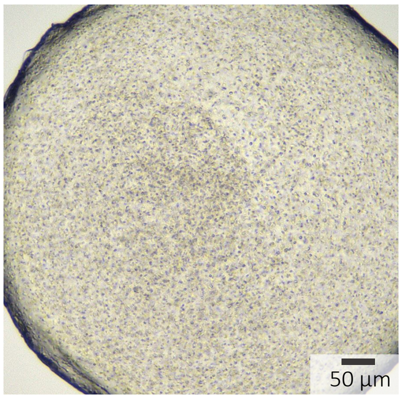

300 mM ammonium chloride

+ 31 % (v/v) PEG 400
+ 100 mM HEPES pH 7.0

Figure 104. Exemplary LCP drops from crystallization of TC196 – PSB-21500 (I) with crystals obtained with the indicated conditions. The pictures were taken after 35 days of incubation.

In parallel to the growth of the crystals presented above, another purification and crystallization trial of TC196 in complex with PSB-21500 was performed. However, this time, the purification procedure was differed slightly as outlined in the upcoming section 3.14.2.

3.14.2 Crystallization of TC196 with PSB-21500 (II)

The main change within this crystallization trial involved an extended ligand incubation and an additional salt exchange step at the end of the purification process. Before solubilization of the membrane proteins, the *Sf9* membranes underwent a 2 h pre-incubation with 20 µM PSB-21500 at room temperature to ensure exhaustive binding of the ligand to the A_{2B}AR construct within the membranes. The subsequent steps, including the incubation with Co^{2+} beads, washing and elution were in principal identical to the standard procedure. However, after protein elution, the elution buffer which contained 800 mM NaCl, 220 mM imidazole and 10 % (v/v) glycerol, was exchanged for a buffer without imidazole and glycerol containing only 500 mM of NaCl. Furthermore, each of the wash, elution and salt exchange buffers was supplemented with 2 µM PSB-21500, instead of the previously added 0.1 µM.

These adjustments were made to eliminate any potential confounding factors that might compromise the reproducibility and formation of the protein crystals, such as incomplete occupancy of the protein with ligand, which would result in an inhomogeneous sample. Also, the removal of imidazole is sometimes performed prior to crystallization attempts,[295] as the presence of imidazole might potentially affect crystal formation.[296, 297]

To comprehensively assess the impact of these alterations, the protein was crystallized in the presence of various precipitant solutions. This included the 48-salt screens (ranging from pH 4.0 to 8.0 in increments of one), the commercial screens PEG/Ion 400 and JBScreen LCP, and the two fine screens with di-ammonium hydrogen phosphate and ammonium chloride that were also utilized in the first crystallization trial of TC196 with PSB-21500. To ensure a sufficient protein quantity for employing all of these precipitant screens, the protein was purified from a total of 900 mL of biomass. The results of this purification and crystallization are illustrated in Figure 105 below.

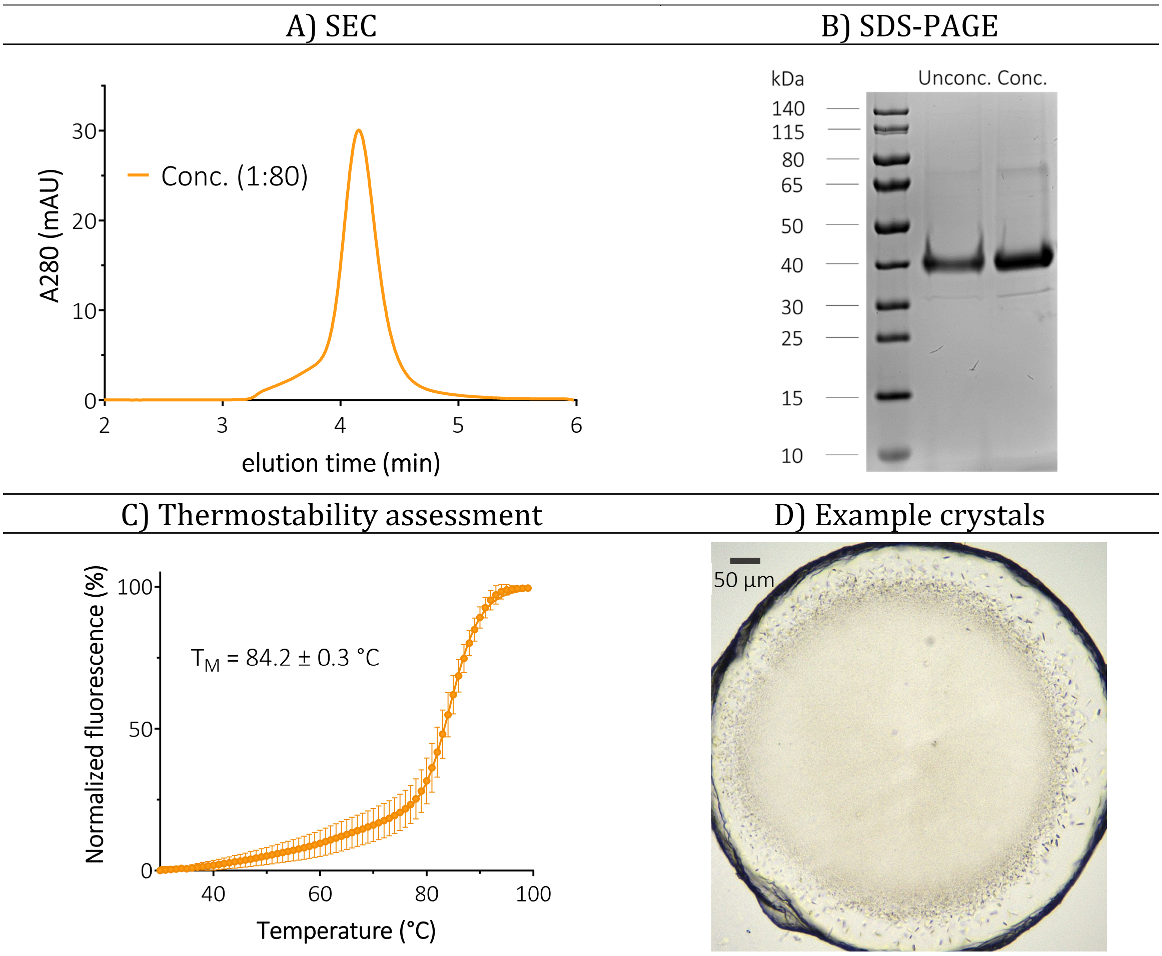

Figure 105. Protein analysis and crystallization of TC196 in complex with PSB-21500 (II). A) Region of interest of the SEC analysis of the concentrated protein sample. B) SDS-PAGE of the (un-) concentrated sample, 10 µL (conc. ~ 1:100 diluted). C) Thermostability assessment of the unconcentrated sample. Nonlinear fit (biphasic) of normalized fluorescence data. The T_M was calculated as the mean ± SD of the inflection point (n=3). D) Exemplary LCP drop from the crystallization experiment.

This second crystallization trial of TC196 with PSB-21500 also led to crystal formation. However, compared to the other concurrent crystallization trial, the crystals remained smaller in size, and did not grow in such manifold conditions. The highest extent of crystallization was observed in the LCP drops to which conditions of the ammonium chloride fine screen were applied, but, as previously shown, crystals that appeared in these conditions typically remained very small (see Figure 104, panel E). Overall, this crystallization was less successful than the previous trial. In this regard, it should be noted that according to the SEC analysis, the protein concentration of the concentrated sample used for this crystallization trial (~ 30 mAU), was significantly reduced compared to the first crystallization trial presented above in section 3.14.1 (peak height ~ 60 mAU). Thus, it is not conclusive whether the buffer exchange, or the potentially suboptimal protein concentration contributed to the decrease in crystal formation.

During this time of the project, leadXpro, a biotechnology company specializing on structure-based drug discovery for membrane proteins, expressed interest in obtaining a co-crystal structure of the A_{2B}AR with our covalent antagonist PSB-21500. Thereupon, a collaboration was initiated. As part of this collaboration, I conducted further crystallization experiments and optimizations using TC190 and TC196 in the laboratories of leadXpro, which are located on the premises of the Paul Scherrer institute (PSI) in Villigen, Switzerland. The upcoming sections will address the most important experiments that were performed during this research stay.

3.15 Research stay at leadXpro

The research stay at leadXpro took place from September of 2022 to March of 2023. Based on the successful construct optimization and the promising outcomes of the latest crystallization experiments that were conducted in Bonn, it was decided to focus all efforts on the optimization of the crystals obtained with constructs TC190 and TC196 in complex with PSB-21500. The main aspect that left room for optimization was the protein concentration and its reproducibility across the purification and crystallization experiments. Moreover, our collaboration partner leadXpro suggested the testing of two additional MAGs alongside the standardly used MO with 10 % cholesterol, to form the LCP. This aspect will be presented and discussed in section 3.15.5 on page 170 ff.

As evident from the crystallization trials presented previously, the protein concentration has a major impact on the crystal formation. Based on literature, a suitable protein concentration for the crystallization of GPCRs in LCP is ≥ 20 mg/mL.[260, 280, 298] In our laboratories in Bonn, the protein concentration of the concentrated samples was indirectly evaluated, by comparison of the peak heights of the SEC chromatograms. However, an absolute value for the protein concentration was not regularly determined in light of the fact that an exact concentration measurement of membrane proteins is challenging. Reasons for that are the high amount of protein needed, and the possible inaccuracy of the available standard methods (like Bradford and Lowry assays) due to their interference with the detergents that are a necessity in buffers used for membrane proteins.[299, 300] Another possibility to measure protein concentrations is by measuring the UV absorbance at 280 nm, considering the unique extinction coefficients of proteins.[299] A valuable advantage of this method is the low volume which is necessary when using a microvolume spectrometer (~ 1 µL/measurement). The UV absorbance (A280 nm) was the method of choice for the protein concentration determination at leadXpro.

To achieve a sufficient volume of protein solution at a concentration of ≥ 20 mg/mL, the over-expression system used for the endogenously low-expressing $A_{2B}AR$ was reevaluated, since the expression levels can vary between different cell lines.[101] A previously performed comparison between expression in *Sf9* and *Tni* cells performed in Bonn, showed no advantage of using *Tni* cells over *Sf9* cells, neither in terms of protein yield nor monodispersity, as indicated by the SEC results (data not shown). In fact, the protein yield for the protein (TC190) expressed in *Tni* cells was even lower than that for the same protein expressed in *Sf9* cells. Nevertheless, the expression systems were once again compared in the new context in the laboratories of leadXpro, and the findings will be presented in the following section 3.15.1.

3.15.1 Small-scale evaluation of expression systems

For the comparison of expression levels of $A_{2B}AR$ constructs in *Sf9* and *Tni* cells, four different constructs, namely TC190, TC197, TC198 and TC200, were expressed under four different conditions:

1. In *Sf9* cells with 1 % of virus (as previously used in Bonn),
2. in *Sf9* cells with 5 % of virus,
3. in *Tni* cells with 1 % of virus (as previously tested in Bonn), and
4. in *Tni* cells with 5 % of virus (as suggested by leadXpro).

In contrast to the small-scale expressions and purifications conducted in Bonn, the procedure for this small-scale experiment at leadXpro provided different results. In short, the proteins were expressed in only 3 mL instead of 40 mL of cell suspension, and directly solubilized from the cell pellets without prior membrane preparation. The solubilization, Co^{2+} resin binding and wash steps followed a shortened procedure, and the amount of the recombinant protein was assessed by SDS-PAGE and SEC analysis. The results of these analyses are presented in the following Figure 106.

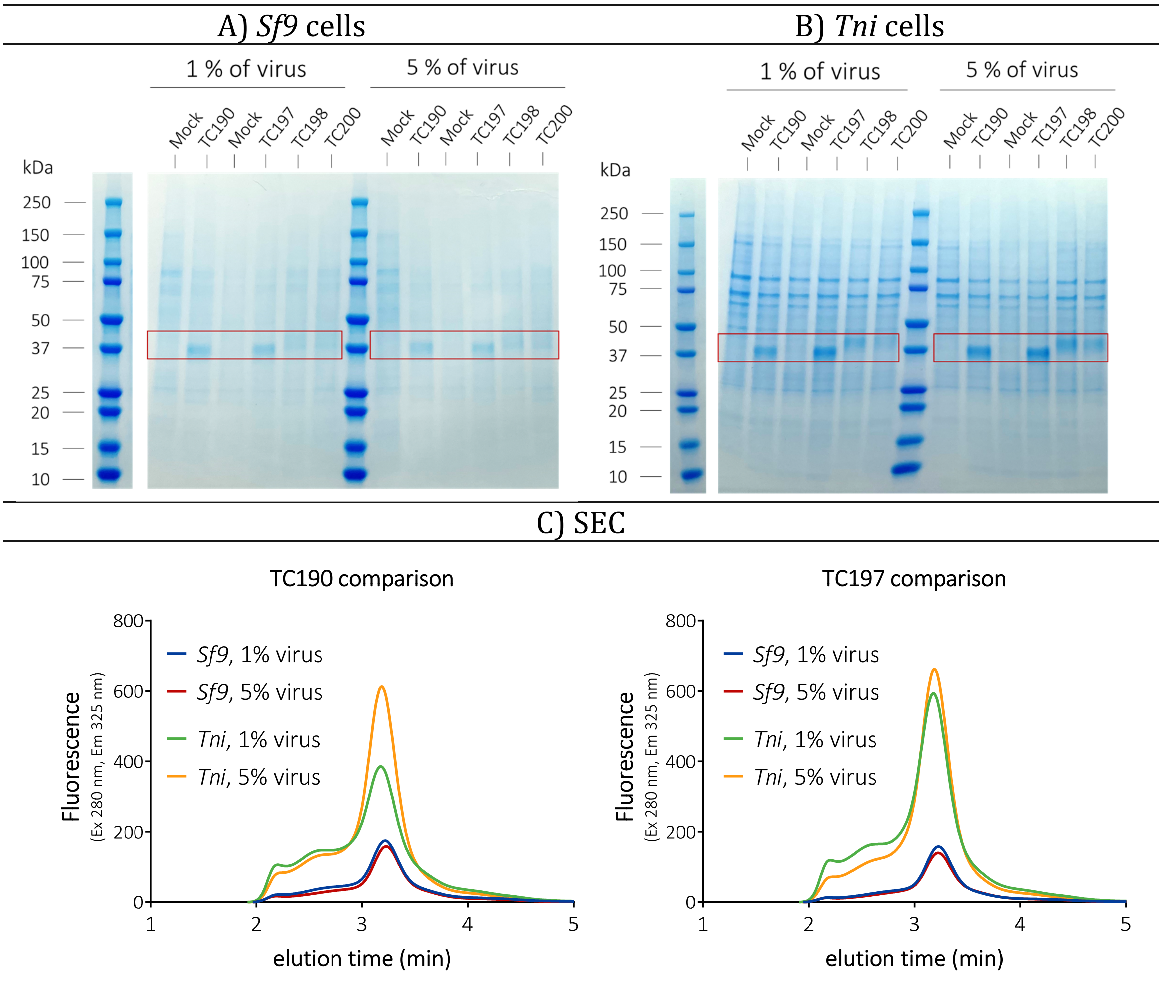

TC190	$A19^{1.44}V$, $C29^{1.54}I$, $G33^{1.58}W$, $A35^{1.60}N$, $S92^{3.39}K$, $N153^{ECL2}Q$, $N163^{ECL2}Q$
TC197	$A19^{1.44}V$, $C29^{1.54}I$, $G33^{1.58}W$, $A35^{1.60}N$, $S92^{3.39}K$, $N153^{ECL2}Q$, $N163^{ECL2}Q$, $A232^{6.33}L$, $C311^{8.64}A$
TC198	$S92^{3.39}K$, $N153^{ECL2}Q$, $N163^{ECL2}Q$, $A232^{6.33}L$, $C311^{8.64}A$
TC200	$S92^{3.39}K$, $N153^{ECL2}Q$, $N163^{ECL2}Q$, $A232^{6.33}L$

Figure 106. Comparison of the small-scale expression of the $A_{2B}AR$ in Sf9 and Tni cells at leadXpro. A) SDS-PAGE analysis of the indicated samples expressed in Sf9 cells. $A_{2B}AR$ bands highlighted in red B) SDS-PAGE analysis of the indicated samples expressed in Tni cells. $A_{2B}AR$ bands highlighted in red. C) Comparison of the SEC results of the region of interest of TC190 and TC197 expressed under different conditions.

In contrast to the outcome of the comparison conducted in our laboratory in Bonn, the results presented in the above-stated Figure 106 indicate a higher protein yield for the $A_{2B}AR$ constructs when expressed in *Tni* cells compared to *Sf9* cells. As evident from the SDS-PAGE results presented in panel A and B the bands corresponding to the $A_{2B}AR$ constructs, highlighted by red boxes, are notably more pronounced in the samples for which *Tni* cells were employed for the expression. Notably, however, the amount of impurities was also significantly increased, which affects the SEC results of the two exemplarily shown constructs TC190 and TC197.

At leadXpro, the HPLC was equipped with a highly sensitive fluorescence detector, in addition to a diode array detector (DAD), which was also used in Bonn. Since the utilized $A_{2B}AR$ constructs did not have any fluorescent tag such as e.g. a green fluorescent protein tag, the detection of the proteins was performed using the tryptophan fluorescence (λ_{ex} 280 nm, λ_{em} 325 nm),[301] which also detects the signal from the protein impurities. The impurities might have contributed to the up to ~ 5-fold higher signal during the SEC analysis of the samples expressed in *Tni* cells, compared to those expressed in *Sf9* cells. The case of TC190, however, proves that the majority of the signal at 3.2 min of elution time indeed corresponds to the recombinant $A_{2B}AR$ constructs. Its main peak height is significantly higher for the sample that was expressed in the presence of 5 %, instead of 1 % virus, even though the amount of impurities was comparable, as estimated visually from the SDS-PAGE. Regarding the SEC results, it is important to note that during the research stay at leadXpro a different SEC column was utilized. Therefore, the elution times of the SEC results cannot be compared with earlier experiments in Bonn. Additionally, the analyses presented below were performed on two different HPLC systems which were run at different flow rates. For that reason, the following SEC results are presented in relation to the elution volume instead of the elution time.

The higher expression of TC190 upon infection of the cells with 5 % of virus is also evident from the SDS-PAGE results (compare main band of the two halves in panel B, Figure 106). The same effect is not observed for construct TC197, where the SDS-PAGE results and the SEC results of the two differently infected samples are almost identical. Since the expression in *Tni* cells with 5 % of virus was the standard procedure performed at leadXpro, and the results with this amount of virus were (slightly) better, all following expressions at leadXpro were performed using these conditions.

In addition to the improved expression conditions, the protein amount was further increased by infecting 2 L of suspension cells, at 4 x 10^6 *Tni* cells/mL, compared to the typical equivalent of ~ 500 mL of suspension cells, at 2 – 3 x 10^6 *Sf9* cells/mL, used in

Bonn. Furthermore, a different purification procedure was utilized in order to capture and purify more of the recombinant proteins. The following two sections, 3.15.2 and 3.15.3, will address the most important large-scale purification experiments that were conducted during the research stay in Switzerland.

3.15.2 Purifications of TC190 in complex with PSB-21500 at leadXpro

3.15.2.1 Purification of TC190 in complex with PSB-21500 (LXP I)

As mentioned above, the purification procedures differed significantly from the standard procedure conducted in Bonn. Briefly, the first purification of TC190 was performed

i. from *Tni* cell biomass of 2 L of cell suspension,
ii. with a standardized 1.5 h long solubilization procedure (with 1 % (w/v) DDM and 0.1 % (w/v) CHS for membranes diluted to 100 mg/mL),
iii. with 2 h of binding with 2 % (v/v) of Co^{2+} beads,
iv. with washing and elution performed on an FPLC (fast protein liquid chromatography) system,
v. and a subsequent quantitative SEC-based purification of the monomeric protein.

The outcomes of these modifications to the purification procedure are depicted in Figure 107.

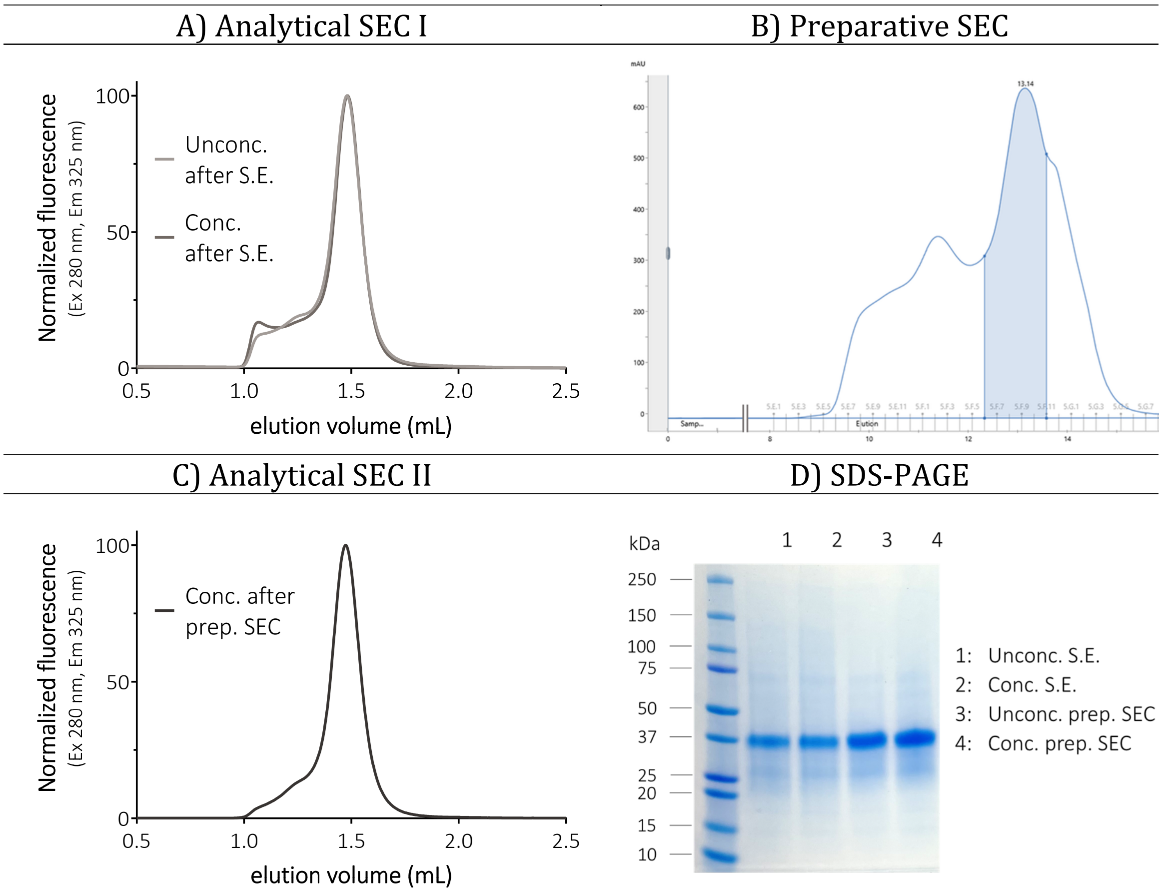

Figure 107. Protein analysis of TC190 in complex with PSB-21500 (LXP I). A) Region of interest of the SEC analysis of the (un-)conc. protein sample after salt exchange (~ 1 µg of protein each). B) Region of interest of the prep. SEC result (blue: pooled fractions). C) Region of interest of the SEC analysis of the conc. pooled protein sample after the prep. SEC (~ 1 µg of protein each). D) SDS-PAGE results of the indicated samples (~ 5 µg of protein each).

As evident from the results presented above, the first purification of TC190 in the laboratories of leadXpro was successful. Panel A shows the analytical SEC results of the samples after the exchange of the elution buffer by a buffer without imidazole (20 mM HEPES pH 7.5, 300 mM NaCl, 10 % glycerol, 0.02 % DDM, 0.002 % CHS). Compared to the standard analytical SEC results for TC190 in complex with PSB-21500 which were previously obtained in Bonn, the protein seemed to exhibit more aggregation. Most of this aggregated protein was subsequently separated from the main fraction by preparative SEC (see results in panel B, pooled fractions highlighted in blue). However, some residual aggregated protein species was either not fully separated by the preparative SEC in the first place, or a fraction of the protein aggregated once again upon concentration of the sample to its final concentration of 25 mg/mL. The monodispersity of the final concentrated sample was similar to the monodispersity of the TC190 samples used for crystallization in Bonn, however, presumably its protein concentration was higher.

Since the absolute protein concentration was not measured in Bonn, for reasons stated above, a direct comparison of the protein yields is not possible. Also, an estimation of the peak heights of the SEC results is not reasonable, since the SEC columns and detectors used for the analyses were different. In terms of protein yield it is interesting to note that for this purification, the total amount of protein after elution and salt exchange was approximately 9.4 mg, whereas the protein amount of the final sample was merely 0.9 mg (~ 35 µL of protein solution at a concentration of 25 mg/mL). Consequently, in the course of concentrating the sample for preparative SEC, during preparative SEC itself, and during the final concentrating step, over 90 % of the initially purified protein was lost.

Regarding the purity, all four analyzed probes displayed a similar, good level of purity, which indicates that the various peaks observed during the preparative SEC (see panel B) were caused by the A_{2B}AR construct and not by substantial impurities.

Taken together, the monodispersity, concentration and purity of the final sample was suitable for the conduction of the very first crystallization experiment of TC190 in complex with PSB-21500 at leadXpro. For the initial crystallization, approximately 20 µL of the final protein solution was used, while approximately 15 µL were frozen and available for a second crystallization experiment for optimization of potential crystal hits with the exact same protein. The results of the crystallization trials conducted with this protein are presented in section 3.15.4. But first, the outcomes of the second purification of TC190 in complex with PSB-21500 will be presented.

3.15.2.2 Purification of TC190 in complex with PSB-21500 (LXP II)

The next purification experiment of TC190 with PSB-21500 was performed similarly to the first purification presented above. The only noteworthy difference was the increase from 300 mM of NaCl to 800 mM of NaCl in all buffers, as typically used in Bonn. This was done to investigate whether the previous, lower levels of NaCl might have contributed to the elevated aggregation observed prior to the preparative SEC. Additionally, the removal of the imidazole from the protein solution by salt exchange was not performed this time, due to the fact that during the preparative SEC the buffer is exchanged as well, and that this time this step was conducted right after the elution of the protein. The results of this purification procedure are depicted in Figure 108.

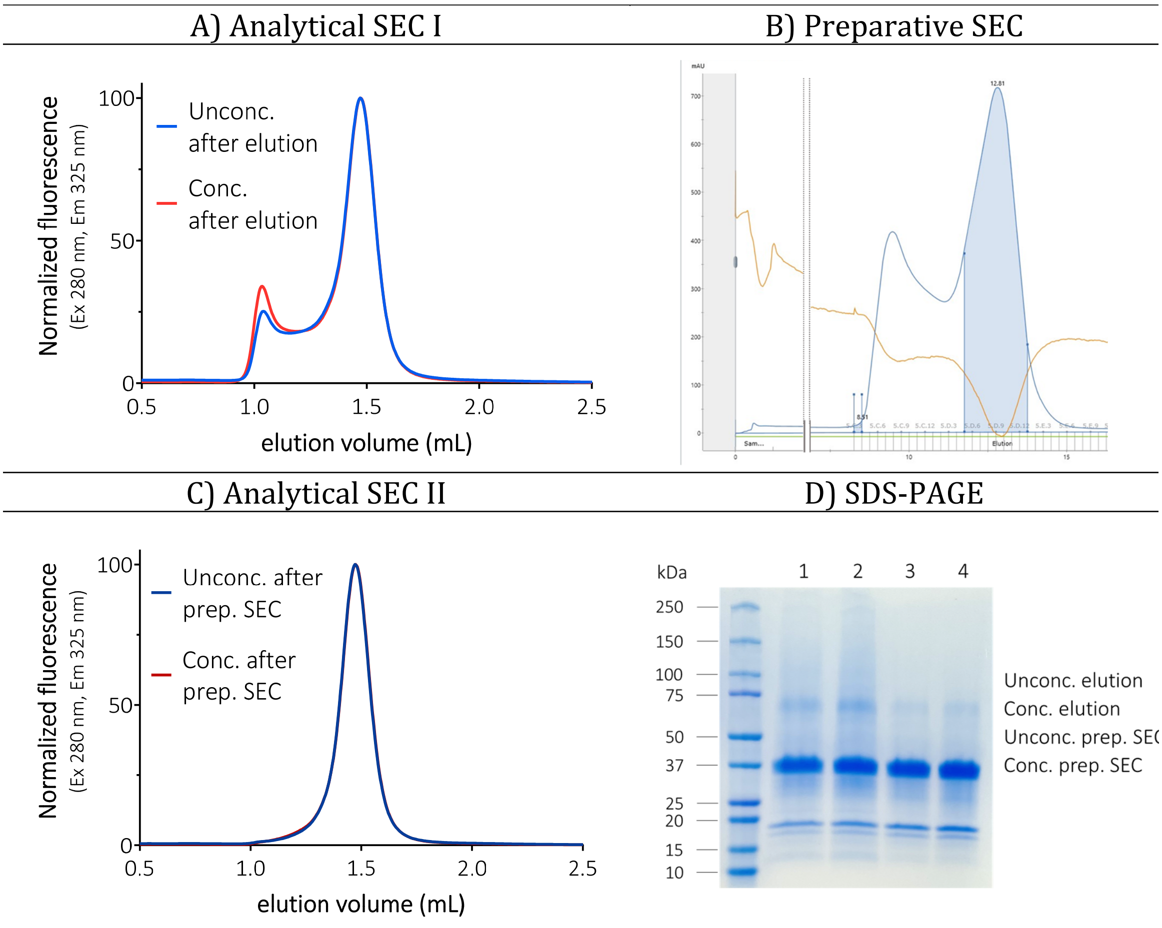

Figure 108. Protein analysis of TC190 in complex with PSB-21500 (LXP II). A) Region of interest of the SEC analysis of the (un-)conc. protein sample after elution (~ 1 µg of protein each). B) Region of interest of the prep. SEC result (blue: pooled fractions). C) Region of interest of the SEC analysis of the (un-)conc. pooled protein sample after the prep. SEC (~ 1 µg of protein each). D) SDS-PAGE results of the indicated samples (~ 5 µg of protein each).

Similarly to the purification presented previously, the protein samples of this second purification of TC190 in the presence of PSB-21500 exhibited a notable aggregation signal upon elution (see panel A). In the chromatogram of the preparative SEC, however, fewer distinct protein peaks were observed. For example, no additional peak was observed after the main peak and also prior to the main peak only one pronounced aggregation peak was visible. As before, the fractions corresponding to monomeric A_{2B}AR were pooled (highlighted in blue) and concentrated, this time to a final concentration of 28 mg/mL. In the subsequent qualitative SEC analysis (see panel C) the unconcentrated and concentrated protein samples both displayed a perfectly monodisperse peak, despite the high protein concentration. This was a clear improvement over the concentrated protein samples obtained in Bonn which were purified without the polishing step of the preparative SEC.

Interestingly, however, the protein showed a significant contamination in the SDS-PAGE analysis with a different protein that was just under 20 kDa in size. The fact that this protein was not separated in the preparative SEC suggests that it might have been attached to the receptor during the process. Chaperones, such as the heat shock protein (HSP) 70 with a molecular weight of approximately 70 kDa, are a typical contaminant of recombinant proteins that oftentimes remain attached during the purification process.[302] Besides HSP70, also small ATP-independent HSPs were identified in insect cells,[303] exhibiting sizes of approximately 20 kDa,[304] which could potentially be the cause for these persistent impurities.

On a more positive note, the protein loss in the course of this purification was less pronounced, compared to the previous purification. From the initial 8.3 mg of protein which was eluted from the Co^{2+} resin, 2.2 mg of protein were still present in the final sample after the preparative SEC and all concentration steps. The protein was aliquoted into five 15 µL aliquots from which one aliquot was immediately used for crystallization, and the other ones were once again flash frozen in liquid nitrogen for subsequent potential optimization of crystals.

Besides TC190, also the newer crystallization construct TC196 was investigated for its potential to form crystals in this new setting in the laboratories of leadXpro. The following section will focus on the two most important purifications of TC196 in complex with PSB-21500 performed in Switzerland.

3.15.3 Purifications of TC196 in complex with PSB-21500 at leadXpro

3.15.3.1 Purification of TC196 in complex with PSB-21500 (LXP I)

As addressed in the preliminary remarks to the first purification of TC190 at leadXpro, the purification process which was performed for the above-stated two purifications differed in many aspects from the standard purification procedure performed in Bonn. Since both TC190 samples exhibited a more pronounced aggregation peak compared to the samples in Bonn (before preparative SEC), it was of interest to perform the same or at a least similar purification process as in Bonn in this new setting. Additionally, this gave rise to the opportunity to compare the amount of purified protein after each of the purification methods. Most features of the purification procedure were identical to that performed in Bonn, however, some steps were still adapted.

The general conditions of the purification procedure were as follows:

i. The purification was performed from *Tni* cell biomass of 2 L of cell suspension,
ii. with a standardized 2 h long solubilization procedure (with 1 % (w/v) DDM and 0.1 % (w/v) CHS for membranes diluted to 100 mg/mL),
iii. with overnight binding to 1.5 mL of Co^{2+} beads (in contrast to the previously used ~ 7 mL),
iv. and subsequent wash and elution steps performed on a gravity flow column.

In this protocol, no preparative SEC was performed. Further details on this purification procedure can be found in the Appendix. Figure 109 presents the results of this purification.

A) Analytical SEC	B) SDS-PAGE

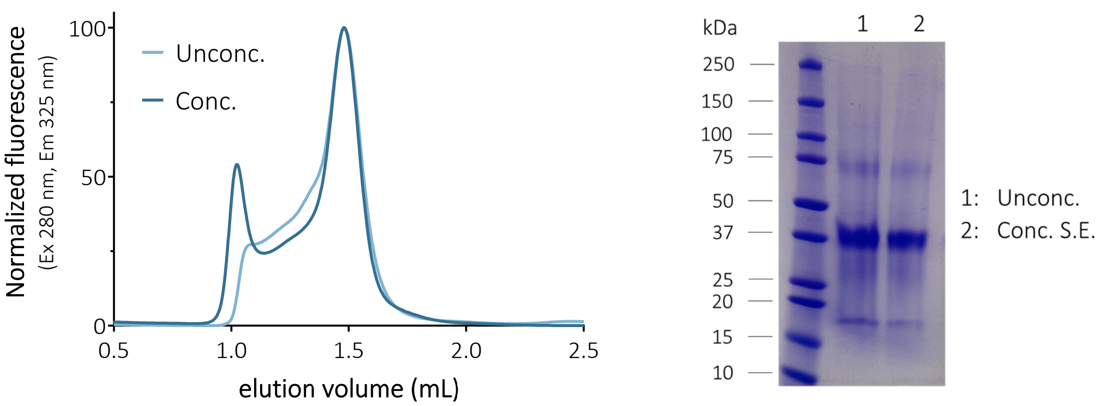

Figure 109. Protein analysis of TC196 in complex with PSB-21500 (LXP I). A) Region of interest of the SEC analysis of the (un-)conc. protein sample (~ 1 µg of protein each). B) SDS-PAGE results of the indicated samples (~ 5 µg of protein each).

The purification resulted in a more pronounced aggregation signal during the analytical SEC analysis, compared to the previous two purifications of TC190, especially in the case of the concentrated sample, which had a final protein concentration of 30 mg/mL. Considering that the purification was performed similarly to the standard method in Bonn, the results suggest that the few aspects which were still different, might be responsible for the increased aggregation. One major difference was the utilization of *Tni* instead of *Sf9* cells for the expression of the protein, even though in our laboratories in Bonn, the monodispersity of the protein derived was identical for both cell lines. Another difference was the standardization of the solubilization procedure based on the weight of the pure membrane after its membrane preparation. However, as presented in the upcoming section 3.16 on page 176 ff., this method was continued for all purifications performed in Bonn, subsequent to this research stay, and none of the eluted protein samples exhibited such a degree of aggregation. Lastly, at leadXpro the detergent stock solution contained 10 % of DDM and 1 % of CHS, whereas the stock solution concentrations are 10 % of DDM and 2 % of CHS in Bonn. Based on experience, however, the halving of the CHS concentration is unlikely to be responsible for the observed effect. Consequently, the reason for the elevated aggregation remained unknown.

Considering the comparison of protein yields, the adapted protocol resulted in a significantly lower amount of protein with only 1.5 mg of protein present in the eluted sample, compared to the previously obtained > 8 mg of protein. All of the samples were purified from the biomass of a 2 L infection of *Tni* cells. Most likely, the over four-fold reduction of Co^{2+} resin significantly influenced the capturing of the recombinant protein, despite its theoretical binding capacity of 5 – 15 mg of protein per mL of resin.[278] However, since no preparative SEC was performed, the protein yield was preserved in the course of the concentration process and finally, 1.2 mg of protein was available for the subsequent crystallization trials.

The purity of the sample seemed sufficient for crystallization, but unfortunately, the SDS-PAGE result lacked clarity to properly distinguish potential impurities from the background. The protein band at a size of approximately 20 kDa was also observed upon this purification, but to a lesser extent than previously (see panel D in Figure 108).

Despite the decreased monodispersity of the sample, the crystallization trials performed with this protein were among the most successful ones performed in the course of the research stay. The results of these experiments are detailed in section 3.15.5, on page 170 ff.

In addition to this, another noteworthy purification of TC196 performed with leadXpro’s purification protocol is presented in the upcoming section 3.15.3.2.

3.15.3.2 Purification of TC196 in complex with PSB-21500 (LXP II)

This second purification of TC196 in complex with the covalent antagonist PSB-21500 was performed identically to the two purifications of TC190, described earlier, including the utilization of 6 mL of Co^{2+} resin and preparative SEC as a polishing step.

The outcome of this purification is detailed in Figure 110, stated below.

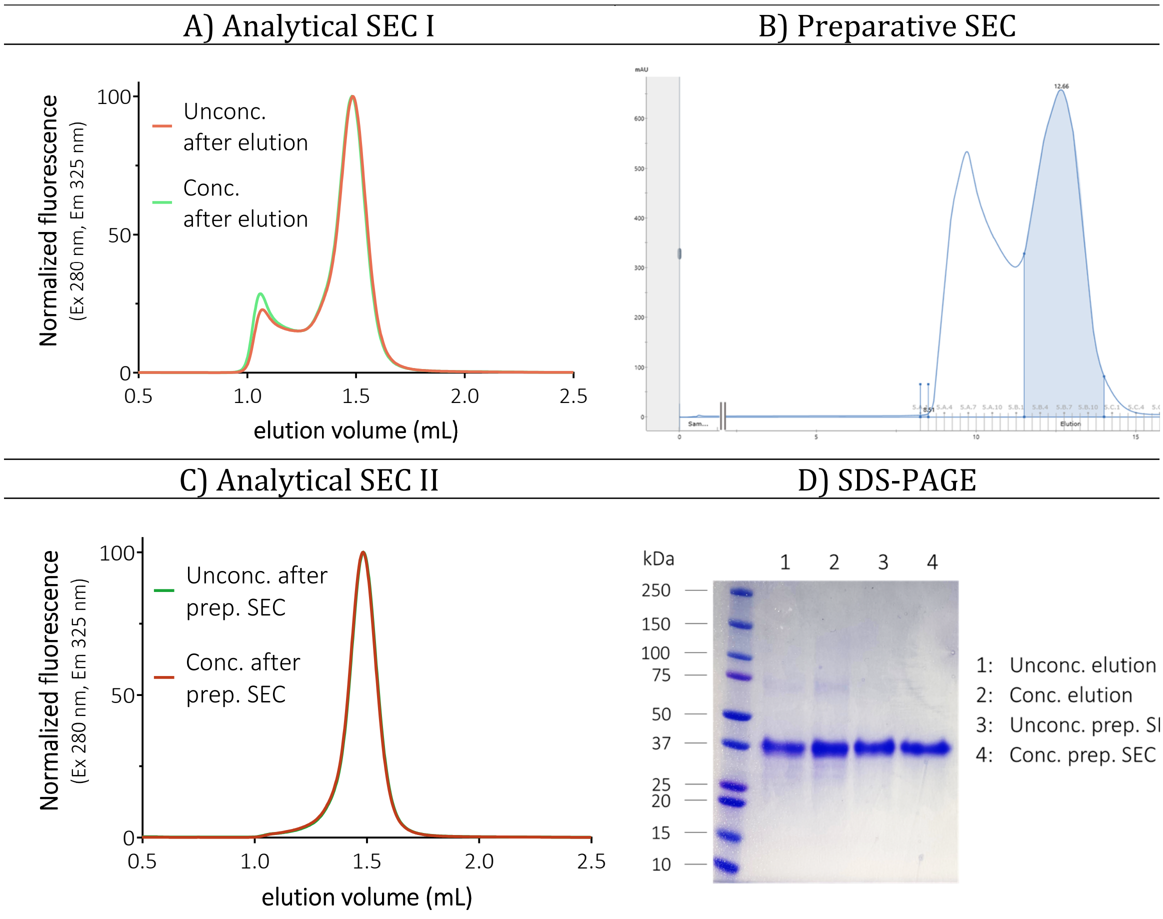

Figure 110. Protein analysis of TC196 in complex with PSB-21500 (LXP II). A) Region of interest of the SEC analysis of the (un-)conc. protein sample after elution (~ 1 µg of protein each). B) Region of interest of the prep. SEC result (blue: pooled fractions). C) Region of interest of the SEC analysis of the (un-)conc. pooled protein sample after the prep. SEC (~ 1 µg of protein each). D) SDS-PAGE results of the indicated samples (~ 5 µg of protein each).

The monodispersity of the eluted sample from this purification was achieved to the degree of the two TC190 purifications and, consequently, was much improved over the purification of TC196 presented in the section above. The chromatogram plotted in the course of the preparative SEC (see panel B) illustrates that a large amount of the eluted protein, which was 8.7 mg protein in total, had to be separated in order to remove all aggregates and to retrieve a homogenous protein sample. The homogeneity of the pooled sample was confirmed by a second analytical SEC, provided in panel C. Regarding the purity, the SDS-PAGE result attested a high purity of all analyzed protein samples without any impurities.

After the final purification and subsequent concentration of the sample, the 100 µL of protein solution was aliquoted and flash-frozen in 15 µL aliquots and individually thawed for crystallization experiments. The final protein concentration of the sample was 31 mg/mL (approximately 3.1 mg of total protein yield). The results of the crystallization with this second TC196 sample are detailed in section 3.15.5 as well. But first, the most important crystallizations performed with TC190 will be described.

3.15.4 Crystallizations of TC190 in complex with PSB-21500 at leadXpro

The first crystallization of construct TC190 at leadXpro was performed with the protein whose purification was detailed in section 3.15.2.1. Generally, the crystallization was performed similarly to those previously performed in Bonn. For this initial crystallization trial, the LCP was formed by mixing the protein solution with the lipid monoolein (MO, with 10 % cholesterol), and the 40 nL large LCP drops were covered with 800 nL of precipitant solution. The precipitant screens utilized for this crystallization were mostly commercial ones, e.g. PEG/Ion 400, but also three custom screens were utilized, which were based on previous crystal hits obtained in Bonn.

Considering the large number of crystallization experiments performed at leadXpro, the summary will only concentrate on the successful crystal hits. For this first crystallization trial, the most noteworthy crystal growth was observed in the LCP drop presented in the following Figure 111.

TC190 + PSB-21500 (LXP I)

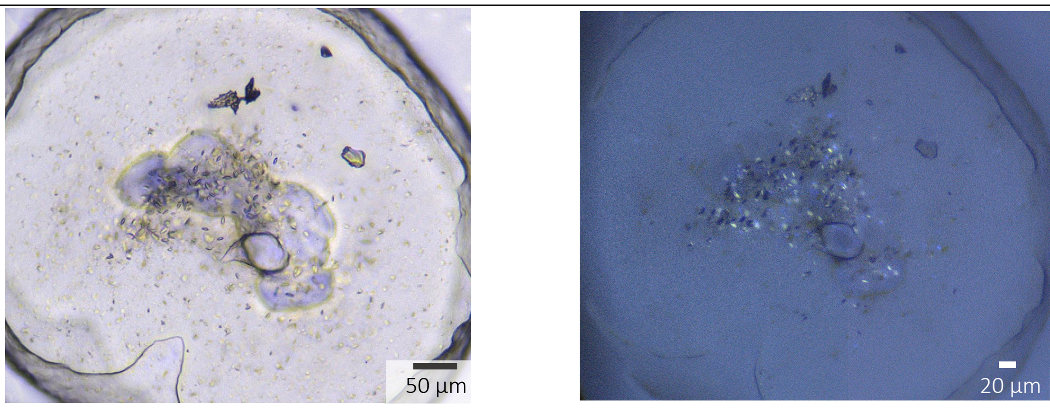

100 mM magnesium chloride hexahydrate,
100 mM tri-sodium citrate dihydrate pH 5.0,
40 % (v/v) PEG 200

Figure 111. Best crystals obtained in the first crystallization trial at leadXpro. Left: Picture of the LCP drop in visible light. Right: Picture of the same LCP drop in cross-polarized light for improved visibility of the crystals. Pictures were taken after 5 days.

The crystallization trials of construct TC190, optimized in Bonn, also yielded crystals in the laboratories of leadXpro in the first trial. One of the advantages of leadXpro's location at the PSI is the possibility of recurring beamtime at the Swiss Light Source synchrotron. Therefore, despite their small size, the crystals were harvested after 5 days and tested for their diffraction. Encouragingly, the measurement confirmed the protein nature of these crystals, which diffracted to up to 9 Å. This diffraction was already better than the diffraction observed for the crystals that were grown in Bonn.

Based on these results, fine screens of the utilized precipitant solution were designed in an attempt to improve crystal size and diffraction. In these fine screens, various concentrations of the salt magnesium chloride hexahydrate, ranging from 50 – 300 mM, various PEG 200 concentrations, ranging from 25 % – 44 %, and various buffers with pH values ranging from 4.2 – 8.0 were tested. They were employed in another crystallization experiment with TC190, however this time, with the second purified TC190 protein, that exhibited a higher monodispersity and slightly higher protein concentration, as detailed in section 3.15.2.2. Additionally, all commercial precipitant screens were tested once again. Figure 112 presents the noteworthy crystals of that subsequent crystallization trial with TC190.

TC190 + PSB-21500 (LXP II)

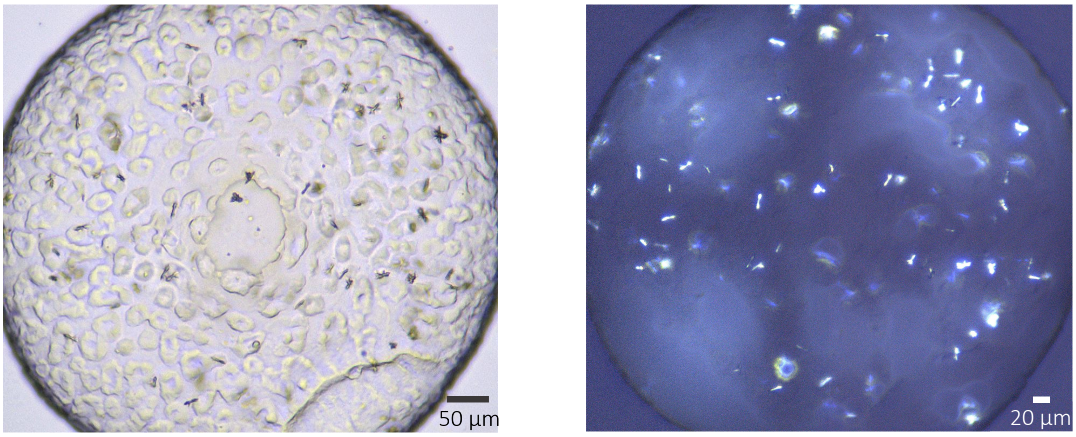

75 mM magnesium sulfate heptahydrate,
100 mM bicine pH 8.0
30 % (v/v) PEG 400

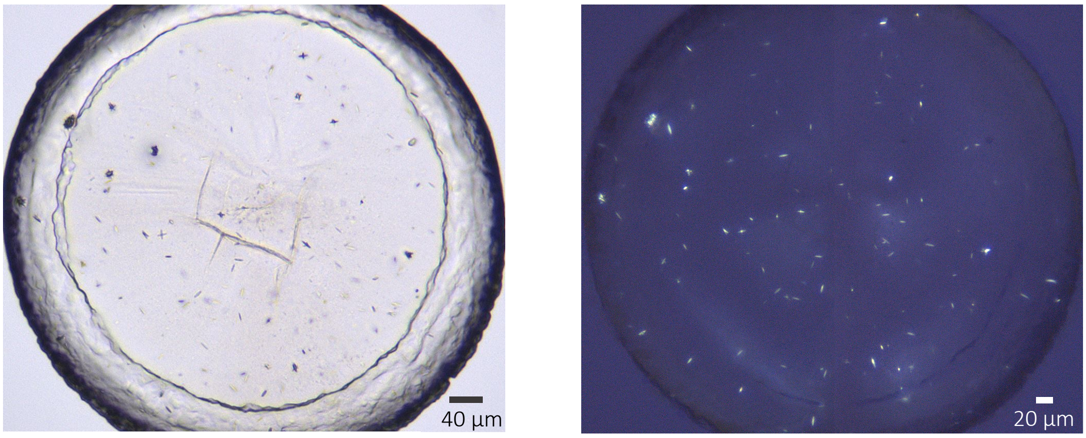

100 mM magnesium chloride hexahydrate,
100 mM Bis-Tris propane pH 7.0
30 % (v/v) PEG 200

Figure 112. Crystals obtained in one of the crystallization trials with TC190 performed at leadXpro. Left: Pictures of the LCP drops in visible light. Right: Picture of the same LCP drops in cross-polarized light for improved visibility of the crystals. Pictures were taken after 5 days.

As witnessed also for the crystal optimization attempts in Bonn, the fine screens were only moderately successful. The crystals depicted in the lower half of Figure 112 were among the only crystals that grew in one of the optimized precipitant screens. The crystals in the upper half of the figure were among the only crystals that resulted from this particular commercial screen. Generally, although crystal growth was observed in each trial, the number of crystal hits was lower compared to previous crystallization experiments of TC190 with PSB-21500 in Bonn. Nevertheless, these crystals were harvested after 7 days and subjected to X-ray diffraction measurement. However, none of the crystals yielded reflections that could be attributed to protein.

Since the initial crystal hits in the magnesium chloride hexahydrate-based condition (in Figure 111) exhibited a relatively strong diffraction, it was decided to pursue the optimization. Thus, several different additional fine screens of precipitant conditions were tested in a series of several crystallization experiments. The fine screens included e.g. additives at different concentrations, or addition of the utilized covalent antagonist PSB-21500, in case the antagonist was not yet bound to each protein at the time of the crystallization. Several other aspects were strategically changed for these crystallization trials as well, including the type of glass sandwich plate onto which the LCP drop and precipitant solutions are pipetted, the incubation temperature of the glass plates, as well as the volume of the LCP drops. Also, the first fine screens and commercial screens were tested once again. However, all these attempts did not result in any improved or even noteworthy crystal growth, despite the high protein concentration of the sample and its ideal monodispersity.

Yet, several weeks after the first fine-screening experiment was conducted, which also yielded the crystals presented in Figure 112, an extensive crystal growth was noticed in one of the LCP drops, covered with an initially optimized fine-screen condition. The upcoming Figure 113 displays those crystals.

TC190 + PSB-21500 (LXP II)

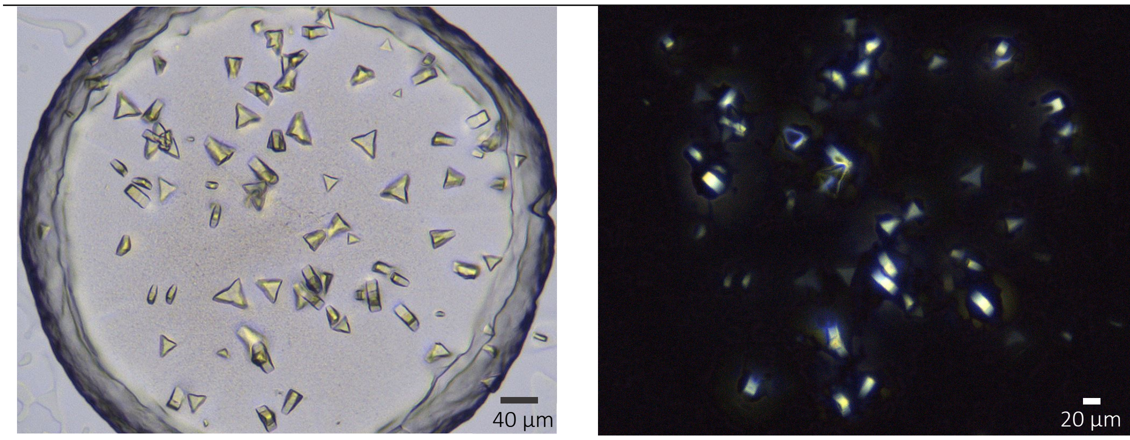

50 mM magnesium chloride hexahydrate,
100 mM tri-sodium citrate dihydrate pH 5.0,
30 % (v/v) PEG 200

Figure 113. Best crystals of TC190 in complex with PSB-21500 obtained at leadXpro. Left: Picture of the LCP drop in visible light. Right: Picture of the same LCP drop in cross-polarized light for improved visibility of the crystals. Pictures were taken after 28 days.

Upon discovery of these crystals, it was unsure whether they were protein or salt crystals, based on their high polarization and the fact that these crystals were the only ones in hundreds of LCP drops that exhibited such a large size (~ 35 µm), form and especially thickness (~ 10 µm). The crystals were harvested after six weeks of incubation at 20 °C and tested for their X-ray diffraction. Fortunately, these crystals were indeed protein crystals, yet unfortunately, they diffracted only up to 7 Å. Two examples of diffraction images are provided in Figure 114.

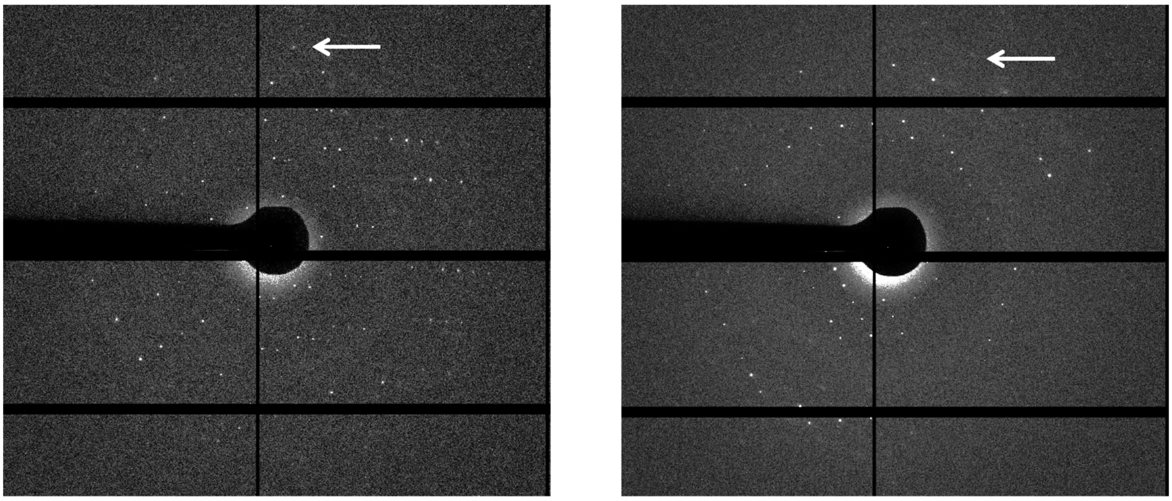

Figure 114. Diffraction images of protein diffraction observed from crystals presented in Figure 113.

Given their theoretically already suitable size for acquisition of high-resolution diffraction data and the meanwhile exhaustive optimization of magnesium chloride hexahydrate-based conditions without any success, it was concluded that the maximum potential of protein crystals obtained under these conditions had been reached. Therefore, the attention was redirected towards another promising crystal hit, which was achieved with the related protein TC196, as presented below.

3.15.5 Crystallizations of TC196 in complex with PSB-21500 at leadXpro

All the crystals of TC190 presented here, grew in LCP formed with the lipid mixture of MO and cholesterol. However, as outlined in the introduction (see section 1.7.6, page 42), the LCP can also be formed with other lipids, such as monopalmitolein (MP) and monovaccenin (MV).[237, 263] Both of these lipids were tested in crystallization experiments with TC196. For the initial evaluation of TC196's crystallization potential with these lipids, the commercially available precipitant screens were employed. As before, only the noteworthy crystal hits of TC196 will be presented and discussed.

Firstly, attention will be given to the crystals obtained with the partly aggregated protein from the purification TC196 + PSB-21500 (LXP II), in the LCP formed with MP. Figure 115 depicts the most interesting crystals from this trial.

TC196 + PSB-21500 (LXP I)	
A)	B)
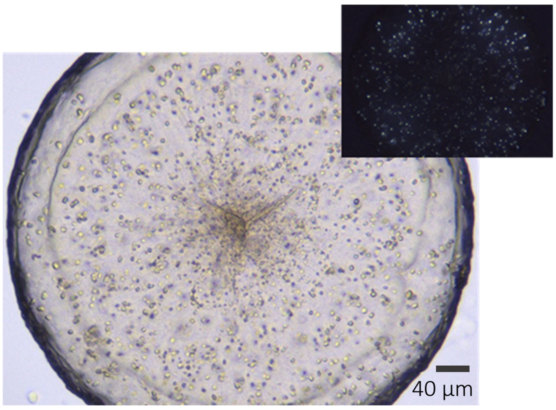	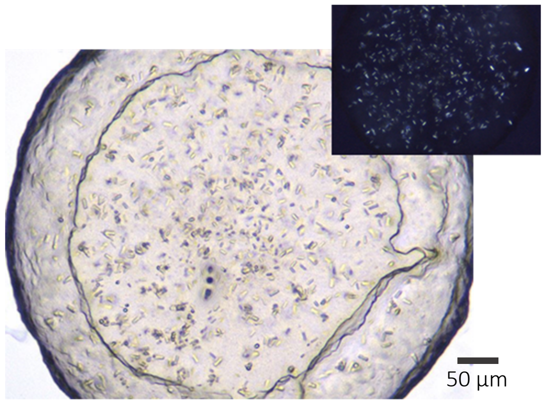
150 mM potassium sodium tartrate, 100 mM Bis-Tris propane pH 6.4, 27.5 % (v/v) PEG 400	10 mM sodium chloride, 100 mM sodium citrate tribasic dihydrate pH 5.0, 40 % (v/v) PEG 200
Diffraction up to 14 Å	Diffraction up to 11 Å
C)	D)
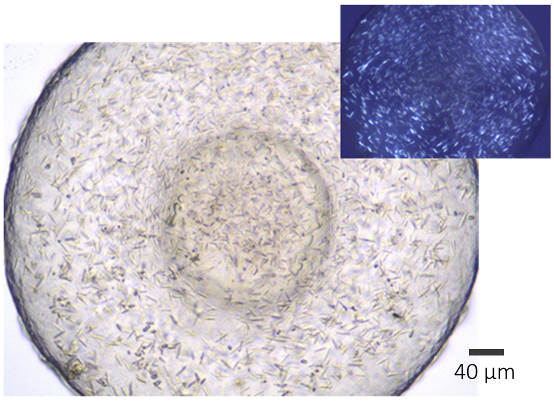	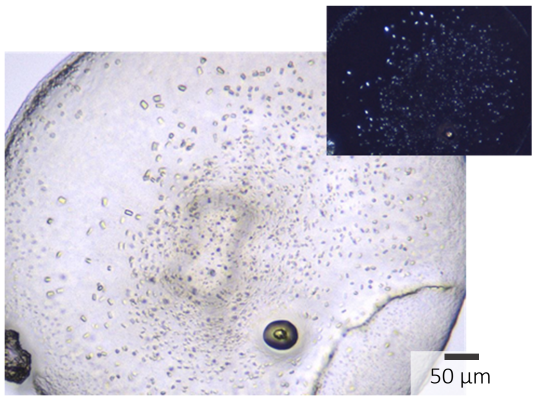
100 mM sodium citrate tribasic dihydrate pH 5.0, 30 % (v/v) PEG 300	400 mM di-sodium tartrate dihydrate, 30 % (v/v) PEG 400
Diffraction up to 16 Å	Diffraction up to 9 Å

Figure 115. Crystals obtained in one of the crystallization trials with TC196 in MP-based LCP performed at leadXpro. Pictures of the LCP drops in visible light, with pictures taken in cross-polarized light provided in the right upper corner. Pictures were taken after 5 – 14 days.

In comparison to a previous crystallization experiment of the same protein sample in LCP formed with MO that did not yield any noteworthy crystals, the protein was more prone to crystallize in the MP-based LCP. In this trial, crystals were observed under various conditions. Of those, the crystals from the four LCP drops presented in Figure 115 were selected for X-ray diffraction measurements. Despite their modest size, reflection spots were visible at a resolution of up to 9 Å for the crystals shown in panel D, and up to 11 Å for those depicted in panel C. Subsequently, fine-screens of precipitant solutions were designed based on these two conditions, and one that produced crystals in panel A of the above-stated figure, since it was similar to the one used for the crystals in panel D. They were utilized in several subsequent crystallization trials with TC196 (protein TC196 + PSB-21500 (LXP II)), but unfortunately, no notable crystal growth was observed.

However, the primary focus regarding the crystallization of TC196 was on crystals that grew in MV-based LCP. The first crystallization trial with MV-LCP was performed in parallel to the one presented above, also with the partly aggregated sample of TC196 (LXP I). As observed for MP, the MV-based LCP facilitated crystal growth in several wells, as illustrated in the upcoming Figure 116.

TC196 + PSB-21500 (LXP I)	
A)	B)
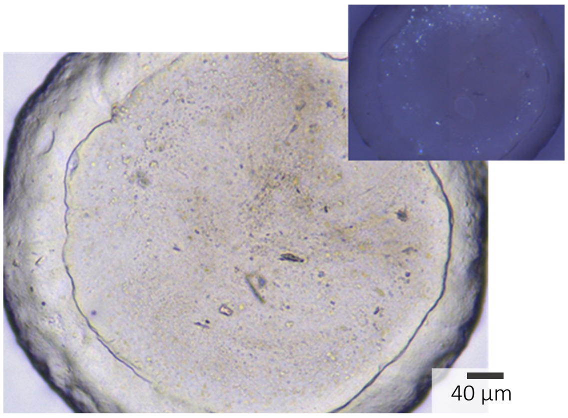	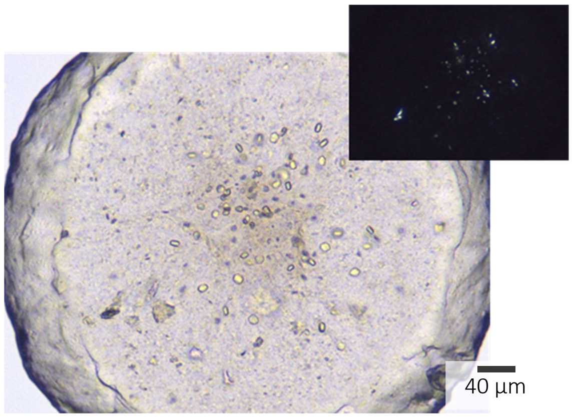
200 mM lithium sulfate, 100 mM sodium citrate tribasic dihydrate pH 5.0, 30 % (v/v) PEG 400	300 mM ammonium dihydrogen phosphate, 10 mM magnesium chloride hexahydrate, 100 mM sodium citrate tribasic dihydrate pH 4.5, 30 % (v/v) PEG 400
Diffraction not measured	Diffraction up to 6 Å
C)	D)
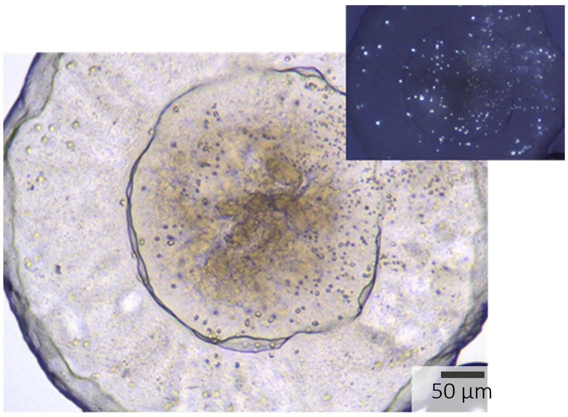	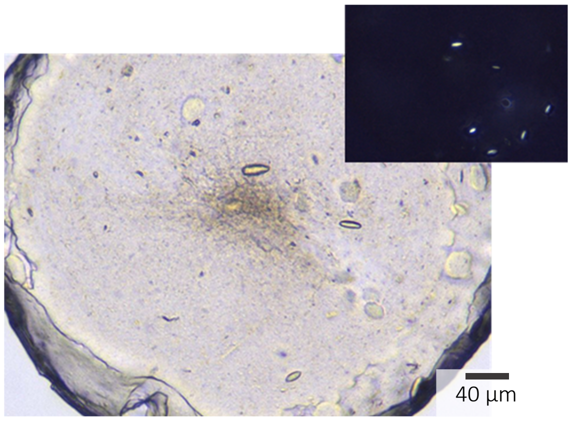
100 mM magnesium acetate tetrahydrate, 100 mM ADA pH 6.5, 39 % (v/v) PEG 400	150 mM potassium sodium tartrate, 100 mM Bis-Tris propane pH 6.4, 27.5 % (v/v) PEG 400
Diffraction up to 9 Å	Diffraction up to 8 Å

Figure 116. Crystals obtained in one of the crystallization trials with TC196 in MV-based LCP performed at leadXpro. Pictures of the LCP drops are provided in visible and cross-polarized light. Pictures were taken after 8 – 14 days.

Crystals from three of the four LCP drops presented before were tested for their X-ray diffraction at the Swiss Light Source. As annotated in the figure, the crystals grown in MV-based LCP diffracted similarly and even better than all other A_{2B}AR crystals up to this point, including the remarkably large crystals of TC190 discussed previously, which diffracted only to 7 Å. The best diffraction data was obtained from the 15 µm large crystals depicted in panel B of Figure 116, which diffracted up to 6 Å. Two diffraction images of the respective measurement are provided in Figure 117.

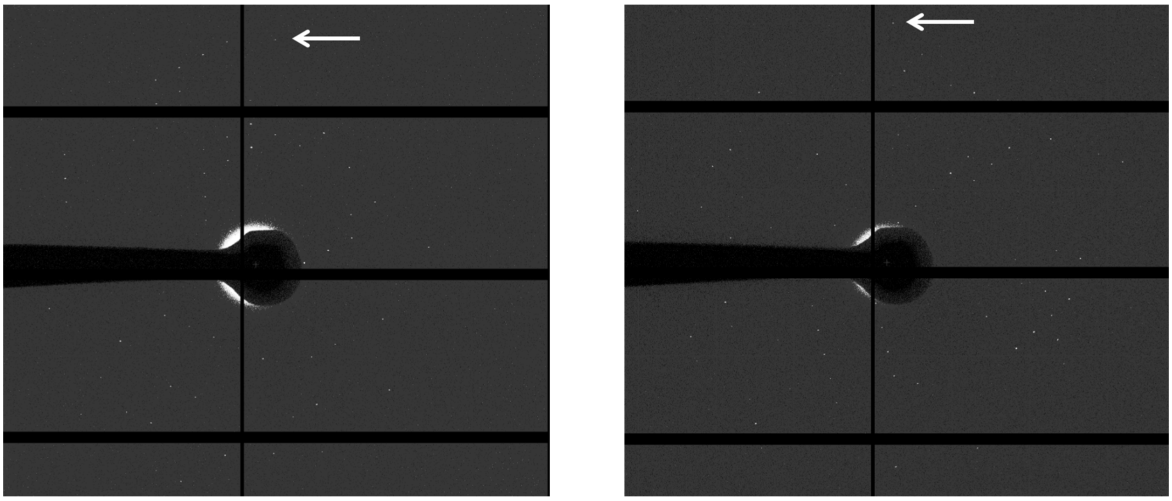

Figure 117. Diffraction images of protein diffraction observed from crystals presented in panel B of Figure 116

Based on the precipitant solution of these crystals, further fine screens were designed in an attempt to reproduce and improve the crystal size and diffraction quality. In these fine screens, either the ammonium dihydrogen phosphate concentration (100 – 500 mM), or the magnesium chloride hexahydrate concentration (0 – 100 mM) was varied alongside the PEG 400 concentration (25 – 40 % (v/v)). Later on, additional precipitant screens were employed in which different additives, buffers and PEGs were tested as well. In total, over 3000 LCP drops were covered in various precipitant solutions that were all based on the one that facilitated the growth of the crystals presented in panel B of Figure 116. For most of these crystallization trials, the protein TC196 + PSB-21500 (LXP II, detailed in section 3.15.3.2) was utilized, which displayed a significantly higher monodispersity compared to the protein which was used for the initial crystal hit.

Unfortunately, the reproducibility and especially the optimization of these crystals was very limited. This can partly be explained by the nature of the MV-based LCP which, by experience, demands a very high accuracy of the mixing ratio of the aqueous protein solution and the lipid in order to form a stable LCP. Considering the relatively low volumes of approximately 15 µL of protein solution which is worked with, it is technically challenging to fulfill the required accuracy when mixing the LCP, which is performed by hand using two glass Hamilton-syringes. For that reason, phase shifts of the MV-based LCP were often observed, resulting in mesophases which were highly birefringent under cross-polarized light. In these phases, crystals are less likely to grow and if they grow, they are more difficult to detect and harvest.[231] The following Figure 118 illustrates some of the better visible protein crystals that were grown in a MV-LCP and tested for their diffraction.

TC196 + PSB-21500 (LXP II)	
A)	B)
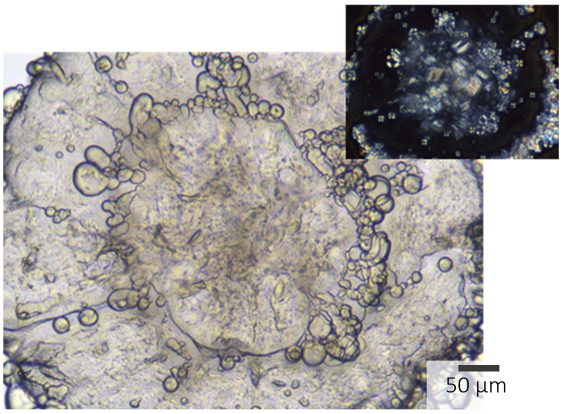	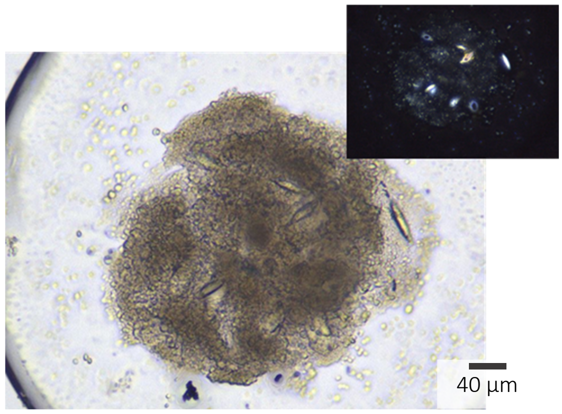
350 mM ammonium dihydrogen phosphate, 25 mM magnesium chloride hexahydrate, 100 mM Tris-HCl pH 7.5, 32 % (v/v) PEG 400	350 mM ammonium dihydrogen phosphate, 25 mM magnesium chloride hexahydrate, 100 mM Bis-Tris propane pH 6.5, 38 % (v/v) PEG 400
Diffraction up to 9 Å	Diffraction up to 9 Å
C)	D)
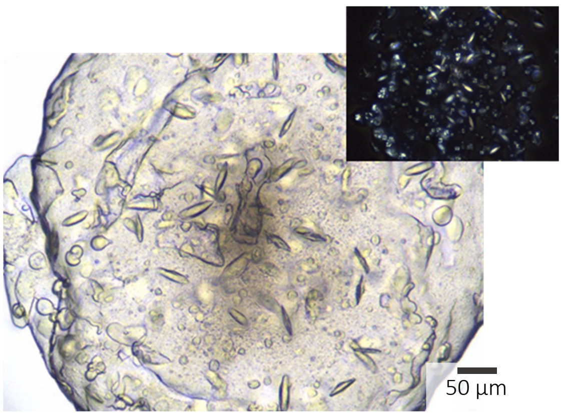	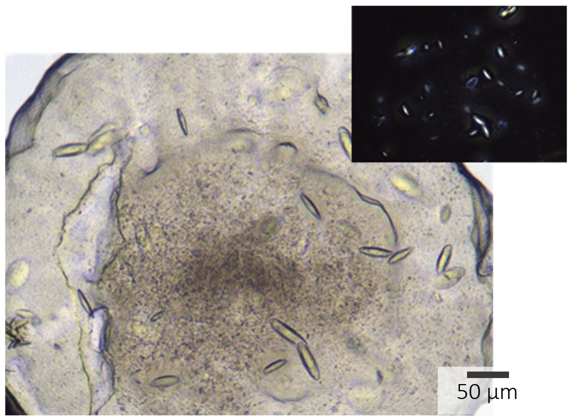
350 mM ammonium dihydrogen phosphate, 25 mM magnesium chloride hexahydrate, 100 mM Tricine-HCl pH 7.5, 32 % (v/v) PEG 400	350 mM ammonium dihydrogen phosphate, 25 mM magnesium chloride hexahydrate, 100 mM Tris-HCl pH 7.5, 34 % (v/v) PEG 400
Diffraction up to 7 Å	Diffraction up to 9 Å

Figure 118. Crystals obtained in further crystallization trials with TC196 in MV-based LCP performed at leadXpro. Pictures of the LCP drops are provided in visible and cross-polarized light. Pictures were taken after 5 – 8 days.

With their size of up to 50 µm, these crystals were among the largest A_{2B}AR crystals obtained. Also, they were grown in MV-based LCP, which previously seemed superior, and in the presence of similar precipitant solutions to the ones that yielded the best diffracting crystals up to that point. Yet, none of these crystals, neither of these crystallization trials nor any others, exceeded the diffraction quality of the 15 µm large crystals presented in panel B of Figure 116.

3.15.6 Conclusion of the research stay at leadXpro

Throughout the six-month research visit in Switzerland, 20 crystallization trials using 10 distinct protein samples were conducted, and only a small subset is presented here. Numerous crystal hits were observed and several of the most promising hits were selected for extensive optimization, during which a multitude of aspects were modified, from the lipids used to form the LCP, to the protein detergent, precipitant solution, incubation temperatures, glass plates, presence of ligand and LCP drop volume. However, in all cases, the reproducibility and optimization of the crystals was challenging, which was in line with the previous experiences from our laboratory in Bonn.

While some crystals reached sizes theoretically suitable for collecting high-resolution diffraction data, their diffraction did not surpass 6 Å, rendering them inadequate for solving even a low-resolution crystal structure of the A_{2B}AR.

Therefore, it became apparent that most likely the packing of the A_{2B}AR molecules within the crystals was the limiting factor for the quality of the crystals. For that reason, it was decided to once again reevaluate the different fusion partners, since these partners strongly co-determine the crystal packing.[106, 305]

3.16 Fusion partner screening based on TC190

As noted at the very beginning of the Results and Discussion chapter, on page 48, all available fusion partners were applied to both the ICL3 and the *N*-terminus of the receptor in the early stages of this project as part of my master's thesis. At that time, bRIL inserted between L213$^{5.69}$ and H221$^{6.22}$ near the ICL3 resulted in the most monodisperse sample among all of the tested constructs.[252] Consequently, it was chosen as the standard fusion partner. Earlier in this doctoral thesis, the exact insertion position of bRIL in the ICL3, as well as the fusions with the T4 lysozyme fragment in the ICL3 and *N*-terminally were reconsidered and analyzed with a more stable $A_{2B}AR$ construct (see section 3.7, page 89). Still, the bRIL fusion between $L213^{5.69}$ and $H221^{6.22}$ provided the highest monodispersity of the protein. It is important to mention that, when all fusion partners were initially applied to the ICL3, the same insertion site was used for each fusion partner. In hindsight, this approach is not ideal as the distance between the ends of each fusion partner varies.[106] Therefore, the insertion position of each fusion partner must be carefully adjusted. For the reevaluation of fusion partners based on construct TC190, which will be presented below, the ideal insertion positions were determined with support by leadXpro. $A_{2B}AR$-fusion protein constructs were modeled using AlphaFold[203] to assess the insertion positions, as described in literature.[306–308] The crucial criterion for the evaluation of these models was whether the helices of TM5 and/or TM6 of the $A_{2B}AR$ seamlessly extended to the α-helical structures on (one of) the *N*-/*C*-terminal ends of the fusion partners, to form a favorable rigid end-to-end fusion.[307, 309]

Based on these considerations, the following refined constructs were designed, presented in Table 6:

Table 6. Overview of refined constructs based on TC190 with different fusion proteins.

Construct	Fusion partner	Insertion position
TC226	*Pyrococcus abysii* glycogen synthase (PGS)	Between 5.69 and 6.25
TC227	Optimized variant 1 of bRIL (OB1)	Between 5.69 and 6.22
TC228	bRIL	Between 5.69 and 6.21
TC229	*Desulfovibrio vulgaris* flavodoxin	Between 5.68 and 6.27
TC230	T4L	Between 5.68 and 6.24
TC231	Undisclosed fusion protein 1 from leadXpro (LXP-FP1)	Between 5.70 and 6.25
TC232	Undisclosed fusion protein 1 from leadXpro (LXP-FP1)	Between 5.73 and 6.25
TC233	Undisclosed fusion protein 2 from leadXpro (LXP-FP2)	Between 5.69 and 6.24

The amino acid sequence of each fusion partner is provided in section 7.2 of the appendix.

In addition to these constructs featuring different fusion proteins, three constructs were designed displaying gradual truncation of the ECL2. This was driven by observations, that e.g. in case of the closely related $A_{2A}AR$, the well-structured ECL2 formed crystal contacts with the fusion partner of another receptor molecule (e.g. PDB ID 4EIY).[65] In the $A_{2B}AR$, the ECL2 is longer,[52] and potentially less rigid, which might interfere with the formation of crystal contacts between the molecules. Therefore, despite the significant role of the ECL2 in ligand affinity and selectivity for the $A_{2A}AR$ versus the and $A_{2B}AR$,[92] these variations were considered and their AlphaFold models were evaluated. As for the $A_{2A}AR$, the ECL2 of the $A_{2B}AR$ was predicted to form a small α-helical domain attached to the extracellular tips of TM4 and TM5 by unstructured amino acid sequences, and a disulfide bridge between $C154^{ECL2}$ and $C166^{ECL2}$ of the ECL2. For the constructs TC223 – TC 225, the long, unstructured loop which is confined by the disulfide bridge was truncated by six, eight and ten amino acids, respectively, as detailed in Table 7.

Table 7. Exact truncation positions of TC223 – TC225.

Construct	ECL2 truncation
TC223	$W158^{ECL2}$ to $N163^{ECL2}$
TC224	$P157^{ECL2}$ to $E164^{ECL2}$
TC225	$W156^{ECL2}$ to $S165^{ECL2}$

Figure 119 depicts the AlphaFold models of the ECL2 of TC190 (untruncated), TC233, TC224 and TC225, and their comparison with the ECL2 of the $A_{2A}AR$ (in red) forming crystal contacts with the bRIL fusion protein (in orange) of another $A_{2A}AR$ molecule.

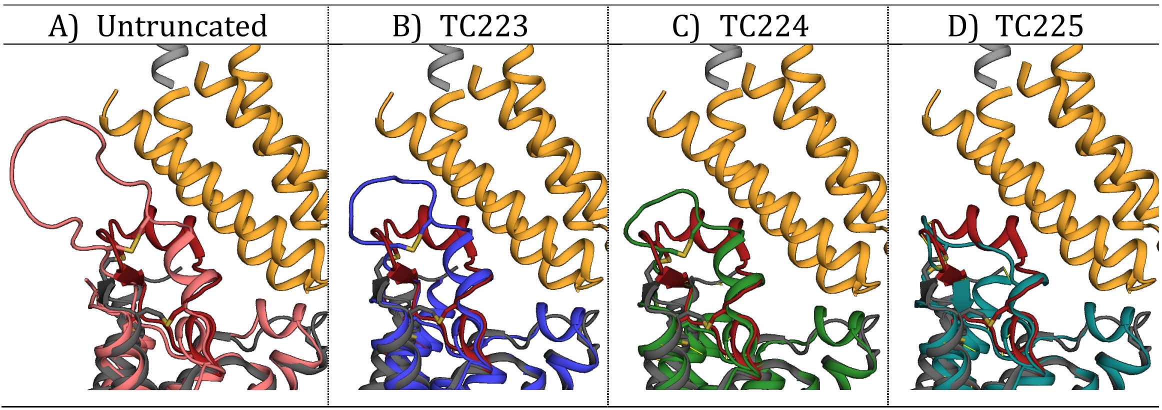

Figure 119. Inspection of the crystal contacts between A_{2A}AR's ECL2 with the bRIL fusion protein of another A_{2A}AR molecule. Red: A_{2A}AR molecule 1, orange: A_{2A}AR molecule 2 (PDB-ID 4EIY)[65]. For comparison, the modeled ECL2 of constructs TC190 (in pink), TC223 (in blue), TC224 (in green) and TC225 (in turquoise) are overlaid with the A_{2A}AR structure.

Considering the large and presumably unstructured region in the native ECL2 of the A_{2B}AR (see pink structure in panel A above), it seems plausible that the ECL2 could potentially compromise the ordered crystal packing of the receptor. When designing the ECL2 variants, we ensured that the predicted disulfide bridge would still be formed, as indicated by the AlphaFold model (see panels B to D).

With the anticipation that these 11 constructs might improve the size and diffraction quality of the crystals without requiring extensive fine-screening efforts, all of the refined constructs were subjected to crystallization trials.

To address the potentially insufficient protein concentration in the previous crystallization trials performed in Bonn, it was decided to purify each of the constructs from 2 L of *Sf*9 cell biomass, in contrast to the previous volumes of 450 or 900 mL. For improved reproducibility, the target concentration for each construct was aimed at 30 mg/mL, determined by measuring the absorbance at 280 nm with a microvolume spectrophotometer. To prevent potential destabilization of the proteins[310] during the three-day purification and crystallization process, and to mitigate any potential negative impact of imidazole during crystallization,[296, 297] a salt exchange (S.E.) was carried out after each protein elution step. This procedure allowed for the removal of the imidazole and, additionally, allowed for a reduction in detergent concentration (by 2/5th, for most of the purifications). Otherwise, the detergent could accumulate upon concentration of the protein,[311] which could impede the crystallization of the GPCR in LCP.[312, 313] The covalent antagonist PSB-21500, which was extensively utilized in the previous crystallization experiments, was employed for all crystallizations involving the refined constructs.

The following sections present and discuss the results of the crystallization trials in the order in which the experiments were performed. Since two purifications and crystallizations were consistently conducted in parallel, and each round of experiments showed distinct characteristics that influenced the next purifications, simultaneous discussion of the results is useful. Unfortunately, this order did not coincide with the chronological order of the constructs, due to the lack of all respective DNAs in the beginning of this crystallization series. For clarity, each of the following sections will include a schematic representation illustrating the basic architecture of the corresponding constructs.

3.16.1 Crystallization of TC223 and TC226 in complex with PSB-21500 (I)

The first purifications of the series that were conducted, were the ones of TC223 and TC226. In contrast to the subsequent purifications that will be presented hereafter, this purification was performed in the course of just two instead of three days, in an effort to minimize stress on the protein. To achieve this, the solubilization lasted only 90 min, instead of the usual 3 h, and the incubation with the Co^{2+} beads was reduced to 2 h instead of overnight. The other steps of the purification were performed according to the standard protocol, provided in section 5.2.3 on page 243 ff. For the crystallizations, only commercial precipitant screens, namely PEG/Ion 400, JBScreen LCP and MemMeso and MemGoldMeso (later two from Molecular Dimensions), were utilized.

The results of the purifications and crystallizations for TC223 and TC226 are presented in the following Figure 120 and Figure 121.

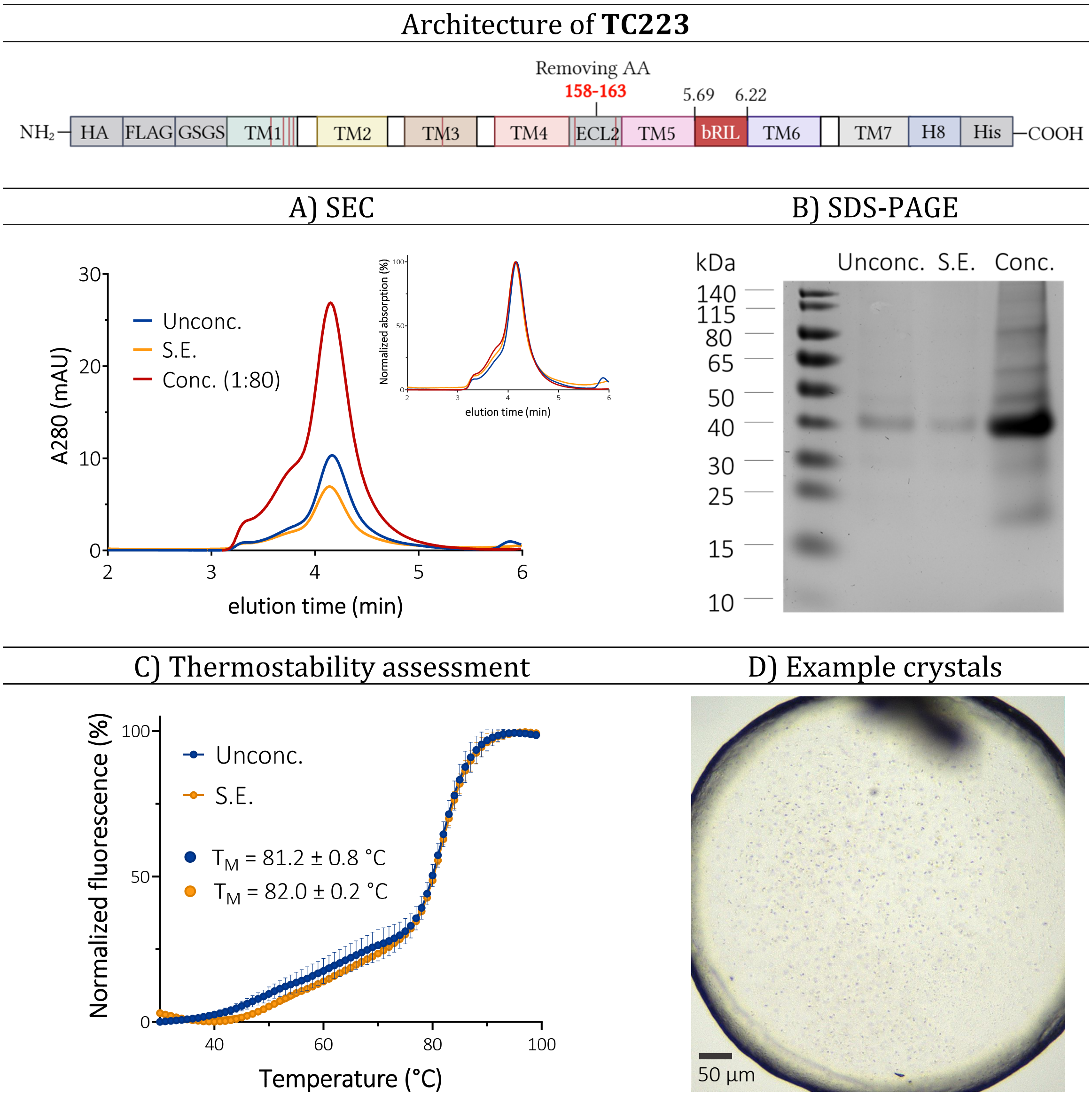

Figure 120. Protein analysis and crystallization of TC223 in complex with PSB-21500 (I). A) Region of interest of the SEC analysis of the protein samples (normalized results in the top right corner). B) SDS-PAGE of the unconc., S.E. and conc. samples, 10 µL each (conc. ~ 1:100 diluted). C) Thermostability assessment of the unconc. and S.E. samples. Nonlinear fit (biphasic) of normalized fluorescence data. The T_M was calculated as the mean ± SD of the later inflection point (n=3). D) Exemplary LCP drop from the crystallization experiment.

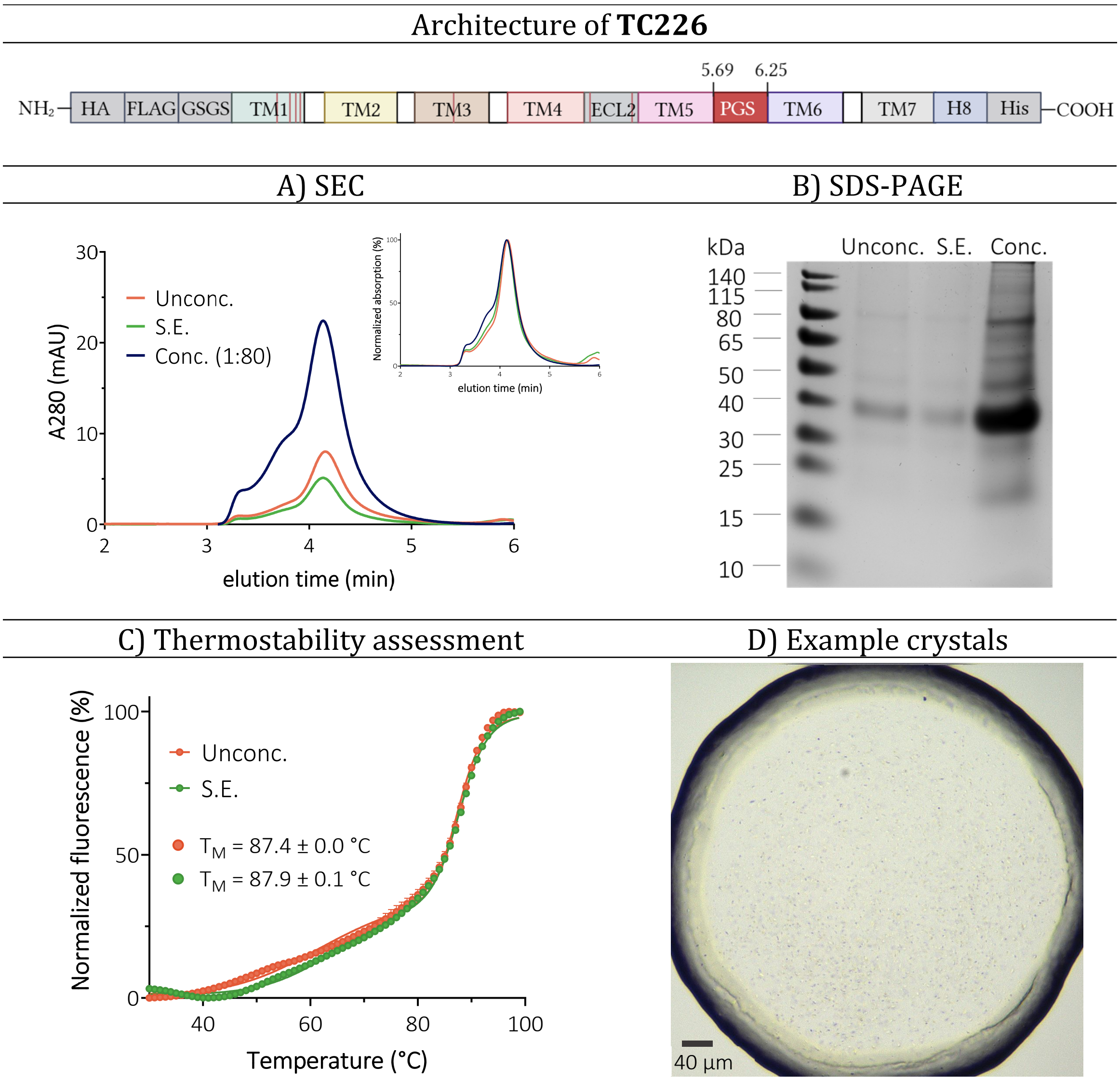

Figure 121. Protein analysis and crystallization of TC226 in complex with PSB-21500 (I). A) Region of interest of the SEC analysis of the protein samples (normalized results in the top right corner). B) SDS-PAGE of the unconc., S.E. and conc. samples, 10 µL each (conc. ~ 1:100 diluted). C) Thermostability assessment of the unconc. and S.E. samples. Nonlinear fit (biphasic) of normalized fluorescence data. The T_M was calculated as the mean ± SD of the later inflection point (n=3). D) Exemplary LCP drop from the crystallization experiment.

As evident from panel D of each figure, both TC223 and TC226 yielded some minor crystal growth, which, however, did not surpass the crystals previously observed for TC190 in terms of quantity and quality. Potentially, the protein sample was not sufficiently pure, which most likely was caused by the lack of a small concentration of imidazole (typically 20 mM) during Co^{2+} resin incubation. Additionally, the protein amount obtained from these purifications fell short of the expectations, with a final concentration of approximately 10 mg/mL each, as measured by the spectrophotometer (A280 nm) considering the proteins' calculated extinction coefficient (according to Expasy's ProtParam tool).[314] This lower protein quantity, despite the 2 L of biomass that was utilized for the purification, could be attributed to two reasons:

i. The modifications on the constructs, here the truncation of the ECL2 by six amino acids (TC223) and the utilization of the PGS fusion protein (TC226), and
ii. the short solubilization time of 90 min and/or the short incubation time with the Co^{2+} resin of just 2h.

Based on experience, GPCRs fused to PGS typically show lower expression, compared to analogous constructs with different fusion partners. Concerning the second aspect, during my research stay, the resin incubation typically lasted for 2 – 3 h as well, however, with a bead volume approximately four times higher than that used for this purification (6 mL vs. 1.5 mL). Although both, 6 mL and 1.5 mL of the Co^{2+} resin, which has a binding capacity of 10 – 15 mg of protein/mL, theoretically should have more than enough capacity to bind all of the expressed protein,[278] the reduction apparently significantly decreased the amount of captured recombinant protein. Using a large amount of resin results in challenges, such as the need for a high elution volume (e.g. 18 mL for 6 mL of resin), unless the elution can be performed with an FPLC system. This high elution volume could lead to subsequent issues like detergent accumulation during the protein concentration (concentration factors up to 1000-fold), which could potentially affect LCP formation and consequently the crystallization experiment as a whole.

To overcome this limitation, it was decided to extend the duration of the subsequent purifications by an extra day, to allow for an elongated solubilization of 3 h and an overnight incubation with Co^{2+} resin, as done for all the previous large-scale purifications in Bonn. On the second day, the protein only underwent the washing and elution from the beads and the salt exchange, before it was approximately 10-fold concentrated and stored on ice in the cold room at 4 °C. Another benefit of the three-day purification was, that the time-consuming protein concentration (up to 6 h with resuspension every 10 min) and the crucial crystallization could be carried out during more manageable working hours.

Another contributing factor for the less abundant crystallization events, observed for TC223 and especially TC226, may have been the declined monodispersity of the constructs compared to the previous crystallizations with constructs TC190 or TC196. However, as seen before and will be observed again in the following crystallization trials, increased aggregation does not necessarily impede the formation of protein crystals. Also, this earlier-eluting protein peak could potentially have been caused not only by aggregated $A_{2B}AR$ but also by some of the impurities observed for these two samples. In order to properly evaluate the crystallization potential of TC223 and TC226, both samples were purified once again at the end of this crystallization series, with improved purity as well as higher protein concentration (see section 3.16.6 and 3.16.7). Generally, however, the purpose of these refined constructs was to identify an $A_{2B}AR$ construct, that readily improves the crystals' characteristics, without time-consuming optimization and repetition of the experiments. Therefore, small crystal hits presented here and hereafter were not further optimized in the course of this thesis, since all of the subsequent crystallizations were performed in the final weeks of this doctoral project.

3.16.2 Crystallization of TC231 and TC233 in complex with PSB-21500

The purification of TC231 and TC233 were performed as discussed in section 3.16.1 above, in the course of three days, with elongated solubilization and resin incubation time. As before, the crystallization was conducted using the four commercial screens PEG/Ion 400, JBScreen LCP, MemMeso and MemGoldMeso.

The results of the purification and crystallization of TC231 and TC233 are illustrated in the following Figure 122 and Figure 123.

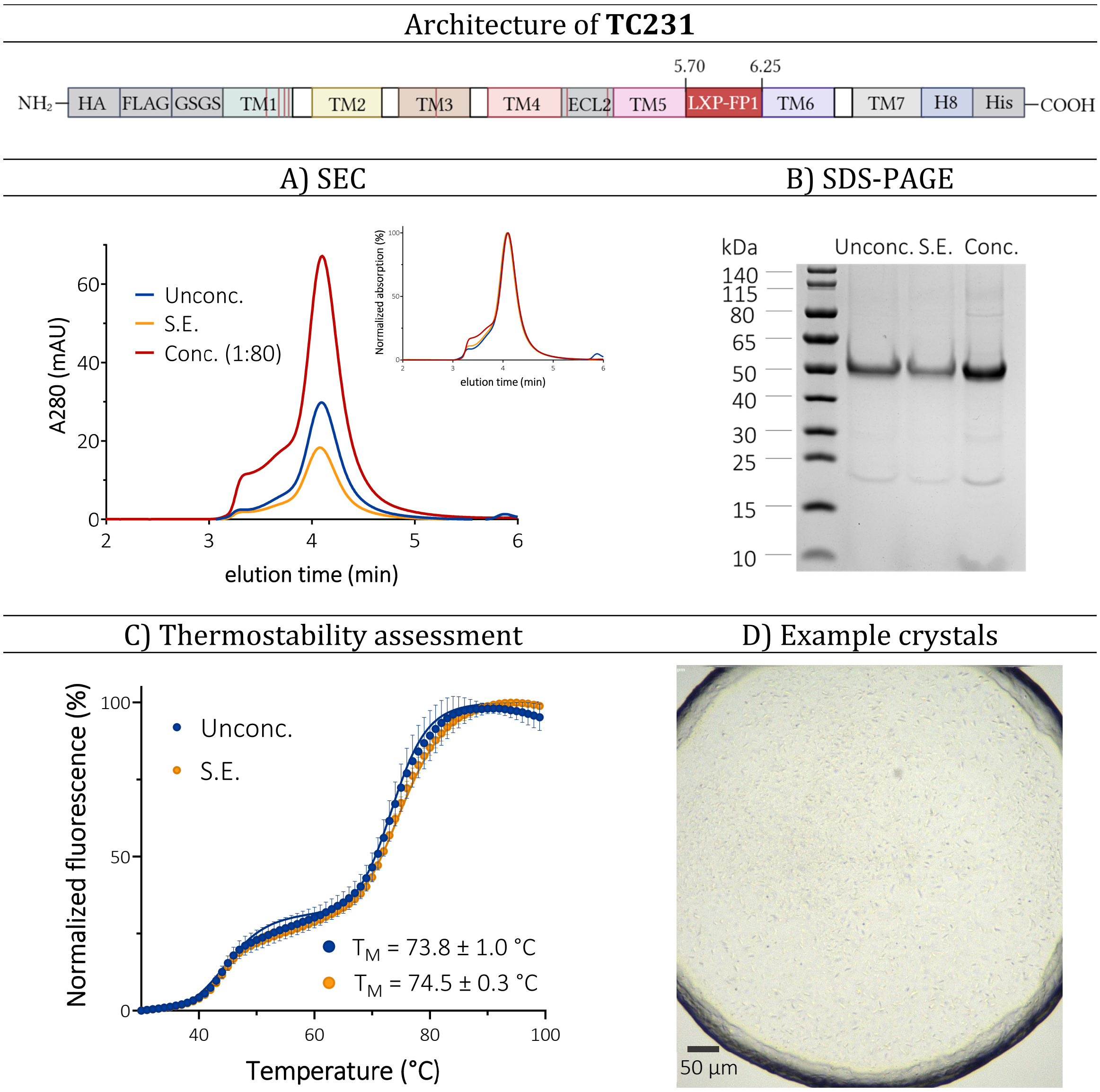

Figure 122. Protein analysis and crystallization of TC231 in complex with PSB-21500. A) Region of interest of the SEC analysis of the protein samples (normalized results in the top right corner). B) SDS-PAGE of the unconc., S.E. and conc. samples, 10 µL each (conc. ~ 1:100 diluted). C) Thermostability assessment of the unconc. and S.E. samples. Nonlinear fit (biphasic) of normalized fluorescence data. The T_M was calculated as the mean ± SD of the later inflection point (n=3). D) Exemplary LCP drop from the crystallization experiment.

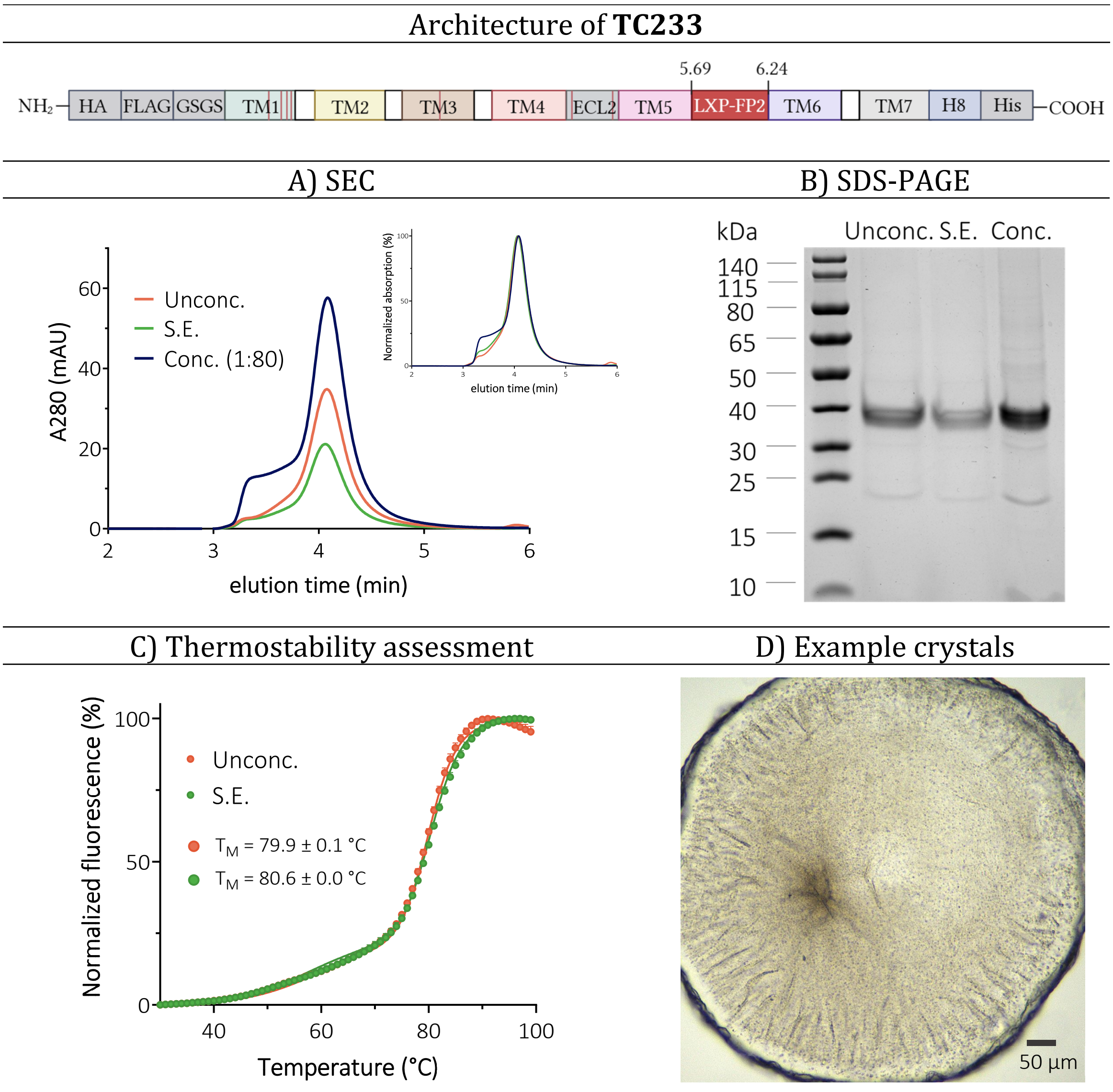

Figure 123. Protein analysis and crystallization of TC233 in complex with PSB-21500. A) Region of interest of the SEC analysis of the protein samples (normalized results in the top right corner). B) SDS-PAGE of the unconc., S.E. and conc. samples, 10 µL each (conc. ~ 1:100 diluted). C) Thermostability assessment of the unconc. and S.E. samples. Nonlinear fit (biphasic) of normalized fluorescence data. The T_M was calculated as the mean ± SD of the later inflection point (n=3). D) Exemplary LCP drop from the crystallization experiment.

The purification of the $A_{2B}AR$ constructs featuring the two undisclosed fusion proteins from leadXpro was more successful. The impurities, which were observed in the previous two purifications, were significantly reduced to a point where essentially only one unintended protein band around approximately 25 kDa was visible in the SDS-PAGE. Furthermore, both the monodispersity and protein concentration, as indicated by the SEC results, were improved for these two constructs. The measured protein concentration, as determined by the spectrophotometer (A280 nm), was approximately 25 mg/mL for both constructs, when the minimal sample volume (limited by the dead stop volume of the concentrators) was reached. Therefore, it fell slightly short of the aimed concentration of 30 mg/mL, but was still an improvement over the previous two purifications. The only downside in the proteins' characteristics was that, especially for TC231, the lower thermostability of ~ 74 °C, was worse compared to all other previously purified constructs in complex with PSB-21500. It seems that this particular fusion protein did not have a thermostabilizing effect on the receptor. Moreover, the protein concentration after an additional elution step was determined, which revealed that the protein still eluted beyond the typical three column volumes (CV) of elution buffer. This required additional elution and salt exchange steps, which is suboptimal regarding the potential accumulation of detergents due to the increased sample volume, as discussed earlier. For the subsequent purifications, the imidazole concentration was therefore increased from 220 mM to 300 mM.

As indicated in the panels D of Figure 122 and Figure 123, both fusion proteins still facilitated the crystal growth of the $A_{2B}AR$, with TC231 exhibiting more substantial crystal growth compared to the more thermostable TC233. However, in both cases, the crystals neither grew in the presence of many different precipitant solutions, nor did they exhibit a larger size that would be promising for a successful structure determination. The largest crystals observed in these two crystallizations were from TC231, which grew in the presence of 75 mM sodium chloride, 130 mM magnesium chloride, 32 % (v/v) PEG 400 and 100 mM tri-sodium citrate dihydrate at pH 4.5. They grew around 20 µm in length, but displayed weak growth in the other two dimensions (depicted in Figure 124 below).

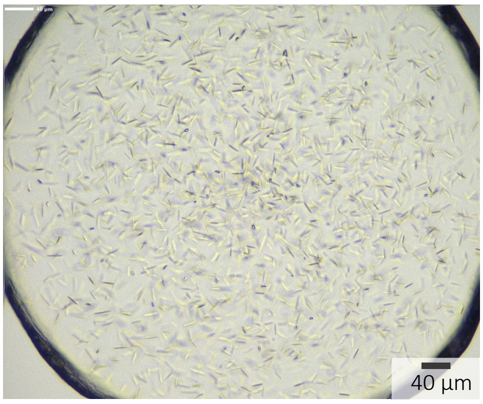

Figure 124. Best crystals obtained from the crystallization of TC231.

The crystals presented here in Figure 124 were sent to our cooperation partner leadXpro at the PSI, to test these crystals for their diffraction. In the measurement, the crystals indeed showed protein diffraction, but only up to 18 Å.

In conclusion, the constructs TC231 and TC233 did not result in the anticipated extensive crystal growth and diffraction quality, despite the almost optimal conditions of purity, monodispersity, protein concentration and thermostability. On a more positive note, however, the changes in the purification procedure proved mostly successful and required only smaller modifications for the next purifications.

3.16.3 Crystallization of TC224 and TC225 in complex with PSB-21500

The next purifications were performed on the constructs TC224 and TC225. As illustrated by the scheme in the top of each figure, both of these constructs featured a modified ELC2, truncated by 8 and 10 amino acids, respectively. The outcomes of their purification and crystallization are summarized in the upcoming Figure 125 and Figure 126.

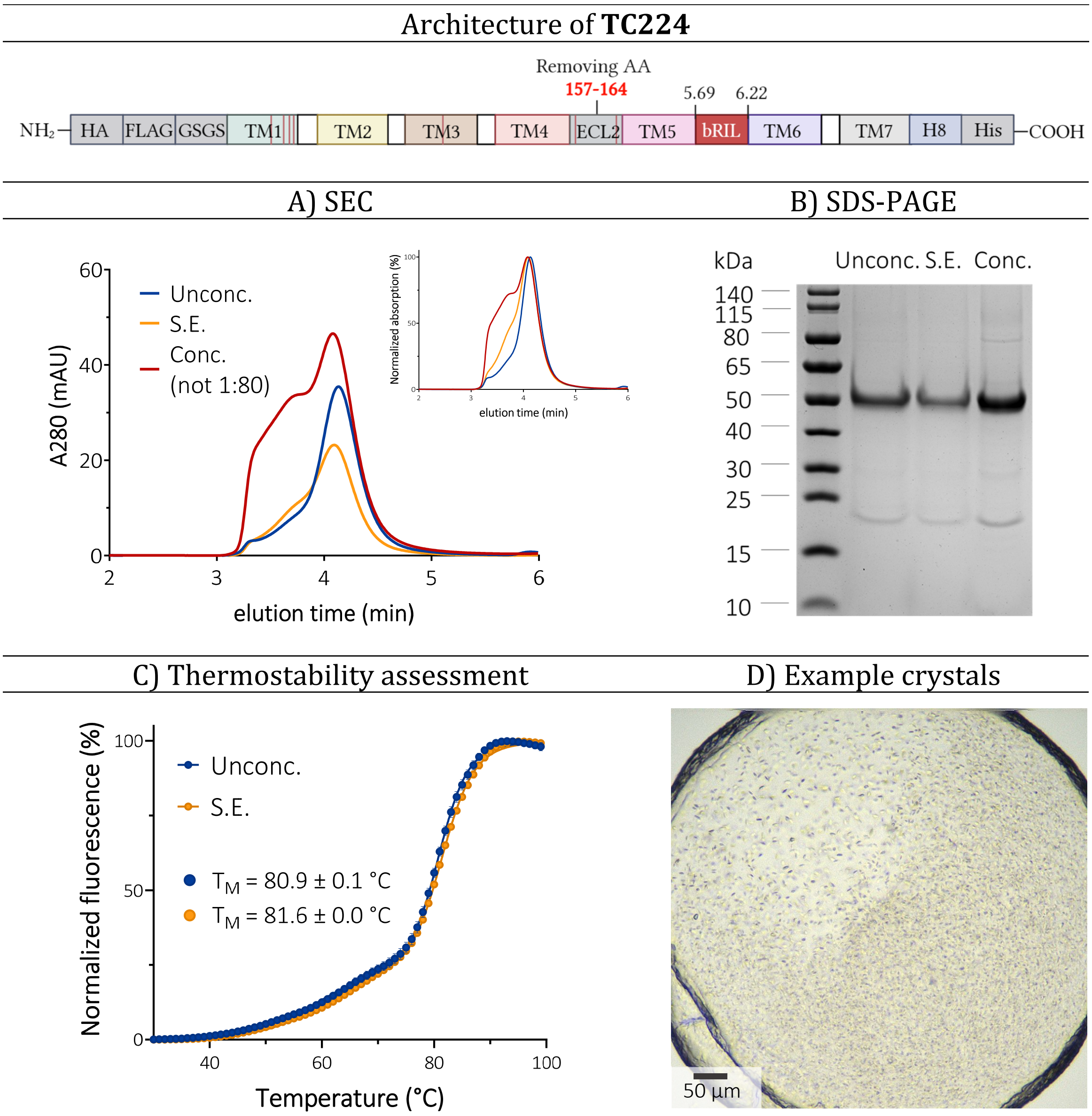

Figure 125. Protein analysis and crystallization of TC224 in complex with PSB-21500. A) Region of interest of the SEC analysis of the protein samples (normalized results in the top right corner). B) SDS-PAGE of the unconc., S.E. and conc. samples, 10 µL each (conc. ~ 1:100 diluted). C) Thermostability assessment of the unconc. and S.E. samples. Nonlinear fit (biphasic) of normalized fluorescence data. The T_M was calculated as the mean ± SD of the later inflection point (n=3). D) Exemplary LCP drop from the crystallization experiment.

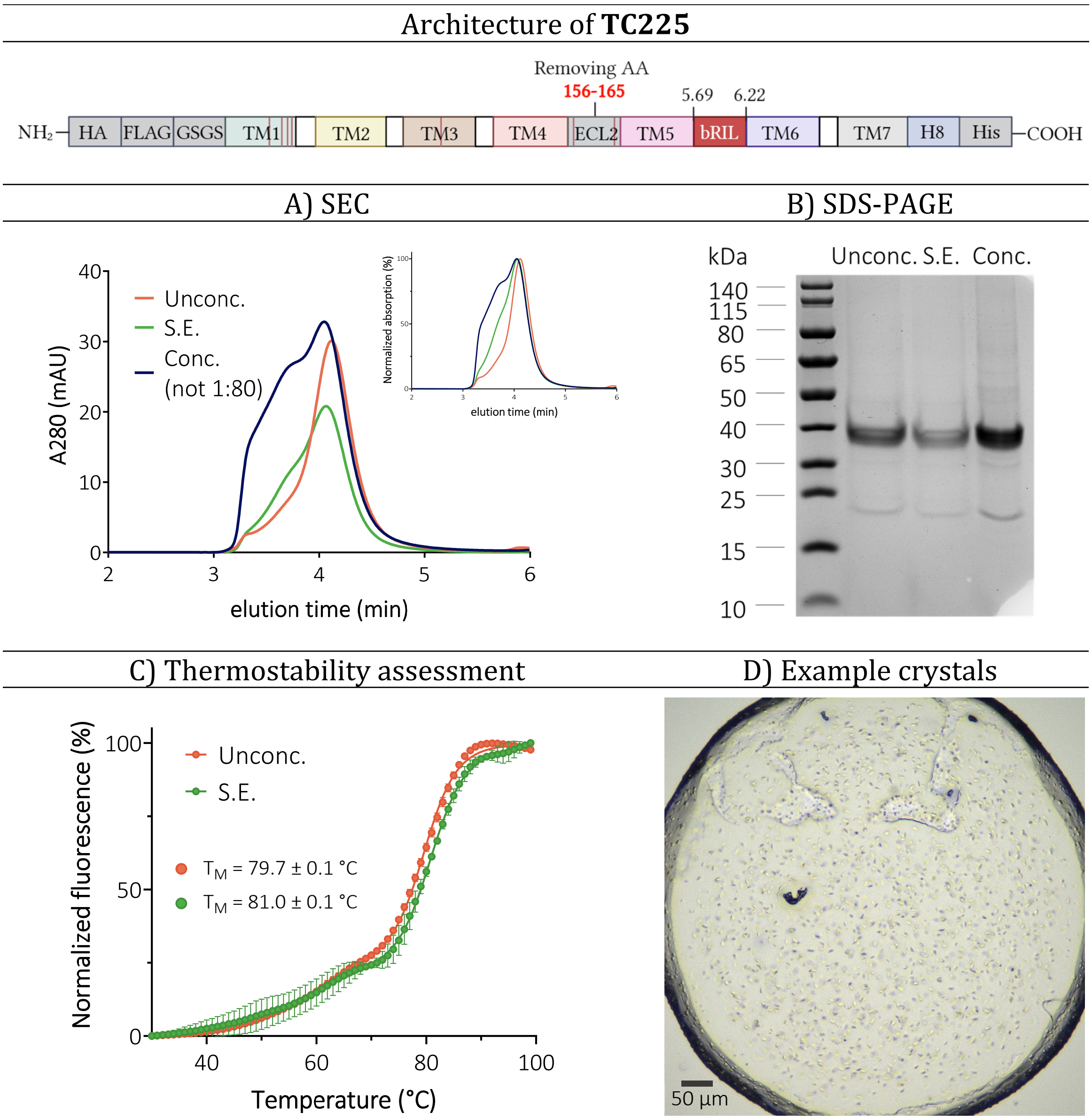

Figure 126. Protein analysis and crystallization of TC225 in complex with PSB-21500. A) Region of interest of the SEC analysis of the protein samples (normalized results in the top right corner). B) SDS-PAGE of the unconc., S.E. and conc. samples, 10 µL each (conc. ~ 1:100 diluted). C) Thermostability assessment of the unconc. and S.E. samples. Nonlinear fit (biphasic) of normalized fluorescence data. The T_M was calculated as the mean ± SD of the later inflection point (n=3). D) Exemplary LCP drop from the crystallization experiment.

As evident from the SEC data, the monodispersity of these two constructs, particularly after their salt exchange and concentration, was severely compromised. Both concentrated samples displayed a substantial signal for protein eluting between 3.2 min to 3.8 min, despite undergoing an essentially identical purification process, compared to the constructs presented in the previous chapter. The only difference was a moderate increase in the imidazole concentration from 220 mM to 300 mM. Unfortunately, unaffected by the increased imidazole concentration, the protein elution was still incomplete after 3 CV. Consequently, additional elution and salt exchange steps were required once again. Considering that the SDS-PAGE results confirmed a good purity for both of the samples, the premature elution time cannot be attributed to impurities in the samples.

In general, however, major modifications were performed on all of the $A_{2B}AR$ constructs in this series, which were not evaluated before their large-scale purification for two reasons. Firstly, the DNAs, which were synthesized by BioCat, arrived only gradually in the course of several weeks. At this stage of the project the significant read-out was no longer the monodispersity or thermostability of the proteins, but their ability to crystallize, which unfortunately is not predictable by evaluation of small-scale purifications. Either way, due to the major modifications on the proteins, the occurrence of elevated aggregation peaks or reduced thermostability is not as unexpected for these constructs as it would be for the extensively characterized constructs TC190 and TC196. Despite the substantial presence of presumed aggregation peaks, both proteins exhibited noteworthy crystal growth under several conditions. The most significant crystals of TC224 and TC225, which grew in LCP drops covered with the same precipitant solution, are depicted in the following Figure 127.

TC224 + PSB-21500	TC225 + PSB-21500

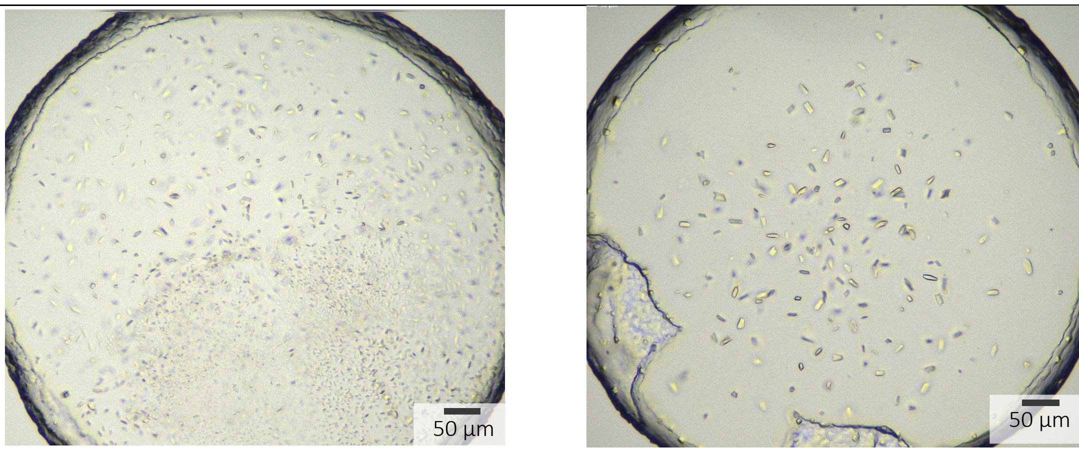

90 mM tri-sodium citrate, 120 mM ammonium sulfate, 100 mM Tris pH 8.7,
37 % (v/v) PEG 400

Figure 127. Largest crystals obtained from the crystallizations of TC224 and TC225. The pictures were taken after 21 days of incubation time.

With sizes ranging up to 15 to 20 µm, these crystals were the largest among all crystals observed for the refined constructs that were tested up to that point. Crystals from both of these LCP drops were tested for their diffraction, and both exhibited weak reflections of up to approximately 9 Å. Clearly, such weak diffraction is not sufficient for structure determination, but considering that these were only the initial crystal hits a fine screen based on these conditions would still be of interest. The subsequent crystallization efforts, however, were directed towards the remaining fusion partner constructs.

For the sake of completeness, it should be noted that the concentrations of the two samples that produced these crystals, were measured to be slightly below 20 mg/mL when the minimal sample volume was reached, and therefore fell short of targeted 30 mg/mL.

3.16.4 Crystallization of TC228 and TC232 in complex with PSB-21500

As briefly mentioned in the section above, the previous increase of the imidazole concentration from 220 mM to 300 mM was not sufficient to completely elute the protein in the 3 CVs. Those 3 CVs represent the maximum elution volume, which enables the salt exchange to be performed in one step instead of two, thereby limiting the final sample volume to 7 mL instead of 14 mL for each protein. Consequently, for this subsequent purification, the imidazole concentration was once again increased, this time to 350 mM. Beyond that, the purification process was not changed, despite the increased aggregation observed before, because it was not clear whether the observed effect was due to the purification procedure, the constructs or the sample collection procedure.

The outcomes of the next two purifications and crystallizations, conducted with constructs TC228 and TC232, are presented in the following Figure 128 and Figure 129.

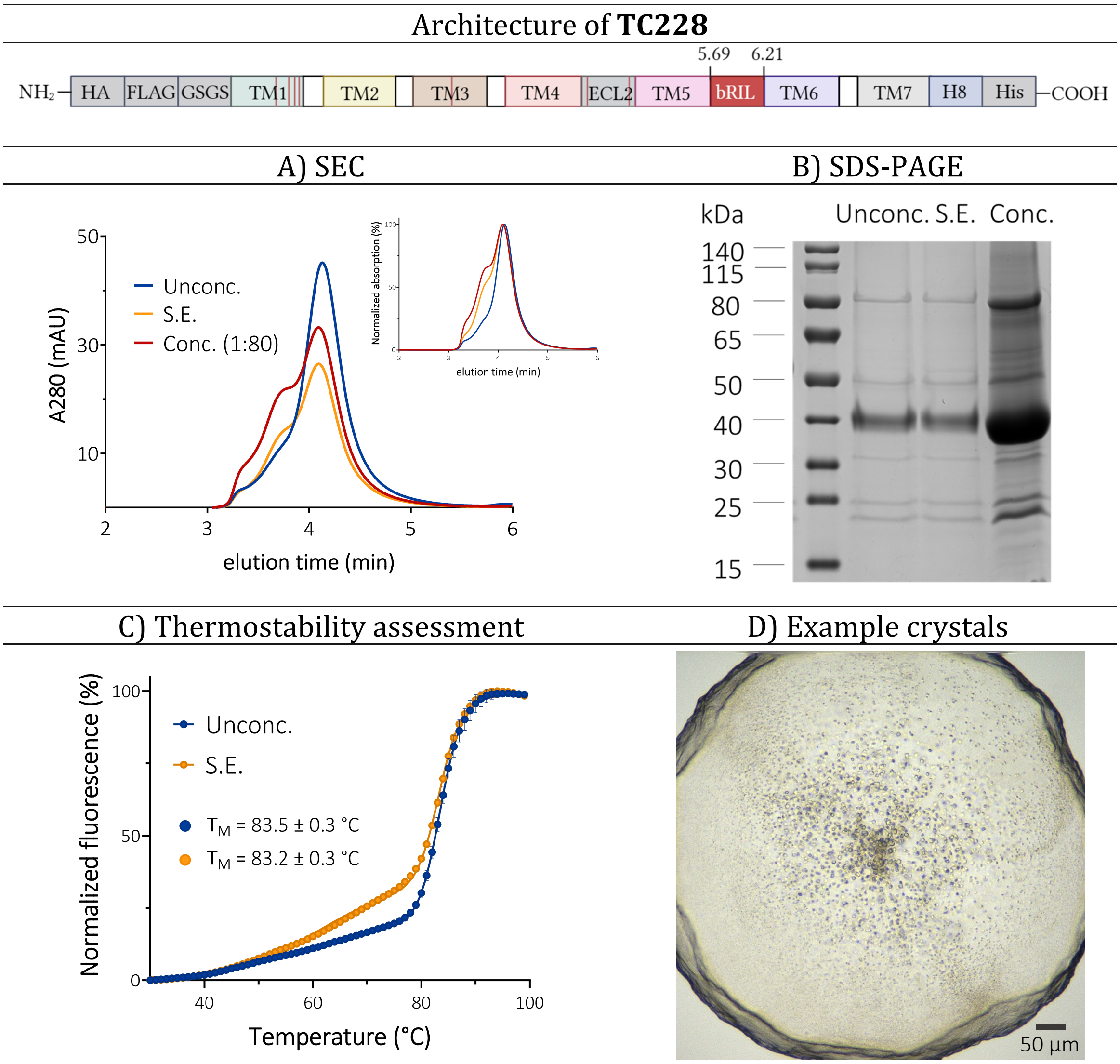

Figure 128. Protein analysis and crystallization of TC228 in complex with PSB-21500. A) Region of interest of the SEC analysis of the protein samples (normalized results in the top right corner). B) SDS-PAGE of the unconc., S.E. and conc. samples, 10 µL each (conc. ~ 1:100 diluted). C) Thermostability assessment of the unconc. and S.E. samples. Nonlinear fit (biphasic) of normalized fluorescence data. The T_M was calculated as the mean ± SD of the later inflection point (n=3). D) Exemplary LCP drop from the crystallization experiment.

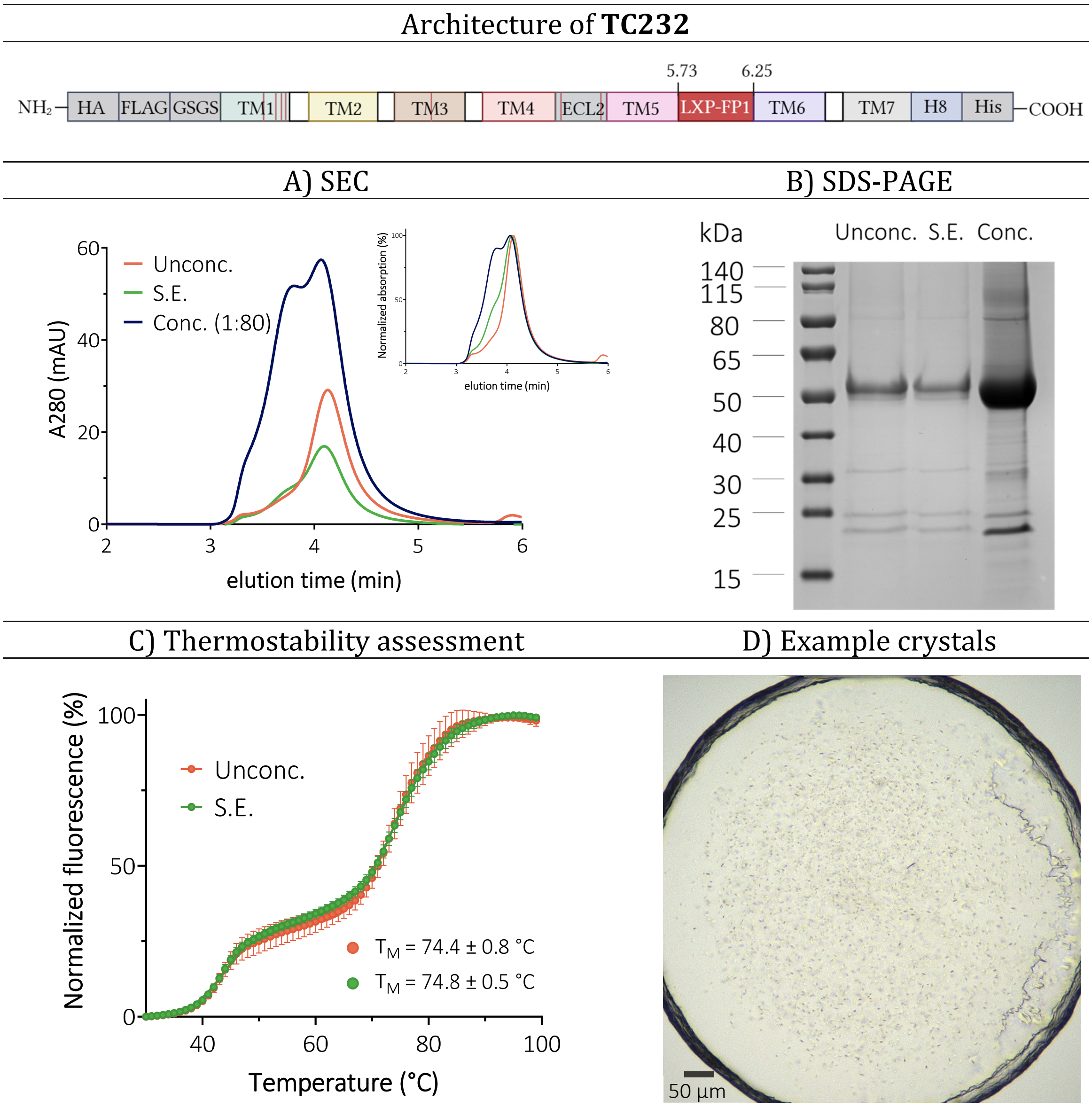

Figure 129. Protein analysis and crystallization of TC232 in complex with PSB-21500. A) Region of interest of the SEC analysis of the protein samples (normalized results in the top right corner). B) SDS-PAGE of the unconc., S.E. and conc. samples, 10 µL each (conc. ~ 1:100 diluted). C) Thermostability assessment of the unconc. and S.E. samples. Nonlinear fit (biphasic) of normalized fluorescence data. The T_M was calculated as the mean ± SD of the later inflection point (n=3). D) Exemplary LCP drop from the crystallization experiment.

Also, for these two purifications, an increase in protein aggregation was observed upon salt exchange and concentration of the protein. TC232, featuring one of the undisclosed fusion proteins from leadXpro, exhibited a particularly pronounced aggregation peak. Another $A_{2B}AR$ construct, namely TC231, whose ICL3 was also replaced by the LXP-FP1, was purified as part of the second round of purifications and did not exhibit such aggregation. The difference between these two constructs, TC231 and TC232, is that for TC232 the insertion site is extended from position 5.70 to 5.73 by three amino acids, corresponding to almost one whole right-handed α-helical turn.[315] In the AlphaFold models, the α-helix of TM5 indeed merged with the α-helix of the fusion protein for both constructs. Based on this, and also the fact that the eluted protein did not exhibit a similar aggregation peak, it is not plausible that the strong aggregation can be attributed to the construct TC232 itself. The same is true for construct TC228, which also showed no considerable aggregation upon elution, and whose insertion position of bRIL (5.69 to 6.21) was modeled to be similar to its closely related parent construct TC190 (insertion position 5.69 to 6.22).

Regarding the purity of the samples, the SDS-PAGE results revealed notable impurities of various sizes, with one particularly prominent protein band around 25 kDa, which was consistently observed for all other proteins of this purification series, albeit to a lesser extent. Despite the increased imidazole concentration for elution, however, no parameters of the purification process were changed compared to the previous two experiments. Unfortunately, even with 350 mM of imidazole, the protein elution was still not entirely complete after 3 CVs, however, this time, no additional elution and salt exchange steps were performed.

For both of these samples, the protein concentration was measured before and after the overnight storage between day two and day three of the purification. Interestingly, it was noted that after the storage, the protein concentration was halved. In general, for all the purifications presented herein, where the protein concentration of the eluted sample and the final sample was measured, a significant loss in protein was observed. This occurred despite the use of concentrators with an appropriate molecular weight cut-off of 100 kDa, which should retain the A_{2B}AR constructs (≥ 50 kDa in size) embedded in the DDM micelles (≥ 60 kDa in size).[316, 317] Regrettably, the final concentration of the samples used for crystallization were challenging to measure reliably, due to fluctuations in the measurements. For TC232, the concentration of the protein sample in the final volume of ~ 20 µL was measured to be approximately 11.5 mg/mL. In contrast, for TC228, the same protein concentration was already measured when the volume was still ~ 50 µL. Consequently, according to these measurements, the protein concentration of TC228 at a final volume of ~ 20 µL should have been significantly higher than that of TC232. However, contradictory to this, the SEC results indicate that protein TC232 was indeed more concentrated compared to TC228, with peak heights of ~ 60 mAU (A280 nm), compared to ~ 45 mAU (A280 nm), respectively.

Regardless of the apparent shortcomings of these two purifications, crystal formation was observed for both of the proteins. Compared to the previous protein samples of TC224 and TC225, however, the crystals were less abundant and smaller in size, as evident from the following pictures of two LCP drops harboring the best crystals of each construct (Figure 130).

TC228 + PSB-21500	TC232 + PSB-21500
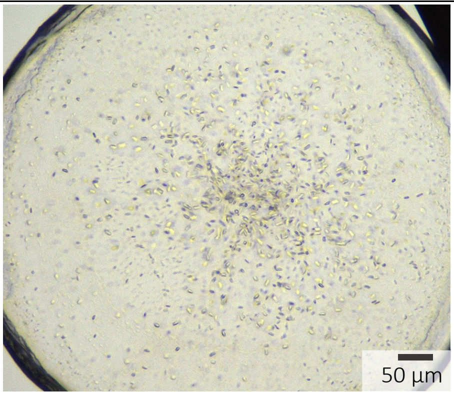	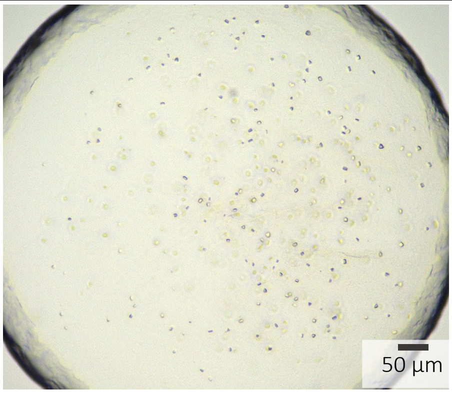
100 mM sodium chloride, 100 mM HEPES pH 7.0. 30 % (v/v) PEG400	100 mM tri-sodium citrate dihydrate pH 5.0, 30 % (v/v) PEG 500 MME

Figure 130. Best crystals obtained from the crystallizations of TC228 and TC232. The pictures were taken after 21 days of incubation time.

Considering the 5 µm to 10 µm size of these crystals, they were not large enough for the purpose of this crystallization series, aiming to identify an A_{2B}AR construct with improved crystallization potential that yields sufficiently large crystals without much optimization. In fact, these initial crystal hits were no improvement over those which were previously observed for the widely used crystallization constructs TC190 or TC196 either. The contribution of the suboptimal SEC results or the observed impurities to this small crystal size is not clear. Potentially, these crystallizations could be repeated and improved in the future. For the next purification, two different constructs, namely TC227 and TC230 were evaluated for their ability to form crystals.

3.16.5 Crystallization of TC227 and TC230 in complex with PSB-21500

For the purifications of TC227 and TC230, the purification protocol underwent another slight modification. In response to the elevated impurity observed for the previous two samples, the amount of washing performed on the Co^{2+} beads was increased by using nearly twice the volume of WB2 (now almost 20 CV), which contained 50 mM imidazole. Controversially, despite the increase in aggregation which was observed before, the salt exchange was still performed. This decision aimed to maintain the comparability of the crystallization experiments and was influenced by the positive results obtained with previous samples, such as TC225, which were achieved without imidazole in the final sample buffer. As presented below, the crystallization, particularly of TC230, proved to be the most successful one of all crystallization trials of the A_{2B}AR performed to date.

The results of the purifications and crystallizations of TC227 and TC230 will be presented in the upcoming Figure 131 and Figure 132.

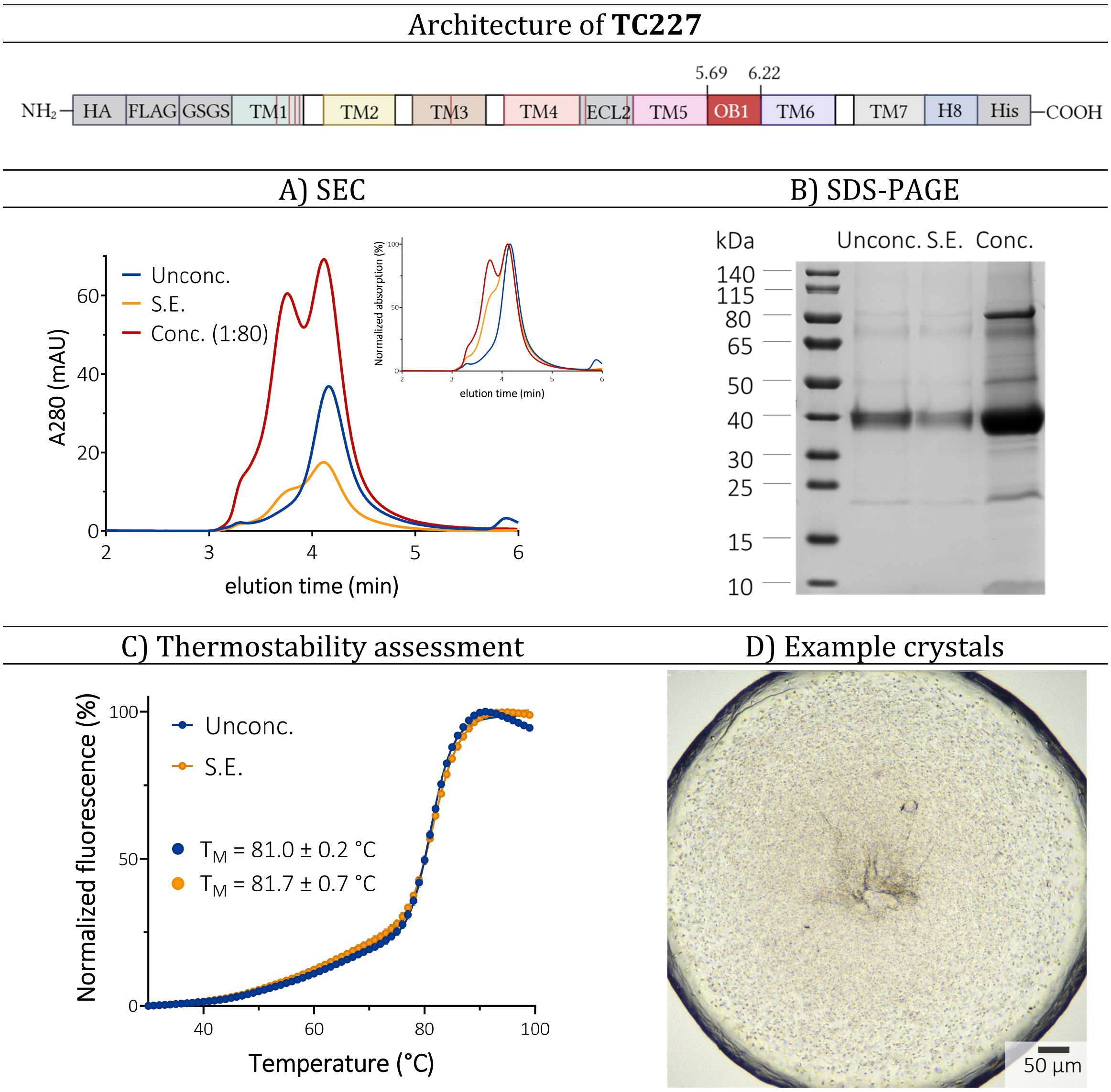

Figure 131. Protein analysis and crystallization of TC227 in complex with PSB-21500. A) Region of interest of the SEC analysis of the protein samples (normalized results in the top right corner). B) SDS-PAGE of the unconc., S.E. and conc. samples, 10 µL each (conc. ~ 1:100 diluted). C) Thermostability assessment of the unconc. and S.E. samples. Nonlinear fit (biphasic) of normalized fluorescence data. The T_M was calculated as the mean ± SD of the later inflection point (n=3). D) Exemplary LCP drop from the crystallization experiment.

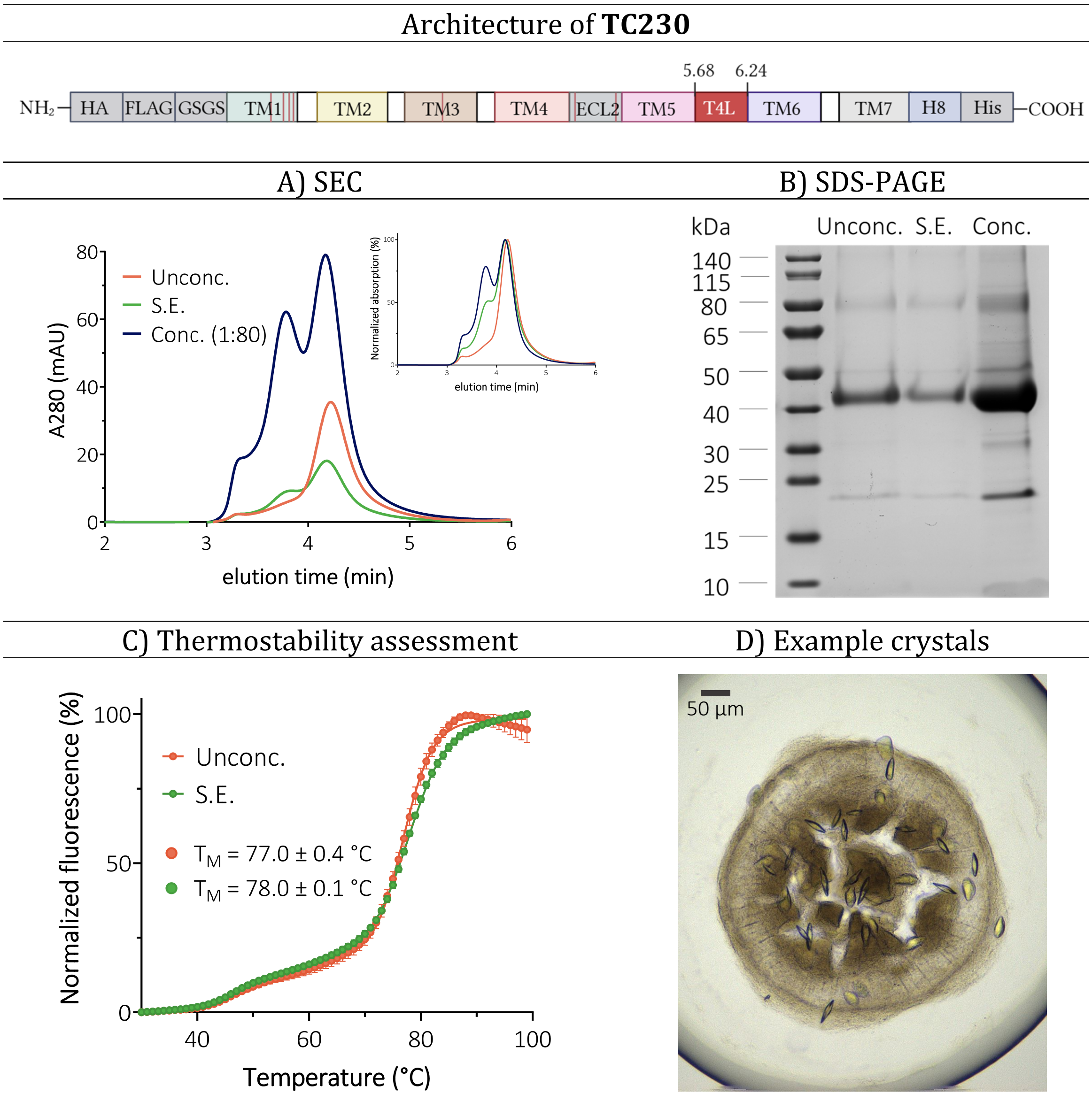

Figure 132. Protein analysis and crystallization of TC230 in complex with PSB-21500. A) Region of interest of the SEC analysis of the protein samples (normalized results in the top right corner). B) SDS-PAGE of the unconc., S.E. and conc. samples, 10 µL each (conc. ~ 1:100 diluted). C) Thermostability assessment of the unconc. and S.E. samples. Nonlinear fit (biphasic) of normalized fluorescence data. The T_M was calculated as the mean ± SD of the later inflection point (n=3). D) Exemplary LCP drop from the crystallization experiment.

The proteins purified in this round of purifications behaved similarly to the ones of the previous experiments. Both samples demonstrated sufficient thermostability with a T_M of over 75 °C, most likely attributed to the presence of the covalent ligand PSB-21500, along with a substantial and sharp aggregation peak. As a result of the more extensive washing of the Co^{2+} beads, the protein was slightly purer than the previous samples, albeit the purity was still not ideal. When comparing the purities of different samples, it is essential to consider the amount of protein loaded onto the gel.

For most of the previous SDS-PAGE analyses, less concentrated protein samples were loaded, which were more comparable to the unconc. samples in the SDS-PAGE results of TC227 and TC230, and potential impurities were therefore less evident. The reason for the more prominent protein bands of TC227 and TC230 samples is their high protein concentration. For TC227, the final protein concentration, as measured by the spectrophotometer (A280 nm), reached 30 mg/mL, as desired. However, determining the final concentration of TC230 was troublesome, likely due to ligand interference, and the final concentration measurement testified a concentration of only 10 mg/mL. Similar to the observations on TC228 and TC232 as detailed in the previous section, these concentration measurements did not align with the signals observed in the SEC analysis, where TC230 exhibited an even higher signal than TC227. Consequently, it can be assumed that both samples exhibited a sufficiently high protein concentration for crystallization.

Indeed, as mentioned in the introduction to this section, the crystallization of TC230 marked the most successful crystallization of the $A_{2B}AR$ to date. To asses both constructs' propensity to crystallize, the standard four commercial precipitant screens were employed. The most noteworthy crystals of TC227 are depicted in Figure 133, and Figure 134 presents the results of TC230's crystallization trial.

TC227 + PSB21500

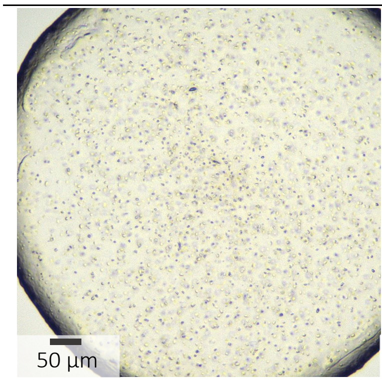

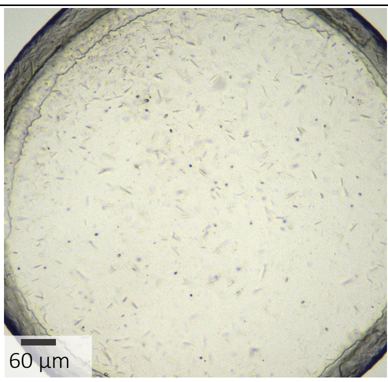

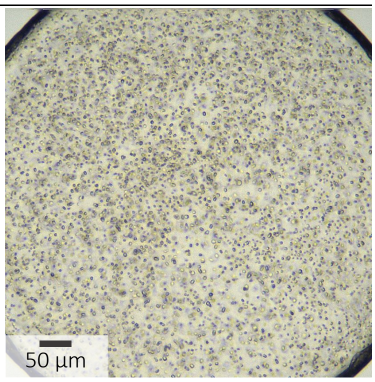

–	100 mM sodium chloride 100 mM lithium nitrate	–
+ 30 % (v/v) PEG 400 + 100 mM tri-sodium citrate dihydrate pH 5.0	+ 4 % (v/v) 2-Methyl-2,4-pentanediol + 100 mM tri-sodium citrate dihydrate pH 5.6	+ 30 % (v/v) PEG 500 MME + 100 mM tri-sodium citrate dihydrate pH 5.0

Figure 133. LCP drops with the most interesting crystals from the TC227 crystallization trial. The crystals grew in precipitant solutions indicated beneath their images, and were pictured after 21 days of incubation time.

TC230 + PSB-21500 (I)		
A)	B)	C)
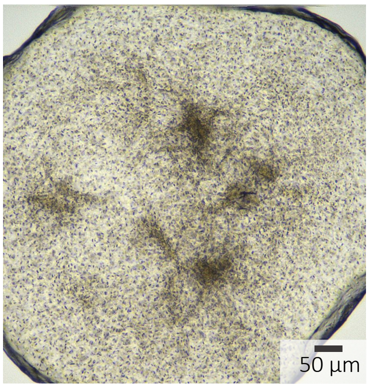	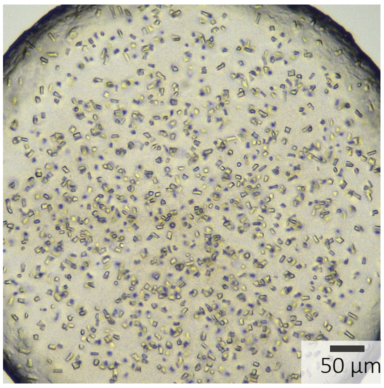	
100 mM di-ammonium hydrogen phosphate	100 mM sodium chloride	100 mM sodium chloride
+ 37 % (v/v) PEG 300 + 100 mM Bis-Tris propane pH 6.5	+ 30 % (v/v) PEG 400 + 100 mM tri-sodium citrate dihydrate pH 5.0	+ 30 % (v/v) PEG 500 DME + 100 mM tri-sodium citrate dihydrate pH 5.0
D)	E)	F)
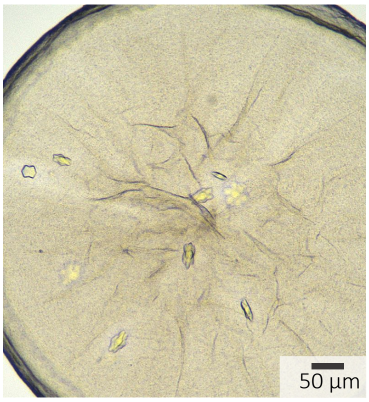	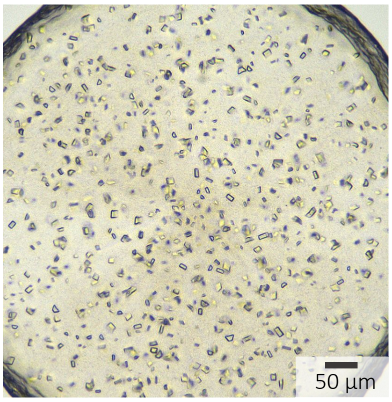	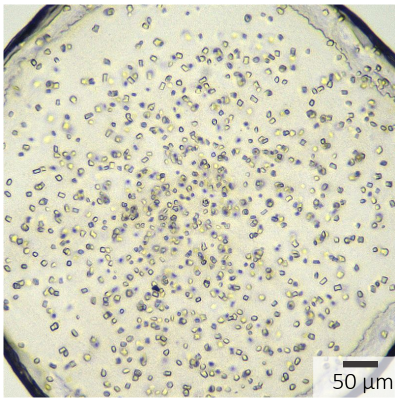
100 mM sodium chloride	200 mM lithium sulfate	220 mM potassium nitrate
+ 30 % (v/v) PEG 500 MME + 100 mM tri-sodium citrate dihydrate pH 5.0	+ 10 % (v/v) PEG 1000 + 100 mM phosphate/ citrate pH 4.2	+ 30 % (v/v) PEG 400 + 100 mM tri-sodium citrate dihydrate pH 6.0

Figure 134. LCP drops with the most interesting crystals from the first TC230 crystallization trial. The crystals grew in precipitant solutions indicated beneath their images, and were pictures after 21 days of incubation time.

The crystals of TC230, as shown in panel C and D of Figure 134, were among the largest crystals obtained in this crystallization series and exhibited a size of ~ 40 µm each. Compared to some of the best crystals obtained with the other $A_{2B}AR$ constructs, e.g. TC231 or TC225, these crystals were two- to three-fold larger, and importantly, they grew in all three dimensions. Luckily, the precipitant screen which facilitated the growth of these crystals was utilized twice in this crystallization trial, and the crystals from the respective second LCP drops were identical to those presented above. Consequently, a great number of crystals was available for harvesting and measurement. The harvesting, which was performed by Dr. Tobias Claff, was particularly challenging for the crystals depicted in panel C, since this LCP drop had transitioned into a more liquid sponge phase,[318] causing the crystals to adhere less securely to the loops that were used for their removal from the drops.[231]

The X-ray diffraction measurement of these crystals was performed at the PSI by our cooperation partner leadXpro. Encouragingly, the crystals presented in panel C and D both diffracted below 4 Å, with single diffraction spots observed at 3.5 Å. This diffraction data represents the best data which has been achieved for the $A_{2B}AR$ throughout the entire course of this project, and it allowed the solving of the very first crystal structure of the $A_{2B}AR$ at a resolution of 4.0 Å. The discussion of this antagonist-bound structure of the $A_{2B}AR$ will follow after the presentation of all crystallization trials, in section 3.17 on page 210. Unfortunately, the resolution of the obtained crystal structure is not sufficient for a comprehensive analysis of the interactions of the amino acid side chains with the ligand and with each other. Consequently, further optimization of these initial crystal hits will be necessary to enhance the resolution and to elucidate these details.

In addition, the crystals presented in panel B of Figure 134 were also tested for their X-ray diffraction and also those crystals diffracted up to 7 Å. Considering their smaller size of just ~ 10 µm, this further substantiates the optimization potential of the utilized construct TC230.

TC230 is the refined construct based on TC190, which incorporated T4L as a fusion partner in the ICL3. As outlined during the description of the construct optimization, the T4L fusion has been applied to several constructs in the past. Initially, it was tested both *N*-terminally and in the ICL3 of the unmutated $A_{2B}AR$, which was performed in the course of my master's thesis.[252] More recently, it was employed in a stabilized $A_{2B}AR$ construct, featuring the $S92^{3.39}K$ mutation (see Figure 61 on page 89). In this case, T4L was also employed in the ICL3, but the insertion position was not optimized. Back then, the fusion protein was inserted between the residues 5.69 and 6.22 of the $A_{2B}AR$, whereas in TC230 the insertion site was between 5.68 and 6.24. Small modifications in the junction between the receptor and the fusion partner can lead to a distortion of the α-helical domain in this region, which can have a large impact on the receptor's monodispersity. Indeed, the monodispersity of the previous ICL3-T4L construct, namely TC132, was significantly inferior compared to the analogous construct featuring bRIL in its ICL3, whose insertion position (5.69 to 6.22) was presumably already ideal, based on the recent AlphaFold model. In contrast to that, the monodispersity of the eluted unconcentrated TC230 construct with its optimized T4L insertion position closely resembled that of the parent construct TC190, featuring bRIL in its ICL3 (compare panel A of Figure 132 e.g. to panel A of Figure 87 on page 126).

The examination of the low-resolution crystal structure, which will be presented in section 3.17 on page 210 ff., suggested potential strategies to further optimize the size and particularly the diffraction quality of the crystals based on the observed crystal packing. First and foremost, however, the repetition of the crystallization with a more homogenous sample would be advisable.

As before, the reason for the increased aggregation of the samples was still unclear, especially considering that for the first two rounds of purifications (see Figure 120 to Figure 123) the salt exchange did not result in this effect. One possible explanation, which was explored in the following purifications, was that the sudden removal of the increased imidazole concentration might have destabilized the protein. This theory was based on the fact that for all purifications after the initial two rounds, an elevated imidazole concentration of 300 mM to 350 mM was employed, in contrast to the 220 mM which were used initially. The upcoming section 3.16.6 will address this theory in the context of the first purification and crystallization of TC229, and the repeated purification and crystallization of TC223.

3.16.6 Crystallization of TC223 (II) and TC229 in complex with PSB-21500

To investigate the hypothesis concerning the impact of the salt exchange, the imidazole concentration was reverted to 220 mM for the purifications of TC223 and TC229. In order to still ensure complete elution of the recombinant proteins from the Co^{2+} beads under these conditions, the first CV of elution buffer was passed through the resin column without the typical 10 min incubation, and the flow through was fractionated in fractions of approximately 100 µL. These fractions were then each analyzed for their protein content by measurement using the microvolume spectrophotometer (at A280 nm). Only the fractions displaying a distinct protein signal were pooled. Since the threshold imidazole concentration for the release of the protein from the resin was reached only gradually, up to 1 CV of “empty” elution buffer (a mixture of the elution buffer and wash buffer 2 which contained only 50 mM of imidazole) was discarded. Consequently, additional CVs of elution buffer were added to the Co^{2+} beads, and the 3 CVs of the eluted sample that contained the highest protein content were used for the subsequent steps.

The outcomes of these two purifications and crystallizations are presented in the following Figure 135 and Figure 136.

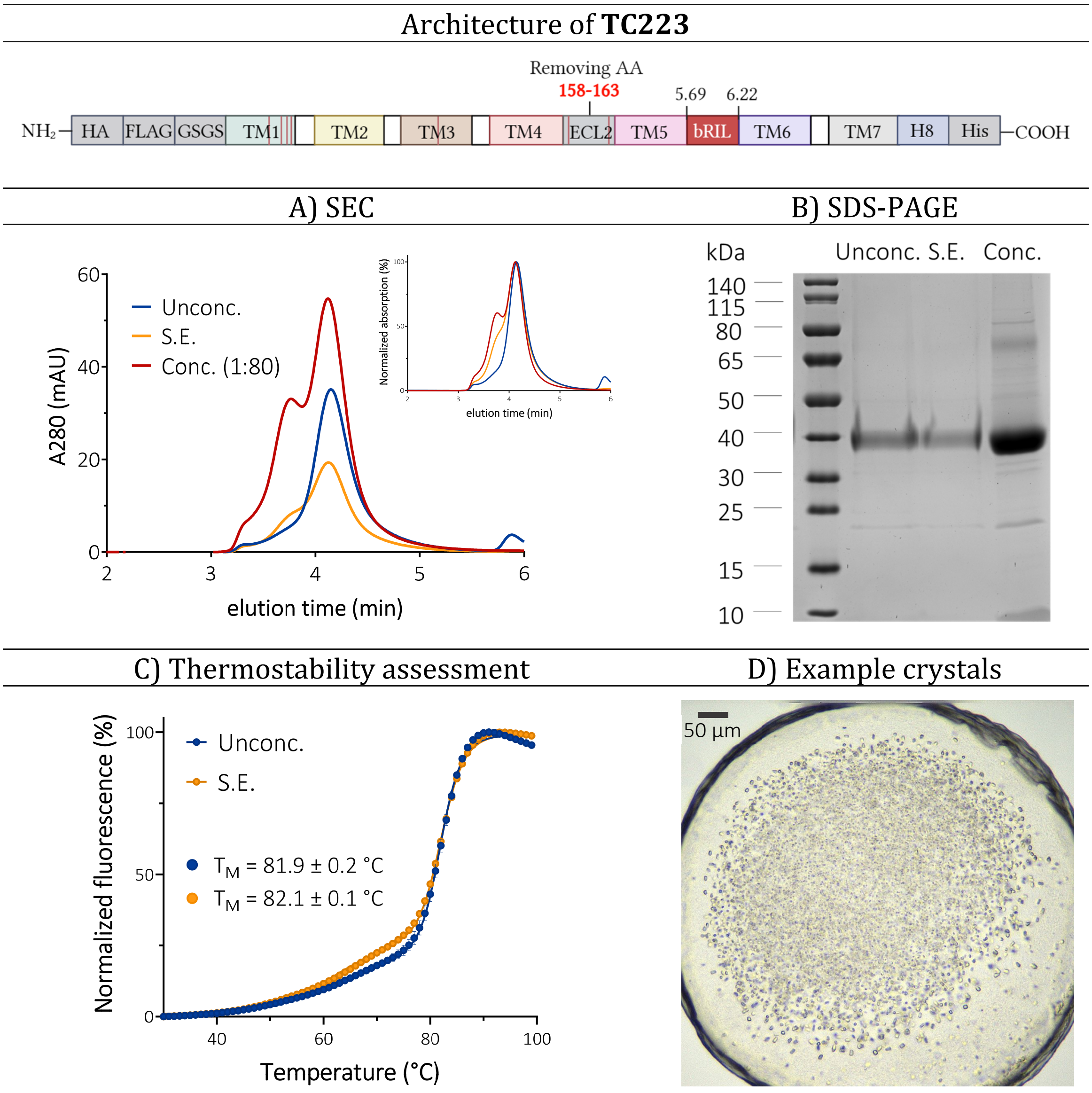

Figure 135. Protein analysis and crystallization of TC223 in complex with PSB-21500 (II). A) Region of interest of the SEC analysis of the protein samples (normalized results in the top right corner). B) SDS-PAGE of the unconc., S.E. and conc. samples, 10 µL each (conc. ~ 1:100 diluted). C) Thermostability assessment of the unconc. and S.E. samples. Nonlinear fit (biphasic) of normalized fluorescence data. The T_M was calculated as the mean ± SD of the later inflection point (n=3). D) Exemplary LCP drop from the crystallization experiment.

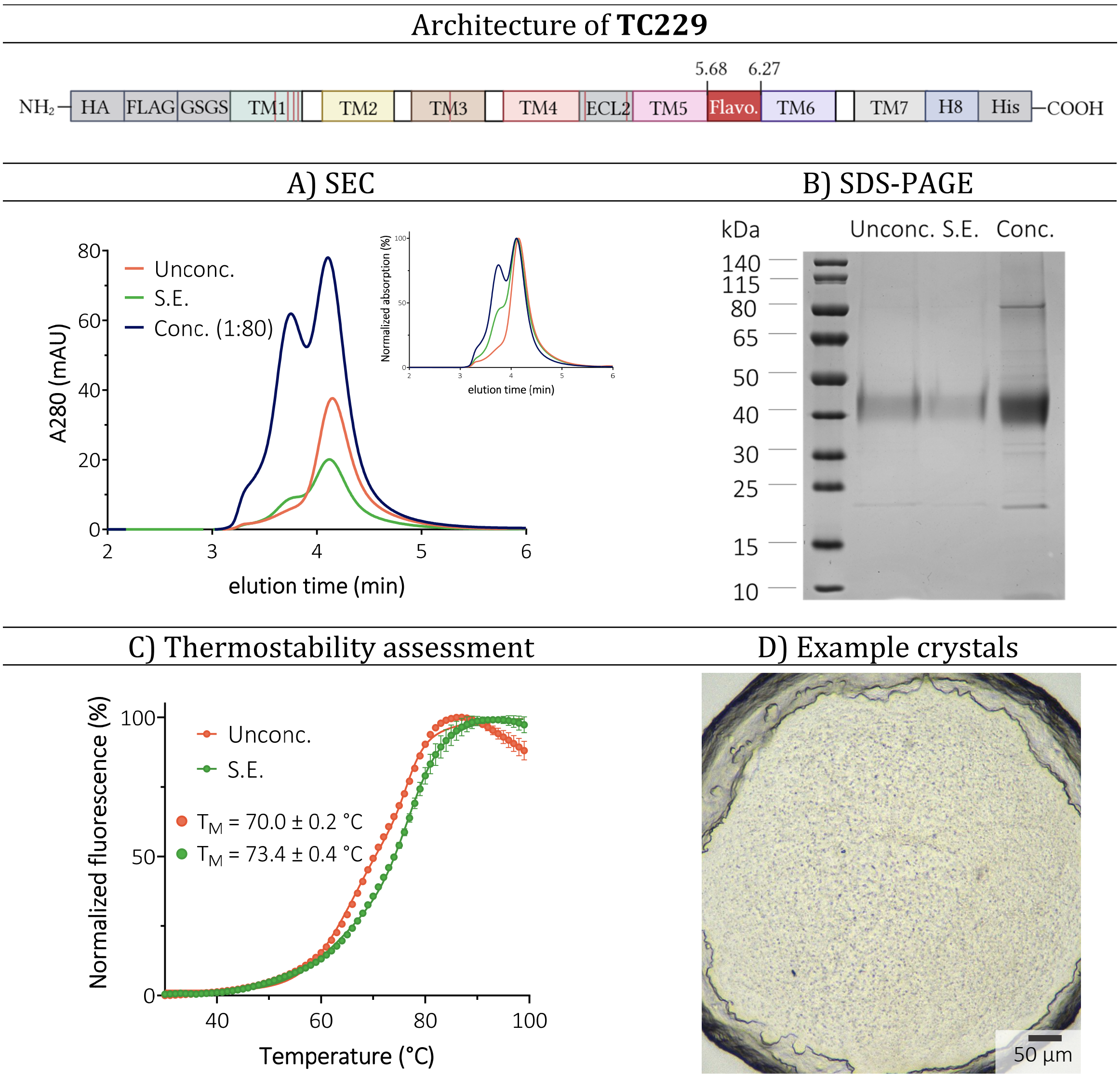

Figure 136. Protein analysis and crystallization of TC229 in complex with PSB-21500. A) Region of interest of the SEC analysis of the protein samples (normalized results in the top right corner). B) SDS-PAGE of the unconc., S.E. and conc. samples, 10 µL each (conc. ~ 1:100 diluted). C) Thermostability assessment of the unconc. and S.E. samples. Nonlinear fit (Boltzmann sigmoidal) of normalized fluorescence data. The T_M was calculated as the mean ± SD of the later inflection point (n=3). D) Exemplary LCP drop from the crystallization experiment.

The SEC results depicted in the respective panels A of Figure 135 and Figure 136 testify, that the cause for the elevated aggregation for the majority of these large-scale purifications was indeed not the elevated imidazole concentration. In this case, the proteins TC223 and TC229 were eluted with the original 220 mM of imidazole and upon the salt exchange they still exhibited distinct aggregation peaks between 3.3 min and 3.9 min of elution time. The comparison of this second purification of TC223 with its first purification, presented in Figure 120 on page 181, confirms the previous consideration that the inhomogeneity of the samples was caused by the purification process rather than an inherent instability of the constructs themselves. At this stage, the only remaining explanation was that, for all later purifications, a new batch of PD-10 salt exchange columns was used.

However, as noted before, the samples exhibiting the increased aggregation still showed crystal formation; therefore, an initial evaluation of their crystallization potential was still applicable. In the case of TC223 (II) and TC229, despite their satisfactory purity and protein concentration, determined to be 23 mg/mL and 29 mg/mL, respectively, only minor crystal formation was observed in several LCP drops. Still, compared to the first crystallization trial of TC223, crystal growth was more abundant, most likely due to the higher protein concentration. This emphasized the need to also repeat the purification and crystallization of TC226, which was the second protein that was purified in the first round of purifications (see section 3.16.1).

3.16.7 Crystallization of TC226 in complex with PSB-21500 (II)

The final crystallization experiment of this series was conducted with construct TC226. After the previous protein purification and concentration, the protein exhibited a concentration of only 10 mg/mL, which was not sufficient to facilitate extensive crystal growth. Additionally, the protein displayed notable impurities that might have hindered crystal growth as well. The outcomes of this second purification of TC226 are presented in Figure 137.

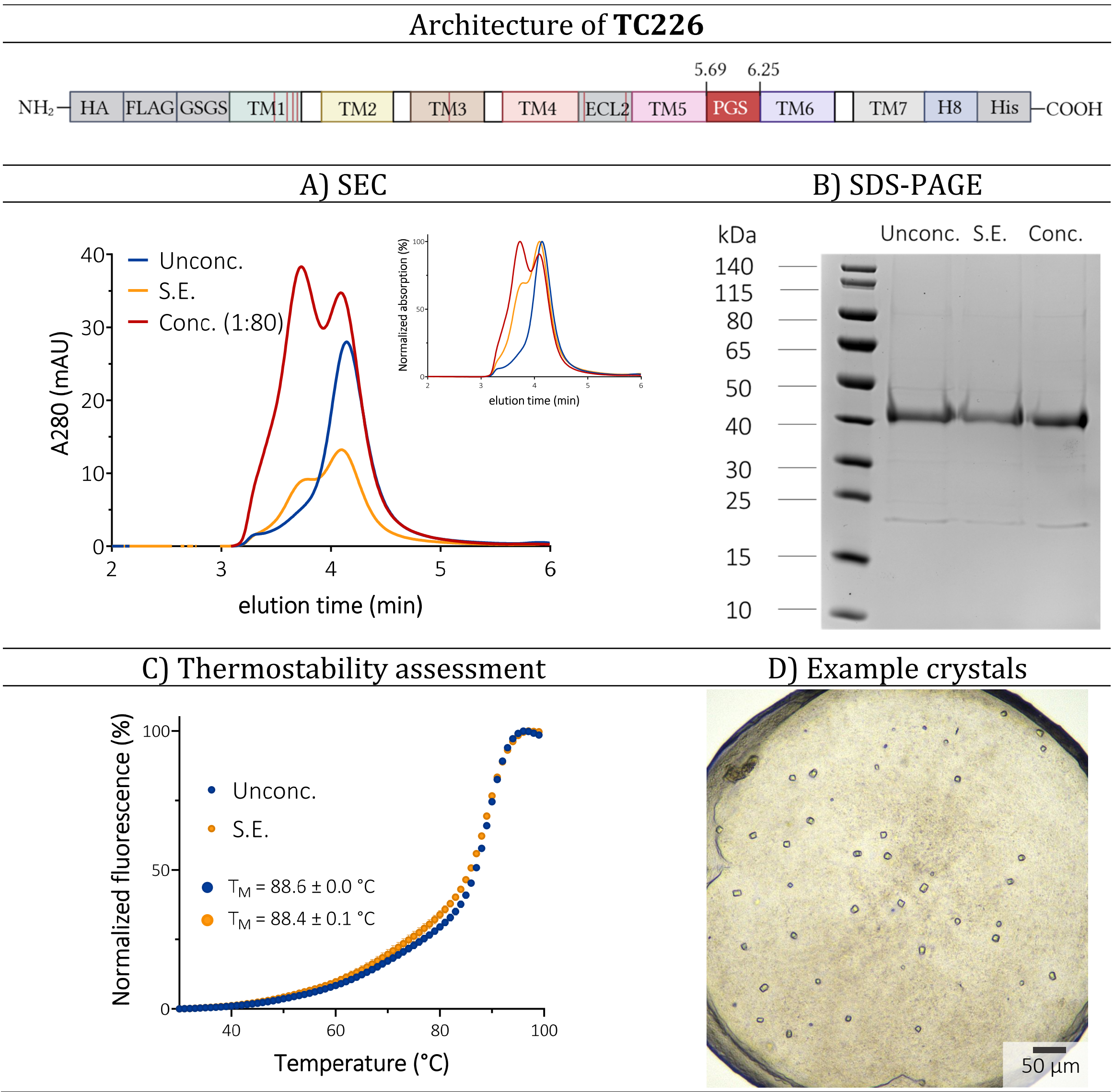

Figure 137. Protein analysis and crystallization of TC226 in complex with PSB-21500 (II). A) Region of interest of the SEC analysis of the protein samples (normalized results in the top right corner). B) SDS-PAGE of the unconc., S.E. and conc. samples, 15 µL each (conc. ~ 1:100 diluted). C) Normalized fluorescence data from thermostability assessment of the unconc. and S.E. samples. The T_M was calculated as the mean ± SD of the later inflection point of the nonlinear biphasic fits (n=2). D) Exemplary LCP drop from the crystallization experiment.

As already observed for construct TC223, the second sample of TC226 exhibited a significantly pronounced aggregation signal in the SEC analysis, and this time, the aggregation peak even exceeded the height of the peak at the favorable elution time of approximately 4.1 min. Apart from the decline in monodispersity, all other characteristics of the protein were improved compared to the first purification. The protein showed superior purity in the SDS-PAGE analysis, and a slightly higher thermostability as well. More importantly, the protein concentration was increased from formerly 10 mg/mL to approximately 25 mg/mL, which presumably positively affected crystal formation. In the second crystallization, numerous crystallization events were observed. Many of the crystals did not grow beyond the microcrystal size, but some grew similarly large as the recently observed well-diffracting crystals of TC230 (see Figure 134). The most noteworthy crystals of TC226's second crystallization trial are depicted in Figure 138.

TC226 + PSB-21500 (II)	
A)	B)
	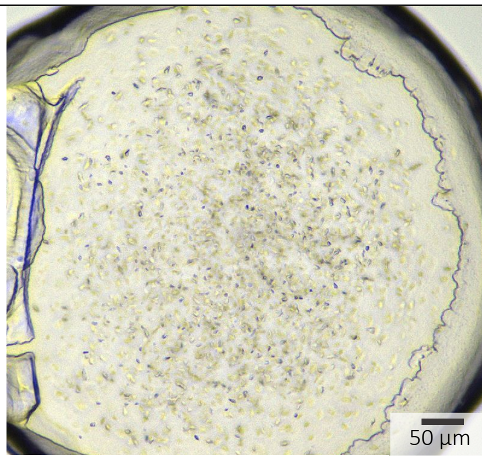
50 mM magnesium citrate nonahydrate, 100 mM ADA pH 7.0, 34 % (v/v) PEG 400	40 mM EDTA, 100 mM HEPES pH 7.0, 15 % (v/v) PEG 300
C)	D)
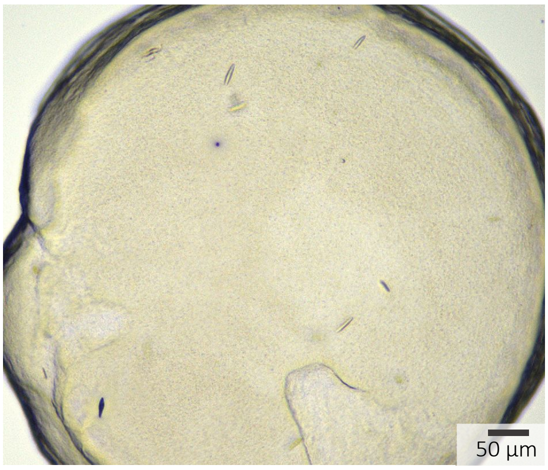	
100 mM sodium chloride, 100 mM tri-sodium citrate dihydrate pH 5.0, 30 % (v/v) PEG 500 MME	100 mM magnesium chloride hexahydrate, 100 mM tri-sodium citrate dihydrate pH 5.0, 40 % (v/v) PEG 200

Figure 138. LCP drops with the most interesting crystals from the second TC226 crystallization trial. The crystals grew in precipitant solutions indicated beneath their images, which were taken after 21 days of incubation time.

As seen in panel D of the above figure, crystals that developed in the presence of the precipitant solution containing magnesium chloride hexahydrate displayed a particularly even shape and promising size of approximately 40 µm. The presence of this salt previously facilitated the growth of protein crystals at various occasions, especially in the context of the crystallization experiments conducted during the research stay in Switzerland. But also the precipitant solution covering the LCP drop depicted in panel C, where crystals grew up to ~ 25 µm in size, has recently given rise to promising crystals, in particular the flower-shaped crystals of TC230 depicted in panel D of Figure 134, which diffracted up to 3.5 Å.

The 40 µm-large crystals depicted in panel D of Figure 138 were harvested and sent to the DESY for evaluation of their X-ray diffraction properties. This time, the measurement was performed by Dr. Renato Weiße from the research group of Prof. Dr. Norbert Sträter at Leipzig University at the DESY. Unfortunately, also these crystals diffracted only up to 7 Å. Therefore, the crystals of construct TC230 remained the best-diffracting crystals that were obtained in the course of this thesis. The 4 Å resolution crystal structure that was obtained from their diffraction data will be presented in the following section.

3.17 Crystal structure of the A_{2B}AR in complex with PSB-21500 at 4.0 Å resolution

Construct TC230 gave rise to well-diffracting crystals in the presence of two similar precipitant solutions:

i. 100 mM sodium chloride, 30 % PEG dimethyl ether (DME) 500, 100 mM tri-sodium citrate dihydrate pH 5.0, and
ii. 100 mM sodium chloride, 30 % PEG methyl ether (MME) 500, 100 mM tri-sodium citrate dihydrate pH 5.0.

Diffraction data was collected at the PXII beamline at the PSI, and crystals from both LCP drops diffracted up to 3.5 Å. The structure of the A_{2B}AR was solved at a resolution of 4.0 Å based on the diffraction data from a single crystal grown in the presence of the PEG MME 500-containing precipitant solution (ii.). The AlphaFold models of the A_{2B}AR and T4L were used as two independent search models in the molecular replacement procedure to solve the phase problem. The data collection was performed by our cooperation partner leadXpro, and refinements of the structure were performed by leadXpro and by Dr. Renato H. Weiße (Leipzig University).

Since the structure does not have sufficient resolution to define the position of most of the amino acid side chains, the insights into the exact interactions of the protein with the antagonist PSB-21500 and other structural details are limited. Still, some interesting information can be obtained from the structure, e.g. regarding the packing of the protein molecules within the crystals.

The crystal packing as well as a view on the general orientation of the fusion partner T4L, inserted between TM5 and TM6 of the receptor, are illustrated in Figure 139.

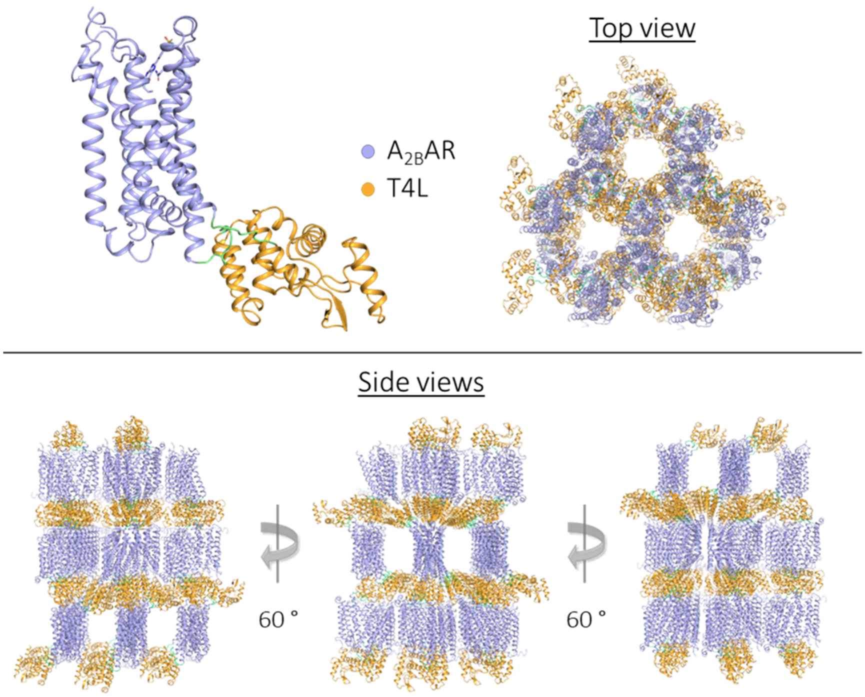

Figure 139. Overview of the crystal packing and orientation of the T4L fusion protein within the TC230 crystals.

The $A_{2B}AR$ fusion protein (TC230) crystallized in the trigonal space group $P3_121$. Crystal contacts, i.e. the interactions between the protein molecules in the crystal, are formed mostly between the T4L protein and the extracellular and intracellular loops of the $A_{2B}AR$. Lateral contacts between the GPCRs are substantially mediated by helix 8. The symmetry of the packing of the molecules resulted in distinct solvent channels within the crystal, as illustrated in the top right panel and bottom half of Figure 139.

In each TC230 molecule of the asymmetric unit, the fusion partner T4L projects sideways from the $A_{2B}AR$. This is in contrast to a T4L fusion construct of the $A_{2A}AR$ (PDB-ID: 3EML) which crystallized with a tighter packing and its structure was resolved at significantly higher resolution (2.6 Å).[180] There, the fusion protein is less tilted, as depicted in the upper half of Figure 140 shown below.

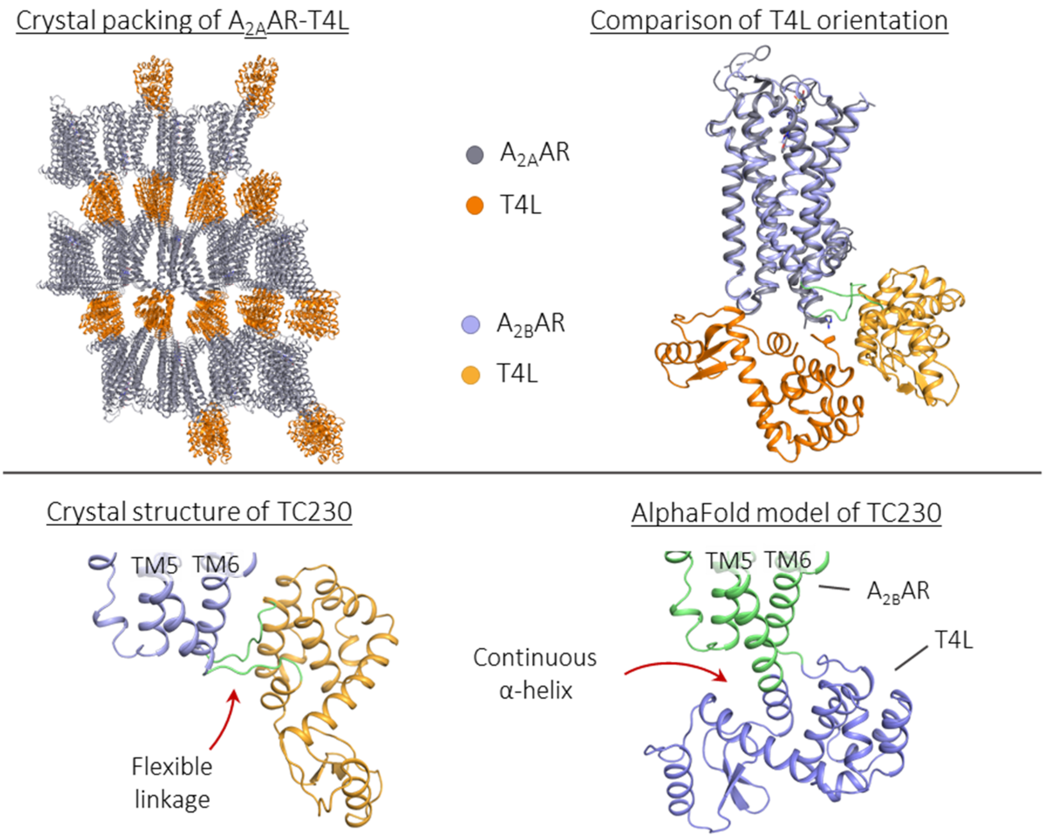

Figure 140. Comparison of the T4L orientation between the A_{2A}- and $A_{2B}AR$ crystal structures, as well as the AlphaFold model of TC230.[203] PDB-ID for $A_{2A}AR$-T4L: 3EML.[180]

Compared to the AlphaFold model of TC230,[203] the orientation of the fusion protein observed in the crystal structure is very different. The AlphaFold models were built to guide the decision on the exact insertion position for each of the fusion proteins that were evaluated following the research stay at leadXpro. For the T4L fusion protein, the AlphaFold model suggested that its insertion between the amino acids 5.68 and 6.24 of the $A_{2B}AR$ would result in a continuous and rigid α-helix between TM5 of the receptor and the fusion protein. In that case, the T4L would have projected beneath the receptor, instead of sideways. However, in contrast to the model, the observed linkage between TM5 and T4L in the crystal structure of TC230 is not an extended α-helix, but forms a loop structure. This difference to the AlphaFold model and the ill-defined electron density of residues 208-210 indicates flexibility of the linker region, illustrated in green in the TC230 crystallographic model of Figure 140. Rigidifying the linkage by gradual shortening of TM5 might be a promising strategy to further improve the crystal packing and consequently the diffraction quality of the crystals.

Another information that can be obtained from the elucidated structure is that it presents the PSB-21500-bound $A_{2B}AR$ construct in the inactive state. As described in section 1.3.1 of the introduction, the structural arrangements between the active and inactive states of class A GPCRs often differs substantially. The most obvious difference is the outward swing of TM6 upon activation, which is one of the aspects that enable the interaction between the receptors and the G proteins.[55] For the presentation of the NECA-bound $A_{2B}AR$ cryo-EM structure (PDB-ID 7XY7,[111] see section 1.6.3) the outward swing of TM6 was assessed based on a published inactive-state crystal structure of the $A_{2A}AR$. Now, for the first time, this comparison can be performed with an inactive-state structure of the $A_{2B}AR$, illustrated in Figure 141.

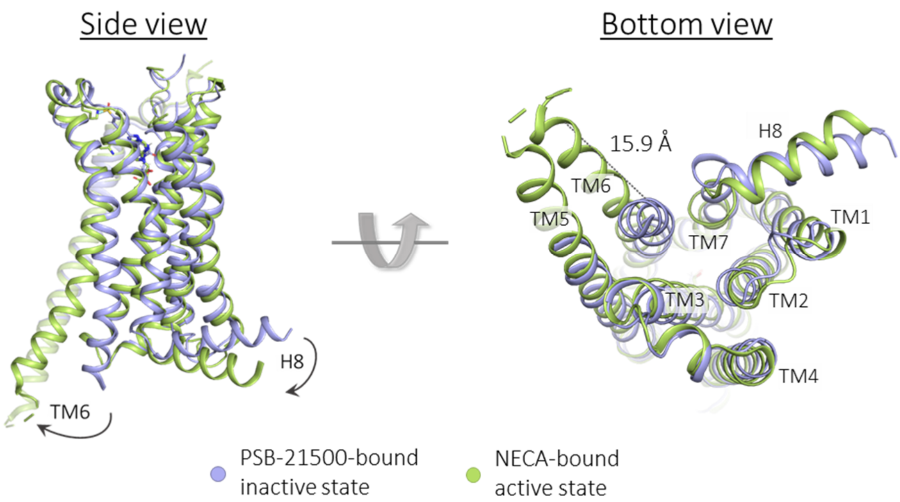

Figure 141. Comparison of the helix arrangements of the active NECA-bound and the inactive PSB-21500-bound $A_{2B}AR$ structures. PDB-ID of the NECA-bound structure: 7XY7. For clarity, the crystal structure is shown without T4L in the ICL3.

This comparison reveals that the antagonist-bound crystal structure of the $A_{2B}AR$ construct TC230 is indeed locked in its inactive-state, in contrast to the active-state structure obtained with the agonist NECA. The most pronounced differences between the structures is the outward swing of the intracellular tip of TM6 by ~ 16 Å upon activation, slightly more than the ~ 13 Å outward movement observed between the NECA-bound and antagonist-bound A_{2A}AR-T4L construct (PDB-IDs 6GDG[192], 3EML[180]). Also, a different position of helix 8 was observed between the active and inactive A_{2B}AR structures, which was not observed in case of the two A_{2A}AR structures, mentioned before, where the helix 8 is in an identical position as in our crystal structure.[180, 192] The authors of the A_{2B}AR-NECA paper speculated that the tilted conformation of helix 8 is an intrinsic feature of the receptor.[111] Our new crystal structure of the antagonist-bound A_{2B}AR appears to contradict this notion. However, it should be noted that helix 8 is involved in the formation of crystal contacts that could potentially influence the helix' position. Yet, the position of helix 8 as seen in our crystal structure aligns well with all examined structures of the A_{2A}AR,[65, 107, 180, 200, 319–321] including the one solved by cryo-EM.[192] Interestingly, the tilted helix 8 is observed in each of the four active-state cryo-EM structures, which were independently solved by two different research groups. This suggests a uniqueness of the A_{2B}AR upon activation. Other major rearrangements such as a repositioning of TM5 or an inward movement of TM7 are not evident from active- and inactive-state structures. Unfortunately, a more detailed comparison of the other features involved in activation of class A GPCRs is not possible, due to the limited resolution of the obtained A_{2B}AR crystal structure.

The same applies to the orthosteric binding pocket. The amino acid side chains lining the ligand binding pocket are not resolved in the structure, however, partial electron density was observed for the ligand PSB-21500. The position of the PSB-21500 electron density within the helix bundle, as well as a superimposition with the NECA-bound A_{2B}AR structure are depicted in Figure 142.

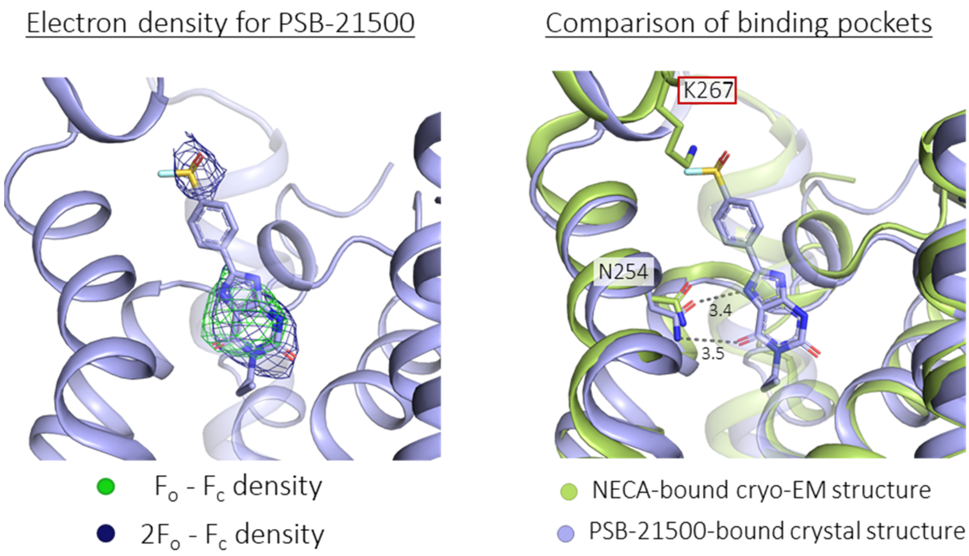

Figure 142. Ligand binding pocket insights. Left: Depiction of the electron density observed for PSB-21500 in the crystal structure. The same structure was refined without ligand to generate the positive F_o-F_c type density. Right: Superposition of the PSB-21500-bound crystal structure with the NECA-bound cryo-EM structure (without NECA, PDB-ID: 7XY7) to illustrate the positions of N254$^{6.55}$ and K267^{ECL3}. The exact side chain rotamer of N254$^{6.55}$ in the crystal structure is not supported by electron density.

Based on the electron density, the ligand was modeled into the orthosteric binding pocket of the receptor. Considering its position, PSB-21500 likely forms hydrogen bond interactions with residue N254$^{6.55}$, even though the electron density for the asparagine side chain is not sufficiently clear to define its exact rotamer, and its position presented in Figure 142 is hypothesized based on the co-crystal structures of other AR subtypes, and the adenosine- and NECA-bound cryo-EM structures of the A_{2B}AR. The interaction with N254$^{6.55}$ was also observed in each of the agonist-bound structures of the A_{2B}AR (see section 1.6.3), as well in structures of the A_1- and A_{2A}AR in complex with xanthine-based antagonists.[259, 281] The xanthine-derivative PSB-21500 was previously demonstrated to bind covalently to the A_{2B}AR (see Figure 143). However, in the structure of TC230 in complex with PSB-21500 the electron density does not indicate the presence of a covalent link. Nevertheless, superposition with the NECA-bound structure implies a close proximity of residue K267^{ECL3} which likely represents the interaction partner of PSB-21500 to form a covalent sulfonamide.

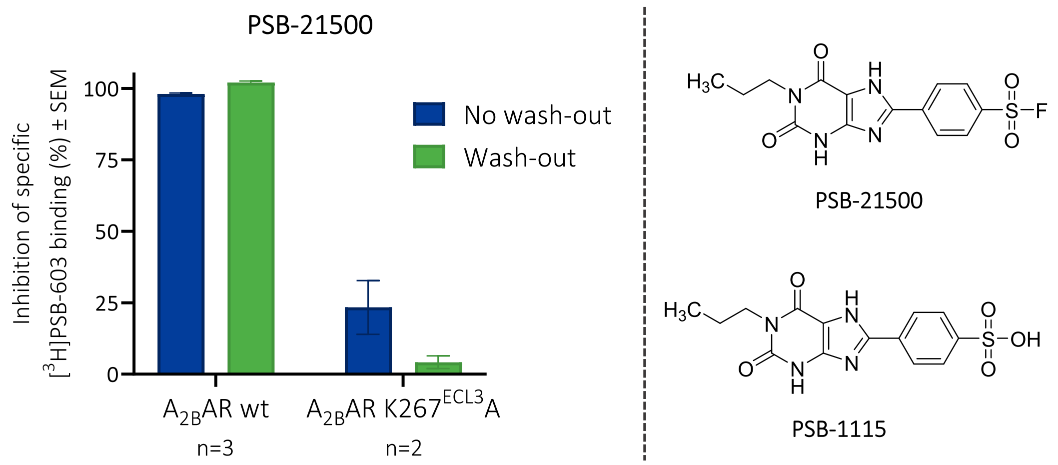

K$_i$/K$_D$ in nM vs. [^{3}H]PSB-603 (mean ± SEM, n=3) // Binding mode (rev./irrev.)				
Compound	wt A_{2B}AR		A_{2B}AR K267^{ECL3}A	
PSB-603	**0.553** ± 0.103	n.d.	**0.346** ± 0.049	n.d.
PSB-1115	**152** ± 12	rev.	**430** ± 30***	n.d.
PSB-21500	**10.6** ± 0.9	irrev.	**27.3** ± 1.9**	rev.

Figure 143. Binding of PSB-21500 to the wt A_{2B}AR and the K267^{ECL3}A-mutated A_{2B}AR. Data obtained for the wt receptor was previously published in Temirak et al.[284] Data for the K267^{ECL3}-mutant was obtained accordingly by Dr. Jonathan G. Schlegel. For wash-out experiment with the K267^{ECL3}A-mutant, PSB-21500 was employed at a concentration of 110 nM (10x the apparent K_i to the wt A_{2B}AR) during incubation with CHO-S membranes recombinantly expressing the receptor. Abbreviations: n.d. = not determined, rev. = reversible, irrev. = irreversible.

As demonstrated in our recent publication,[284] specific binding of the A_{2B}AR antagonist radioligand [^{3}H]PSB-603 to the wt receptor was completely inhibited upon pre-incubation with PSB-21500 at a concentration of 110 nM, which could not be restored by extensive washing. However, upon mutation of K267^{ECL3} to alanine, binding of [^{3}H]PSB-603 was only partly prevented by pre-incubation with 110 nM PSB-21500 (by approximately 25 %). After washing, the inhibitory effects were gone (< 5%), indicating removal of PSB-21500. The affinity of PSB-21500 for the K267^{ECL3}A-mutated receptor was reduced by ~ 2.6-fold, similar to the reduction in affinity of ~ 2.8-fold observed for the parent compound PSB-1115 without the reactive sulfonyl fluoride group. Our data clearly demonstrates that mutation of K267^{ECL3} to alanine, which does not have a nucleophilic side chain suitable for covalent linkage, results in reversible binding of PSB-21500. This stands in contrast to the wt A_{2B}AR where PSB-21500 binds in a covalent, irreversible manner.[284] Thus, K267^{ECL3} is identified as the covalent binding partner for PSB-21500, despite the missing electron density for the linkage in our crystal structure.

Although the exact interactions of the ligand with K267^{ECL3} and the other residues in the orthosteric binding pocket could not be elucidated in this 4.0 Å resolution crystal structure, interesting initial insights into the PSB-21500-bound inactive state of the receptor were obtained. Nevertheless, a co-crystal structure at higher resolution would surely help to unravel further interesting details about this unique member of the AR family.

4 Conclusions

The elucidation of protein structures harbors great potential for the advancement of drug development.[322] One interesting emerging drug target is the A_{2B}AR,[124] due to its unique pharmacological profile, and upregulation under pathological conditions.[179, 184] Antagonists targeting the receptor hold particular promise for cancer and pain treatment,[175, 179] yet no antagonist-bound structure of the receptor has been reported. The aim of this thesis was to address the knowledge gap by generation of A_{2B}AR crystallization constructs, that facilitate A_{2B}AR crystallization in lipidic cubic phase (LCP), and ultimately elucidate the first antagonist-bound structure of the A_{2B}AR.

I. Generation of A_{2B}AR crystallization constructs

In the course of this project, the previously low-expressing and unstable A_{2B}AR was transformed into a well-expressing, highly stable receptor suitable for crystallization experiments. The generation of the crystallization constructs comprised the conceptualization, cloning, expression, purification and analysis of 233 different A_{2B}AR constructs, of which 174, namely TC59 – TC233, were processed in the course of this thesis. The favorable characteristics of the final crystallization constructs were achieved by addition of seven deliberately selected and combined point mutations, as well as an *N*-terminal linker sequence.

Four of the seven favorable point mutations, present in all successfully employed crystallization constructs, were introduced into the lower half of TM1, which is not expected to be involved in ligand binding. Most of the TM1 mutations were discovered by mutating every single amino acid that differs between the A_{2B}AR and the related A_{2A}AR to the respective analogous amino acid of the A_{2A}AR, and comparing the elution profile of the resulting constructs by analytical SEC and a CPM-based thermostability assessment. This strategy was based on the earlier observation that the A_{2B}AR is more stable after exchange of its entire TM1 for that of the A_{2A}AR.[252] Two additional mutations are located in the ECL2 of the receptor, where the two N-glycosylation sites were removed by replacing the respective asparagine residues by related glutamine residues to reduce potential heterogeneity.[102] The most crucial point mutation to increase receptor stability was the mutation S92$^{3.39}$K in the conserved Na^+ binding pocket. After the discovery of this mutation's positive effect on the stability of the A$_{2B}$AR, it had also been successfully employed for the stabilization of the A$_{2A}$- and the A$_3$AR.[259, 268] In case of the A$_{2A}$AR, the mutation facilitated the structure elucidation in complex with several ligands, which confirmed the structural basis for this mutation's effect: It permanently mimics the presence of the inactive state-stabilizing effect of the Na^+ ion through the protonated amino group in the side chain of the introduced lysine.[73, 107, 259] Lastly, the *N*-terminal linker sequence GSGS, introduced between a hemagglutinin tag and a FLAG tag of the A$_{2B}$AR constructs, further enhanced the protein yield of the receptor to a level that was sufficient for successful crystallization of the protein.

Figure 144 illustrates the modifications present in nearly all constructs that were employed for crystallization trials in this thesis.

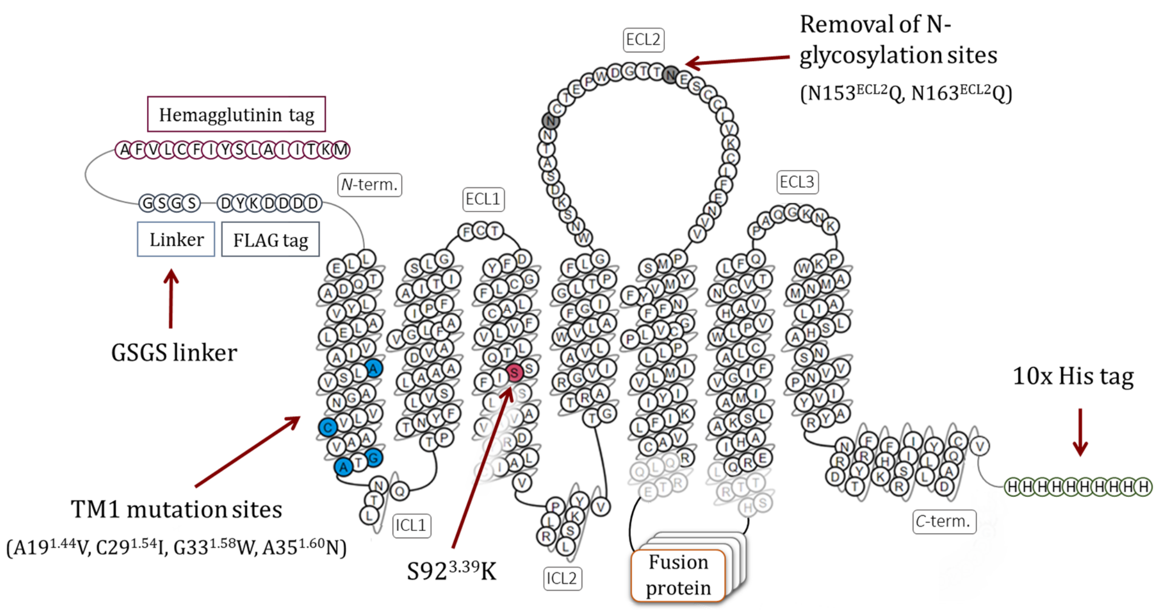

Figure 144. Snake plot representation of all modifications present in most of the utilized crystallization constructs of the A$_{2B}$AR. Snake plot modified from GPCRdb.[52]

II. Crystallization of the A$_{2B}$AR in LCP

A total of 17 different crystallization constructs, most of which were bearing various fusion proteins, but also different *N*- or *C*-terminal tags and linkers, were utilized in 49 different crystallization trials, performed using the LCP method. In these trials, the crystallization potential of the receptor was assessed in the presence of three different LCP-forming lipids, five different antagonists and thousands of different precipitant solution mixtures.

Generally, only the crystallization trials conducted with the xanthine-based in-house antagonists PSB-09120 and PSB-21500 resulted in notable crystal growth. The first protein crystals of the A_{2B}AR, evidenced by X-ray diffraction data, were obtained with construct TC190 in the presence of the newly developed covalent antagonist PSB-21500.[284] Of all crystallization constructs, TC190 was utilized most extensively in crystallization trials, alongside TC196, and their crystallization potential, specifically in the presence of PSB-21500, was thoroughly investigated. Part of these experiments were performed during a research stay at the biotechnology company leadXpro, located on the premises of the Paul-Scherrer Institute in Villigen, Switzerland. While sufficiently large protein crystals of 40 – 50 µm in size were produced from both of these constructs, their diffraction was limited to 6 – 7 Å, despite an exhaustive screening of different crystallization conditions. The limited reproducibility and diffraction quality of the A_{2B}AR crystals was attributed to an unfavorable packing of the molecules within the crystals. Therefore, based on construct TC190, eleven additional crystallization constructs with various other fusion proteins were crystallized in order to expand the possibilities of crystal packing and to detect a superior fusion partner and/or insertion site that would facilitate the growth of well-diffracting protein crystals.

That goal has been achieved with construct TC230, which yielded ~ 40 µm-large crystals in the presence of the covalent antagonist PSB-21500 in two different precipitant solutions, without extensive optimization, as had been necessary for the previous comparably large crystals of TC190. Even more importantly, the TC230 crystals exhibited improved X-ray diffraction of up to 3.5 Å. This diffraction data enabled the elucidation of the first antagonist-bound crystal structure of the A_{2B}AR at 4.0 Å resolution.

Figure 145 depicts the crystals which yielded the diffraction data used to solve the crystal structure of the A_{2B}AR.

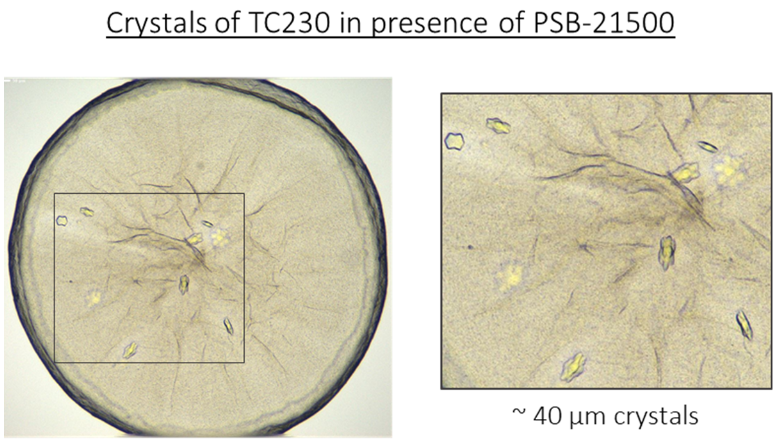

Figure 145. Picture of the TC230 crystals that enabled the structure determination of the $A_{2B}AR$.

III. Antagonist-bound crystal structure of the $A_{2B}AR$

Due to the limited resolution, most of the amino acid side chains are not resolved in the crystal structure. Therefore, a detailed analysis of ligand interactions is not feasible. Nevertheless, interesting information can be obtained from the structure:

i. Based on the α-helical arrangement, specifically of TM6, the structure proves that the antagonist-bound $A_{2B}AR$ with the Na^+-mimicking mutation $S92^{3.39}K$ is indeed present in the inactive state. Furthermore, a discrepancy regarding the position of the intracellular helix 8 is observed among the active and inactive state structures, that is not seen in the structures of the A_1- and $A_{2A}AR$. This potentially suggests a unique feature of $A_{2B}AR$ activation, which should be further explored.

ii. Although no electron density for amino acid side chains in the orthosteric pocket, or for the covalent linkage of PSB-21500 to the receptor, is observed, partial electron density for the ligand enabled its placement in the orthosteric binding pocket. The superposition with the recently published NECA-bound cryo-EM structure of the $A_{2B}AR$ implies a spatial proximity of residue $K267^{ECL3}$ to the suspected position of the sulfonyl fluoride warhead of PSB-21500. This suggests $K267^{ECL3}$ to be the covalent binding partner for the ligand, which was confirmed by radioligand binding data on the $A_{2B}AR$ $K267^{ECL3}A$ mutant. Moreover, the crystal structure indicates that the position of PSB-21500 in the orthosteric binding pocket is compatible with hydrogen bonding interactions of $N254^{6.55}$ with the C6-carbonyl group and *N*H7 of its xanthine scaffold. Importantly, however, the electron density for N254[6.55] is not sufficient to determine the side chain rotamer. Therefore, this hypothesis resides on the general position of PSB-21500 within the binding pocket, and identical interactions previously observed in X-ray structures of the A_1- and A_{2A}AR bound to xanthine derivatives.[281]

iii. Lastly, the obtained crystal structure provides insights into the packing of the molecules within the crystal and the position of the fusion partner T4L inserted into the ICL3 of the receptor. Examination of the insertion site revealed that the connection of the receptor and T4L is not formed by a continuous rigid α-helix, as predicted based on the AlphaFold model of the A_{2B}AR construct. Instead, the proteins are connected by a likely flexible linker. A slight movement of the insertion position between T4L and TM5 of the receptor might result in the anticipated rigid fusion and consequently promote the growth of even better-diffracting crystals, that could provide insights into further details which are still missing from the obtained crystal structure.

Figure 146 illustrates the obtained crystal structure of the A_{2B}AR in complex with PSB-21500.

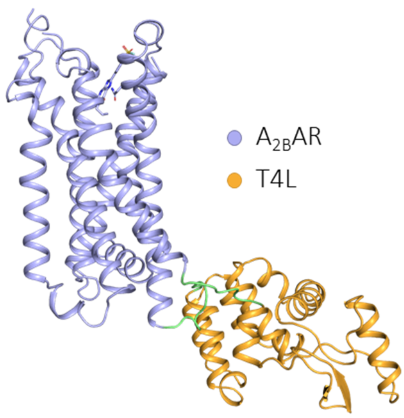

Figure 146. Solved crystal structure of the A_{2B}AR in complex with PSB-21500.

In summary, within this study, the previously low-expressing and unstable A_{2B}AR was transformed into a well-expressing and highly-stable protein. In complex with our new xanthine-based covalent antagonist PSB-21500, the optimized protein constructs showed a thermostability increase of approximately 30 °C compared to initial A_{2B}AR constructs. A total of 49 crystallization experiments with 17 different crystallization constructs culminated in the growth of up to 50 μm-large protein crystals and the elucidation of the first antagonist-bound crystal structure of the $A_{2B}AR$ at a resolution of 4.0 Å. The solved crystal structure provides valuable insights into the antagonist binding mode at the $A_{2B}AR$, and offers a clear strategy for future structural biology projects on this unique adenosine receptor subtype.

5 Experimental Part

5.1 Materials

5.1.1 DNA and primer

Table 8. Types of nucleic acids and their source.

Material	Source
Primer	Microsynth AG, Balgach, Switzerland
Plasmid	BioCat GmbH, Heidelberg, Germany

5.1.2 Molecular biology supply

Table 9. Enzymes used for molecular biology and their source.

Enzyme	Source
Phusion high fidelity polymerase	New England Biolabs, Ipswich, USA
Q5 high-fidelity polymerase	New England Biolabs, Ipswich, USA
Restriction enzymes, including DpnI	New England Biolabs, Ipswich, USA
RNAse A	Qiagen, Venlo, Netherlands
Taq polymerase	New England Biolabs, Ipswich, USA

Table 10. Bacteria used for molecular biology and their source.

Bacteria	Source
DH5α E. coli	Produced in-house, initial stock from ThermoFisher Scientic, Waltham, USA
DH10bac E. coli	ThermoFisher Scientic, Waltham, USA

Table 11. Reagents used for molecular biology and their source.

Reagents	Source
GC buffer, 5x	New England Biolabs, Ipswich, USA
DMSO	New England Biolabs, Ipswich, USA
dNTP mix, 10 mM each	New England Biolabs, Ipswich, USA
Resuspension buffer (P1)	Qiagen, Venlo, Netherlands
Lysis buffer (P2)	Qiagen, Venlo, Netherlands
Neutralization buffer (P3)	Qiagen, Venlo, Netherlands
Water, DEPC-treated	New England Biolabs, Ipswich, USA

Table 12. Kits used for molecular biology and their source.

Kit	Source
Zymoclean Gel DNA Recovery Kit	Zymo Research, Irvine, USA
ZymoPURE Plasmid Miniprep Kit	Zymo Research, Irvine, USA

Table 13. Antibiotics used for molecular biology and their source.

Antibiotic	Concentration	Source
Ampicillin sodium	100 mg/mL in H_2O	Cayman Chemical, Ann Arbor, MI, USA
Gentamicin sulfate	7 mg/mL in H_2O	Carl Roth, Karlsruhe, Germany
Kanamycin sulfate	50 mg/mL in H_2O	Carl Roth, Karlsruhe, Germany
Tetracycline	10 mg/mL in 70 % EtOH	Carl Roth, Karlsruhe, Germany

All water-based antibiotics were filter-sterilized through a 0.2 µm filter. Each antibiotic was stored at – 20 °C and diluted 1:1000 fold before use.

Table 14. Additives used for molecular biology and their source.

Additive	Concentration	Source
IPTG	40 mg/mL in H_2O	Carl Roth, Karlsruhe, Germany
X-Gal	100 mg/mL in H_2O	VWR, Radnor, USA

Both additives were filter-sterilized through a 0.2 µm filter and stored at – 20 °C. Before their use, they were diluted 1:1000 fold.

5.1.3 Cell culture supply

Table 15. Cells used for insect cell culture and their source.

Cells	Source
Sf9 insect cells	Oxford Expression Technologies, Oxford, UK
Tni insect cells	Oxford Expression Technologies, Oxford, UK

Table 16. Medium and reagents used for insect cell culture and their source.

Medium and reagents	Source
Anti-Gp64 PE-conjugated antibody	ThermoFisher Scientic, Waltham, USA
Anti-FLAG FITC-conjugated antibody	GenScript Biotech, Piscataway, USA
ESF921 cell culture medium	Expression Systems, Davis, USA
Transfection medium	Expression Systems, Davis, USA
X-tremeGENE HP DNA transfection reagent	Sigma-Aldrich, St. Louis, USA

Table 17. Material used for cell culture and their source.

Cell culture material	Source
125 mL Erlenmeyer flask	Corning, Corning, USA
125 mL Optimum Growth flask	Thomson, Oceanside, USA
500 mL Optimum Growth flask	Thomson, Oceanside, USA

1.6 L Optimum Growth flask	Thomson, Oceanside, USA
24-well deep well block, round bottom	Cytiva, Marlborough, USA

5.1.4 Protein purification supply

Table 18. Reagents used for protein purification and their source.

Reagent	Source
Cholesterol hemisuccinate	Sigma-Aldrich, St. Louis, USA
Dodecyl-β-D-maltoside	Anatrace Products LLC, Maumee, USA
Iodoacetamide	TCI, Tokyo, Japan
Protease inhibitor tablets, EDTA-free	Roche, Basel, Switzerland
TALON metal affinity resin	Takara Bio, Kusatu, Japan

Table 19. Material and machines used for protein purification and their source.

Material and machines	Source
Chromatography column (10 mL)	Bio-Rad, Hercules, USA
Chromatography column (0.8 mL)	Bio-Rad, Hercules, USA
Econo-Column chromatography column	Bio-Rad, Hercules, USA
PD-10 desalting column	Cytiva, Marlborough, USA
Superdex 200 increase 5/150 GL	Cytiva, Marlborough, USA
Superdex 200 increase 10/300 GL	Cytiva, Marlborough, USA
Vivaspin 6, 100 kDa MWCO concentrator	Sartorius, Göttingen, Germany
Vivaspin 500, 100 kDa MWCO concentrator	Sartorius, Göttingen, Germany
Avanti JXN-26 high capacity centrifuge	Beckman Coulter, Inc., Brea, USA
Optima L-100 XP ultracentrifuge	Beckman Coulter, Inc., Brea, USA

Table 20. Buffers used for protein purification and their composition.

Buffer	Composition
Elution buffer	25 mM HEPES pH 7.5, 0.8 M NaCl, 0.025 % DDM, 0.005 % CHS, 10 % (v/v) glycerol, 220 mM imidazole
High osmotic buffer	10 mM HEPES pH 7.5, 10 mM $MgCl_2$, 20 mM KCl, 1 M NaCl
Low osmotic buffer	10 mM HEPES pH 7.5, 10 mM $MgCl_2$, 20 mM KCl
Membrane resuspension buffer	10 mM HEPES pH 7.5, 10 mM $MgCl_2$, 20 mM KCl, 30 % (v/v) glycerol
Pre-wash buffer	50 mM HEPES pH 7.5, 0.8 M NaCl, 0.1 % DDM, 0.02 % CHS, 10 % (v/v) glycerol
Solubilization buffer	100 mM HEPES pH 7.5, 1.6 M NaCl, 2 % DDM, 0.4 % CHS
Wash buffer 1 (WB1)	50 mM HEPES pH 7.5, 0.8 M NaCl, 0.1 % DDM, 0.02 % CHS, 10 % (v/v) glycerol, 25 mM imidazole pH 7.5
Wash buffer 2 (WB2)	50 mM HEPES pH 7.5, 0.8 M NaCl, 0.05 % DDM, 0.01 % CHS, 10 % (v/v) glycerol, 50 mM imidazole pH 7.5

5.1.5 Protein crystallization supply

Table 21. Reagents used for protein crystallization.

Reagent	Source
Monoolein and cholesterol (10:1, premixed)	Anatrace Products LLC, Maumee, USA
Monopalmitolein	Nu-Chek Prep Inc., Elysian, USA
Monovaccenin	Nu-Chek Prep Inc., Elysian, USA
PEG/Ion 400 crystallization screen	Hampton Research, Aliso Viejo, USA
JBScreen LCP crystallization screen	Jena Bioscience GmbH, Jena, Germany
MemMeso crystallization screen	Molecular Dimensions Ltd., Sheffield, UK
MemGoldMeso crystallization screen	Molecular Dimensions Ltd., Sheffield, UK
Additive Screen HT	Hampton Research, Aliso Viejo, USA

StockOptions salt screen	Hampton Research, Aliso Viejo, USA
StockOptions pH buffer kit	Hampton Research, Aliso Viejo, USA
StockOptions sodium citrate buffer kit	Hampton Research, Aliso Viejo, USA
PEG 400	Hampton Research, Aliso Viejo, USA
PEG monomethyl ether 500	Sigma-Aldrich, St. Louis, USA

Table 22. Materials and machines used for protein crystallization.

Material and machines	Source
GASTIGHT 100 µL glass syringe	Hamilton Company, Reno, USA
Mosquito LCP syringe coupling	SPT Labtech Ltd, Melbourn, UK
Needle, 26 gauge, 0.375''	Hamilton Company, Reno, USA
LCP sandwich set	Paul Marienfeld GmbH & Co. KG, Lauda-Königshofen, Germany
Pressurized gas cleaner	DURABLE Hunke & Jochheim GmbH & Co. KG, Iserlohn, Germany
NT8 protein crystallization robot	Formulatrix IHL Ltd., Dubai, UAE
Rock Imager 54 protein crystallization imager	Formulatrix IHL Ltd., Dubai, UAE

5.1.6 Protein analysis supply

Table 23. Reagents used for protein analysis and their source.

Reagent	Source
CPM	ThermoFisher Scientic, Waltham, USA
Coomassie R-250	Carl Roth GmbH & Co. KG, Karlsruhe, Germany
ECL substrate	ThermoFisher Scientic, Waltham, USA
PageRuler prestained protein ladder	ThermoFisher Scientic, Waltham, USA

Table 24. Material and machines used for protein analysis and their source.

Material and machines	Source
Nanofilm SEC-250, 4.6 x 250 mm	Sepax Technologies, Newark, USA
Superdex 200 increase 5/150 GL	Cytiva, Marlborough, USA
Superdex 200 increase 10/300 GL	Cytiva, Marlborough, USA
1260 Infinity LC System	Agilent, Santa Clara, USA
Mini-PROTEAN electrophoresis chamber	Bio-Rad, Hercules, USA
Trans-Blot Turbo Transfer System	Bio-Rad, Hercules, USA
Colibri Microvolume Spectrometer	Berthold Detection Systems GmbH & Co. KG, Pforzheim, Germany
Rotor-Gene Q 6plex real-time PCR machine	Qiagen, Venlo, Netherlands
Guava easycyte 5-HT	Merck KGaA, Darmstadt, Germany

Table 25. Buffers used for protein analysis and their composition.

Buffer	Composition
HPLC buffer	25 mM HEPES pH 7.5, 0.5 M NaCl, 2 % (v/v) glycerol, 0.05 % DDM, 0.01 % CHS
PBS-T	1.15 g/L Na_2HPO_4, 0.2 g/L KCl, 0.2 g/L KH_2PO_4, 8 g/L NaCl, 0.1 % Tween 20
SDS-PAGE buffer	50 mM MOPS, 50 mM Tris, 1 mM EDTA, 0.1 % SDS
Transfer buffer	48 mM Tris, 39 mM glycine, 10 % ethanol, 0.1 % SDS

5.1.7 Crystal harvesting and shipment supply

Table 26. Materials and machines used for crystal harvesting and shipment.

Material and machines	Source
Microscope	Olympus Life Science, Waltham, USA
Dual Thickness MicroMounts, various sizes	MiTeGen, Ithaca, USA
B5 goniometer bases	MiTeGen, Ithaca, USA
Uni-Puck Starter Kit	Jena Bioscience GmbH, Jena, Germany

5.1.8 Software

The analytical SEC and thermostability data were analyzed using GraphPad Prism (Graphpad Software, Inc.) version 7.0.0 and 10.0.3. All illustrations of protein structures were performed with PyMol (Schrödinger, Inc.) version 2.3.4, except for Figure 1 and Figure 16 which were illustrated using ChimeraX (UCSF) version 1.7.[323] BioRender (www.biorender.com) was employed to generate Figure 2, Figure 7, Figure 10, Figure 19 and Figure 20.

5.2 Methods

As mentioned in section 1.7.1 of the introduction, the crystallization of membrane proteins, such as the $A_{2B}AR$, often requires extensive sequence modifications including point mutations and the introduction of fusion proteins, linkers and various tags. On this account, any membrane protein crystallography project begins with extensive construct optimization, until the protein shows sufficient stability and yield, to be utilized in a crystallization experiment.

5.2.1 Molecular biology

To attain a sufficient protein yield, the high-level expression of the protein of interest is one of the central prerequisites. For the expression of the recombinant $A_{2B}AR$, we utilized *Spodoptera frugiperda* (*Sf9*) and *Trichoplusia ni* (*Tni*) insect cells in an adapted protocol of the Bac-to-Bac Baculovirus Expression System by Invitrogen. This system works by transferring an expression cassette, carried by the pFastBac1™ donor plasmid, into a baculovirus shuttle vector (referred to as "bacmid") through site-specific transposition.[324] For this reason, all $A_{2B}AR$ constructs were cloned into the pFastBac1™ vector, and all receptor sequence modifications were carried out in this setting.

5.2.1.1 $A_{2B}AR$ sequence modification

The sequence modifications, discussed in this thesis, were all performed in-house, with the exception of the constructs TC223 to TC233, which were synthesized by BioCat.

<u>Point mutations and deletions</u>

All primers that were utilized to introduce point mutations and sequence deletions were designed using the Agilent Quikchange Primer Design Program. They were deployed in the polymerase chain reaction (PCR) protocol, given in Table 27. Table 28 specifies the thermocycler program that was typically used.

Table 27. Pipetting scheme for the Quikchange PCR.

Reagent	Amount
5x GC buffer	5 µL
Template DNA	100 – 150 ng
dNTP mixture, 10 mM each	0.6 µL
Forward Primer, 5 µM	0.6 µL
Reverse Primer, 5 µM	0.6 µL
DMSO	0.25 µL
Phusion high fidelity DNA polymerase (2000 U/mL)	0.3 µL
PCR grade water	Ad 26 µL

Table 28. Thermocycler program for the Quikchange PCR.

Step	Temperature (°C)	Time (s)	
Initial denaturation	98	180	
Denaturation	98	30	20 cycles
Annealing	58	45	
Elongation	72	300	
Final elongation	72	600	

Overlap extension PCR

For the introduction and exchange of larger sequence parts, such as the fusion partners, the overlap extension PCR was used. It requires two steps:

I. The generation of "mega primers" in a first PCR, containing the desired insert, flanked by approximately 25 bp long 3' and 5' ends, that are specific for the intended insertion site within the vector.
II. A second PCR, in which the generated "mega primers" bind to the vector with their 3' and 5' ends and enable the amplification of the chimeric sequence.

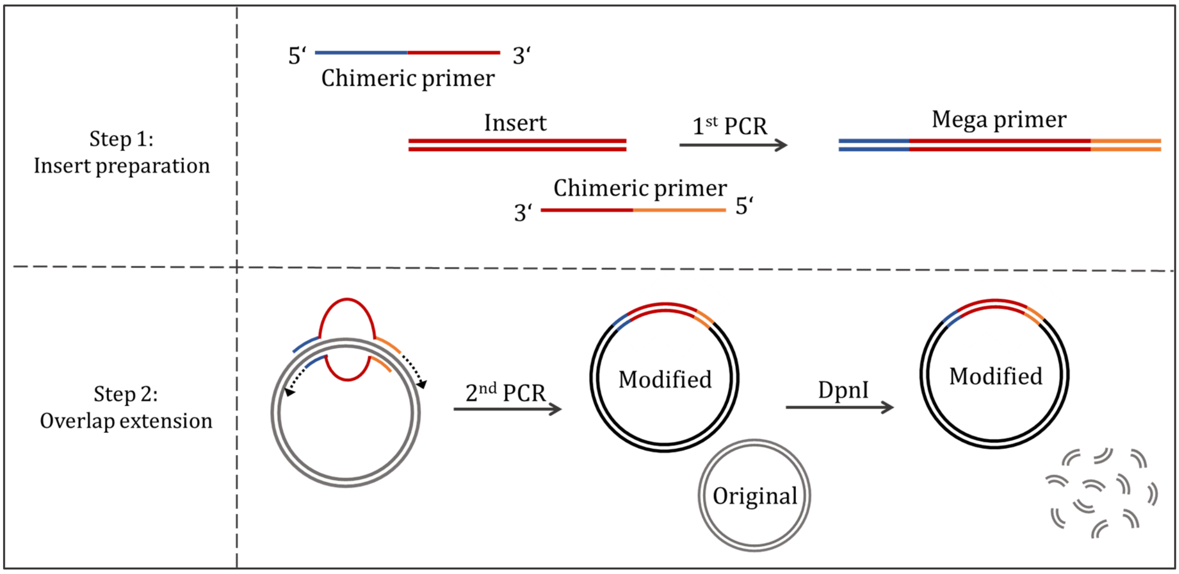

Figure 147. Outline of the overlap extension PCR procedure.

The pipetting scheme and thermocycler program for the "insert preparation" PCR is given in the following Table 29 and Table 30.

Table 29. Pipetting scheme for the insert preparation PCR.

Reagent	Amount
5x Q5 reaction buffer	10 µL
Template DNA	0.5 µL
dNTP mixture, 2.5 mM each	1 µL
Forward Primer, 5 µM	2 µL
Reverse Primer, 5 µM	2 µL
Q5 high fidelity DNA polymerase (2000 U/mL)	0.5 µL
PCR grade water	34 µL

Table 30. Thermocycler program for the insert preparation PCR.

Step	Temperature (°C)	Time (s)	
Initial denaturation	95	180	
Denaturation	95	30	30 cycles
Annealing	55	60	
Elongation	68	90	
Final elongation	68	600	

The amplified “mega primers” were purified by application to a 1.5 – 2 % agarose gel, followed by their extraction from the gel using the Zymoclean Gel DNA recovery kit. The primers were then utilized in the second “overlap extension” PCR. The pipetting scheme, as well as the thermocycler program of this PCR, are given in Table 31 and Table 32, respectively.

Table 31. Pipetting scheme for the overlap extension PCR.

Reagent	Amount
5x GC buffer	4 µL
Template DNA	0.2 µL
dNTP mixture, 10 mM each	0.6 µL
$MgCl_2$, 50 mM	0.2 µL
Mega primer	200 ng
Phusion high fidelity DNA polymerase (2000 U/mL)	0.4 µL
PCR grade water	Ad 20 µL

Table 32. Thermocycler program for the overlap extension PCR.

Step	Temperature (°C)	Time (s)	
Initial denaturation	98	180	
Denaturation	95	30	25 cycles
Annealing	58	60	
Elongation	72	300	
Final elongation	72	300	

5.2.1.2 Plasmid amplification and preparation

<u>Transformation in DH5α E. coli bacteria</u>

Prior to their transformation, all PCR products were digested with DpnI (10 – 20 U/reaction) for 30 min to 120 min to remove the plasmids of bacterial origin. Without heat inactivation, 5 µL of the PCR products was added to 50 µL of DH5α E. coli suspension and incubated on ice for 30 min. The heat shock was executed for 45 sec in a 42 °C water bath. After a short incubation on ice, 100 µL of LB medium was added and the bacteria were shaken at 350 rpm for 60 min at 37 °C. Afterwards, the complete volume was spread on LB agar plates containing 100 µg/mL ampicillin. The plates were incubated overnight at 37 °C.

<u>Overnight cultures, plasmid DNA preparation & verification</u>

Overnight cultures were set up by picking 1-2 single colonies per construct from the LB agar plates with pipette tips and submerging them in 5 mL of LB medium each, to which 100 µg/mL ampicillin was freshly added. The cultures were incubated shaking overnight at 37 °C, 220 rpm in a bacteriological incubator. The next day, the bacteria were spun down at 4000 g for 10 min, and amplified plasmid DNA was isolated using the ZymoPURE Plasmid Miniprep Kit from Zymo Research. Typical yields were 300 – 500 ng/µL. 1 – 2 µg of plasmid DNA was sent to Eurofins Genomics for sequencing. The standard sequencing primers are given in the following:

pFastBacF: 5'-TCCGGATTATTCATACCGTCCC-3'

pBakPAC-FP: 5'-TAAAATGATAACCATCTCGC-3'

pFastBacR: 5'- CCTCTACAAATGTGGTATGGCTG-3'

5.2.1.3 Generation of recombinant bacmid DNA

In order to obtain recombinant bacmid DNA, that can be used for the production of baculovirus, the gene of interest needs to be integrated into a baculovirus shuttle vector. This integration takes place through site-specific transposition, enabled by the presence of the mini-Tn7 transposon sequences in the pFastBac1™ plasmid, as well as the mini-*att*Tn7 target site on the bacmid DNA within the DH10bac E. coli cells.[324]

<u>Transformation in DH10bac E. coli cells</u>

Practically, this generation of recombinant bacmid DNA was achieved by adding 500 ng of purified of the pFastBac1™ plasmid to 50 µL chemically competent DH10bac E. coli cells cells and applying a heat shock of 42 °C for 45 sec. Subsequently, 800 µL of room-temperature LB medium was added and the suspension was incubated for 4 h at 37 °C, shaking at 350 rpm. Later, a fraction of the bacteria was added to LB agar plates containing 10 µg/mL tetracycline, 7 µg/mL gentamicin, 50 µg/mL kanamycin, 40 µg/mL IPTG 100 µg/mL X-Gal. The plates were incubated at 37 °C for 48 h, before differentiating between blue and white colonies.

The blue color of colonies indicates that the previously outlined transposition was not successful, therefore resulting in an undisrupted expression of the LacZα peptide, which, in consequence, restores the function of an otherwise deficient ß-galactosidase. The then functional ß-galactosidase cleaves its substrate, the colorless X-Gal, into galactose and 5-bromo-4-chloro-3-hydroxyindole, that dimerizes and oxidizes to form blue 5,5'-dibromo-4,4'-dichloro-indigo. Upon successful transposition of the gene of interest, however, the expression of the LacZα peptide is impeded. As a result, no functional β-galactosidase and no blue product is formed, which provides the possibility to differentiate between clones in which the transposition was successful or unsuccessful.[324, 325]

Bacmid DNA preparation and verification

Therefore, the next step towards the baculovirus production was to set up overnight cultures from the white colonies, and purify the recombinant bacmid DNA from the bacteria. Due to its large size and in contrast to the plasmid DNA preparation mentioned in chapter 5.2.1.2, the bacmid DNA was isolated by precipitation in 2-propanol, instead of binding and elution from a silica-based matrix. Typically, 5 mL of overnight culture resulted in a DNA concentration of approximately 2000 ng/μL in 30 μL.

To further verify the presence of the gene of interest within the purified bacmid DNA, a bacmid verification PCR was performed. Table 33 and Table 34 specify the pipetting scheme and thermocycler program that was used for this PCR.

Table 33. Pipetting scheme for the bacmid verification PCR.

Reagent	Amount
10x Taq buffer	2.5 μL
Bacmid DNA	1 μL
dNTP mixture, 10 mM each	0.5 μL
pUC/M13 forward primer	0.5 μL
pUC/M13 reverse primer	0.5 μL
Taq DNA polymerase (5000 U/mL)	0.15 μL
PCR grade water	Ad 25 μL

Table 34. Thermocycler program for the bacmid verification PCR.

Step	Temperature (°C)	Time (s)	
Initial denaturation	95	30	
Denaturation	95	30	25 cycles
Annealing	58	60	
Elongation	68	180	
Final elongation	72	300	

The primers that are utilized in this PCR bind to regions of the bacmid DNA that flank the site of transposition. Therefore, if the purified bacmid DNA does not contain the gene of interest, a DNA fragment of only 300 bp in size is amplified. In the other case, parts of the transposed pFastBac1™ vector as well as the full gene of interest are amplified, resulting in a DNA fragment of 2300 bp + size of gene of interest. An agarose gel electrophoresis with an 1 % agarose gel is performed to visualize the PCR products and differentiate between an "empty" and a recombinant bacmid. This allows for an additional layer of assurance regarding the existence of the gene of interest in the bacmid DNA, before the transfection of the bacmid is performed.

5.2.2 Protein expression

5.2.2.1 Transfection of bacmid DNA for baculovirus production

For the transfection, 5 µL of the freshly purified and verified bacmid DNA was gently mixed with 103 µL of transfection mix, consisting of 100 µL transfection medium and 3 µL of the transfection reagent X-tremeGENE HP. Upon incubation for 15 min at room temperature (RT), the mixture was added to one well of a 24 deep-well plate, filled with 2.5 mL of a *Sf9* cell suspension that was at a density of 1 x 10^6 cells/mL. The cells were incubated for 96 h in a thermoshaker set at 27 °C, 400 rpm. After this incubation, the cell suspension was centrifuged for 15 min at 570 g to harvest the virus-containing supernatant (P0). The virus was stored at 4 °C in the dark, until further use.

5.2.2.2 Gp64 assay

Each time, the success of the transfection was evaluated by flowcytometry in the "Gp64 assay". Gp64 (glycoprotein 64) is the major baculoviral glycoprotein which is expressed on the surface of infected insect cells,[326] therefore quantification of Gp64 expression levels allows for conclusions regarding the efficiency of infection.

For this assay, 5 µL of the transfected cell suspension was combined with 5 µL of a phycoerythrin (PE)-conjugated anti-Gp64 antibody solution, which was diluted 1:100 in Tris-buffered saline (TBS) with 4 % bovine serum albumin (BSA). The mixture was incubated for 20 min at 4 °C, before the addition of 90 µL TBS and measurement in the flow cytometer. Upon excitation of the probes at 496 nm, their fluorescence was measured and quantified at an emission wavelength of 578 nm.

5.2.2.3 Expression of recombinant protein

Depending on the scope of the subsequent experiments, the proteins of interest were either expressed in small- or large-scale. For the optimization of the construct, the various proteins were evaluated in regards to their monodispersity and (thermal) stability. This could be achieved with comparably small amounts of protein, wherefore small-scale expressions were sufficient for these initial tests. Once the protein was sufficiently stable for crystallization, large-scale expressions were necessary in order to yield the required amount of protein.

Small-scale expression

For the small-scale expressions, 400 µL of the above-mentioned P0 was used to infect 40 mL of *Sf9* suspension cells at a density of 2 – 3 x 10^6 cells/mL. Typically, the infection was performed for 48 h at 27 °C and 160 rpm on a 20 mm amplitude shaker. After the incubation period, the cells were spun down for 15 min at 4,000 g, to separate the cells from the virus-containing supernatant (P1). The pelleted cells, expressing the recombinant protein, were stored at - 80 °C until further use. This same routine was also utilized to further amplify the P1 virus, to generate the more potent P2, or even P3 virus prior to large scale expressions.

Large-scale expression

Large-scale expressions were performed by adding 6 mL of either P1, P2 or P3 virus to 1 L of *Sf9* suspension cells at a density of 2 – 3 x 10^6 cells/mL. Again, the cells were typically incubated for 48 h to 72 h at 27 °C and 160 rpm on a 20 mm amplitude shaker. To harvest the cells, the suspension was spun down for 30 min at 4,000 g. After the removal of the supernatant, the pelleted cells were resuspended in approximately 30 mL of phosphate-buffered saline (PBS) and spun down once more for 20 min at 4,000 g. As before, the supernatant was removed and the biomass stored at - 80 °C until further use.

5.2.2.4 FLAG assay

In order to evaluate the success of each expression, the FLAG assay is utilized. With the exception of using a different antibody, the FLAG assay is based on the same approach as the Gp64 assay. 5 µL of infected cell suspension was incubated with 5 µL of a fluorophore-conjugated antibody solution, and incubated for 20 min at 4 °C, before addition of another 90 µL of TBS and measurement in a flow cytometer. However, instead of the anti-Gp64 antibody, two different solutions of fluorescein isothiocyanate (FITC)-conjugated anti-FLAG antibody was used, one with 0.15 % Triton X-100 to permeabilize the cells,[327] and one without. Also, the 10 µg/mL of the membrane impermeant 7-aminoactinomycin D (7-AAD) was added to both antibody solutions, which is a fluorochrome that binds to double-stranded DNA and therefore stains non-viable cells.[328] In this set-up, it is possible to quantify

i. the surface expression of the FLAG-tagged protein,
ii. the total expression (due to addition of Triton X-100),
iii. the viability of the cells.

Also, by comparison of the surface and total expression, the assay allows for conclusions regarding the localization of the protein of interest. The readout for this assay is performed at λ_{ex} 488 nm and λ_{em} 525 ± 15 nm for the FITC signal, and λ_{ex} 488 nm and λ_{em} 695 ± 25 nm for the 7-AAD signal.

5.2.3 Protein purification

In the subsequent section, the standard protocols for the small- and large-scale protein purifications are outlined. To obtain detailed information regarding the specifics of each significant purification discussed in this thesis, please consult section 7.1 in the appendix, which provides a comprehensive compilation of all relevant aspects.

5.2.3.1 Membrane preparation

For both the small-scale analysis of proteins and the crystallization of proteins, a sample with a high degree of purity is necessary. Since the A_{2B}AR is a membrane protein, it is helpful to remove the large amount of soluble proteins and other soluble contaminants prior to the actual purification, in a process called membrane preparation.

Small-scale

The cells from small-scale expression experiments were lyzed by resuspension in 25 mL of low osmotic buffer, containing an adequate amount of EDTA-free protease inhibitor, using a glass dounce homogenizer. Upon centrifugation for 30 min at 48,000 – 57,000 g at 4 °C, the supernatant was discarded and the pellets were resuspended in 25 mL of high osmotic buffer, which additionally contained 1 M NaCl. Once again, the suspension was centrifuged at 48,000 – 57,000 g at 4 °C for 30 – 45 min. Lastly, the pellets were resuspended in a final volume of 3 mL of resuspension buffer by dounce homogenization, flash frozen in liquid nitrogen and stored at - 80 °C until further use.

Large-scale

Two different protocols for the membrane preparation from large-scale expressions were used:

a. A protocol involving five membrane washing steps for expressions up to 1 L.
b. An adapted protocol involving only three, modified washing steps for expressions from 2 L of cell suspensions.

For the first protocol, the cells from a 1 L expression were disrupted by dounce homogenization with approximately 120 mL of low osmotic buffer with the respective amount of EDTA-free protease inhibitor. Afterwards, the cells were centrifuged at 48,000 – 57,000 g at 4 °C for 30 – 45 min. The supernatant was discarded and the washing with low osmotic buffer was repeated once more. Upon this, the pellets were homogenized threefold with approximately 120 mL of high osmotic buffer each time, with centrifugation steps in between at 48,000 – 57,000 g and 4 °C, for 45 min. The washed membranes were then homogenized with 50 mL of resuspension buffer, flash frozen in liquid nitrogen and stored at - 80 °C until further use.

For the adapted protocol, the cells from a 2 L expression were dounce homogenized in 300 mL low osmotic buffer with the appropriate amount of protease inhibitor. The suspension was stirred for 1 h at 4 °C, prior to the centrifugation step for 1 h at 57,000 g and 4 °C. The pellet of the lyzed cells was then resuspended in 300 mL high osmotic buffer in a dounce homogenizer, and again stirred for 1 h at 4 °C prior to the centrifugation at 57,000 g at 4 °C for 1 h. This washing step with high osmotic buffer was repeated once more, and finally the membrane pellets were weighed and homogenized in resuspension buffer. Depending on the weight of the membranes, the amount of resuspension buffer was adapted to yield a final concentration of 200 mg/mL of membrane, to enhance the reproducibility and comparability between different experiments. Again, the resuspended membranes were flash frozen in liquid nitrogen and stored at - 80 °C until further use.

5.2.3.2 Solubilization

In order to purify a membrane protein, it must be extracted from its native membrane environment. To do so without denaturating the protein, mild detergents such as Dodecyl-β-D-maltoside (DDM), lauryl maltose neopentyl glycol (LMNG), and cholesteryl hemisuccinate (CHS) are added to the sample in the process called solubilization. The process is very similar between a small-scale and large-scale purification.

Small-scale

For the small-scale solubilization, the frozen, resuspended membranes were thawed on ice. By choice, the protein was either purified in apo state, or 25 – 50 µM of ligand were added to the sample and incubated for 30 min while slowly turning end-over-end at 4 °C. This allows the ligand to bind before the addition of the thiol-alkylating agent iodoacetamide, which was added at a concentration of 2 mg/mL, and also incubated for 30 min while turning end-over-end at 4 °C. Afterwards, the solubilization buffer with the detergents was added. The final condition during the small-scale purifications were typically as follows: 50 mM HEPES, 800 mM NaCl, 1 % DDM, 0.2 % CHS and 12.5 – 25 µM ligand. The membranes were incubated in this buffer for 3 h, turning end-over-end at 4 °C, again. After this incubation period, the samples were centrifuged for 30 min at 10,000 – 20,000 g and the membrane protein-containing supernatant was collected for further use.

Large-scale

The large-scale solubilization was performed similarly to the small-scale solubilization described above. The membranes were thawed on ice, and the desired type and concentration of ligand was added to the sample, and incubated for 30 min at 4 °C, turning end-over-end. Next, iodoacetamide was added at a concentration of 1 – 2 mg/mL and the samples were incubated in the same way. The solubilization buffer was added and the samples incubated for 2 – 3 h, as described before. The final concentration of the buffer components was typically 50 mM HEPES, 800 mM NaCl, 0.75 – 1.5 % DDM, 0.15 – 0.3 % CHS and 12.5 – 25 µM ligand. In case the membrane concentration was determined beforehand, the samples were diluted to 100 mg/mL of membrane, for the process of solubilization. After the incubation, the solubilized protein was separated from the membranes by centrifugation at 48,000 – 57,000 g for 30 – 60 min. The supernatant was collected for the further purification procedure.

5.2.3.3 Immobilized metal affinity chromatography

During the solubilization, not only the protein of interest, but all membrane proteins get extracted from the native membrane. Therefore, the next step in the purification procedure was the immobilized metal affinity chromatography (IMAC), that enables the separation of the protein of interest from the other membrane proteins.

Small-scale

In small-scale purifications, 20 mM of imidazole (pH 7.5) was mixed into the solubilization supernatant, before the addition of typically 12.5 µL of Talon metal affinity resin. The samples were incubated overnight at 4 °C, slowly turning end-over-end.

Large-scale

When performing large-scale purifications, the amount of Talon metal affinity resin added to each sample ranged from 250 µL to 2 mL, depending on the amount of biomass used for solubilization. Also in this case, each sample was mixed with imidazole (pH 7.5) to reach a final concentration of 20 mM. The incubation of the supernatant with the resin varied from 3 h to overnight, with end-over-end rotation at 4 °C in both cases.

5.2.3.4 Column purification

Small-scale

The next morning, the resin was spun down for 5 min at 100 g to pellet it and remove the majority of the supernatant. The residual supernatant was used to resuspend the resin, and transfer it to an empty plastic column. The resin was washed with 750 µL of wash buffer 1, containing 25 mM imidazole, and 500 µL of wash buffer 2, containing 50 mM imidazole. The protein was eluted from the resin by addition of 1 x 25 µL and 2 x 50 µL elution buffer, containing 220 mM imidazole. Between each step, the columns were briefly centrifuged to remove unwanted, residual buffer and to prevent variations in the elution volume, that could lead to incorrect conclusions about the protein yield.

Large-scale

After its incubation time with the solubilized sample, the resin was spun down at 100 g for 5 min before the majority of the supernatant was removed. To ensure a good drainage of the wash and elution buffers from the packed resin later, the residual solubilization buffer was most often removed by pre-washing the resin 3 times in 5 x the respective amount of resin. The amount of resin is also referred to as one column volume (CV). The buffer used for this pre-wash step consisted of 50 mM HEPES pH 7.5, 800 mM NaCl, 0.1 % DDM; 0.02 % CHS and 10 % glycerol.

Subsequently, the resin was transferred to chromatography columns to further wash the resin and elute the protein of interest. The utilized columns were either empty gravity-flow chromatography columns or XK chromatography columns, which were attached to a FPLC system for faster and more precise washing and eluting of the protein.

In both cases, the wash and elution conditions were as follows:

i. 10 – 30 CV wash buffer I:
50 mM HEPES (pH 7.5), 800 mM NaCl, 0.1 % DDM, 0.02 % CHS, 10 % glycerol, 10 mM $MgCl_2$, 8 mM ATP (pH 7.0), 25 mM imidazole (pH 7.5)
ii. 10 – 20 CV wash buffer II:
25 mM HEPES (pH 7.5), 800 mM NaCl, 0.05 % DDM, 0.01 % CHS, 10 % glycerol, 50 mM imidazole (pH 7.5)
iii. 3 – 6 CV elution buffer:
25 mM HEPES (pH 7.5), 800 mM NaCl, 0.025 % DDM, 0.005 % CHS, 10 % glycerol, 220 mM imidazole (pH 7.5)

When the empty gravity-flow chromatography columns were used, the elution buffer was added to the resin in three separate steps, with 10 min of incubation time each. In contrast, when utilizing an FPLC system, the elution buffer was not incubated with the resin. Instead, the resin was continuously washed with the elution buffer, and only the eluted fractions that contained protein, as detected by the FPLC system's UV-detector at 280 nm, were pooled.

5.2.3.5 Preparation of the protein for crystallizations

Large-scale

Successful crystallization experiments require a high concentration, purity and monodispersity of the protein sample. Enhancing the purity and monodispersity of the protein sample must not solely depend on optimizing the purification procedures or the protein stabilization, as detailed in section 1.7 of the introduction. Another approach to improve these characteristics involves the additional application of a preparative SEC, which enables the separation of differently disperse protein populations.

To perform the preparative SEC, the eluted protein of interest was concentrated to an appropriate volume of approximately 600 – 700 µL. For the concentration, the protein was transferred to either Vivaspin or Amicon concentrators with a MWCO of 100 kDa, and centrifuged at 1000 – 2000 g until the desired volume was reached, with resuspension every 5 – 10 min. Afterwards, the protein was injected onto an equilibrated preparative SEC column, namely a Superdex 200 Increase 10/300 GL column. The equilibration and running buffer typically consisted of 25 mM HEPES (pH 7.5), 800 mM NaCl, 0.02 % DDM and 0.002 % CHS. After injection of the protein, the column was washed with 1 CV of running buffer and the flow-through was fractionated in fractions of 250 µL. The fractions with the desired, monodisperse protein of interest were pooled.

Only few of the purifications mentioned in this thesis were additionally processed by the preparative SEC, as detailed in section 7.1 in the appendix. Most of the proteins were either finally concentrated directly after their elution from the Talon metal affinity resin, or after an intermediary desalting step.

The desalting step, for example, enabled the removal of the high concentration of imidazole (220 mM) which is present in the elution buffer and potentially affects the protein stability. For this purpose, 2.5 mL of the freshly eluted protein was each loaded onto one PD-10 desalting column, which had previously been equilibrated with 10 CV of the desired buffer (typically 25 mM HEPES (pH 7.5), 800 mM NaCl, 0.025 % DDM and 0.005 % CHS, 10 % glycerol). The protein was eluted in the desired buffer by addition of another 3.5 mL of this buffer to the column.

For the final concentration, the protein samples were transferred to Vivaspin or Amicon concentrators with a molecular weight cut-off (MWCO) of 100 kDa, and centrifuged at 500 – 2000 g until the desired volume or concentration was reached. The concentration was assessed using a UV/Vis spectrophotometer, taking into consideration the protein’s extinction coefficient, which was calculated using the ProtParam tool provided by the Swiss Institute of Bioinformatics. After the final concentration, the protein sample was typically spun down at > 20,000 g, at 4 °C for 15 min to remove any insoluble aggregates that may have formed during the concentration of the sample.

5.2.4 Crystallization in LCP

As noted in section 1.7.6 of the introduction, the crystallization of membrane proteins, such as the A_{2B}AR, often relies on the use of the membrane-mimetic LCP.[206]

5.2.4.1 Formation of the LCP

The protocol for the formation of the LCP depends on the hosting lipid component, which is used. During this study, three different hosting lipids, namely MO, MP and MV were used. The most commonly used MAG, MO, was additionally doped with 10 % cholesterol, which is extensively used as an additive lipid for LCP crystallizations of GPCRs to increase their stability.[206, 238]

To form the LCPs, each lipid had to be thoroughly mixed in a distinct ratio with the freshly prepared, concentrated protein solution. For LCP made from MO/cholesterol (9:1) this ratio is 3:2, e.g. 30 µL of MO/cholesterol (9:1) was mixed with 20 µL of the protein solution. For LCP made with monopalmitolein (MP) or monovaccenin (MV), however, that ratio was 1:1, hence e.g. 20 µL of these lipids had to be mixed with 20 µL of protein solution. The mixing was performed by using two 100 µL (Hamilton) glass syringes which could be connected with a low-volume syringe coupler.

To facilitate the pipetting and mixing of the lipids, that had previously been kept in aliquots at - 20 °C, the lipids were melted at 40 – 50 °C for a few minutes, before an excess of the lipid was transferred to a likewise prewarmed glass syringe. Next, the desired amount of protein solution was pipetted into the second, room tempered glass syringe, and the exact volume was visually determined. Thereupon, the syringe coupler was connected to the protein-filled syringe, and the protein solution was carefully pushed into the coupler. The respective surplus of lipid was released from its syringe, until only the desired amount of lipid was left. The lipid syringe was then connected to the coupler as well. After a short incubation period, that enabled the equalization of the temperatures of the components, the components were thoroughly mixed by moving them back and forth trough the coupler with the plungers of the syringes. To prevent friction and heating of the sample, the mixing was performed at approximately 1 stroke/s. The mixing was stopped when a uniformly transparent LPC appeared. When this was achieved, all of the LCP was pushed into the one syringe, which originally harbored the protein solution, so that the second syringe and the coupler could be removed. Then, a low-volume needle was tightly mounted onto the LCP-filled syringe to prepare for the subsequent dispensing of the LCP, described in the following section.

5.2.4.2 Setting up 96-well crystallization plates

To grow crystals in LCP, typically a small volume of the protein-infused LCP is dispensed on 96-well glass sandwich plates, which is subsequently overlaid with an excess of a precipitant solution.

The precipitant solutions usually consist of the following components:

i. A buffer, e.g. HEPES, Tris, or sodium citrate,
ii. one or multiple salts,
iii. PEG of a certain average molecular weight, e.g. PEG 400,
iv. and optionally an additive.

They are typically set up or provided in a 96-well format, where each well is filled with a different type or concentration of the above-mentioned components.

To screen the influence on the crystal formation of as many precipitant solutions as possible, just 40 – 50 nL of the LCP is placed on each well of the 96-well glass plate. Given this limited volume, as well as the high viscosity of the LCP, the dispensing was not performed by hand, but by use of specific humidity-controlled pipetting robots, such as the NT8 robot from Formulatrix. Crystallization robots enable the consistent dispensing of the LCP and precipitant solution, prevent water evaporation and destabilization of the sample, and therefore improve the reproducibility of the crystallization trials.

For setting up the crystallization plates, the robots were instructed to dispense 40 – 50 nL of LCP from the glass syringe onto each well of the base of a 96-well glass sandwich plate. Following that, 800 µL of precipitant solution were coated on each LCP drop. The relative humidity during this procedure was set to 80 %, and the temperature was typically around 20 °C. The drops were sealed with a second glass plate, which was tightly attached to the sticky film on the base glass plate in order to prevent evaporation of water during the incubation of the 96-well crystallization plates. Subsequently, the plates were incubated for several weeks in a temperature-controlled imager set to 20 °C, which photographed each drop at specific times. The pictures were taken in normal, and optionally cross-polarized light. The crystals were identified by visual inspection of said images.

5.2.5 Protein analysis

Many proteins, particularly membrane proteins, will not crystallize in their wildtype (wt) form. For this reason, many sequence modifications on the $A_{2B}AR$ were required to stabilize the receptor sufficiently for crystallization attempts, as previously introduced and described (see chapter 5.2.1.1). In order to characterize the protein and to assess the effect of said sequence modifications, the purified proteins were analyzed in several ways, which will be described in this following section.

5.2.5.1 Sodium dodecyl sulfate – Polyacrylamide gel electrophoresis

To assess the actual purity of the purified proteins, a sodium dodecyl sulfate – polyacrylamide gel electrophoresis (in short SDS-PAGE) was routinely performed. For this cause, 10 % Bis-Tris gels were hand cast according to the following recipe (for four gels), provided in Table 35 and Table 36.

Table 35. Pipetting scheme for the resolving gel of 10 % Bis-Tris gels.

Reagent	Amount
Water	6.5 mL
1 M Bis-Tris (pH 6.5 – 6.7)	6.5 mL
30 % acrylamide/bis-acrylamide (37.5:1)	6.5 mL
10 % (w/v) APS	120 µL
TEMED	48 µL

After mixing the components of the resolving gel, the solution was quickly poured between the two glass plates of each gel cassette, up to approximately 2 cm below the rim of the smaller glass plate. To even out the fluid level, the resolving gel was coated with 70 % isopropanol during the polymerization. Once the polymerization was complete, the isopropanol was removed, and the stacking gel was mixed according to the following recipe.

Table 36. Pipetting scheme for the stacking gel of 10 % Bis-Tris gels.

Reagent	Amount
Water	5.6 mL
1 M Bis-Tris (pH 6.5 – 6.7)	2.4 mL
30 % acrylamide/bis-acrylamide (37.5:1)	1.6 mL
10 % (w/v) APS	48 µL
TEMED	32 µL

The stacking gel was cast on top of the resolving gel. A suitable 10-well comb was inserted between the glass plates, and the gels were incubated until the polymerization was completed. Afterwards, the gels were either used directly, or stored at 4 °C until further use.

To perform the SDS-PAGE, the Bis-Tris gels were placed in an electrophoresis chamber, which was filled with the following fresh running buffer: 50 mM 3-(morpholin-4-yl)propane-1-sulfonic acid (MOPS), 50 mM Tris, 1 mM EDTA and 0.1 %

SDS. The protein was mixed with the respective amount of 4X NuPAGE LDS sample buffer. At times, the sample buffer was additionally equipped with 200 mM of dithiothreitol (DTT) to reduce the disulfide bonds of the protein. The samples and 4 µL of PageRuler Prestained Protein Ladder from Thermo Fisher Scientific were loaded in the wells. The stacking of the samples was accomplished by using 50 V (constant), before the voltage was increased to 150 – 200 V (constant) for the separation of the proteins.

After the gels were run, they were removed from the glass plates and heated up in Coomassie R-250 staining solution, which was prepared according to the following recipe, given in Table 37.

Table 37. Recipe for Coomassie R-250 staining solution.

Reagent	Amount
Water	670 mL
Acetic acid, glacial	250 mL
Ethanol	80 mL
Coomassie Brilliant Blue R-250	1.25 g

Afterwards, the unspecifically bound Coomassie dye was removed from the gel through repeated heating of the gel in water, until the protein bands were clearly visible.

The gels were imaged using the ChemiDoc MP Imaging System from Bio-Rad.

5.2.5.2 Western Blot

Some protein samples were additionally analyzed by Western Blot, to confirm the successful purification and presence of the protein of interest, or to compare the expression levels of different proteins. For that purpose, an SDS-PAGE of the proteins was performed, as described above, and the proteins were subsequently transferred to a nitrocellulose membrane. For successful transfer, the gel and the nitrocellulose membrane were equilibrated for few minutes in transfer buffer, consisting of 48 mM Tris, 39 mM glycine, 10 % ethanol and 0.1 % SDS. Gel and membrane were then stacked between two, transfer buffer-soaked, whatman papers, in the semi-dry Trans-Blot Turbo transfer system from Bio-Rad. The proteins were transferred in approximately 15 min at 1.3 A (constant) and 25 V (maximum). The completeness of the transfer was estimated by visual inspection of the prestained protein ladder. Afterwards, the membrane was incubated for at least 45 min in blocking buffer, consisting of 5 % w/v skim milk powder dissolved in PBS with 0.1 % Tween 20 (PBS-T). The desired primary antibody was diluted in fresh blocking buffer according to the manufacturer's instructions and was added to the membrane for overnight incubation at 4 °C. The next morning, the membranes were washed with blocking buffer for a total of 20 min with 4 changes of blocking buffer. The secondary antibody was also diluted in fresh blocking buffer, according to the manufacturer's instruction (e.g. 1:4000 for horseradish peroxidase (HRP)-conjugated anti-mouse antibody), and incubated with the membrane for at least 90 min at RT. Upon incubation, the membranes were washed with PBS-T for 4 times, 5 – 10 min, followed by a 5th wash step for approximately 30 min. The proteins were detected by addition of 800 µL of enhanced chemiluminescence (ECL) substrate, which intensifies the chemiluminescence signal emitted by reaction of the HRP with its substrate luminol.[329]

The membranes were imaged using the ChemiDoc MP Imaging System from Bio-Rad in chemiluminescence and Ponceau S mode. The pictures were superimposed to see the chemiluminescence signal and the protein ladder in the same image.

5.2.5.3 Analytical SEC

One of the characteristics of unstable proteins is their abundant formation of aggregates.[330] Under denaturating conditions, such as an SDS-PAGE, it is not possible to differentiate between aggregated proteins or stable, monodisperse proteins, since also the aggregated protein is disrupted by the SDS.[331] Therefore, alternative methods, such as analytical SEC, must be used to evaluate a protein's aggregation and monodispersity.

An Agilent Technologies 1260 Infinity HPLC system was outfitted with an analytical SEC column to carry out these analyses. In most cases, a Sepax NanoFilm SEC-250 column (4.6x250 mm, 5 µm particle size, 250 Å pore size) was employed, which was used with the following HPLC running buffer:

25 mM HEPES (pH 7.5), 500 mM NaCl, 2 % glycerol, 0.05 % DDM, 0.01 % CHS

To ensure that the sample would be consistently cooled, the autosampler compartment and column oven were pre-cooled to 4 °C and 12 °C, respectively, before the analyses. After small-scale and large-scale purifications (but before concentration), the typical injection volume was 30 µL. In order to evaluate their monodispersity upon concentration, and possibly estimate their protein concentration, also the concentrated protein samples were examined by analytical SEC. On that account, the concentrated samples were diluted 80-fold, before 30 µL of said dilution was injected onto the column. Each run was carried out for 20 min, at a flow rate of 0.5 mL/min. The proteins were detected by the use of a diode array detector, determining the protein's absorbance at a wavelength of 280 nm.

The results were analyzed using Graphpad Prism 7.0.0 or 10.0.3.

5.2.5.4 Thermostability assay

Another way to examine the stability of purified membrane proteins in various conditions, is the thermostability assay with CPM.

For this assay, the regents were mixed according to the following instructions, provided in Table 38:

Table 38. Pipetting scheme for the CPM assay.

Reagent	Amount
CPM working solution	1 µL
Unconcentrated protein	1 – 5 µL
Optional: 1 mM ligand stock	1 µL
HPLC running buffer	Ad 50 µL

The CPM working solution refers to a 40-fold dilution of a CPM stock solution (4 mg/mL in DMSO), which was freshly diluted with HPLC running buffer, right before its use. Since the protein yield varied from each purification, the optimal amount of protein was empirically determined and adjusted for each protein. The optional addition of ligand (to a final concentration of 20 µM) was used to evaluate the potentially stabilizing or destabilizing effects of a ligand on an apo purified protein. Each CPM measurement was additionally carried out using a blank sample, to eliminate background signals, e.g. from the ligands, for the analysis of the results. The pipetting scheme used for these blank samples was essentially the same as for the protein sample; the only difference was that instead of the protein, the same amount of the respective protein's buffer was pipetted.

Upon combination of all reagents, the samples were thoroughly vortexed and incubated at RT for 10 min. Then, the samples were transferred to the thermocycler for their measurement. Upon excitation of the samples at 365 nm, the probes emitted a fluorescence at 460 nm, which was determined at each temperature point ranging from 25(-30) to 99 °C.

The results were analyzed using the Graphpad Prism 7.0.0 or 10.0.3 software, by plotting the fluorescence signals against the temperature, normalizing the results, and fitting them according to the Boltzmann sigmoidal (least squares) fit, with the top value constantly set to 100:

$$\mathrm{Y} = \mathrm{Bottom} + \frac{(100 - \mathrm{Bottom})}{1 + \exp\left(\frac{\mathrm{V50} - \mathrm{x}}{\mathrm{Slope}}\right)}$$

In some cases, the results were better described by a biphasic sigmoid fit. Here, the top value was constantly set to 100 as well:

$$\mathrm{Span} = 100 - \mathrm{Bottom}$$

$$\mathrm{Section\ 1} = \frac{(\mathrm{Span} \times \mathrm{Frac})}{1 + \left(\frac{\mathrm{EC50\_1}}{\mathrm{X}}\right)^{nH1}}$$

$$\mathrm{Section\ 2} = \frac{(\mathrm{Span} \times (1 - \mathrm{Frac}))}{1 + \left(\frac{\mathrm{EC50\_2}}{\mathrm{X}}\right)^{nH2}}$$

$$\mathrm{Y} = \mathrm{Bottom} + \mathrm{Section\ 1} + \mathrm{Section\ 2}$$

In these equations, “Frac” represents the fraction of the response that is attributable to the first section of the curve, and nH1 and nH2 are the Hill slope factors that characterize the slopes of the two phases of the curve.[332] X is the independent variable, in this case the temperature (in °C).

5.2.5.5 Thermal analytical SEC

In some cases, thermostability assessment of the $A_{2B}AR$ in complex with certain ligands was not possible, due to their or their impurities’ interference with the measurement of the fluorescence at 460 nm. Therefore, the thermostabilizing effect of these ligands was estimated and compared by application of a thermal analytical SEC.

For this method, the proteins were incubated in a water bath for 5 – 10 min, which was set to a temperature slightly below the estimated melting temperature (T_M). After the exact incubation time, the proteins were instantly cooled on ice, and centrifuged at 4 °C, > 14,000 g for 10 min, before their injection onto the analytical SEC column. The thermostability of all equally treated samples could be compared, by evaluating the extent of the left-shift of the protein peaks, which happens upon heat shocking the protein, due to the formation of aggregates.

5.2.6 Crystal harvesting

As previously mentioned in chapter 5.2.4.2, the crystallization plates were typically incubated and photographed in the Rock Imager for several weeks. This extended duration is necessary, since protein crystals often require these prolonged incubation periods to reach their final size. When crystals seemed suitable for X-ray diffraction analysis and had ideally reached their maximum size, they were removed from the LCP and flash-frozen in liquid nitrogen for storage and transportation.

For this harvesting of the crystals, the crystallization plates were transferred to a microscope and the thin glass cover was opened along the edges of the respective well containing suitable crystals. This was achieved by scratching along the edges of the well of interest with a glass cutter pencil. The cover plate was lifted from the well with a fine tweezer. At times, a few microliters of the respective precipitant solution, that covered the LCP drop during the incubation, was added on top of the LCP to prolong the disintegration of the LCP. The crystals were extracted from the LCP using MiTeGen's Dual Thickness MicroMounts loops, selecting a loop size that roughly matched the crystal's dimensions. Once a crystal sat on a loop, the loop was quickly removed from the LCP and plunged into liquid-nitrogen, which was ideally free of any ice crystals. All loops were placed into pre-cooled pucks, which in turn were placed into a cryo express dry shipper for storage and shipment to the beamline.

The harvesting of the crystals presented in this thesis was either conducted by Dr. Tobias Claff or Dr. Robert K. Y. Cheng.

5.2.7 Data collection and processing

The diffraction data which resulted in the elucidation of the 4.0 Å crystal structure of the A_{2B}AR collected at the Swiss Light Source beamline X10SA equipped with an EIGER 16M detector. The harvested crystal was exposed to the X-ray beam with a 30 µm aperture. A dataset was collected using an unattenuated beam at 0.2° oscillation and 0.05 s exposure per image. A total of 180° were collected per dataset. Raw diffraction data were integrated and merged using XDS[333] and scaled using AIMLESS from the CCP4 suite.[334] The structure was solved by molecular replacement with Phaser,[335] using the AlphaFold model of the A_{2B}AR (with flexible termini removed) and T4 lysozyme as independent search models.[203] Iterative model building was carried out using sigma-A weighted $2m|F_o|-|DF_c|$ and $m|F_o|-D|F_c|$ maps in Coot[336], Phenix.Rosetta_refine[337, 338] and reciprocal space refinement using Phenix_refine.[337, 339]

The diffraction data collection was performed by Dr. Robert K. Y. Cheng from leadXpro (Villigen, Switzerland), and refinements of the structure were performed by Dr. Robert K. Y. Cheng and Dr. Renato H. Weiße (Leipzig University).

Final data collection and refinement statistic are reported in Table 39.

Table 39. Diffraction data and refinement statistics.

Data collection	
Wavelength (Å)	1.00006
Resolution (Å)	37.33-3.99 (4.46-3.99)
Resolution aniso (Å)	3.99, 3.99
Space group	P 3_1 2 1
Unit cell dimensions (Å;°)	72.20, 72.20, 232.62; 90.00, 90.00 120.00
Unique reflections	6518 (1793)
Multiplicity	9.5 (10.2)
Completeness (%)	99.9 (100.0)
Mean I/s(I)	7.5 (1.3)
R-meas	0.242 (1.925)
R-merge	0.229 (1.827)
R-pim	0.078 (0.600)
$CC_{1/2}$	0.999 (0.571)
Wilson B (Å^2)	167.69
Refinement	
Resolution (Å)	37.33-3.99 (5.02-3.99)
R-work	0.3026 (0.3500)
R-free	0.3855 (0.4022)
Number of non-hydrogen atoms, B-value (Å^2)	
Protein	3481, 187.83
Heterogen	24, 184.40
Solvent	0
Rmsd bonds (Å)	0.001
Rmsd angles (°)	0.343
Ramachandran favored (%)	94.52
Ramachandran allowed (%)	5.48
Ramachandran outliers (%)	0.00
Rotamer outliers (%)	2.15
MolProbity clashscore	3.38

6 References

(1) Weng, G.; Bhalla, U. S.; Iyengar, R. Complexity in biological signaling systems. *Science* **1999**, *284*, 92–96.

(2) Bourret, R. B. Signal transduction meets systems biology: deciphering specificity determinants for protein-protein interactions. *Mol. Microbiol.* **2008**, *69*, 1336–1340.

(3) Yewdall, N. A.; Mason, A. F.; van Hest, J. C. M. The hallmarks of living systems: towards creating artificial cells. *Interface Focus* **2018**, *8*, 20180023.

(4) Wacker, D.; Stevens, R. C.; Roth, B. L. How ligands illuminate GPCR molecular pharmacology. *Cell* **2017**, *170*, 414–427.

(5) Heldin, C.-H.; Lu, B.; Evans, R.; Gutkind, J. S. Signals and receptors. *Cold Spring Harbor Perspect. Biol.* **2016**, *8*, a005900.

(6) Salon, J. A.; Lodowski, D. T.; Palczewski, K. The significance of G protein-coupled receptor crystallography for drug discovery. *Pharmacol. Rev.* **2011**, *63*, 901–937.

(7) Fredriksson, R.; Schiöth, H. B. The repertoire of G-protein-coupled receptors in fully sequenced genomes. *Mol. Pharmacol.* **2005**, *67*, 1414–1425.

(8) Almén, M. S.; Nordström, K. J. V.; Fredriksson, R.; Schiöth, H. B. Mapping the human membrane proteome: a majority of the human membrane proteins can be classified according to function and evolutionary origin. *BMC Biol.* **2009**, *7*, 50.

(9) Venkatakrishnan, A. J.; Deupi, X.; Lebon, G.; Tate, C. G.; Schertler, G. F.; Babu, M. M. Molecular signatures of G protein-coupled receptors. *Nature* **2013**, *494*, 185–194.

(10) Hilger, D.; Masureel, M.; Kobilka, B. K. Structure and dynamics of GPCR signaling complexes. *Nat. Struct. Mol. Biol.* **2018**, *25*, 4–12.

(11) Gao, Y.; Hu, H.; Ramachandran, S.; Erickson, J. W.; Cerione, R. A.; Skiniotis, G. Structures of the rhodopsin-transducin complex: Insights into G-protein activation. *Mol. Cell* **2019**, *75*, 781-790.e3.

(12) Koppisetti, R. K.; Fulcher, Y. G.; Jurkevich, A.; Prior, S. H.; Xu, J.; Lenoir, M.; Overduin, M.; van Doren, S. R. Ambidextrous binding of cell and membrane bilayers by soluble matrix metalloproteinase-12. *Nat. Commun.* **2014**, *5*, 5552.

(13) Simon, M. I.; Strathmann, M. P.; Gautam, N. Diversity of G proteins in signal transduction. *Science* **1991**, *252*, 802–808.

(14) Syrovatkina, V.; Alegre, K. O.; Dey, R.; Huang, X.-Y. Regulation, signaling, and physiological functions of G-proteins. *J. Mol. Biol.* **2016**, *428*, 3850–3868.

(15) Kim, H. R.; Xu, J.; Maeda, S.; Duc, N. M.; Ahn, D.; Du, Y.; Chung, K. Y. Structural mechanism underlying primary and secondary coupling between GPCRs and the Gi/o family. *Nat. Commun.* **2020**, *11*, 3160.

(16) Albert, P. R.; Robillard, L. G protein specificity: traffic direction required. *Cell. Signalling* **2002**, *14*, 407–418.

(17) Xiao, R. P. Beta-adrenergic signaling in the heart: dual coupling of the β_2-adrenergic receptor to G_s and G_i proteins. *Sci. STKE* **2001**, *2001*, re15.

(18) Voss, J. H.; Mahardhika, A. B.; Inoue, A.; Müller, C. E. Agonist-dependent coupling of the promiscuous adenosine A_{2B} receptor to Gα protein subunits. *ACS Pharmacol. Transl. Sci.* **2022**, *5*, 373–386.

(19) Downes, G. B.; Gautam, N. The G protein subunit gene families. *Genomics* **1999**, *62*, 544–552.

(20) Calebiro, D.; Koszegi, Z.; Lanoiselée, Y.; Miljus, T.; O'Brien, S. G protein-coupled receptor-G protein interactions: a single-molecule perspective. *Physiol. Rev.* **2021**, *101*, 857–906.

(21) Katritch, V.; Cherezov, V.; Stevens, R. C. Diversity and modularity of G protein-coupled receptor structures. *Trends Pharmacol. Sci.* **2012**, *33*, 17–27.

(22) Manglik, A.; Kruse, A. C. Structural basis for G protein-coupled receptor activation. *Biochemistry* **2017**, *56*, 5628–5634.

(23) Hofmann, K. P.; Lamb, T. D. Rhodopsin, light-sensor of vision. *Prog. Retinal Eye Res.* **2023**, *93*, 101116.

(24) Hecht, S.; Shlaer, S.; Pirenne, M. H. Energy, quanta, and vision. *J. Gen. Physiol.* **1942**, *25*, 819–840.

(25) Stryer, L. Visual excitation and recovery. *J. Biol. Chem.* **1991**, *266*, 10711–10714.

(26) Pugh, E. N. The discovery of the ability of rod photoreceptors to signal single photons. *J. Gen. Physiol.* **2018**, *150*, 383–388.

(27) Smith, S. O. Mechanism of activation of the visual receptor rhodopsin. *Annu. Rev. Biophys.* **2023**, *52*, 301–317.

(28) Wright, S. C.; Bouvier, M. Illuminating the complexity of GPCR pathway selectivity - advances in biosensor development. *Curr. Opin. Struct. Biol.* **2021**, *69*, 142–149.

(29) Sriram, K.; Insel, P. A. G protein-coupled receptors as targets for approved drugs: How many targets and how many drugs? *Mol. Pharmacol.* **2018**, *93*, 251–258.

(30) Wettschureck, N.; Offermanns, S. Mammalian G proteins and their cell type specific functions. *Physiol. Rev.* **2005**, *85*, 1159–1204.

(31) Gurevich, V. V.; Gurevich, E. V. GPCR signaling regulation: The role of GRKs and arrestins. *Front. Pharmacol.* **2019**, *10*, 125.

(32) Khan, S. M.; Sleno, R.; Gora, S.; Zylbergold, P.; Laverdure, J.-P.; Labbé, J.-C.; Miller, G. J.; Hébert, T. E. The expanding roles of Gβγ subunits in G protein-coupled receptor signaling and drug action. *Pharmacol. Rev.* **2013**, *65*, 545–577.

(33) Chen, H.; Zhang, S.; Zhang, X.; Liu, H. QR code model: a new possibility for GPCR phosphorylation recognition. *Cell Commun. Signaling* **2022**, *20*, 23.

(34) Krupnick, J. G.; Benovic, J. L. The role of receptor kinases and arrestins in G protein-coupled receptor regulation. *Annu. Rev. Pharmacol. Toxicol.* **1998**, *38*, 289–319.

(35) Grundmann, M.; Merten, N.; Malfacini, D.; Inoue, A.; Preis, P.; Simon, K.; Rüttiger, N.; Ziegler, N.; Benkel, T.; Schmitt, N. K.; Ishida, S.; Müller, I.; Reher, R.; Kawakami, K.; Inoue, A.; Rick, U.; Kühl, T.; Imhof, D.; Aoki, J.; König, G. M.; Hoffmann, C.; Gomeza, J.; Wess, J.; Kostenis, E. Lack of beta-arrestin signaling in the absence of active G proteins. *Nat. Commun.* **2018**, *9*, 341.

(36) Rajagopal, S.; Rajagopal, K.; Lefkowitz, R. J. Teaching old receptors new tricks: biasing seven-transmembrane receptors. *Nat. Rev. Drug Discov.* **2010**, *9*, 373–386.

(37) Jean-Charles, P.-Y.; Kaur, S.; Shenoy, S. K. G protein-coupled receptor signaling through β-arrestin-dependent mechanisms. *J. Cardiovasc. Pharmacol.* **2017**, *70*, 142–158.

(38) Sprang, S. R. Invited review: Activation of G proteins by GTP and the mechanism of Gα-catalyzed GTP hydrolysis. *Biopolymers* **2016**, *105*, 449–462.

(39) Lam, M.; Lamanna, E.; Bourke, J. E. Regulation of airway smooth muscle contraction in health and disease. *Adv. Exp. Med. Biol.* **2019**, *1124*, 381–422.

(40) Cooper, C. B. Airflow obstruction and exercise. *Respir. Med.* **2009**, *103*, 325–334.

(41) Rosenbaum, D. M.; Rasmussen, S. G. F.; Kobilka, B. K. The structure and function of G-protein-coupled receptors. *Nature* **2009**, *459*, 356–363.

(42) Hilger, D. The role of structural dynamics in GPCR-mediated signaling. *FEBS J.* **2021**, *288*, 2461–2489.

(43) Hu, G.-M.; Mai, T.-L.; Chen, C.-M. Visualizing the GPCR network: Classification and evolution. *Sci. Rep.* **2017**, *7*.

(44) Wingert, B.; Doruker, P.; Bahar, I. Activation and speciation mechanisms in class A GPCRs. *J. Mol. Biol.* **2022**, *434*, 167690.

(45) Palczewski, K.; Kumasaka, T.; Hori, T.; Behnke, C. A.; Motoshima, H.; Fox, B. A.; Le Trong, I.; Teller, D. C.; Okada, T.; Stenkamp, R. E.; Yamamoto, M.; Miyano, M. Crystal structure of rhodopsin: A G protein-coupled receptor. *Science* **2000**, *289*, 739–745.

(46) Choe, H.-W.; Kim, Y. J.; Park, J. H.; Morizumi, T.; Pai, E. F.; Krauss, N.; Hofmann, K. P.; Scheerer, P.; Ernst, O. P. Crystal structure of metarhodopsin II. *Nature* **2011**, *471*, 651–655.

(47) Nakamichi, H.; Okada, T. Crystallographic analysis of primary visual photochemistry. *Angew. Chem. Int. Ed Engl.* **2006**, *45*, 4270–4273.

(48) Nakamichi, H.; Okada, T. Local peptide movement in the photoreaction intermediate of rhodopsin. *Proc. Natl. Acad. Sci. U. S. A.* **2006**, *103*, 12729–12734.

(49) Kang, Y.; Zhou, X. E.; Gao, X.; He, Y.; Liu, W.; Ishchenko, A.; Barty, A.; White, T. A.; Yefanov, O.; Han, G. W.; Xu, Q.; Waal, P. W. de; Ke, J.; Tan, M. H. E.; Zhang, C.; Moeller,

A.; West, G. M.; Pascal, B. D.; van Eps, N.; Caro, L. N.; Vishnivetskiy, S. A.; Lee, R. J.; Suino-Powell, K. M.; Gu, X.; Pal, K.; Ma, J.; Zhi, X.; Boutet, S.; Williams, G. J.; Messerschmidt, M.; Gati, C.; Zatsepin, N. A.; Wang, D.; James, D.; Basu, S.; Roy-Chowdhury, S.; Conrad, C. E.; Coe, J.; Liu, H.; Lisova, S.; Kupitz, C.; Grotjohann, I.; Fromme, R.; Jiang, Y.; Tan, M.; Yang, H.; Li, J.; Wang, M.; Zheng, Z.; Li, D.; Howe, N.; Zhao, Y.; Standfuss, J.; Diederichs, K.; Dong, Y.; Potter, C. S.; Carragher, B.; Caffrey, M.; Jiang, H.; Chapman, H. N.; Spence, J. C. H.; Fromme, P.; Weierstall, U.; Ernst, O. P.; Katritch, V.; Gurevich, V. V.; Griffin, P. R.; Hubbell, W. L.; Stevens, R. C.; Cherezov, V.; Melcher, K.; Xu, H. E. Crystal structure of rhodopsin bound to arrestin by femtosecond X-ray laser. *Nature* **2015**, *523*, 561–567.

(50) Chen, Q.; Plasencia, M.; Li, Z.; Mukherjee, S.; Patra, D.; Chen, C.-L.; Klose, T.; Yao, X.-Q.; Kossiakoff, A. A.; Chang, L.; Andrews, P. C.; Tesmer, J. J. G. Structures of rhodopsin in complex with G-protein-coupled receptor kinase 1. *Nature* **2021**, *595*, 600–605.

(51) Deupi, X. Relevance of rhodopsin studies for GPCR activation. *Biochim. Biophys. Acta, Bioenerg.* **2014**, *1837*, 674–682.

(52) Pándy-Szekeres, G.; Caroli, J.; Mamyrbekov, A.; Kermani, A. A.; Keserű, G. M.; Kooistra, A. J.; Gloriam, D. E. GPCRdb in 2023: state-specific structure models using AlphaFold2 and new ligand resources. *Nucleic Acids Res.* **2023**, *51*, D395-D402.

(53) Rosenbaum, D. M.; Cherezov, V.; Hanson, M. A.; Rasmussen, S. G. F.; Thian, F. S.; Kobilka, T. S.; Choi, H.-J.; Yao, X.-J.; Weis, W. I.; Stevens, R. C.; Kobilka, B. K. GPCR engineering yields high-resolution structural insights into β_2-adrenergic receptor function. *Science* **2007**, *318*, 1266–1273.

(54) Chan, H. C. S.; Li, Y.; Dahoun, T.; Vogel, H.; Yuan, S. New binding sites, new opportunities for GPCR drug discovery. *Trends Biochem. Sci.* **2019**, *44*, 312–330.

(55) Zhou, Q.; Yang, D.; Wu, M.; Guo, Y.; Guo, W.; Zhong, L.; Cai, X.; Dai, A.; Jang, W.; Shakhnovich, E. I.; Liu, Z.-J.; Stevens, R. C.; Lambert, N. A.; Babu, M. M.; Wang, M.-W.; Zhao, S. Common activation mechanism of class A GPCRs. *eLife* **2019**, *8*.

(56) Katritch, V.; Cherezov, V.; Stevens, R. C. Structure-function of the G protein–coupled receptor superfamily. *Annu. Rev. Pharmacol. Toxicol.* **2013**, *53*, 531–556.

(57) Latorraca, N. R.; Venkatakrishnan, A. J.; Dror, R. O. GPCR dynamics: Structures in motion. *Chem. Rev.* **2017**, *117*, 139–155.

(58) Katritch, V.; Fenalti, G.; Abola, E. E.; Roth, B. L.; Cherezov, V.; Stevens, R. C. Allosteric sodium in class A GPCR signaling. *Trends Biochem. Sci.* **2014**, *39*, 233–244.

(59) Venkatakrishnan, A. J.; Deupi, X.; Lebon, G.; Heydenreich, F. M.; Flock, T.; Miljus, T.; Balaji, S.; Bouvier, M.; Veprintsev, D. B.; Tate, C. G.; Schertler, G. F. X.; Babu, M. M. Diverse activation pathways in class A GPCRs converge near the G protein-coupling region. *Nature* **2016**, *536*, 484–487.

(60) Weis, W. I.; Kobilka, B. K. The molecular basis of G protein-coupled receptor activation. *Annu. Rev. Biochem.* **2018**, *87*, 897–919.

(61) Ballesteros, J. A.; Weinstein, H. Integrated methods for the construction of three-dimensional models and computational probing of structure-function relations in G protein-coupled receptors. *J. Neurosci. Methods* **1995**, *25*, 366–428.

(62) Filipek, S. Molecular switches in GPCRs. *Curr. Opin. Struct. Biol.* **2019**, *55*, 114–120.

(63) Venkatakrishnan, A. J.; Ma, A. K.; Fonseca, R.; Latorraca, N. R.; Kelly, B.; Betz, R. M.; Asawa, C.; Kobilka, B. K.; Dror, R. O. Diverse GPCRs exhibit conserved water networks for stabilization and activation. *Proc. Natl. Acad. Sci. U. S. A.* **2019**, *116*, 3288–3293.

(64) Hauser, A. S.; Kooistra, A. J.; Munk, C.; Heydenreich, F. M.; Veprintsev, D. B.; Bouvier, M.; Babu, M. M.; Gloriam, D. E. GPCR activation mechanisms across classes and macro/microscales. *Nat. Struct. Mol. Biol.* **2021**, *28*, 879–888.

(65) Liu, W.; Chun, E.; Thompson, A. A.; Chubukov, P.; Xu, F.; Katritch, V.; Han, G. W.; Roth, C. B.; Heitman, L. H.; IJzerman, A. P.; Cherezov, V.; Stevens, R. C. Structural basis for allosteric regulation of GPCRs by sodium ions. *Science* **2012**, *337*, 232–236.

(66) Fenalti, G.; Giguere, P. M.; Katritch, V.; Huang, X.-P.; Thompson, A. A.; Cherezov, V.; Roth, B. L.; Stevens, R. C. Molecular control of δ-opioid receptor signalling. *Nature* **2014**, *506*, 191–196.

(67) Miller-Gallacher, J. L.; Nehmé, R.; Warne, T.; Edwards, P. C.; Schertler, G. F. X.; Leslie, A. G. W.; Tate, C. G. The 2.1 Å resolution structure of cyanopindolol-bound β_1-

adrenoceptor identifies an intramembrane Na^+ ion that stabilises the ligand-free receptor. *PLoS ONE* **2014**, *9*, e92727.

(68) Wang, S.; Wacker, D.; Levit, A.; Che, T.; Betz, R. M.; McCorvy, J. D.; Venkatakrishnan, A. J.; Huang, X.-P.; Dror, R. O.; Shoichet, B. K.; Roth, B. L. D_4 dopamine receptor high-resolution structures enable the discovery of selective agonists. *Science* **2017**, *358*, 381–386.

(69) Zarzycka, B.; Zaidi, S. A.; Roth, B. L.; Katritch, V. Harnessing ion-binding sites for GPCR pharmacology. *Pharmacol. Rev.* **2019**, *71*, 571–595.

(70) Horstman, D. A.; Brandon, S.; Wilson, A. L.; Guyer, C. A.; Cragoe, E. J.; Limbird, L. E. An aspartate conserved among G-protein receptors confers allosteric regulation of alpha 2-adrenergic receptors by sodium. *J. Biol. Chem.* **1990**, *265*, 21590–21595.

(71) Hishinuma, S.; Kosaka, K.; Akatsu, C.; Uesawa, Y.; Fukui, H.; Shoji, M. Asp73-dependent and -independent regulation of the affinity of ligands for human histamine H_1 receptors by Na. *Biochem. Pharmacol.* **2017**, *128*, 46–54.

(72) Hori, T.; Okuno, T.; Hirata, K.; Yamashita, K.; Kawano, Y.; Yamamoto, M.; Hato, M.; Nakamura, M.; Shimizu, T.; Yokomizo, T.; Miyano, M.; Yokoyama, S. Na^+-mimicking ligands stabilize the inactive state of leukotriene B_4 receptor BLT1. *Nat. Chem. Biol.* **2018**, *14*, 262–269.

(73) Claff, T.; Klapschinski, T. A.; Tiruttani Subhramanyam, U. K.; Vaaßen, V. J.; Schlegel, J. G.; Vielmuth, C.; Voß, J. H.; Labahn, J.; Müller, C. E. Single stabilizing point mutation enables high-resolution co-crystal structures of the adenosine A_{2A} receptor with preladenant conjugates. *Angew. Chem. Int. Ed Engl.* **2022**, *61*, e202115545.

(74) Kimura, K. T.; Asada, H.; Inoue, A.; Kadji, F. M. N.; Im, D.; Mori, C.; Arakawa, T.; Hirata, K.; Nomura, Y.; Nomura, N.; Aoki, J.; Iwata, S.; Shimamura, T. Structures of the 5-HT_{2A} receptor in complex with the antipsychotics risperidone and zotepine. *Nat. Struct. Mol. Biol.* **2019**, *26*, 121–128.

(75) Pert, C. B.; Pasternak, G.; Snyder, S. H. Opiate agonists and antagonists discriminated by receptor binding in brain. *Science* **1973**, *182*, 1359–1361.

(76) White, K. L.; Eddy, M. T.; Gao, Z.-G.; Han, G. W.; Lian, T.; Deary, A.; Patel, N.; Jacobson, K. A.; Katritch, V.; Stevens, R. C. Structural connection between activation

microswitch and allosteric sodium site in GPCR signaling. *Structure* **2018**, *26*, 259-269.

(77) Barbhaiya, H.; McClain, R.; Ijzerman, A.; Rivkees, S. A. Site-directed mutagenesis of the human A_1 adenosine receptor: influences of acidic and hydroxy residues in the first four transmembrane domains on ligand binding. *Mol. Pharmacol.* **1996**, *50*, 1635–1642.

(78) Gao, Z. G.; IJzerman, A. P. Allosteric modulation of A_{2A} adenosine receptors by amiloride analogues and sodium ions. *Biochem. Pharmacol.* **2000**, *60*, 669–676.

(79) Gutiérrez-de-Terán, H.; Massink, A.; Rodríguez, D.; Liu, W.; Han, G. W.; Joseph, J. S.; Katritch, I.; Heitman, L. H.; Xia, L.; IJzerman, A. P.; Cherezov, V.; Katritch, V.; Stevens, R. C. The role of a sodium ion binding site in the allosteric modulation of the A_{2A} adenosine G protein-coupled receptor. *Structure* **2013**, *21*, 2175–2185.

(80) Gao, Z.-G.; Melman, N.; Erdmann, A.; Kim, S. G.; Müller, C. E.; IJzerman, A. P.; Jacobson, K. A. Differential allosteric modulation by amiloride analogues of agonist and antagonist binding at A_1 and A_3 adenosine receptors. *Biochem. Pharmacol.* **2003**, *65*, 525–534.

(81) Bertarelli, D. C. G.; Diekmann, M.; Hayallah, A. M.; Rüsing, D.; Iqbal, J.; Preiss, B.; Verspohl, E. J.; Müller, C. E. Characterization of human and rodent native and recombinant adenosine A_{2B} receptors by radioligand binding studies. *Purinergic Signal.* **2006**, *2*, 559–571.

(82) Hinz, S.; Lacher, S. K.; Seibt, B. F.; Müller, C. E. BAY60-6583 acts as a partial agonist at adenosine A_{2B} receptors. *J. Pharmacol. Exp. Ther.* **2014**, *349*, 427–436.

(83) Pándy-Szekeres, G.; Munk, C.; Tsonkov, T. M.; Mordalski, S.; Harpsøe, K.; Hauser, A. S.; Bojarski, A. J.; Gloriam, D. E. GPCRdb in 2018: adding GPCR structure models and ligands. *Nucleic Acids Res.* **2018**, *46*, 440-446.

(84) Zhang, D.; Zhao, Q.; Wu, B. Structural studies of G protein-coupled receptors. *Mol. Cells* **2015**, *38*, 836–842.

(85) Wheatley, M.; Wootten, D.; Conner, M. T.; Simms, J.; Kendrick, R.; Logan, R. T.; Poyner, D. R.; Barwell, J. Lifting the lid on GPCRs: the role of extracellular loops. *Br. J. Pharmacol.* **2012**, *165*, 1688–1703.

(86) Karnik, S. S.; Gogonea, C.; Patil, S.; Saad, Y.; Takezako, T. Activation of G-protein-coupled receptors: a common molecular mechanism. *Trends Endocrinol. Metab.* **2003**, *14*, 431–437.

(87) Noda, K.; Saad, Y.; Graham, R. M.; Karnik, S. S. The high affinity state of the β2-adrenergic receptor requires unique interaction between conserved and non-conserved extracellular loop cysteines. *J. Biol. Chem.* **1994**, *269*, 6743–6752.

(88) Davidson, F. F.; Loewen, P. C.; Khorana, H. G. Structure and function in rhodopsin: replacement by alanine of cysteine residues 110 and 187, components of a conserved disulfide bond in rhodopsin, affects the light-activated metarhodopsin II state. *Proc. Natl. Acad. Sci. U. S. A.* **1994**, *91*, 4029–4033.

(89) Nicoli, A.; Dunkel, A.; Giorgino, T.; Graaf, C. de; Di Pizio, A. Classification model for the second extracellular loop of class A GPCRs. *J. Chem. Inf. Model.* **2022**, *62*, 511–522.

(90) Filippo, E. de; Namasivayam, V.; Zappe, L.; El-Tayeb, A.; Schiedel, A. C.; Müller, C. E. Role of extracellular cysteine residues in the adenosine A_{2A} receptor. *Purinergic Signal.* **2016**, *12*, 313–329.

(91) Woolley, M. J.; Conner, A. C. Understanding the common themes and diverse roles of the second extracellular loop (ECL2) of the GPCR super-family. *Mol. Cell. Endocrinol.* **2017**, *449*, 3–11.

(92) Filippo, E. de; Hinz, S.; Pellizzari, V.; Deganutti, G.; El-Tayeb, A.; Navarro, G.; Franco, R.; Moro, S.; Schiedel, A. C.; Müller, C. E. A_{2A} and A_{2B} adenosine receptors: The extracellular loop 2 determines high (A_{2A}) or low affinity (A_{2B}) for adenosine. *Biochem. Pharmacol.* **2020**, *172*, 113718.

(93) Wang, Y.; Liu, W.; Xu, Y.; He, X.; Yuan, Q.; Luo, P.; Fan, W.; Zhu, J.; Zhang, X.; Cheng, X.; Jiang, Y.; Xu, H. E.; Zhuang, Y. Revealing the signaling of complement receptors C3aR and C5aR1 by anaphylatoxins. *Nat. Chem. Biol.* **2023**, *19*, 1351–1360.

(94) Patwardhan, A.; Cheng, N.; Trejo, J. Post-translational modifications of G protein-coupled receptors control cellular signaling dynamics in space and time. *Pharmacol. Rev.* **2021**, *73*, 120–151.

(95) Zhang, B.; Li, S.; Shui, W. Post-translational modifications of G protein-coupled receptors revealed by proteomics and structural biology. *Front. Chem.* **2022**, *10*, 843502.

(96) Goth, C. K.; Petäjä-Repo, U. E.; Rosenkilde, M. M. G protein-coupled receptors in the sweet spot: Glycosylation and other post-translational modifications. *ACS Pharmacol. Transl. Sci.* **2020**, *3*, 237–245.

(97) Rands, E.; Candelore, M. R.; Cheung, A. H.; Hill, W. S.; Strader, C. D.; Dixon, R. A. Mutational analysis of beta-adrenergic receptor glycosylation. *J. Biol. Chem.* **1990**, *265*, 10759–10764.

(98) Markkanen, P. M. H.; Petäjä-Repo, U. E. N-glycan-mediated quality control in the endoplasmic reticulum is required for the expression of correctly folded delta-opioid receptors at the cell surface. *J. Biol. Chem.* **2008**, *283*, 29086–29098.

(99) Lanctôt, P. M.; Leclerc, P. C.; Escher, E.; Leduc, R.; Guillemette, G. Role of N-glycosylation in the expression and functional properties of human AT_1 receptor. *Biochemistry* **1999**, *38*, 8621–8627.

(100) Pal, S.; Chattopadhyay, A. Extramembranous regions in G protein-coupled receptors: Cinderella in receptor biology? *J. Membr. Biol.* **2019**, *252*, 483–497.

(101) Wiseman, D. N.; Otchere, A.; Patel, J. H.; Uddin, R.; Pollock, N. L.; Routledge, S. J.; Rothnie, A. J.; Slack, C.; Poyner, D. R.; Bill, R. M.; Goddard, A. D. Expression and purification of recombinant G protein-coupled receptors: A review. *Protein Expression Purif.* **2020**, *167*, 105524.

(102) Milić, D.; Veprintsev, D. B. Large-scale production and protein engineering of G protein-coupled receptors for structural studies. *Front. Pharmacol.* **2015**, *6*, 66.

(103) Shi, X.; Jarvis, D. L. Protein N-glycosylation in the baculovirus-insect cell system. *Curr. Drug Targets* **2007**, *8*, 1116–1125.

(104) Massotte, D. G protein-coupled receptor overexpression with the baculovirus-insect cell system: a tool for structural and functional studies. *Biochim. Biophys. Acta Biomembr.* **2003**, *1610*, 77–89.

(105) Warne, T.; Chirnside, J.; Schertler, G. F. X. Expression and purification of truncated, non-glycosylated turkey β-adrenergic receptors for crystallization. *Biochim. Biophys. Acta, Biomembr.* **2003**, *1610*, 133–140.

(106) Chun, E.; Thompson, A. A.; Liu, W.; Roth, C. B.; Griffith, M. T.; Katritch, V.; Kunken, J.; Xu, F.; Cherezov, V.; Hanson, M. A.; Stevens, R. C. Fusion partner toolchest for the stabilization and crystallization of G protein-coupled receptors. *Structure* **2012**, *20*, 967–976.

(107) Claff, T.; Schlegel, J. G.; Voss, J. H.; Vaaßen, V. J.; Weiße, R. H.; Cheng, R. K. Y.; Markovic-Mueller, S.; Bucher, D.; Sträter, N.; Müller, C. E. Crystal structure of adenosine A_{2A} receptor in complex with clinical candidate Etrumadenant reveals unprecedented antagonist interaction. *Commun. Chem.* **2023**, *6*, 106.

(108) Zhang, C.; Srinivasan, Y.; Arlow, D. H.; Fung, J. J.; Palmer, D.; Zheng, Y.; Green, H. F.; Pandey, A.; Dror, R. O.; Shaw, D. E.; Weis, W. I.; Coughlin, S. R.; Kobilka, B. K. High-resolution crystal structure of human protease-activated receptor 1. *Nature* **2012**, *492*, 387–392.

(109) Thal, D. M.; Sun, B.; Feng, D.; Nawaratne, V.; Leach, K.; Felder, C. C.; Bures, M. G.; Evans, D. A.; Weis, W. I.; Bachhawat, P.; Kobilka, T. S.; Sexton, P. M.; Kobilka, B. K.; Christopoulos, A. Crystal structures of the M_1 and M_4 muscarinic acetylcholine receptors. *Nature* **2016**, *531*, 335–340.

(110) Yang, D.; Zhou, Q.; Labroska, V.; Qin, S.; Darbalaei, S.; Wu, Y.; Yuliantie, E.; Xie, L.; Tao, H.; Cheng, J.; Liu, Q.; Zhao, S.; Shui, W.; Jiang, Y.; Wang, M.-W. G protein-coupled receptors: structure- and function-based drug discovery. *Signal Transduct. Target. Ther.* **2021**, *6*, 7.

(111) Chen, Y.; Zhang, J.; Weng, Y.; Xu, Y.; Lu, W.; Liu, W.; Liu, M.; Hua, T.; Song, G. Cryo-EM structure of the human adenosine A_{2B} receptor-Gs signaling complex. *Sci. Adv.* **2022**, *8*, eadd3709.

(112) Hedderich, J. B.; Persechino, M.; Becker, K.; Heydenreich, F. M.; Gutermuth, T.; Bouvier, M.; Bünemann, M.; Kolb, P. The pocketome of G-protein-coupled receptors reveals previously untargeted allosteric sites. *Nat. Commun.* **2022**, *13*, 2567.

(113) Nussinov, R.; Tsai, C.-J. The different ways through which specificity works in orthosteric and allosteric drugs. *Curr. Pharm. Des.* **2012**, *18*, 1311–1316.

(114) Egyed, A.; Kiss, D. J.; Keserű, G. M. The impact of the secondary binding pocket on the pharmacology of class A GPCRs. *Front. Pharmacol.* **2022**, *13*, 847788.

(115) Mohr, K.; Tränkle, C.; Kostenis, E.; Barocelli, E.; Amici, M. de; Holzgrabe, U. Rational design of dualsteric GPCR ligands: quests and promise. *Br. J. Pharmacol.* **2010**, *159*, 997–1008.

(116) Congreve, M.; Dias, J. M.; Marshall, F. H. Structure-based drug design for G protein-coupled receptors. *Prog. Med. Chem.* **2014**, *53*, 1–63.

(117) Heng, B. C.; Aubel, D.; Fussenegger, M. An overview of the diverse roles of G-protein coupled receptors (GPCRs) in the pathophysiology of various human diseases. *Biotechnol. Adv.* **2013**, *31*, 1676–1694.

(118) Schöneberg, T.; Liebscher, I. Mutations in G Protein-Coupled Receptors: Mechanisms, pathophysiology and potential therapeutic approaches. *Pharmacol. Rev.* **2021**, *73*, 89–119.

(119) Congreve, M.; Graaf, C. de; Swain, N. A.; Tate, C. G. Impact of GPCR structures on drug discovery. *Cell* **2020**, *181*, 81–91.

(120) Smith, J. S.; Lefkowitz, R. J.; Rajagopal, S. Biased signalling: from simple switches to allosteric microprocessors. *Nat. Rev. Drug Discov.* **2018**, *17*, 243–260.

(121) Kenakin, T. Biased receptor signaling in drug discovery. *Pharmacol. Rev.* **2019**, *71*, 267–315.

(122) DeWire, S. M.; Violin, J. D. Biased ligands for better cardiovascular drugs: dissecting G-protein-coupled receptor pharmacology. *Circ. Res.* **2011**, *109*, 205–216.

(123) Hauser, A. S.; Attwood, M. M.; Rask-Andersen, M.; Schiöth, H. B.; Gloriam, D. E. Trends in GPCR drug discovery: new agents, targets and indications. *Nat. Rev. Drug Discov.* **2017**, *16*, 829–842.

(124) Kutryb-Zając, B.; Kawecka, A.; Nasadiuk, K.; Braczko, A.; Stawarska, K.; Caiazzo, E.; Koszałka, P.; Cicala, C. Drugs targeting adenosine signaling pathways: A current view. *Biomed. Pharmacother.* **2023**, *165*, 115184.

(125) van Calker, D.; Müller, M.; Hamprecht, B. Adenosine regulates via two different types of receptors, the accumulation of cyclic AMP in cultured brain cells. *J. Neurochem.* **1979**, *33*, 999–1005.

(126) Fredholm, B. B.; IJzerman, A. P.; Jacobson, K. A.; Klotz, K. N.; Linden, J. International union of pharmacology. XXV. Nomenclature and classification of adenosine receptors. *Pharmacol. Rev.* **2001**, *53*, 527–552.

(127) Borea, P. A.; Varani, K.; Gessi, S.; Merighi, S.; Vincenzi, F., Eds. *The adenosine receptors*; *Springer International Publishing:* Cham, **2018**.

(128) Burnstock, G. Purine and purinergic receptors. *Brain Neurosci. Adv.* **2018**, *2*, 2398212818817494.

(129) Fredriksson, R.; Lagerström, M. C.; Lundin, L.-G.; Schiöth, H. B. The G protein-coupled receptors in the human genome form five main families. Phylogenetic analysis, paralogon groups, and fingerprints. *Mol. Pharmacol.* **2003**, *63*, 1256–1272.

(130) Hattori, M.; Gouaux, E. Molecular mechanism of ATP binding and ion channel activation in P2X receptors. *Nature* **2012**, *485*, 207–212.

(131) Menzies, R. I.; Tam, F. W.; Unwin, R. J.; Bailey, M. A. Purinergic signaling in kidney disease. *Kidney Int.* **2017**, *91*, 315–323.

(132) Jacobson, K. A. Introduction to adenosine receptors as therapeutic targets. *Handb. Exp. Pharmacol.* **2009**, 1–24.

(133) Borea, P. A.; Gessi, S.; Merighi, S.; Varani, K. Adenosine as a multi-signalling guardian angel in human diseases: When, where and how does it exert its protective effects? *Trends Pharmacol. Sci.* **2016**, *37*, 419–434.

(134) Köse, M.; Schiedel, A. C. Nucleoside/nucleobase transporters: drug targets of the future? *Future Med. Chem.* **2009**, *1*, 303–326.

(135) Zimmermann, H.; Zebisch, M.; Sträter, N. Cellular function and molecular structure of ecto-nucleotidases. *Purinergic Signal.* **2012**, *8*, 437–502.

(136) Greiner, J. V.; Glonek, T. Intracellular ATP concentration and implication for cellular evolution. *Biology* **2021**, *10*.

(137) Vultaggio-Poma, V.; Falzoni, S.; Salvi, G.; Giuliani, A. L.; Di Virgilio, F. Signalling by extracellular nucleotides in health and disease. *Biochim. Biophys. Acta Mol. Cell Res.* **2022**, *1869*, 119237.

(138) Linden, J. Adenosine in tissue protection and tissue regeneration. *Mol. Pharmacol.* **2005**, *67*, 1385–1387.

(139) Bruns, R. F. Role of adenosine in energy supply/demand balance. *Nucleosides Nucleotides* **1991**, *10*, 931–943.

(140) Chen, J.-F.; Eltzschig, H. K.; Fredholm, B. B. Adenosine receptors as drug targets--what are the challenges? *Nat. Rev. Drug Discov.* **2013**, *12*, 265–286.

(141) Gupta, A.; Lokhandwala, Y.; Rai, N.; Malviya, A. Adenosine-A drug with myriad utility in the diagnosis and treatment of arrhythmias. *J. Arrhythm.* **2021**, *37*, 103–112.

(142) Iskandrian, A. S. Adenosine myocardial perfusion imaging. *J. Nucl. Med.* **1994**, *35*, 734–736.

(143) DiMarco, J. P.; Miles, W.; Akhtar, M.; Milstein, S.; Sharma, A. D.; Platia, E.; McGovern, B.; Scheinman, M. M.; Govier, W. C. Adenosine for paroxysmal supraventricular tachycardia: dose ranging and comparison with verapamil. Assessment in placebo-controlled, multicenter trials. The Adenosine for PSVT Study Group. *Ann. Intern. Med.* **1990**, *113*, 104–110.

(144) Müller, C. E.; Jacobson, K. A. Recent developments in adenosine receptor ligands and their potential as novel drugs. *Biochim. Biophys. Acta, Biomembr.* **2011**, *1808*, 1290–1308.

(145) Elkholy, K. O.; Hegazy, O.; Okunade, A.; Aktas, S.; Ajibawo, T. Regadenoson stress testing: A comprehensive review with a focused update. *Cureus* **2021**, *13*, e12940.

(146) IJzerman, A. P.; Jacobson, K. A.; Müller, C. E.; Cronstein, B. N.; Cunha, R. A. International union of basic and clinical pharmacology. CXII: Adenosine receptors: A further update. *Pharmacol. Rev.* **2022**, *74*, 340–372.

(147) Fredholm, B. B. Notes on the history of caffeine use. *Handb. Exp. Pharmacol.* **2011**, 1–9.

(148) Baratloo, A.; Rouhipour, A.; Forouzanfar, M. M.; Safari, S.; Amiri, M.; Negida, A. The role of caffeine in pain management: A brief literature review. *Anesth. Pain Med.* **2016**, *6*, e33193.

(149) Nehlig, A.; Daval, J. L.; Debry, G. Caffeine and the central nervous system: mechanisms of action, biochemical, metabolic and psychostimulant effects. *Brain Res. Rev.* **1992**, *17*, 139–170.

(150) Grizzi, F.; Chiriva-Internati, M. Cancer: looking for simplicity and finding complexity. *Cancer Cell Int.* **2006**, *6*, 4.

(151) Marusyk, A.; Polyak, K. Tumor heterogeneity: causes and consequences. *Biochim. Biophys. Acta, Rev. Cancer* **2010**, *1805*, 105–117.

(152) Tomasetti, C.; Li, L.; Vogelstein, B. Stem cell divisions, somatic mutations, cancer etiology, and cancer prevention. *Science* **2017**, *355*, 1330–1334.

(153) Weinberg, R. A. *The biology of cancer*; *Garland Science/Taylor & Francis:* New York, NY, **2014**.

(154) Alberts, B.; Johnson, A.; Lewis, J.; Raff, M.; Roberts, K.; Walter, P. *Molecular biology of the cell*; *Garland Science Taylor & Francis Group:* New York, NY, **2002**.

(155) Evans, E. J.; DeGregori, J. Cells with cancer-associated mutations overtake our tissues as we age. *Aging Cancer* **2021**, *2*, 82–97.

(156) Finn, O. J. Immuno-oncology: understanding the function and dysfunction of the immune system in cancer. *Ann. Oncol.* **2012**, *23 Suppl 8*, viii6-9.

(157) Vinay, D. S.; Ryan, E. P.; Pawelec, G.; Talib, W. H.; Stagg, J.; Elkord, E.; Lichtor, T.; Decker, W. K.; Whelan, R. L.; Kumara, H. M. C. S.; Signori, E.; Honoki, K.; Georgakilas, A. G.; Amin, A.; Helferich, W. G.; Boosani, C. S.; Guha, G.; Ciriolo, M. R.; Chen, S.; Mohammed, S. I.; Azmi, A. S.; Keith, W. N.; Bilsland, A.; Bhakta, D.; Halicka, D.; Fujii, H.; Aquilano, K.; Ashraf, S. S.; Nowsheen, S.; Yang, X.; Choi, B. K.; Kwon, B. S. Immune evasion in cancer: Mechanistic basis and therapeutic strategies. *Semin. Cancer Biol.* **2015**, *35 Suppl*, S185-S198.

(158) Leone, R. D.; Emens, L. A. Targeting adenosine for cancer immunotherapy. *J. Immunother. Cancer* **2018**, *6*, 57.

(159) Linnemann, C.; Schildberg, F. A.; Schurich, A.; Diehl, L.; Hegenbarth, S. I.; Endl, E.; Lacher, S.; Müller, C. E.; Frey, J.; Simeoni, L.; Schraven, B.; Stabenow, D.; Knolle, P. A. Adenosine regulates CD8 T-cell priming by inhibition of membrane-proximal T-cell receptor signalling. *Immunology* **2009**, *128*, e728-37.

(160) Ohta, A. A metabolic immune checkpoint: Adenosine in tumor microenvironment. *Front. Immunol.* **2016**, *7*, 109.

(161) Vigano, S.; Alatzoglou, D.; Irving, M.; Ménétrier-Caux, C.; Caux, C.; Romero, P.; Coukos, G. Targeting adenosine in cancer immunotherapy to enhance T-cell function. *Front. Immunol.* **2019**, *10*, 925.

(162) Xia, C.; Yin, S.; To, K. K. W.; Fu, L. CD39/CD73/A_{2A}R pathway and cancer immunotherapy. *Mol. Cancer* **2023**, *22*, 44.

(163) Bao, R.; Shui, X.; Hou, J.; Li, J.; Deng, X.; Zhu, X.; Yang, T. Adenosine and the adenosine A_{2A} receptor agonist, CGS21680, upregulate CD39 and CD73 expression through E2F-1 and CREB in regulatory T cells isolated from septic mice. *Int. J. Mol. Med.* **2016**, *38*, 969–975.

(164) Palmer, T. M.; Trevethick, M. A. Suppression of inflammatory and immune responses by the A_{2A} adenosine receptor: an introduction. *Br. J. Pharmacol.* **2008**, *153 Suppl 1*, S27-34.

(165) Thompson, E. A.; Powell, J. D. Inhibition of the adenosine pathway to potentiate cancer immunotherapy: Potential for combinatorial approaches. *Annu. Rev. Med.* **2021**, *72*, 331–348.

(166) Dziedzic, K.; Węgrzyn, P.; Gałęzowski, M.; Bońkowska, M.; Grycuk, K.; Satała, G.; Wiatrowska, K.; Wiklik, K.; Brzózka, K.; Nowak, M. Release of adenosine-induced immunosuppression: Comprehensive characterization of dual A_{2A}/A_{2B} receptor antagonist. *Int. Immunopharmacol.* **2021**, *96*, 107645.

(167) Kazemi, M. H.; Raoofi Mohseni, S.; Hojjat-Farsangi, M.; Anvari, E.; Ghalamfarsa, G.; Mohammadi, H.; Jadidi-Niaragh, F. Adenosine and adenosine receptors in the immunopathogenesis and treatment of cancer. *J. Cell. Physiol.* **2018**, *233*, 2032–2057.

(168) Allard, D.; Turcotte, M.; Stagg, J. Targeting A_2 adenosine receptors in cancer. *Immunol. Cell Biol.* **2017**, *95*, 333–339.

(169) Sepúlveda, C.; Palomo, I.; Fuentes, E. Role of adenosine A_{2B} receptor overexpression in tumor progression. *Life Sci.* **2016**, *166*, 92–99.

(170) Fredholm, B. B.; Irenius, E.; Kull, B.; Schulte, G. Comparison of the potency of adenosine as an agonist at human adenosine receptors expressed in Chinese hamster ovary cells. *Biochem. Pharmacol.* **2001**, *61*, 443–448.

(171) Fredholm, B. B. Adenosine, an endogenous distress signal, modulates tissue damage and repair. *Cell Death Differ.* **2007**, *14*, 1315–1323.

(172) Feoktistov, I.; Biaggioni, I. Adenosine A_{2B} receptors. *Pharmacol. Rev.* **1997**, *49*, 381–402.

(173) Aherne, C. M.; Kewley, E. M.; Eltzschig, H. K. The resurgence of A_{2B} adenosine receptor signaling. *Biochim. Biophys. Acta, Biomembr.* **2011**, *1808*, 1329–1339.

(174) Kwon, J. H.; Lee, J.; Kim, J.; Jo, Y. H.; Kirchner, V. A.; Kim, N.; Kwak, B. J.; Hwang, S.; Song, G.-W.; Lee, S.-G.; Yoon, Y.-I.; Park, G.-C.; Tak, E. HIF-1α regulates A_{2B} adenosine receptor expression in liver cancer cells. *Exp. Ther. Med.* **2019**, *18*, 4231–4240.

(175) Abo-Salem, O. M.; Hayallah, A. M.; Bilkei-Gorzo, A.; Filipek, B.; Zimmer, A.; Müller, C. E. Antinociceptive effects of novel A_{2B} adenosine receptor antagonists. *J. Pharmacol. Exp. Ther.* **2004**, *308*, 358–366.

(176) Bilkei-Gorzo, A.; Abo-Salem, O. M.; Hayallah, A. M.; Michel, K.; Müller, C. E.; Zimmer, A. Adenosine receptor subtype-selective antagonists in inflammation and hyperalgesia. *Naunyn Schmiedeberg's Arch. Pharmacol.* **2008**, *377*, 65–76.

(177) Khadela, A.; Soni, S.; Megha, K.; Shah, A. C.; Pandya, A. J.; Kothari, N.; Shah, I.; Avinash, C. B. Contracting triple-negative breast cancer with immunotherapeutic armamentarium: recent advances and clinical prospects. *Med. Oncol.* **2022**, *40*, 48.

(178) Augustin, R. C.; Leone, R. D.; Naing, A.; Fong, L.; Bao, R.; Luke, J. J. Next steps for clinical translation of adenosine pathway inhibition in cancer immunotherapy. *J. Immunother. Cancer* **2022**, *10*.

(179) Gao, Z.-G.; Jacobson, K. A. A_{2B} adenosine receptor and cancer. *Int. J. Mol. Sci.* **2019**, *20*.

(180) Jaakola, V.-P.; Griffith, M. T.; Hanson, M. A.; Cherezov, V.; Chien, E. Y. T.; Lane, J. R.; IJzerman, A. P.; Stevens, R. C. The 2.6 angstrom crystal structure of a human A_{2A} adenosine receptor bound to an antagonist. *Science* **2008**, *322*, 1211–1217.

(181) Sherbiny, F. F.; Schiedel, A. C.; Maass, A.; Müller, C. E. Homology modelling of the human adenosine A_{2B} receptor based on X-ray structures of bovine rhodopsin, the β_2-adrenergic receptor and the human adenosine A_{2A} receptor. *J. Comput. Aided Mol. Des.* **2009**, *23*, 807–828.

(182) Martinelli, A.; Ortore, G. Molecular modeling of adenosine receptors. *Methods Enzymol.* **2013**, *522*, 37–59.

(183) Dal Ben, D.; Buccioni, M.; Lambertucci, C.; Thomas, A.; Volpini, R. Simulation and comparative analysis of binding modes of nucleoside and non-nucleoside agonists at the A2B adenosine receptor. *In Silico Pharmacol.* **2013**, *1*, 24.

(184) Müller, C. E.; Baqi, Y.; Hinz, S.; Namasivayam, V. Medicinal chemistry of A_{2B} adenosine receptors. In *The adenosine receptors.* Borea, P. A.; Varani, K.; Gessi, S.; Merighi, S.; Vincenzi, F., Eds.; Springer International Publishing: Cham; pp. 137–168.

(185) Cai, H.; Xu, Y.; Guo, S.; He, X.; Sun, J.; Li, X.; Li, C.; Yin, W.; Cheng, X.; Jiang, H.; Xu, H. E.; Xie, X.; Jiang, Y. Structures of adenosine receptor A_{2B}R bound to endogenous and synthetic agonists. *Cell Discov.* **2022**, *8*, 140.

(186) Graaf, C. de; Foata, N.; Engkvist, O.; Rognan, D. Molecular modeling of the second extracellular loop of G-protein coupled receptors and its implication on structure-based virtual screening. *Proteins* **2008**, *71*, 599–620.

(187) Schiedel, A. C.; Hinz, S.; Thimm, D.; Sherbiny, F.; Borrmann, T.; Maass, A.; Müller, C. E. The four cysteine residues in the second extracellular loop of the human adenosine A_{2B} receptor: role in ligand binding and receptor function. *Biochem. Pharmacol.* **2011**, *82*, 389–399.

(188) García-Nafría, J.; Tate, C. G. Structure determination of GPCRs: cryo-EM compared with X-ray crystallography. *Biochem. Soc. Trans.* **2021**, *49*, 2345–2355.

(189) Duan, J.; Xu, P.; Zhang, H.; Luan, X.; Yang, J.; He, X.; Mao, C.; Shen, D.-D.; Ji, Y.; Cheng, X.; Jiang, H.; Jiang, Y.; Zhang, S.; Zhang, Y.; Xu, H. E. Mechanism of hormone and allosteric agonist mediated activation of follicle stimulating hormone receptor. *Nat. Commun.* **2023**, *14*, 519.

(190) Zhang, X.; Johnson, R. M.; Drulyte, I.; Yu, L.; Kotecha, A.; Danev, R.; Wootten, D.; Sexton, P. M.; Belousoff, M. J. Evolving cryo-EM structural approaches for GPCR drug discovery. *Structure* **2021**, *29*, 963-974.e6.

(191) Duan, J.; Shen, D.-D.; Zhou, X. E.; Bi, P.; Liu, Q.-F.; Tan, Y.-X.; Zhuang, Y.-W.; Zhang, H.-B.; Xu, P.-Y.; Huang, S.-J.; Ma, S.-S.; He, X.-H.; Melcher, K.; Zhang, Y.; Xu, H. E.; Jiang, Y. Cryo-EM structure of an activated VIP1 receptor-G protein complex revealed by a NanoBiT tethering strategy. *Nat. Commun.* **2020**, *11*, 4121.

(192) García-Nafría, J.; Lee, Y.; Bai, X.; Carpenter, B.; Tate, C. G. Cryo-EM structure of the adenosine A_{2A} receptor coupled to an engineered heterotrimeric G protein. *eLife* **2018**, *7*.

(193) Draper-Joyce, C. J.; Bhola, R.; Wang, J.; Bhattarai, A.; Nguyen, A. T. N.; Cowie-Kent, I.; O'Sullivan, K.; Chia, L. Y.; Venugopal, H.; Valant, C.; Thal, D. M.; Wootten, D.; Panel, N.; Carlsson, J.; Christie, M. J.; White, P. J.; Scammells, P.; May, L. T.; Sexton, P. M.; Danev, R.; Miao, Y.; Glukhova, A.; Imlach, W. L.; Christopoulos, A. Positive allosteric mechanisms of adenosine A_1 receptor-mediated analgesia. *Nature* **2021**, *597*, 571–576.

(194) Carpenter, B.; Nehmé, R.; Warne, T.; Leslie, A. G. W.; Tate, C. G. Structure of the adenosine A_{2A} receptor bound to an engineered G protein. *Nature* **2016**, *536*, 104–107.

(195) Thimm, D.; Schiedel, A. C.; Sherbiny, F. F.; Hinz, S.; Hochheiser, K.; Bertarelli, D. C. G.; Maass, A.; Müller, C. E. Ligand-specific binding and activation of the human adenosine A_{2B} receptor. *Biochemistry* **2013**, *52*, 726–740.

(196) Alnouri, M. W.; Jepards, S.; Casari, A.; Schiedel, A. C.; Hinz, S.; Müller, C. E. Selectivity is species-dependent: Characterization of standard agonists and antagonists at human, rat, and mouse adenosine receptors. *Purinergic Signal.* **2015**, *11*, 389–407.

(197) Carpenter, B.; Lebon, G. Human adenosine A_{2A} receptor: Molecular mechanism of ligand binding and activation. *Front. Pharmacol.* **2017**, *8*, 898.

(198) Segala, E.; Guo, D.; Cheng, R. K. Y.; Bortolato, A.; Deflorian, F.; Doré, A. S.; Errey, J. C.; Heitman, L. H.; IJzerman, A. P.; Marshall, F. H.; Cooke, R. M. Controlling the

dissociation of ligands from the adenosine A_{2A} receptor through modulation of salt bridge strength. *J. Med. Chem.* **2016**, *59*, 6470–6479.

(199) Liao, S.-M.; Du, Q.-S.; Meng, J.-Z.; Pang, Z.-W.; Huang, R.-B. The multiple roles of histidine in protein interactions. *Chem. Cent. J.* **2013**, *7*, 44.

(200) Lebon, G.; Warne, T.; Edwards, P. C.; Bennett, K.; Langmead, C. J.; Leslie, A. G. W.; Tate, C. G. Agonist-bound adenosine A_{2A} receptor structures reveal common features of GPCR activation. *Nature* **2011**, *474*, 521–525.

(201) Amelia, T.; van Veldhoven, J. P. D.; Falsini, M.; Liu, R.; Heitman, L. H.; van Westen, G. J. P.; Segala, E.; Verdon, G.; Cheng, R. K. Y.; Cooke, R. M.; van der Es, D.; IJzerman, A. P. Crystal structure and subsequent ligand design of a nonriboside partial agonist bound to the adenosine A_{2A} receptor. *J. Med. Chem.* **2021**, *64*, 3827–3842.

(202) Guaita, M.; Watters, S. C.; Loerch, S. Recent advances and current trends in cryo-electron microscopy. *Curr. Opin. Struct. Biol.* **2022**, *77*, 102484.

(203) Jumper, J.; Evans, R.; Pritzel, A.; Green, T.; Figurnov, M.; Ronneberger, O.; Tunyasuvunakool, K.; Bates, R.; Žídek, A.; Potapenko, A.; Bridgland, A.; Meyer, C.; Kohl, S. A. A.; Ballard, A. J.; Cowie, A.; Romera-Paredes, B.; Nikolov, S.; Jain, R.; Adler, J.; Back, T.; Petersen, S.; Reiman, D.; Clancy, E.; Zielinski, M.; Steinegger, M.; Pacholska, M.; Berghammer, T.; Bodenstein, S.; Silver, D.; Vinyals, O.; Senior, A. W.; Kavukcuoglu, K.; Kohli, P.; Hassabis, D. Highly accurate protein structure prediction with AlphaFold. *Nature* **2021**, *596*, 583–589.

(204) Terwilliger, T. C.; Liebschner, D.; Croll, T. I.; Williams, C. J.; McCoy, A. J.; Poon, B. K.; Afonine, P. V.; Oeffner, R. D.; Richardson, J. S.; Read, R. J.; Adams, P. D. AlphaFold predictions are valuable hypotheses and accelerate but do not replace experimental structure determination. *Nat. Methods* **2023**.

(205) Waltenspühl, Y.; Ehrenmann, J.; Klenk, C.; Plückthun, A. Engineering of challenging G protein-coupled receptors for structure determination and biophysical studies. *Molecules* **2021**, *26*.

(206) Bertheleme, N.; Chae, P. S.; Singh, S.; Mossakowska, D.; Hann, M. M.; Smith, K. J.; Hubbard, J. A.; Dowell, S. J.; Byrne, B. Unlocking the secrets of the gatekeeper:

methods for stabilizing and crystallizing GPCRs. *Biochim. Biophys. Acta, Biomembr.* **2013**, *1828*, 2583–2591.

(207) Cherezov, V.; Rosenbaum, D. M.; Hanson, M. A.; Rasmussen, S. G. F.; Thian, F. S.; Kobilka, T. S.; Choi, H.-J.; Kuhn, P.; Weis, W. I.; Kobilka, B. K.; Stevens, R. C. High-resolution crystal structure of an engineered human β_2-adrenergic G protein-coupled receptor. *Science* **2007**, *318*, 1258–1265.

(208) Hua, T.; Vemuri, K.; Pu, M.; Qu, L.; Han, G. W.; Wu, Y.; Zhao, S.; Shui, W.; Li, S.; Korde, A.; Laprairie, R. B.; Stahl, E. L.; Ho, J.-H.; Zvonok, N.; Zhou, H.; Kufareva, I.; Wu, B.; Zhao, Q.; Hanson, M. A.; Bohn, L. M.; Makriyannis, A.; Stevens, R. C.; Liu, Z.-J. Crystal structure of the human cannabinoid receptor CB_1. *Cell* **2016**, *167*, 750-762.e14.

(209) Yin, J.; Babaoglu, K.; Brautigam, C. A.; Clark, L.; Shao, Z.; Scheuermann, T. H.; Harrell, C. M.; Gotter, A. L.; Roecker, A. J.; Winrow, C. J.; Renger, J. J.; Coleman, P. J.; Rosenbaum, D. M. Structure and ligand-binding mechanism of the human OX_1 and OX_2 orexin receptors. *Nat. Struct. Mol. Biol.* **2016**, *23*, 293–299.

(210) Xiang, J.; Chun, E.; Liu, C.; Jing, L.; Al-Sahouri, Z.; Zhu, L.; Liu, W. Successful strategies to determine high-resolution structures of GPCRs. *Trends Pharmacol. Sci.* **2016**, *37*, 1055–1069.

(211) Magnani, F.; Serrano-Vega, M. J.; Shibata, Y.; Abdul-Hussein, S.; Lebon, G.; Miller-Gallacher, J.; Singhal, A.; Strege, A.; Thomas, J. A.; Tate, C. G. A mutagenesis and screening strategy to generate optimally thermostabilized membrane proteins for structural studies. *Nat. Protoc.* **2016**, *11*, 1554–1571.

(212) Warne, T.; Serrano-Vega, M. J.; Baker, J. G.; Moukhametzianov, R.; Edwards, P. C.; Henderson, R.; Leslie, A. G. W.; Tate, C. G.; Schertler, G. F. X. Structure of a β_1-adrenergic G-protein-coupled receptor. *Nature* **2008**, *454*, 486–491.

(213) Ratkeviciute, G.; Cooper, B. F.; Knowles, T. J. Methods for the solubilisation of membrane proteins: the micelle-aneous world of membrane protein solubilisation. *Biochem. Soc. Trans.* **2021**, *49*, 1763–1777.

(214) Lee, S.; Ghosh, S.; Jana, S.; Robertson, N.; Tate, C. G.; Vaidehi, N. How do branched detergents stabilize GPCRs in micelles? *Biochemistry* **2020**, *59*, 2125–2134.

(215) Seddon, A. M.; Curnow, P.; Booth, P. J. Membrane proteins, lipids and detergents: not just a soap opera. *Biochim. Biophys. Acta* **2004**, *1666*, 105–117.

(216) Thompson, A. A.; Liu, J. J.; Chun, E.; Wacker, D.; Wu, H.; Cherezov, V.; Stevens, R. C. GPCR stabilization using the bicelle-like architecture of mixed sterol-detergent micelles. *Methods* **2011**, *55*, 310–317.

(217) McPherson, A.; Gavira, J. A. Introduction to protein crystallization. *Acta Crystallogr., Sect. F: Struct. Biol. Cryst. Commun.* **2014**, *70*, 2–20.

(218) Mahmoodi, S.; Pourhassan-Moghaddam, M.; Wood, D. W.; Majdi, H.; Zarghami, N. Current affinity approaches for purification of recombinant proteins. *Cogent Biol.* **2019**, *5*, 1665406.

(219) Ghosh, E.; Kumari, P.; Jaiman, D.; Shukla, A. K. Methodological advances: the unsung heroes of the GPCR structural revolution. *Nat. Rev. Mol. Cell Biol.* **2015**, *16*, 69–81.

(220) Porath, J. Immobilized metal ion affinity chromatography. *Protein Expression Purif.* **1992**, *3*, 263–281.

(221) Prasanna, R. R.; Vijayalakshmi, M. A. Immobilized metal-ion affinity systems for recovery and structure–function studies of proteins at molecular, supramolecular, and cellular levels. *Pure Appl. Chem.* **2010**, *82*, 39–55.

(222) Blowers, D. P. Immobilized metal ion chromatography. In *Encyclopedia of Separation Science;* Elsevier; pp. 277–283.

(223) Fekete, S.; Beck, A.; Veuthey, J.-L.; Guillarme, D. Theory and practice of size exclusion chromatography for the analysis of protein aggregates. *J. Pharm. Biomed. Anal.* **2014**, *101*, 161–173.

(224) Nagy, K.; Vékey, K. Separation methods. In *Medical Applications of Mass Spectrometry;* Elsevier; pp. 61–92.

(225) Mancusso, R.; Karpowich, N. K.; Czyzewski, B. K.; Wang, D.-N. Simple screening method for improving membrane protein thermostability. *Methods* **2011**, *55*, 324–329.

(226) Kwan, T. O. C.; Reis, R.; Siligardi, G.; Hussain, R.; Cheruvara, H.; Moraes, I. Selection of biophysical methods for characterisation of membrane proteins. *Int. J. Mol. Sci.* **2019**, *20*.

(227) Mastroberardino, P. G.; Orr, A. L.; Hu, X.; Na, H. M.; Greenamyre, J. T. A FRET-based method to study protein thiol oxidation in histological preparations. *Free Radic. Biol. Med.* **2008**, *45*, 971–981.

(228) Alexandrov, A. I.; Mileni, M.; Chien, E. Y. T.; Hanson, M. A.; Stevens, R. C. Microscale fluorescent thermal stability assay for membrane proteins. *Structure* **2008**, *16*, 351–359.

(229) Senisterra, G.; Chau, I.; Vedadi, M. Thermal denaturation assays in chemical biology. *Assay Drug Dev. Technol.* **2012**, *10*, 128–136.

(230) Li, D.; Howe, N.; Dukkipati, A.; Shah, S. T. A.; Bax, B. D.; Edge, C.; Bridges, A.; Hardwicke, P.; Singh, O. M. P.; Giblin, G.; Pautsch, A.; Pfau, R.; Schnapp, G.; Wang, M.; Olieric, V.; Caffrey, M. Crystallizing membrane proteins in the lipidic mesophase. Experience with human prostaglandin E_2 synthase 1 and an evolving strategy. *Cryst. Growth Des.* **2014**, *14*, 2034–2047.

(231) Caffrey, M.; Cherezov, V. Crystallizing membrane proteins using lipidic mesophases. *Nat. Protoc.* **2009**, *4*, 706–731.

(232) Ishchenko, A.; Abola, E. E.; Cherezov, V. Crystallization of membrane proteins: An overview. *Methods Mol. Biol.* **2017**, *1607*, 117–141.

(233) Kermani, A. A. A guide to membrane protein X-ray crystallography. *FEBS J.* **2021**, *288*, 5788–5804.

(234) Timofeev, V.; Samygina, V. Protein crystallography: Achievements and challenges. *Crystals* **2023**, *13*, 71.

(235) Kors, C. A.; Wallace, E.; Davies, D. R.; Li, L.; Laible, P. D.; Nollert, P. Effects of impurities on membrane-protein crystallization in different systems. *Acta Crystallogr., Sect. D: Biol. Crystallogr.* **2009**, *65*, 1062–1073.

(236) Grisshammer, R. New approaches towards the understanding of integral membrane proteins: A structural perspective on G protein-coupled receptors. *Protein Sci.* **2017**, *26*, 1493–1504.

(237) Caffrey, M. A comprehensive review of the lipid cubic phase or in meso method for crystallizing membrane and soluble proteins and complexes. *Acta Crystallogr., Sect. F: Struct. Biol. Cryst. Commun.* **2015**, *71*, 3–18.

(238) Li, D.; Caffrey, M. Structure and functional characterization of membrane integral proteins in the lipid cubic phase. *J. Mol. Biol.* **2020**, *432*, 5104–5123.

(239) Li, D.; Lee, J.; Caffrey, M. Crystallizing membrane proteins in lipidic mesophases. A host lipid screen. *Cryst. Growth Des.* **2011**, *11*, 530–537.

(240) Liu, W.; Ishchenko, A.; Cherezov, V. Preparation of microcrystals in lipidic cubic phase for serial femtosecond crystallography. *Nat. Protoc.* **2014**, *9*, 2123–2134.

(241) Zabara, A.; Chong, J. T. Y.; Martiel, I.; Stark, L.; Cromer, B. A.; Speziale, C.; Drummond, C. J.; Mezzenga, R. Design of ultra-swollen lipidic mesophases for the crystallization of membrane proteins with large extracellular domains. *Nat. Commun.* **2018**, *9*, 544.

(242) Li, D.; Shah, S. T. A.; Caffrey, M. Host lipid and temperature as important screening variables for crystallizing integral membrane proteins in lipidic mesophases. Trials with aiacylglycerol kinase. *Cryst. Growth Des.* **2013**, *13*, 2846–2857.

(243) Misquitta, L. V.; Misquitta, Y.; Cherezov, V.; Slattery, O.; Mohan, J. M.; Hart, D.; Zhalnina, M.; Cramer, W. A.; Caffrey, M. Membrane protein crystallization in lipidic mesophases with tailored bilayers. *Structure* **2004**, *12*, 2113–2124.

(244) Zhou, X. E.; Gao, X.; Barty, A.; Kang, Y.; He, Y.; Liu, W.; Ishchenko, A.; White, T. A.; Yefanov, O.; Han, G. W.; Xu, Q.; Waal, P. W. de; Suino-Powell, K. M.; Boutet, S.; Williams, G. J.; Wang, M.; Li, D.; Caffrey, M.; Chapman, H. N.; Spence, J. C. H.; Fromme, P.; Weierstall, U.; Stevens, R. C.; Cherezov, V.; Melcher, K.; Xu, H. E. X-ray laser diffraction for structure determination of the rhodopsin-arrestin complex. *Sci. Data* **2016**, *3*, 160021.

(245) Birch, J.; Axford, D.; Foadi, J.; Meyer, A.; Eckhardt, A.; Thielmann, Y.; Moraes, I. The fine art of integral membrane protein crystallisation. *Methods* **2018**, *147*, 150–162.

(246) Rupp, B. Origin and use of crystallization phase diagrams. *Acta Crystallogr., Sect. F: Struct. Biol. Cryst. Commun.* **2015**, *71*, 247–260.

(247) Sun, Y.; Huang, P. Adenosine A_{2B} receptor: From cell biology to human diseases. *Front. Chem.* **2016**, *4*, 37.

(248) Jiang, J.; Seel, C. J.; Temirak, A.; Namasivayam, V.; Arridu, A.; Schabikowski, J.; Baqi, Y.; Hinz, S.; Hockemeyer, J.; Müller, C. E. A_{2B} adenosine receptor antagonists with picomolar potency. *J. Med. Chem.* **2019**, *62*, 4032–4055.

(249) Seibt, B. F.; Schiedel, A. C.; Thimm, D.; Hinz, S.; Sherbiny, F. F.; Müller, C. E. The second extracellular loop of GPCRs determines subtype-selectivity and controls efficacy as evidenced by loop exchange study at A_2 adenosine receptors. *Biochem. Pharmacol.* **2013**, *85*, 1317–1329.

(250) Guan, X. M.; Kobilka, T. S.; Kobilka, B. K. Enhancement of membrane insertion and function in a type IIIb membrane protein following introduction of a cleavable signal peptide. *J. Biol. Chem.* **1992**, *267*, 21995–21998.

(251) Koh, S. S.; Hengartner, C. J.; Young, R. A. Baculoviral transfer vectors for expression of FLAG fusion proteins in insect cells. *Biotechniques* **1997**, *23*, 622-4, 626-7.

(252) Vaaßen, V. J. *Stabilization of the adenosine A_{2B} receptor for crystallization:* Rheinische Friedrich-Wilhelms-Universität Bonn, **2019**.

(253) Xu, F.; Wu, H.; Katritch, V.; Han, G. W.; Jacobson, K. A.; Gao, Z.-G.; Cherezov, V.; Stevens, R. C. Structure of an agonist-bound human A_{2A} adenosine receptor. *Science* **2011**, *332*, 322–327.

(254) Oomens, A. G.; Monsma, S. A.; Blissard, G. W. The baculovirus GP64 envelope fusion protein: synthesis, oligomerization, and processing. *Virology* **1995**, *209*, 592–603.

(255) Monsma, S. A.; Oomens, A. G.; Blissard, G. W. The GP64 envelope fusion protein is an essential baculovirus protein required for cell-to-cell transmission of infection. *J. Virol.* **1996**, *70*, 4607–4616.

(256) Rohrmann, G. F. Polyhedrin structure. *J. Gen. Virol.* **1986**, *67 (Pt 8)*, 1499–1513.

(257) Roy, A.; Kucukural, A.; Zhang, Y. I-TASSER: a unified platform for automated protein structure and function prediction. *Nat. Protoc.* **2010**, *5*, 725–738.

(258) Yasuda, S.; Kajiwara, Y.; Toyoda, Y.; Morimoto, K.; Suno, R.; Iwata, S.; Kobayashi, T.; Murata, T.; Kinoshita, M. Hot-spot residues to be mutated common in G protein-coupled receptors of class A: Identification of thermostabilizing mutations followed by determination of three-dimensional structures for two example receptors. *J. Phys. Chem. B* **2017**, *121*, 6341–6350.

(259) Claff, T. *X-ray crystallography of G protein-coupled receptors. Exploring interactions with drug molecules:* Rheinische Friedrich-Wilhelms-Universität Bonn, **2022**.

(260) Zhao, Q.; Wu, B. Ice breaking in GPCR structural biology. *Acta Pharmacol. Sin.* **2012**, *33*, 324–334.

(261) Nagae, M.; Yamaguchi, Y. Function and 3D structure of the N-glycans on glycoproteins. *Int. J. Mol. Sci.* **2012**, *13*, 8398–8429.

(262) Esmail, S.; Manolson, M. F. Advances in understanding N-glycosylation structure, function, and regulation in health and disease. *Eur. J. Cell Biol.* **2021**, *100*, 151186.

(263) Munk, C.; Mutt, E.; Isberg, V.; Nikolajsen, L. F.; Bibbe, J. M.; Flock, T.; Hanson, M. A.; Stevens, R. C.; Deupi, X.; Gloriam, D. E. An online resource for GPCR structure determination and analysis. *Nat. Methods* **2019**, *16*, 151–162.

(264) Coleman, J. L. J.; Ngo, T.; Smith, N. J. The G protein-coupled receptor *N*-terminus and receptor signalling: N-tering a new era. *Cell. Signalling* **2017**, *33*, 1–9.

(265) Glukhova, A.; Thal, D. M.; Nguyen, A. T.; Vecchio, E. A.; Jörg, M.; Scammells, P. J.; May, L. T.; Sexton, P. M.; Christopoulos, A. Structure of the adenosine A_1 receptor reveals the basis for subtype selectivity. *Cell* **2017**, *168*, 867-877.e13.

(266) Audet, M.; Villers, K.; Velasquez, J.; Chu, M.; Hanson, C.; Stevens, R. C. Small-scale approach for precrystallization screening in GPCR X-ray crystallography. *Nat. Protoc.* **2020**, *15*, 144–160.

(267) Cherezov, V.; Abola, E.; Stevens, R. C. Recent progress in the structure determination of GPCRs, a membrane protein family with high potential as pharmaceutical targets. *Methods Mol. Biol.* **2010**, *654*, 141–168.

(268) Schlegel, J. G. *Converting the elusive G protein-coupled adenosine A_3 receptor into a super-stable, well-characterized receptor model for structural studies:* Rheinische Friedrich-Wilhelms-Universität Bonn, **2023**.

(269) Lera Ruiz, M. de; Lim, Y.-H.; Zheng, J. Adenosine A_{2A} receptor as a drug discovery target. *J. Med. Chem.* **2014**, *57*, 3623–3650.

(270) El Maatougui, A.; Azuaje, J.; González-Gómez, M.; Miguez, G.; Crespo, A.; Carbajales, C.; Escalante, L.; García-Mera, X.; Gutiérrez-de-Terán, H.; Sotelo, E. Discovery of Potent and Highly Selective A_{2B} Adenosine Receptor Antagonist Chemotypes. *J. Med. Chem.* **2016**, *59*, 1967–1983.

(271) Hayallah, A. M.; Sandoval-Ramírez, J.; Reith, U.; Schobert, U.; Preiss, B.; Schumacher, B.; Daly, J. W.; Müller, C. E. 1,8-disubstituted xanthine derivatives: synthesis of potent A_{2B}-selective adenosine receptor antagonists. *J. Med. Chem.* **2002**, *45*, 1500–1510.

(272) Borrmann, T.; Hinz, S.; Bertarelli, D. C. G.; Li, W.; Florin, N. C.; Scheiff, A. B.; Müller, C. E. 1-alkyl-8-(piperazine-1-sulfonyl)phenylxanthines: development and characterization of adenosine A_{2B} receptor antagonists and a new radioligand with subnanomolar affinity and subtype specificity. *J. Med. Chem.* **2009**, *52*, 3994–4006.

(273) Vecchio, E. A.; Chuo, C. H.; Baltos, J.-A.; Ford, L.; Scammells, P. J.; Wang, B. H.; Christopoulos, A.; White, P. J.; May, L. T. The hybrid molecule, VCP746, is a potent adenosine A_{2B} receptor agonist that stimulates anti-fibrotic signalling. *Biochem. Pharmacol.* **2016**, *117*, 46–56.

(274) Linden, J.; Thai, T.; Figler, H.; Jin, X.; Robeva, A. S. Characterization of human A_{2B} adenosine receptors: radioligand binding, western blotting, and coupling to Gq in human embryonic kidney 293 cells and HMC-1 mast cells. *Mol. Pharmacol.* **1999**, *56*, 705–713.

(275) Fredholm, B. B.; IJzerman, A. P.; Jacobson, K. A.; Linden, J.; Müller, C. E. International union of basic and clinical pharmacology. LXXXI. Nomenclature and classification of adenosine receptors - an update. *Pharmacol. Rev.* **2011**, *63*, 1–34.

(276) Kim, S.-A.; Marshall, M. A.; Melman, N.; Kim, H. S.; Müller, C. E.; Linden, J.; Jacobson, K. A. Structure-activity relationships at human and rat A_{2B} adenosine receptors of xanthine derivatives substituted at the 1-, 3-, 7-, and 8-positions. *J. Med. Chem.* **2002**, *45*, 2131–2138.

(277) Jacobson, K. A.; IJzerman, A. P.; Linden, J. 1,3-dialkylxanthine derivatives having high potency as antagonists at human A_{2B} adenosine receptors. *Drug Dev. Res.* **1999**, *47*, 45–53.

(278) Clontech Laboratories, Inc. TALON® metal affinity resins user manual. Retrieved 06.11.2023 from https://www.takarabio.com/documents/User%20Manual/TALON%20Metal%20Affinity%20Resins%20User%20Manual%20%28PT1320/TALON%20Metal%20Affinity%20Resins%20User%20Manual%20%28PT1320-1%29_031716.pdf.

(279) Rucktooa, P.; Cheng, R. K. Y.; Segala, E.; Geng, T.; Errey, J. C.; Brown, G. A.; Cooke, R. M.; Marshall, F. H.; Doré, A. S. Towards high throughput GPCR crystallography: In meso soaking of adenosine A_{2A} receptor crystals. *Sci. Rep.* **2018**, *8*, 41.

(280) Ishchenko, A.; Stauch, B.; Han, G. W.; Batyuk, A.; Shiriaeva, A.; Li, C.; Zatsepin, N.; Weierstall, U.; Liu, W.; Nango, E.; Nakane, T.; Tanaka, R.; Tono, K.; Joti, Y.; Iwata, S.; Moraes, I.; Gati, C.; Cherezov, V. Toward G protein-coupled receptor structure-based drug design using X-ray lasers. *IUCrJ* **2019**, *6*, 1106–1119.

(281) Cheng, R. K. Y.; Segala, E.; Robertson, N.; Deflorian, F.; Doré, A. S.; Errey, J. C.; Fiez-Vandal, C.; Marshall, F. H.; Cooke, R. M. Structures of human A_1 and A_{2A} adenosine receptors with xanthines reveal determinants of selectivity. *Structure* **2017**, *25*, 1275-1285.e4.

(282) Rial, D. V.; Ceccarelli, E. A. Removal of DnaK contamination during fusion protein purifications. *Protein Expression Purif.* **2002**, *25*, 503–507.

(283) Hampton Research. Additive Screen™ user guide. Retrieved 06.11.2023 from https://hamptonresearch.com/uploads/support_materials/HR2-428_Documents.pdfhttps://hamptonresearch.com/uploads/support_materials/HR2-428_Documents.pdf.

(284) Temirak, A.; Schlegel, J. G.; Voss, J. H.; Vaaßen, V. J.; Vielmuth, C.; Claff, T.; Müller, C. E. Irreversible antagonists for the adenosine A_{2B} receptor. *Molecules* **2022**, *27*.

(285) Rosenbaum, D. M.; Zhang, C.; Lyons, J. A.; Holl, R.; Aragao, D.; Arlow, D. H.; Rasmussen, S. G. F.; Choi, H.-J.; Devree, B. T.; Sunahara, R. K.; Chae, P. S.; Gellman, S. H.; Dror, R. O.; Shaw, D. E.; Weis, W. I.; Caffrey, M.; Gmeiner, P.; Kobilka, B. K. Structure and function of an irreversible agonist-β_2 adrenoceptor complex. *Nature* **2011**, *469*, 236–240.

(286) Weichert, D.; Kruse, A. C.; Manglik, A.; Hiller, C.; Zhang, C.; Hübner, H.; Kobilka, B. K.; Gmeiner, P. Covalent agonists for studying G protein-coupled receptor activation. *Proc. Natl. Acad. Sci. U. S. A.* **2014**, *111*, 10744–10748.

(287) Granier, S.; Kobilka, B. A new era of GPCR structural and chemical biology. *Nat. Chem. Biol.* **2012**, *8*, 670–673.

(288) Weichert, D.; Gmeiner, P. Covalent molecular probes for class A G protein-coupled receptors: advances and applications. *ACS Chem. Biol.* **2015**, *10*, 1376–1386.

(289) Dong, J.; Krasnova, L.; Finn, M. G.; Sharpless, K. B. Sulfur(VI) fluoride exchange (SuFEx): another good reaction for click chemistry. *Angew. Chem. Int. Ed Engl.* **2014**, *53*, 9430–9448.

(290) Beatty, J.; Debien, L.; Jeffrey, J. Azolopyrimidine for the treatment of cancer-related disorders. Patent number WO 2018/136700, **2018**.

(291) U.S. National Library of Medicine. A phase I-II study to test the safety and efficacy of PD1 (AB122) and adenosine receptor (AB928) antagonists with chemotherapy after short-course radiation for rectal cancer. Identifier NCT05024097. Retrieved 18.12.2023 from https://classic.clinicaltrials.gov/ct2/show/NCT05024097.

(292) U.S. National Library of Medicine. An open label study evaluating the efficacy and safety of etrumadenant (AB928) based treatment combinations in participants with metastatic colorectal cancer. Identifier NCT04660812. Retrieved 18.12.2023 from https://classic.clinicaltrials.gov/ct2/show/NCT04660812.

(293) U.S. National Library of Medicine. Study to evaluate monotherapy and combination immunotherapies in participants with PD-L1 positive non-small cell lung cancer. Identifier NCT04262856. Retrieved 18.12.2023 from https://classic.clinicaltrials.gov/ct2/show/NCT04262856.

(294) U.S. National Library of Medicine. Neoadjuvant atezolizumab-based combination therapy in men with localized prostate cancer prior to radical prostatectomy. Identifier NCT03821246. Retrieved 18.12.2023 from https://classic.clinicaltrials.gov/ct2/show/NCT03821246.

(295) Newby, Z. E. R.; O'Connell, J. D.; Gruswitz, F.; Hays, F. A.; Harries, W. E. C.; Harwood, I. M.; Ho, J. D.; Lee, J. K.; Savage, D. F.; Miercke, L. J. W.; Stroud, R. M. A general protocol for the crystallization of membrane proteins for X-ray structural investigation. *Nat. Protoc.* **2009**, *4*, 619–637.

(296) Nannenga, B. L.; Iadanza, M. G.; Vollmar, B. S.; Gonen, T. Overview of electron crystallography of membrane proteins: crystallization and screening strategies using negative stain electron microscopy. *Curr. Protoc. Protein Sci.* **2013**, *Chapter 17*, 17.15.1 - 17.15.11.

(297) Bhat, E. A.; Abdalla, M.; Rather, I. A. Key factors for successful protein purification and crystallization. *Glob. J. Biotechnol. Biomater. Sci.* **2018**, *4*, 1–7.

(298) Salom, D.; Padayatti, P. S.; Palczewski, K. Crystallization of G protein-coupled receptors. *Methods Cell Biol.* **2013**, *117*, 451–468.

(299) Noble, J. E.; Bailey, M. J. A. Quantitation of protein. *Methods Enzymol.* **2009**, *463*, 73–95.

(300) Simonian, M. H.; Smith, J. A. Spectrophotometric and colorimetric determination of protein concentration. *Curr. Protoc. Mol. Biol.* **2006**, *Chapter 10*, Unit 10.1A.

(301) Ghisaidoobe, A. B. T.; Chung, S. J. Intrinsic tryptophan fluorescence in the detection and analysis of proteins: a focus on Förster resonance energy transfer techniques. *Int. J. Mol. Sci.* **2014**, *15*, 22518–22538.

(302) Morales, E. S.; Parcerisa, I. L.; Ceccarelli, E. A. A novel method for removing contaminant Hsp70 molecular chaperones from recombinant proteins. *Protein Sci.* **2019**, *28*, 800–807.

(303) King, A. M.; MacRae, T. H. Insect heat shock proteins during stress and diapause. *Annu. Rev. Entomol.* **2015**, *60*, 59–75.

(304) Kato, K.; Goto, S.; Inaguma, Y.; Hasegawa, K.; Morishita, R.; Asano, T. Purification and characterization of a 20-kDa protein that is highly homologous to alpha B crystallin. *J. Biol. Chem.* **1994**, *269*, 15302–15309.

(305) Kobe, B.; Ve, T.; Williams, S. J. Fusion protein-assisted protein crystallization. *Acta Crystallogr., Sect. F: Struct. Biol. Cryst. Commun.* **2015**, *71*, 861–869.

(306) Zhang, K.; Wu, H.; Hoppe, N.; Manglik, A.; Cheng, Y. Fusion protein strategies for cryo-EM study of G protein-coupled receptors. *Nat. Commun.* **2022**, *13*, 4366.

(307) Liu, S.; Li, W. Protein fusion strategies for membrane protein stabilization and crystal structure determination. *Crystals* **2022**, *12*, 1041.

(308) Lees, J. A.; Dias, J. M.; Rajamohan, F.; Fortin, J.-P.; O'Connor, R.; Kong, J. X.; Hughes, E. A. G.; Fisher, E. L.; Tuttle, J. B.; Lovett, G.; Kormos, B. L.; Unwalla, R. J.; Zhang, L.; Dechert Schmitt, A.-M.; Zhou, D.; Moran, M.; Stevens, K. A.; Fennell, K. F.; Varghese, A. E.; Maxwell, A.; Cote, E. E.; Zhang, Y.; Han, S. An inverse agonist of orphan receptor GPR61 acts by a G protein-competitive allosteric mechanism. *Nat. Commun.* **2023**, *14*, 5938.

(309) Kwon, N.-Y.; Kim, Y.; Lee, J.-O. The application of helix fusion methods in structural biology. *Curr. Opin. Struct. Biol.* **2020**, *60*, 110–116.

(310) Platts, L.; Darby, S. J.; Falconer, R. J. Control of globular protein thermal stability in aqueous formulations by the positively charged amino acid excipients. *J. Pharm. Sci.* **2016**, *105*, 3532–3536.

(311) Kaufmann, T. C.; Engel, A.; Rémigy, H.-W. A novel method for detergent concentration determination. *Biophys. J.* **2006**, *90*, 310–317.

(312) Misquitta, Y.; Caffrey, M. Detergents destabilize the cubic phase of monoolein: implications for membrane protein crystallization. *Biophys. J.* **2003**, *85*, 3084–3096.

(313) Ai, X.; Caffrey, M. Membrane protein crystallization in lipidic mesophases: detergent effects. *Biophys. J.* **2000**, *79*, 394–405.

(314) Duvaud, S.; Gabella, C.; Lisacek, F.; Stockinger, H.; Ioannidis, V.; Durinx, C. Expasy, the Swiss Bioinformatics Resource Portal, as designed by its users. *Nucleic Acids Res.* **2021**, *49*, W216-W227.

(315) Parry, D. A. D.; Fraser, R. D. B.; Squire, J. M. Fifty years of coiled-coils and alpha-helical bundles: a close relationship between sequence and structure. *J. Struct. Biol.* **2008**, *163*, 258–269.

(316) Strop, P.; Brunger, A. T. Refractive index-based determination of detergent concentration and its application to the study of membrane proteins. *Protein Sci.* **2005**, *14*, 2207–2211.

(317) Slotboom, D. J.; Duurkens, R. H.; Olieman, K.; Erkens, G. B. Static light scattering to characterize membrane proteins in detergent solution. *Methods* **2008**, *46*, 73–82.

(318) Wadsten, P.; Wöhri, A. B.; Snijder, A.; Katona, G.; Gardiner, A. T.; Cogdell, R. J.; Neutze, R.; Engström, S. Lipidic sponge phase crystallization of membrane proteins. *J. Mol. Biol.* **2006**, *364*, 44–53.

(319) Doré, A. S.; Robertson, N.; Errey, J. C.; Ng, I.; Hollenstein, K.; Tehan, B.; Hurrell, E.; Bennett, K.; Congreve, M.; Magnani, F.; Tate, C. G.; Weir, M.; Marshall, F. H. Structure of the adenosine A_{2A} receptor in complex with ZM241385 and the xanthines XAC and caffeine. *Structure* **2011**, *19*, 1283–1293.

(320) Hino, T.; Arakawa, T.; Iwanari, H.; Yurugi-Kobayashi, T.; Ikeda-Suno, C.; Nakada-Nakura, Y.; Kusano-Arai, O.; Weyand, S.; Shimamura, T.; Nomura, N.; Cameron, A. D.; Kobayashi, T.; Hamakubo, T.; Iwata, S.; Murata, T. G-protein-coupled receptor inactivation by an allosteric inverse-agonist antibody. *Nature* **2012**, *482*, 237–240.

(321) Ohno, Y.; Suzuki, M.; Asada, H.; Kanda, T.; Saki, M.; Miyagi, H.; Yasunaga, M.; Suno, C.; Iwata, S.; Saito, J.-I.; Uchida, S. In vitro pharmacological profile of KW-6356, a novel adenosine A_{2A} receptor antagonist/inverse agonist. *Mol. Pharmacol.* **2023**, *103*, 311–324.

(322) Batool, M.; Ahmad, B.; Choi, S. A structure-based drug discovery paradigm. *Int. J. Mol. Sci.* **2019**, *20*.

(323) Meng, E. C.; Goddard, T. D.; Pettersen, E. F.; Couch, G. S.; Pearson, Z. J.; Morris, J. H.; Ferrin, T. E. UCSF ChimeraX: Tools for structure building and analysis. *Protein Sci.* **2023**, *32*, e4792.

(324) Invitrogen. Bac-to-Bac® baculovirus expression system. Retrieved 13.06.2023 from https://tools.thermofisher.com/content/sfs/manuals/bactobac_man.pdf.

(325) Green, M. R.; Sambrook, J. Screening Bacterial Colonies Using X-Gal and IPTG: α-Complementation. *Cold Spring Harb. Protoc.* **2019**, *14*, 790–794.

(326) Kingsley, D. H.; Behbahani, A.; Rashtian, A.; Blissard, G. W.; Zimmerberg, J. A discrete stage of baculovirus GP64-mediated membrane fusion. *Mol. Biol. Cell* **1999**, *10*, 4191–4200.

(327) Mattei, B.; Lira, R. B.; Perez, K. R.; Riske, K. A. Membrane permeabilization induced by Triton X-100: The role of membrane phase state and edge tension. *Chem. Phys. Lipids* **2017**, *202*, 28–37.

(328) Johnson, S.; Nguyen, V.; Coder, D. Assessment of cell viability. *Curr. Protoc. Cytom.* **2013**, *Chapter 9*, 9.2.1-9.2.26.

(329) Durrant, I. Enhanced chemiluminescent detection of horseradish peroxidase labeled probes. *Methods Mol. Biol.* **1994**, *31*, 147–161.

(330) Vagenende, V.; Yap, M. G. S.; Trout, B. L. Mechanisms of protein stabilization and prevention of protein aggregation by glycerol. *Biochemistry* **2009**, *48*, 11084–11096.

(331) Engelsman, J. den; Garidel, P.; Smulders, R.; Koll, H.; Smith, B.; Bassarab, S.; Seidl, A.; Hainzl, O.; Jiskoot, W. Strategies for the assessment of protein aggregates in pharmaceutical biotech product development. *Pharm. Res.* **2011**, *28*, 920–933.

(332) GraphPad. Equation: Biphasic dose-response. Retrieved 09.10.2023 from https://www.graphpad.com/guides/prism/latest/curve-fitting/reg_biphasic_dose_response.htm?q=Equation+Biphasic+dose-response.

(333) Kabsch, W. Integration, scaling, space-group assignment and post-refinement. *Acta Crystallogr., Sect. D: Biol. Crystallogr.* **2010**, *66*, 133–144.

(334) Agirre, J.; Atanasova, M.; Bagdonas, H.; Ballard, C. B.; Baslé, A.; Beilsten-Edmands, J.; Borges, R. J.; Brown, D. G.; Burgos-Mármol, J. J.; Berrisford, J. M.; Bond, P. S.; Caballero, I.; Catapano, L.; Chojnowski, G.; Cook, A. G.; Cowtan, K. D.; Croll, T. I.; Debreczeni, J. É.; Devenish, N. E.; Dodson, E. J.; Drevon, T. R.; Emsley, P.; Evans, G.; Evans, P. R.; Fando, M.; Foadi, J.; Fuentes-Montero, L.; Garman, E. F.; Gerstel, M.; Gildea, R. J.; Hatti, K.; Hekkelman, M. L.; Heuser, P.; Hoh, S. W.; Hough, M. A.; Jenkins, H. T.; Jiménez, E.; Joosten, R. P.; Keegan, R. M.; Keep, N.; Krissinel, E. B.; Kolenko, P.; Kovalevskiy, O.; Lamzin, V. S.; Lawson, D. M.; Lebedev, A. A.; Leslie, A. G. W.; Lohkamp, B.; Long, F.; Malý, M.; McCoy, A. J.; McNicholas, S. J.; Medina, A.; Millán, C.; Murray, J. W.; Murshudov, G. N.; Nicholls, R. A.; Noble, M. E. M.; Oeffner, R.; Pannu, N. S.; Parkhurst, J. M.; Pearce, N.; Pereira, J.; Perrakis, A.; Powell, H. R.; Read, R. J.; Rigden, D. J.; Rochira, W.; Sammito, M.; Sánchez Rodríguez, F.; Sheldrick, G. M.; Shelley, K. L.; Simkovic, F.; Simpkin, A. J.; Skubak, P.; Sobolev, E.; Steiner, R. A.; Stevenson, K.; Tews, I.; Thomas, J. M. H.; Thorn, A.; Valls, J. T.; Uski, V.; Usón, I.; Vagin, A.; Velankar, S.; Vollmar, M.; Walden, H.; Waterman, D.; Wilson, K. S.; Winn, M. D.; Winter, G.; Wojdyr, M.; Yamashita, K. The CCP4 suite: integrative software for macromolecular crystallography. *Acta Crystallogr., Sect. D: Struct. Biol.* **2023**, *79*, 449–461.

(335) McCoy, A. J.; Grosse-Kunstleve, R. W.; Adams, P. D.; Winn, M. D.; Storoni, L. C.; Read, R. J. Phaser crystallographic software. *J. Appl. Crystallogr.* **2007**, *40*, 658–674.

(336) Emsley, P.; Lohkamp, B.; Scott, W. G.; Cowtan, K. Features and development of Coot. *Acta Crystallogr., Sect. D: Biol. Crystallogr.* **2010**, *66*, 486–501.

(337) Afonine, P. V.; Grosse-Kunstleve, R. W.; Echols, N.; Headd, J. J.; Moriarty, N. W.; Mustyakimov, M.; Terwilliger, T. C.; Urzhumtsev, A.; Zwart, P. H.; Adams, P. D. Towards automated crystallographic structure refinement with phenix.refine. *Acta Crystallogr., Sect. D: Struct. Biol.* **2012**, *68*, 352–367.

(338) DiMaio, F.; Echols, N.; Headd, J. J.; Terwilliger, T. C.; Adams, P. D.; Baker, D. Improved low-resolution crystallographic refinement with Phenix and Rosetta. *Nat. Methods* **2013**, *10*, 1102–1104.

(339) Liebschner, D.; Afonine, P. V.; Baker, M. L.; Bunkóczi, G.; Chen, V. B.; Croll, T. I.; Hintze, B.; Hung, L.-W.; Jain, S.; McCoy, A. J.; Moriarty, N. W.; Oeffner, R. D.; Poon, B.

K.; Prisant, M. G.; Read, R. J.; Richardson, J. S.; Richardson, D. C.; Sammito, M. D.; Sobolev, O. V.; Stockwell, D. H.; Terwilliger, T. C.; Urzhumtsev, A. G.; Videau, L. L.; Williams, C. J.; Adams, P. D. Macromolecular structure determination using X-rays, neutrons and electrons: recent developments in Phenix. *Acta Crystallogr., Sect. D: Struct. Biol.* **2019**, *75*, 861–877.

7 Appendix

7.1 Detailed information on the large-scale protein purifications of the presented crystallization trials

The following tables will provide a comprehensive overview of the relevant information of the proteins utilized in the crystallization experiments presented in this thesis. Unless specified otherwise, the buffer compositions correspond to those provided in chapter 5.1.4 on page 229.

7.1.1 Crystallization of TC111 in complex with PA50

Amount of biomass	Equivalent of 450 mL of *Sf9* cells, infected at 2-3 x 10^6 cells/mL.		
Membrane preparation	Dounce homogenization 2x with hypotonic buffer, 3x with hypertonic buffer.		
Solubilization conditions	For 3 h with 0.5 % DDM and 0.1 % CHS. Final ligand concentration 12.5 µM.		
Resin incubation	375 µL beads, incubated with sample overnight.		
Resin wash conditions	40 CV of WB1 (+ 25 µM ligand), 27 CV of WB2 (+ 25 µM ligand).		
Elution	5 CV of EB (+ 25 µM ligand) added in 4 steps, with 10 min incubation each.		
Salt Exchange	No	Additional ligand added	No
Preparative SEC	No	Protein concentration	N.d.
Additional notes	–		

7.1.2 Crystallization of TC169 in complex with PA51

Amount of biomass	Equivalent of 450 mL of *Sf9* cells, infected at 2-3 x 10^6 cells/mL.		
Membrane preparation	Dounce homogenization 2x with hypotonic buffer, 3x with hypertonic buffer.		
Solubilization conditions	For 3 h with 0.5 % DDM and 0.1 % CHS. Final ligand concentration 12.5 µM.		
Resin incubation	500 µL beads, incubated with sample overnight.		
Resin wash conditions	30 CV of WB1 (+ 50 µM ligand), 20 CV of WB2 (+ 50 µM ligand).		
Elution	4 CV of EB (+ 50 µM ligand) added in 4 steps, with 10 min incubation each.		
Salt Exchange	No	Additional ligand added	No
Preparative SEC	No	Protein concentration	N.d.
Additional notes	–		

7.1.3 Crystallization of TC168 in complex with PSB-09120 (I)

Amount of biomass	Equivalent of 900 mL of *Sf9* cells, infected at 2-3 x 10^6 cells/mL.		
Membrane preparation	Dounce homogenization 2x with hypotonic buffer, 3x with hypertonic buffer.		
Solubilization conditions	For 3 h with 0.5 % DDM and 0.1 % CHS. Final ligand concentration 25 µM.		
Resin incubation	350 µL beads, incubated with sample overnight.		
Resin wash conditions	30 CV of WB1 (+ 50 µM ligand), 20 CV of WB2 (+ 50 µM ligand).		
Elution	6 CV of EB (+ 50 µM ligand) added in 4 steps, with 10 min incubation each.		
Salt Exchange	No	Additional ligand added	No
Preparative SEC	No	Protein concentration	N.d.
Additional notes	–		

7.1.4 Crystallization of TC168 in complex with PSB-09120 (II)

Amount of biomass	Equivalent of 900 mL of *Sf9* cells, infected at 2-3 x 10^6 cells/mL.		
Membrane preparation	Dounce homogenization 2x with hypotonic buffer, 3x with hypertonic buffer.		
Solubilization conditions	For 3 h with 0.5 % DDM and 0.1 % CHS. Final ligand concentration 12.5 µM.		
Resin incubation	300 µL beads, incubated with sample overnight.		
Resin wash conditions	33 CV of WB1 (+ 25 µM ligand), 25 CV of WB2 (+ 25 µM ligand).		
Elution	6 CV of EB (+ 50 µM ligand) added in 4 steps, with 10 min incubation each.		
Salt Exchange	No	Additional ligand added	No
Preparative SEC	No	Protein concentration	N.d.
Additional notes	–		

7.1.5 Crystallization of TC168 in complex with PSB-09120 (III)

Amount of biomass	Equivalent of 900 mL of *Sf9* cells, infected at 2-3 x 10^6 cells/mL.		
Membrane preparation	Dounce homogenization 2x with hypotonic buffer, 3x with hypertonic buffer.		
Solubilization conditions	For 3 h with 0.75 % DDM and 0.15 % CHS. Final ligand concentration 12.5 µM.		
Resin incubation	500 µL beads, incubated with sample overnight.		
Resin wash conditions	40 CV pre-WB, 20 CV of WB1 (+ 25 µM ligand), 15 CV of WB2 (+ 25 µM ligand).		
Elution	4 CV of EB (+ 50 µM ligand) added in 4 steps, with 10 min incubation each.		
Salt Exchange	No	Additional ligand added	No
Preparative SEC	No	Protein concentration	N.d.
Additional notes	–		

7.1.6 Crystallization of TC190 in complex with PSB-21500 (I)

Amount of biomass	Equivalent of 450 mL of *Sf9* cells, infected at 2-3 x 10^6 cells/mL.
Membrane preparation	Dounce homogenization 2x with hypotonic buffer, 3x with hypertonic buffer.
Solubilization conditions	For 3 h with 0.75 % DDM and 0.15 % CHS. Final ligand concentration 1 µM.
Resin incubation	250 µL beads, incubated with sample overnight.

Resin wash conditions	40 CV pre-WB, 15 CV of WB1 (+ 0.1 µM ligand), 10 CV of WB2 (+ 0.1 µM ligand).		
Elution	4 CV of EB (+ 0.1 µM ligand) added in 4 steps, with 10 min incubation each.		
Salt Exchange	No	Additional ligand added	No
Preparative SEC	No	Protein concentration	N.d.
Additional notes	–		

7.1.7 Crystallization of TC190 in complex with PSB-21500 (II)

Amount of biomass	Equivalent of 450 mL of *Sf9* cells, infected at 2-3 x 10^6 cells/mL.		
Membrane preparation	Dounce homogenization 2x with hypotonic buffer, 3x with hypertonic buffer.		
Solubilization conditions	2 µM of ligand pre-incubated with membrane at RT for 2h. Solubilization for 3 h with 0.75 % DDM and 0.15 % CHS. Final ligand concentration 1 µM.		
Resin incubation	250 µL beads, incubated with sample overnight.		
Resin wash conditions	40 CV pre-WB, 30 CV of WB1 (+ 0.1 µM ligand), 20 CV of WB2 (+ 0.1 µM ligand).		
Elution	6 CV of EB (+ 0.1 µM ligand) added in 3 steps, with 10 min incubation each.		
Salt Exchange	No	Additional ligand added	No
Preparative SEC	No	Protein concentration	N.d.
Additional notes	–		

7.1.8 Crystallization of TC190 in complex with PSB-21500 (III)

Amount of biomass	Equivalent of 450 mL of *Sf9* cells, infected at 2-3 x 10^6 cells/mL.		
Membrane preparation	Dounce homogenization 2x with hypotonic buffer, 3x with hypertonic buffer.		
Solubilization conditions	2 µM of ligand pre-incubated with membrane at RT for 2 h. Solubilization for 3 h with 0.75 % DDM and 0.15 % CHS. Final ligand concentration 1 µM.		
Resin incubation	250 µL beads, incubated with sample overnight.		
Resin wash conditions	40 CV pre-WB, 30 CV of WB1 (+ 0.1 µM ligand), 20 CV of WB2 (+ 0.1 µM ligand).		
Elution	6 CV of EB (+ 0.1 µM ligand) added in 3 steps, with 10 min incubation each.		
Salt Exchange	No	Additional ligand added	No
Preparative SEC	No	Protein concentration	N.d.
Additional notes	–		

7.1.9 Crystallization of TC190 in complex with PSB-21500 (IV)

Amount of biomass	Equivalent of 450 mL of *Sf9* cells, infected at 2-3 x 10^6 cells/mL.		
Membrane preparation	Dounce homogenization 2x with hypotonic buffer, 3x with hypertonic buffer.		
Solubilization conditions	2 µM of ligand pre-incubated with membrane at RT for 2 h. Solubilization for 3 h with 0.75 % DDM and 0.15 % CHS. Final ligand concentration 1 µM.		
Resin incubation	250 µL beads, incubated with sample overnight.		
Resin wash conditions	40 CV pre-WB, 30 CV of WB1 (no ligand), 20 CV of WB2 (no ligand).		
Elution	6 CV of EB (no ligand) added in 3 steps, with 10 min incubation each.		
Salt Exchange	No	Additional ligand added	No
Preparative SEC	No	Protein concentration	N.d.
Additional notes	–		

7.1.10 Crystallization of TC190 in complex with PSB-21500 (V)

Amount of biomass	Equivalent of 450 mL of *Sf9* cells, infected at 2-3 x 10^6 cells/mL.		
Membrane preparation	Dounce homogenization 2x with hypotonic buffer, 3x with hypertonic buffer.		
Solubilization conditions	2 µM of ligand pre-incubated with membrane at RT for 2 h. Solubilization for 3 h with 0.75 % DDM and 0.15 % CHS. Final ligand concentration 1 µM.		
Resin incubation	250 µL beads, incubated with sample overnight.		
Resin wash conditions	40 CV pre-WB, 30 CV of WB1 (no ligand), 20 CV of WB2 (no ligand).		
Elution	6 CV of EB (no ligand) added in 3 steps, with 10 min incubation each.		
Salt Exchange	No	Additional ligand added	No
Preparative SEC	No	Protein concentration	N.d.
Additional notes	–		

7.1.11 Crystallization of TC190 in complex with AB928

Amount of biomass	Equivalent of 450 mL of *Sf9* cells, infected at 2-3 x 10^6 cells/mL.		
Membrane preparation	Dounce homogenization 2x with hypotonic buffer, 3x with hypertonic buffer.		
Solubilization conditions	For 3 h with 0.75 % DDM and 0.15 % CHS. Final ligand concentration 25 µM.		
Resin incubation	250 µL beads, incubated with sample overnight.		
Resin wash conditions	40 CV pre-WB, 30 CV of WB1 (+ 50 µM ligand), 20 CV of WB2 (+ 50 µM ligand).		
Elution	6 CV of EB (+ 25 µM ligand) added in 3 steps, with 10 min incubation each.		
Salt Exchange	No	Additional ligand added	No
Preparative SEC	No	Protein concentration	N.d.
Additional notes	–		

7.1.12 Crystallization of TC190 in complex with PA51

Amount of biomass	Equivalent of 450 mL of *Sf9* cells, infected at 2-3 x 10^6 cells/mL.		
Membrane preparation	Dounce homogenization 2x with hypotonic buffer, 3x with hypertonic buffer.		
Solubilization conditions	For 3 h with 0.75 % DDM and 0.15 % CHS. Final ligand concentration 25 µM.		
Resin incubation	250 µL beads, incubated with sample overnight.		
Resin wash conditions	40 CV pre-WB, 30 CV of WB1 (+ 10 µM ligand), 20 CV of WB2 (+ 25 µM ligand).		
Elution	6 CV of EB (+ 25 µM ligand) added in 3 steps, with 10 min incubation each.		
Salt Exchange	No	Additional ligand added	No
Preparative SEC	No	Protein concentration	N.d.
Additional notes	–		

7.1.13 Crystallization of TC190 in complex with PSB-09120 (I)

Amount of biomass	Equivalent of 450 mL of *Sf9* cells, infected at 2-3 x 10^6 cells/mL.
Membrane preparation	Dounce homogenization 2x with hypotonic buffer, 3x with hypertonic buffer.
Solubilization conditions	For 3 h with 0.75 % DDM and 0.15 % CHS. Final ligand concentration 12.5 µM.
Resin incubation	250 µL beads, incubated with sample overnight.

Resin wash conditions	40 CV pre-WB, 30 CV of WB1 (+ 25 µM ligand), 20 CV of WB2 (+ 25 µM ligand).		
Elution	6 CV of EB (+ 25 µM ligand) added in 3 steps, with 10 min incubation each.		
Salt Exchange	No	Additional ligand added	No
Preparative SEC	No	Protein concentration	N.d.
Additional notes	–		

7.1.14 Crystallization of TC190 in complex with PSB-09120 (II)

Amount of biomass	Equivalent of 450 mL of *Sf*9 cells, infected at 2-3 x 10^6 cells/mL.		
Membrane preparation	Dounce homogenization 2x with hypotonic buffer, 3x with hypertonic buffer.		
Solubilization conditions	For 3 h with 0.75 % DDM and 0.15 % CHS. Final ligand concentration 25 µM.		
Resin incubation	250 µL beads, incubated with sample overnight.		
Resin wash conditions	40 CV pre-WB, 30 CV of WB1 (+ 25 µM ligand), 20 CV of WB2 (+ 25 µM ligand).		
Elution	6 CV of EB (+ 25 µM ligand) added in 3 steps, with 10 min incubation each.		
Salt Exchange	No	Additional ligand added	No
Preparative SEC	No	Protein concentration	N.d.
Additional notes	–		

7.1.15 Crystallization of TC196 with PSB-21500 (I)

Amount of biomass	Equivalent of 450 mL of *Sf*9 cells, infected at 2-3 x 10^6 cells/mL.		
Membrane preparation	Dounce homogenization 2x with hypotonic buffer, 3x with hypertonic buffer.		
Solubilization conditions	For 3 h with 0.75 % DDM and 0.15 % CHS. Final ligand concentration 1 µM.		
Resin incubation	250 µL beads, incubated with sample overnight.		
Resin wash conditions	40 CV pre-WB, 30 CV of WB1 (1 µM ligand), 20 CV of WB2 (1 µM ligand).		
Elution	6 CV of EB (1 µM ligand) added in 3 steps, with 10 min incubation each.		
Salt Exchange	No	Additional ligand added	No
Preparative SEC	No	Protein concentration	N.d.
Additional notes	–		

7.1.16 Crystallization of TC196 with PSB-21500 (II)

Amount of biomass	Equivalent of 900 mL of *Sf*9 cells, infected at 2-3 x 10^6 cells/mL.		
Membrane preparation	Dounce homogenization 2x with hypotonic buffer, 3x with hypertonic buffer.		
Solubilization conditions	20 µM of ligand pre-incubated with membrane at RT for 2 h. Solubilization for 3 h with 0.75 % DDM and 0.15 % CHS. Final ligand concentration 10 µM.		
Resin incubation	250 µL beads, incubated with sample overnight.		
Resin wash conditions	40 CV pre-WB, 30 CV of WB1 (+ 2 µM ligand), 20 CV of WB2 (+ 2 µM ligand).		
Elution	6 CV of EB (+ 2 µM ligand) added in 3 steps, with 10 min incubation each.		
Salt Exchange	To 50 mM HEPES pH 7.5, 500 mM NaCl, 0.025 % DDM, 0.005 % CHS		
Preparative SEC	No	Protein concentration	N.d.
Additional ligand added	No	Additional notes	–

7.1.17 Purification of TC190 in complex with PSB-21500 (LXP I)

Amount of biomass	Equivalent of 2 L of *Tni* cells, infected at 4 x 10^6 cells/mL.
Membrane preparation	Dounce homogenization with hypotonic buffer (1h incubation, stirring), afterwards topped up with 2-fold hypertonic buffer (1h incubation, stirring).
Solubilization conditions	Membrane concentration during solubilization 100 mg/mL. Solubilization for 1.5 h with 1 % DDM and 0.1 % CHS. Final ligand concentration 0.5 µM.
Solubilization buffer composition	10 mM HEPES pH 7.5, 300 mM NaCl, 20 mM KCl, 10 mM MgCl2, 10 mM CaCl2, 5% glycerol, 2 mg/mL iodoacetamide, 10 µg/mL DNAse, 10 mM imidazole pH 7.5, 0.5 µM PSB-21500, 1% DDM, 0.1 % CHS
Resin incubation	8 mL beads, incubated with sample for 1.5 h.
Resin wash conditions	On FPLC, 15 CV of WB1 (no ligand), no WB2 due to premature elution.
Elution	On FPLC, 1.3 CV of EB, no incubation time.
WB1 composition	20 mM HEPES pH 7.5, 300 mM NaCl, 0.02 % DDM, 0.002 % CHS, 20 mM imidazole
EB composition	20 mM HEPES pH 7.5, 300 mM NaCl, 0.02 % DDM, 0.002 % CHS, 125 mM imidazole
Salt Exchange	To 20 mM HEPES pH 7.5, 300 mM NaCl, 0.02 % DDM, 0.002 % CHS, 10 % glycerol

Preparative SEC	Yes	Protein concentration (mg/L)	25
Additional ligand added	20 µM	Additional notes	–

7.1.18 Purification of TC190 in complex with PSB-21500 (LXP II)

Amount of biomass	Equivalent of 2 L of *Tni* cells, infected at 4 x 10^6 cells/mL.
Membrane preparation	Dounce homogenization with hypotonic buffer (1h incubation, stirring), afterwards topped up with 2-fold hypertonic buffer (1h incubation, stirring).
Solubilization conditions	Membrane concentration during solubilization 100 mg/mL. Solubilization for 1.5 h with 1 % DDM and 0.1 % CHS. Final ligand concentration 0.5 µM.
Solubilization buffer composition	20 mM HEPES pH 7.5, 800 mM NaCl, 10 % glycerol, 2 mg/mL iodoacetamide, 10 µg/mL DNAse, 10 mM imidazole pH 7.5, 1 µM PSB21500, 1% DDM, 0.1 % CHS
Resin incubation	7 mL beads, incubated with sample for 3 h.
Resin wash conditions	On FPLC, 10 CV of WB1 (no ligand), 10 CV of WB2 (no ligand),
Elution	On FPLC, 1 CV of EB, no incubation time.
WB1 composition	25 mM HEPES pH 7.5, 850 mM NaCl, 0.02 % DDM, 0.002 % CHS, 20 mM imidazole
WB2 composition	25 mM HEPES pH 7.5, 850 mM NaCl, 0.02 % DDM, 0.002 % CHS, 50 mM imidazole
EB composition	25 mM HEPES pH 7.5, 850 mM NaCl, 0.02 % DDM, 0.002 % CHS, 220 mM imidazole
Salt Exchange	To 20 mM HEPES pH 7.5, 300 mM NaCl, 0.02 % DDM, 0.002 % CHS, 10 % glycerol

Preparative SEC	Yes	Protein concentration (mg/L)	28
Additional ligand added	20 µM	Additional notes	–

7.1.19 Purification of TC196 in complex with PSB-21500 (LXP I)

Amount of biomass	Equivalent of 2 L of *Tni* cells, infected at 4 x 10^6 cells/mL.
Membrane preparation	Dounce homogenization 1x with hypotonic buffer, 2x with hypertonic buffer.
Solubilization conditions	For 3 h with 1 % DDM and 0.1 % CHS. Final ligand concentration 1 µM.
Resin incubation	1.5 mL beads, incubated with sample overnight.
Resin wash conditions	13 CV pre-WB, 27 CV of WB1 (no ligand), 20 CV of WB2 (no ligand).
Elution	3 CV of EB (no ligand) added in 3 steps, with 10 min incubation each.

Salt Exchange	No	Additional ligand added	20 µM
Preparative SEC	No	Protein concentration (mg/mL)	30
Additional notes	–		

7.1.20 Purification of TC196 in complex with PSB-21500 (LXP II)

Amount of biomass	Equivalent of 2 L of *Tni* cells, infected at 4 x 10^6 cells/mL.
Membrane preparation	Dounce homogenization with hypotonic buffer (1h incubation, stirring), afterwards topped up with 2-fold hypertonic buffer (1h incubation, stirring).
Solubilization conditions	Membrane concentration during solubilization 100 mg/mL. Solubilization for 1.5 h with 1 % DDM and 0.1 % CHS. Final ligand concentration 0.5 µM.
Solubilization buffer composition	20 mM HEPES pH 7.5, 800 mM NaCl, 10 % glycerol, 2 mg/mL iodoacetamide, 10 µg/mL DNAse, 10 mM imidazole pH 7.5, 1 µM PSB21500, 1% DDM, 0.1 % CHS
Resin incubation	6 mL beads, incubated with sample for 3 h.
Resin wash conditions	On FPLC, 5 CV of WB1 (no ligand), 10 CV of WB2 (no ligand),
Elution	On FPLC, 1.2 CV of EB, no incubation time.
WB1 composition	25 mM HEPES pH 7.5, 850 mM NaCl, 0.02 % DDM, 0.002 % CHS, 20 mM imidazole
WB2 composition	25 mM HEPES pH 7.5, 850 mM NaCl, 0.02 % DDM, 0.002 % CHS, 50 mM imidazole
EB composition	25 mM HEPES pH 7.5, 850 mM NaCl, 0.02 % DDM, 0.002 % CHS, 220 mM imidazole

Salt Exchange	No	Additional ligand added	20 µM
Preparative SEC	Yes	Protein concentration (mg/L)	28
Additional notes	–		

7.1.21 Crystallization of TC223 and TC226 in complex with PSB-21500 (I)

Amount of biomass	Equivalent of 2 L of *Sf9* cells each, infected at 2-3 x 10^6 cells/mL.
Membrane preparation	Dounce homogenization 2x with hypotonic buffer, 2x with hypertonic buffer.
Solubilization conditions	Membrane concentration during solubilization 100 mg/mL. Solubilization for 1.5 h with 1 % DDM and 0.2 % CHS. Final ligand concentration 5 µM.
Resin incubation	1.5 mL beads, incubated with sample for 2h.
Resin wash conditions	17 CV pre-WB, 17 CV of WB1 (+ 2 µM ligand), 17 CV of WB2 (+ 2 µM ligand).
Elution	3 CV of EB (+ 5 µM ligand) added in 3 steps, with 10 min incubation each.

Salt Exchange	To 25 mM HEPES pH 7.5, 800 mM NaCl, 0.015 % DDM, 0.003 % CHS, 10 % glycerol		
Preparative SEC	No	Protein concentration (mg/L)	9.7 (TC223) / 9.9 (TC226)
Additional ligand added	No	Additional notes	–

7.1.22 Crystallization of TC231 and TC233 in complex with PSB-21500

Amount of biomass	Equivalent of 2 L of *Sf9* cells each, infected at 2-3 x 10^6 cells/mL.
Membrane preparation	Dounce homogenization 2x with hypotonic buffer, 2x with hypertonic buffer.
Solubilization conditions	Membrane concentration during solubilization 100 mg/mL. Solubilization for 3 h with 1 % DDM and 0.2 % CHS. Final ligand concentration 5 µM.
Resin incubation	2 mL beads, incubated with sample overnight.
Resin wash conditions	10 CV pre-WB, 10 CV of WB1 (+ 2 µM ligand), 10 CV of WB2 (+ 2 µM ligand).
Elution	5 CV of EB (+ 5 µM ligand) added in 6 steps, with 10 min incubation each.

Salt Exchange	To 25 mM HEPES pH 7.5, 800 mM NaCl, 0.015 % DDM, 0.003 % CHS, 10 % glycerol		
Preparative SEC	No	Protein concentration (mg/L)	26 (TC231) / 24 (TC233)
Additional ligand added	+ 10 µM	Additional notes	–

7.1.23 Crystallization of TC224 and TC225 in complex with PSB-21500

Amount of biomass	Equivalent of 2 L of *Sf9* cells each, infected at 2-3 x 10^6 cells/mL.		
Membrane preparation	Dounce homogenization 2x with hypotonic buffer, 2x with hypertonic buffer.		
Solubilization conditions	Membrane concentration during solubilization 100 mg/mL. Solubilization for 3 h with 1 % DDM and 0.2 % CHS. Final ligand concentration 5 µM.		
Resin incubation	2 mL beads, incubated with sample overnight.		
Resin wash conditions	10 CV pre-WB, 10 CV of WB1 (+ 2 µM ligand), 10 CV of WB2 (+ 2 µM ligand).		
Elution	4 CV of EB (+ 5 µM ligand) added in 6 steps, with 10 min incubation each.		
Salt Exchange	To 25 mM HEPES pH 7.5, 800 mM NaCl, 0.015 % DDM, 0.003 % CHS, 10 % glycerol		
Preparative SEC	No	Protein concentration (mg/L)	19 (TC224) / 20 (TC225)
Additional ligand added	+ 10 µM	Additional notes	EB with 300 mM imidazole

7.1.24 Crystallization of TC228 and TC232 in complex with PSB-21500

Amount of biomass	Equivalent of 2 L of *Sf9* cells each, infected at 2-3 x 10^6 cells/mL.		
Membrane preparation	Dounce homogenization 2x with hypotonic buffer, 2x with hypertonic buffer.		
Solubilization conditions	Membrane concentration during solubilization 100 mg/mL. Solubilization for 3 h with 1 % DDM and 0.2 % CHS. Final ligand concentration 5 µM.		
Resin incubation	2 mL beads, incubated with sample overnight.		
Resin wash conditions	10 CV pre-WB, 10 CV of WB1 (+ 2 µM ligand), 10 CV of WB2 (+ 2 µM ligand).		
Elution	3 CV of EB (+ 5 µM ligand) added in 4 steps, with 10 min incubation each.		
Salt Exchange	To 25 mM HEPES pH 7.5, 800 mM NaCl, 0.015 % DDM, 0.003 % CHS, 10 % glycerol		
Preparative SEC	No	Protein concentration (mg/L)	N.d.
Additional ligand added	+ 10 µM	Additional notes	EB with 350 mM imidazole

7.1.25 Crystallization of TC227 and TC230 in complex with PSB-21500

Amount of biomass	Equivalent of 2 L of *Sf9* cells each, infected at 2-3 x 10^6 cells/mL.		
Membrane preparation	Dounce homogenization 2x with hypotonic buffer, 2x with hypertonic buffer.		
Solubilization conditions	Membrane concentration during solubilization 100 mg/mL. Solubilization for 3 h with 1 % DDM and 0.2 % CHS. Final ligand concentration 5 µM.		
Resin incubation	2 mL beads, incubated with sample overnight.		
Resin wash conditions	10 CV pre-WB, 10 CV of WB1 (+ 2 µM ligand), 18 CV of WB2 (+ 2 µM ligand).		
Elution	4 CV of EB (+ 5 µM ligand) added in 5 steps, with 10 min incubation each.		
Salt Exchange	To 25 mM HEPES pH 7.5, 800 mM NaCl, 0.015 % DDM, 0.003 % CHS, 10 % glycerol		
Preparative SEC	No	Protein concentration (mg/L)	31 (TC227) / 10 (TC230)
Additional ligand added	+ 10 µM	Additional notes	EB with 350 mM imidazole

7.1.26 Crystallization of TC223 (II) and TC229 in complex with PSB-21500

Amount of biomass	Equivalent of 2 L of *Sf9* cells each, infected at 2-3 x 10^6 cells/mL.		
Membrane preparation	Dounce homogenization 2x with hypotonic buffer, 2x with hypertonic buffer.		
Solubilization conditions	Membrane concentration during solubilization 100 mg/mL. Solubilization for 3 h with 1 % DDM and 0.2 % CHS. Final ligand concentration 5 µM.		
Resin incubation	2 mL beads, incubated with sample overnight.		
Resin wash conditions	10 CV pre-WB, 10 CV of WB1 (+ 2 µM ligand), 18 CV of WB2 (+ 2 µM ligand).		
Elution	3 CV of EB (+ 5 µM ligand) added in 4 steps, with 10 min incubation each.		
Salt Exchange	To 25 mM HEPES pH 7.5, 800 mM NaCl, 0.015 % DDM, 0.003 % CHS, 10 % glycerol		
Preparative SEC	No	Protein concentration (mg/L)	23 (TC223) / 29 (TC229)
Additional ligand added	+ 10 µM	Additional notes	-

7.1.27 Crystallization of TC226 in complex with PSB-21500 (II)

Amount of biomass	Equivalent of 2 L of *Sf9* cells, infected at 2-3 x 10^6 cells/mL.		
Membrane preparation	Dounce homogenization 2x with hypotonic buffer, 2x with hypertonic buffer.		
Solubilization conditions	Membrane concentration during solubilization 100 mg/mL. Solubilization for 3 h with 1 % DDM and 0.2 % CHS. Final ligand concentration 5 µM.		
Resin incubation	2 mL beads, incubated with sample overnight.		
Resin wash conditions	10 CV pre-WB, 10 CV of WB1 (+ 2 µM ligand), 18 CV of WB2 (+ 2 µM ligand).		
Elution	3 CV of EB (+ 5 µM ligand) added in 4 steps, with 10 min incubation each.		
Salt Exchange	To 25 mM HEPES pH 7.5, 800 mM NaCl, 0.025 % DDM, 0.005 % CHS, 10 % glycerol		
Preparative SEC	No	Protein concentration (mg/L)	24 (TC226)
Additional ligand added	+ 10 µM	Additional notes	-

7.2 Sequence information on all $A_{2B}AR$ constructs

7.2.1 Detailed list of the modifications on all $A_{2B}AR$ constructs

The following table will provide a comprehensive overview over all modifications that were applied to each of the presented $A_{2B}AR$ constructs. Importantly, all constructs from TC1 up to TC59 were evaluated as part of my master's thesis.[252]

Construct	Plasmid	Truncation		Mutations	BW numbers	Fusion partner	Junction site	Tags	
		N-term.	*C*-term.					*N*-term.	*C*-term.
TC1	pFastBac1	1	316-332	-	-	bRIL	5.69 to 6.22	HA-FLAG	10xHis-tag
TC15	pFastBac1	1	316-332	A_{2A}AR TM1	1.28-1.60	bRIL	5.69 to 6.22	HA-FLAG	10xHis-tag
TC25	pFastBac1	1	316-332	D53N	2.5	bRIL	5.69 to 6.22	HA-FLAG	10xHis-tag
TC26	pFastBac1	1	316-332	D53G	2.5	bRIL	5.69 to 6.22	HA-FLAG	10xHis-tag
TC27	pFastBac1	1	316-332	D53A	2.5	bRIL	5.69 to 6.22	HA-FLAG	10xHis-tag
TC29	pFastBac1	1	316-332	L88N	3.35	bRIL	5.69 to 6.22	HA-FLAG	10xHis-tag
TC30	pFastBac1	1	316-332	L96A	3.43	bRIL	5.69 to 6.22	HA-FLAG	10xHis-tag
TC33	pFastBac1	1	316-332	N286D	7.49	bRIL	5.69 to 6.22	HA-FLAG	10xHis-tag
TC34	pFastBac1	1	316-332	S92A	3.39	bRIL	5.69 to 6.22	HA-FLAG	10xHis-tag
TC35	pFastBac1	1	316-332	S92R	3.39	bRIL	5.69 to 6.22	HA-FLAG	10xHis-tag
TC59	pFastBac1	1	316-332	C29I, C210R	1.54, 5.66	bRIL	5.69 to 6.22	HA-FLAG	10xHis-tag
TC62	GP64-pFastBac1	1	316-332	A_{2A}AR TM1	1.28-1.60	bRIL	5.69 to 6.22	HA-FLAG	10x His-tag
TC63	GP64-pFastBac1	1	316-332	-	-	bRIL	5.69 to 6.22	HA-FLAG	10x His-tag
TC69	pFastBac1	2	316-332	-	-	T4L	N-terminal	HA-FLAG	10x His-tag
TC73	GP64-pFastBac1	1	316-332	A_{2A}AR TM1	1.28-1.60	bRIL	5.69 to 6.22	-	10xHis-tag
TC74	pFastBac1	1	316-332	A_{2A}AR TM1	1.27-1.60	bRIL	5.69 to 6.22	-	10xHis-tag
TC78	GP64-pFastBac1	1	316-332	L3P	1.28	bRIL	5.69 to 6.22	HA-FLAG	10xHis-tag
TC79	pFastBac1	1	316-332	E4I	1.29	bRIL	5.69 to 6.22	HA-FLAG	10xHis-tag
TC80	pFastBac1	1	316-332	T5M	1.3	bRIL	5.69 to 6.22	HA-FLAG	10xHis-tag

Construct	Plasmid	Truncation		Mutations	BW numbers	Fusion partner	Junction site	Tags	
		N-term.	*C*-term.					*N*-term.	*C*-term.
TC81	pFastBac1	1	316-332	Q6G	1.31	bRIL	5.69 to 6.22	HA-FLAG	10xHis-tag
TC82	pFastBac1	1	316-332	D7S	1.32	bRIL	5.69 to 6.22	HA-FLAG	10xHis-tag
TC83	pFastBac1	1	316-332	A8S	1.33	bRIL	5.69 to 6.22	HA-FLAG	10xHis-tag
TC84	pFastBac1	1	316-332	L9V	1.34	bRIL	5.69 to 6.22	HA-FLAG	10xHis-tag
TC85	pFastBac1	1	316-332	V11I	1.35	bRIL	5.69 to 6.22	HA-FLAG	10xHis-tag
TC86	pFastBac1	1	316-332	A12T	1.36	bRIL	5.69 to 6.22	HA-FLAG	10xHis-tag
TC87	pFastBac1	1	316-332	L13V	1.37	bRIL	5.69 to 6.22	HA-FLAG	10xHis-tag
TC88	pFastBac1	1	316-332	V16A	1.41	bRIL	5.69 to 6.22	HA-FLAG	10xHis-tag
TC89	pFastBac1	1	316-332	A19V	1.44	bRIL	5.69 to 6.22	HA-FLAG	10xHis-tag
TC90	GP64-pFastBac1	1	316-332	S21A	1.46	bRIL	5.69 to 6.22	HA-FLAG	10xHis-tag
TC91	GP64-pFastBac1	1	316-332	V22I	1.47	bRIL	5.69 to 6.22	HA-FLAG	10xHis-tag
TC92	GP64-pFastBac1	1	316-332	A23L	1.48	bRIL	5.69 to 6.22	HA-FLAG	10xHis-tag
TC93	pFastBac1	1	316-332	A30W	1.55	bRIL	5.69 to 6.22	HA-FLAG	10xHis-tag
TC94	pFastBac1	1	316-332	G33W	1.58	bRIL	5.69 to 6.22	HA-FLAG	10xHis-tag
TC95	pFastBac1	1	316-332	T34L	1.59	bRIL	5.69 to 6.22	HA-FLAG	10xHis-tag
TC96	pFastBac1	1	316-332	A35N	1.6	bRIL	5.69 to 6.22	HA-FLAG	10xHis-tag
TC97	pFastBac1	1	316-332	N36S	ICL1	bRIL	5.69 to 6.22	HA-FLAG	10xHis-tag
TC103	pFastBac1	1	316-332	S92K	3.39	bRIL	5.69 to 6.22	HA-FLAG	10xHis-tag
TC104	pFastBac1	1	316-332	W247A	6.48	bRIL	5.69 to 6.22	HA-FLAG	10xHis-tag

Construct	Plasmid	Truncation		Mutations	BW numbers	Fusion partner	Junction site	Tags	
		N-term.	*C*-term.					*N*-term.	*C*-term.
TC108	GP64-pFastBac1	1	316-332	S92K	3.39	bRIL	5.69 to 6.22	HA-FLAG	10x His-tag
TC109	GP64-pFastBac1	1	316-332	A232E	6.33	bRIL	5.69 to 6.22	HA-FLAG	10x His-tag
TC110	GP64-pFastBac1	1	316-332	S92K, A232E	3.39, 6.33	bRIL	5.69 to 6.22	HA-FLAG	10x His-tag
TC111	GP64-pFastBac1	1	316-332	S92K, A232E, A_{2A}AR TM1	3.39, 6.33, 1.28-1.60	bRIL	5.69 to 6.22	-	10x His-tag
TC117	GP64-pFastBac1	1	316-332	S92K, A_{2A}AR TM1	3.39, 1.28-1.60	bRIL	5.69 to 6.22	-	10x His-tag
TC119	GP64-pFastBac1	1	316-332	A232D	6.33	bRIL	5.69 to 6.22	HA-FLAG	10x His-tag
TC120	GP64-pFastBac1	1	316-332	S92K, A232D	3.39, 6.33	bRIL	5.69 to 6.22	HA-FLAG	10x His-tag
TC121	GP64-pFastBac1	1	316-332	C29I, S92K	1.54, 3.39	bRIL	5.69 to 6.22	HA-FLAG	10x His-tag
TC122	GP64-pFastBac1	1	316-332	S92K, C210R	3.39, 5.66	bRIL	5.69 to 6.22	HA-FLAG	10x His-tag
TC132	GP64-pFastBac1	1	316-332	S92K	3.39	T4L	5.69 to 6.22	HA-FLAG	10xHis-tag
TC133	GP64-pFastBac1	4	316-332	S92K	3.39	T4L	N-terminal	HA-FLAG	10xHis-tag
TC134	GP64-pFastBac1	1	316-332	S92K, N153Q, N163Q	3.39, ECL2	bRIL	5.69 to 6.22	-	10x His-tag
TC135	GP64-pFastBac1	1	316-332	S92K, N153Q, N163Q	3.39, ECL2	bRIL	5.69 to 6.22	FLAG	10x His-tag
TC137	GP64-pFastBac1	1	316-332	C29I, A35N, S92K, N153Q, N163Q	1.54, 1.60, 3.39, ECL2	bRIL	5.69 to 6.22	FLAG	10x His-tag
TC138	GP64-pFastBac1	1	316-332	A19V, C29I, G33W, A35N, S92K, N153Q, N163Q	1.44, 1.54, 1.58, 1.60, 3.39, ECL2	bRIL	5.69 to 6.22	HA-FLAG	10x His-tag

Construct	Plasmid	Truncation		Mutations	BW numbers	Fusion partner	Junction site	Tags	
		N-term.	*C*-term.					*N*-term.	*C*-term.
TC140	GP64-pFastBac1	1	316-332	S92K, N153Q, N163Q	3.39, ECL2	bRIL	5.67 to 6.22	HA-FLAG	10x His-tag
TC141	GP64-pFastBac1	1	316-332	S92K, N153Q, N163Q	3.39, ECL2	bRIL	5.66 to 6.22	HA-FLAG	10x His-tag
TC142	GP64-pFastBac1	1	316-332	S92K, N153Q, N163Q	3.39, ECL2	bRIL	5.65 to 6.22	HA-FLAG	10x His-tag
TC143	GP64-pFastBac1	1	316-332	S92K, N153Q, N163Q	3.39, ECL2	bRIL	5.64 to 6.22	HA-FLAG	10x His-tag
TC144	GP64-pFastBac1	1	316-332	S92K, N153Q, N163Q	3.39, ECL2	bRIL	5.70 to 6.22	HA-FLAG	10x His-tag
TC145	GP64-pFastBac1	1	316-332	S92K, N153Q, N163Q	3.39, ECL2	bRIL	5.71 to 6.22	HA-FLAG	10x His-tag
TC146	GP64-pFastBac1	1	316-332	S92K, N153Q, N163Q	3.39, ECL2	bRIL	5.72 to 6.22	HA-FLAG	10x His-tag
TC147	GP64-pFastBac1	1	316-332	S92K, N153Q, N163Q	3.39, ECL2	bRIL	5.73 to 6.22	HA-FLAG	10x His-tag
TC148	GP64-pFastBac1	1	316-332	S92K, N153Q, N163Q	3.39, ECL2	bRIL	5.69 to 6.23	HA-FLAG	10x His-tag
TC149	GP64-pFastBac1	1	316-332	S92K, N153Q, N163Q	3.39, ECL2	bRIL	5.69 to 6.24	HA-FLAG	10x His-tag
TC150	GP64-pFastBac1	1	316-332	S92K, N153Q, N163Q	3.39, ECL2	bRIL	5.69 to 6.25	HA-FLAG	10x His-tag
TC151	GP64-pFastBac1	1	316-332	S92K, N153Q, N163Q	3.39, ECL2	bRIL	5.69 to 6.26	HA-FLAG	10x His-tag
TC152	GP64-pFastBac1	1	316-332	S92K, N153Q, N163Q	3.39, ECL2	bRIL	5.69 to 6.27	HA-FLAG	10x His-tag
TC153	GP64-pFastBac1	1	316-332	C29I, S92K, N153Q, N163Q, C210R	1.54, 3.39, ECL2, 5.66	bRIL	5.69 to 6.22	HA-FLAG	10xHis-tag
TC154	GP64-pFastBac1	1	316-332	S92K, N153Q, N163Q	3.39, ECL2	bRIL	5.69 to 6.22	HA-FLAG	10xHis-tag

Construct	Plasmid	Truncation		Mutations	BW numbers	Fusion partner	Junction site	Tags	
		N-term.	*C*-term.					*N*-term.	*C*-term.
TC161	GP64-pFastBac1	1	316-332	A19V, C29I, G33W, S92K, N153Q, N163Q	1.44, 1.54, 1.58, 3.39, ECL2	bRIL	5.69 to 6.22	HA-FLAG	10x His-tag
TC162	GP64-pFastBac1	1	316-332	A19V, C29I, S92K, N153Q, N163Q	1.44, 1.54, 3.39, ECL2	bRIL	5.69 to 6.22	HA-FLAG	10x His-tag
TC163	GP64-pFastBac1	1	316-332	C29I, G33W, S92K, N153Q, N163Q	1.54, 1.58, 3.39, ECL2	bRIL	5.69 to 6.22	HA-FLAG	10x His-tag
TC164	GP64-pFastBac1	1	316-332	A19V, G33W, A35N, S92K, N153Q, N163Q	1.44, 1.58, 1.60, 3.39, ECL2	bRIL	5.69 to 6.22	HA-FLAG	10x His-tag
TC168	GP64-pFastBac1	1	316-332	A19V, C29I, G33W, A35N, S92K, N153Q, N163Q	1.44, 1.54, 1.58, 1.60, 3.39, ECL2	bRIL	5.69 to 6.22	FLAG	10x His-tag
TC169	GP64-pFastBac1	1	316-332	A19V, C29I, G33W, A35N, S92K, N153Q, N163Q	1.44, 1.54, 1.58, 1.60, 3.39, ECL2	bRIL	5.69 to 6.22	HA-NNST-FLAG	10x His-tag
TC170	GP64-pFastBac1	1	316-332	A19V, C29I, G33W, A35N, S92K, N153Q, N163Q	1.44, 1.54, 1.58, 1.60, 3.39, ECL2	bRIL	5.69 to 6.22	HA-NNST-HA-FLAG	10x His-tag
TC171	GP64-pFastBac1	1	316-332	A19V, C29I, G33W, A35N, S92K, N153Q, N163Q	1.44, 1.54, 1.58, 1.60, 3.39, ECL2	bRIL	5.69 to 6.22	NNST-HA-FLAG	10x His-tag
TC190	GP64-pFastBac1	1	316-332	A19V, C29I, G33W, A35N, S92K, N153Q, N163Q	1.44, 1.54, 1.58, 1.60, 3.39, ECL2	bRIL	5.69 to 6.22	HA-GSGS-FLAG	10x His-tag
TC192	GP64-pFastBac1	1	316-332	S92K	3.39	bRIL	5.69 to 6.22	HA-GSGS-FLAG	10x His-tag
TC196	GP64-pFastBac1	1	316-332	A19V, C29I, G33W, A35N, S92K, N153Q, N163Q, A232L	1.44, 1.54, 1.58, 1.60, 3.39, ECL2, 6.33	bRIL	5.69 to 6.22	HA-GSGS-FLAG	10x His-tag
TC197	GP64-pFastBac1	1	316-332	A19V, C29I, G33W, A35N, S92K, N153Q, N163Q, A232L, C311A	1.44, 1.54, 1.58, 1.60, 3.39, ECL2, 6.33, 8.64	bRIL	5.69 to 6.22	HA-GSGS-FLAG	10x His-tag
TC198	GP64-pFastBac1	1	316-332	S92K, N153Q, N163Q, A232L, C311A	3.39, ECL2, 6.34, 8.64	bRIL	5.69 to 6.22	HA-GSGS-FLAG	10x His-tag
TC199	GP64-pFastBac1	1	310-332	A19V, C29I, G33W, A35N, S92K, N153Q, N163Q, A232L	1.44, 1.54, 1.58, 1.60, 3.39, ECL2, 6.33	bRIL	5.69 to 6.22	HA-GSGS-FLAG	10x His-tag
TC200	GP64-pFastBac1	1	310-332	S92K, N153Q, N163Q, A232L	3.39, ECL2, 6.34	bRIL	5.69 to 6.22	HA-GSGS-FLAG	10x His-tag

Construct	Plasmid	Truncation		Mutations	BW numbers	Fusion partner	Junction site	Tags	
		N-term.	*C*-term.					*N*-term.	*C*-term.
TC223	GP64-pFastBac1	1	316-332	A19V, C29I, G33W, A35N, S92K, N153Q, N163Q, Δ W158-N163	1.44, 1.54, 1.58, 1.60, 3.39, ECL2	bRIL	5.69 to 6.22	HA-GSGS-FLAG	10x His-tag
TC224	GP64-pFastBac1	1	316-332	A19V, C29I, G33W, A35N, S92K, N153Q, N163Q, Δ P157-E164	1.44, 1.54, 1.58, 1.60, 3.39, ECL2	bRIL	5.69 to 6.22	HA-GSGS-FLAG	10x His-tag
TC225	GP64-pFastBac1	1	316-332	A19V, C29I, G33W, A35N, S92K, N153Q, N163Q, Δ W156-S165	1.44, 1.54, 1.58, 1.60, 3.39, ECL2	bRIL	5.69 to 6.22	HA-GSGS-FLAG	10x His-tag
TC226	GP64-pFastBac1	1	316-332	A19V, C29I, G33W, A35N, S92K, N153Q, N163Q	1.44, 1.54, 1.58, 1.60, 3.39, ECL2	PGS	5.69 to 6.25	HA-GSGS-FLAG	10x His-tag
TC227	GP64-pFastBac1	1	316-332	A19V, C29I, G33W, A35N, S92K, N153Q, N163Q	1.44, 1.54, 1.58, 1.60, 3.39, ECL2	OB1	5.69 to 6.22	HA-GSGS-FLAG	10x His-tag
TC228	GP64-pFastBac1	1	316-332	A19V, C29I, G33W, A35N, S92K, N153Q, N163Q	1.44, 1.54, 1.58, 1.60, 3.39, ECL2	bRIL	5.69 to 6.21	HA-GSGS-FLAG	10x His-tag
TC229	GP64-pFastBac1	1	316-332	A19V, C29I, G33W, A35N, S92K, N153Q, N163Q	1.44, 1.54, 1.58, 1.60, 3.39, ECL2	Flavodoxin	5.68 to 6.27	HA-GSGS-FLAG	10x His-tag
TC230	GP64-pFastBac1	1	316-332	A19V, C29I, G33W, A35N, S92K, N153Q, N163Q	1.44, 1.54, 1.58, 1.60, 3.39, ECL2	T4L	5.68 to 6.24	HA-GSGS-FLAG	10x His-tag
TC231	GP64-pFastBac1	1	316-332	A19V, C29I, G33W, A35N, S92K, N153Q, N163Q	1.44, 1.54, 1.58, 1.60, 3.39, ECL2	LXP-FP1	5.70 to 6.25	HA-GSGS-FLAG	10x His-tag
TC232	GP64-pFastBac1	1	316-332	A19V, C29I, G33W, A35N, S92K, N153Q, N163Q	1.44, 1.54, 1.58, 1.60, 3.39, ECL2	LXP-FP1	5.73 to 6.25	HA-GSGS-FLAG	10x His-tag
TC233	GP64-pFastBac1	1	316-332	A19V, C29I, G33W, A35N, S92K, N153Q, N163Q	1.44, 1.54, 1.58, 1.60, 3.39, ECL2	LXP-FP2	5.69 to 6.24	HA-GSGS-FLAG	10x His-tag

7.2.2 Amino acid sequences of the human wt $A_{2B}AR$

MLLETQDALYVALELVIAALSVAGNVLVCAAVGTANTLQTPTNYFLVSLAAADVAVGLFAI
PFAITISLGFCTDFYGCLFLACFVLVLTQSSIFSLLAVAVDRYLAICVPLRYKSLVTGTRARGV
IAVLWVLAFGIGLTPFLGWNSKDSATNNCTEPWDGTTNESCCLVKCLFENVVPMSYMVYF
NFFGCVLPPLLIMLVIYIKIFLVACRQLQRTELMDHSRTTLQREIHAAKSLAMIVGIFALCW
LPVHAVNCVTLFQPAQGKNKPKWAMNMAILLSHANSVVNPIVYAYRNRDFRYTFHKIISR
YLLCQADVKSGNGQAGVQPALGVGL

7.2.3 Amino acid sequences of the employed fusion partners

7.2.3.1 PGS

GIDCSFWNESYLTGSRDERKKSLLSKFGMDEGVTFMFIGRFDRGQKGVDVLLKAIEILSSKK
EFQEMRFIIIGKGDPELEGWARSLEEKHGNVKVITEMLSREFVRELYGSVDFVIIPSYFEPFG
LVALEAMCLGAIPIASAVGGLRDIITNETGILVKAGDPGELANAILKALELSRSDLSKFRENC
KKRAMSFS

7.2.3.2 OB1

ADLEDRWRTLEDNLRVIERAANAAEVREALTRMRAAAEDAQRATPPALEDRSPASPEME
DFRHGFDILVGQIDDALRLADEGRVAEAQAAAEELRTTRNAYIQKYL

7.2.3.3 bRIL

ADLEDNWETLNDNLKVIEKADNAAQVKDALTKMRAAALDAQKATPPKLEDKSPDSPEM
KDFRHGFDILVGQIDDALKLANEGKVKEAQAAAEQLKTTRNAYIQKYL

7.2.3.4 Flavodoxin

AKALIVYGSTTGNTEYTAETIARELADAGYEVDSRDAASVEAGGLFEGFDLVLLGCSTWGD
DSIELQDDFIPLFDSLEETGAQGRKVACFGCGDSSHEYFCGAVDAIEEKLKNLGAEIVQDGL
RIDGDPRAARDDIVGWAHDVRGAI

7.2.3.5 T4L

NIFEMLRIDEGLRLKIYKDTEGYYTIGIGHLLTKSPSLNAAKSELDKAIGRNTNGVITKDEAE
KLFNQDVDAAVRGILRNAKLKPVYDSLDAVRRAALINMVFQMGETGVAGFTNSLRMLQQ
KRWDEAAVNLAKSRWYNQTPNRAKRVITTFRTGTWDAY

7.2.3.6 LXP-FP1

Undisclosed.

7.2.3.7 LXP-FP2

Undisclosed.

Danksagung

Über mehr als fünf Jahre hinweg hat die strukturbiologische Arbeit an dem Adenosin-A_{2B}-Rezeptor meinen Alltag geprägt. Für dieses überaus spannende und abwechslungsreiche Projekt, sowie die hervorragende Betreuung während dieser tollen fünf Jahre möchte ich mich herzlich bei Prof. Dr. Christa E. Müller bedanken. Sie hat mich, und dieses besondere Projekt, trotz so mancher Rückschläge, ausnahmslos mit großem Enthusiasmus unterstützt und gefördert. Ihre tiefe Unterstützung umfasste ebenfalls die Ermöglichung meines sechsmonatigen Forschungsaufenthalts in der Schweiz, für den ich überaus dankbar bin.

In diesem Hinblick gilt mein Dank ebenso dem Biotechnologie-Unternehmen leadXpro und insbesondere Dr. Michael Hennig. Vielen Dank für die herzliche Einladung zu diesem Forschungsaufenthalt, während dem ich so viele wertvolle neue Einblicke in die strukturbiologische Arbeit, sowie in das Arbeiten in der Industrie gewinnen durfte. Des Weiteren hat leadXpro das Projekt auch über meinen Aufenthalt hinaus durch Messzeit an der Swiss Light Source sowie der Bereitstellung von Materialien unterstützt, wofür ich mich ebenfalls herzlich bedanke. Für die fachliche Unterstützung möchte ich mich allen voran bei Dr. Robert K. Y. Cheng und Dr. Matilde Trabuco bedanken, die sich während meines Aufenthaltes täglich meinen Fragen und Problemen gestellt haben. Ebenso möchte ich mich bei Dr. Robert K. Y. Cheng und allen weiteren Beteiligten für die Vermessung der Kristalle, die zu Auflösung der 4.0 Å Kristallstruktur geführt haben, bedanken.

Finanziell wurde mein Forschungsaufenthalt von der Bonn International Graduate School of Drug Sciences unterstützt. Dafür danke ich insbesondere dem Vorstand der BIGS DrugS und Dr. Amelie Fiene.

Bei Prof. Dr. Finn Hansen möchte ich mich ausdrücklich für sein Mitwirken in der Prüfungskommission und die Erstellung des Zweitgutachtens zu dieser Arbeit bedanken. Mein herzlicher Dank gilt ebenso Prof. Dr. Martin Baunach, für die Übernahme des Vorsitzes der Kommission, und PD Dr. Marianne Engeser für das Mitwirken als weiteres Mitglied der Kommission.

Im Laufe dieses Projektes wurde eine Vielzahl von Liganden für die Stabilisierung des Adenosin-A_{2B}-Rezeptors eingesetzt, die mir Dank der Arbeit von vielen talentierten Chemikern zur Verfügung standen. Für die Entwicklung und Synthese dieser Liganden möchte ich im besonderen Maße Dr. Ahmed Temirak und Dr. Jörg Hockemeyer danken, sowie allen weiteren Kollegen die an der Bereitstellung der verwendeten Liganden mitgewirkt haben.

Mein weiterer Dank gilt Prof. Dr. Norbert Sträter und Dr. Renato H. Weiße von der Universität Leipzig. Sie haben am Deutschen Elektronen-Synchroton bereitwillig jeden noch so kleinen Kristall vermessen, die aufgelöste Kristallstruktur verfeinert, sowie hilfreiche Unterstützung bei der Dateninterpretation geleistet.

Für die hervorragende Organisation im Labor möchte ich herzlich PD Dr. Anke Schiedel, Dr. Dominik Thimm, Katharina Sylvester, Christiane Bous und Christin Vielmuth danken. Euer Mitwirken unter anderem in Form von Bestellungen, praktischen Tipps und der Organisation der Substanzbibliothek war ein wichtiger Bestandteil der reibungslosen Arbeit im Labor. Vielen Dank dafür!

Neben dem spannenden Projekt war auch die großartige Arbeitsatmosphäre ein ausschlaggebender Aspekt, der die letzten fünf Jahre für mich zu etwas Besonderem gemacht haben.

Dafür gilt mein allergrößter Dank allen voran Dr. Tobias Claff und Dr. Jonathan G. Schlegel, mit denen ich alle Höhen und Tiefen teilen durfte, und die mich immer mit ihrer praktischen, theoretischen und moralischen Hilfestellung unterstützt haben, im fachlichen sowie privaten Hinblick. Eure Freundschaft möchte ich nicht mehr missen und ich hoffe, dass wir uns auch in Zukunft nicht aus den Augen verlieren.

Ebenso herzlich möchte ich mich bei Jessica Nagel und Andhika B. Mahardhika für die schöne gemeinsame Zeit bedanken, insbesondere während der letzten Monate meiner praktischen Arbeit. Ohne Eure tatkräftige Unterstützung und Euer offenes Ohr hätte ich diese intensive Zeit sicherlich nicht gemeistert.

Weitere (ehemalige) Doktoranden bei denen ich mich für die vielen schönen, gemeinsamen Stunden im Labor - und außerhalb - bedanken möchte sind Dr. Georg W. Rolshoven, Ghazl Al Hamwi, Helay Baburi, Dr. Jan H. Voß, Dr. Lukas L. Wendt, Dr. Martin Mangold, Dr. Robin S. Gedschold, Salahuddin Mirza und Sana R. Mulani.

Mein letzter Dank gilt meinen Freunden und meiner Familie, die mir in den letzten Jahren stets großes Verständnis und Unterstützung entgegengebracht haben. Besonders hervorheben möchte ich dabei meine Eltern, die es mir ermöglicht haben, diese beruflichen Laufbahn einzuschlagen, ohne meine Entscheidungen je infrage zu stellen. Für Eure bedingungslose Unterstützung, Euren klugen Rat und Euren Glauben an mich werde ich Euch immer dankbar sein.